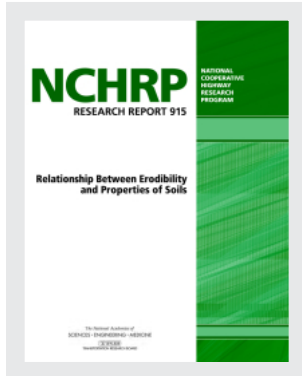


This PDF is available at <http://nap.edu/25470>

SHARE



## Relationship Between Erodibility and Properties of Soils (2019)

### DETAILS

328 pages | 8.5 x 11 | PAPERBACK

ISBN 978-0-309-49354-3 | DOI 10.17226/25470

GET THIS BOOK

FIND RELATED TITLES

### CONTRIBUTORS

Jean-Louis Briaud, Iman Shafii, Hamn-Ching Chen, and Zenon Medina-Cetina; National Cooperative Highway Research Program; Transportation Research Board; National Academies of Sciences, Engineering, and Medicine

### SUGGESTED CITATION

National Academies of Sciences, Engineering, and Medicine 2019. *Relationship Between Erodibility and Properties of Soils*. Washington, DC: The National Academies Press. <https://doi.org/10.17226/25470>.

Visit the National Academies Press at [NAP.edu](#) and login or register to get:

- Access to free PDF downloads of thousands of scientific reports
- 10% off the price of print titles
- Email or social media notifications of new titles related to your interests
- Special offers and discounts



Distribution, posting, or copying of this PDF is strictly prohibited without written permission of the National Academies Press.  
[\(Request Permission\)](#) Unless otherwise indicated, all materials in this PDF are copyrighted by the National Academy of Sciences.

Copyright © National Academy of Sciences. All rights reserved.

NATIONAL COOPERATIVE HIGHWAY RESEARCH PROGRAM

NCHRP RESEARCH REPORT 915

**Relationship Between Erodibility  
and Properties of Soils**

J.-L. Briaud

I. Shafii

H.-C. Chen

Z. Medina-Cetina

TEXAS A&M TRANSPORTATION INSTITUTE

College Station, TX

*Subscriber Categories*

Bridges and Other Structures • Geotechnology

---

Research sponsored by the American Association of State Highway and Transportation Officials  
in cooperation with the Federal Highway Administration

---

The National Academies of  
SCIENCES • ENGINEERING • MEDICINE



2019

## NATIONAL COOPERATIVE HIGHWAY RESEARCH PROGRAM

Systematic, well-designed, and implementable research is the most effective way to solve many problems facing state departments of transportation (DOTs) administrators and engineers. Often, highway problems are of local or regional interest and can best be studied by state DOTs individually or in cooperation with their state universities and others. However, the accelerating growth of highway transportation results in increasingly complex problems of wide interest to highway authorities. These problems are best studied through a coordinated program of cooperative research.

Recognizing this need, the leadership of the American Association of State Highway and Transportation Officials (AASHTO) in 1962 initiated an objective national highway research program using modern scientific techniques—the National Cooperative Highway Research Program (NCHRP). NCHRP is supported on a continuing basis by funds from participating member states of AASHTO and receives the full cooperation and support of the Federal Highway Administration, United States Department of Transportation.

The Transportation Research Board (TRB) of the National Academies of Sciences, Engineering, and Medicine was requested by AASHTO to administer the research program because of TRB's recognized objectivity and understanding of modern research practices. TRB is uniquely suited for this purpose for many reasons: TRB maintains an extensive committee structure from which authorities on any highway transportation subject may be drawn; TRB possesses avenues of communications and cooperation with federal, state, and local governmental agencies, universities, and industry; TRB's relationship to the National Academies is an insurance of objectivity; and TRB maintains a full-time staff of specialists in highway transportation matters to bring the findings of research directly to those in a position to use them.

The program is developed on the basis of research needs identified by chief administrators and other staff of the highway and transportation departments, by committees of AASHTO, and by the Federal Highway Administration. Topics of the highest merit are selected by the AASHTO Special Committee on Research and Innovation (R&I), and each year R&I's recommendations are proposed to the AASHTO Board of Directors and the National Academies. Research projects to address these topics are defined by NCHRP, and qualified research agencies are selected from submitted proposals. Administration and surveillance of research contracts are the responsibilities of the National Academies and TRB.

The needs for highway research are many, and NCHRP can make significant contributions to solving highway transportation problems of mutual concern to many responsible groups. The program, however, is intended to complement, rather than to substitute for or duplicate, other highway research programs.

## NCHRP RESEARCH REPORT 915

Project 24-43  
ISSN 2572-3766 (Print)  
ISSN 2572-3774 (Online)  
ISBN 978-0-309-48075-8

Library of Congress Control Number 2019950229

© 2019 National Academy of Sciences. All rights reserved.

### COPYRIGHT INFORMATION

Authors herein are responsible for the authenticity of their materials and for obtaining written permissions from publishers or persons who own the copyright to any previously published or copyrighted material used herein.

Cooperative Research Programs (CRP) grants permission to reproduce material in this publication for classroom and not-for-profit purposes. Permission is given with the understanding that none of the material will be used to imply TRB, AASHTO, FAA, FHWA, FMCSA, FRA, FTA, Office of the Assistant Secretary for Research and Technology, PHMSA, or TDC endorsement of a particular product, method, or practice. It is expected that those reproducing the material in this document for educational and not-for-profit uses will give appropriate acknowledgment of the source of any reprinted or reproduced material. For other uses of the material, request permission from CRP.

### NOTICE

The research report was reviewed by the technical panel and accepted for publication according to procedures established and overseen by the Transportation Research Board and approved by the National Academies of Sciences, Engineering, and Medicine.

The opinions and conclusions expressed or implied in this report are those of the researchers who performed the research and are not necessarily those of the Transportation Research Board; the National Academies of Sciences, Engineering, and Medicine; or the program sponsors.

The Transportation Research Board; the National Academies of Sciences, Engineering, and Medicine; and the sponsors of the National Cooperative Highway Research Program do not endorse products or manufacturers. Trade or manufacturers' names appear herein solely because they are considered essential to the object of the report.

*Published research reports of the*

### NATIONAL COOPERATIVE HIGHWAY RESEARCH PROGRAM

*are available from*

Transportation Research Board  
Business Office  
500 Fifth Street, NW  
Washington, DC 20001

*and can be ordered through the Internet by going to*

<http://www.national-academies.org>

*and then searching for TRB*

Printed in the United States of America

*The National Academies of*  
**SCIENCES • ENGINEERING • MEDICINE**

The **National Academy of Sciences** was established in 1863 by an Act of Congress, signed by President Lincoln, as a private, non-governmental institution to advise the nation on issues related to science and technology. Members are elected by their peers for outstanding contributions to research. Dr. Marcia McNutt is president.

The **National Academy of Engineering** was established in 1964 under the charter of the National Academy of Sciences to bring the practices of engineering to advising the nation. Members are elected by their peers for extraordinary contributions to engineering. Dr. John L. Anderson is president.

The **National Academy of Medicine** (formerly the Institute of Medicine) was established in 1970 under the charter of the National Academy of Sciences to advise the nation on medical and health issues. Members are elected by their peers for distinguished contributions to medicine and health. Dr. Victor J. Dzau is president.

The three Academies work together as the **National Academies of Sciences, Engineering, and Medicine** to provide independent, objective analysis and advice to the nation and conduct other activities to solve complex problems and inform public policy decisions. The National Academies also encourage education and research, recognize outstanding contributions to knowledge, and increase public understanding in matters of science, engineering, and medicine.

Learn more about the National Academies of Sciences, Engineering, and Medicine at [www.national-academies.org](http://www.national-academies.org).

---

The **Transportation Research Board** is one of seven major programs of the National Academies of Sciences, Engineering, and Medicine. The mission of the Transportation Research Board is to increase the benefits that transportation contributes to society by providing leadership in transportation innovation and progress through research and information exchange, conducted within a setting that is objective, interdisciplinary, and multimodal. The Board's varied committees, task forces, and panels annually engage about 7,000 engineers, scientists, and other transportation researchers and practitioners from the public and private sectors and academia, all of whom contribute their expertise in the public interest. The program is supported by state transportation departments, federal agencies including the component administrations of the U.S. Department of Transportation, and other organizations and individuals interested in the development of transportation.

Learn more about the Transportation Research Board at [www.TRB.org](http://www.TRB.org).

# COOPERATIVE RESEARCH PROGRAMS

## CRP STAFF FOR NCHRP RESEARCH REPORT 915

*Christopher J. Hedges, Director, Cooperative Research Programs  
Lori L. Sundstrom, Deputy Director, Cooperative Research Programs  
Camille Crichton-Summers, Senior Program Officer  
Megan A. Chamberlain, Senior Program Assistant  
Eileen P. Delaney, Director of Publications  
Natalie Barnes, Associate Director of Publications  
Janet M. McNaughton, Senior Editor*

## NCHRP PROJECT 24-43 PANEL

### Field of Soils and Geology—Area of Mechanics and Foundations

*John G. Delphia, Texas DOT, Austin, TX (Chair)  
Nathalia R. Chandler, South Carolina DOT, Columbia, SC  
Leo L. Fontaine, Connecticut DOT, Newington, CT  
Martin W. McIlroy, MGE Engineering, Sacramento, CA  
Vernon R. Schaefer, Iowa State University, Ames, IA  
Heather Z. Shoup, Illinois DOT, Springfield, IL  
Ming Xiao, Pennsylvania State University, University Park, PA  
Jennifer E. Nicks, FHWA Liaison*

## AUTHOR ACKNOWLEDGMENTS

The research reported herein was performed under NCHRP Project 24-43 by the Texas A&M Transportation Institute, Texas A&M University System (TAMU). Jean-Louis Briaud, P.E., Distinguished Professor of Civil Engineering at TAMU, was the project director and principal investigator. The other authors of this report are Iman Shafii, research assistant and doctoral candidate, TAMU (currently geotechnical engineer, Fugro USA Land); Hamn-Ching Chen, Joint Professor of Civil Engineering and Ocean Engineering, TAMU; and Zenon Medina-Cetina, Associate Professor of Civil Engineering, TAMU.

The investigators wish to thank many people for their input and cooperation. These include Stephane Bonelli of the University of Grenoble, France; Anna Shidlovskaya of the University of Mines, Russia; and Tony Wahl of the U.S. Bureau of Reclamation. Thanks also go to Garey Fox, Professor and Department Head, Biosystems and Agricultural Engineering Department, Oklahoma State University, for providing the core part of the mini-JET device. The authors also acknowledge Mostafa Bahmani and Yichuan Zhu, both doctoral students at TAMU, for their contributions to this project; the Houston, Texas, office of Fugro USA Land, and the College Station and Conroe, Texas, offices of Terracon Consultants for providing help at many key moments during this project. Finally, the authors thank the staff and lab coordinators in the TAMU Geotechnical Engineering Program, who helped during this project and thereby made this study possible.



## FORWORD

By Camille Crichton-Sumners

Staff Officer  
Transportation Research Board

*NCHRP Research Report 915: Relationship Between Erodibility and Properties of Soils* provides state transportation geotechnical engineers, hydraulic engineers, structural engineers, and other practitioners with a detailed analysis and a searchable Microsoft® Excel spreadsheet, NCHRP-Erosion, that uses statistical techniques to relate geotechnical properties to soil erodibility. Downloadable from the TRB summary web page for this report (search [trb.org](http://trb.org) for “NCHRP Research Report 915”), NCHRP-Erosion is a searchable database that includes compiled erosion data from the literature review and a plethora of erosion tests. It contains equations that may be used to estimate the erosion resistance of soil and determine whether erosion tests are needed.

---

Analysis of the erodibility of geomaterials is important for the study of problems related to soil erosion such as bridge scour, embankment overtopping erosion, and stream stability. Erodibility is a relationship between the soil erosion rate and fluid velocity or hydraulic shear stress. Since different soils have different geotechnical properties, their erosion rates vary. Additionally, existing laboratory and field erosion soil tests yield varied results that make it difficult to achieve consistent and reliable estimates.

Under NCHRP Project 24-43, Texas A&M University (TAMU) was asked to develop equations that quantify soil erodibility on the basis of soil properties. Two approaches were used: (1) development of correlations between the elements of the erosion function (critical velocity, critical shear stress, and slope of the erosion function) with basic soil properties (e.g., plasticity index, mean grain size, unit weight, and shear strength) and (2) use of erosion categories to develop best fit models where the erosion function fits in a zone between boundaries to be directly associated with a single category of the erosion function so that correlations with soil properties can be developed.

TAMU completed an extensive literature search compiling erosion data from multiple sources worldwide and conducted hundreds of erosion and geotechnical property tests. Following detailed statistical analysis, a searchable Microsoft Excel spreadsheet that relates geotechnical properties to soil erodibility was developed. This spreadsheet, NCHRP-Erosion, can be downloaded from the TRB summary web page for *NCHRP Research Report 915*. Through the use of numerical simulations, the researchers also compared soil erosion test methods to inform test method selection. *NCHRP Research Report 915* should be helpful for those responsible for geotechnical analysis within state transportation agencies and other practitioners.

Five appendices to *NCHRP Research Report 915* are gathered in an Appendices Report that is available on the NCHRP Project 24-43 web page on the TRB website ([trb.org](http://trb.org)):

Appendix 1: Erosion Test Results Spreadsheets,  
Appendix 2: Geotechnical Properties Spreadsheets,  
Appendix 3: First and Second Order Statistical Analyses Results,  
Appendix 4: Deterministic Frequentist Regression Analysis, and  
Appendix 5: Probabilistic Calibration Results.



## CONTENTS

<b>1</b>	<b>Summary</b>
<b>11</b>	<b>Chapter 1</b> Introduction
11	1.1 Definition of Erosion
13	1.2 Soil Erodibility and Constitutive Models
15	1.3 Erodibility Parameters
17	1.4 Research Approach and Project Tasks
<b>20</b>	<b>Chapter 2</b> Existing Erosion Tests
20	2.1 Laboratory Erosion Testing
47	2.2 Field Erosion Testing
55	2.3 Summary
<b>56</b>	<b>Chapter 3</b> Existing Correlations Between Soil Erodibility and Soil Properties
56	3.1 Existing Correlations
69	3.2 Influence Factors on Erosion
<b>76</b>	<b>Chapter 4</b> Erosion Experiments
76	4.1 TAMU Soil Erosion Lab and Testing Devices
84	4.2 Test Plan Matrix
85	4.3 Results of Erosion Tests
115	4.4 Soil Geotechnical Properties
<b>117</b>	<b>Chapter 5</b> Organization and Interpretation of the Data
117	5.1 Development and Organization of NCHRP-Erosion
121	5.2 Column Contents in NCHRP-Erosion
125	5.3 NCHRP-Erosion Manual
<b>138</b>	<b>Chapter 6</b> Comparison of Selected Soil Erosion Tests by Numerical Simulation
138	6.1 Results of Numerical Simulation for Nonerodible Soils
153	6.2 Results of Numerical Simulation Including Erosion
<b>168</b>	<b>Chapter 7</b> Development of Correlation Equations
168	7.1 Determining Erosion Resistance Using the USCS
178	7.2 Plots of Critical Velocity and Shear Stress Versus Mean Particle Size
178	7.3 Deterministic (Frequentist) Regression Analysis
258	7.4 Probabilistic (Bayesian) Analysis
<b>280</b>	<b>Chapter 8</b> Most Robust Correlation Equations
280	8.1 Differences Between the EFA, JET, and HET
280	8.2 Deterministic Analysis (Frequentist Regression)

<b>301</b>	<b>Chapter 9 Conclusions and Recommendations</b>
301	9.1 Summary of Chapters 1 Through 8
306	9.2 Recommendations on How to Approach Erosion-Related Design Problems
307	9.3 Example Applications
316	9.4 General Observations on the Effect of Geotechnical Properties on Soil Erodibility
<b>318</b>	<b>Symbols and Abbreviations</b>
<b>320</b>	<b>References</b>
<b>325</b>	<b>Bibliography</b>
<b>327</b>	<b>Appendices</b>

---

Note: Photographs, figures, and tables in this report may have been converted from color to grayscale for printing. The electronic version of the report (posted on the web at [www.trb.org](http://www.trb.org)) retains the color versions.



## SUMMARY

# Relationship Between Erodibility and Properties of Soils

The goal of this project was to develop reliable and simple equations quantifying the erodibility of soils on the basis of soil properties. The reliability must take into account the accuracy required for erosion-related projects, while the simplicity must consider the economic aspects of erosion-related projects. Different soils exhibit different erodibility (e.g., sand, clay); therefore, erodibility is tied to soil properties.

Many researchers have attempted to develop equations quantifying the erodibility of soils without much success. One problem is that erodibility is not a single number, but a relationship between the erosion rate and the water velocity, or the hydraulic shear stress. This erosion function is a curve, and it is difficult to correlate a curve to soil properties. Another problem that needs to be solved is associated with the availability of several erosion testing devices. In the laboratory, these include many erosion tests, such as the pinhole test, the hole erosion test (HET), the jet erosion test (JET), the rotating cylinder test, and the erosion function apparatus (EFA) test. In the field, these include the JET, the North Carolina State University in situ scour evaluation probe test, and the Texas A&M University (TAMU) borehole erosion test and pocket erodometer test. All these tests measure soil erodibility but give different results. It is important to give engineers options so that they can choose one test or another. Therefore, it would be helpful if all these tests could give the same answer. Indeed, the soil does not know the difference between erosion tests, and the erosion function is a fundamental property of the soil. Experimental and numerical efforts were made to advance in this direction. The tasks were as follows:

### Phase I

Task 1: Identification of current knowledge on soil erosion and soil properties.

Task 2: Identification of current soil erodibility data and correlations.

Task 3: Assessment of current and promising erosion tests.

### Phase II

Task 4: Performance of erosion tests with different devices on the same prepared soils.

Task 5: Performance of erosion tests on many different soils to develop erodibility equations.

Task 6: Development of regression equations and validation.

Task 7: Verification, synthesis, and analysis of all data to propose the best solution.

A summary of each chapter is given below.

## Chapter 1. Introduction

Chapter 1 is divided into two parts. The first part presents a definition of erosion and introduces different types of erosion. The general parameters for quantifying soil erodibility and the constitutive models for erosion are briefly discussed. The second part presents the research

## 2 Relationship Between Erodibility and Properties of Soils

approach. The project tasks are described and a summary of how and where within the report each of the tasks is addressed is provided.

### **Chapter 2. Existing Erosion Tests**

Chapter 2 presents a comprehensive literature review on different soil erosion tests. Tests developed all over the world in the past few decades are discussed in terms of their application in the lab or in the field and of their application to surface erosion or internal erosion problems. The advantages and disadvantages of the most important tests are explained, and a summary table about the tests used in statistical analyses in this report is provided at the end of the chapter. The advantages, disadvantages, and applications of the three major erosion tests used in this study—the EFA, the JET, and the HET—are presented in Table S-1.

### **Chapter 3. Existing Correlations Between Soil Erodibility and Soil Properties**

Chapter 3 provides a literature review of the existing correlations between soil erodibility and soil properties. The observations and correlation equations proposed by various researchers in the past century are summarized. The influence factors on erosion, including the less easily obtained engineering properties, are presented and discussed in detail. Table S-2 summarizes these parameters.

### **Chapter 4. Erosion Experiments**

Chapter 4 begins by describing the TAMU Soil Erosion Laboratory. The erosion testing devices built as part of this research project as well as the refurnished and armored erosion function apparatus are presented. The test plan matrix proposed for the project and the results of the hundreds of erosion tests performed during the project are then presented and discussed. Finally, an example of the spreadsheet of geotechnical engineering properties created for each tested sample obtained at TAMU is presented. Appendices 1 and 2 of this report contain the spreadsheets for the erosion test results and soil geotechnical properties, respectively, for all samples tested in this project. [Note: Five appendices to *NCHRP Research Report 915* are gathered in an Appendices Report that is available on the NCHRP Project 24-43 page on the TRB website ([trb.org](http://trb.org)).]

### **Chapter 5. Organization and Interpretation of the Data**

Chapter 5 is largely dedicated to the organization and description of the erosion spreadsheet developed for this project and named “NCHRP-Erosion.” NCHRP-Erosion includes the results of nearly 1,000 erosion tests—approximately 250 erosion tests performed as part of this project and nearly 750 erosion tests collected from all over the world—along with the geotechnical properties of each sample. The process used to compile erosion test data from all over the world is explained, and the contact people and organizations who helped gather the information are mentioned. All the erosion data in NCHRP-Erosion were analyzed according to the procedures described in the report for five erodibility parameters: (1) critical shear stress ( $\tau_c$ ), (2) critical velocity ( $v_c$ ), (3) initial slope of velocity ( $E_v$ ), (4) initial slope of shear stress ( $E\tau$ ), and (5) erosion category (EC). NCHRP-Erosion includes 50 columns and nearly 1,000 rows. Chapter 5 discusses the column contents in detail and concludes with the Inquiry Operation Manual that explains

**Table S-1. Comparison of EFA, JET, and HET.**

Advantages	Drawbacks	Applications
<b>EFA</b>		
<p>1. Minimizes the sample disturbance effect, as it takes the unextruded Shelby tube sample directly from the field.</p> <p>2. Can be used on natural samples as well as man-made samples</p> <p>3. Gives all five erodibility parameters (i.e., <math>v_c</math>, <math>\tau_c</math>, <math>E_v</math>, <math>E_t</math>, and EC). Can give the erosion function directly.</p> <p>4. Can monitor the erosion rate in real time rather than by interpolating or extrapolating using indirect equations.</p> <p>5. EFA test results are directly used as input to the TAMU-SCOUR method for bridge scour depth predictions (Arneson et al. 2012, Chapter 6).</p> <p>6. EFA can test the erodibility of the soil at any depth as long as a sample can be recovered.</p> <p>7. Gives the erosion function, which is a fundamental measure of erodibility at the element level.</p> <p>8. Can be used to test very soft to hard soils. Very broad applications. The velocity range is from 0.2 to 6 m/s.</p>	<p>1. Shear stress is indirectly measured from velocity using Moody charts, which might not be accurate. Also, the average flow velocity is used in the calculation.</p> <p>2. In some cases, obtaining samples is difficult and costly. The test needs to be done on the sample before the sample is affected by long periods of storage.</p> <p>3. Particles larger than about 40 mm cannot be tested with confidence, as the diameter of the sampling tube is 75 mm.</p> <p>4. The EFA device is fairly expensive (around \$50,000 in 2018).</p>	<p>1. Bridge scour.</p> <p>2. Meander migration.</p> <p>3. Levee overtopping.</p> <p>4. Soil improvement.</p> <p>5. Internal erosion of dams.</p>
<b>JET</b>		
<p>1. Can be run both in the field and in the lab.</p> <p>2. The latest version of the JET, the mini-JET, is simple, quick, and inexpensive compared with other types of erosion tests.</p> <p>3. Can be performed on any surface—vertical, horizontal, or inclined.</p> <p>4. Very good as an index erodibility test.</p>	<p>1. Particles larger than 30 mm cannot be tested with confidence because of the small size of the sample.</p> <p>2. Coarse-grained soils (i.e., noncohesive sand and gravel) tend to fall back into the open hole during the jet erosion process, thereby making the readings dubious.</p> <p>3. Very small-scale test application.</p> <p>4. Typically used for man-made samples. Natural samples are more difficult to test.</p> <p>5. The flow within the eroded hole and at the soil boundary is complex and difficult to analyze.</p> <p>6. Gives only three of the five possible erodibility parameters (<math>\tau_c</math>, <math>E_t</math>, and EC).</p> <p>7. The elements of erosion are inferred rather than measured directly.</p> <p>8. There are multiple interpretation techniques for predicting the critical shear stress, and these give significantly different results.</p>	<p>1. Agriculture erosion.</p> <p>2. Levees.</p>
<b>HET</b>		
<p>1. Direct similitude with piping erosion in earth dams.</p> <p>2. Can apply to a wide range of pressure heads and therefore a wide range of hydraulic shear stress at the soil–water interface.</p>	<p>1. The sample needs to be cohesive and strong enough to stand under its own weight. Therefore, the test cannot be run on loose cohesionless soils or soft cohesive soils.</p> <p>2. Very difficult to run on intact samples in Shelby tubes from the field. Only good for remolded, recompacted samples in the lab.</p> <p>3. Preparation of the test is difficult and time consuming.</p> <p>4. No direct monitoring of the erosion process. The erosion rate needs to be inferred and extrapolated.</p> <p>5. The hydraulic shear stress is inferred rather than directly measured.</p> <p>6. The data reduction process is quite subjective.</p> <p>7. Gives only three of the five possible erodibility parameters (<math>\tau_c</math>, <math>E_t</math>, and EC).</p> <p>8. The flow within the eroded hole and at the soil boundary is complex.</p>	<p>1. Internal erosion of earth dams.</p> <p>2. Suffusion.</p> <p>3. Levee breach.</p> <p>4. Soil improvement.</p>

## 4 Relationship Between Erodibility and Properties of Soils

**Table S-2. Soil and water properties that influence the erosion resistance of soils.**

More Typically Obtained Properties	Less Typically Obtained Properties
<ul style="list-style-type: none"> <li>• Plasticity index</li> <li>• Liquidity index</li> <li>• Unit weight</li> <li>• Water content</li> <li>• Undrained shear strength</li> <li>• Percentage passing sieve #200</li> <li>• Percentage of clay particles</li> <li>• Percentage of silt particles</li> <li>• Mean grain size</li> <li>• Coefficient of uniformity</li> <li>• Percentage of compaction (for man-made soils only)</li> <li>• Soil swell potential</li> <li>• Soil void ratio</li> </ul>	<ul style="list-style-type: none"> <li>• Specific gravity of solids</li> <li>• Soil dispersion ratio</li> <li>• pH (flowing water and pore water)</li> <li>• Salinity of eroding fluid</li> <li>• Organic content</li> <li>• Soil cation exchange cap</li> <li>• Soil clay minerals</li> <li>• Soil sodium adsorption ratio</li> <li>• Soil activity</li> <li>• Soil temperature</li> <li>• Density of cracks</li> </ul>

how to search for specific data within the spreadsheet. NCHRP-Erosion can be downloaded from the TRB website ([trb.org](http://trb.org)) by searching for “NCHRP Research Report 915”.

## Chapter 6. Comparison of Selected Soil Erosion Tests by Numerical Simulation

Chapter 6 presents a comparison of selected soil erosion tests [i.e., EFA, HET, JET, and the borehole erosion test (BET)] by means of numerical simulations software. The chapter is divided into two sections: (1) numerical simulations for nonerodible soils and (2) numerical simulations including the erosion process. The first part of the chapter deals with the evolution of hydraulic shear stress and the velocity profile with the assumption that the soil is not erodible. It is observed that there was a discrepancy between the Moody chart predictions and the numerical simulations and that the Moody charts generally overestimated the shear stress. This discrepancy was more pronounced in higher shear stress values (up to 100% difference between the Moody chart prediction and the numerical simulation in one case). In the second part of the chapter, the erosion function is assigned to the water–soil interface, and the erosion is numerically simulated with a moving boundary for selected erosion tests. The results of the numerical simulations are compared with the actual observations for each test. The findings show that the erosion function obtained from the EFA test for each sample can reasonably be used to produce a scour-versus-time plot similar to what the results of the JET, HET, and BET experiments would produce. However, the variety of interpretation techniques used for each test to obtain the shear stress in the soil–water interface leads to different erosion functions. Therefore, one must be aware of the interpretation techniques that each test uses to obtain the erosion function (erosion rate versus shear stress).

## Chapter 7. Development of Correlation Equations

Chapter 7 is dedicated to the main goal of the study, namely, the development of correlation equations. This chapter is divided into four major parts. The first part presents a preliminary and quick method for determining the erosion resistance of a soil by using only the Unified Soil Classification System (USCS) classification of the soil and associated erosion categories. The plot of the erosion rate versus velocity based on the USCS categories is shown in Figure S-1. The width of each box associated with a USCS category represents the zone in which 90% of the EFA results for such samples would fall within the erosion category chart. For instance,

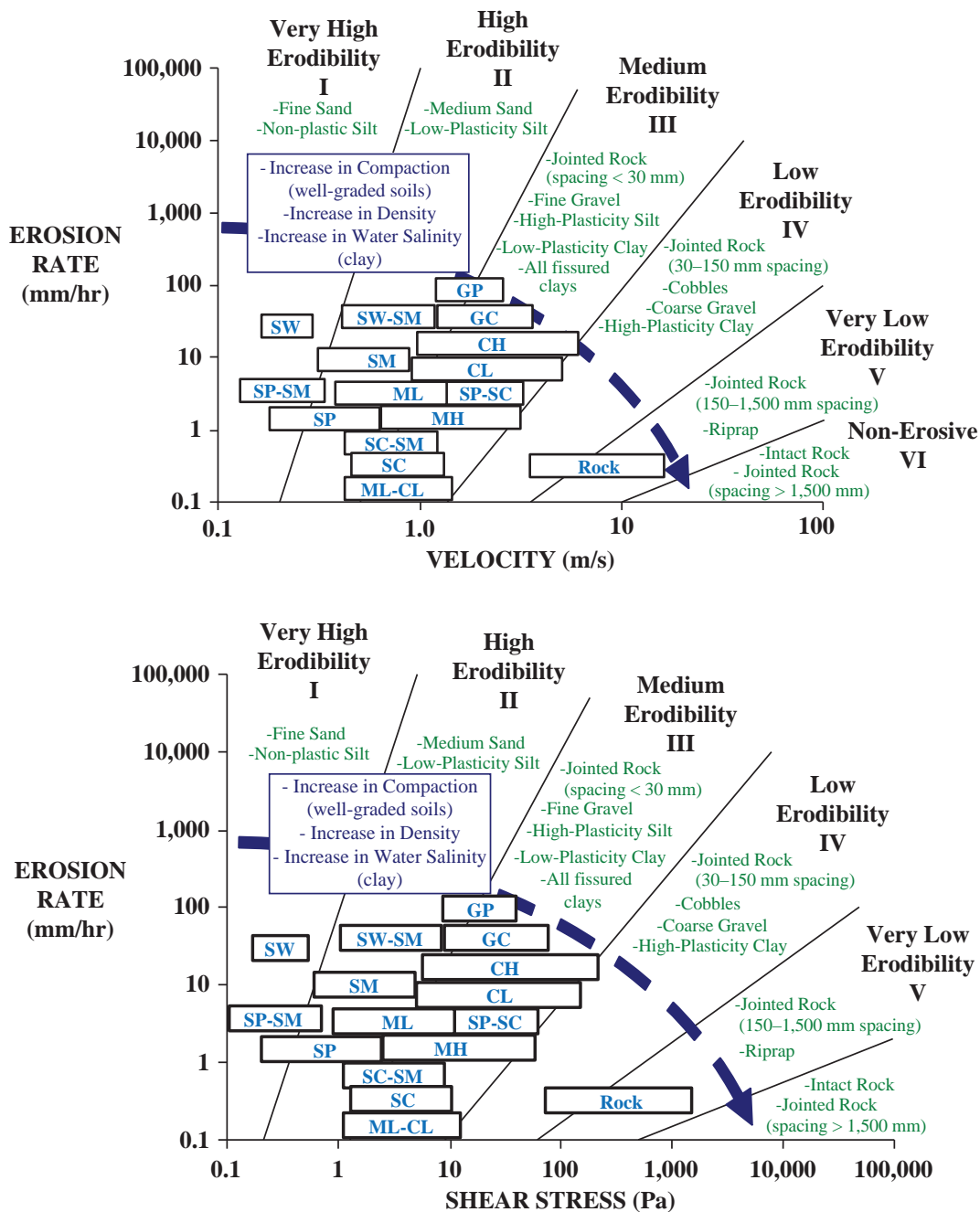


Figure S-1. Erosion category charts with USCS symbols.

## 6 Relationship Between Erodibility and Properties of Soils

**Table S-3. Selected models for critical shear stress,  $\tau_c$ .**

Group No.	Independent Variables <sup>a</sup>	Data Set <sup>b</sup>	Model Expression <sup>c</sup>	R <sup>2</sup>	Cross-Validation Score
124	$\gamma, A, WC, S_u, PF, D_{50}$	EFA/Fine ( $n = 44$ )	$\tau_c = (158.06) \times \gamma^5 \times A^{-0.46} \times WC^{10.03} \times S_u^{1.83} \times PF^{-18.28} \times D_{50}^{-4.21}$	0.94	0.66
77	$C_u, \gamma, D_{50}$	EFA/Coarse ( $n = 28$ )	$\tau_c = (1.58) \times C_u^{-0.04} \times \gamma^{0.02} \times D_{50}^{0.77}$	0.93	0.99
113	$PC, \gamma, WC, S_u, D_{50}$	JET/Global ( $n = 28$ )	$\tau_c = -0.248 \times PC - 1.23 \times \gamma + 0.21 \times WC + 0.07 \times S_u - 36.89 \times D_{50} + 31.82$	0.50	0.10
19	$PI, S_u, D_{50}$	HET/Global ( $n = 21$ )	$\tau_c = (25.07) \times PI^{0.27} \times S_u^{0.55} \times D_{50}^{0.5}$	0.64	0.43

<sup>a</sup>See Chapter 7, Section 7.3.1.

<sup>b</sup> $n$  = number of data points.

<sup>c</sup>Parameter values given by deterministic regression.

if the soil type at a geotechnical site is classified as SM (silty sand) according to the USCS, it would most likely (with close to 90% confidence on the basis of the EFA results compiled in NCHRP-Erosion) fall into Category II (high erodibility). Similarly, a soil classified as CH (fat clay) would most likely fall into Category III (medium erodibility), and an SP (poorly graded sand) would fall within Categories I and II (very high to high erodibility).

The second part of Chapter 7 deals with improving existing plots of critical velocity/critical shear stress versus mean particle size ( $D_{50}$ ). It is observed that for soils with a mean particle size greater than 0.3 mm, the following relationships exist between the critical velocity/shear stress and mean particle size:  $v_c$  (m/s) = 0.315( $D_{50}$  (mm))<sup>0.5</sup> and  $\tau_c$  (Pa) =  $D_{50}$  (mm). It is also concluded that for fine-grained soils, there is no direct relationship between critical velocity/shear stress and mean particle size. However, the data could be bracketed with an upper-bound and a lower-bound equation.

The third part of Chapter 7 presents the frequentist regression technique. The step-by-step procedure for implementing the frequentist regression technique, the experimental design, and the model selection process are discussed, and the results of the regressions are presented. The best correlation equations are determined by a four-filter process including (1)  $R^2$ , (2) the mean square error, (3) the statistical  $F$ -test, and (4) the cross-validation test. Plots of the probability of overpredicting (POO) and probability of underpredicting (POU) are also presented for the selected equations. Tables S-3 to S-7 show the selected equations for each erodibility parameter and for each data set.

**Table S-4. Selected models for critical velocity,  $v_c$ .**

Group No.	Independent Variables <sup>a</sup>	Data Set <sup>b</sup>	Model Expression <sup>c</sup>	R <sup>2</sup>	Cross-Validation Score
117	$PC, WC, S_u, D_{50}$	EFA/Fine ( $n = 46$ )	$v_c = (2.518 \times 10^{-5}) \times PC^{0.2} \times WC^{2.06} \times S_u^{0.51} \times D_{50}^{-0.13}$	0.80	0.80
27	$PI, \gamma, WC, D_{50}$	EFA/Coarse ( $n = 15$ )	$v_c = (3 \times 10^{-15}) \times PI^{1.24} \times \gamma^{8.11} \times WC^{0.54} \times D_{50}^{-2.35}$	0.88	0.72

<sup>a</sup>See Chapter 7, Section 7.3.1.

<sup>b</sup> $n$  = number of data points.

<sup>c</sup>Parameter values given by deterministic regression.

**Table S-5. Selected models for erosion category, EC.**

Group No.	Independent Variables <sup>a</sup>	Data Set <sup>b</sup>	Model Expression <sup>c</sup>	R <sup>2</sup>	Cross-Validation Score
132	A, WC, S <sub>u</sub> , D <sub>50</sub>	EFA/Fine (n = 44)	EC = (0.1933) × A <sup>-0.06</sup> × WC <sup>0.51</sup> × S <sub>u</sub> <sup>0.09</sup> × D <sub>50</sub> <sup>-0.12</sup>	0.55	0.53
91	C <sub>u</sub> , WC, VST, D <sub>50</sub>	EFA/Coarse (n = 11)	EC = (1.12) × C <sub>u</sub> <sup>0.1</sup> × WC <sup>-0.28</sup> × VST <sup>0.02</sup> × D <sub>50</sub> <sup>-0.44</sup> for 0.074 < D <sub>50</sub> < 0.3	0.92	0.80
88	PL, S <sub>u</sub> , D <sub>50</sub>	JET/Global (n = 28)	EC = -0.022 × PL + 0.0031 × S <sub>u</sub> - 5.5 × D <sub>50</sub> + 3.34	0.70	0.58
12	PI, γ, S <sub>u</sub>	HET/Fine (n = 21)	EC = (1.67) × PI <sup>0.04</sup> × γ <sup>0.15</sup> × S <sub>u</sub> <sup>0.03</sup>	0.70	0.54
48	C <sub>c</sub> , γ, WC	HET/Coarse (n = 28)	EC = (1.045) × C <sub>c</sub> <sup>-0.25</sup> × γ <sup>0.45</sup> × WC <sup>-0.04</sup>	0.77	0.78

<sup>a</sup>See Chapter 7, Section 7.3.1.<sup>b</sup>n = number of data points.<sup>c</sup>Parameter values given by deterministic regression.**Table S-6. Selected models for velocity slope, E<sub>v</sub>.**

Group No.	Independent Variables <sup>a</sup>	Data Set <sup>b</sup>	Model Expression <sup>c</sup>	R <sup>2</sup>	Cross-Validation Score
86	C <sub>u</sub> , γ, WC, D <sub>50</sub>	EFA/Coarse (n = 28)	E <sub>v</sub> = (88,969.4) × C <sub>u</sub> <sup>-1.77</sup> × γ <sup>-2.26</sup> × WC <sup>0.34</sup> × D <sub>50</sub> <sup>-1.69</sup>	0.86	0.64
126	D <sub>50</sub> , γ, WC, PF, A	EFA/Fine (n = 74)	E <sub>v</sub> = (1.682339 × 10 <sup>13</sup> ) × D <sub>50</sub> <sup>5.10</sup> × γ <sup>-9.20</sup> × WC <sup>-1.13</sup> × PF <sup>4.69</sup> × A <sup>-0.01</sup>	0.79	0.52

<sup>a</sup>See Chapter 7, Section 7.3.1.<sup>b</sup>n = number of data points.<sup>c</sup>Parameter values given by deterministic regression.**Table S-7. Selected models for shear stress slope, E<sub>τ</sub>.**

Group No.	Independent Variables <sup>a</sup>	Data Set <sup>b</sup>	Model Expression <sup>c</sup>	R <sup>2</sup>	Cross-Validation Score
77	C <sub>u</sub> , γ, D <sub>50</sub>	EFA/Coarse (n = 28)	E <sub>τ</sub> = (3,228.7) × C <sub>u</sub> <sup>-2.8</sup> × γ <sup>-1.58</sup> × D <sub>50</sub> <sup>-2.91</sup>	0.91	0.64
134	A, γ, PF, D <sub>50</sub>	EFA/Fine (n = 72)	E <sub>τ</sub> = (1.429078 × 10 <sup>13</sup> ) × A <sup>-0.47</sup> × γ <sup>-10.43</sup> × PF <sup>6.14</sup> × D <sub>50</sub> <sup>7.52</sup>	0.90	0.51
40	γ, WC, PF, D <sub>50</sub>	HET/Coarse (n = 62)	E <sub>τ</sub> = (2.951) × γ <sup>26.08</sup> × WC <sup>-7.48</sup> × PF <sup>-19.96</sup> × D <sub>50</sub> <sup>-5.32</sup>	0.86	0.55
108	LL, PL, γ, PC, S <sub>u</sub>	HET/Fine (n = 21)	E <sub>τ</sub> = (9 × 10 <sup>-6</sup> ) × LL <sup>-0.35</sup> × PL <sup>1.59</sup> × γ <sup>3.3</sup> × PC <sup>-0.48</sup> × S <sub>u</sub> <sup>-0.19</sup>	0.81	0.51
5	PI, γ, WC	JET/Coarse (n = 25)	E <sub>τ</sub> = (55,637,006,351,614) × PI <sup>-0.19</sup> × γ <sup>-6.39</sup> × WC <sup>-3.67</sup>	0.90	0.67
15	PI, WC, S <sub>u</sub>	JET/Fine (n = 24)	E <sub>τ</sub> = (396,599.6) × PI <sup>-2.54</sup> × WC <sup>4.58</sup> × S <sub>u</sub> <sup>-4.91</sup>	0.93	0.23

<sup>a</sup>See Chapter 7, Section 7.3.1.<sup>b</sup>n = number of data points.<sup>c</sup>Parameter values given by deterministic regression.

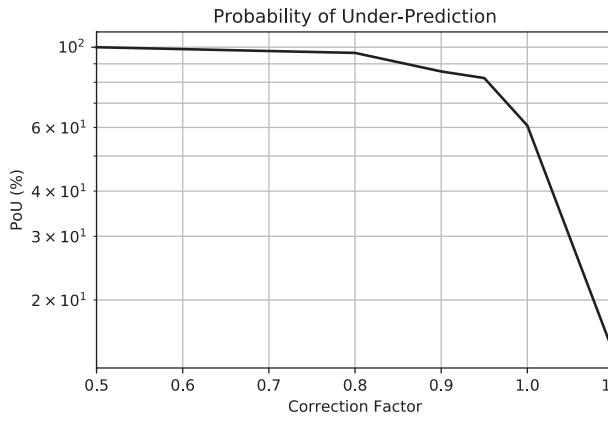
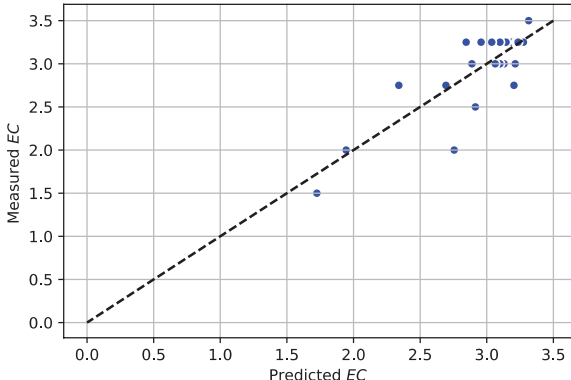
## 8 Relationship Between Erodibility and Properties of Soils

The last part of Chapter 7 deals with a probabilistic approach as opposed to the deterministic approach presented in the previous section. The probabilistic approach is based on the Bayesian inference method. The methodology of the Bayesian inference method and its results are presented in Section 7.4 as well as in Appendix 5.

## Chapter 8. Most Robust Correlation Equations

This chapter focuses on the recommended correlation equations (Tables S-3 to S-7) based on the work presented in Chapter 7 and provides instructions on how best to use them. Table S-8 shows an example of the proposed equation charts for erosion category based on the JET data. This table presents the recommended correlation equation for predicting the erosion category for  $D_{50} < 0.3$  mm. Along with each proposed equation, these tables give two plots: one showing the POU (or the POO, where applicable) versus the correction factor and one showing the predicted EC versus the measured EC. Such plots provide great insight on using each equation. Also, a column containing some remarks is provided on the right side of each equation. This column includes the values of  $R^2$  and the cross-validation (C.V.) score. The same sort of table is presented for different erodibility parameters and different erosion tests.

**Table S-8. Proposed equation for erosion category (EC) based on the JET data.**

$D_{50} < 0.3$ mm	$EC = -0.022 \times PL + 0.0031 \times S_u - 5.5 \times D_{50} + 3.34$  <b>Group 88: <math>EC = f(PL, S_u, D_{50})</math></b> 	Remarks
	$R^2 = 0.70$ <b>C.V. score = 0.58</b> <ul style="list-style-type: none"> <li>1. Refer to Group 88 in Table 76 for further information on the statistical significance of the proposed equation.</li> <li>2. The POU versus correction factor plot is based on the data used to develop the proposed equation.</li> <li>3. To reach 90% confidence that the predicted EC is less than the actual EC, the predicted value should be multiplied by 0.85.</li> </ul>	

## Chapter 9. Conclusions and Recommendations

Chapter 9 presents the general conclusions resulting from the work done in this project, recommendations on how to approach erosion-related design problems, and general observations on the effect of geotechnical properties on soil erodibility.

### Recommendations on How to Approach Erosion-Related Design Problems

#### *Step 1. Probe NCHRP-Erosion*

Chapter 5 of this report discusses the development of the NCHRP-Erosion database. This global spreadsheet is a searchable tool that allows the engineer to filter the data on the basis of multiple criteria. The first approach to evaluating the erodibility of a desired site is through probing NCHRP-Erosion. The engineer can use information on as many geotechnical properties as are available for the site (e.g., USCS category, AASHTO classification, Atterberg limits, unit weight, and so forth), and filter NCHRP-Erosion on the basis of those criteria with the goal of finding soil samples that are similar to the target soil. After the filtering, the obtained soil samples may be tested with one or more erosion tests (e.g., EFA, BET, JET, HET). The engineer then can see which erodibility parameters he or she must expect from the soil without having to conduct different erosion tests. Probing NCHRP-Erosion also helps the engineer compare the results of these different erosion tests on similar soil samples.

#### *Step 2. Use the USCS Erosion Charts to Estimate Erosion Resistance*

Section 7.1 shows that the erosion functions for soils with a given USCS category do not generally fall distinctly into a single erosion category but rather seem to plot approximately across two categories. As discussed in the summary of Chapter 7 above, the proposed erosion category-USCS category chart can be used as another preliminary tool for estimating the erodibility of any sample. Knowledge of the erosion category of a soil can lead to useful information about the erosion resistance of that soil; however, it should be noted that such results are not accurate enough for design purposes.

#### *Step 3. Use the Deterministic Regression Results*

Section 7.3 presents a comprehensive deterministic approach for selecting the best correlation equations between geotechnical properties and erodibility parameters. The most robust equations were repeated and are presented in a tabulated format in Section 8.2. The proposed equations were developed on the basis of the data obtained in different erosion tests (EFA, JET, and HET). The advance knowledge on each test is extremely useful in choosing the best equation. Before the proposed equations in Section 8.2 are used, the advantages and disadvantages of each erosion test should be studied carefully. POU/POO plots help the engineer find the correction factor needed to reach a certain confidence that the predicted value is under- or overpredicted. These plots can be very useful for design purposes.

#### *Step 4. Use the Bayesian Inference Results*

One of the issues with conventional deterministic approaches is that they fail to capture uncertainty by accounting only for the mean value of the unknown parameter. Therefore, Section 7.4 is dedicated to the performance of a probabilistic analysis with the Bayesian inference approach. The comprehensive deterministic frequentist regression analysis performed in Section 7.3 is the foundation of the Bayesian inference analysis performed in Section 7.4. The selected correlation equations that use the deterministic approach are analyzed by Bayesian

## 10 Relationship Between Erodibility and Properties of Soils

inference. The engineer can evaluate the sensitivity of the predicted value with regard to one or more model parameters. All possible values that an erodibility parameter can get for each selected equation are presented in the form of a probability distribution. Examples of the Bayesian inference analysis are presented in Section 7.4. Appendix 5 presents the entire results of the Bayesian inference analysis.

### **General Observations on the Effect of Geotechnical Properties on Soil Erodibility**

The following findings on the relationships between geotechnical properties and erodibility parameters are also reported in Chapter 9:

- An increase in mean particle size ( $D_{50}$ ) leads to an increase in the erosion resistance of soils with  $D_{50}$  greater than 0.3 mm. However, regardless of the erosion test type, an increase in  $D_{50}$  leads to a decrease in the erosion resistance of soils with  $D_{50}$  less than 0.3 mm.
- In fine-grained soils ( $D_{50} < 0.074$  mm), a decrease in the coefficient of curvature or coefficient of uniformity ( $C_c$  and  $C_u$ ) leads to an increase in soil erosion resistance.
- In both fine- and coarse-grained soils, an increase in the percentage of clay leads to an increase in the erosion resistance of the soil.
- An increase in the plasticity index (PI) in general leads to an increase in the erosion resistance in both coarse-grained and fine-grained soils (especially soils with  $D_{50}$  less than 0.3 mm); however, there are a few exceptions to this statement.
- An increase in the plastic limit (PL) leads to an increase in the erosion resistance in fine-grained soils. This influence was found to be more pronounced in the EFA data set than in the JET and HET data sets.
- In many cases, the wet unit weight ( $\gamma$ ) and the undrained shear strength ( $S_u$ ) (for soils with  $D_{50}$  less than 0.3 mm) were directly proportional to the erosion resistance.
- Water content (WC) seemed to have a positive impact on the erosion resistance of finer soils in general. However, WC showed a negative effect on the erosion resistance of coarse-grained soils in the EFA test. It appears that WC alone is poorly correlated with the erosion resistance.

Overall, the geotechnical properties were found to have a mixed and complex relationship with erosion resistance in general. Nevertheless, the aforementioned observations as well as the proposed equations can be used as a first step in estimating the erosion resistance of many soils. If, by using such relationships, the erosion issue is clearly not a problem, it is unlikely that further effort is necessary. However, if the use of such equations leads to uncertainty, it is desirable to run erosion tests on site-specific samples.



## CHAPTER 1

# Introduction

## 1.1 Definition of Erosion

The phenomenon of erosion is the result of interaction between three main components: the erodible material, the eroding fluid (in most cases water), and the geometry of the obstacle affecting the flow. In this process, the fluid generates the “load,” the erodible material provides the resistance, and the obstacle induces the disturbance. Briaud (2008) divided erodible materials into three categories:

- Soil: those earth elements that can be classified by the Unified Soil Classification System (USCS);
- Rock: those earth elements that have an unconfined compressive strength of the intact rock core of more than 500 kPa with joint spacing of at least 0.1 m;
- Intermediate geomaterials: any earth material between rock and soil.

Erodibility can be defined as the behavior of the eroding material when subjected to the flow of the eroding fluid. Eroding water is quantified by its velocity, and the geometry of the obstacle is characterized by its dimensions. Figure 1 shows the forces acting on a soil particle at the surface of the interface between the water and the soil.

Given their application in nature, erosion phenomena can be divided into two groups:

1. Internal erosion, which is important for seepage through embankment dams, levees, and canal side embankments, and
2. Surface erosion, which is important for bridge scour, overtopping of levees, dams, highway embankments, and meander migration.

### 1.1.1 Internal Erosion

The type of erosion in which the soil particles are transported within the body of an earth structure, such as an embankment dam from the upstream source to the downstream by the eroding fluid is known as “internal erosion” (Wan and Fell 2002). On the basis of the process in which the eroded particles are carried from an embankment dam or its foundation, internal erosion is subdivided into two types: piping and suffusion.

#### 1.1.1.1 Piping

Piping is mainly the result of backward erosion due to the high exit gradient at the downstream part of an embankment or the boundary between a coarse-grained downstream zone of a rockfill dam and its core. Basically, the high exit gradient detaches the particles and initiates the internal erosion. This erosion process leads to the formation of a continuous tunnel

## 12 Relationship Between Erodibility and Properties of Soils

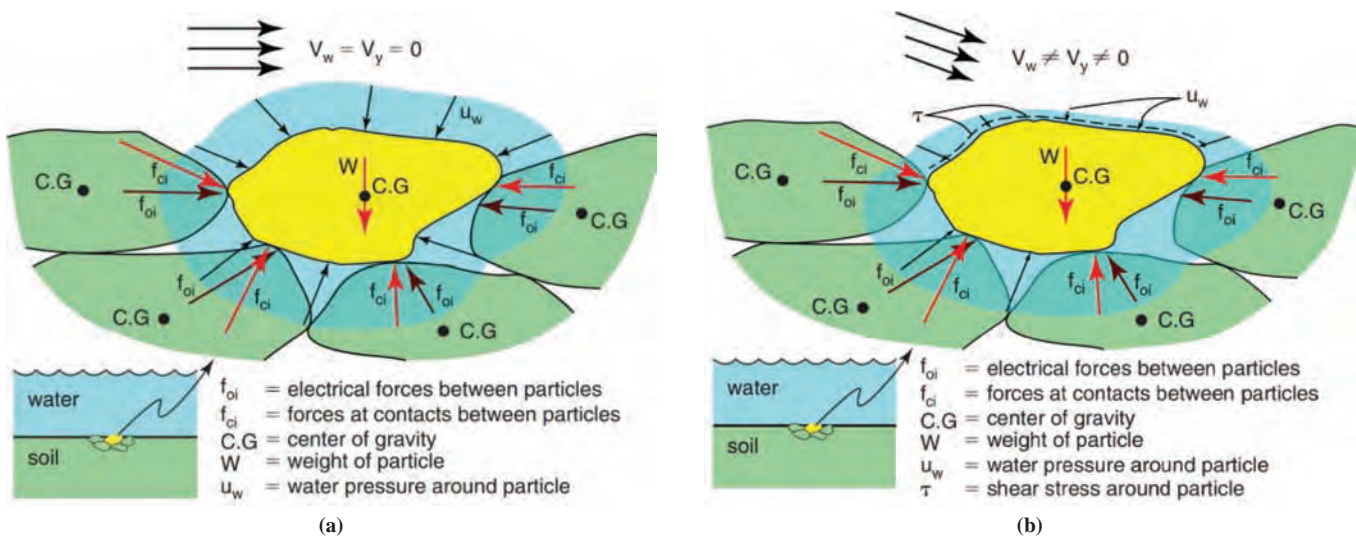


**Figure 1.** Free body diagram of a soil particle or rock block in two different stages: (a) no-flow condition and (b) with water flow (Briaud 2008).

in the embankment, which is known as a “pipe.” Other factors, such as hydraulic fracturing or poor compaction of the soil, also potentially might cause some cracking through the core of the dam, which can result in piping. Similar to the definition made by Terzaghi and Peck (1948), the phenomenon of heave in dams can be named as a special case of piping that happens when the effective stress of the soil at the toe is decreased due to a high seepage gradient.

### 1.1.1.2 Suffusion

The internal instability of fusion mostly happens in soils in which the distribution of grain size does not meet the requirements of self-filtering conditions, such as poorly graded soils (Wan and Fell 2002). Suffusion is the result of replacement and erosion of very fine soils that exist in a matrix of coarser particles by the eroding flow. The Comité Français des Grande Barrages (1997) reports several dam failures in France that were caused mainly by suffusion.

Von Thun (1996) describes seepage and piping failures as the primary dam safety problem in the western United States. Indeed, a study on the relative risk of failure of dams in the United States revealed that 60% of all failures of embankment dams higher than 15.2 m (50 ft) in the western United States were caused by piping.

### 1.1.2 Surface Erosion

Surface erosion occurs on the surface of the soil, such as in river beds and during overtopping flow of levees and embankments, wave action, and plunge pools. Similar to the erosion shown in Figure 1, surface erosion happens in three main stages:

1. A drag force and the resulting shear stress are developed on the surface at the interface between the soil particles/rock block and the eroding fluid.
2. The eroding fluid causes a decrease in the normal stress induced on the surface of the soil particles/rock block; that is, as the velocity of the eroding fluid increases in the space surrounding the soil particles, given to the rule of conservation of energy and Bernoulli’s principle, the normal pressure induced by the eroding fluid decreases to maintain the flow.

3. Due to the turbulence in the water, the normal stress and the induced shear stress on the hydraulic interface between the eroding fluid and soil fluctuate. At high velocities, these fluctuations create cyclic loading of the soil particle, which allows erosion to occur more easily (Croad 1981; Hofland et al. 2005).

The combination of the drag shear force, the uplift normal force, and their fluctuations acts together to remove the soil particle/rock block and initiate the surface erosion process.

The process outlined above is mainly observed in granular soils and fractured cohesive soils. In intact unfractured clayey soils, the individual clay particles can form microaggregates (from a single to dozens of micrometers) and macroaggregates (from dozens to thousands of micrometers) (Osipov et al. 1989). The erosion behavior of clayey soils depends on the presence of these micro and macroaggregates in the matrix, on the ability of the particles to coagulate, on the size and shape of the particles, and on the clay's ability to resist disaggregation when submerged in water. The nature and the magnitude of the structural or cohesion forces also play a very important role in understanding the erodibility of clayey soils. The strength of the structural forces can vary significantly and depends on their nature and on the soil properties.

Surface erosion is the key element in bridge scour. Scour around bridge supports is the most common cause of bridge failure (Arneson et al. 2012). More than 80% of all bridges in the United States (approximately 500,000 bridges) are located over water that highlights the significance of studying surface erosion. Studies have shown that in 60% of the cases where bridge collapse has happened, the failure was due to the scour at and beneath the bridge supports (Briaud et al. 1999).

## 1.2 Soil Erodibility and Constitutive Models

This project dealt with the first category of erodible materials defined by Briaud (2008): soils. It is well understood that knowledge of the erodibility of soil is the key step in probing and controlling the serious safety hazards caused by erosion, such as bridge scour, embankment and floodwall overtopping erosion, dam spillway erosion, and stream stability.

Despite the large number of contributions to soil erosion and despite the development of several testing methods, both in the field and in laboratories, no unified method for estimating the erodibility characteristics of soils has been achieved so far. One of the complexities in trying to unify methods of measuring erodibility is that some researchers have tested man-made soils to impose specific conditions or have reproduced field conditions in the lab, while others have tested samples collected from the field. Intact samples from the field and reproduced/remolded samples in the laboratory are often different in some aspects, such as stress history and chemical and organic content. These differences can sometimes lead to different erodibility characteristics. It is critical to learn about as many engineering properties of the tested soils as possible to achieve all different factors that influence the erosion resistance of soils.

The only way to come up with a common reliable model for estimating the erodibility characteristics of each soil is to first identify the major parameters involved in the erosion process. The erodibility of a material can be defined as the relationship between the erosion rate of the material ( $\dot{z}$ ) and the velocity ( $v$ ) of eroding fluid at the interface between the material and water.

$$\dot{z} = f(v) \quad (1)$$

where  $\dot{z}$  is the erosion rate (depth/time) and  $v$  is the velocity of eroding fluid (length/time).

Equation 1, however, is not satisfactory enough, because the velocity varies in direction and intensity in the flow field (Briaud 2008). Indeed, the water velocity profile reaches a value of zero

## 14 Relationship Between Erodibility and Properties of Soils

at the interface between the water and the soil. A more fundamental definition is the relationship between the erosion rate and the shear stress at the soil–water interface.

$$\dot{z} = f(\tau) \quad (2)$$

where  $\dot{z}$  is the erosion rate (depth/time), and  $\tau$  is the hydraulic shear stress at the interface (force/length square). However, the velocity is often used because it is easier to get a feel for velocity than for shear stress.

In an effort to normalize Equation 1, the erodibility of a soil can be defined as the relationship between the erosion rate  $\dot{z}$  and the mean depth velocity  $v$  of the water in excess of the critical velocity  $v_c$  (Figure 2). The following equation is proposed by Shafii et al. (2016) as an example of a relationship between soil erodibility and mean depth velocity:

$$\dot{z}/v_c = \alpha((v - v_c)/v_c)^m \quad (3)$$

where  $\alpha$  and  $m$  are unitless coefficients depending on the properties of the soil. Also, a normalized version of Equation 2 has been proposed:

$$\dot{z}/v_c = \alpha'((\tau - \tau_c)/\tau_c)^{m'} \quad (4)$$

where  $\alpha'$  and  $m'$  are unitless coefficients depending on the properties of the soil. The erosion function described by Equation 4 represents the constitutive law of the soil for erosion problems, much as a stress–strain curve would represent the constitutive law of the soil for a settlement problem. While a definition based on shear stress is an improvement over one based on velocity, it is still not completely satisfactory, as the shear stress is not the only stress that contributes to the erosion rate. Indeed, the fluctuations in normal stress and shear stress due to turbulence intensity apply pulsations that can suck the soil particle or cluster of soil particles out of position and then entrain it in the flow through the drag force. A more complete description of the erosion function is proposed in Equation 5 (Shafii et al. 2016):

$$\frac{\dot{z}}{v} = \alpha \left( \frac{\tau - \tau_c}{\rho v^2} \right)^m + \beta \left( \frac{\Delta \tau}{\rho v^2} \right)^n + \gamma \left( \frac{\Delta \sigma}{\rho v^2} \right)^p \quad (5)$$

where

$\dot{z}$  = erosion rate (mm/h),

$v$  = mean depth water velocity (m/s),

$\tau$  = hydraulic shear stress ( $N/m^2$ ),

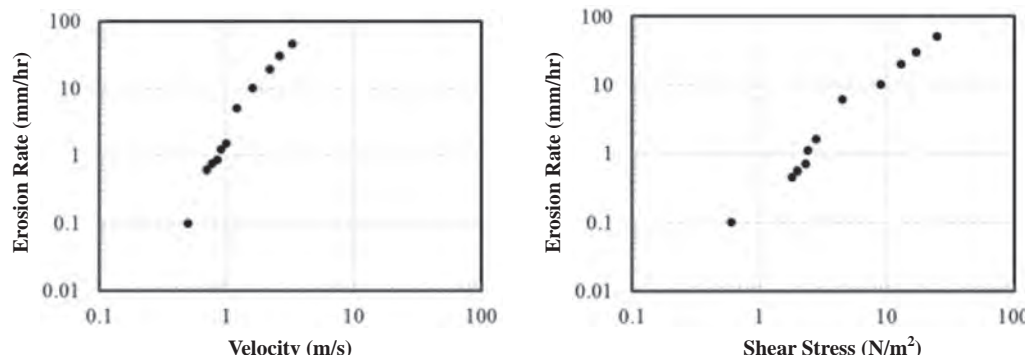


Figure 2. Examples of erosion function (Briaud 2013).

$\tau_c$  = threshold or critical shear stress ( $N/m^2$ ) below which no erosion occurs,

$\rho$  = mass density of water ( $kg/m^3$ ),

$\Delta\tau$  = turbulent fluctuation of hydraulic shear stress ( $N/m^2$ ), and

$\Delta\sigma$  = turbulent fluctuation of net uplift normal stress ( $N/m^2$ ).

All other quantities are parameters characterizing the soil being eroded. While this model is quite thorough, it is rather impractical at this time to determine all the parameters needed in Equation 5 on a site-specific and routine basis. At present, Equations 3 and 4 are broadly accepted and form the basis of this project (Shafii et al. 2016). After using a video analysis technique to investigate and measure the hydrodynamic forces on gravel particles, Shafii et al. (2019) have recently introduced a more practical erosion model:

$$\frac{\dot{z}}{0.1} = \left( \frac{\tau}{\tau_c} \right)^\alpha \times \left( \frac{\sigma}{\sigma_c} \right)^\beta \quad (6)$$

where

$\dot{z}$  = erosion rate ( $mm/h$ ),

$\tau_c$  = critical shear stress ( $Pa$ ) associated with an erosion rate of  $0.1\ mm/h$ ,

$\sigma_c$  = critical normal stress ( $Pa$ ) associated with an erosion rate of  $0.1\ mm/h$ , and

$\alpha$  and  $\beta$  = unitless erosion model parameters.

Equation 6 is expected to capture the influence of both shear and normal stresses during erosion.

One example application of erosion functions is to model the development of scour holes in bridges. Li et al. (2002) at Texas A&M University (TAMU) developed a method for calculating the maximum scour depth around bridge piers. In this method, the eroding flow generates a shear stress on the soil–water interface that initiates the scour. The shear stress generated at the bottom of the scour hole decreases as the scour depth increases. This process continues until there is an equilibrium depth in which the erosion resistance of the soil (critical shear stress) at the soil–water interface equals the shear stress imposed by the eroding flow. This idea has recently been endorsed by the Federal Highway Administration (FHWA).

## 1.3 Erodibility Parameters

The erosion functions presented in Section 1.2 (Equation 2 to Equation 6) can all be used to help quantify the erosion behavior of soils; however, none of these equations has been able to capture erodibility with 100% accuracy. Therefore, the model parameters defined in these equations (i.e.,  $\alpha'$  and  $m'$  in Equation 4;  $\alpha$  and  $\beta$  in Equation 6) cannot be determined definitively. One of the important goals of this study was to organize and analyze many different erosion test results in a way such that these data would become comparable. The following erodibility parameters have been used because they are widely accepted among hydraulic and geotechnical engineers and have simple and easily understood definitions.

### 1.3.1 Erosion Rate

The erosion rate of a soil can be identified in many different ways, depending on the erosion testing method. This rate can be generally expressed in three main forms:

1. Rate of change in the depth of a soil surface under a specific hydraulic shear stress induced by the eroding fluid flow (e.g., erosion function apparatus, jet erosion test, etc.);

## 16 Relationship Between Erodibility and Properties of Soils

2. Rate of change in the soil volume during a specific time period while the soil is subjected to a hydraulic shear stress induced by the eroding fluid flow; and
3. Rate of change in the eroded soil mass, which is sometimes presented as the rate of mass removal per unit area (e.g., hole erosion test).

### 1.3.2 Slope of Erosion Function

Another important erodibility parameter is the normalized erosion rate against the flow velocity or the hydraulic shear stress. As shown in Figure 2, the result of an erosion test can be presented in two different forms: erosion rate versus velocity and erosion rate versus hydraulic shear stress. There are different methods for determining the slope of erosion function. In this report, the slope of the erosion rate versus velocity curve is designated as  $E_v$ , and the slope of erosion rate versus shear stress is designated as  $E_\tau$ . In Chapter 5, the procedure for determining  $E_v$  and  $E_\tau$  is detailed for each test result.

### 1.3.3 Critical Velocity/Shear Stress

Critical velocity/shear stress refers to the initiation of the erosion process. Basically, the critical velocity ( $v_c$ ) in an erosion test refers to the maximum velocity that the soil can resist without getting eroded. In terms of the hydraulic shear stress, this value is known as “critical shear stress” ( $\tau_c$ ). Depending on the type of erosion test, researchers have used different definitions and different techniques to identify the critical velocity and critical shear stress. In this study, critical velocity and critical shear stress were determined by using the same procedure independent of the type of erosion test. This procedure is discussed in Chapter 5.

### 1.3.4 Erosion Category

Briaud (2008) and Hanson and Simon (2001) developed category charts to make it easier to identify the erodibility of soils. Figure 3 shows the erosion categories developed by Briaud (2008) in his 2007 Ralph B. Peck Lecture. In that chart, the erosion categories are bound by lines in the  $\dot{z}$  versus  $v$  and the  $\dot{z}$  versus  $\tau$  plots. These charts were based on many years of erosion testing at TAMU. The lines giving the boundaries between categories originate at the critical velocity and critical shear stress. Table 1 shows the critical values for the velocity and the shear stress for each erosion category in Figure 3.

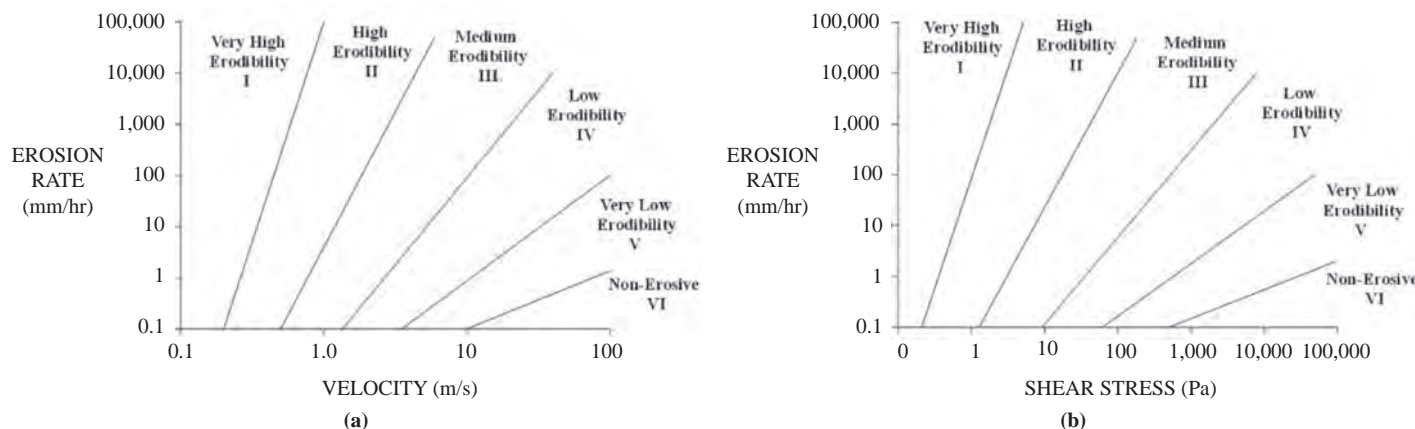


**Figure 3.** Erosion categories for soils and rocks on basis of (a) velocity and (b) shear stress, as proposed by Briaud (2008).

**Table 1. Threshold velocity and shear stress associated with each erosion category.**

Category Number	Erosion Category Description	$v_c$ (m/s)	$\tau_c$ (Pa)
I	Very high erodibility geomaterials	0.1	0.1
II	High erodibility geomaterials	0.2	0.2
III	Medium erodibility geomaterials	0.5	1.3
IV	Low erodibility geomaterials	1.35	9.3
V	Very low erodibility geomaterials	3.5	62.0
VI	Nonerosive materials	10.0	500.0

Source: Briaud 2008.

## 1.4 Research Approach and Project Tasks

The goal of this project was to develop reliable and simple equations that link the erodibility of soils to commonly determined soil properties. The use of the results is to provide valuable input in erosion studies on topics such as bridge scour, river meander migration, roadway embankment overtopping, and others. The equations optimize the balance between reliability and simplicity. Reliability must take into account the accuracy required for highway projects, while simplicity must consider the economic aspects of such projects. During this study, the following seven tasks were accomplished:

1. Identification of current knowledge on erosion and soil properties;
2. Identification of current soil erodibility data correlations;
3. Assessment of current and promising erosion tests;
4. Performance of erosion tests with different devices on the same soils;
5. Performance of erosion tests on many different soils to develop erodibility equations;
6. Development of regression equations and validation; and
7. Verification, synthesis, and analysis of all data to propose the best solution.

### 1.4.1 Identification of Current Knowledge on Erosion and Soil Properties

Defining erodibility was the first step. Soil erodibility is not a single number, but a relationship between the hydraulic load (water velocity or shear stress) and the soil resistance (erosion rate). The relationship equations proposed in this study link the elements of the erosion function (critical velocity, critical shear stress, and initial slope of the erosion rate versus velocity or shear stress curve) to various soil properties.

In the identification of current geotechnical laboratory tests, this study focused on the most typically obtained soil properties in regression equations. Among those soil properties are mean grain size, plasticity index, water content, percentage passing the #200 sieve, unit weight, and undrained shear strength. In the identification of current practices for testing erosion, the objective was to learn about all of the available erosion testing devices and then to focus on the most commonly used erosion tests, both in the laboratory and in the field. This knowledge is documented in Chapter 2 of this report.

### **1.4.2 Identification of Current Soil Erodibility Data Correlations**

In the identification of current erodibility data correlations, available data on the following subjects were collected: soil erodibility parameters (i.e., critical velocity, critical shear stress, initial slope of the erosion rate versus velocity or shear stress curve), and common soil properties. The existing erodibility correlations are documented in Chapter 3 of this report. Additionally, a global spreadsheet developed as part of this study is presented in Chapter 5.

### **1.4.3 Assessment of Current and Promising Erosion Tests**

The most commonly available laboratory and in situ erosion tests are reviewed in Chapter 2. Each test has advantages and limitations. These tests were also assessed with respect to issues such as the range of soil types that can be tested, the cost of the test, the cost of the device, and the best applications. These comparisons help the engineer select the best tests for a given situation. The assessment is documented at the end of Chapter 2.

The critical issue associated with these different devices and tests is that they do not give the same erosion parameters; that is, they do not lead to the same type of results. To solve this problem, numerical simulations were used. These simulations led to a common data reduction process of erosion tests and a common output of all erosion tests, brought uniformity to erosion studies, and kept all soil erosion testing options open for the engineer. Information on the numerical simulations is documented in Chapter 6 of this report.

### **1.4.4 Performance of Erosion Tests with Different Devices on the Same Soils**

This task was dedicated to testing the same soil with different erosion testing devices. The soils tested were man-made soils because the use of such soils was the only way to be sure that identical and reproducible samples could be prepared and tested. These soils included, at a minimum, a gravel, a compacted sand, a compacted silt, and a compacted high-plasticity clay. All soil properties tests, all pocket erodometer tests, and all erosion function apparatus, jet erosion, and borehole erosion tests were performed at the Erosion Laboratory at TAMU. For the in situ tests, the borehole erosion test and the pocket erodometer test were conducted at the RELLIS sand and clay sites at TAMU. These results are documented in Chapter 4 of this report.

### **1.4.5 Performance of Erosion Tests on Many Different Soils to Develop Erodibility Equations**

This task was dedicated to testing the different soil samples with different erosion testing devices at TAMU. The data obtained from the erosion tests performed during this project, along with data collected from all over the world, were used to develop the regressions equations. Chapter 4 of this report as well as Appendices 1 and 2 document the results of the erosion and geotechnical tests performed in this study. [Note: Five appendices to *NCHRP Research Report 915* are gathered in an Appendices Report that is available on the NCHRP Project 24-43 page on the TRB website ([trb.org](http://trb.org)).]

### **1.4.6 Development of Regression Equations and Validation**

This task was dedicated to developing regression equations correlating the erodibility parameters and the geotechnical properties of soils. Two major statistical methods were used:

1. A frequentist approach with plots of probability of overpredicting and probability of underpredicting for the selected models. As part of this approach, first- and second-order statistical

analyses were conducted. This analysis was followed by regression and optimization techniques (i.e., cross validation).

2. A probabilistic approach using Bayesian inference. The main benefit of the use of Bayesian inference is the definition of a metric of confidence on the model predictions. The results of these statistical approaches are extensively documented in Chapter 7 of this report and in Appendices 3 to 5.

#### **1.4.7 Verification, Synthesis, and Analysis of All Data to Propose the Best Solution**

Once all the testing and the statistical/correlation analysis were conducted, all aspects of the project were synthesized and analyzed to present a complete solution package to address the main objective of this research. Also, the classification charts presented in Figure 3, which link the likely soil erosion function to the soil classification as a first step in any soil erosion problem, were updated. These results are documented in Chapter 8 of this report.



## CHAPTER 2

# Existing Erosion Tests

This chapter describes some of the most common tests developed over the past century to quantify soil erodibility. The drawbacks and advantages of these testing methods are evaluated and identified. Generally, erosion testing is divided into the following two types:

1. Laboratory erosion testing and
2. Field erosion testing.

The erosion tests presented in this chapter are divided into two sections: laboratory tests and field tests. Some of the erosion tests have applications in both the laboratory and the field; however, they are discussed only once, in either Section 2.1 or Section 2.2.

## 2.1 Laboratory Erosion Testing

### 2.1.1 Erosion Function Apparatus

In the early 1990s, the idea of the erosion function apparatus (EFA) was first developed and established by Briaud at Texas A&M University (TAMU) (Briaud et al. 1999, 2001a, 2001b). Today, the EFA is being manufactured by Humboldt, Inc., and is used widely by many engineering organizations. This test was originally developed to evaluate the erodibility of a wide range of both cohesive and noncohesive soils, including gravel, sand, clay, and silt. Figure 4 shows a schematic diagram and image of the EFA device.

Soil samples are taken by using ASTM standard Shelby tubes with an outside diameter of 76.2 mm (ASTM D1587). With soft rocks, a rock core sample can be extracted and placed into a Shelby tube for rock erosion testing. A pump is used to drive water, the eroding fluid, into a 1.2-m-long rectangular cross section of  $101.6 \times 50.8$  mm, as shown in Figure 4. The water flow can be adjusted with a valve, and the average water velocity is measured by a flow meter in line with the flow. One end of the Shelby tube is placed on the bottom of a circular plate that is connected to a piston. The piston is designed to push the sample up into the flow when necessary. The sample is pushed upward until it becomes flush with the bottom of the rectangular cross section pipe.

The test procedure is as follows (Briaud et al. 2001b):

1. Place one end of the Shelby tube on the circular plate piston and push it up until it becomes flush with the bottom surface of the rectangular cross-section pipe.
2. Fill the rectangular pipe with water and wait for 1 hour.
3. Initiate the flow with a small flow velocity, typically 0.2 m/s.
4. Start recording time. Hold the sample surface flush with the bottom of the rectangular pipe during the induced flow velocity. The test operator needs to make sure that the soil surface

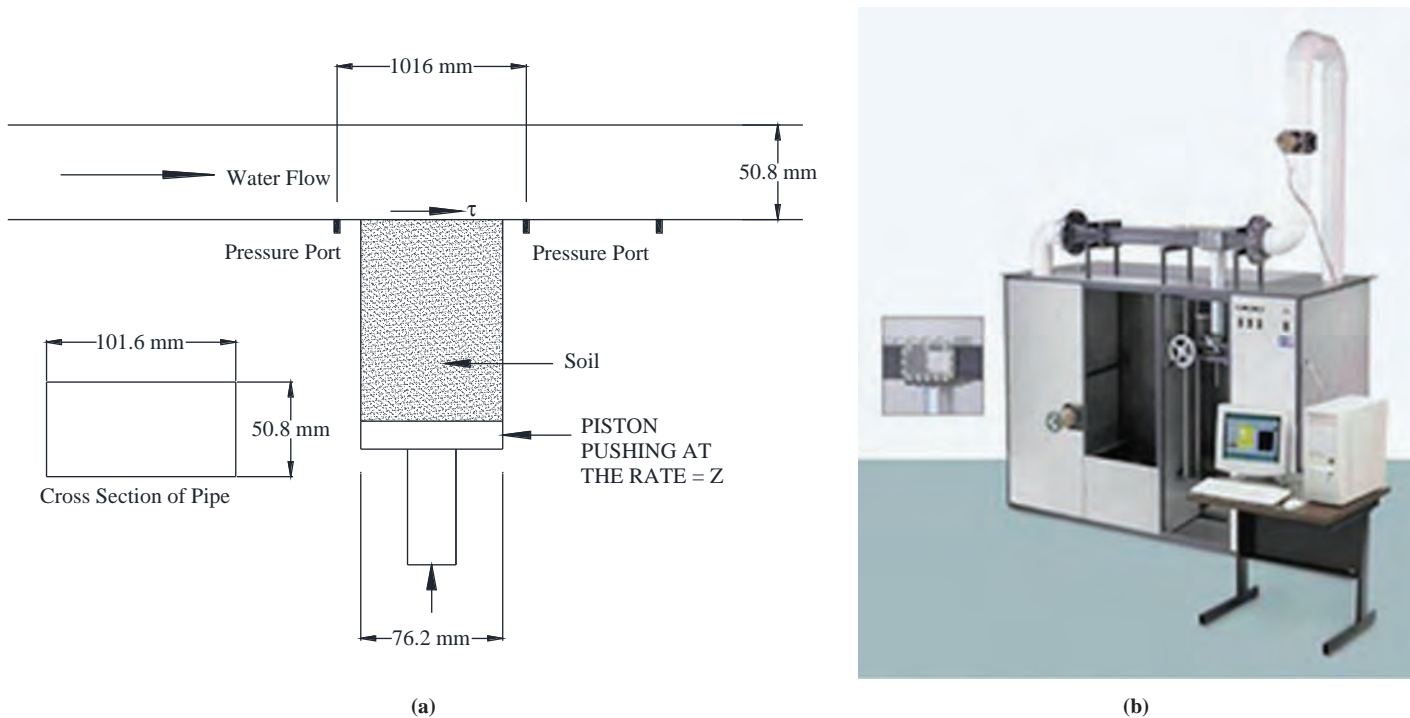


**Figure 4.** EFA: (a) schematic diagram and (b) image (courtesy of TAMU).

is kept flush at all times by pushing the soil with the piston as it is eroded by the water and maintaining a level interface. Continue this procedure until 50 mm of the soil is eroded or 30 min have passed. Read the protrusion height by observing the change in the height of the bottom of the piston.

5. Repeat Steps 3 and 4 for a new and higher flow velocity (i.e., 0.2 m/s, 0.6 m/s, 1 m/s, 1.5 m/s, 2 m/s, 3 m/s, 4.5 m/s, and 6 m/s).

The scour rate versus flow velocity is plotted. Figure 2 (Chapter 1) shows an example of EFA test results as both erosion rate versus velocity and erosion rate versus shear stress. The shear stress on the eroded surface of the soil is calculated by using the Moody chart (Moody 1944).

$$\tau = \frac{1}{8} f \rho v^2 \quad (7)$$

where

$\tau$  = shear stress (Pa),

$\rho$  = density of water ( $1,000 \text{ kg/m}^3$ ),

$v$  = flow velocity (m/s), and

$f$  = friction factor obtained from Moody chart.

### Advantages

1. Minimize the sample disturbance effect, as it takes the sample directly from the field using Shelby tubes.
2. Can be used for natural samples as well as man-made samples.
3. Gives the critical velocity and the critical shear stress. Can give the erosion function directly.
4. EFA test results are directly used as input to the TAMU-SCOUR method for bridge scour depth predictions [see Hydraulic Engineering Circular No. 18 (Arneson et al. 2012, Chapter 6)].

## 22 Relationship Between Erodibility and Properties of Soils

5. The EFA can test the erodibility of the soil at any depth as long as a sample can be recovered.
6. While the EFA test is a surface erosion test, it can be used to evaluate internal erosion as well, because the EFA erosion function represents the erodibility of the soil at the element level.
7. The EFA can be used to test from very soft to very hard soils. This test has very broad applications.

### Drawbacks

1. Shear stress is indirectly measured from the average velocity according to the Moody chart, so the measurement might not be accurate. Also, the average flow velocity is used in the calculations instead of the actual velocity profile.
2. In cases in which field samples are required, obtaining samples is difficult and costly. The test needs to be done on the sample before the sample is affected by long periods of storage.
3. Particles larger than 40 mm cannot be tested with confidence, as the diameter of the sampling tube is 75 mm.
4. The EFA is a fairly expensive device (around \$50,000 to purchase).

Several other organizations have utilized the concepts and principles of the EFA and developed similar devices, such as the Sediment Erosion Rate Flume (SERF) and the ex situ scour testing device (ESTD), which are also presented in this chapter.

### 2.1.2 Sediment Erosion Rate Flume

The SERF was developed by Sheppard and his colleagues at the University of Florida to measure the erodibility of cohesive and noncohesive sediments (Trammel 2004). Figure 5 shows a schematic diagram and photograph of the SERF.

The SERF has a 9-ft-long rectangular channel with dimensions of  $5.08 \times 20.32$  cm elevated at 5.5 ft that is fed by two 500-gallons-per-minute parallel pumps from a large 1,100-gallon water tank. The flow channel is designed to have a 1-ft straightener in the beginning to reduce the turbulence of the water discharge. The specimen cross section is placed in the center of the rectangular channel at the base of the flume. Flow is driven through a 3-ft-long channel and right after reaches the specimen's cross section. It then proceeds another 4 ft of the channel and is directed to the reservoir tank. The reason that two pumps are used is to account for harder

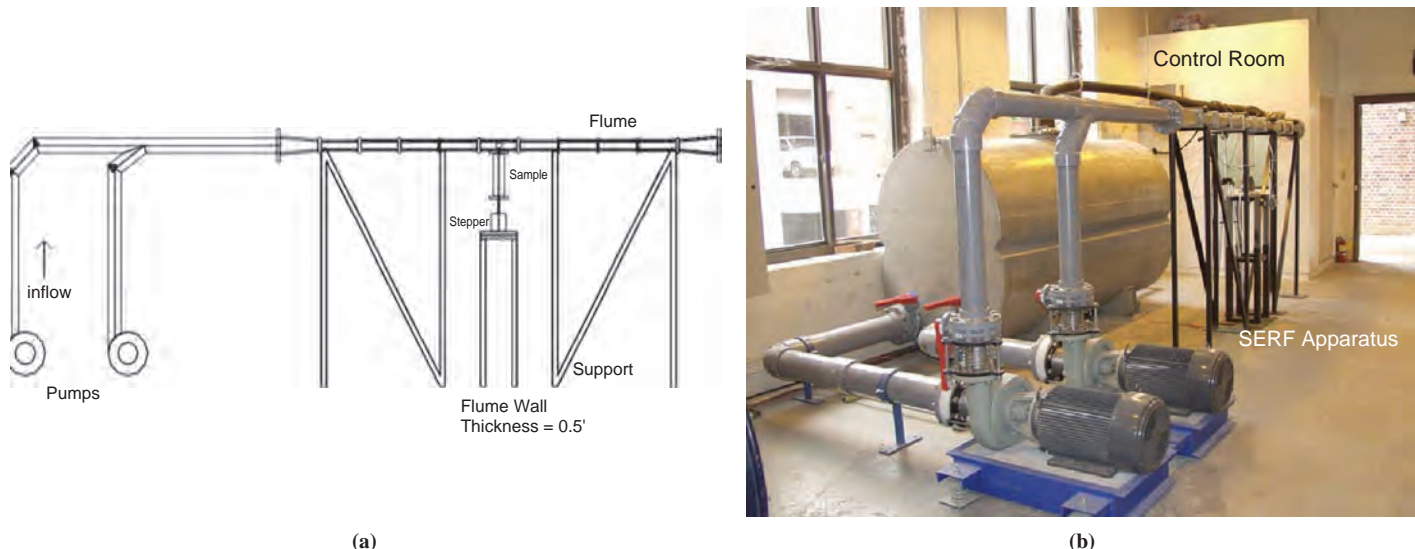


**Figure 5. SERF apparatus at the University of Florida (a) schematic diagram and (b) photograph (Trammel 2004).**

soil samples, for which both pumps can be running. Also, erosion of the Shelby tube size sample is continuously monitored by the control computer with a video camera attached next to the test section. An array of sonic SeaTek transponders is attached at the top of the flume right above the test section; these transponders give the mean elevation of the sample surface, which is used to prompt the computer to advance the piston and keep the sample surface flush with the bottom of the flume. Basically, the SERF is controlled and monitored automatically by computer software. The summation of upward movements recorded and steps by the motor for a specific flow velocity (shear stress) divided by that particular time period reflects the erosion rate.

SERF includes pressure ports at 2 ft upstream and downstream from the center of the test section. The pressure drop in the flume is calculated with the following equation:

$$\tau = \frac{(\Delta p \times \text{area})}{(2w + 2h) \times L} \quad (8)$$

where

$\tau$  = hydraulic shear stress (Pa),

$\Delta p$  = recorded pressure drop (Pa),

area = cross-section area of the rectangular channel,

$L$  = distance between pressure ports (4 ft), and

$2w + 2h$  = hydraulic radius in the channel.

In addition to similar advantages mentioned for the EFA, the SERF is independent of the operator and runs with an automated system.

### **Advantages**

1. Can be used for natural and man-made samples.
2. Can give the erosion function directly.
3. Runs with an automated system.

### **Drawbacks**

1. The SERF is no longer being used; the device requires a bulky setup.
2. The automation of the process requires the use of very expensive instruments that also require significant expertise when they break down or need to be adjusted.
3. The samples have to be prepared in the cylinder of the test device. This limits the use of the SERF to disturbed or man-made samples.

### **2.1.3 Ex Situ Scour Testing Device**

The ESTD was developed by Kerenyi and his colleagues at the Federal Highway Administration (FHWA) Turner–Fairbank Highway Research Center (Shan et al. 2015). The purpose was to simulate the velocity profile for open channel conditions. Figure 6 shows a schematic diagram along with a photograph of this test device.

A cylindrical soil specimen with a diameter of 63.5 mm and height of 15 mm is placed on the top of a direct force gauge. A 580-mm rectangular channel with dimensions of 12 × 2 cm connects the inlet tank to the outlet tank. As with the EFA, a flow meter is attached to the device to measure the flow velocity in the channel. A moving belt, as shown in Figure 6, is used to entrain the water and reproduce the expected log-law velocity profile in the field. The roughness of the channel is controlled by attaching a range of wide grit of sandpapers to the bottom of the channel surface. Instead of calculating the hydraulic shear stress at the interface of the eroding fluid and the soil indirectly from velocity or pressure drop, a direct force gauge is used

## 24 Relationship Between Erodibility and Properties of Soils

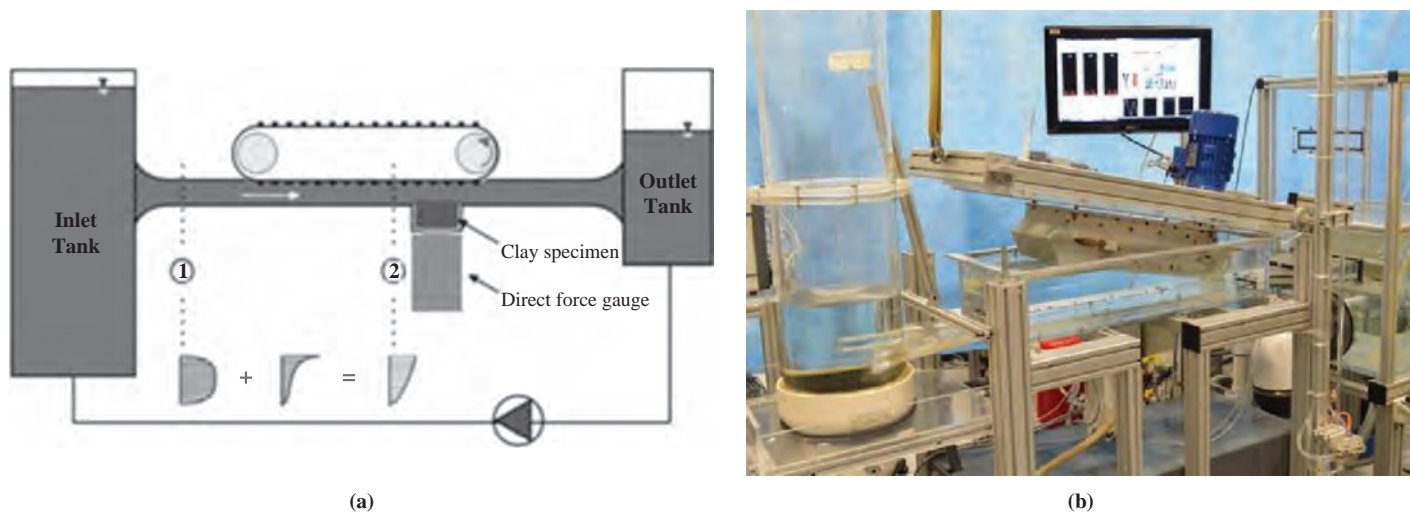


**Figure 6.** ESTD: (a) schematic diagram and (b) photograph (Shan et al. 2015).

to instantaneously capture both normal forces and shear stress induced on the soil surface. Samples for the ESTD are prepared in the lab, typically with a Pugger-Mixer, which prevents the existence of air bubbles in the specimen. Samples are left in water to slake before the ESTD test is performed. The advantages and drawbacks of the ESTD are listed below.

### Advantages

1. The ESTD is automated.
2. The ESTD is designed to reproduce an open channel flow condition.
3. The existence of sensors that measure the vertical force and shear stress directly is very helpful.
4. The effect of turbulence can be studied more precisely by using the results of the vertical force on the interface.

### Drawbacks

1. Setting up the ESTD is time consuming (up to 2 days).
2. The ESTD cannot reflect actual field conditions, as the soil specimens are all handmade in the lab; that is, an intact sample from the field cannot be tested directly in the ESTD.

### 2.1.4 Sediment Erosion at Depth Flume

The High Shear Stress flume, or SEDflume (sediment erosion at depth flume), was originally developed at the University of Santa Barbara for the purpose of measuring sediment erosion at high shear stress and with shallow depth (McNeil et al. 1996). It has been used by researchers for coastal applications and by the U.S. Army Corps of Engineers. The primary application of this device is studying the sediment transport and suspension rate during high-stress floods. Figure 7 shows a schematic diagram and photograph of the SEDflume.

The channel of the flume is 120 cm long, and the rectangular cross section is 10 × 2 cm, as shown in Figure 7. The SEDflume also exists as a portable lab that can be moved to a site. At the end of the straight channel is a 15-cm-long section where the top of the soil sample is exposed. The rectangular soil sample is 1 m long and has cross-section dimensions of 15 cm long × 10 cm wide. Test samples are either collected directly from the site or recreated in the lab by using a sediment slurry. In deeper waters, divers might be needed to place the coring tube

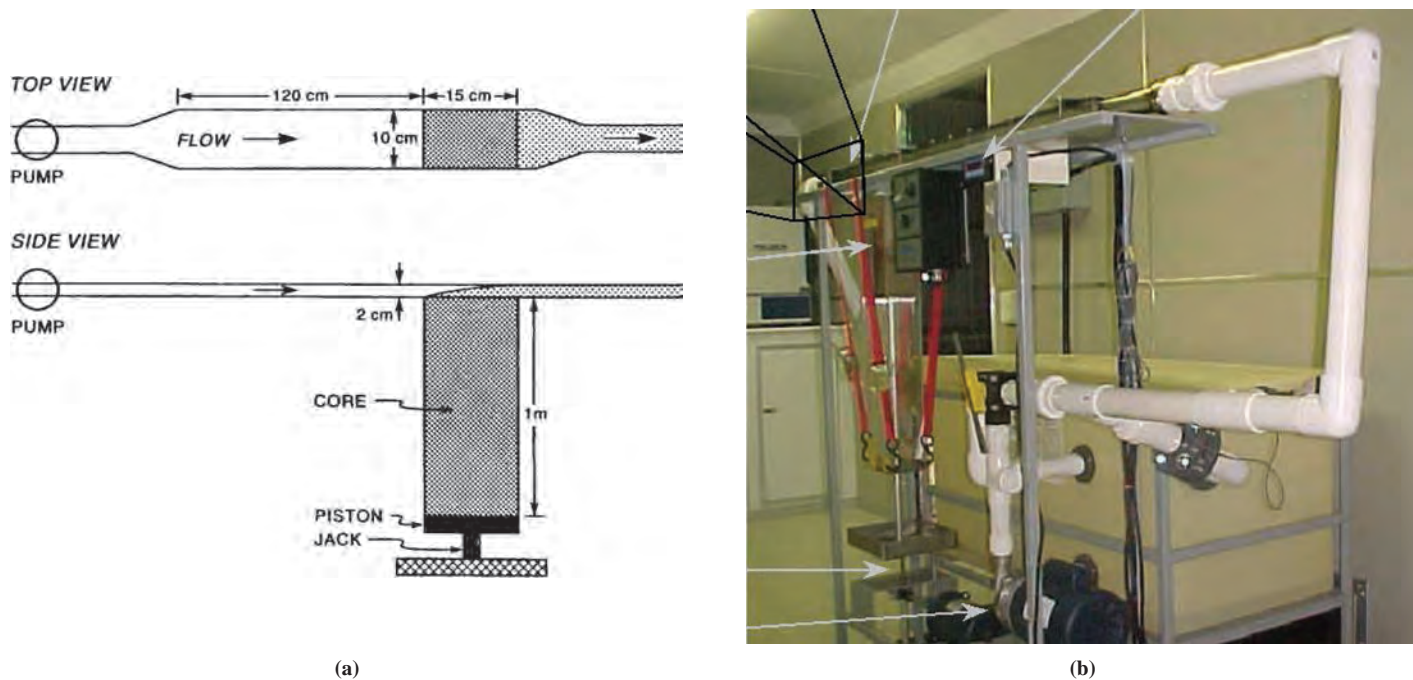


**Figure 7. SEDflume: (a) schematic diagram (McNeil et al. 1996) and (b) photograph (U.S. Army Corps of Engineers).**

and extract a sample from the site. In soft soils, the sampler can be pushed into the soil, whereas in stiffer soils, a Vibracoring head can be used. The test sample is then placed on a piston with a hydraulic jack, which is used to manually adjust the height of the sample. As with the EFA, the operator needs to keep the sample flush with the flume surface. The flow also is adjusted by a valve, and a flow meter is attached to the flume to measure the flow rate of the eroding fluid. Water that is powered by a pump flows into the flume, and testing proceeds in the following steps (McNeil et al. 1996):

1. Place one end of the rectangular coring tube on a piston located at the bottom of the test section.
2. Use the piston to extrude the sample upward until it becomes flush with the bottom of the flume surface.
3. Make sure that as the soil surface erodes, a level interface is maintained between the sample and the bottom of flume surface.
4. Record the amount of eroded sediments by recording the upward movement of piston.
5. Repeat Steps 2 to 4 for higher flow velocities and, thus, higher shear stress values.

As is done for the EFA, the shear stress is calculated with Equation 7. The advantages and drawbacks of the SEDflume are as follows:

#### **Advantages**

1. The field version helps minimize the sample disturbance effect. Also, with the field version, the existing water in the field can be used in the test.
2. The SEDflume directly measures the erosion rate versus shear stress curve from the field and determines the critical shear stress

#### **Drawbacks**

1. The shear stress calculation is based on the mean flow velocity and the use of the Moody chart instead of on direct measurements.

## 26 Relationship Between Erodibility and Properties of Soils

2. The lab apparatus is very bulky and costly (more than \$100,000). Preparation of samples is time consuming, as is the test setup in the field.
3. Only disturbed or reconstructed samples can be tested.
4. There are several limitations in sample collection, especially for offshore conditions.

Roberts et al. (2003) developed a device similar to the SEDflume called the Adjustable Shear Stress Erosion and Transport (ASSET) Flume. The ASSET Flume was designed to be larger than the SEDflume to overcome a problem common to all flume tests: the effects of the channel wall on the flow. The other difference between the ASSET Flume and the SEDflume is that in the ASSET Flume, the eroded sediments are collected and then dried to obtain the bed load and suspended fractions in the flume.

### 2.1.5 Some Other Flume Tests

In addition to the EFA and similar tests, several researchers have performed flume tests to study the erodibility potential of different soils. Gibbs (1962) conducted some large-scale flume tests in the laboratory on intact soil samples [mostly clay of low plasticity (CL) and silt (ML)] from canal banks. The purpose of his tests was to investigate the influence of different plasticity properties and in situ density of the soils on the erosion resistance of these soils. Gibbs' findings are summarized in the next chapter of this report.

A few years later, Lyle and Smerdon (1965) of TAMU constructed a laboratory flume test to study the effect of soil properties (especially compaction) on the erosion resistance of soils. They conducted erosion tests on seven Texas soils in a 22-m-long hydraulic flume with a 76- × 40-cm cross-sectional area. The slope of the flume was 0.2%. The 5.5-m-long sample soil was placed in the center cross section of the flume. The velocity of the water flow was measured by using six pitot tubes installed at six different points of the flow. The depth of flow was also measured accurately by using 17 piezometers along the flow channel. The shear stress induced on the eroded surface was calculated as the product of the hydraulic gradient and water unit weight. Lyle and Smerdon then defined the critical shear stress as the shear stress that initiates the erosion of the soil. The samples that were replicated by using the suspended samplers during each increase in the flow were tested in the lab, and the plasticity index and void ratio (compaction) were recorded. The critical shear stress was then plotted against the compaction and plasticity properties of the soil. The findings of Lyle and Smerdon (1965) are discussed further in the next chapter of the report.

Kandiah and Arulanandan (1974) also used flume tests to study the erodibility of Yolo clay loam. The main purpose of their research was to compare the erodibility results obtained from the flume test and the rotating cylinder test. Also, the effect of compaction and water content on the critical shear stress was investigated. Some of Kandiah and Arulanandan's findings are discussed in the next chapter of this report.

Arulanandan and Perry (1983) studied the erodibility potential of dam core materials used for better representing the common dam filter design method that was being practiced during that time. To quantify the critical shear stress imparted on the cracks within the core of the dam, Arulanandan and Perry used both flume tests and rotating cylinder tests.

Research on evaluating soil properties continued, and different researchers used different approaches to find the erodibility parameters. Shaikh et al. (1988a) performed flume tests to evaluate the influence of clay material and compaction of soil on the erosion resistance of soils. To do so, they constructed a 250-cm-long rectangular channel with a 15.5- × 11-cm cross section (see Figure 8). The slope of the flume was adjustable. As shown in Figure 8, three samples that were 15.2 cm long with a 10.5- × 2.25-cm cross section could be tested at the

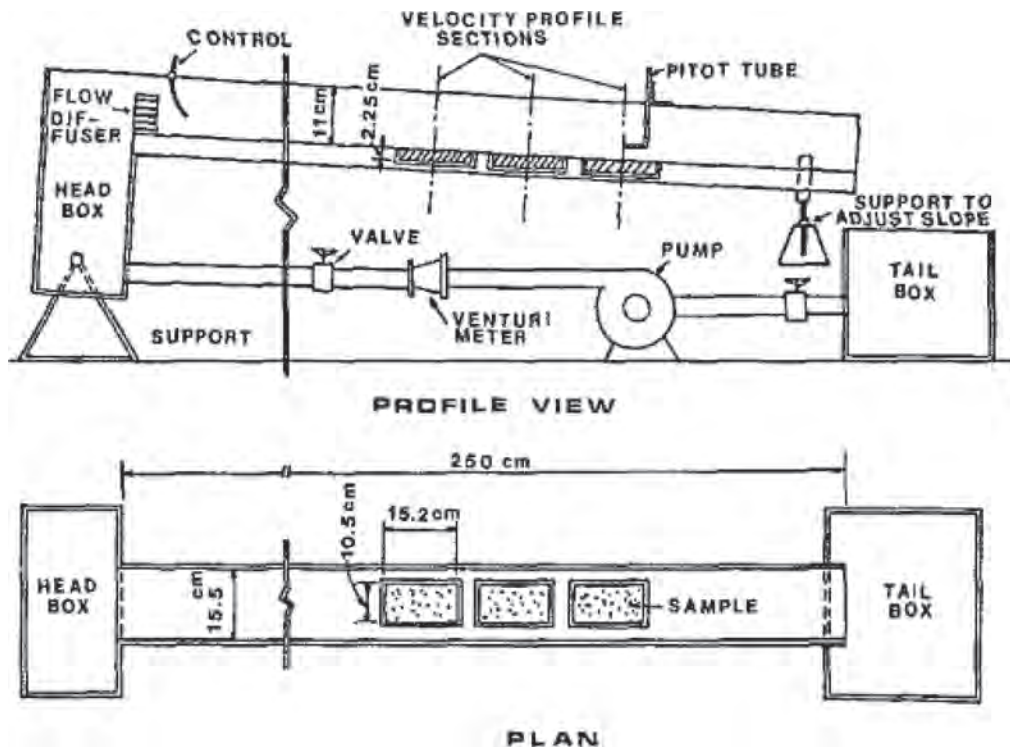


**Figure 8.** Schematic diagram of flume test used by Shaikh et al. (1988b).

same time with the same slope. The flow depth could be adjusted between 80 cm and 210 cm. The flow velocity was also measured with a pitot tube, as shown in Figure 8.

Chow (1959) calculated the shear stress induced on the surface of the sample by using the smooth channel flow equation:

$$\frac{V}{V^*} = 5.5 + 5.75 \log \left( \frac{V^* \times y}{\nu} \right) \quad (9)$$

where

$$V^* = \text{shear velocity} \left( \frac{\tau}{\rho_w} \right),$$

$V$  = velocity of flow at a depth  $y$  in the turbulent zone,

$\rho_w$  = water density, and

$\nu$  = viscosity of water.

Shaikh et al. (1988a) defined the erosion rate as the rate of weight removal in a given time. Then they could plot the erosion rate ( $N/m^2/min$ ) versus hydraulic shear stress (Pa).

Six years later, Ghebreiyessus et al. (1994) developed a new enclosed flume test to study soil resistance to erosion as well as the influence of geotechnical parameters in soil erodibility. For this purpose, a 250-cm-long rectangular flume with a 20.3- × 2.5-cm cross section was constructed (Figure 9). The flume dimensions were selected to generate a steady flow condition according to Chow's (1959) equations.

The test samples were cylindrical, with a 10.2-cm inner diameter and were mounted on a mechanical piston to maintain a level interface with the bottom surface of the flume. Erosion

## 28 Relationship Between Erodibility and Properties of Soils

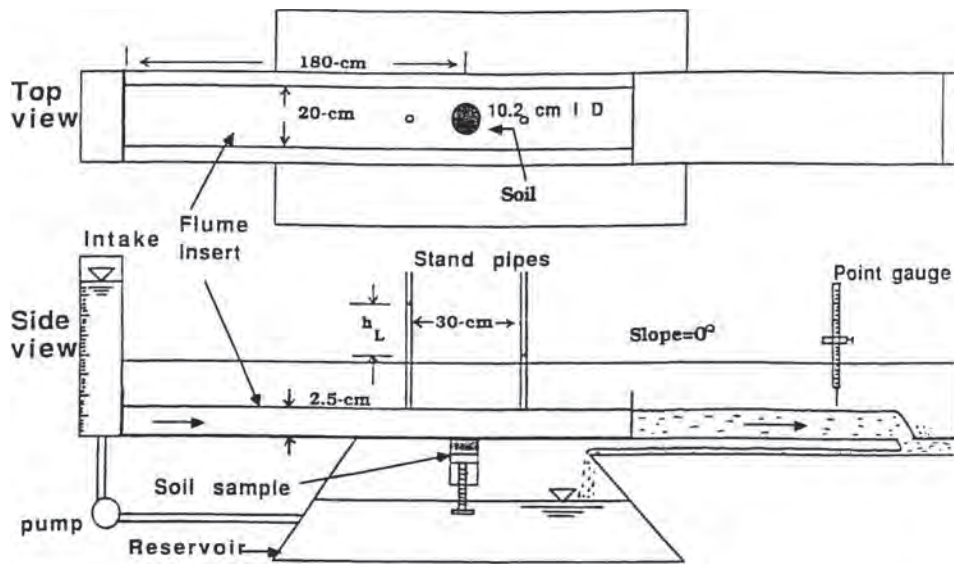


**Figure 9. Schematic diagram of constructed enclosed flume (Ghebreiyessus et al. 1994).**

rates were calculated as the rate of dried mass removal in a given time. The shear stress on the soil sample was predicted as

$$\tau = \frac{\gamma_w \times h_L \times R}{L} \quad (10)$$

where

$\tau$  = hydraulic shear stress (Pa) on the soil surface;

$h_L$  = head loss (m) measured by using two standpipes, one at each side of the sample;

$R$  = hydraulic radius (m) of the flume;

$L$  = length (m) of flume; and

$\gamma_w$  = unit weight ( $\text{N/m}^3$ ) of water.

Several other attempts were also made to develop a flume erosion-testing apparatus. Some examples are the attempts made at Georgia Institute of Technology by Navarro (2004), Hobson (2008), and Wang (2013) to modify the EFA method.

### 2.1.6 Jet Erosion Test

The jet erosion test (JET), which can be credited to Hanson (1990a, 1990b), was developed at the U.S. Department of Agriculture, Agricultural Research Service. Hanson first developed this testing device for the purpose of measuring soil erodibility in situ. The JET was standardized as ASTM D5852 in 1995 and includes both in situ and lab versions. It included a nozzle with a diameter of 13 mm, which was held 22 cm away from the center of soil surface. Figure 10 shows a schematic diagram and photograph of the in situ version of the JET apparatus. A pin profiler is used after each jet sequence to read the change in the depth of the hole made in the soil by the jet (Hanson 1990a, 1990b).

The JET has been modified since its inception. Hanson and Hunt (2007) developed a new laboratory version of the JET apparatus. The circular jet submergence tank in this version has a diameter of 305 mm and a height of 305 mm. Scour readings are made by using a point gauge

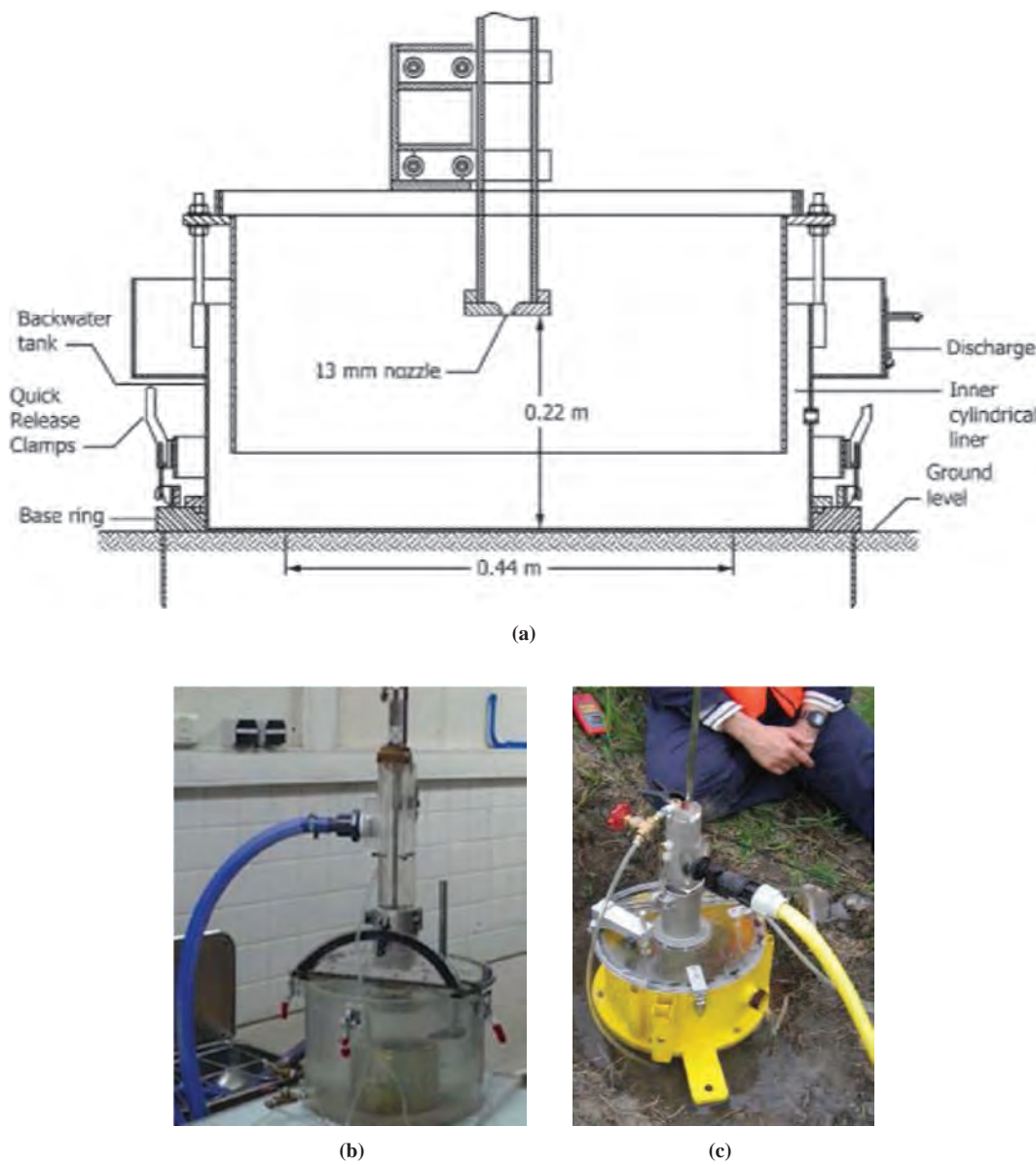


**Figure 10.** JET: (a) schematic diagram of submerged JET apparatus for field testing (ASTM D5852-95) and photographs of (b) lab version of JET (Hanson and Hunt 2007) and (c) in situ version of JET (Hanson and Cook 2004).

that is aligned with the orifice and measures the scour in the center of the specimen. The soil specimen is compacted in a 4-in. standard compaction mold that is centered in a submergence tank and placed below the jet nozzle. The distance between the nozzle and the soil surface in the standard compaction mold is 33 mm. The JET is currently used by some departments of transportation and engineering firms.

The step-by-step procedure of a JET done in the laboratory is as follows (Hanson and Hunt 2007):

1. Compact the sample in the 4-in. standard compaction mold and trim the top surface.
2. Center the specimen in the submergence tank right below the jet orifice. Fill the tank with water.

## 30 Relationship Between Erodibility and Properties of Soils

3. Adjust the pressure head at the jet orifice to be 775 mm.
4. Direct the water jet at a given velocity perpendicularly to the soil surface and record the depth of the hole made by the jet as a function of time (not more than 2 hours), while holding the jet in a stationary position.

The last version of the JET is a miniature of the original JET apparatus, called the mini-JET. It was first used in the field by Simon et al. (2010) at 35 sites in Oregon (Al-Madhhachi et al. 2013). Compared with the previous versions, it is easily portable and can be used both in the field and the lab on the 4-in. standard compaction mold sample. The submergence tank in the mini-JET has a dimension of 101.6 mm, and height of 70 mm. The adjustable mini-JET nozzle is 3.18 mm in diameter, and the head pressure at the nozzle is typically 450 to 610 mm.

Figure 11 shows the stress distribution at the soil surface proposed by Hanson and Cook (2004). The erosion rate is calculated as the slope of the curve linking the depth of the hole to the time of jetting. The shear stress associated with the jetting process is calculated as a function of the maximum stress due to the jet velocity at the nozzle using the following equation:

$$\tau = C_f \times \rho \times U_0^2 \times \left( \frac{J_p}{J_i} \right)^2 \quad (11)$$

where

$C_f$  = coefficient of friction (typically 0.00416),  
 $U_0$  = velocity of the jet at the origin ( $\sqrt{2gh}$ ),  
 $\rho$  = fluid density,  
 $J_i$  = initial jet orifice height from soil surface, and  
 $J_p$  = potential core length ( $6.3 \times$  nozzle diameter).

The critical shear stress,  $\tau_c$ , is defined as the stress that exists when the hole is deep enough that the jet is no longer adequate to cause additional downward erosion (Hanson and Cook 2004).

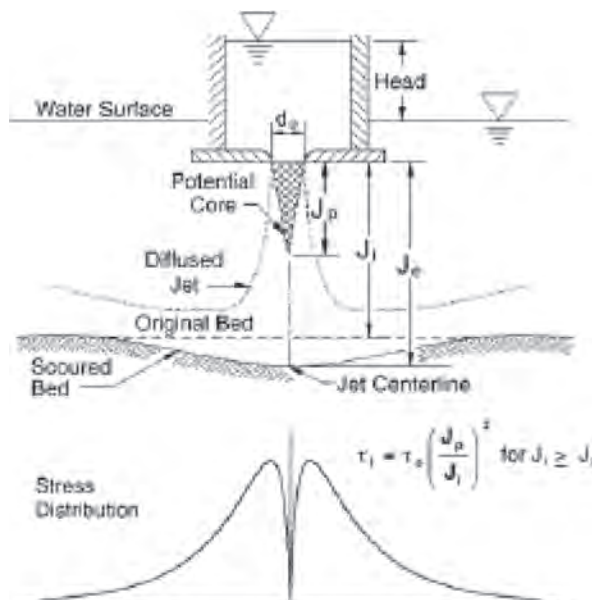


Figure 11. Stress distribution at soil surface in JET (Hanson and Cook 2004).

To describe the relationship between the JET erosion rate and the jet velocity or calculated shear stress (erosion function), Hanson and colleagues used a linear relationship and called the slope of the line the erosion coefficient,  $K_D$  (Hanson 1991, 1992; Hanson and Cook 2004):

$$\dot{z} = K_D (\tau - \tau_c) \quad (12)$$

Based on many JETs performed over time, Hanson classified the erodibility of soils according to their  $K_D$  value as shown in Figure 12.

### **Advantages**

1. The JET can be run both in the field and in the lab.
2. The latest version of the JET is simple, quick, and inexpensive (around \$15,000 to purchase) compared with other types of erosion test.
3. The JET can be performed on any surface—vertical, horizontal, and inclined (Hanson et al. 2002).
4. The JET is good as an index erodibility test.

### **Drawbacks**

1. Particles larger than 30 mm cannot be tested with confidence because of the small size of the sample.
2. Coarse-grained soils (i.e., noncohesive sand and gravel) tend to fall back into the open hole during the jet erosion process, thereby making the readings dubious.
3. The scale of the test application is very small.
4. The JET is typically used for man-made samples. Natural samples are more difficult to test.
5. The flow within the eroded hole and at the soil boundary is complex and difficult to analyze.

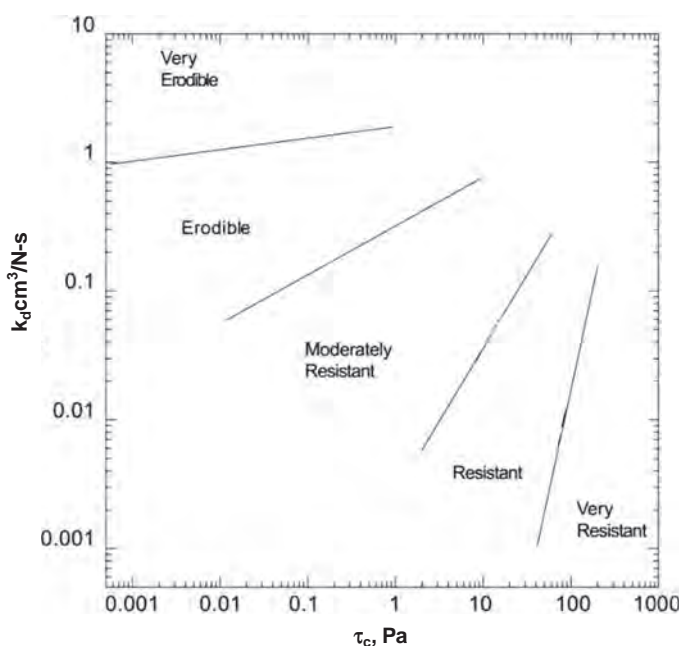


**Figure 12.** JET: Hanson's classification according to erosion coefficient (Hanson and Simon 2001; Chedid et al. 2018).

## 32 Relationship Between Erodibility and Properties of Soils

6. The JET gives only three erodibility parameters [ $\tau_c$ ,  $E\tau$ , and the erosion category (EC)] out of the five possible parameters.
7. The elements of erosion are inferred rather than measured directly.
8. There are multiple interpretation techniques for predicting the critical shear stress, and these techniques give significantly different results.

Prior to Hansen (1990a, 1990b), a few scholars had conducted some studies on erodibility of soils by shooting a jet into the surface of the soil. Sections 2.1.7 and 2.1.8 summarize some of that work.

### 2.1.7 Jet Apparatus to Measure the Tractive Resistance of Cohesive Channel Beds

Dunn (1959) used a jet test to calculate the critical shear stress of cohesive channel beds. This test contained a vertical submerged impinging jet perpendicular to the soil surface. Dunn observed that the location of the maximum shear stress was the same for different pressure heads at the nozzle.

To measure the induced shear stress, Dunn used a device that included a steel plate that was almost fully covered with soil particles, except for a 1-in.<sup>2</sup> area at the location of maximum shear stress that was not covered with any soil. Dunn also measured the vane shear strength of the tested samples. Using this approach, he was able to observe the change in maximum shear stress with change in vane shear strength for each soil sample. Dunn found that the vane shear strength was proportional to the maximum shear stress at the start of the erosion process. Dunn proposed that the most important soil properties affecting resistance to erosion were the percentage of clay and silt, the soil plasticity, and the grain size distribution. A summary of his findings in correlating erodibility parameters with soil properties is presented in the Chapter 3. This jet apparatus was conceptually similar to the JET developed later by Hanson (1990a, 1990b) and, therefore, has advantages and drawbacks, similar to those listed for the JET.

### 2.1.8 Submerged Jet Test at the University of Texas

Moore and Masch (1962) developed a submerged jet test at the University of Texas. In the proposed test, the change in the scour depth of the sample was obtained for different jet velocities, but the hydraulic shear stress at the soil surface was not calculated. Moore and Masch used a cylindrical sample with a diameter of 127 mm (5 in.) and height of 101.6 mm (4 in.). The jet velocity was kept constant for more than 1 h; meanwhile, the eroded weight of the sample was recorded every 10 min. The change in the depth of the hole was calculated by using the volume of the soil removed. The same procedure was repeated for higher velocities, and the data were compared.

It was inferred that the depth of the hole in the sample can be affected by the following parameters: velocity of the submerged jet, diameter of the impinging jet, head pressure at the jet nozzle, viscosity of the eroding fluid, and the scour resistance of the sediments (Moore and Masch 1962). Figure 13 shows a schematic diagram of the vertical jet scour test. This jet apparatus was conceptually similar to the JET developed later by Hanson (1990a, 1990b) and, therefore, had advantages and drawbacks similar to those listed for the JET.

Moore and Masch defined a variable called the scour rate index,  $K_s$ . This parameter is the slope in

$$\left( \frac{S_{ave}}{h_0} \right) \text{ versus } \left( \frac{t\mu}{\rho d^2} \right)$$

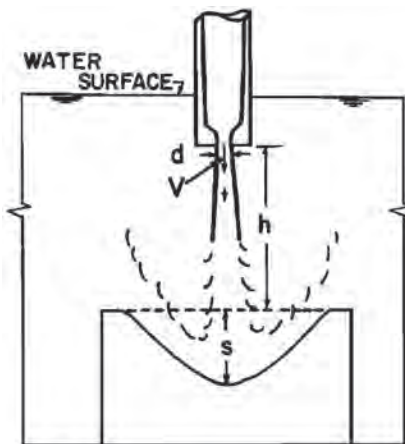


**Figure 13. Schematic diagram of vertical jet scour test developed by Moore and Masch (1962).**

where

$S_{ave}$  = depth of scour hole for a specific jet velocity,

$h_0$  = distance from jet orifice to soil surface,

$t$  = time of scour for a specific velocity,

$\mu$  = viscosity of eroding fluid,

$\rho$  = eroding fluid density, and

$d$  = nozzle diameter.

Moore and Masch could observe that measured  $K_s$  was linearly correlated with the Reynolds number. The work of Moore and Masch was studied and used by Hanson for his JET analysis.

### 2.1.9 Rotating Cylinder Apparatus Developed at University of Texas

In addition to trying a submerged jet test, Moore and Masch (1962) developed a new scour-testing apparatus that worked by subjecting the sample to a rotating flow around the side of the cylinder. The main purpose for implementing this device was that, by that time, other available tests for predicting the erodibility of soil [i.e., the jet apparatus developed by Dunn (1959)] could not accurately measure the hydraulic shear stress on the surface of the soil.

A cylinder of cohesive soil 76.2 mm (3 in.) in diameter and 76.2 mm (3 in.) in length was used as the test specimen. The testing apparatus included a larger translucent cylinder that had the option to rotate around the vertical axis. The maximum rotation speed that the apparatus could handle was 2,500 rpm. The test specimen was then placed into the cylinder coaxially, and the residual space between the sample and translucent cylinder was filled with the eroding fluid. The fluid rotation would apply the shear stress onto the soil surface. Figure 14 shows a schematic diagram of the rotating cylinder testing device.

As shown in Figure 14, the soil sample was constructed around a flexure pivot, which could help calculate the torque directly applied to the sides of the sample. The induced torque on the sample was then calculated and, thus, the shear stress could be backcalculated. One of the challenges that Moore and Masch had was to choose the right liquid as the shear transmitter in the annular space of the cylinder. They found that the use of some liquids, such as glycerin, would form a resistive layer on the soil surface. Finally, they decided to use water in the annular

## 34 Relationship Between Erodibility and Properties of Soils

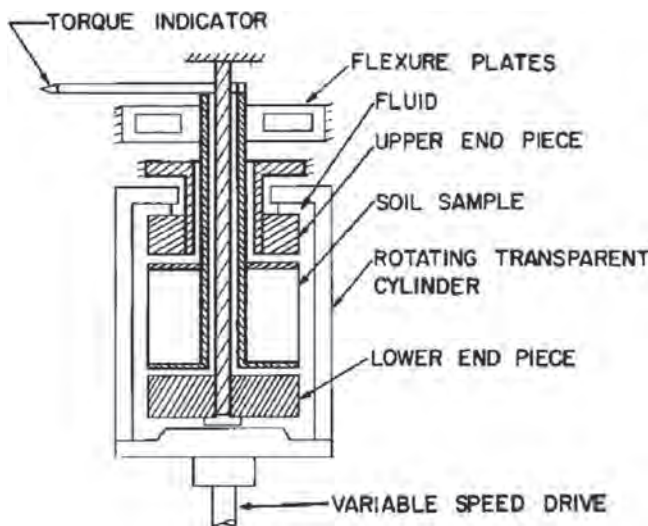


**Figure 14.** Schematic diagram of rotating cylinder test developed by Moore and Masch (1962).

space to transmit the shear stress onto the side surface of the sample. The test procedure is as follows:

1. Place the cylindrical 76.2-mm-diameter sample in the apparatus.
2. Fill the empty space with water.
3. Increase the rotating speed until the occurrence of surface scour can be observed.
4. Record the reading of the torque. Use the calculated torque to measure the shear stress.

It is worth mentioning that to calibrate the test, the operator needed to induce a known torque on a dummy sample. Then the rpm required to rotate the sample was recorded. In this way, a plot of different rpms and different torques would be obtained. Moore and Masch recommended choosing the rate of mass removal during a particular time period as the erosion rate. The rotating cylinder test apparatus was later used and modified by some researchers. Masch et al. (1965) worked more on the recommendations made by Moore and Masch (1962) and subsequently developed the original guideline for the rotating cylinder test. Arulanandan et al. (1973) slightly modified the previous version of the rotating cylinder and studied the effect of clay mineralogy on the erodibility of the soils by conducting some tests on Yolo loam. Kandiah and Arulanandan (1974) also used the rotating cylinder test and compared their results with the results of a flume test on the Yolo clay loam. Arulanandan et al. (1975) used the modified rotating cylinder to study the effect of pore fluid composition and also the concentration of salt in the eroding fluid. The soil samples they used were remolded saturated soils. A summary of the results of Arulanandan and colleagues is presented in Section 3.1 of this report.

Some of the advantages and drawbacks of the early version of the rotating cylinder test are as follows:

#### **Advantages**

1. Contrary to most erosion tests, a very small amount of water is needed.
2. The shear stress can be directly estimated by using the induced torque on the side surface of the specimen.
3. The test can generate very high shear stresses.
4. The influence of the physicochemical properties of the eroding fluid (i.e., pH, salinity) on erosion rate can be easily studied.

### Drawbacks

1. Owing to the existence of the shaft within the soil sample in the apparatus, the test can only be conducted on remolded samples.
2. The samples need to be cohesive and strong enough to stand under their own weight; therefore, testing of coarse-grained soils and soft clays and silts is not possible.
3. There is no direct measurement of torque, as the induced torque is calibrated on the basis of the results from dummy samples.

### 2.1.10 Improved Rotating Cylinder Test

Chapuis and Gatien (1986) used the same principles of the rotating cylinder apparatus developed by Moore and Masch (1962) and improved the testing technique in order to be able to test not only remolded samples but also intact samples. Before this, the rotating cylinder test could only run erodibility tests on reconstructed clays and recreated mixtures in the lab. As mentioned earlier, the clay samples were reconstructed around a center shaft that made it possible to measure the torque on the sample. In the apparatus developed by Chapuis and Gatien (1986), no flexure pivot was in the middle of the sample; therefore, the intact sample could be placed between the upper and bottom ends of the device. Figure 15 shows a photograph of the testing apparatus.

The other advantage of this version of the rotating cylinder compared with earlier versions was that it could directly measure the torque through a pulley weight system. The weight system

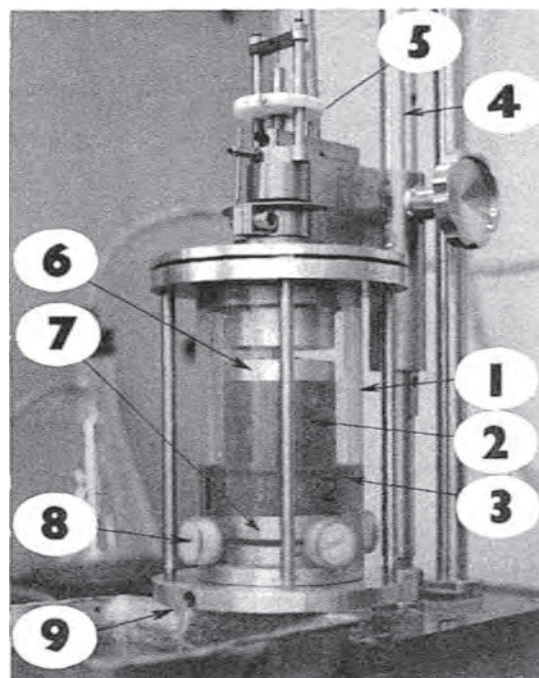


*Figure 15. Photograph of improved rotating cylinder test: (1) rotating outer cylinder, (2) soil sample, (3) eroding fluid in annular space, (4) guiding shaft for installation, (5) torque measurement system, (6) head, (7) base, (8) access for cleaning, and (9) gravity drainage (Chapuis and Gatien 1986).*

### 36 Relationship Between Erodibility and Properties of Soils

included masses ranging from 0 to 40 g and had a precision of 0.1 g. The device could also produce a maximum 1,750 rpm rotational speed. It was observed that the roughness of the side surface of the soil was constantly changing during a test, and therefore was affecting the shear stress measurements.

The step-by-step procedure of the improved rotating cylinder test was as follows (Chapuis and Gatien 1986):

1. Place the clay sample (75 mm in diameter; height 89 mm) into the cylindrical cell of the apparatus.
2. Depending on the purpose of the test, fill the annular space around the sample with the eroding liquid (water or other chemical liquids).
3. Induce a stationary torque to the sample by using the pulley weight system.
4. On the same rpm, record the induced shear stress for stages of 10 to 30 min.
5. After each stage, collect the eroded samples, oven dry, and record the eroded mass for that particular time under that particular shear stress.

#### ***Advantages***

1. A small amount of water is enough as compared with most other erosion tests.
2. High shear stresses can be generated.
3. The test can be conducted on remolded and intact samples.
4. The test directly measures the torque through a pulley weight system.

#### ***Drawbacks***

1. The samples need to be cohesive and strong enough to stand under their own weight; therefore, testing of coarse-grained soils and soft clays and silts is not possible.
2. The test device is expensive to build (more than \$30,000).

### **2.1.11 Rotating Erosion Test Apparatus**

Following a similar concept, Kerr (2001) and Sheppard et al. (2006) modified the previous versions of the rotating cylinder test. The modified version, which is called the rotating erosion testing apparatus (RETA), was constructed at University of Florida. This test was modified to be used only for stiff clays and hard rocks such as sandstone and limestone. It basically holds the same constraint that exists in previous versions of the rotating cylinder test: use of a self-supporting sample. The RETA can be run for several days, which is required for more erosion-resistant materials such as rock. The samples tested with RETA can be both 61 mm (2.4 in.) and 101.6 mm (4 in.) with a height of 101.6 mm (4 in.).

The test apparatus is equipped with a torque transducer at its base and a load cell to record the weight of the sample. The apparatus is also equipped with a water cooling system to reduce the temperature for long tests (more than 72 h for rocks). The central shaft still exists; therefore, intact samples are not usable unless a center hole can be drilled through them. After the hole is drilled, the sample is oven dried and placed in the device to saturate. During the saturation, the device applies a very small torque to the sample for at least a day to remove any loose material. Sheppard et al. (2006) believed that the results of shear stress would be unexpectedly large if the loose material was not removed before the test was performed. After the sample is saturated, it is inserted into a sleeve and placed in the RETA cylinder for the test. Figure 16 shows a schematic diagram and photograph of the testing machine.

#### ***Advantages***

1. Can be run for very long time (more than 72 h for rocks).
2. Can generate very high shear stress values.

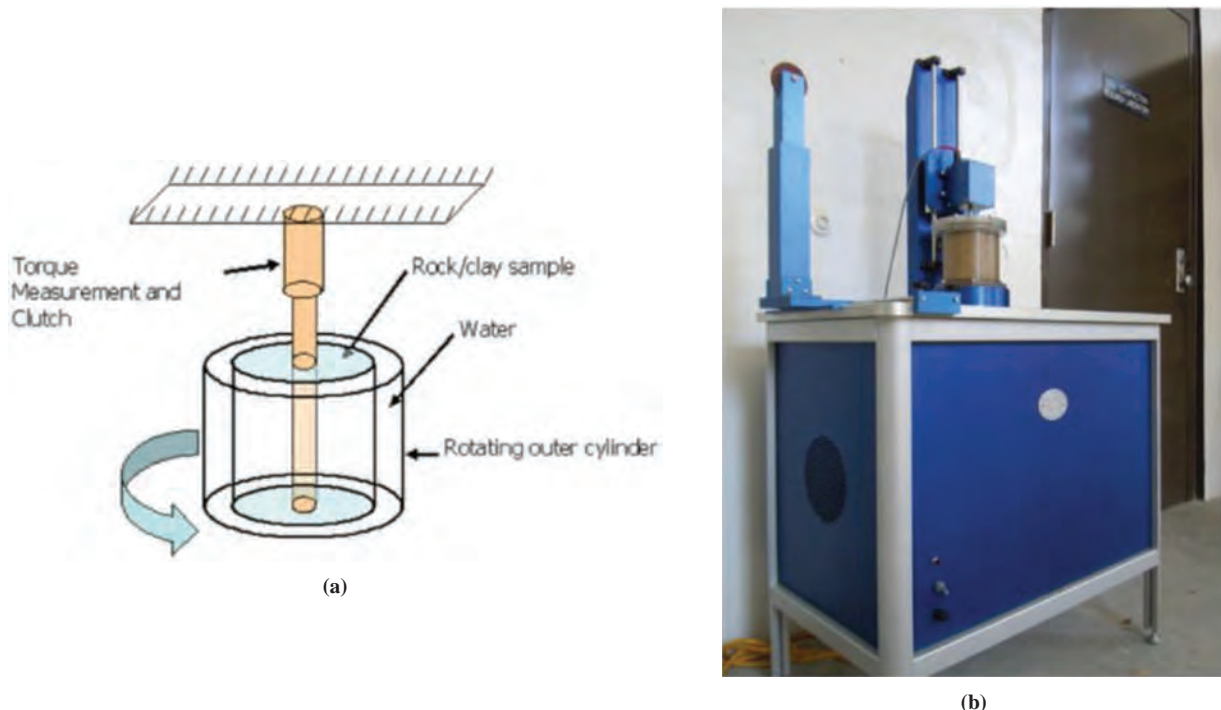


**Figure 16.** RETA: (a) schematic diagram and (b) photograph at the University of Florida (Bloomquist et al. 2012).

3. The apparatus is equipped with a torque transducer.
4. The flow temperature can be controlled during the test.

#### Drawbacks

1. The apparatus is modified to be used only for stiff clay and hard rock such as limestone.
2. Intact samples are not usable unless a center hole can be drilled through them.
3. As with earlier versions, samples need to be self-supporting.
4. The test device is bulky and expensive to build (more than \$30,000).

#### 2.1.12 Pinhole Erosion Test

Sherard et al. (1976a) developed a laboratory test to qualitatively measure the erodibility of fine-grained soils. In this test, distilled water is passed through a drilled hole under a pressure head of 51 mm in the center of the sample, and the erosion resistance of the soil is observed. The hole punched in the center of the sample has a diameter of 1 mm. The test was particularly designed to study and simulate the leakage effect in both dispersive and nondispersive fine-grained soils, which was the case in most earth embankments. The pinhole test was later standardized as ASTM D4647. The test consists of compacting a 38-mm-long soil sample in a plastic cylinder with an inside diameter of 33 mm. A truncated jet nozzle with a diameter of 1.5 mm directs the water through the 1-mm diameter punched hole in the center of the cylindrical specimen. Figure 17 depicts a schematic diagram of the test apparatus.

In observing the appearance of the flowing water and final size of the hole in the tested sample, Sherard et al. (1976) noticed considerable differences in the behavior of dispersive and non-dispersive clays subjected to water flow. With some limitations, the test could be done on intact field samples.

### 38 Relationship Between Erodibility and Properties of Soils

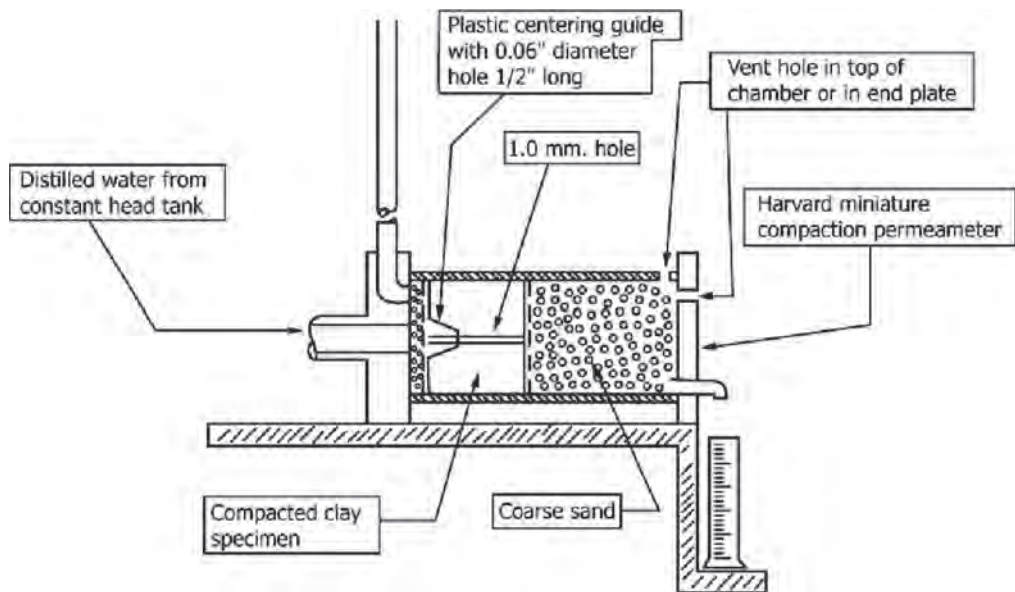


**Figure 17. Schematic diagram of pinhole erosion test apparatus (ASTM D4647).**

The procedure for the pinhole erosion test is as follows:

1. Create a 38-mm-long sample by compacting the soil in the test cylinder above the coarse sand space, which is covered by a wire screen (Figure 17).
2. Make sure that the soil specimen is representative of the field conditions in terms of moisture content and dry unit weight.
3. Push the truncated cone jet nozzle into the center of the cylindrical sample.
4. Using the test wire punch, punch a 1-mm-diameter hole in the center of the sample.
5. Remove the wire punch, place a wire screen on the top of sample, and fill the remaining space with coarse sand.
6. Start the test by shooting the jet into the hole with a pressure head of 51 mm.
7. Continue the test up to 5 min. Depending on the cloudiness of the effluent and the measured flow rate, decide to continue the test or not for higher pressure heads, as described in the ASTM standard.

Table 2 is used to interpret the results of the pinhole erosion test. On the basis of the criteria defined in Table 2, the erosion resistance of soil is classified as one of the nine defined categories.

#### *Advantages*

1. Simulates the leakage in dispersive and nondispersive fine-grained soils.
2. Standardized as ASTM.
3. Directly measures the dispersibility of clay soils.
4. Costs relatively less to build the device as compared with other erosion tests (less than \$10,000).

#### *Drawbacks*

1. Qualitative results.
2. Mostly applicable for remolded samples; however, can be run on intact samples with some limitations.
3. Not applicable for coarse-grained soils (i.e., coarse sand and gravel).

**Table 2. Interpretation of the results of the pinhole erosion test (ASTM D4647).**

Dispersive Classification	Head, mm	Test time for given head, min.	Final flow rate through specimen, mL/s	Cloudiness of flow at end of test		Hole size after test, mm
				from side	from top	
D1	50	5	1.0–1.4	dark	very dark	≥2.0
D2	50	10	1.0–1.4	moderately dark	dark	>1.5
ND4	50	10	0.8–1.0	slightly dark	moderately dark	≤1.5
ND3	180	5	1.4–2.7	barely visible	slightly dark	≥1.5
	380	5	1.8–3.2			
ND2	1020	5	>3.0	clear	barely	<1.5
ND1	1020	5	≤3.0	perfectly clear	perfectly clear	1.0
Method B						
D	50	10	...	slightly dark to dark	very dark to moderately dark	≥1.5
SD	180–380	5	...	barely visible	slightly dark	≥1.5
ND	380	5	...	clear	barely visible to clear	<1.5

### 2.1.13 Drill Hole Test

Lefebvre et al. (1985) developed a new technique for predicting the internal erosion resistance of natural clays. The concern was the erodibility of the natural clays in the eastern part of Canada. The test was inspired by the earlier version of the pinhole erosion test. The testing apparatus uses a 10-cm-long cylindrical sample with a diameter of 35.5 mm. At the center of the sample, a 6.35-mm hole is drilled. Schematic diagrams of the test are shown in Figure 18. The test is conducted by circulating water through the bored hole into the sample. The pressure drop through the sample is measured with a differential manometer connected to both sides of the sample. A tank is used to produce a 143-cm pressure head and thereafter direct the flow through the sample. The flow is adjusted with a valve and measured by a flow meter.

The adjusting valve is used to increase the flow velocity 0.5 m/s every 15 min. The deposited sediment in the reservoir tank is dried and weighed to measure the mass removal rate for that particular velocity. The average diameter of the hole is recorded after each step. The shear stress is calculated according to the pressure drop measured by the manometers. The results are reported as removed mass versus velocity or shear stress.

Lefebvre et al. (1985) also observed that the change in roughness of the hole during the test can be interpreted by using the Moody diagram (Moody 1944) when the friction factor and the Reynolds number are known. Erosion at the clay particle level is accompanied by an increase in the smoothness of the hole (decrease in relative roughness), while erosion of lumps of clay particles leads to an increase in hole roughness.

#### Advantages

- Has a larger hole diameter than the pinhole erosion test (6.35 mm vs. 1 mm), which minimizes the soil disturbance.
- Yields quantitative erodibility results.
- Costs relatively less to build the device as compared with other erosion test devices (less than \$15,000).

#### Drawbacks

- Shear stress is indirectly measured by using Moody charts, which might not be accurate.
- The test is mostly applicable for remolded samples; however, it can be run on intact samples with some limitations.
- The test is not applicable for coarse-grained soils (i.e., coarse sand and gravel).

## 40 Relationship Between Erodibility and Properties of Soils

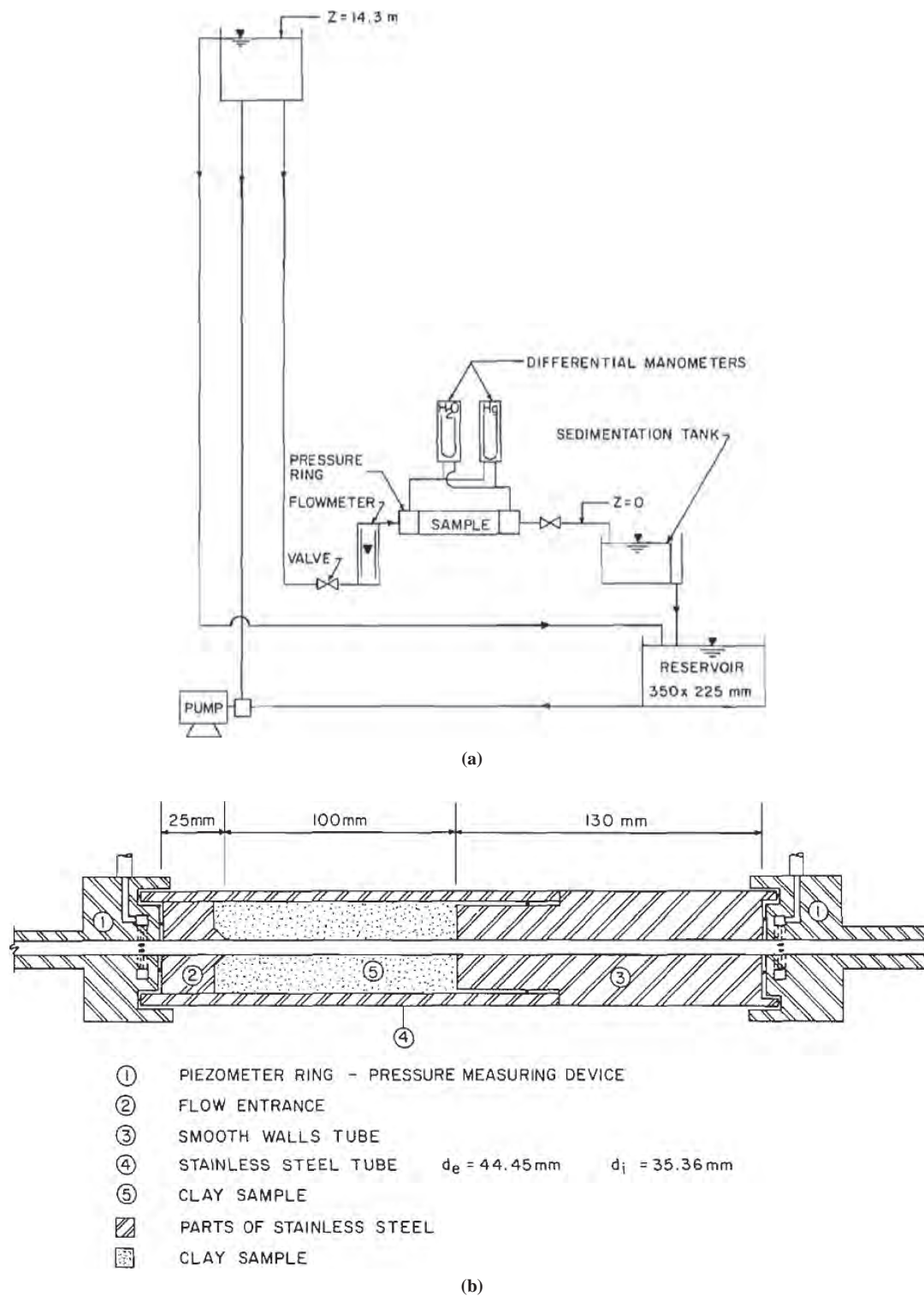


**Figure 18.** Schematic diagrams of (a) entire drill hole test assembly and (b) sample setup of drill hole test (Lefebvre et al. 1985).

### 2.1.14 Hole Erosion Test

The hole erosion test (HET) is a laboratory erosion test that evolved from the older pinhole erosion test and can be credited to Robin Fell in Australia (Wan and Fell 2002; Wahl et al. 2009a, 2009b; Benahmed and Bonelli 2012). The test consists of drilling a hole 6 mm in diameter through a soil sample and forcing water to flow through the hole at a chosen velocity while recording the rate of mass removal per unit area as a function of time to obtain an erosion rate ( $\text{kg/s/m}^2$ ) (Figure 19). The soil is compacted in a standard compaction mold 100 mm (4 in.) in diameter. As in the drill hole test, the sample is connected to a tank that can maintain a variable head ranging from 50 to 800 mm. The flow is also controlled through a valve. The cost of building the device ranges from \$20,000 to \$35,000.

The rate of mass removal per unit area is calculated as

$$\frac{\rho_d}{2} \times \frac{d\phi}{d_t}$$

where

$d\phi$  = change in diameter of the hole,  
 $\rho_d$  = dry unit weight of the sample, and  
 $d_t$  = change in time.

Because the diameter of the hole cannot be monitored during the test, this value is indirectly predicted by using the measured flow rate, the hydraulic gradient, and Equations 13 and 14 (in SI units). Equation 13 refers to laminar flow conditions, and Equation 14 refers to turbulent flow. Turbulent flow is associated with a Reynold's number higher than 5,000.

$$\phi_t = \left( \frac{16 \times Q_t \times f_{\text{Laminar},t}}{\pi \rho_w g s_t} \right)^{\frac{1}{3}} \quad (13)$$

$$\phi_t = \left( \frac{64 \times Q_t^2 \times f_{\text{Turbulent},t}}{\pi^2 \rho_w g s_t} \right)^{\frac{1}{5}} \quad (14)$$

where

$Q_t$  = flow rate at time  $t$ ,  
 $f_{\text{Laminar},t}$  and  $f_{\text{Turbulent},t}$  = estimated friction factors at time  $t$ ,  
 $\rho_w$  = water unit weight,  
 $g$  = ground gravity acceleration, and  
 $s_t$  = hydraulic gradient obtained from manometers at both ends of sample.

In these equations, the friction factors are estimated by using the recorded hole diameter before and after the test.

The test results link the rate of mass removal per unit area to the net shear stress above critical; the shear stress on the wall of the hole is estimated with Equation 15. This equation is obtained after consideration of force equilibrium on the body of the eroding fluid along the preformed hole at a particular time,  $t$ .

$$\tau = \rho_w \times g \times s_t \times \frac{\phi}{4} \quad (15)$$

## 42 Relationship Between Erodibility and Properties of Soils

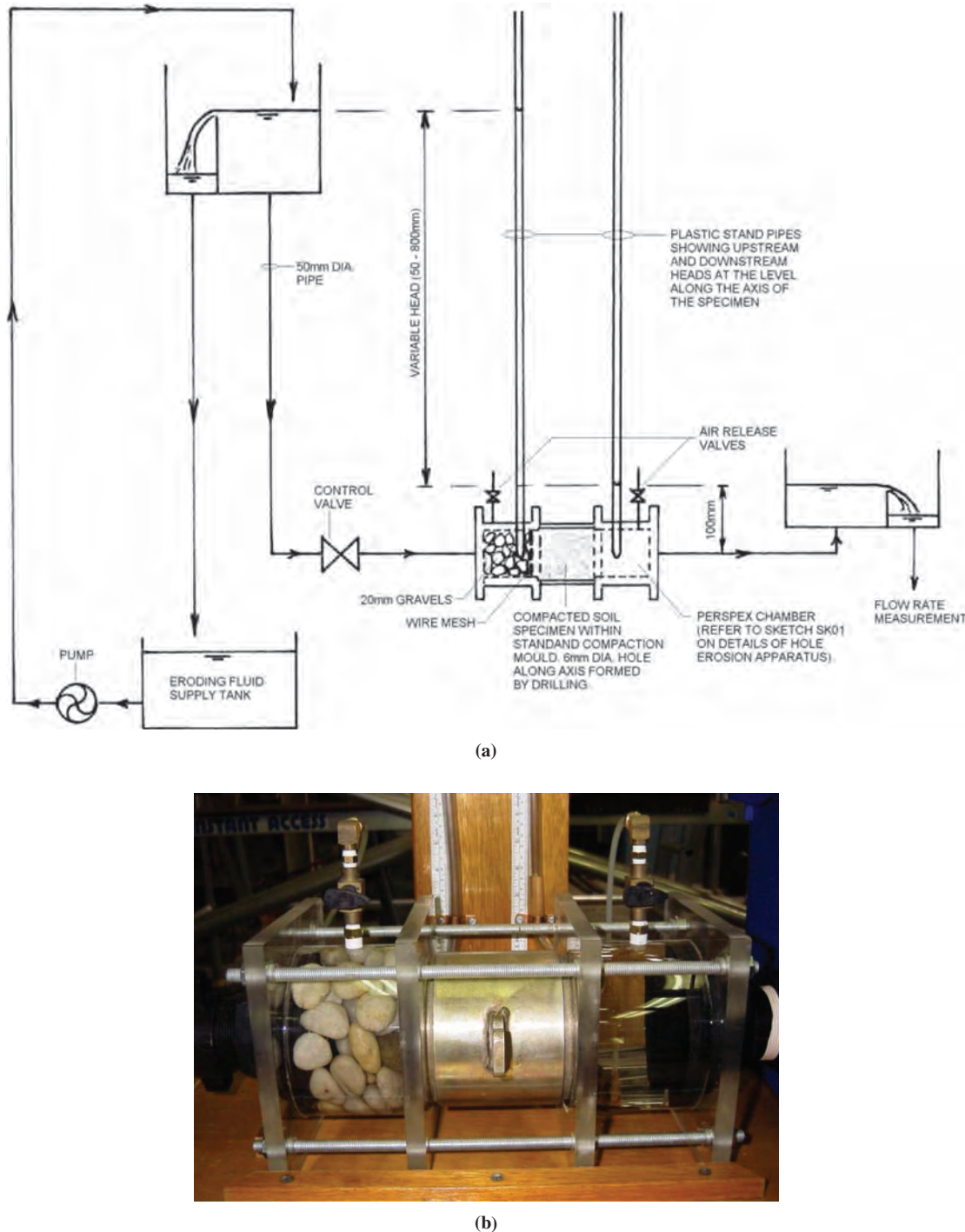


**Figure 19.** HET: (a) schematic diagram and (b) photograph of sample setup.

where

$\rho_w$  = density of water,  
 $s_t$  = hydraulic gradient across the hole, and  
 $\phi$  = diameter at time  $t$ .

The equation used for the erosion function is linear:

$$\dot{m} = C_e(\tau - \tau_c) \quad (16)$$

where  $C_e$  (s/m) is the erosion coefficient and  $\dot{m}$  is the rate of mass removal. The erosion rate index is then defined as

$$I_{HET} = -\log(C_e) \quad (17)$$

Wan and Fell (2002) went on to propose some erosion categories based on  $I_{HET}$  (Table 3).

#### Advantages

1. There is direct similitude with piping erosion in earth dams.
2. A wide range of pressure heads, and therefore a wide range of hydraulic shear stress at the soil–water interface, can be applied.

#### Drawbacks

1. The sample needs to be cohesive and strong enough to stand under its own weight. Therefore, the test cannot be run on cohesionless samples.
2. The test is very difficult to run on intact samples in Shelby tubes from the field. It is better for remolded samples in the lab.
3. Preparation of the test is difficult and time consuming (up to days).
4. The erosion process cannot be directly monitored. The erosion rate needs to be extrapolated and inferred.
5. The hydraulic shear stress is inferred rather than directly measured.
6. The data reduction process is subjective.
7. The flow within the eroded hole and at the soil boundary is complex and difficult to analyze.

### 2.1.15 Slot Erosion Test

The slot erosion test (SET) was also developed by Wan and Fell (2002) in Australia. The concept of the SET is very similar to that of the HET, except that the sample in the SET is different. The test (Figure 20) consists of drilling a 2.2-mm-wide, 10-mm-deep slot at the surface of a 1-m-long rectangular soil sample and having water within the slot at a chosen

**Table 3. HET: Fell's classification according to the erosion index (Wan and Fell 2002).**

Group No.	Erosion Rate Index, $I_{HET}$	Description
1	<2	Extremely rapid
2	2–3	Very rapid
3	3–4	Moderately rapid
4	4–5	Moderately slow
5	5–6	Very slow
6	>6	Extremely slow

## 44 Relationship Between Erodibility and Properties of Soils

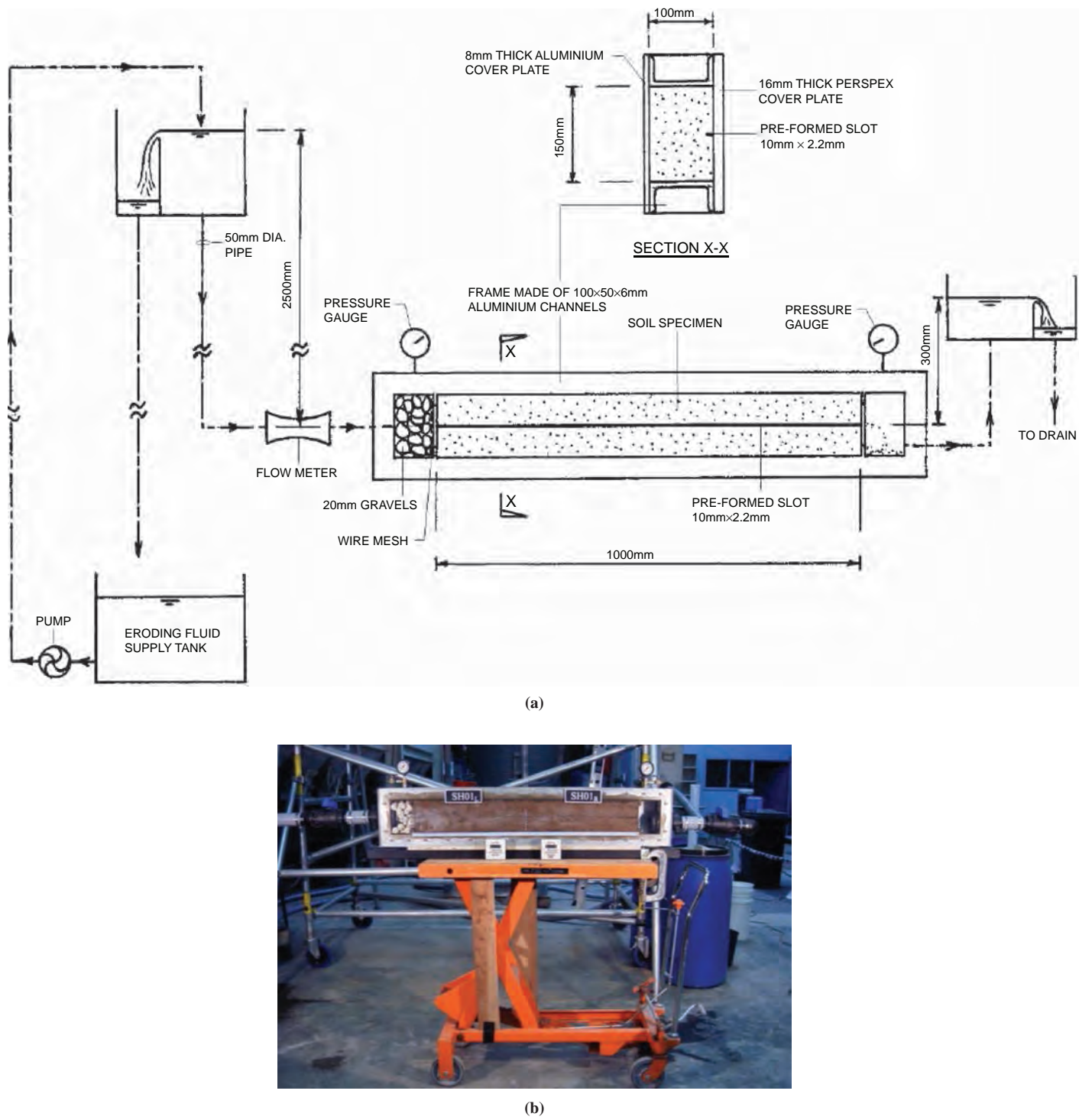


Figure 20. SET: (a) schematic diagram and (b) photograph of sample setup.

velocity while the rate of mass removal per unit area as a function of time is recorded to obtain an erosion rate ( $\text{kg/s/m}^2$ ). The cost of building the device ranges from \$20,000 to \$35,000.

As with the HET, Equation 15 is used to calculate the shear stress. In the SET, the hydraulic diameter

$$\left( \frac{A_{\text{slot}}}{P_w} \right)$$

is used instead of

$$\frac{\phi}{4}$$

in Equation 15.  $A_{\text{slot}}$  refers to the cross-sectional area of the preformed slot, and  $P_w$  is the wetted perimeter.  $I_{\text{SET}}$  is also calculated with the same procedure used to calculate  $I_{\text{HET}}$  (Equation 17).

All the described tests that study internal erosion require that the soil be self-supporting (cohesive). Cohesionless soils cannot preserve an open hole or slot. Therefore, in cases in which noncohesive soils form a high-stress portion of the embankment, the HET, SET, drill hole, and pinhole tests cannot appropriately simulate actual field conditions. The advantages and drawbacks of the SET are same as those identified for the HET. For that reason, new internal erosion test devices are being developed. Some of these devices are described below.

### 2.1.16 Stress-Controlled Erosion Apparatus

Chang and Zhang (2011) developed a new test for studying internal erosion in soils at Hong Kong University. They ran some tests on a man-made cohesionless soil. A schematic diagram and photograph of this test are shown in Figure 21. The test consists of a triaxial system that is fed by a water supply system and controlled by a computer. The porous stone used in this apparatus is modified to accommodate the high permeability of the soil tested in this experiment. The soil sample is 10 cm in diameter and 10 cm high and is mounted on a hollow base with a 10-mm-thick, 95-mm-diameter perforated plate. Water flow seeps through the hollow base and the perforated plate and the soil sample.

Before the internal erosion testing is begun, a 10-kPa confining pressure is applied to the sample. Then, de-aired water is injected slowly into the specimen from the bottom base to saturate the sample. During the erosion test, the vertical deformation of the sample is measured with a linear variable differential transformer (LVDT), and the radial deformations can be measured with a video camera. The test is controlled by adjusting the hydraulic gradient of the seepage water through the sample. A soil collection system is placed at the bottom of the triaxial system. Each hydraulic gradient is maintained for a 10-min period, and the eroded mass of soil is collected, dried, and weighted.

#### *Advantages*

1. Has direct similitude with internal erosion in earth dams.
2. Works properly for cohesionless samples.
3. Uses advanced measurement techniques for axial and radial deformations.
4. Can control multiple criteria (i.e., confining pressure, hydraulic gradient) during the test.

#### *Drawbacks*

1. Requires costly setup (more than \$30,000 to build).
2. May not be efficient for very low-permeability clays and rocks.
3. Hard to test on intact samples, owing to the size of the sample.

## 46 Relationship Between Erodibility and Properties of Soils

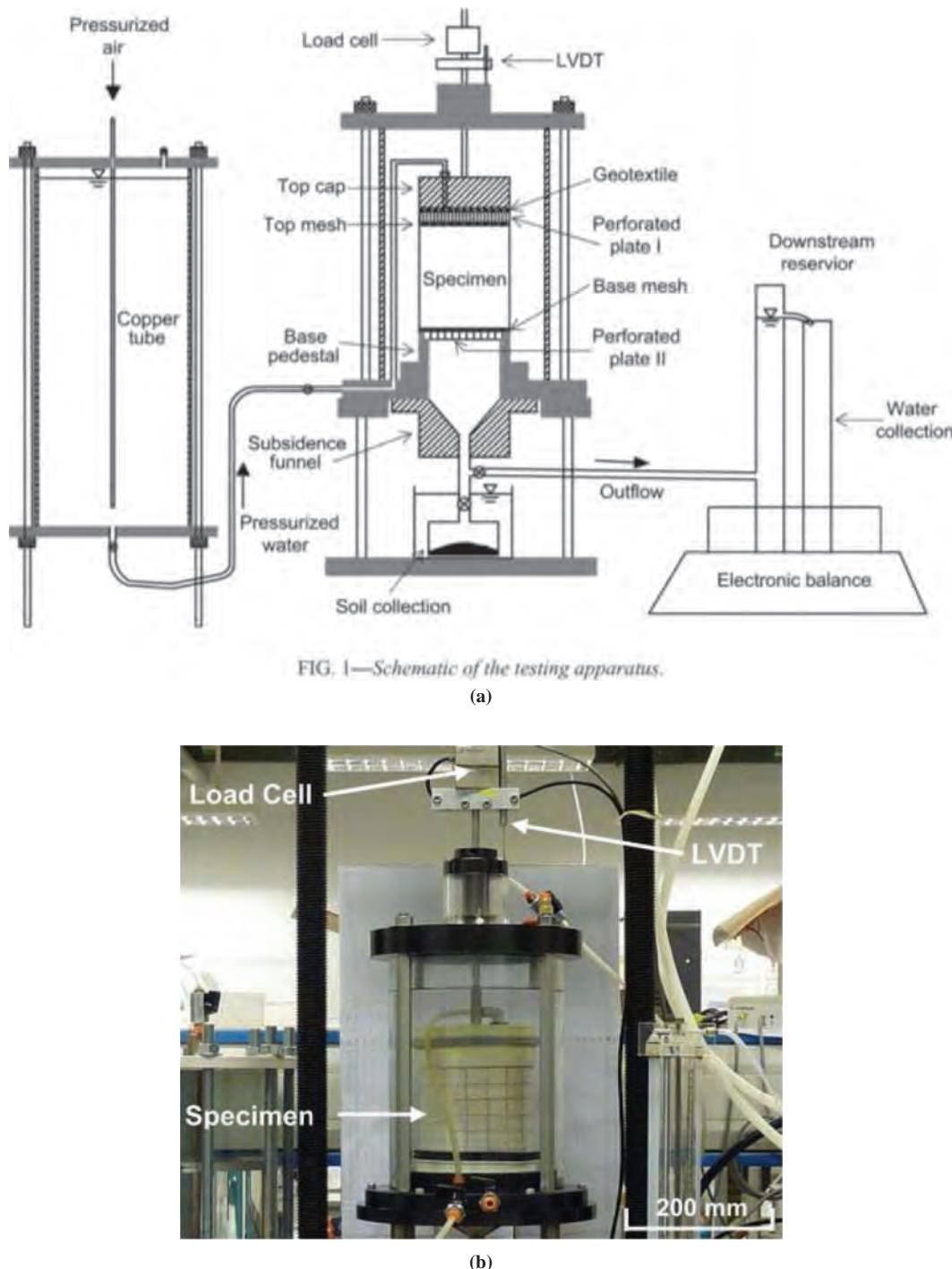


**Figure 21.** Stress-controlled erosion apparatus: (a) schematic diagram and (b) photograph (Chang and Zhang 2011).

### 2.1.17 True Triaxial Piping Test Apparatus

Richards and Reddy (2010) developed a true triaxial piping test apparatus (TTPTA) at the University of Illinois at Chicago to study the internal erosion in both cohesive and cohesion-less soils. The test consists of applying a wide range of confining pressures, with measurements of pore pressure and hydraulic gradient in a true triaxial cell (Figure 22). The results of this test give the critical hydraulic gradient as well as the critical velocity.

#### *Advantages*

1. Has direct similitude with internal erosion.
2. Works properly for both cohesionless and cohesive samples.
3. Uses advanced measurement techniques for deformations.
4. Can control multiple criteria (i.e., confining pressure, hydraulic gradient) during the test.

#### *Drawbacks*

1. Relatively complicated and costly setup (more than \$30,000 to build).
2. May not be efficient for very low-permeability clays and rocks.
3. Hard to test on intact samples because of the size of the sample.

### 2.1.18 Constant Gradient Piping Test Apparatus

Fleshman and Rice (2013) developed a new test apparatus to evaluate the hydraulic conditions required for starting piping erosion. The testing apparatus is shown in Figure 23. The sample is held in a sample holder, while a constant hydraulic gradient is imposed throughout the sample. During the test, the differential head is increased and the pore pressure and the soil behavior are monitored.

Fleshman and Rice (2013) used this testing device on various sandy soils with different grain size distribution, specific gravity, and gradation, and recorded the critical hydraulic condition (i.e., critical gradient) in which the piping erosion was initiated. It was observed that the initiation of the erosion occurs in four stages: (1) the first observable movement of particles, (2) progression of heave, (3) boil formation, and (4) final or total heave.

#### *Advantages*

1. Has direct similitude with piping erosion.
2. Includes automated saturation instrumentation and advanced measurement of flow and head.

#### *Drawbacks*

1. Used only to evaluate the initiation of piping rather than to give the entire erosion function.
2. No measurement of soil axial and radial deformations.
3. Efficient only for sandy soils.
4. Sample preparation is relatively difficult. The test is not designed for intact samples.

## 2.2 Field Erosion Testing

### 2.2.1 Pocket Erodometer Test

The pocket erodometer test (PET) was developed by Briaud et al. (2012) at TAMU. The pocket erodometer is a regulated mini jet impulse-generating device in the form of a plastic water gun. The jet is aimed horizontally at the vertical face of the sample. The jet velocity is calibrated to be always 8 m/s, and the nozzle is kept 50 mm from the soil surface. The depth of the hole in the surface of the sample created by 20 impulses of water is recorded. The eroded

## 48 Relationship Between Erodibility and Properties of Soils

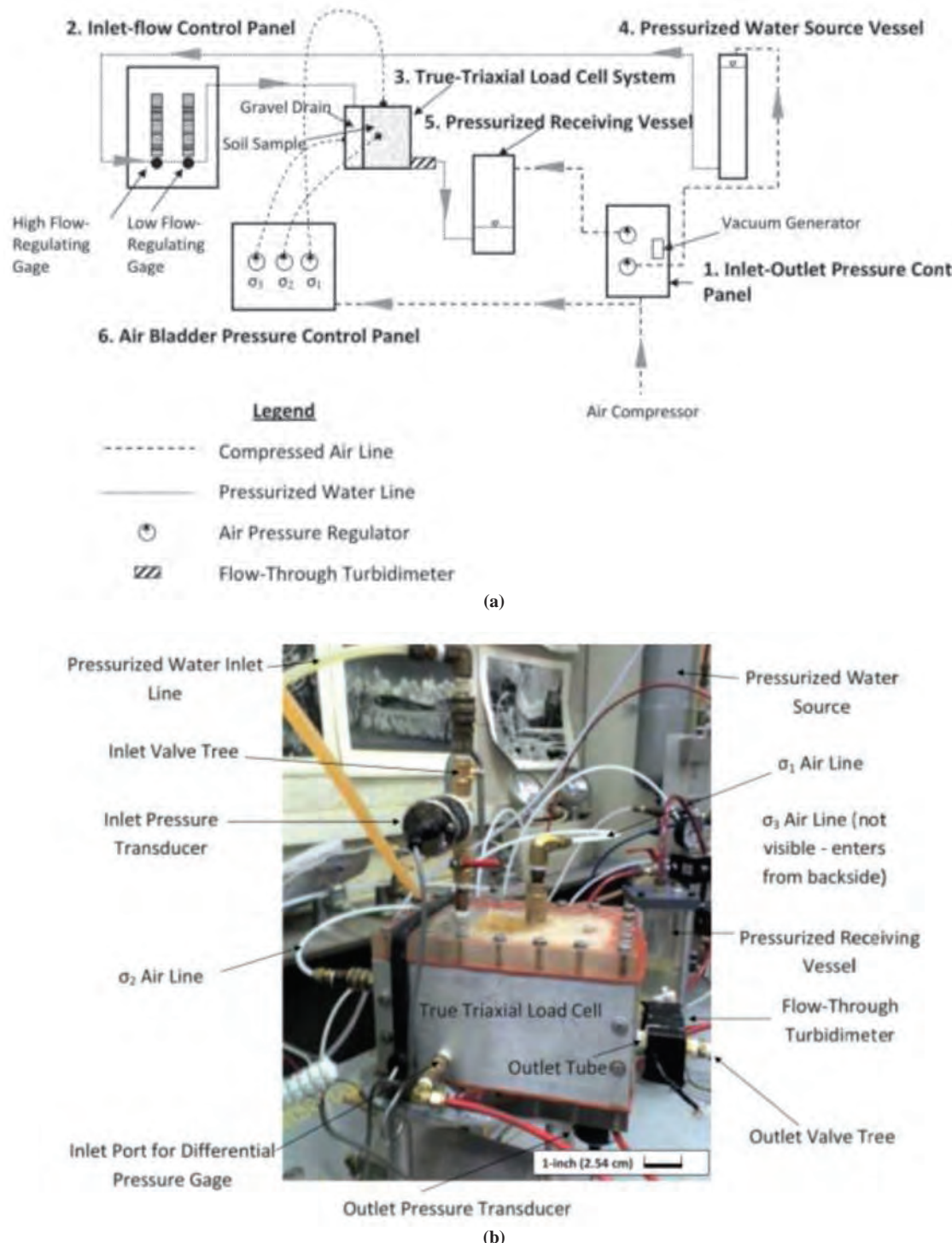
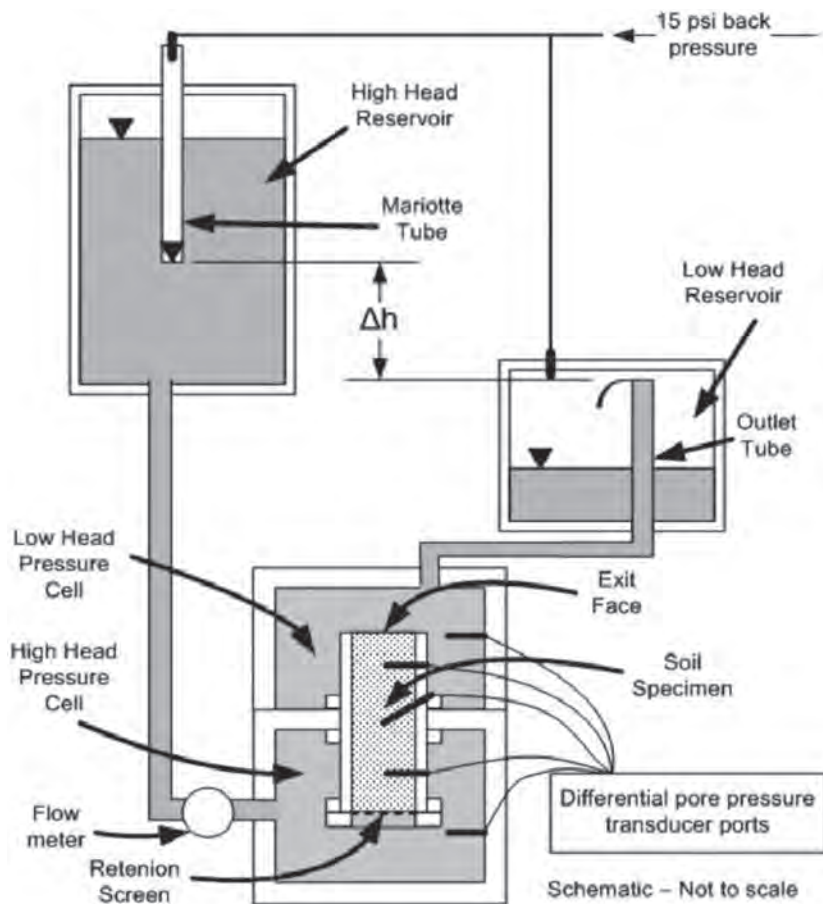


Figure 22. TTPTA: (a) schematic diagram and (b) photograph (Richards and Reddy 2010).



**Figure 23.** Schematic diagram of the constant gradient piping test apparatus (Fleshman and Rice 2013).

depth is compared with an erosion chart to determine the erosion category of the soil, which helps the geotechnical engineer with preliminary design of erosion projects.

Many different options were considered during the development of the pocket erodometer, including the most appropriate device, velocity range, direction of application, distance from the face of the sample, and repeatability from one person to another. Figure 24 shows the schematic diagram of the PET, along with a photograph from the test (Briaud et al. 2012). The original device selected for the pocket erodometer is  $105 \times 77 \times 18$  mm. The diameter of the nozzle is about 0.5 mm. The jet velocity of 8 m/s was chosen because it eroded most tested specimens.

The pocket erodometer needs to be calibrated before the test to reproduce the velocity of 8 m/s at the nozzle. The following equation is used to calibrate the velocity of the impinging jet at the nozzle:

$$v = \frac{x}{\left(\frac{2H}{g}\right)^{0.5}} \quad (18)$$

where  $x$  and  $H$  are as shown in the schematic diagram of the PET depicted in Figure 24 and  $v$  is the initial horizontal velocity right at the nozzle.

## 50 Relationship Between Erodibility and Properties of Soils

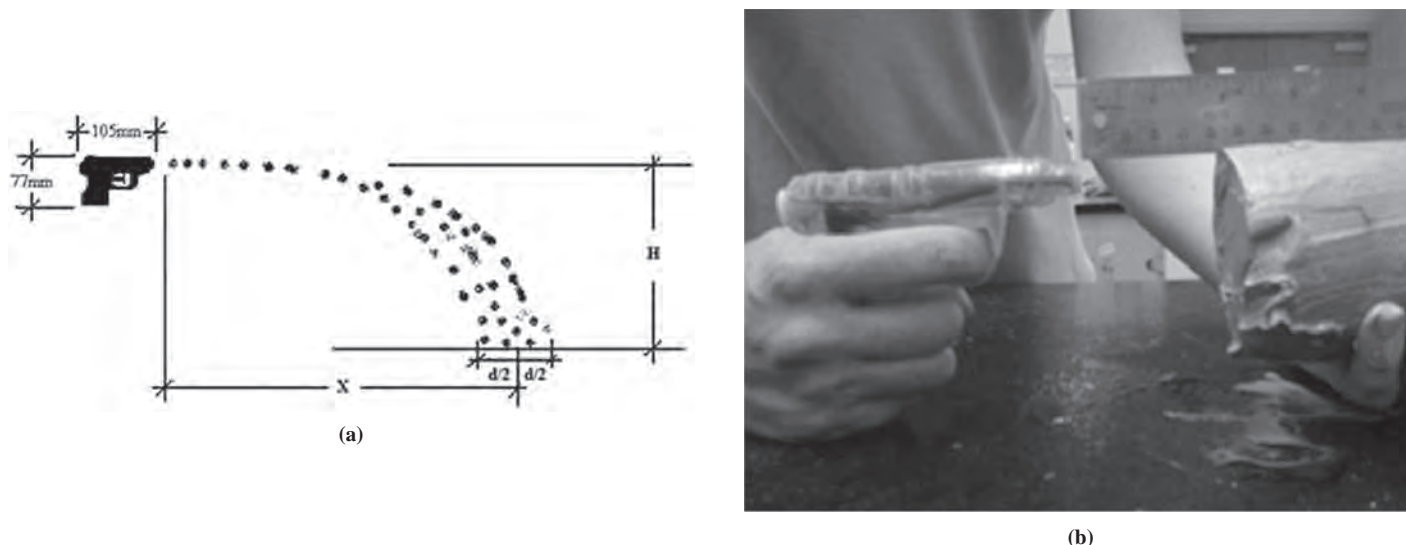


**Figure 24.** PET: (a) schematic diagram and (b) photograph (Briaud et al. 2012).

The height of the erodometer (shown as H in Figure 24) must be kept constant during the calibration process. Also, external forces such as wind should be avoided. The PET can be done with any type of apparatus that can meet the requirements of this test and reproduce 8 m/s velocity at the nozzle with  $\pm 0.5$  m/s with an impulse time period of near 0.15 s. Briaud et al. (2012) conducted the PET on many samples from different levees and compared the results with EFA results that had been obtained. The comparisons resulted in an erosion category chart based on the PET depth ranges (Figure 25). The step-by-step process of the PET is as follows (Briaud et al. 2012):

1. Place the sample horizontally, either by laying it on a flat surface or by holding it in your hand. (Note: The test must not be run with the jet pointed vertically.)
2. Smooth the surface to remove any uneven soil. Beginning with a smooth and vertical surface makes it easier to measure the erosion depth.
3. Point the pocket erodometer at the smooth end of the sample, 50 mm away from the face.
4. Keeping the jet of water from the PET aimed horizontally at a constant location, squeeze the trigger 20 times at a rate of 1 squeeze per second, forming an indentation in the surface of the sample. Each squeeze should fully compress the trigger, and then the trigger should be fully released before it is compressed again.

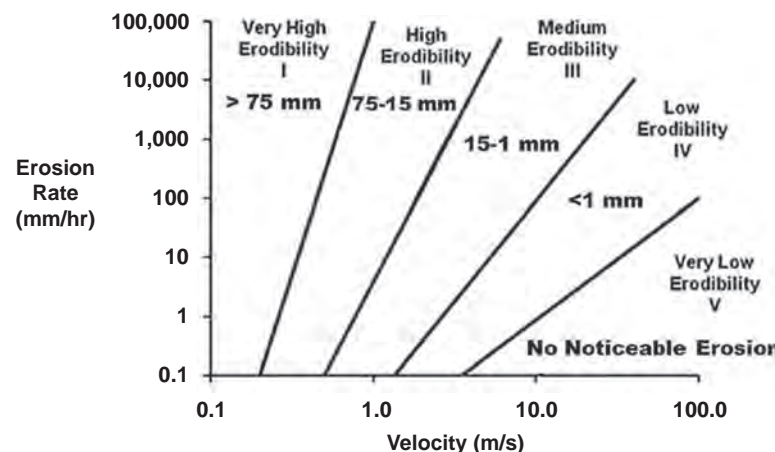


**Figure 25.** Erosion depth ranges of PET depicted on erosion categories proposed by EFA.

5. Using the end of a digital caliper or an appropriate measuring tool, measure the depth of the hole created.
6. The test should be repeated at least three times in different locations across the face of the sample, and an average should be used to ensure a good estimate.
7. Use Figure 25 to determine the erosion category.

#### **Advantages**

1. The cost is very low (\$25 per test).
2. The device is very handy and simple to operate, both in the field and in the laboratory.
3. The test gives a quick and crude estimate of soil erodibility.

#### **Drawbacks**

1. The PET is on a very small scale.
2. The test gives only the erosion category, with no measurement of critical shear stress or critical velocity.
3. The test is useful only for preliminary field evaluation and not good for design purposes.

### **2.2.2 In Situ Erosion Evaluation Probe**

Gabr et al. (2013) developed an erosion testing device called the in situ erosion evaluation probe (ISEEP) at North Carolina State University. The test is conducted by advancing a vertical jet probe into the subsurface soil and measuring the rate of advancement.

As discussed earlier, all other in situ tests were limited to evaluating the scour potential of the soil solely on the ground surface (e.g., JET, SEDflume), and the EFA was the only test that could evaluate the erodibility of the natural soil associated with a particular depth. The flow velocities of the ISEEP are normally much less than the imparted velocities in the EFA. ISEEP can investigate the erodibility of any soil at any depth, provided the probe can penetrate by erosion.

The results of ISEEP are reported on the basis of the concept of stream power, which was first presented by Annandale and Parkhill (1995), who believed that this concept would better represent the erodibility potential of an eroding fluid as compared with velocity or shear stress. Annandale (2006) used Equations 19 and 20 to define stream power,  $P$ .

$$P = \gamma_w q H \quad (19)$$

$$P = \tau U_0 \quad (20)$$

where

$P$  = stream power (watts per unit area),

$\gamma_w$  = water unit weight,

$q$  = flow discharge in unit area,

$H$  = energy head,

$\tau$  = shear stress, and

$U_0$  = velocity.

Equation 20 shows that the stream power is a function of both the shear stress and the velocity. Figure 26 shows a photograph of the ISEEP device, which was tested at the North Carolina State University lab before being used in the field.

The jet nozzle is a truncated cone probe that is guided into the soil as the soil is being eroded by the impinging jet. The eroded material moves up through the annulus space between the probe and the wall of the hole created by erosion. The water velocity at the nozzle is controlled digitally by a variable speed pump on the ground surface. The rate of advancement into the soil

## 52 Relationship Between Erodibility and Properties of Soils

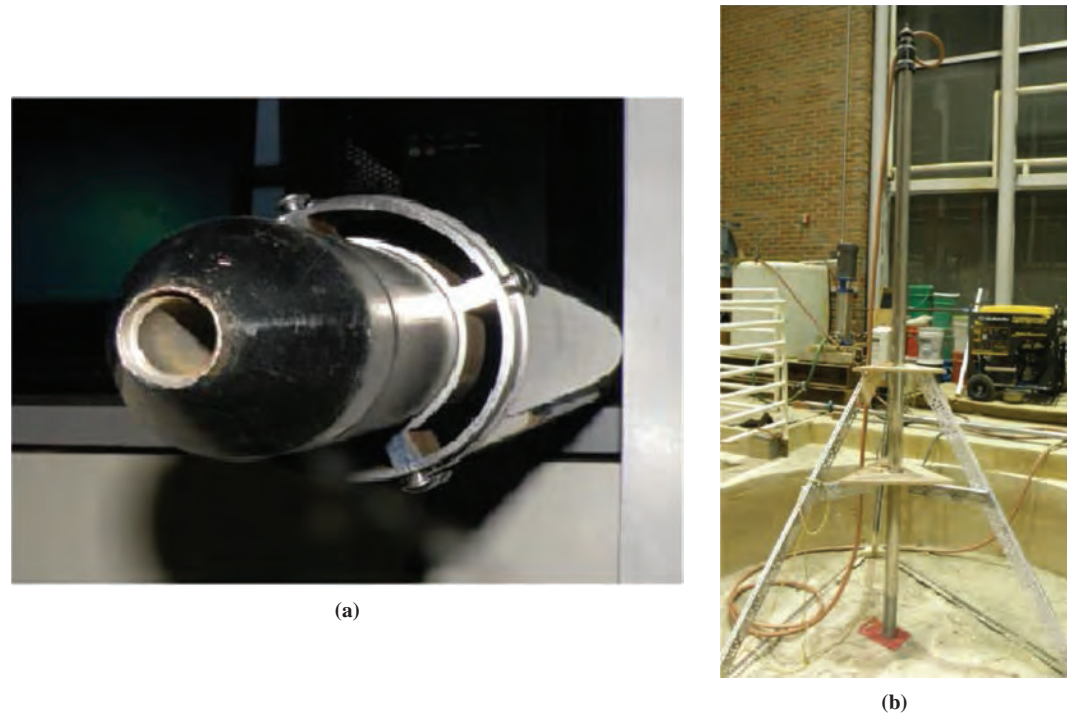


**Figure 26.** ISEEP: (a) truncated cone probe and (b) apparatus prototype at North Carolina State University (Gabr et al. 2013).

subsurface is measured and represents the erosion rate. The body of the probe is divided into sections so that the length can be adjusted for deep locations in the field. The orifice of the jet nozzle is 19 mm (0.75 in.) long, and the nozzle velocity can go up to 12 m/s. During penetration, the advancement is recorded with a video camera.

The results of this test are reported as the rate of advancement (penetration) versus the stream power value,  $P$ . The bed shear stress is obtained from Equation 21 on the basis of Julien's (1995) study:

$$\tau = C \rho_w U^2 \quad (21)$$

where

$\tau$  = bed shear stress,  
 $U$  = jet velocity,  
 $\rho_w$  = water density, and  
 $C$  = diffusion coefficient that varies depending on flow condition.

Some advantages and drawbacks of the ISEEP are as follows:

### **Advantages**

1. The ISEEP can evaluate the erodibility of any soil at any depth with a wide range of jet velocity.
2. There is no need for sample extraction and procurement.

### **Drawbacks**

1. The penetration may be limited if the probe fails to erode the soil. The ISEEP is better for use in sandy soils.

2. The use of the stream power makes it difficult to compare this device with other erosion devices.
3. The test device is fairly expensive to build (more than \$20,000), and difficult to interpret.

### 2.2.3 Borehole Erosion Test

The borehole erosion test (BET) is an in situ test developed by Briaud at TAMU (Briaud et al. 2017a). The purpose of this test is to quantify the erodibility of the soil layers as a function depth, as follows:

1. Drill a hole into the ground, say 100 mm in diameter, 10 m deep.
2. Remove the drilling rods and measure the initial diameter of the borehole with a borehole caliper.
3. Reinsert the rods to the bottom of the hole and circulate water down the rod and up the outside annulus of the hole for a given time, say 15 minutes.
4. Remove the rods and measure the diameter of the hole with the borehole caliper.
5. Calculate the erosion rate. The increase in diameter of the borehole at a certain depth given by the calipers divided by the flow time is the erosion rate of the soil at that depth for the flow velocity applied during the test.

Profiles of erosion rate for different velocities can be prepared in this fashion.

Figure 27 shows a schematic diagram of the BET and field work photographs. The advantages and drawbacks of the BET areas follows:

#### Advantages

1. Only typically available field equipment (i.e., common drilling rig for wet rotary boring, flow meter in line with the drilling rig pump, and borehole caliper) is used to perform a BET; therefore, this test can be performed in many drilling projects.

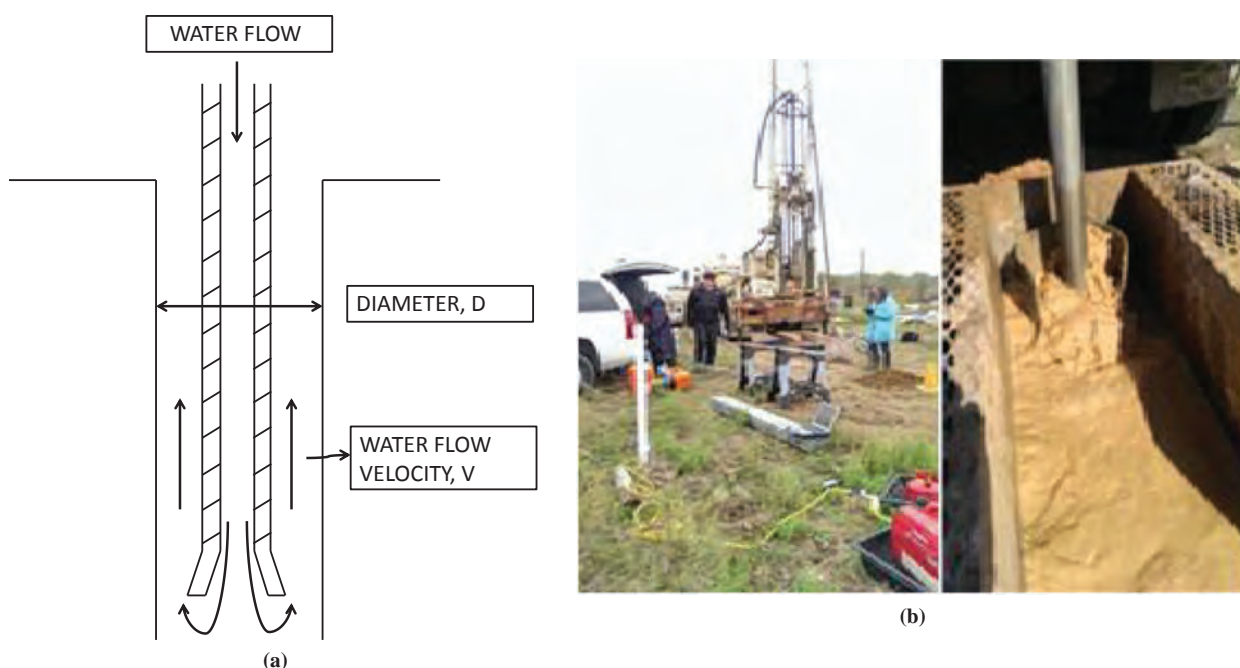


**Figure 27.** BET: (a) schematic diagram and (b) photographs of the test at the Riverside campus at TAMU (Briaud et al. 2017).

## 54 Relationship Between Erodibility and Properties of Soils

2. Each test gives the erosion function for all layers traversed, since a complete borehole diameter profile is obtained from the caliper. Many tests on many samples would be required if laboratory tests were to be conducted.
3. The BET has two component tests: the lateral erosion test associated with the increase in diameter of the borehole and the bottom erosion test associated with the increase in depth below the bottom of the drilling rods during the flow. The latter is much like an *in situ* JET.
4. The BET can be used in any soil or rock in which a hole can be drilled.

### **Drawbacks**

1. The shear stress is obtained from the Moody chart.
2. The test is limited by the pump flow available on the drill rig.
3. The hole needs to be capable of staying open.
4. In sand boreholes, the addition of bentonite during drilling needs to be controlled, so as not to affect the erosion resistance.
5. Because of gravity, the velocity over a given distance changes and needs to be taken into account.
6. Erosion of layers above the tip of the pipe could be altered by the sediment transport from the lower layers. For example, Sheppard (2002) showed that equilibrium scour depths are reduced by the presence of suspended fine sediments.
7. Borehole measurements with the caliper may not be accurate as a result of material sloughing off.

### **2.2.4 In Situ Scour Testing Device**

The in situ scour testing device (ISTD) is the most recent field erosion test device that is currently under development by FHWA. Zinner et al. (2016) presented the concept behind the ISTD and its application in pier scour studies. This device has a cylindrical shape and can be used in a boring test rig and fit into the steel casing of a hollow stem auger to evaluate the erodibility of soil at any depth. The ISTD generates a horizontal flow at the bottom of the borehole. Figure 28 shows a diagram of the cylindrical ISTD concept. So far, the ISTD is applicable only for soils that are below the groundwater table and that have a maximum *N*-value of 30. Also, the ISTD is generally limited to upper soil layers, as the mechanical parts are limited. Development of the ISTD by FHWA is on-going.

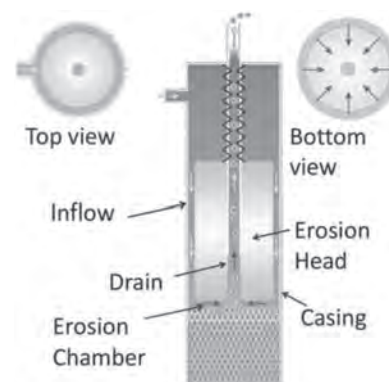


**Figure 28. Schematic diagram of the cylindrical ISTD concept (Zinner et al. 2016).**

**Table 4. Summary of all types of erosion tests in terms of their application.**

Laboratory Erosion Tests	In Situ Erosion Tests
<ul style="list-style-type: none"> <li>• Lab jet erosion test (JET)</li> <li>• Hole erosion test (HET)</li> <li>• Pinhole erosion test</li> <li>• Drill hole erosion test</li> <li>• Slot erosion test (SET)</li> <li>• Rotating cylinder test (RCT) and improved versions</li> <li>• Rotating erosion testing apparatus (RETA)</li> <li>• EFA and similar versions of it (e.g., SEDflume, SERF, ESTD)</li> <li>• Stress-controlled erosion apparatus</li> <li>• True triaxial piping test apparatus (TTPTA)</li> <li>• Constant gradient piping test apparatus</li> </ul>	<ul style="list-style-type: none"> <li>• Field jet erosion test (JET)</li> <li>• In situ erosion evaluation probe (ISEEP) from North Carolina State University</li> <li>• Borehole erosion test (BET)</li> <li>• Pocket erodometer test (PET)</li> <li>• Adjustable Shear Stress Erosion and Transport (ASSET) flume</li> <li>• In situ scour testing device (ISTD)</li> <li>• Field flume tests</li> </ul>

**Table 5. Some erosion tests with information about their application.**

Erosion Test	Range of Soil Types That Can Be Tested	Range of Shear Stress (Pa) That Can Be Applied	Cost of Device <sup>a</sup>	Reliability of Results
Lab JET	Sands to clays	<100	Low	Good
In situ JET	Sands to clays	<500	Medium	Good
EFA	Sands to clays	<165	High	Good
HET	Clayey soils	≤800	High	Good
SET	Clayey soils	≤400	High	Medium
RETA	Clayey soils	<100	High	Medium
PET	Sands to clays	<20	Very Low	Medium
ISEEP	Sands to clays	<650	High	Good
BET	Sands to clays	<600	Medium	Good

<sup>a</sup>Very low: <\$5,000; low: \$5,000 to \$15,000; medium: \$15,000 to \$30,000; high: ≥\$30,000.

## 2.3 Summary

A summary of all the erosion tests reviewed in this chapter is presented in Table 4 in terms of their application in the field or the lab. Table 5 shows some of the most common and important erosion tests with information regarding their ability to measure shear stress, the soil type that can be tested, and the cost associated with them.



## CHAPTER 3

# Existing Correlations Between Soil Erodibility and Soil Properties

It is well accepted that different soils have different critical velocities and different erosion rates beyond the critical threshold; therefore, soil erodibility depends on the soil's properties. At the same time, a reliable and broadly accepted relationship between soil erodibility and soil properties has not been found. However, a number of attempts have been made on the basis of erosion test databases, which are more or less populated. Some of these attempts are reviewed in this chapter.

### 3.1 Existing Correlations

Dunn (1959) carried out submerged JET examinations of remolded samples of sand and of fine-grained soils such as silty clay. He proposed a relationship between the critical shear stress obtained by using a 1-in<sup>2</sup> steel plate in the location of maximum observed scour and two basic soil properties that he believed were the most influential parameters. This relationship was proposed for the soils with a plasticity index ranging from 5 to 16:

$$\tau_c = 0.001 \times (S_v + 180) \times \tan(30 + 1.73 \times PI) \quad (22)$$

where

$S_v$  = shear strength of the soil (psi), measured with a rotating vane;

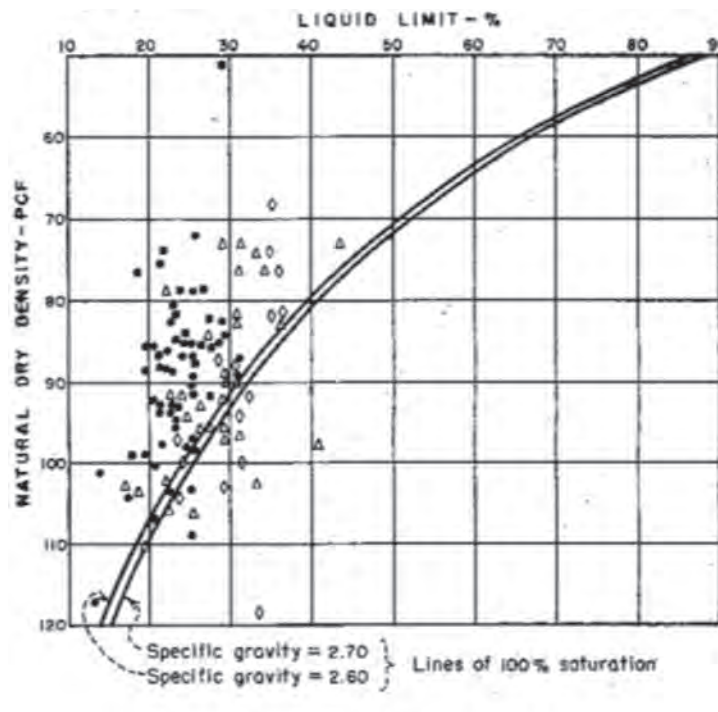
$\tau_c$  = critical hydraulic shear stress (psi);

PI = plasticity index (%), and

the unit of the angle in the tangent is degrees.

Gibbs (1962) conducted flume tests on undisturbed samples [mostly clay of low plasticity (CL) and silt (ML)] from 45 case studies to assess the influence of field density on erosion resistance of the soil. Gibbs plotted his results versus field density and liquid limit. Recorded critical shear stresses ranged from 0.7 Pa to 2.87 Pa. Gibbs observed that clays were more resistant to erosion than was coarser material. Also, the highly plastic samples generally showed more resistance to erosion as compared with low plasticity soils. Gibbs observed that gradation of a soil is an important parameter in the erosion resistance of coarser soils, while for finer samples, plasticity seems to be more effective. Although no good relation was found between dry density and critical shear stress, liquid limit generally seemed to be proportional to critical shear stress in several cases. Consequently, Gibbs (1962) recommended four categories based on the results of flume tests on the tested samples (Figure 29b).

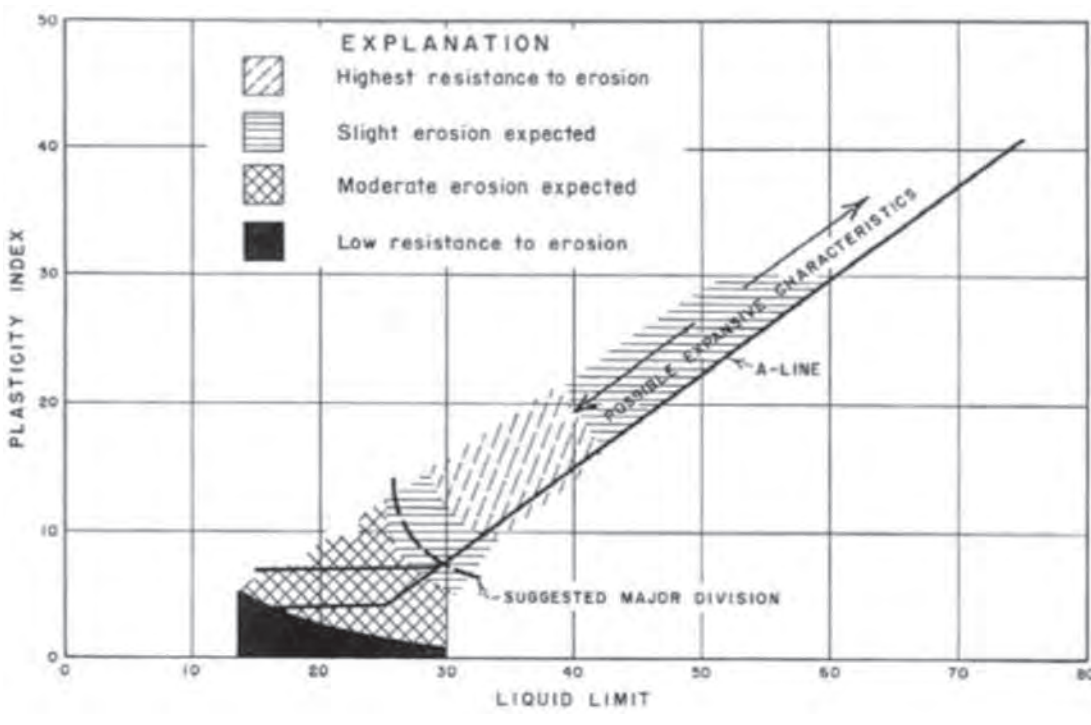
A few years after Gibbs (1962), Lyle and Smerdon (1965) performed some flume tests on seven Texas soils. They studied both the individual and combined influence of different engineering properties such as degree of compaction and PI on the erosion resistance of the soils. The soils tested in their study comprised two nonplastic soils (Amarillo fine sandy loam and



**EXPLANATION**  
**TRAITIVE FORCE FROM TESTS**

- - 0.045 - 0.060
- △ - 0.035 - 0.045
- - 0.025 - 0.035
- - 0.015 - 0.025

(a)



(b)

Figure 29. (a) Flume test results of critical shear stress versus natural dry density and liquid limit and (b) proposed erosion categories (Gibbs 1962).

## 58 Relationship Between Erodibility and Properties of Soils

Lufkin fine sandy loam), and five plastic soils (Reagan silty clay loam, San Saba clay, Houston black clay, Lake Charles clay, and Lufkin Clay).

For each soil tested, the average particle size, percentage of clay, dispersion ratio, vane shear strength, and PI were measured. In addition to the physical engineering properties, the percentage of organic matter, the calcium/sodium (Ca/Na) ratio, and the cation exchange potential were obtained for each soil. Lyle and Smerdon (1965) first studied the effect of compaction (void ratio), and linearly correlated the void ratio and the critical shear stress. Table 6, which refers to the void ratio of soil, shows the results of these linear regressions.

After examining the test results, Lyle and Smerdon (1965) concluded that, in addition to the void ratio, the following parameters were also influential, in order of decreasing impact: PI, dispersion ratio, percentage of organic matter, vane shear strength, cation exchange potential, average particle size ( $D_{50}$ ), Ca/Na ratio, and percentage of clay. Thereafter, Lyle and Smerdon (1965) proposed linear regressions for each of these parameters combined with the void ratio.

Table 7 shows the results of these linear regressions. Neither the  $R^2$  value nor any other parameter representing the significance level of the proposed equations was reported along with the results. After these equations were established, further efforts were made to involve more parameters; some link was observed between the Ca/Na ratio and the slope of the critical shear stress–void ratio plot.

Smerdon and Beasley (1961) performed flume tests on 11 cohesive Missouri soils to investigate the relationships between the main engineering properties of soils and critical shear stress measured in the flume tests. The proposed empirical equations were as follows:

$$\tau_c = 0.0034(I_w)^{0.84} \quad (23)$$

$$\tau_c = 10.2(D_r)^{-0.63} \quad (24)$$

$$\tau_c = 3.54 * 10^{-28.1D_{50}} \quad (25)$$

$$\tau_c = 0.493 * 10^{0.0182P_c} \quad (26)$$

where  $\tau_c$  = critical shear stress (Pa) and  $D_{50}$  = particle size.

**Table 6. Results of linear regression study on correlations between critical shear stress and void ratio (Lyle and Smerdon 1965).**

Test Series No.	Regression Equation	t-value	Significance Level
1	$\tau_c(\text{psf}) = 0.0255 - 0.00714 \times e$	12.93	0.05
2	$\tau_c(\text{psf}) = 0.0279 - 0.00316 \times e$	na	0.01
3	$\tau_c(\text{psf}) = 0.0271 - 0.00577 \times e$	11.5	0.1
4	$\tau_c(\text{psf}) = 0.036 - 0.01778 \times e$	13.45	0.05
5	$\tau_c(\text{psf}) = 0.07387 - 0.0338 \times e$	2.53	0.4
6	$\tau_c(\text{psf}) = 0.0323 - 0.00653 \times e$	21.3	0.05
7	$\tau_c(\text{psf}) = 0.0640 - 0.00959 \times e$	0.604	0.7

Note: psf = pounds per square foot; na = not applicable.

**Table 7. Proposed regression equations linking the critical shear stress with void ratio and other soil properties (Lyle and Smerdon 1965).**

Soil Property	General Equation
Plasticity index ( $I_w$ )	$\tau_c = 0.00771 + 0.0233(1.2 - e) + [0.00079 + 0.00035(e - 1.2)]I_w$
Dispersion ratio ( $D_r$ )	$\tau_c = [0.0322 + 0.0086(1.2 - e)](10) - (n)D_r$ where $n = 0.00452(10)^{0.32(e-1.2)}$
Percentage of organic matter ( $P_{om}$ )	$\tau_c = [0.0105 + 0.0124(1.2 - e)]P_{om}(n)$ where $n = 0.765(10)^{-0.42(1.2-e)}$
Vane shear strength ( $S_v$ )	$\tau_c = [0.0140 + 0.00192(1.2 - e)](\frac{S_v}{10})(n)$ where $n = 0.205(10)^{-0.61(1.2-e)}$
Cation exchange capacity (CEC)	$\tau_c = [0.00429 + 0.0136(1.2 - e)] + [0.0140 + 0.00116(e - 1.2)] \log(\text{CEC})$
Mean particle size ( $M$ )	$\tau_c = [0.01199 + 0.0101(1.2 - e)] - [0.00589 + 0.0009(e - 1.2)] \log(M)$
Calcium/sodium ratio ( $R_{cn}$ )	$\tau_c = [0.02024 + 0.0235(1.2 - e)] + [0.00264 + 0.00812(e - 1.2)] \log(R_{cn})$
Percentage of clay (PC)	$\tau_c = [0.0141 + 0.0075(1.2 - e)](10)^{0.00621PC}$

Partheniades (1965) proposed the following model to link the erosion rate to the shear stress of fine-grained soils. This model was used later on by Hanson and Cook (2004) with an exponent  $a$  equal to 1 and by Briaud et al. (2001b) with an exponent different from 1.

$$\dot{z} = k_d(t_a - \tau_c)^a \quad (27)$$

where

$\dot{z}$  = erosion rate (m/s),

$k_d$  = erodibility coefficient ( $\text{m}^3/\text{N} * \text{s}$ ),

$a$  = exponent typically assumed to be 1,

$\tau_a$  = applied shear stress on the soil boundary (Pa), and

$\tau_c$  = critical shear stress (Pa).

Neill (1967) proposed an equation to predict the critical velocity of coarse-grained soils on the basis of experimental data on six sizes of graded gravels, two sizes of uniform glass balls, and cellulose acetate balls ranging in diameter from 6 to 30 mm. The depth of flow is included in the equation proposed by Neill (1967), which would indicate that critical shear stress is not merely a soil property (Clark and Wynn 2007).

$$\frac{\rho Y_{mc}^2}{\gamma_s D_g} = 2.50 \left( \frac{D_g}{d} \right)^{-0.20} \quad (28)$$

where

$V_{mc}$  = competent mean velocity for first displacement of bed material,

$D_g$  = effective diameter of bed grains,

$d$  = depth of flow,

$\gamma_s$  =  $g(\rho_s - \rho)$ ,

$g$  = acceleration due to gravity,

$\rho$  = fluid mass density, and

$\rho_s$  = bed-material mass density.

## 60 Relationship Between Erodibility and Properties of Soils

Kandiah and Arulanandan (1974) also performed both flume tests and rotating cylinder tests on saturated and unsaturated Yolo clay loam. The influence of the sodium adsorption ratio (SAR) as well as the salt concentration of the sample on soil erodibility was investigated. SAR is defined in Equation 29.

$$\text{SAR} = [\text{Na}] / \sqrt{0.5[(\text{Ca}^{++}) + (\text{Mg}^{++})]} \quad (29)$$

Kandiah and Arulanandan also studied the influence of the water content of the compacted samples on flaking. They concluded that an increase in salt concentration leads to a decrease in critical shear stress, whereas an increase in SAR would raise the critical shear stress. They also found that the water content of the sample in the saturated state does not have a significant impact on erodibility. However, in the case of an unsaturated compacted sample, it was observed that an increase in moisture content led to an increase in critical shear stress.

Sargunan (1977) also used the rotating cylinder test to study the impact of mineralogy, soil pore fluid, and the chemistry of the eroding fluid on the erodibility of cohesive soils. However, this study did not lead to proposed regression equations. Sargunan tried Na instead of Ca or magnesium (Mg) and observed that the critical shear stress typically decreased when the SAR increased. Also, it was found that an increase in salt concentration at a given SAR led to an increase in critical shear stress. However, Sargunan indicated that the influence of mineralogy was more significant when the SAR was relatively high.

Arulanandan and Perry (1983) challenged the contemporary filter design method, in which dam engineers of the time were using widely graded sand–gravel combinations as a filter for the core materials without taking erosion into account. Arulanandan and Perry concluded that using the classification plot based on plasticity proposed by Gibbs (1962) (Figure 29), was not sufficient to categorize erodibility, as some dam failures were observed in the “high resistance to erosion” zone of Gibbs’ (1962) proposed plot. Using flume tests and rotating cylinder tests, Arulanandan and Perry studied 29 dams that consisted of both dispersive and nondispersive core materials and performed erodibility tests on them. As a result, three general categories were proposed for the erodibility of core materials in dams:

1. **Erodible soils.** These are soils that have a critical shear stress less than 0.4 Pa. Filter tests are highly recommended to ensure the success of a filter in resisting erosion.
2. **Moderately erodible soils.** These are soils that have a critical shear stress between 0.4 and 0.9 Pa. Testing similar to that recommended for erodible soils is needed to certify the filter material.
3. **Erosion-resistant soils.** A regular filter design procedure can be implemented in these cases.

Another finding of Arulanandan and Perry (1983) was that a nondispersive clay is not necessarily an erosion-resistant clay, owing to many factors such as clay type, composition of the eroding fluid as well as the pore fluid, pH, organic matter, temperature, and structure of the soil. This was also shown by Acciardi (1984), who found that some soils classified as dispersive clay on the basis of a pinhole test were found in the third category (erosion-resistant soils) of the Arulanandan and Perry category chart. Arulanandan and Perry proposed plots for saturated remolded soils to relate the critical shear stress and eroding fluid concentration. Figure 30 shows two of the proposed plots relating the eroding fluid concentration with the erosion rate and critical shear stress.

Chen and Anderson (1987) investigated damages due to overtopping in 21 embankments in five U.S. states. They proposed the following equations for critical shear stress ( $\tau_c$ ) and erosion rate ( $E$ ):

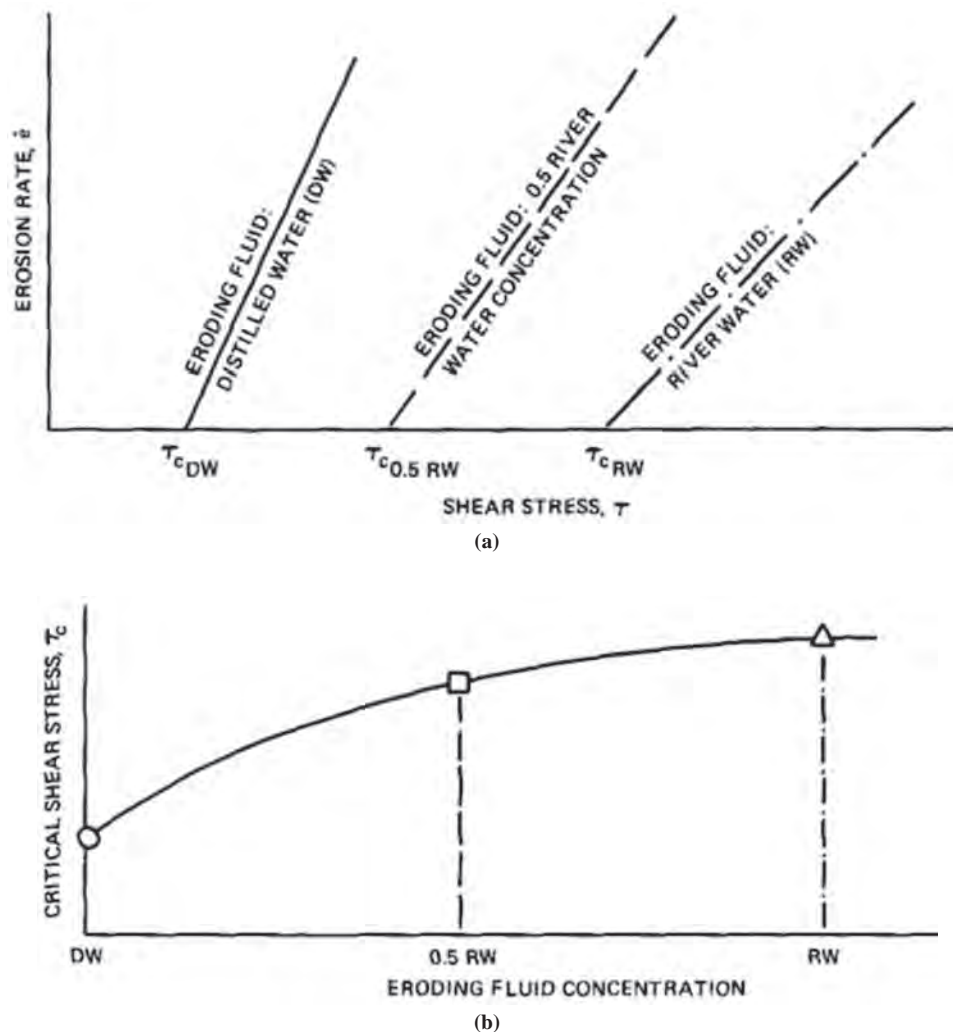


**Figure 30.** Proposed charts by Arulanandan and Perry (1983) for relating erosion rate, critical shear stress, and eroding fluid concentration: (a) effect of eroding fluid on erosion rate and shear stress and (b) critical shear stress versus eroding fluid concentration.

- Noncohesive material for a shear Reynolds number greater than 70:

$$\tau_c = 0.05(\gamma_s - \gamma)D_{50} \quad (30)$$

where

- $\gamma_s$  = unit weight of soil,
- $\gamma$  = unit weight of water, and
- $D_{50}$  = median particle size of soil

- Cohesive material (uncompacted, ranging from a silty loam soil to a highly cohesive clay soil):

$$\tau_c = 0.0034(PI)^{0.84} \quad (31)$$

- Cohesive material (normally compacted):

$$\tau_c = 0.019(PI)^{0.58} \quad (32)$$

## 62 Relationship Between Erodibility and Properties of Soils

- Highly cohesive soil such as clay ( $PI \geq 10$ ):

$$E = 0.000086(\tau - \tau_c)^{0.91} \quad (33)$$

- Low-cohesive soil such as sandy clay ( $PI \leq 5$ ):

$$E = 0.00022(PI)^{0.43} \quad (34)$$

- Noncohesive sand/gravel soil:

$$E = 0.00324(PI)^{1.3} \quad (35)$$

where

$E$  = erosion rate (cubic feet per second-foot),  
 $\tau$  = shear stress (pounds per square foot),  
 $\tau_c$  = critical shear stress (pounds per square foot)  
 $\gamma_s$  = soil unit weight (pounds per cubic foot),  
 $\gamma$  = water unit weight (pounds per cubic foot),  
 $PI$  = plasticity index (percent), and  
 $D_{50}$  = mean grain size (inches).

Chen and Anderson later created monographs using Equations 30 to 35 to predict the damage to embankments caused by flood overtopping.

Shaikh et al. (1988a) used a flume system to study the erodibility of unsaturated compacted clay soils. Various mixtures of materials (e.g., Na-montmorillonite + silica) were used to prepare four samples with different percentages of clay (100%, 70%, 40%, and 10%). According to their tests on the four clayey samples, Shaikh et al. proposed empirical correlations for linking the erosion rate of the compacted clayey samples to the clay percentage and critical shear stress for the range of moisture content and saturation tested. They also found out that the compacted moisture content of the samples did not have a significant effect on erosion rates. The reason was that because the same compaction method was implemented, the orientation of particles was similar for all the samples. They first defined the erosion function as the following linear equation (Shaikh et al. 1988a):

$$\dot{\epsilon} = C\tau \quad (36)$$

where

$\dot{\epsilon}$  = erosion rate ( $N/m^2/min$ ),  
 $\tau$  = hydraulic shear stress, and  
 $C$  = erosion rate coefficient ( $1/min$ ).

Shaikh et al. (1988a) proposed the following relationships between the erosion rate coefficient,  $C$  ( $1/min$ ), percentage of clay (PC), and torvane shear stress ( $S_t$ ) (MPa).

$$C = 4.14 \times (PC)^{-0.91} \quad (37)$$

$$C = 0.157 \times (S_t)^{-1.338} \quad (38)$$

Shaikh et al. (1988b) tested Ca-montmorillonite (a nondispersive clay) and Na-montmorillonite (a dispersive clay) by using a flume system to study the relationships between dispersivity and erodibility of the soil. The dispersivity of the soils was measured according to Sherard et al.

(1976). Again, the effect of the compacted moisture content was believed to be minimal. Shaikh et al. (1988b) proposed the following equation for relating erodibility to the chemistry of the pore water by using the SAR (mEq/L)<sup>0.5</sup>:

$$C = 4.41 \times (\text{SAR})^{-1.34} \quad (39)$$

Hanson (1992) and Hanson and Robinson (1993) used submerged jet tests in the laboratory to investigate the impact of compaction and associated moisture content on the erosion resistance of soils. The soils tested were clays and silty clays with a PI ranging from 7 to 12%. Both static and dynamic compaction methods were used to prepare 29 samples at different moisture contents and compaction efforts. Hanson and Robinson plotted dry density and moisture content versus the unitless jet index ( $J_i$ ) which was defined earlier by Hanson (1991):

$$\frac{D_s}{t} = J_i U_0 \left( \frac{t}{t_1} \right)^{-0.931} \quad (40)$$

where

$D_s$  = maximum scour depth,

$t$  = time of erosion,

$U_0$  = jet velocity at the nozzle, and

$t_1$  = time unit equivalent of 1 s.

Hanson (1991) showed that  $J_i \geq 0.02$  refers to highly erodible materials, while  $J_i < 0.002$  is associated with very low erodible geomaterials.

Comparison between the  $J_i$  values and the moisture content and dry unit weight indicated that  $J_i$  decreases (i.e., erosion resistance increases) when the dry density increases at a constant moisture content. Also, it was concluded that for a given dry unit weight, an increase in moisture content would decrease  $J_i$  (or increase the erosion resistance of the soil) for unsaturated soil samples. For saturated samples, however, an increase in moisture content increases the  $J_i$  value. Hanson and Robinson (1993) also compared the test results with the open channel tests conducted by Robinson (1990) on the same samples and found those results to be in agreement with their findings.

Ghebreiyessus et al. (1994) performed flume tests on Mexico silty loamy soils to study the effect of vane shear strength and bulk density on soil erodibility parameters. Table 8 shows the

**Table 8. Predicted regression models for relationships between erosion rate, shear stress, bulk density, and vane shear strength (Ghebreiyessus et al. 1994).**

Equation No.	Regression Equation	Model $R^2$	F-value	Pr > F
1	$Y = 1.8 + 0.21\tau$	0.25	4	0.07
2	$Y = 41.3 + 0.5\tau - 31 \times \rho_b$	0.68	11	0.002
3	$Y = -4.0 + 5.9\tau + 2.3 \times \rho_b - 4.1 (\tau \times \rho_b)$	0.97	108	0.0001
4	$Y = 5.5 + 0.3\tau - 0.5VE$	0.66	11	0.003
5	$Y = -1.4 + 1.3\tau + 0.04VE - 0.07 (\tau \times VE)$	0.94	55	0.0001

Note:

$Y$  = detachment rate ( $\text{g m}^{-2} \text{s}^{-1}$ ),

$\rho_b$  = bulk density ( $\text{Mg/m}^3$ ),

$\tau$  = shear stress (Pa), and

VE = vane shear strength (kPa).

## 64 Relationship Between Erodibility and Properties of Soils

results of their regression analyses. The erosion or detachment rate is defined here as the rate of mass removal per unit area ( $\text{g m}^{-2}\text{s}^{-1}$ ).

Briaud et al. (2001a) and Briaud (2008) proposed a set of equations to predict the critical velocity and critical shear stress of coarse-grained soils on the basis of many erosion function apparatus (EFA) tests performed at Texas A&M University.

$$v_c (\text{m/s}) = 0.35(D_{50} (\text{mm}))^{0.45} \quad (41)$$

$$\tau_c (\text{Pa}) = D_{50} (\text{mm}) \quad (42)$$

Briaud (2008) concluded that for fine-grained soils, there is no direct relationship between critical velocity/shear stress and mean particle size. However, Briaud (2008) bracketed the data with an upper bound and a lower bound equation as follows:

$$\text{Upper bound: } v_c (\text{m/s}) = 0.03(D_{50} (\text{mm}))^{-1} \quad (43)$$

$$\text{Lower bound: } v_c (\text{m/s}) = 0.1(D_{50} (\text{mm}))^{-0.2} \quad (44)$$

$$\text{Upper bound: } \tau_c (\text{Pa}) = 0.006(D_{50} (\text{mm}))^{-2} \quad (45)$$

$$\text{Lower bound: } \tau_c (\text{Pa}) = 0.05(D_{50} (\text{mm}))^{-0.4} \quad (46)$$

Figure 31 shows the scattered data for both fine-grained soils and coarse-grained soils with the defined upper and lower bounds.

Hanson and Simon (2001) proposed a relationship between the critical shear stress and the erodibility coefficient for soils with 50% to 80% silt size material. The results were based on 83 submerged jet tests in the midwestern United States.

$$k_d = 0.2\tau_c^{-0.5} \quad (47)$$

where  $k_d$  is the erodibility coefficient  $\left( \frac{\text{cm}}{N - \text{sec}} \right)$  and  $\tau_c$  is the critical shear stress (Pa).

Wynn et al. (2004) investigated the influences of vegetation on stream bank erosion at 25 sites in Virginia. They used Hanson's submerged jet test to measure the critical shear stress and erodibility of soils. The critical shear stresses measured ranged from 0 to 22 Pa. Wynn and colleagues concluded that bulk density is the most influential parameter in soil erodibility. Depending on the soil texture, other influential parameters were inferred to be moisture content, root density, pore and stream water chemistry, and freeze-thaw cycling. They categorized the data into three groups. Groups 1 and 2 included plastic soils, while Group 3 was made up of nonplastic soils. Group 1 included plastic soils with higher bulk densities, lower PI, and lower organic content than the soils in Group 2. Table 9 shows the results of regression analyses on the critical shear stress and some engineering properties.

Amos et al. (2004) use two benthic annular flumes and soils from 24 sites to study the stability of the seabed in the Venice Lagoon. Water temperature, salinity, organic content, and bulk densities were controlled under different conditions. Amos and colleagues proposed an equation for natural lacustrine, estuarine, and marine muds that could link the critical shear stress and the wet sediment bulk density:

$$\tau_{cr} = 5.44 \times 10^{-4}(\rho_b) - 0.28 \quad (48)$$

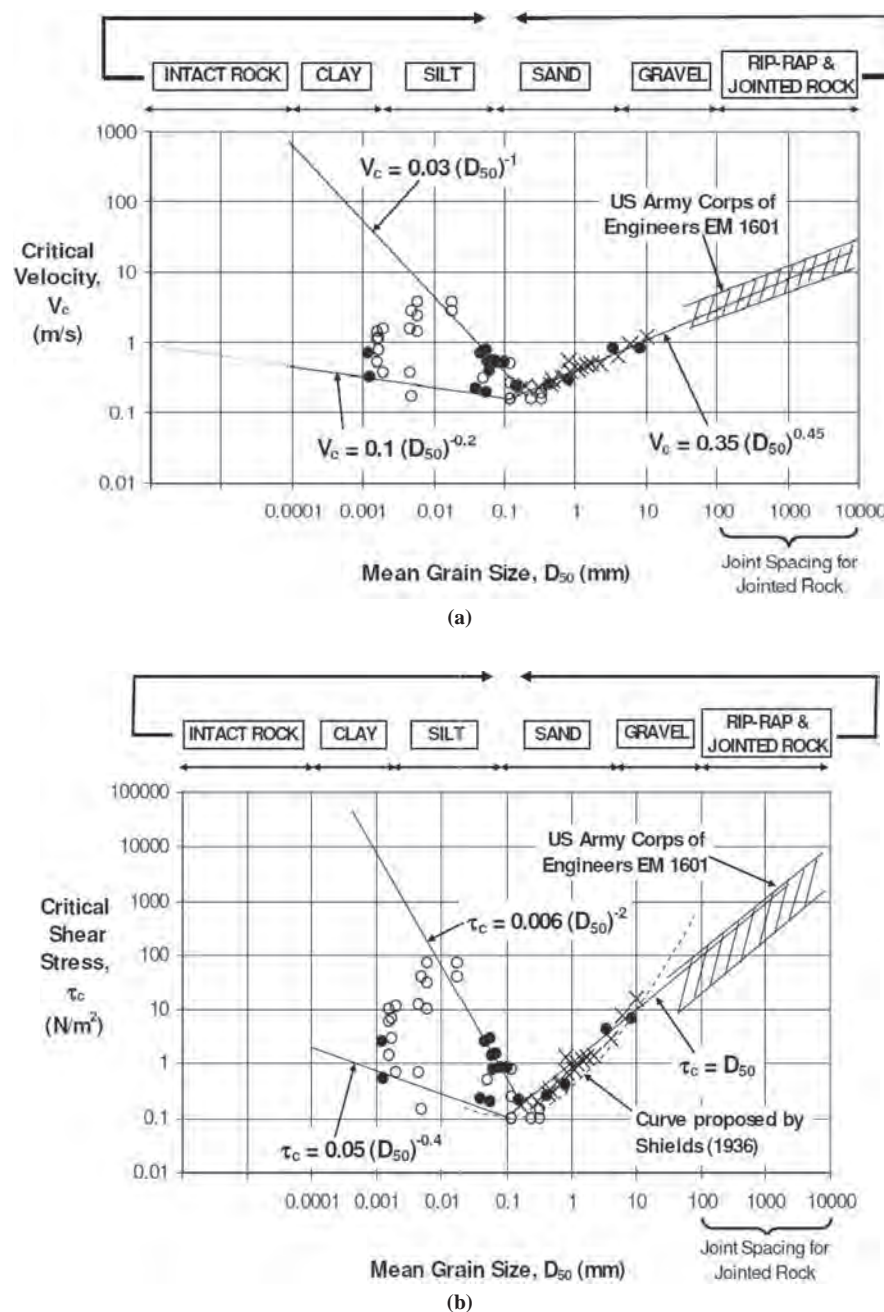


Figure 31. Plots of (a) critical velocity and (b) shear stress versus the mean particle size ( $D_{50}$ ) (Briaud 2008).

## 66 Relationship Between Erodibility and Properties of Soils

**Table 9. Regression equations for soil critical shear stress in southwest Virginia (Wynn et al. 2004).**

Soil Group	Equation	n	p-value	R <sup>2</sup>
All data	$\tau_c^{0.36} = 1.79 + 0.47BD^{2.5} - 0.27 \ln(KIF) - 0.85SWpH^6 - 0.08WT$	42	0.000	0.569
Group 1	$\tau_c^{0.36} = 1.48 + 0.11\sigma - 0.00035sand^2$	9	0.002	0.718
Group 1	$\tau_c^{0.36} = -0.44 + 0.067\sigma + 0.64BD^{2.5}$	18	0.001	0.663
Group 1	$\tau_c^{0.36} = 1.36 + 0.078\sigma - 0.00018sand^2$	18	0.005	0.508
Group 3	$\tau_c^{0.36} = -0.24 + 1.26BD^{2.5} - 0.23MC^{-1} - 0.86S:C^{-0.4}$	15	0.002	0.733
Group 3	$\tau_c^{0.36} = 2.11 + 2.21AS^5 - 1.07RDAM^2 - 1.15SWpH^6 - 0.00044SG^8$	12	0.001	0.913

Note:

KIF = potassium intensity factor,

WT = temperature of water (°C),

BD = bulk density (g/cm<sup>3</sup>), $\sigma$  = standard deviation of particle size distribution,

sand = sand percentage,

MC = moisture content,

S:C = ratio of silt to clay in soil,

SWpH = ratio of pore water to river water pH,

AS = aggregate stability,

SG = soil specific gravity, and

RDAM = related to the difference between median and average periods frozen.

where  $\tau_{cr}$  is the critical shear stress (Pa), and  $\rho_b$  is the sediment wet bulk density (kg/m<sup>3</sup>). Equation 48 is based on 73 sets of data; the  $R^2$  value for Equation 48 is 0.46.

Thoman and Niezgoda (2008) studied the stability of 25 channel sites in Wyoming. To do so, they conducted several in situ JET tests and measured the erodibility parameters; the geotechnical properties were obtained from parallel laboratory tests. They found that the most influential parameters were activity, organic content, cation exchange capacity, soil pH, and dispersion ratio. No linear correlation was found between the critical shear stress and each of the aforementioned geotechnical parameters; however, combining all five parameters, Thoman and Niezgoda (2008) proposed the following equation:

$$\tau_c = 77.28 + 2.20(Act) + 0.26(DR) - 13.49(SG) - 6.40(pH) + 0.12(w) \quad (49)$$

where

 $\tau_c$  = critical shear stress (Pa),

Act = soil activity (ratio of PI to percentage of clay),

DR = dispersion ratio,

SG = specific weight,

pH = chemical index for acidity, and

w = water content (%).

The reliability of the proposed model can be seen in Figure 32. The dashed lines show the one standard deviation range.

Winterwerp and van Kesteren (2004) presented a theoretical derivation of an erosion rate parameter M:

$$M = \frac{c_v \phi_{s,0} \rho_{dry}}{10D_{50}c_u} = \frac{c_v \left( \frac{1}{1 + (W_0 \phi_s / \phi_w)} \right) \rho_{dry}}{10D_{50}c_u} \quad (50)$$

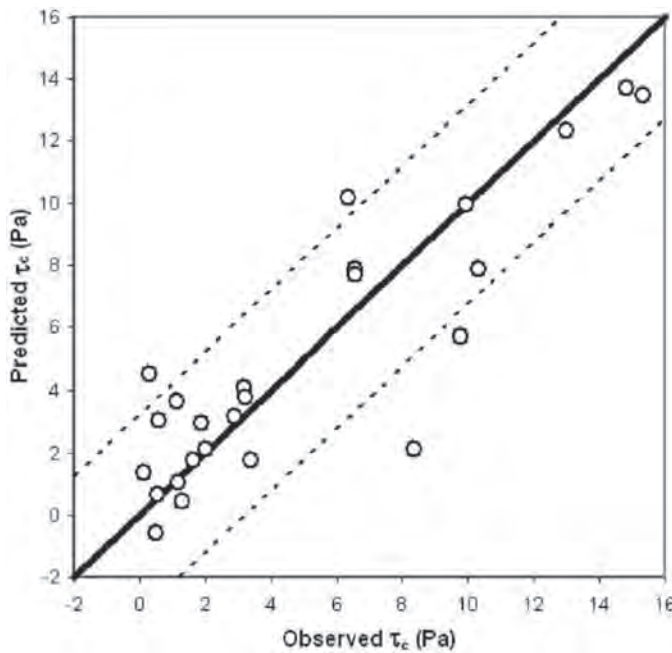


**Figure 32.** Estimated versus actual critical shear stress from the Wyoming channels (Thoman and Niegzoda, 2008).

where

- $c_v$  = vertical consolidation coefficient,
- $\varphi_{s,0}$  = volumetric concentration,
- $W_0$  = water content,
- $\varphi_s$  = density of the primary sediment particles,
- $\varphi_w$  = density of the water,
- $\rho_{dry}$  = dry bulk density,
- $D_{50}$  = mean particle size, and
- $c_u$  = undrained shear strength.

Julian and Torres (2006) developed an equation linking the critical shear stress in pascals to the silt and clay (SC) content (%):

$$\tau_c = 0.1 + 0.1779(\text{SC}) + 0.0028(\text{SC})^2 - 0.0000234(\text{SC})^3 \quad (51)$$

Mostafa et al. (2008) developed a relationship between a nondimensional shear stress of mass erosion and a nondimensional soil parameter.

$$\tau_p^* = -23.67\chi + 17.28 \quad (52)$$

$$\tau_m^* = -107.56\chi + 79.59 \quad (53)$$

with

$$\chi = \frac{\text{LI}}{S_G - 1}$$

**68** Relationship Between Erodibility and Properties of Soils

where

$\tau_p^*$  = nondimensional erosion resistance for particle erosion,

$\tau_m^*$  = nondimensional erosion resistance for mass erosion,

$\chi$  = nondimensional soil parameter,

LI = liquidity index =  $\frac{\omega - \omega_{PL}}{PI}$ , and

$S_G$  = specific gravity based on moist bulk density.

Straub and colleagues (2010, 2013) studied the ultimate pier and contraction scour methods for cohesive soils at 30 bridge sites throughout Illinois. As part of this study, they showed that the unconfined compressive strength of the tested cohesive soils provided a good estimate of the critical shear stress obtained from the EFA (Equation 54):

$$\tau_c = 0.1065 \ln Q_u + 0.209 \quad (54)$$

where  $\tau_c$  (psf) is the critical shear stress and  $Q_u$  (tsf) is the unconfined compressive strength.

Fleshman and Rice (2013) developed a piping erosion test device called the constant gradient piping test apparatus and performed multiple tests on sandy soils to investigate the effect of grain size, gradation, and specific gravity on the critical hydraulic gradient required for piping to start. Although they did not propose a practical correlation equation, Fleshman and Rice (2013) showed that, in general, angular sandy soils have greater piping resistance. Greater piping resistance was also observed when the sandy samples were graded. The specific gravity was also shown to be directly proportional to the piping resistance.

Bones (2014) developed a methodology for predicting critical shear stress by using the Unified Soil Classification System categories. Shan et al. (2015) also proposed general relationships between critical shear stress, water content, unconfined compressive strength, PI, and fine content on the basis of a limited range of cohesive soil.

Singh and Thompson (2015) used the cohesive strength meter in soils with different moisture contents and measured the in situ critical shear stress in fields and grassed waterways. The study showed that the critical shear stress varies with moisture content and is not constant for a soil. It was also observed that critical shear stress is proportional to soil moisture until it is below the plastic limit. Singh and Thompson (2015) proposed the following equation for the case in which the soil moisture content is less than the plastic limit in grassed waterways. The  $R^2$  associated with Equation 55 is 0.68.

$$\tau_c = 0.70 \times e^{0.06 \times (\text{moisture content, \%})} \quad (55)$$

Using the EFA and electrical resistivity tomography (ERT), Karim and Tucker-Kulesza (2018) evaluated the erosion resistance of 15 selected bridge sites in Kansas. They observed that the erodibility of a soil changed with the in situ electrical resistivity of the soil. Therefore, ERT could be used as an alternative quick tool for predicting the erodibility of a site instead of performing different erosion tests such as the EFA. By comparing the results of the EFA with ERT for highly erodible sites, Karim and Tucker-Kulesza (2018) indicated that when the electrical resistivity exceeds  $50 \Omega\text{m}$ , there is a 93% chance that the tested soil will be categorized as having high erodibility. ERT was introduced as a crude tool for identifying the critical locations prone to erosion at a site. The selected critical locations then would need further investigation to evaluate their erodibility.

It is very important to evaluate the reliability of these equations, as the scatter in the data may be significant. In the next section of this chapter, the influence of each soil property is discussed in qualitative terms.

## 3.2 Influence Factors on Erosion

### 3.2.1 Broad Geological Properties That Influence Erodibility

The erodibility of soil can vary significantly; therefore, in general, erodibility depends on engineering soil properties. Some of the broad geological properties likely to influence erodibility include

- Soil microstructure and macrostructure,
- Lithification,
- Strength of structural (cohesion) forces between particles and between water molecules and particles,
- Lithology and anisotropy of soil at the different scales (laboratory and in situ),
- Grain size distribution,
- Mineral and chemical composition of soil,
- Geotechnical properties, and
- Presence of fissures in a given soil massive that affect at full scale the field behavior of clay. Scale, specifically, becomes a critical factor when the presence of fissures in the soil is considered. Many laboratory tests are not able to capture the effects of fissures or joints because of the small size of the tested sample.

It is clear that many factors can influence the erosion behavior of a soil. On the basis of the literature review conducted for this report, a list of typical properties that affect the erosion resistance of soils is given in Table 10. This table is divided into two categories: the more typically obtained properties and the less typically obtained properties. As mentioned earlier, the main goal of this project was to develop reliable and simple equations quantifying the erodibility of soils on the basis of soil properties.

### 3.2.2 Effects of Less Typically Obtained Parameters

The fact that the following parameters are not typically obtained does not mean that they are not important when it comes to predicting erosion.

#### 3.2.2.1 Mineralogy and Particle Size Distribution

One of the very important parameters that needs to be carefully studied is the effect of mineralogy and of particle size distribution on the erosion resistance of soils. In terms of grain size

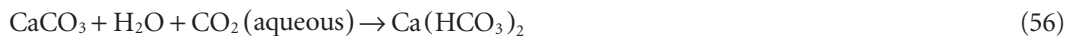
**Table 10. Soil and water properties that influence the erosion resistance of soils.**

More Typically Obtained Properties	Less Typically Obtained Properties
<ul style="list-style-type: none"> <li>• Plasticity index</li> <li>• Liquidity index</li> <li>• Unit weight</li> <li>• Water content</li> <li>• Undrained shear strength</li> <li>• Percentage passing sieve #200</li> <li>• Percentage of clay particles</li> <li>• Percentage of silt particles</li> <li>• Mean grain size</li> <li>• Coefficient of uniformity</li> <li>• Percentage of compaction (for man-made soils only)</li> <li>• Soil swell potential</li> <li>• Soil void ratio</li> </ul>	<ul style="list-style-type: none"> <li>• Specific gravity of solids</li> <li>• Soil dispersion ratio</li> <li>• pH (flowing water and pore water)</li> <li>• Salinity of eroding fluid</li> <li>• Organic content</li> <li>• Soil cation exchange cap</li> <li>• Soil clay minerals</li> <li>• Soil sodium adsorption ratio</li> <li>• Soil activity</li> <li>• Soil temperature</li> <li>• Density of cracks</li> </ul>

## 70 Relationship Between Erodibility and Properties of Soils

distribution, there are four major fractions—gravel, sand, silt, and clay—that affect the erosion resistance of soil under different flow conditions.

**Gravel Fraction (2–20 mm).** The erosion behavior of the gravel fraction depends mostly on the correlation between the weight of the particle and the hydrodynamic force applied to the particle. The mineral composition of gravel is an issue as well and becomes important when the particle is formed by carbonate minerals ( $\text{CaCO}_3$ ). Leaching of carbonate minerals is likely to occur in the presence of aggressive carbon dioxide in aqueous form ( $\text{CO}_2$ ). The following reaction between carbonate minerals and water takes place:



As a result of this reaction, lightly soluble calcium bicarbonate will form and go to an aqueous phase; thereafter, calcium carbonate is gradually destroyed. As a result, the content of hydrogen carbonate ion ( $\text{HCO}_3^-$ ) in the water increases as well as the content of calcium ion ( $\text{Ca}^{2+}$ ). The erosion behavior of the gravel fraction in soil can be important for glacial (moraine) clayey soil containing these fractions.

**Sand Fraction (0.075–2 mm).** The influence of sand particles on soil erosion is similar to that of gravel particles, as the most important factor that affects the erodibility of sand is the particle's weight and its mineral composition.

**Silt Fraction (0.002–0.074 mm).** The silt fraction is the least erosion resistant and soaking resistant of all the fractions. The presence of silt particles in soil may cause the collapse of the structure during wetting. For example, loess is less water resistant because it is made primarily of silt-sized particles (more than 70%). Some clayey soils in semiarid zones such as Texas contain a great amount of silt particles and could erode rapidly.

**Clay Fraction (<0.002 mm).** In clayey soils, the individual clay particles can form microaggregates (from single to dozens of micrometers) and macroaggregates (from dozens to thousands of micrometers) (Osipov et al. 1989). Light microscopes and electron microscopes can be used to identify the microstructure of clayey soil. The erosion behavior of clayey soils depends on the presence of micro- and macroaggregates in the matrix, on the ability of the particles to coagulate, on the size and shape of the particles, and on the clay's ability to resist disaggregation when submerged in water. The most active aggregate formation is associated with the smectite group (e.g., montmorillonite, nontronite, bentonite). In this case, the erodibility of clay containing smectites depends on the strength between the clay aggregates. After the bonds between clay aggregates collapse, the erosion resistance depends on the force between individual clay particles and the strength of those forces.

The clay fraction swells when it interacts with water. The swell potential typically increases with a decrease in water flow velocity. The presence of clay particles in sand creates a cohesion between sand particles that can significantly increase the resistance to erosion. The three major groups of clay minerals are kaolinite, illite, and montmorillonite. These minerals have very different structures, including bonding between layers. Figure 33 shows four general different clay mineral microstructures.

Many studies have been conducted to find out the potential relationships between erodibility and particle size. Particle size should be a factor considered only for coarse-grained soil. For fine-grained soils, particle size alone, without consideration of electrostatic and electromagnetic forces, is not an adequate representative.

Working separately, Maslov (1968) and Justin (1923) obtained very similar results in studying the relationship between critical velocity and size of particles. Table 11 and Figure 34 show

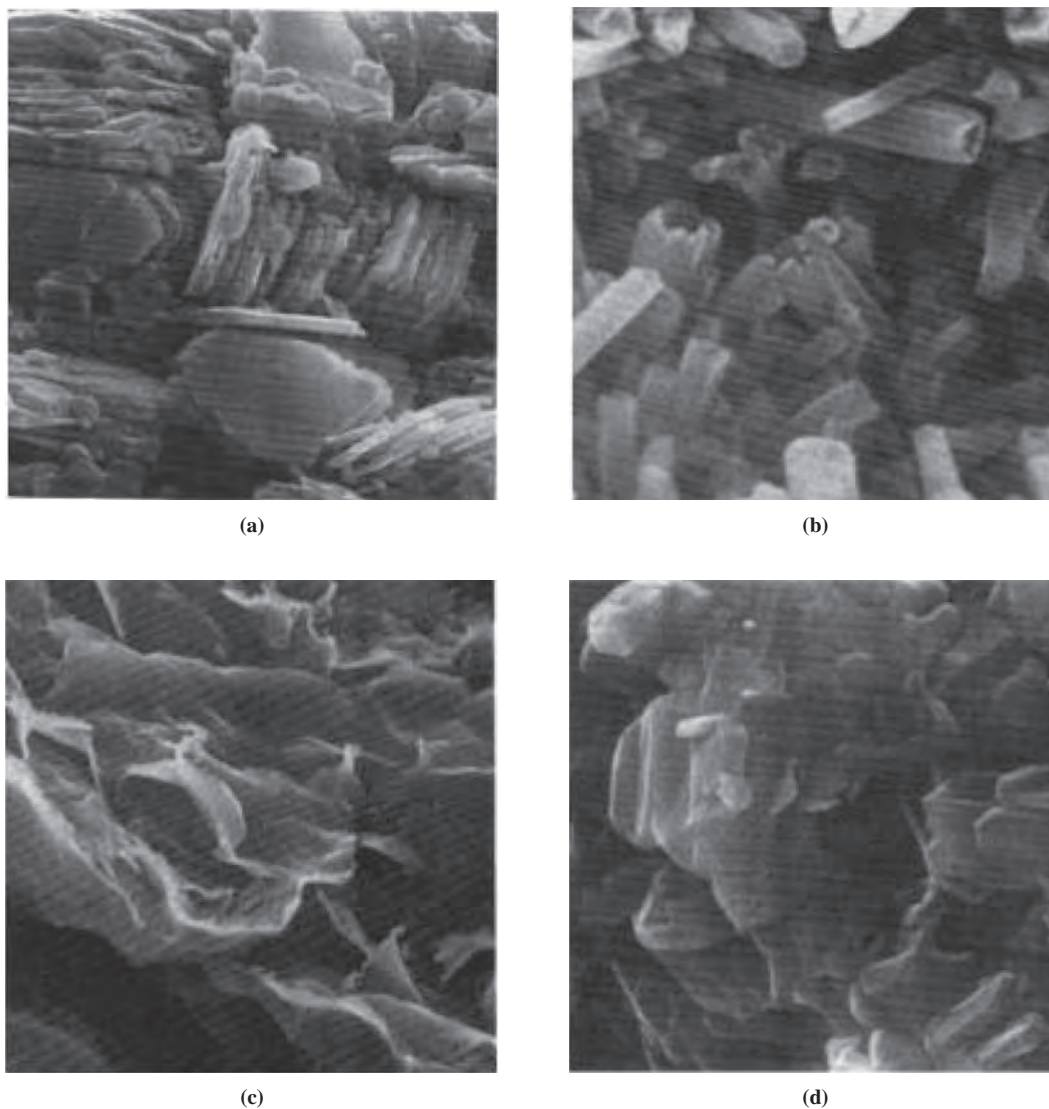


**Figure 33.** Clay mineral microstructure (Mitchell 1993 after Tovey 1971): (a) kaolinite, (b) halloysite, (c) montmorillonite, and (d) illite.

that critical velocity decreases as the diameter of the particle decreases. It was also observed that erosion resistance increases as the number of particles with a diameter of less than 0.05 mm and greater than 0.001 mm increases.

### 3.2.2.2 Structural or Cohesion Forces

The nature and the magnitude of structural or cohesion forces play a very important role in understanding the erodibility of clayey soils. The strength of the structural forces can vary significantly and depends on their nature and on the soil properties. Structural forces may be ion-electrostatic, molecular, magnetic, or chemical in nature.

One of the strongest forces is the chemical force that exists in geomaterials such as igneous rock and clay if the natural water content of the clay is below the plastic limit (Table 12). The nature of this force is electrical interaction between atoms. Once this chemical force fails, it cannot be recovered.

## 72 Relationship Between Erodibility and Properties of Soils

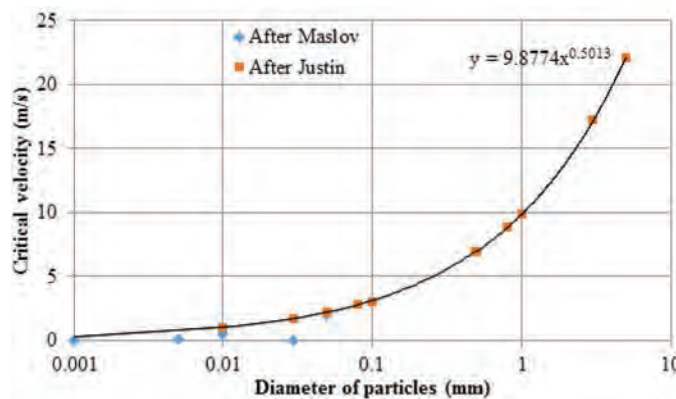
**Table 11.** Critical velocity of water flow ( $V_c$ ) depending on diameter of particles (Maslov 1968 and Justin 1923).

Diameter of Particles (mm)	Critical Velocity (cm/s)	
	Maslov	Justin
5	NA	22.1
3	NA	17.3
1	10	9.85
0.8	NA	8.83
0.5	7	6.97
0.1	3	3.05
0.08	NA	2.79
0.05	2	2.19
0.03	0	1.74
0.01	0.5	0.98
0.005	0.12	NA
0.001	0.02	NA

Note: NA = not available.

Molecular and ion-electrostatic (Coulomb) forces exist mostly in soft clays when the water content reaches the liquid limit. Molecular forces or van der Waals forces are weaker than chemical forces. The strength of the molecular force depends on the water content of the clay as well as on the dispersion ratio. With an increase in dispersion, the magnitude of molecular forces increases. The maximum strength of molecular forces is found in dry clay. As the water content of clay increases, the strength of the molecular force decreases. If the clay becomes wet, the diffusion layer of ions between and around particles causes the formation of the molecular-ion-electronic force, which is very likely to be destroyed by water flow.

Mirzhulava (1967) obtained a relationship between the critical velocity and the cohesion of saturated soils (Figure 35) indicating that the critical velocity of saturated soils increases as soil cohesion increases. The results of this study also show that critical velocity increases with an increase in the undrained shear strength of clay ( $S_u$ ) (Figure 36).

**Figure 34.** Critical velocity of water flow in different soils (Maslov 1968; Justin 1923).

**Table 12.** Type of cohesion forces in fine-grained soils (clayey soils) (Osipov et al. 1989).

Type of Clay	Type of Cohesion Force	Physical Nature of Force	Strength of Single Force (N)
Clayey silt ( $W \gg W_L$ )	Thixotropic and coagulation	Molecular Magnetic	$10^{-3}$ to $10^{-2}$ $10^{-8}$ to $10^{-9}$
Soft clay in quasi-liquid condition ( $W_L > W > W_p$ )	Thixotropic and coagulation, appearance of cementation	Magnetic Molecular Ion-electrostatic	$10^{-8}$ to $10^{-9}$ $10^{-3}$ to $10^{-2}$ $10^{-2}$ to 4
Clay in quasi-plastic condition ( $W \approx W_p$ )	Partially thixotropic and coagulation, partially cementation	Ion-electrostatic Molecular Chemical	$10^{-2}$ to 4 $10^{-3}$ to $10^{-2}$ $10^{-7}$ to $10^{-2}$
Hard clay (like mudstone) ( $W < W_p$ )	Cementation with subordinate significance of coagulation	Ion-electrostatic Chemical Molecular	$10^{-2}$ to 4 $10^{-7}$ to $10^{-2}$ $10^{-3}$ to $10^{-2}$
Very hard clay (like slate) ( $W \ll W_p$ )	Cementation	Ion-electrostatic Chemical	$10^{-2}$ to 4 $10^{-7}$ to $10^{-2}$

Note:  $W$  = water content;  $W_p$  = plastic limit;  $W_L$  = liquid limit.

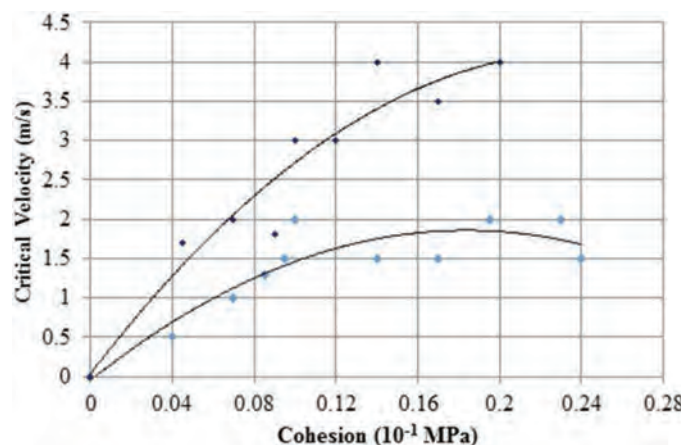


**Figure 35.** Critical velocity versus cohesion for saturated soil (Mirzhulava 1967).

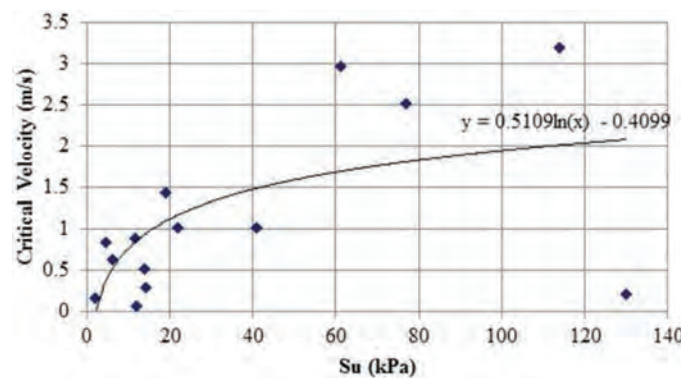


**Figure 36.** Relationship between critical velocity and undrained shear strength of clay (Mirzhulava 1967).

## 74 Relationship Between Erodibility and Properties of Soils

**Table 13. Critical velocity of water flow for carbonated lean clay (Zhordaniaya 1957).**

Water Content (%)	Critical Velocity (m/s)
<b>Disturbed Structure</b>	
3–6	0.15
11–12	0.25
18–20	0.4
23–25	0.5
<b>Undisturbed Structure</b>	
8–10	0.75
16–18	1.35
25–27	2.6

### 3.2.2.3 Disturbance of the Soil Structure

Disturbance of the soil structure also has an impact on erosion resistance. Zhordaniaya (1957) studied the influence of disturbance on the erodibility of carbonated lean clay. Table 13 clearly shows that disturbing the soil structure decreases the critical velocity significantly. The critical velocity of the same carbonated lean clay at a given water content decreases by a factor of 3 to 5 times when going from the undisturbed to the disturbed state. Carbonate soils are prone to having strong cementation but are not very resistant to chemical processes such as dissolution and leaching.

### 3.2.2.4 Chemical Composition of Soil

The chemical composition of soil has an impact on the erodibility of both fine- and coarse-grained soils. Erosion, especially suffusion, is likely to occur in sandy and clayey soils containing soluble salts. This type of erosion corresponds to a dissolution of salt and to a collapse of the corresponding bonds in the soil. The more soluble cases would be those with chloride and sulfate in the soil. The presence of these salts in the chemical composition of the soil accelerates the erosion process, owing to the co-occurrence of mechanical and chemical erosion. Table 14 shows the solubility of different salts in water.

### 3.2.2.5 Organic Content of Soil

Another influential factor in erosion is the presence in soil of biogenic forms (micro-organisms) and abiogenic material (organic matter in colloidal form). Organic colloids with a size of less than 0.0001 mm can clog the pore space and decrease the permeability of the soil. This is more important in coarse-grained soil (sand). The presence of organic colloids in the pore space can create some particle–particle cohesion as well as organic colloid–particle cohesion. This would lead to a decrease in water permeability and increase the resistance to erosion. The adhesion of microorganism cells to soil particles results in the formation of biofilms, which are extracellular substances glued to particles. This bond between the biofilm and the particle can help resistance against erosion.

A microbial enzyme is a product of microbial activity and works to stabilize active clay particles. It has a hydrophobic effect on the clay. Strengthening clayey soils by using enzyme technology is one of the soil improvement methods applied to decrease the hydrophilicity of clays and to protect them from erosion; however, in water erosion, the flow velocity at which the organic matter could be washed away may not be very high.

### 3.2.2.6 Presence of Cracks and Fissures (Micro- and Macroscale)

In a fractured rock or fissured soil mass, water discharges through the existing cracks and fissures. An increase in water discharge through the fissured soil mass provides an increase in the

**Table 14. Solubility of different salts in water.**

Type of Salt	Solubility in Water (g/100 g water)
Sodium chloride (NaCl)	35.8
Potassium chloride (KCl)	34.2
Calcium sulfate (CaSO <sub>4</sub> )	0.2
Calcium carbonate (CaCO <sub>3</sub> )	0.0014
Sodium hydroxide (NaOH)	107.0
Sodium sulfate (Na <sub>2</sub> SO <sub>4</sub> )	32.8
Magnesium chloride (MgCl <sub>2</sub> )	35.3

**Table 15. Critical fluid velocity above which rock erodes, depending on opening of cracks (Bogdanov and Smirnov 1972).**

Options	Opening of Crack (cm)					
	0.01	0.1	0.2	0.5	1.0	2.0
Critical velocity (m/s)	1.5	0.15	0.075	0.03	0.015	0.0075
Critical gradient of head	50	0.5	0.063	0.004	$5 * 10^{-4}$	$6.3 * 10^{-5}$
Coefficient of actual velocity (m/s)	0.003	0.3	1.2	7.5	30	120

Note: Coefficient of actual velocity is an average velocity through a crack at a gradient equal to 1.

opening of the fissures by erosion. Table 15 shows the critical fluid velocity above which rock erodes, depending on the opening of the cracks in the rock mass. The erosion rate changes as the opening of the cracks increases.

### 3.2.2.7 Wet–Dry Cycles

The wet–dry cycles are due to the weather and associated moisture migration in the soil profile by a thermal gradient during the year. These cycles have an impact on the soil erodibility. For example, the formation of shrinkage cracks and then water flowing through the cracks can erode a soil significantly. The density and size of the shrinkage cracks depends on the initial water content of the clay and on its plasticity index. This is particularly important at shallower depths with problems such as overtopping of levees during hurricanes or floods, river bank erosion, surface erosion of highway embankments, and so forth.

As mentioned earlier, the present study focuses on the influences of the most common geotechnical properties (Table 10). The selected properties are some of the more direct influences on erodibility and are commonly measured in the laboratory during geotechnical testing.



## CHAPTER 4

# Erosion Experiments

This chapter presents the results of all the erosion experiments performed as part of NCHRP Project 24-43. Section 4.1 of this chapter describes the Soil Erosion Laboratory at Texas A&M University (TAMU) and the testing devices that were built as part of this project. The design plans as well as photographs of each device that was built are presented in this section. Section 4.2 presents the erosion test plan matrix for the project, and Section 4.3 presents the results of the erosion experiments, namely, the mini-jet erosion test (mini-JET), the erosion function apparatus (EFA), the hole erosion test (HET), the pocket erodometer test (PET), and the borehole erosion test (BET). Finally, Section 4.4 presents the comprehensive information on the geotechnical properties of all tested samples. Appendix 1 of this report includes all detailed results of the erosion tests, and Appendix 2 presents the spreadsheets of the geotechnical properties of each sample. For each sample that was tested in any erosion device, many photographs and videos were taken before, during, and after the tests. The photographs and videos were collected in a file that is held by the authors.

### **4.1 TAMU Soil Erosion Lab and Testing Devices**

The primary step in performing the erosion tests in this study was furnishing the erosion lab with all necessary testing equipment and ensuring that the working conditions at TAMU were satisfactory. HET and JET devices were constructed in the lab, and TAMU's two EFA machines were refurbished. The work done in constructing the HET and JET devices and the refurbishment of the TAMU Soil Erosion Laboratory is summarized below.

#### **4.1.1 Construction of HET Apparatus**

The HET apparatus was constructed at TAMU in accordance with the work done by Wan and Fell (2002) at the University of New South Wales in Australia. A schematic diagram of this device and the design drawings are presented in Figure 37 to Figure 41. Two dummy tests were conducted to make sure that the constructed apparatus was ready for the testing schedule. Figure 42 shows the final version of the HET apparatus in the Soil Erosion Laboratory at TAMU.

#### **4.1.2 Construction of Mini-JET Apparatus**

The core part of the mini-JET device was obtained from the Department of Biosystems and Agricultural Engineering at Oklahoma State University. The JET test assembly was then constructed in the TAMU Soil Erosion Laboratory (Figure 43). Two dummy tests were also conducted to ensure that there was no considerable leakage or hindrance with the testing process. Figure 43 shows photos of the JET assembly.

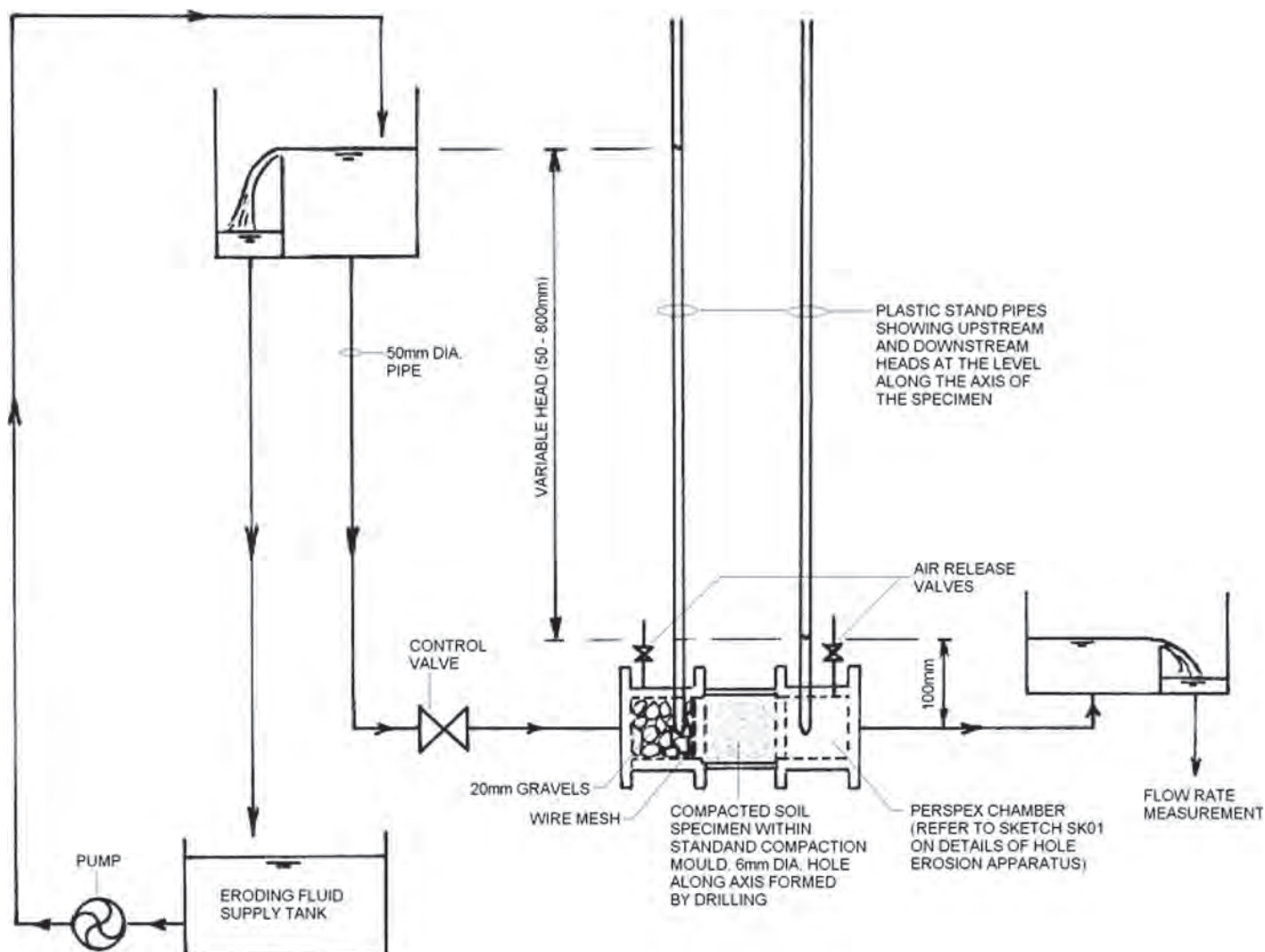
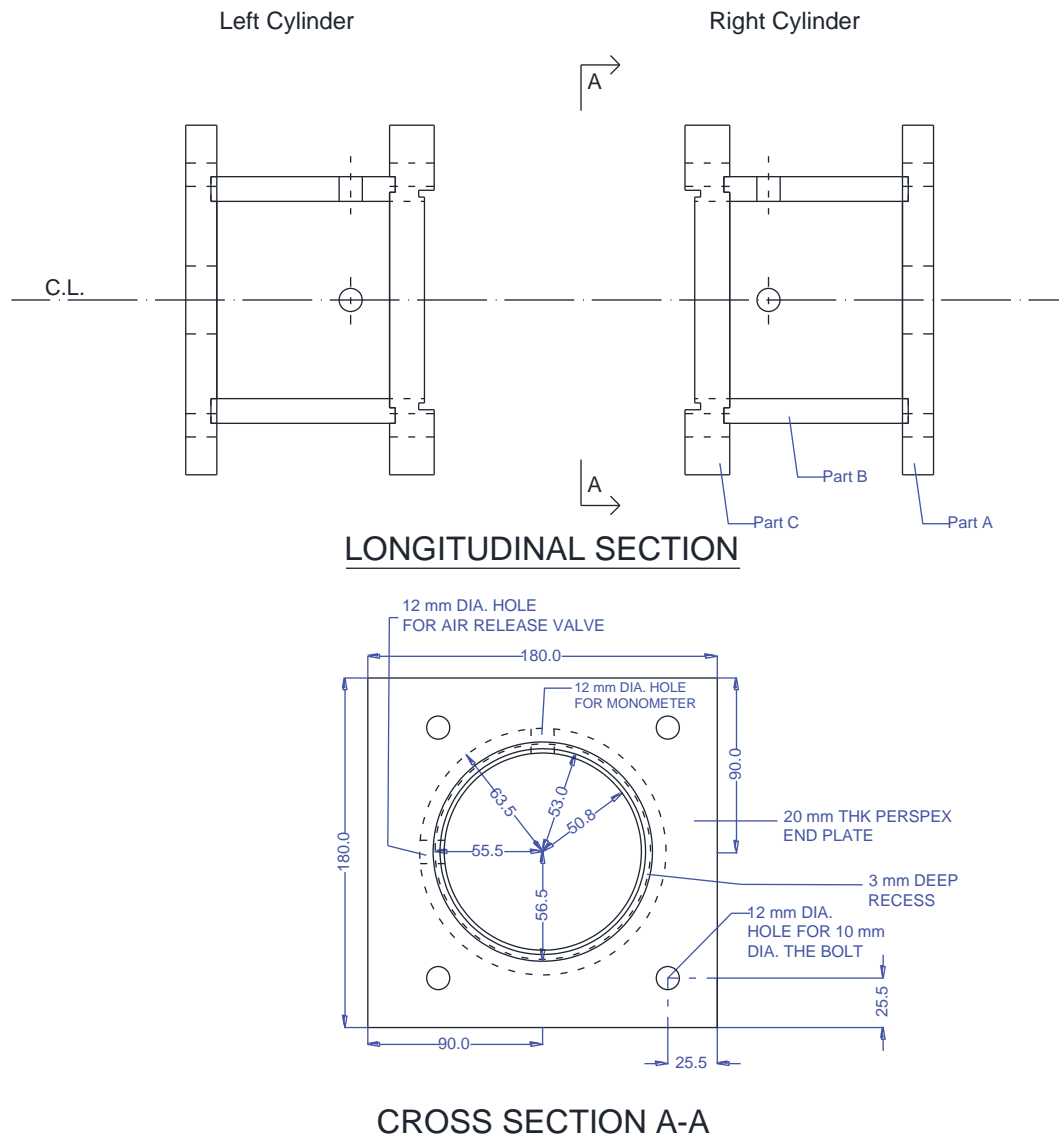
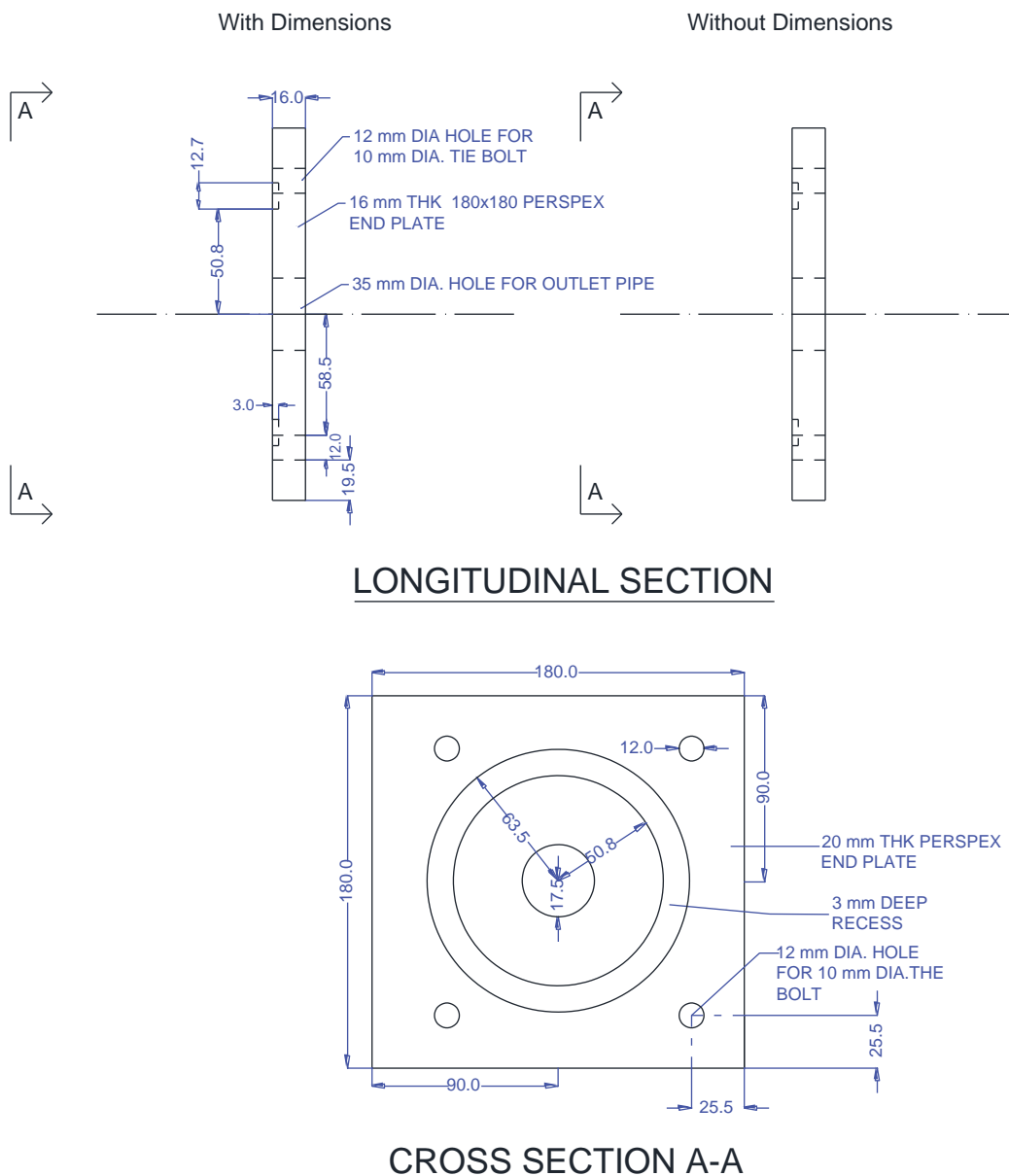


Figure 37. Schematic of HET assembly (Wan and Fell 2002).

## 78 Relationship Between Erodibility and Properties of Soils



**Figure 38.** Drawing of the entire HET assembly at a glance  
(all dimensions in millimeters).



**Figure 39.** Drawings of HET associated with Part A: End Plate (all dimensions in millimeters).

## 80 Relationship Between Erodibility and Properties of Soils

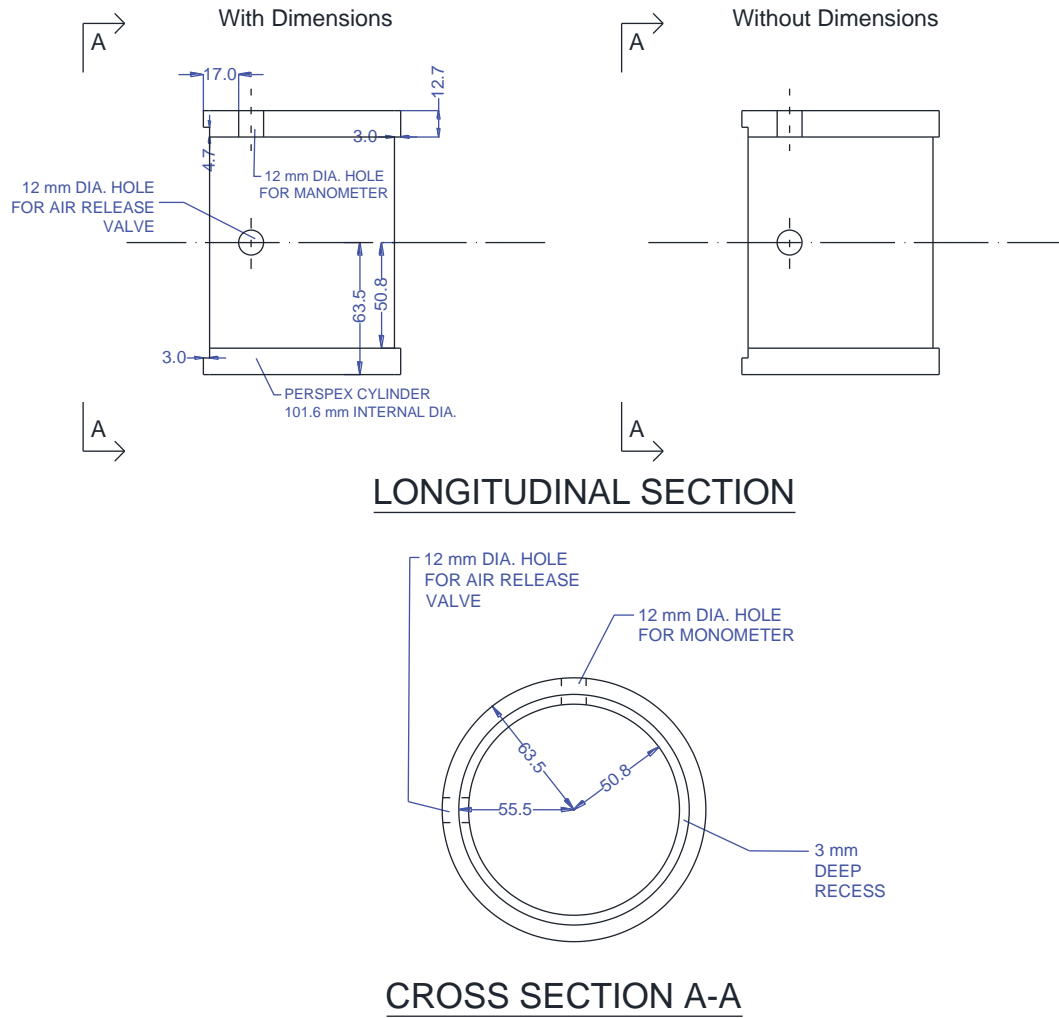
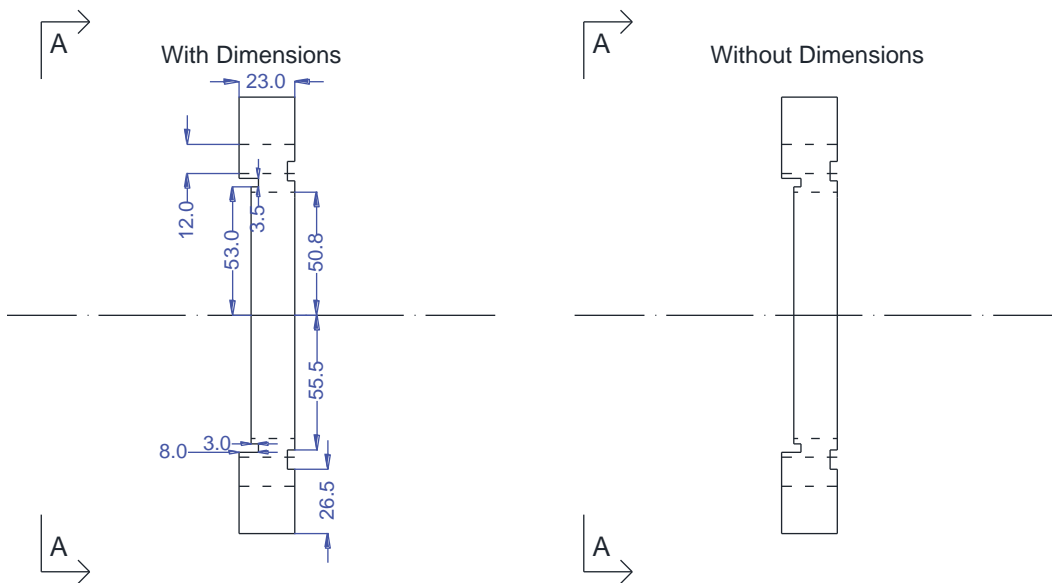
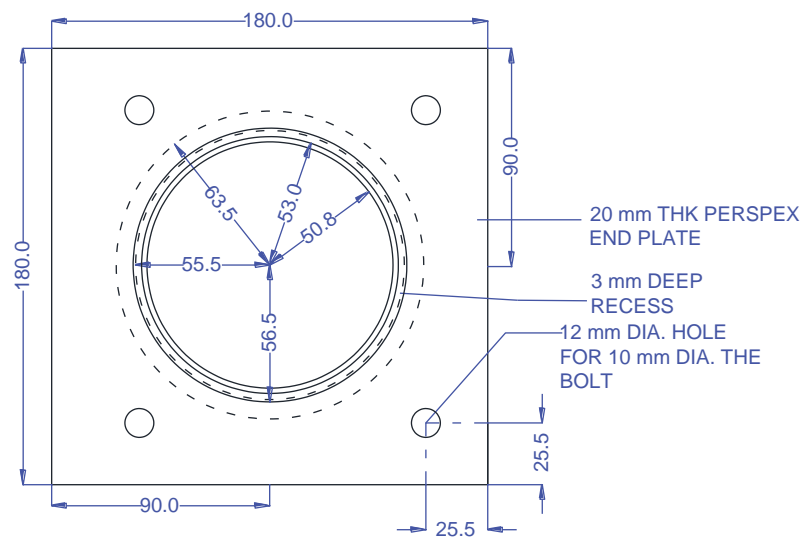


**Figure 40.** Drawings of HET associated with Part B: Middle Cylinder (all dimensions in millimeters).



### LONGITUDINAL SECTION



### CROSS SECTION A-A

**Figure 41.** Drawings of HET associated with Part C: Inlet Plate (all dimensions in millimeters).

## 82 Relationship Between Erodibility and Properties of Soils

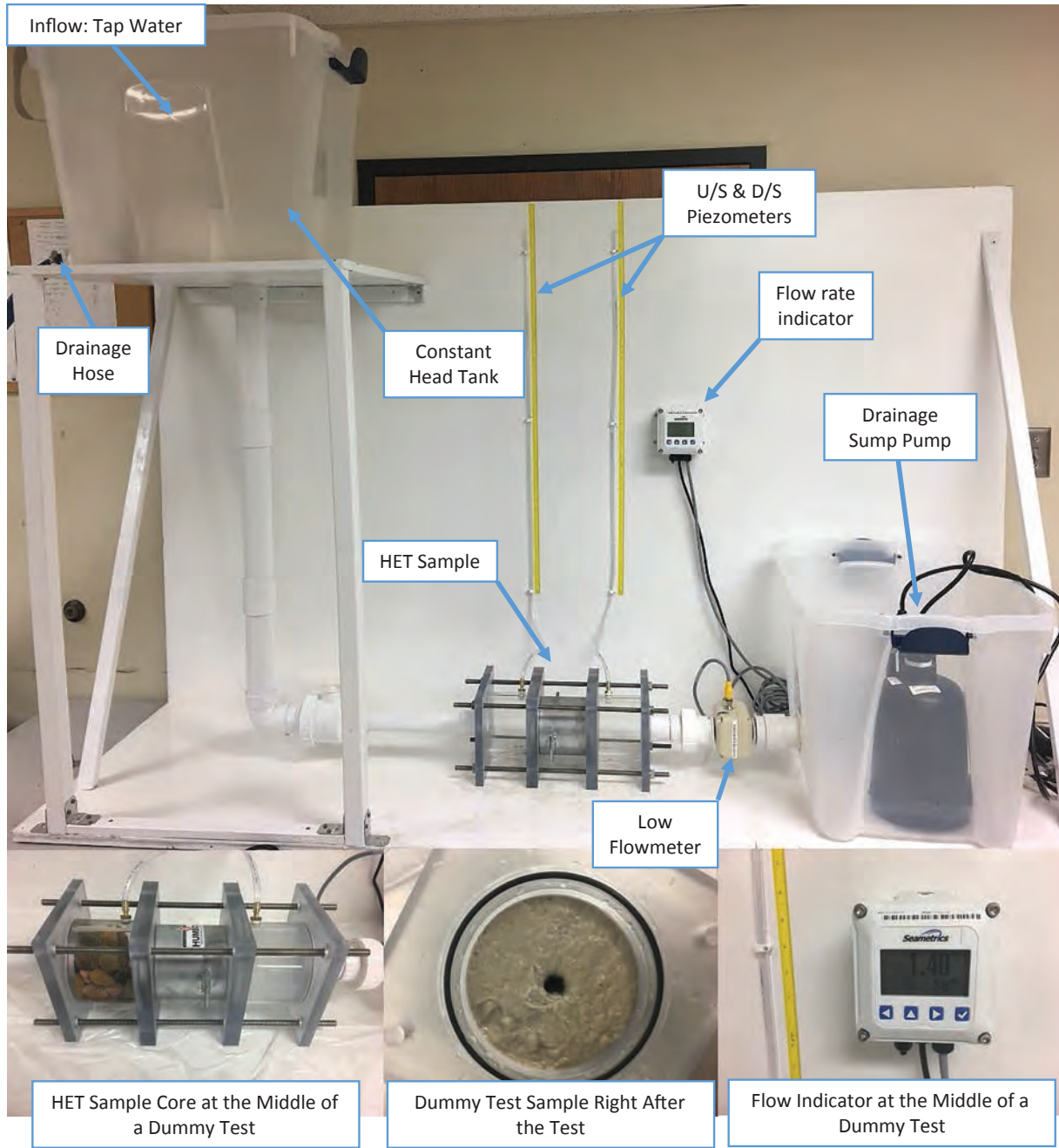
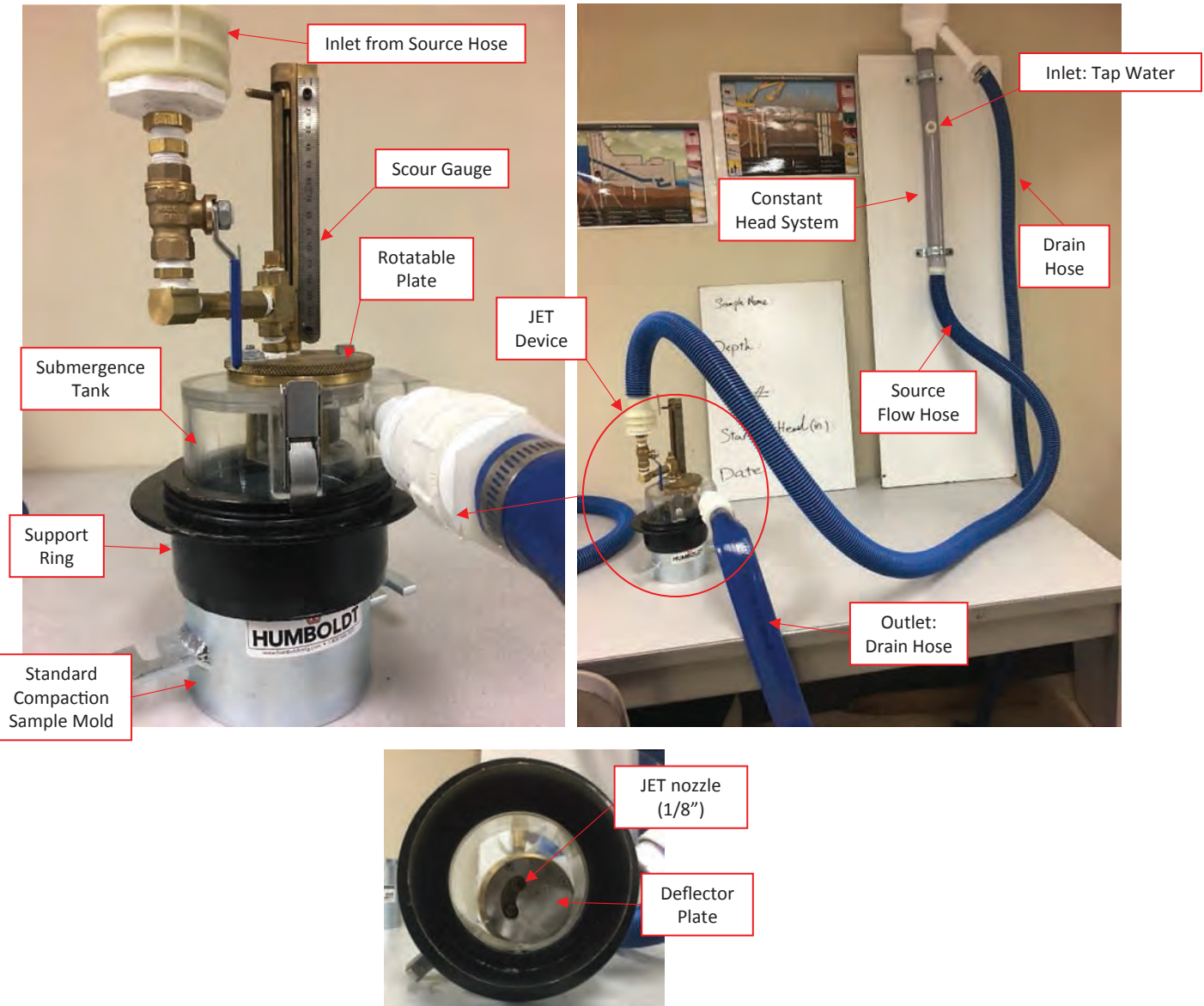


Figure 42. Photos of HET assembly at TAMU (U/S = upstream; D/S = downstream).



**Figure 43.** Photos of JET assembly at TAMU.



**Figure 44.** Photos of the Soil Erosion Laboratory at TAMU showing control desk and the two EFAs.

#### 4.1.3 Refurbishment of EFA Machines and TAMU Soil Erosion Laboratory

The TAMU Soil Erosion Laboratory contains two EFAs. Both machines were repaired and upgraded for the second phase of the project. Figure 44 shows photos of the laboratory, the control desk, and the two EFAs. The difference between the two EFAs is the way the sample extrusion is controlled. In EFA #1, the test operator needs to extrude the sample from the tube manually by pushing the button on the control board of the EFA, while in EFA #2 the extrusion is controlled through the desktop on the control desk; however, one of the operators still needs to stand by the EFA to monitor whether there is any scour on the sample.

#### 4.2 Test Plan Matrix

As discussed in Chapter 1, the majority of the erosion tests proposed in this study consisted of laboratory tests performed with devices developed in the TAMU Soil Erosion Laboratory. The remaining tests were associated with field tests conducted on the clay and sand sites at TAMU's

**Table 16. Experimental test plan proposed for NCHRP Project 24-43.**

Soil Type	Type of Test	Total Number of Tests
Compare Different Devices		
1 clay (man-made)	EFA	16
1 silt (man-made)	JET	
1 sand (man-made)	HET	
1 gravel (man-made)	PET	
Check Repeatability of Results		
1 clay (man-made)	EFA	16
1 silt (man-made)	JET	
1 sand (man-made)	HET	
1 gravel (man-made)	PET	
Organize Demonstration and Comparison of Field Erosion Devices		
1 clay	PET	8
1 sand	BET	
	ISEEP	
	ISTD	
Erosion Tests to Develop Equations		
14 clays	EFA HET JET PET	56
8 silts	EFA HET JET PET	32
6 sands	EFA HET JET PET	24
4 gravels	EFA HET JET PET	16
Total Number of Tests		
Clays, silts, sands, gravels	EFA JET HET PET BET ISEEP ISTD	168

Note: ISEEP = in situ erosion evaluation probe; ISTD = in situ scour testing device.

RELLIS campus. A total of 168 new erosion tests were planned to be performed during this project. Table 16 shows the experimental plan proposed for this project. A testing matrix was proposed in order to perform all erosion tests in accordance with the progress schedule timeline of the project. Table 17 shows the proposed testing matrix for this project.

### 4.3 Results of Erosion Tests

This section presents the results of all the erosion tests performed during this project. As discussed in the previous section, the following erosion test devices were used: EFA, JET, HET, PET, and BET. Detailed information on the geotechnical properties of all tested samples is presented in Section 4.4.

## 86 Relationship Between Erodibility and Properties of Soils

**Table 17. Testing matrix for NCHRP Project 24-43.**

NATIONAL COOPERATIVE HIGHWAY RESEARCH PROGRAM TRANSPORTATION RESEARCH BOARD NATIONAL RESEARCH COUNCIL <b>TESTING MATRIX</b>							
NCHRP Project No.	24-43						
Research Agency	Texas A&M University System						
Laboratory Leader	Iman SHAFII						
FY	TIME FRAME	TASK #	TARGET	Week 1 (9/29 to 10/7)	Week 2 (10/7 to 10/14)	Week 3 (10/14 to 10/21)	Week 4 (10/22 to 10/29)
2016	September 30th to October 30th	4	Perform erosion tests with different devices using the same prepared soil	1 EFA, 1 JET, 1 HET, 1 PET w/ soil properties on <b>Clay</b>	1 EFA, 1 JET, 1 HET, 1 PET w/ soil properties on <b>Silt</b>	1 EFA, 1 JET, 1 HET, 1 PET w/ soil properties on <b>Sand</b>	1 EFA, 1 JET, 1 HET, 1 PET w/ soil properties on <b>Gravel</b>
			Percent completed? ►►►	100	100	100	100
	TIME FRAME	TASK #	TARGET	Week 1 (10/29 to 11/7)	Week 2 (11/7 to 11/14)	Week 3 (11/14 to 11/21)	Week 4 (11/22 to 11/29)
	October 30th to November 30th	4	Check repeatability of results	1 EFA, 1 JET, 1 HET, 1 PET on same as above <b>Clay</b>	1 EFA, 1 JET, 1 HET, 1 PET on same as above <b>Silt</b>	1 EFA, 1 JET, 1 HET, 1 PET on same as above <b>Sand</b>	1 EFA, 1 JET, 1 HET, 1 PET on same as above <b>Gravel</b>
			Percent completed? ►►►	100	100	100	100
	TIME FRAME	TASK #	TARGET	Week 1 (11/29 to 12/7)	Week 2 (12/7 to 12/14)	Week 3 (12/14 to 12/21)	Week 4 (12/22 to 12/29)
	November 30th to December 30th	4	Organize field erosion devices demonstration and comparison	1 PET, (possibly 1 ISEEP) on <b>clay</b> site in RELLIS Campus w/ associated soil properties	1 PET, (possibly 1 ISEEP) on <b>sand</b> site in RELLIS Campus w/ associated soil properties	1 BET, (possibly 1 ISTD) on <b>clay</b> site in RELLIS Campus w/ associated soil properties	1 BET, (possibly 1 ISTD) on <b>sand</b> site in RELLIS Campus w/ associated soil properties
			Percent completed? ►►►	100	100	100	100
FY	TIME FRAME	TASK #	TARGET	Week 1 (12/28 to 1/5)	Week 2 (1/5 to 1/14)	Week 3 (1/14 to 1/21)	Week 4 (1/22 to 1/29)
2017	December 30th to January 30th	5	Erosion tests to develop the equations (14 clay samples)	<b>Holidays (Christmas Break)</b>		1 EFA, 1 JET, 1 HET, 1 PET w/ soil properties on <b>Clay #1</b>	1 EFA, 1 JET, 1 HET, 1 PET w/ soil properties on <b>Clay #2</b>
			Percent completed? ►►►	100	100	100	100
	TIME FRAME	TASK #	TARGET	Week 1 (1/29 to 2/7)	Week 2 (2/7 to 2/14)	Week 3 (2/14 to 2/21)	Week 4 (2/22 to 2/29)
	January 30th to February 30th	5	Erosion tests to develop the equations (14 clay samples)	1 EFA, 1 JET, 1 HET, 1 PET w/ soil properties on <b>Clay #4</b>	1 EFA, 1 JET, 1 HET, 1 PET w/ soil properties on <b>Clay #5</b>	1 EFA, 1 JET, 1 HET, 1 PET w/ soil properties on <b>Clay #6</b>	1 EFA, 1 JET, 1 HET, 1 PET w/ soil properties on <b>Clay #7</b>
			Percent completed? ►►►	100	100	100	100
	TIME FRAME	TASK #	TARGET	Week 1 (2/29 to 3/7)	Week 2 (3/7 to 3/13)	Week 3 (3/13 to 3/19)	Week 4 (3/19 to 3/29)
	February 30th to March 30th	5	Erosion tests to develop the equations (14 clay samples)	1 EFA, 1 JET, 1 HET, 1 PET w/ soil properties on <b>Clay #8</b>	1 EFA, 1 JET, 1 HET, 1 PET w/ soil properties on <b>Clay #9</b>	<b>Holidays (Spring Break)</b>	
			Percent completed? ►►►	100	100	100	100
	TIME FRAME	TASK #	TARGET	Week 1 (3/29 to 4/7)	Week 2 (4/7 to 4/14)	Week 3 (4/14 to 4/21)	Week 4 (4/22 to 4/29)
2017	March 30th to April 30th	5	Erosion tests to develop the equations (14 clay samples)	1 EFA, 1 JET, 1 HET, 1 PET w/ soil properties on <b>Clay #11</b>	1 EFA, 1 JET, 1 HET, 1 PET w/ soil properties on <b>Clay #12</b>	1 EFA, 1 JET, 1 HET, 1 PET w/ soil properties on <b>Clay #13</b>	1 EFA, 1 JET, 1 HET, 1 PET w/ soil properties on <b>Clay #14</b>
			Percent completed? ►►►	100	100	100	100
	TIME FRAME	TASK #	TARGET	Week 1 (4/29 to 5/7)	Week 2 (5/7 to 5/14)	Week 3 (5/14 to 5/21)	Week 4 (5/22 to 5/29)
	April 30th to May 30th	5	Erosion tests to develop the equations (8 silt samples)	1 EFA, 1 JET, 1 HET, 1 PET w/ soil properties on <b>Silt #1</b>	1 EFA, 1 JET, 1 HET, 1 PET w/ soil properties on <b>Silt #2</b>	1 EFA, 1 JET, 1 HET, 1 PET w/ soil properties on <b>Silt #3</b>	1 EFA, 1 JET, 1 HET, 1 PET w/ soil properties on <b>Silt #4</b>
			Percent completed? ►►►	100	100	100	100
	TIME FRAME	TASK #	TARGET	Week 1 (5/29 to 6/7)	Week 2 (6/7 to 6/14)	Week 3 (6/14 to 6/21)	Week 4 (6/22 to 6/29)
	May 30th to June 30th	5	Erosion tests to develop the equations (8 silt samples)	1 EFA, 1 JET, 1 HET, 1 PET w/ soil properties on <b>Silt #5</b>	1 EFA, 1 JET, 1 HET, 1 PET w/ soil properties on <b>Silt #6</b>	1 EFA, 1 JET, 1 HET, 1 PET w/ soil properties on <b>Silt #7</b>	1 EFA, 1 JET, 1 HET, 1 PET w/ soil properties on <b>Silt #8</b>
			Percent completed? ►►►	100	100	100	100
	TIME FRAME	TASK #	TARGET	Week 1 (6/29 to 7/7)	Week 2 (7/7 to 7/14)	Week 3 (7/14 to 7/21)	Week 4 (7/22 to 7/29)
2017	June 30th to July 30th	5	Erosion tests to develop the equations (6 sand samples)	1 EFA, 1 JET, 1 HET, 1 PET w/ soil properties on <b>Sand #1</b>	1 EFA, 1 JET, 1 HET, 1 PET w/ soil properties on <b>Sand #2</b>	1 EFA, 1 JET, 1 HET, 1 PET w/ soil properties on <b>Sand #3</b>	1 EFA, 1 JET, 1 HET, 1 PET w/ soil properties on <b>Sand #4</b>
			Percent completed? ►►►	100	100	100	100
	TIME FRAME	TASK #	TARGET	Week 1 (7/29 to 8/7)	Week 2 (8/7 to 8/14)	Week 3 (8/14 to 8/21)	Week 4 (8/22 to 8/29)
	July 30th to August 30th	5	Erosion tests to develop the equations (finish 6 sands, start on 4 gravel samples)	1 EFA, 1 JET, 1 HET, 1 PET w/ soil properties on <b>Sand #5</b>	1 EFA, 1 JET, 1 HET, 1 PET w/ soil properties on <b>Sand #6</b>	1 EFA, 1 JET, 1 HET, 1 PET w/ soil properties on <b>Gravel #1</b>	1 EFA, 1 JET, 1 HET, 1 PET w/ soil properties on <b>Gravel #2</b>
			Percent completed? ►►►	100	100	100	100
	TIME FRAME	TASK #	TARGET	Week 1 (8/29 to 9/7)	Week 2 (9/7 to 9/14)		
July 30th to August 30th	5	Erosion tests to develop the equations (4 gravel samples)	1 EFA, 1 JET, 1 HET, 1 PET w/ soil properties on <b>Gravel #3</b>	1 EFA, 1 JET, 1 HET, 1 PET w/ soil properties on <b>Gravel #4</b>			
		Percent completed? ►►►	100	100			

**4.3.1 Ensuring the Repeatability of Erosion Tests and Field Demonstration**

The two major topics addressed in this section are

1. Testing the same soil with different erosion testing devices (i.e., EFA, JET, HET, and PET) to evaluate the repeatability of the results for each erosion test, and
2. Organizing field demonstration tests of the PET and the BET.

For the purpose of ensuring the repeatability of the erosion tests, man-made samples of all four types of soils (gravel, sand, silt, and clay) were prepared and tested using the EFA, JET, HET, and PET. Table 18 shows the primary description of the soils tested for the purpose of ensuring repeatability. Thirty-two samples were tested. The first letter in the sample name refers to the soil type. The second letter refers to the first letter of each apparatus type. The number at the end of the sample name is 1 if the sample was being tested for the first time, and 2 if it was being tested for the second time to ensure repeatability. For example, CJ-2 means that the sample is a clay that was tested with the JET for the second time to evaluate the repeatability of this device.

The results of the work done to check the repeatability of erosion tests for each sample are described in the following sections:

- Section 4.3.1.1, Ensuring the Repeatability of the EFA;
- Section 4.3.1.2, Ensuring the Repeatability of the PET;
- Section 4.3.1.3, Ensuring the Repeatability of the HET; and
- Section 4.3.1.4, Ensuring the Repeatability of the JET.

#### **4.3.1.1 Ensuring the Repeatability of the EFA**

**Clay Samples (CE-1 and CE-2).** The prepared clay samples were a mixture of 60% porcelain Grolleg kaolin plus 40% bentonite. Both samples were remolded and compacted to reproduce the target condition listed in Table 18. Results of the EFA tests on CE-1 and CE-2 are presented in Figure 45 and Figure 46 against velocity and shear stress, respectively. Both samples can be categorized as medium erodibility (Category III). The critical velocities for CE-1 and CE-2 were 1.18 and 1.04 m/s, respectively. The critical shear stress values for CE-1 and CE-2 were 7.59 and 5.93 Pa, respectively. The results of each EFA test are also presented in the format of an EFA result spreadsheet in Appendix 1. Figure 47 shows an example of the EFA result spreadsheet for Sample CE-1.

**Silt Samples (ME-1 and ME-2).** The silt samples were 100% porcelain Grolleg. Both samples were remolded and compacted to reproduce the target condition listed in Table 18. Results of the EFA tests on ME-1 and ME-2 are presented in Figure 48 and Figure 49 against velocity and shear

**Table 18. Description of the soils used to ensure repeatability of erosion tests.**

Soil Type	Description	Erosion Test	Sample Name	Target Water Content (%)	Target Wet Unit Weight (kN/m <sup>3</sup> )
Gravel	Pea gravel from Lowes, College Station, Texas	HET	GH-1 & GH-2	10	20
		JET	GJ-1 & GJ-2		
		EFA	GE-1 & GE-2		
		PET	GP-1 & GP-2		
Sand	Mixture of 20% bentonite + 80% silica sand (60–80) from Armadillo Clay & Supplies Co., Austin, Texas	HET	SH-1 & SH-2	10	19
		JET	SJ-1 & SJ-2		
		EFA	SE-1 & SE-2		
		PET	SP-1 & SP-2		
Silt	Porcelain Grolleg kaolin from Armadillo Clay & Supplies Co., Austin, Texas	HET	MH-1 & MH-2	18	16
		JET	MJ-1 & MJ-2		
		EFA	ME-1 & ME-2		
		PET	MP-1 & MP-2		
Clay	Mixture of 60% porcelain Grolleg kaolin + 40% bentonite from Armadillo Clay & Supplies Co., Austin, Texas	HET	CH-1 & CH-2	15	14
		JET	CJ-1 & CJ-2		
		EFA	CE-1 & CE-2		
		PET	CP-1 & CP-2		

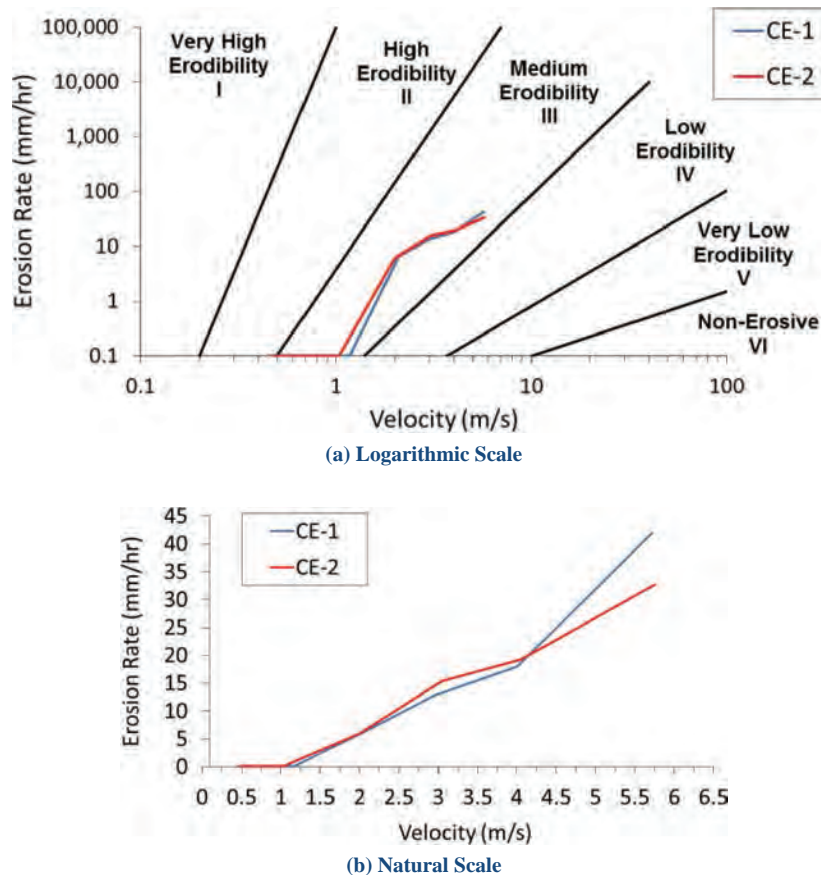


**Figure 45.** EFA test results based on velocity for ensuring the repeatability of the EFA on clay samples.

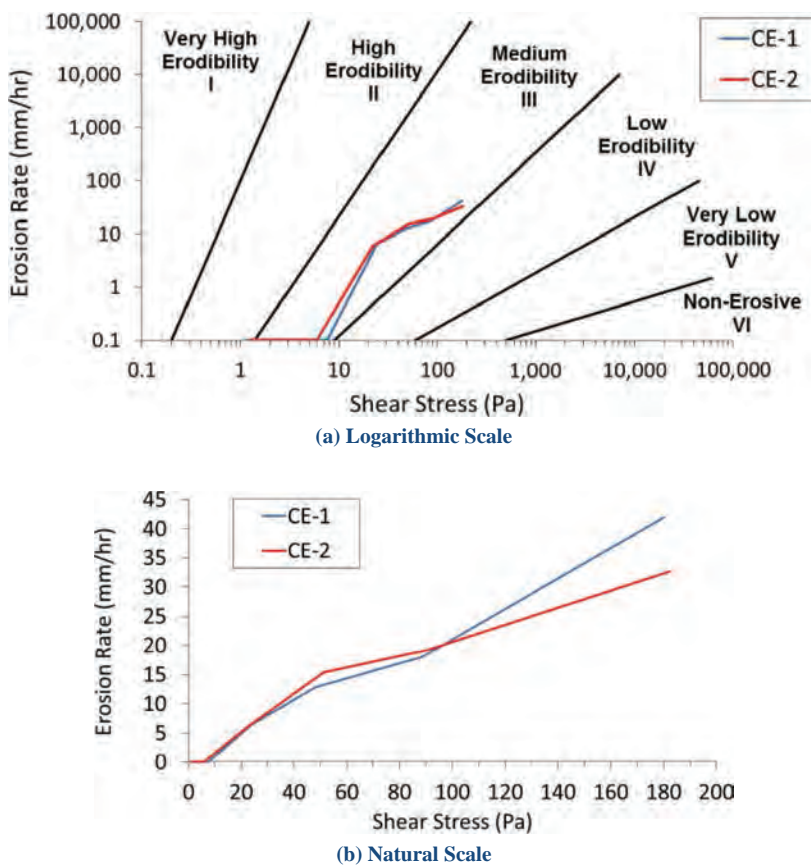


**Figure 46.** EFA test results based on shear stress for ensuring the repeatability of the EFA on clay samples.

Velocity m/sec	Equivalent Roughness mm	Reynolds Number $R_e$	Friction Factor Moodychart	Shear Stress $P_a$	Erosion Reading mm	Test Time sec	Erosion Rate mm/hr
0.445	1.000	27011	0.045	1.113	0	570	0.000
1.175	1.000	71359	0.044	7.598	0	840	0.000
2.102	1.000	127626	0.044	24.303	1	550.002	6.545
2.962	1.000	179859	0.044	48.266	2	559.98	12.858
4.011	1.000	243503	0.044	88.469	3	600	18.000
5.724	1.000	347528	0.044	180.202	7	600	42.000

Velocity (m/sec)	0.445	1.175	2.102	2.962	4.011	5.724
Shear stress ( $P_a$ )	1.113	7.598	24.303	48.266	88.469	180.202
Erosion Rate (mm/hr)	0.100	0.100	6.545	12.858	18.000	42.000

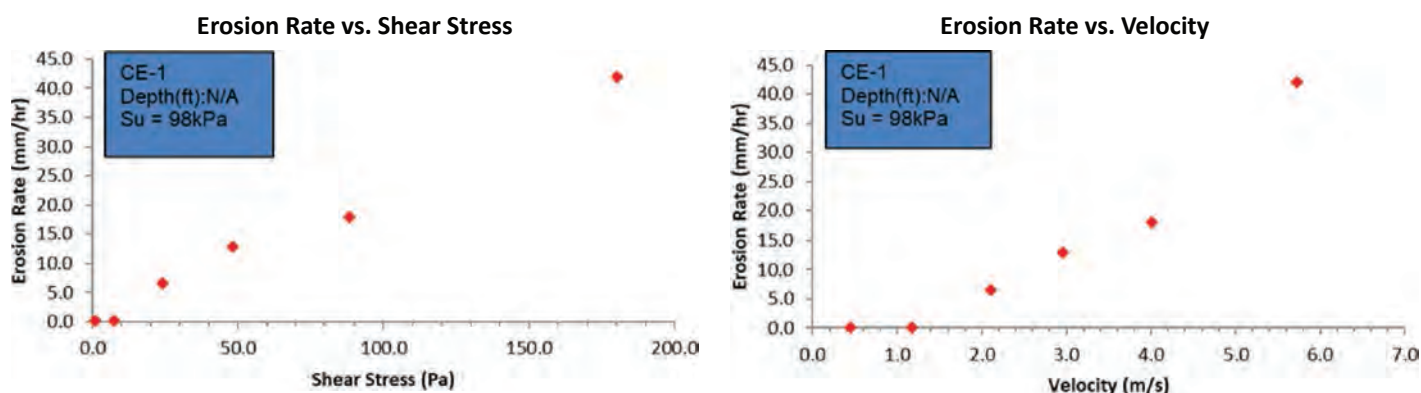


Figure 47. EFA result spreadsheet for CE-1.

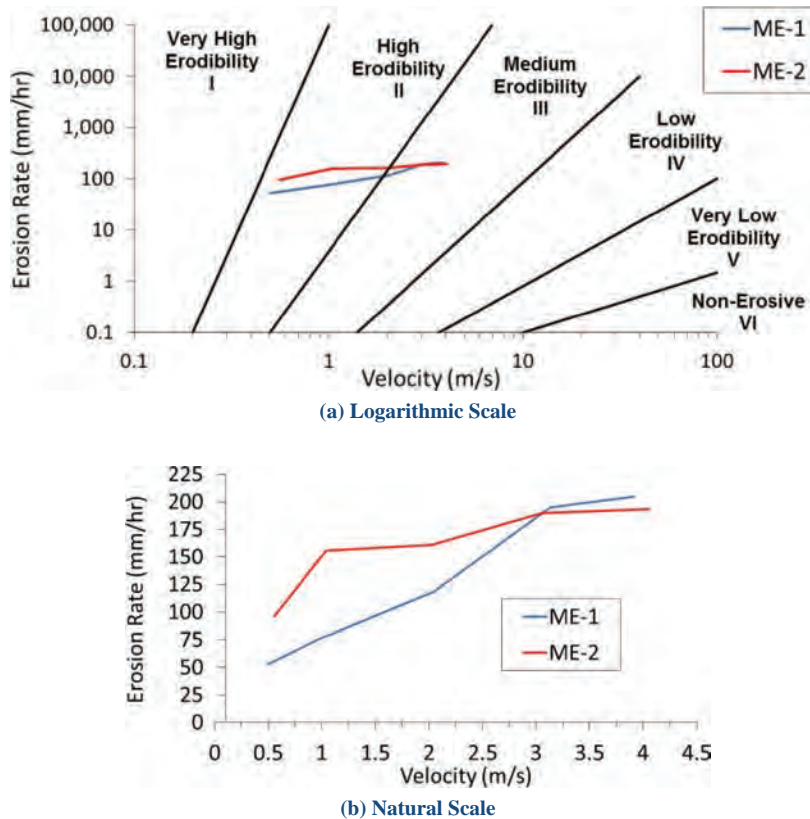
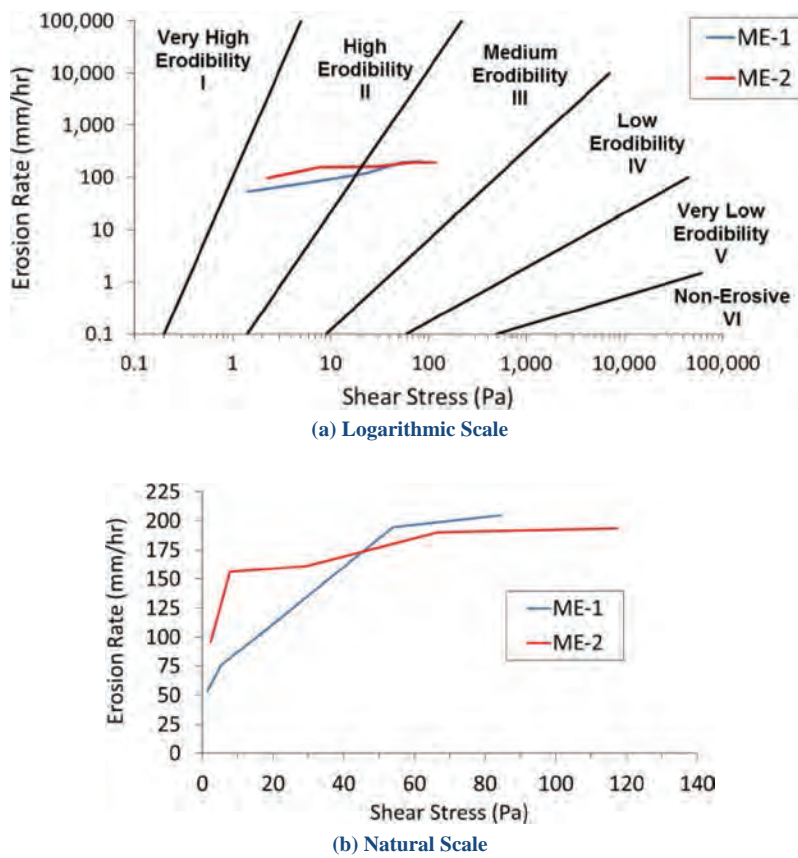


Figure 48. EFA test results based on velocity for ensuring the repeatability of the EFA on silt samples.

## 90 Relationship Between Erodibility and Properties of Soils



**Figure 49.** EFA test results based on shear stress for ensuring the repeatability of the EFA on silt samples.

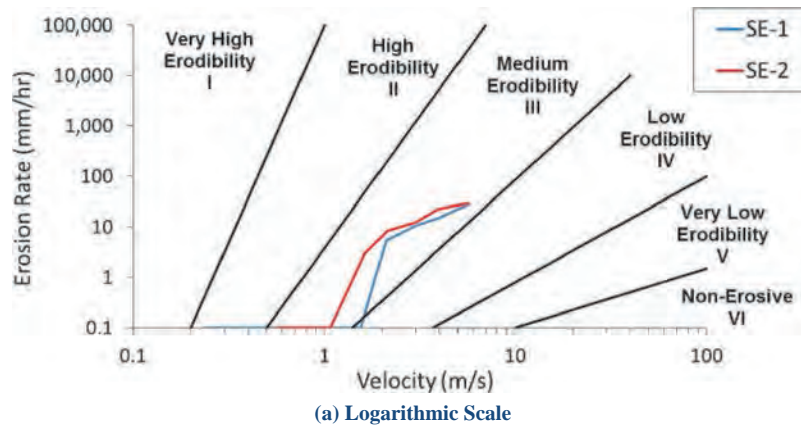
stress, respectively. Both samples can be categorized as high to medium erodibility (Categories II to III). The critical velocities for ME-1 and ME-2 were 0.1 m/s. The critical shear stress values were measured as 0.1 Pa.

**Sand Samples.** The sand samples were a mixture of 20% bentonite and 80% silica sand 60–80. Both samples were remolded and compacted to reproduce the target condition listed in Table 18. Results of the EFA tests on SE-1 and SE-2 are presented in Figure 50 and Figure 51 against velocity and shear stress, respectively. Both samples can be categorized as medium erodibility (Category III).

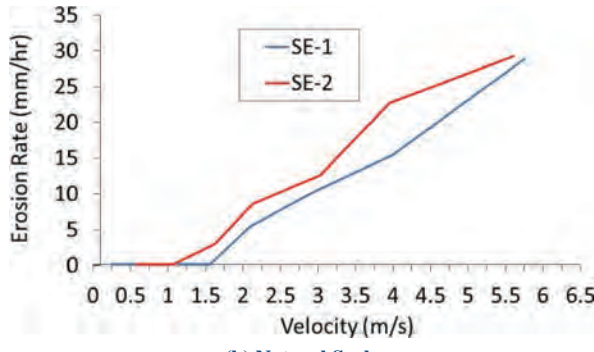
**Gravel Samples.** The gravel samples were pea gravel. Both samples were remolded and compacted to reproduce the target condition listed in Table 18. Results of the EFA tests on GE-1 and GE-2 are presented in Figure 52 and Figure 53 against velocity and shear stress, respectively. Both samples can be categorized as medium to low erodibility (Categories III to IV). The critical velocities for GE-1 and GE-2 were 1.44 and 1.5 m/s, respectively. The critical shear stress values were measured as 17.63 and 19.13 Pa, respectively.

#### 4.3.1.2 Ensuring the Repeatability of the PET

The PET was performed on the top surface of each sample prior to each EFA test. As discussed in Chapter 2, the PET consists of 20 applications of a jet of water at 8 m/s by squeezing the trigger of a water pistol positioned 50 mm from the sample face. The jet hits the sample surface at the same location at one end of the sample. The depth of the hole formed on the

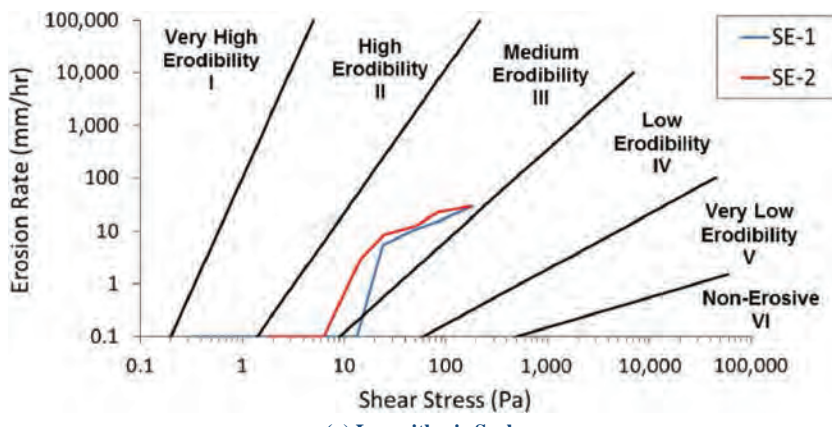


(a) Logarithmic Scale

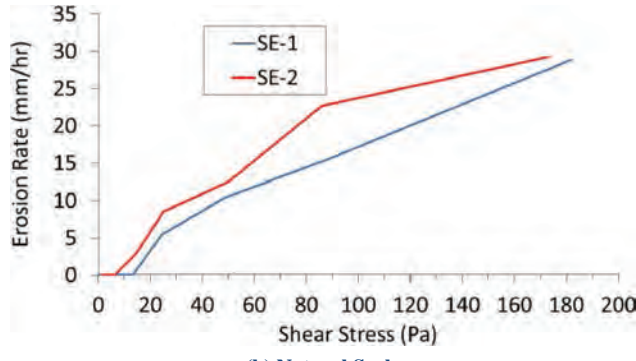


(b) Natural Scale

**Figure 50.** EFA test results based on velocity for ensuring the repeatability of the EFA on sand samples.

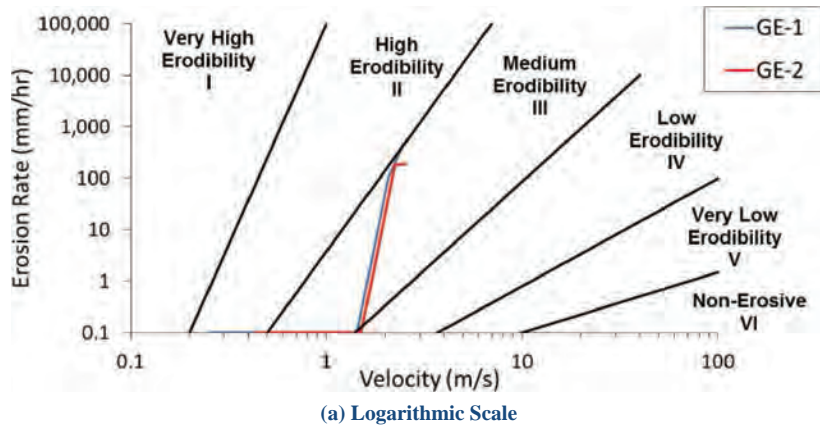


(a) Logarithmic Scale

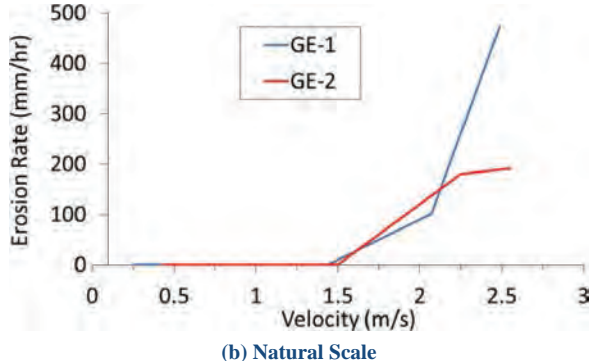


(b) Natural Scale

**Figure 51.** EFA test results based on shear stress for ensuring the repeatability of the EFA on sand samples.

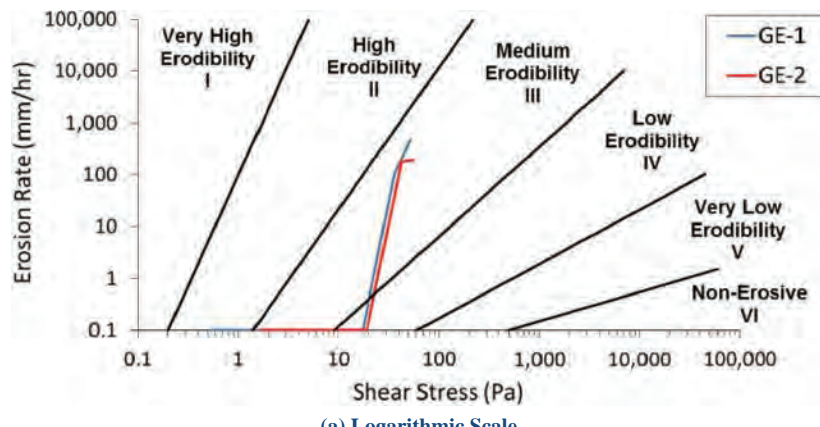


(a) Logarithmic Scale

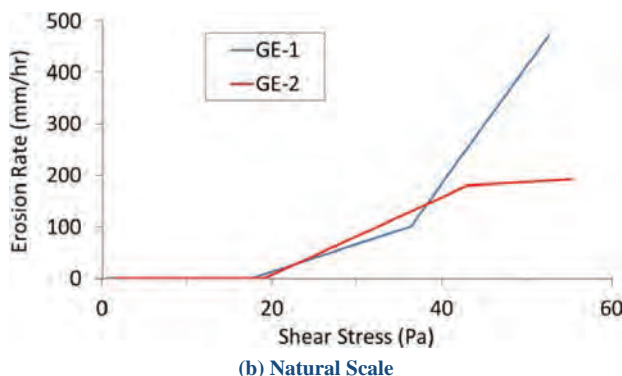


(b) Natural Scale

**Figure 52.** EFA test results based on velocity for ensuring the repeatability of the EFA on gravel samples.



(a) Logarithmic Scale



(b) Natural Scale

**Figure 53.** EFA test results based on shear stress for ensuring the repeatability of the EFA on gravel samples.

**Table 19.** Results of the PET on each sample.

Sample	Result (mm)	Sample	Result (mm)
Clay		Sand	
CP-1	2.11	SP-1	5.4
CP-2	3.0	SP-2	4.22
Silt		Gravel	
MP-1	5.33	GP-1	na
MP-2	5.3	GP-2	na

Note: na = not applicable. It is not feasible to perform the PET on gravel samples.

sample surface is then measured and entered in the PET erosion categories chart. The PET was conducted three times at different areas on the top end of each sample. The results of the PET show reasonable repeatability for each soil type (Table 19).

As discussed in Chapter 2, the results of the PET can be associated with the erosion category chart (Figure 54). All the points fall within the medium erodibility range (Category III) on this chart. Comparison of the results of the PET with the results of EFA shows compliance between the two tests.

#### 4.3.1.3 Ensuring the Repeatability of the HET

**Clay Samples (CH-1 and CH-2).** The clay samples were a mixture of 60% porcelain Grolleg kaolin plus 40% bentonite. Results of the HETs on CH-1 and CH-2 are presented in Figure 55 and Figure 56, respectively. The HET results are plotted as erosion rate (mm/h) against hydraulic shear stress. The HET plots include several fluctuations resulting from the errors associated with the constant head system both upstream and downstream. Note that Wan and Fell (2002) had the same type of curves and estimated the critical shear stress by fitting a best line on each plot. The critical shear stress values were measured as 70 and 67 Pa for CH-1 and CH-2, respectively. As explained in Chapter 2, HET results begin with a decrease in erosion rate and an increase in shear stress; thereafter, both erosion rate and shear stress begin increasing. The first part of the

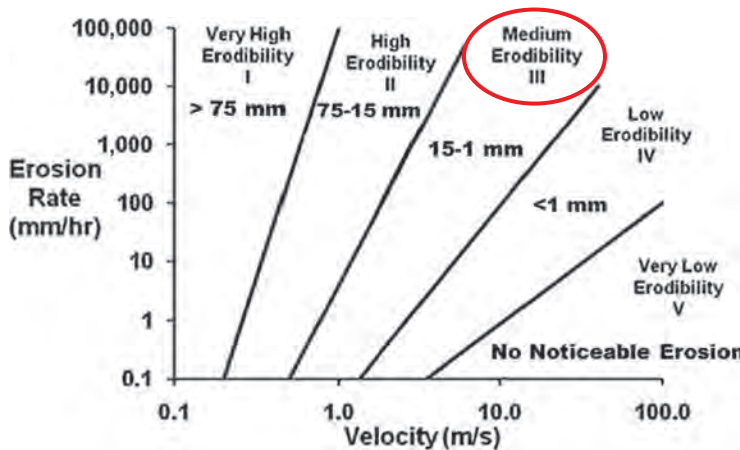


**Figure 54.** Erosion categories for the samples tested with the PET.

## 94 Relationship Between Erodibility and Properties of Soils

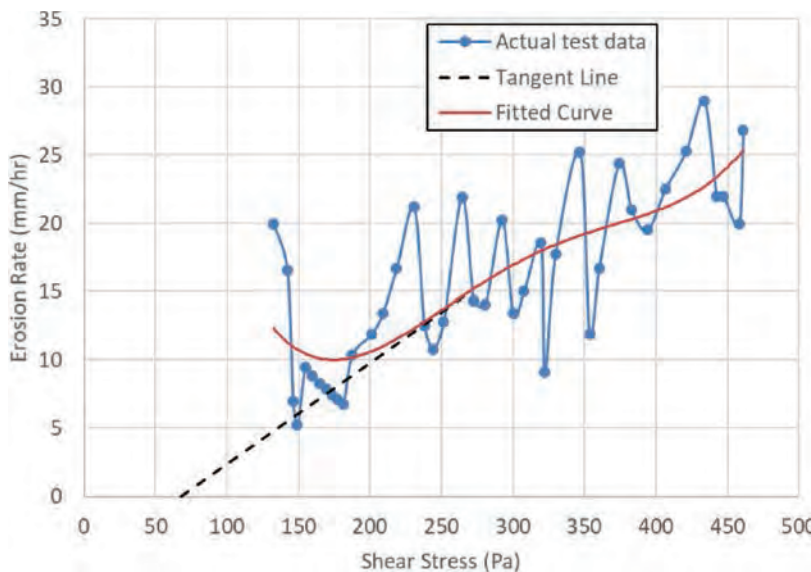


Figure 55. HET data for Sample CH-1.

curve is typically attributed to the thickness of the disturbed zone resulting from drilling the 6 mm hole in the center of the sample. The second part of the curve corresponds to the erosion of the undisturbed soil. To predict the critical shear stress, the erosion part of the fitted erosion curve is extended (see the dashed tangent line in Figure 55) to cross the horizontal axis. The shear stress associated with the obtained point is the critical shear stress. It should be noted that the dashed line is determined according to the operator's interpretation. Therefore, the critical shear stress and slope of shear stress in the HET are subjective.

The erosion part of the CH-1 and CH-2 test result curves were plotted in the erosion category chart. It can be concluded that both samples place in the low erodibility range (Category IV) (Figure 57). The main reason that the curves are in two different shear stress ranges is that the

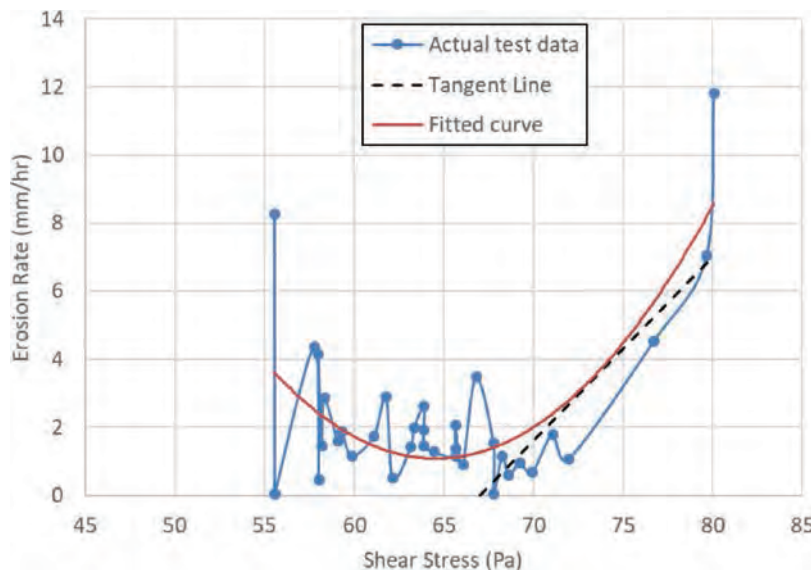
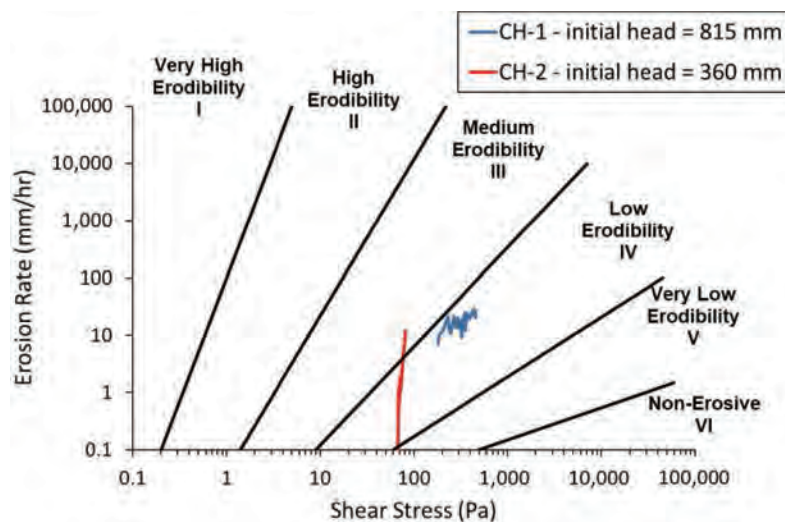


Figure 56. HET data for Sample CH-2.



**Figure 57.** Erosion part of the clay HET curves plotted on the erosion category chart.

initial head condition for CH-1 and CH-2 differed because of the unexpected change in the test condition at the time of test (815 mm and 360 mm, respectively); however, when the erosion part of the curves is tracked, both curves cross the horizontal axis at a critical shear stress of 70 Pa. It is important to notice that higher initial heads in the HET lead to greater shear stress ranges at the soil–water interface. Therefore, the user should be aware of the desired shear stress range before performing HET. For high erodible geomaterials such as silt, the erosion function is better captured in an HET with a low initial head; however, for more erosion-resistant geomaterials such as dense high-plasticity clay, performing the HET with higher initial heads would better capture the erosion function.

The results of all HETs are also presented in the format of an HET result spreadsheet in Appendix 1. Figure 58 shows an example of the HET result spreadsheet for Sample CH-1.

**Silt Samples (MH-1 and MH-2).** The silt samples were 100% porcelain Grolleg kaolin. Results of the HETs for MH-1 and MH-2 are presented in Figure 59 and Figure 60, respectively. The critical shear stress was measured as 50 and 46 Pa for CH-1 and CH-2, respectively. The erosion functions of MH-1 and MH-2 were plotted in the erosion category chart and fell in the medium erodibility category (Category III) (Figure 61). The initial head was 330 mm and 321 mm for MH-1 and MH-2, respectively.

**Sand Samples (SH-1 and SH-2).** As said earlier, the sand samples were a mixture of 20% bentonite plus 80% silica sand 60–80. The HET results for SH-1 and SH-2 are presented in Figure 62 and Figure 63, respectively. The critical shear stress values were measured as 111 and 108 Pa for CH-1 and CH-2, respectively. For the purpose of comparison and populating the NCHRP-Erosion spreadsheet, the erosion part of the SH-1 and SH-2 test result curves was plotted in the erosion category chart. Both erosion curves fell at the boundary between medium and low erodibility (Categories III and IV) (Figure 64). The initial head was 514 and 508 mm for SH-1 and SH-2, respectively.

**Gravel Samples (GH-1 and GH-2).** The HET can only be performed in soils in which a horizontal hole can hold up and be self-supporting (i.e., fine-grained soils). Therefore, the HET was not conducted for the gravel samples.

Time (mins)	Time (s)	Flowrate (gpm)	U/S Tube (l/min)	D/S Tube (in)	Pressure Differential (in)	Pressure Differential		Sample length L (mm)	Gradient S	Flow rate Q (m³/s)	Friction Factor f	If Laminar $f_f$	If Turbulent $f_t$	Hole diameter (m) D	Reynold's No. Re(t)	Diameter D (m)	
						in	mm										
0.00	0	0.54	2.04	32.0	0.00	32.0	813	115	7.067826087	3.4069E-05	136.7985	154.5297	0.0070000	0.0070000	6005.940	6005.940	0.007
1.00	60	0.54	2.04	32.0	0.00	32.0	813	115	7.067826087	3.4069E-05	1.6541E+02	2.4342E+02	0.0074575	0.0076659	5637.470	5484.198	0.007656949
2.00	120	0.55	2.08	32.0	0.00	32.0	813	115	7.067826087	3.4700E-05	1.9403E+02	3.3230E+02	0.0079132	0.0082185	5411.261	5210.237	0.008218461
3.00	180	0.55	2.08	32.0	0.00	32.0	813	115	7.067826087	3.4700E-05	2.2264E+02	4.2119E+02	0.0082845	0.0086175	5168.727	4968.996	0.008450962
4.00	240	0.55	2.08	32.0	0.00	32.0	813	115	7.067826087	3.4700E-05	2.5126E+02	5.1008E+02	0.0086252	0.0089539	4964.550	4782.303	0.008625178
5.00	300	0.55	2.08	32.0	0.00	32.0	813	115	7.067826087	3.4700E-05	2.7987E+02	5.9897E+02	0.0089409	0.0092462	4789.235	4631.100	0.008940912
6.00	360	0.55	2.08	32.0	0.00	32.0	813	115	7.067826087	3.4700E-05	3.0849E+02	6.8785E+02	0.0092358	0.0095057	4636.323	4504.695	0.009235795
7.00	420	0.55	2.08	32.0	0.00	32.0	813	115	7.067826087	3.4700E-05	3.3711E+02	7.7674E+02	0.0095130	0.0097395	4501.240	4396.523	0.009512962
8.00	480	0.55	2.08	32.0	0.00	32.0	813	115	7.067826087	3.4700E-05	3.6572E+02	8.6553E+02	0.0097749	0.0099529	4380.640	4302.276	0.009774856
9.00	540	0.55	2.08	32.0	0.00	32.0	813	115	7.067826087	3.4700E-05	3.9434E+02	9.5452E+02	0.0100234	0.0101494	4272.007	4218.985	0.010023421
10.00	600	0.55	2.08	32.0	0.00	32.0	813	115	7.067826087	3.4700E-05	4.2295E+02	1.0434E+03	0.0102602	0.0103317	4173.407	4144.519	0.010260234
11.00	660	0.55	2.08	32.0	0.00	32.0	813	115	7.067826087	3.4700E-05	4.5175E+02	1.1323E+03	0.0104866	0.0105021	4083.321	4077.303	0.010486593
12.00	720	0.57	2.16	32.0	0.00	32.0	813	115	7.067826087	3.5961E-05	4.8018E+02	1.2212E+03	0.0108318	0.0108154	4096.947	4109.138	0.010831779
14.00	840	0.63	2.38	32.0	0.00	32.0	813	115	7.067826087	3.9747E-05	5.3741E+02	1.3990E+03	0.0116276	0.0115674	4218.294	4240.243	0.011627571
15.00	900	0.67	2.54	32.0	0.00	32.0	813	115	7.067826087	4.2270E-05	5.6603E+02	1.4878E+03	0.0120756	0.0120202	4319.661	4345.909	0.012075647
16.00	960	0.73	2.76	32.0	0.00	32.0	813	115	7.067826087	4.6056E-05	5.9464E+02	1.5767E+03	0.0125666	0.012631821	4489.271	4522.613	0.012631821
17.00	1020	0.82	3.10	32.0	0.00	32.0	813	115	7.067826087	5.1734E-05	6.2326E+02	1.6656E+03	0.0133383	0.0133100	4786.288	4796.455	0.013338291
18.00	1080	0.86	3.26	32.0	0.00	32.0	813	115	7.067826087	5.4258E-05	6.5187E+02	1.7545E+03	0.0137560	0.0137078	4867.324	4884.446	0.013756042
19.00	1140	0.89	3.37	32.0	0.00	32.0	813	115	7.067826087	5.6150E-05	6.8049E+02	1.8484E+03	0.0141449	0.0140852	4909.064	4936.937	0.01414486
20.00	1200	0.95	3.60	32.0	0.00	32.0	813	115	7.067826087	5.9939E-05	7.0910E+02	1.9323E+03	0.0146246	0.0145426	5057.371	5085.894	0.014542584
21.00	1260	1.05	3.97	32.0	0.00	32.0	813	115	7.067826087	6.6245E-05	7.3772E+02	2.0212E+03	0.0153214	0.0152734	5335.497	5352.298	0.015273351
22.00	1320	1.11	4.20	32.0	0.00	32.0	813	115	7.067826087	7.0300E-05	7.6633E+02	2.1101E+03	0.0158071	0.0157517	5467.073	5486.333	0.015751651
23.00	1380	1.17	4.43	32.0	0.00	32.0	813	115	7.067826087	7.3815E-05	7.9495E+02	2.1988E+03	0.0162202	0.0162202	5593.578	5615.855	0.016220165
24.00	1440	1.27	4.81	32.0	0.00	32.0	813	115	7.067826087	8.0125E-05	8.2356E+02	2.2878E+03	0.0169945	0.0168945	5838.691	5852.543	0.016894462
25.00	1500	1.33	5.03	32.0	0.00	32.0	813	115	7.067826087	8.3910E-05	8.5218E+02	2.3767E+03	0.0173940	0.0173410	5971.214	0.017341007	
26.00	1560	1.4	5.30	31.9	0.00	31.9	810	115	7.04573913	9.8326E-05	9.8080E+02	2.4656E+03	0.0179085	0.017842098	6108.962	6108.962	
27.00	1620	1.5	5.68	32.0	0.00	32.0	813	115	7.067826087	9.4635E-05	9.9041E+02	2.5545E+03	0.0185022	0.0184602	6311.171	6326.171	0.018460165
28.00	1680	1.53	5.79	31.8	0.00	31.8	806	115	7.012608696	9.6528E-05	9.3803E+02	2.6484E+03	0.0188673	0.0187641	6313.443	6348.174	0.018764106
29.00	1740	1.62	6.13	31.5	0.00	31.5	800	115	6.957391304	1.0221E-04	9.6664E+02	2.7323E+03	0.0194751	0.0193560	6476.207	6516.038	0.019356047
30.00	1800	1.78	6.74	31.8	0.00	31.8	806	115	7.012608696	1.1209E-04	9.9526E+02	2.8212E+03	0.02021963	0.0202392	6847.182	6861.712	0.020196345
31.00	1860	1.84	6.97	31.9	0.00	31.9	806	115	7.012608696	1.1609E-04	1.0239E+03	2.9100E+03	0.0206584	0.0205933	6984.369	6956.274	0.020593321
32.00	1920	1.93	7.31	31.5	0.00	31.5	800	115	6.957391304	1.2176E-04	1.0525E+03	2.9989E+03	0.0212395	0.0211506	7074.544	7104.285	0.021150577
33.00	1980	2.09	7.91	31.5	0.00	31.5	800	115	6.957391304	1.3186E-04	1.0811E+03	3.0878E+03	0.0220668	0.0219632	7393.915	7408.609	0.021963162
34.00	2040	2.22	8.40	31.3	0.00	31.3	794	115	6.902173913	1.4006E-04	1.1097E+03	3.1757E+03	0.0227106	0.0226628	7610.447	7626.118	0.022662903
35.00	2100	2.35	8.90	31.3	0.00	31.3	794	115	6.902173913	1.4826E-04	1.1389E+03	3.2656E+03	0.0233427	0.0233140	7827.926	7847.575	0.023314048
36.00	2160	2.51	9.50	31.3	0.00	31.3	794	115	6.902173913	1.5836E-04	1.1669E+03	3.3545E+03	0.0240592	0.0240654	8122.274	8120.192	0.024065377
37.00	2220	2.7	10.22	31.3	0.00	31.3	794	115	6.902173913	1.7034E-04	1.1956E+03	3.4434E+03	0.0248514	0.0249081	8458.577	8439.345	0.024908084
38.00	2280	2.92	11.05	31.0	0.00	31.0	787	115	6.846956522	1.8422E-04	1.2242E+03	3.5232E+03	0.0257797	0.0258737	8818.401	8796.355	0.025873748
39.00	2340	3.08	11.66	31.0	0.25	30.8	781	115	6.79173913	1.9432E-04	1.2528E+03	3.6211E+03	0.0265166	0.0266065	9043.113	9012.545	0.026606548
40.00	2400	3.23	12.23	30.9	0.50	30.3	768	115	6.681304348	2.0378E-04	1.2814E+03	3.7100E+03	0.0272926	0.0273388	9213.894	9198.314	0.027338807
41.00	2460	3.39	12.83	30.9	0.50	30.3	768	115	6.681304348	2.1388E-04	1.3100E+03	3.7986E+03	0.0279409	0.0280050	9445.917	9424.321	0.028004957
42.00	2520	3.58	12.55	30.5	1.00	29.5	749	115	6.515652174	2.2586E-04	1.3386E+03	3.8878E+03	0.0289000	0.0289000	9644.294	9644.294	0.0289

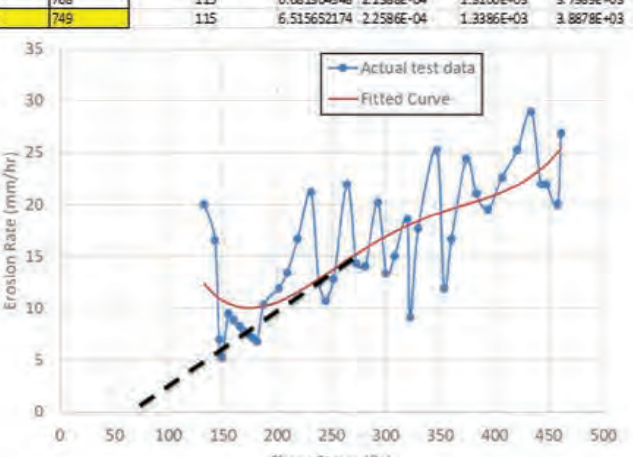


Figure 58. HET result spreadsheet for Sample CH-1.

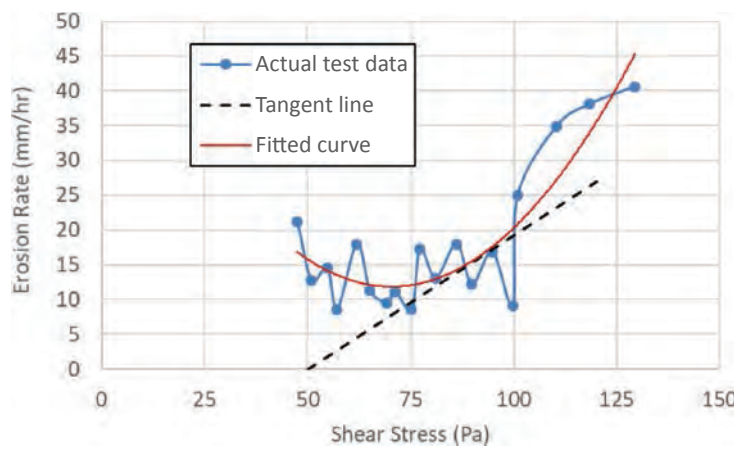


Figure 59. HET data for Sample MH-1.

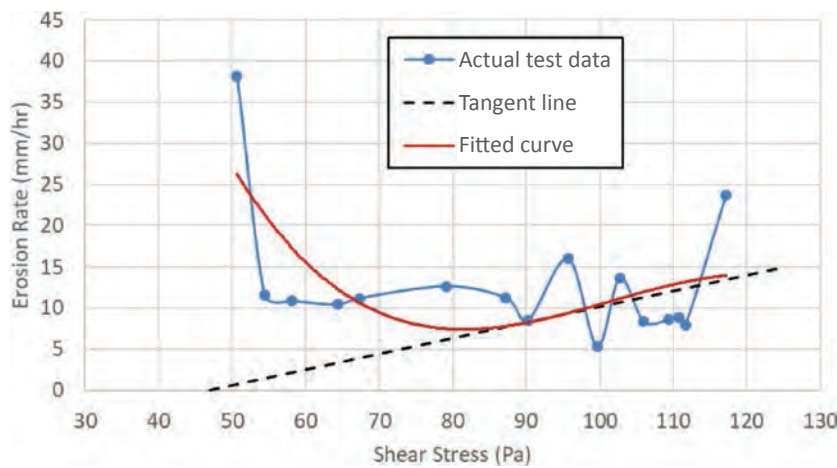


Figure 60. HET data for Sample MH-2.

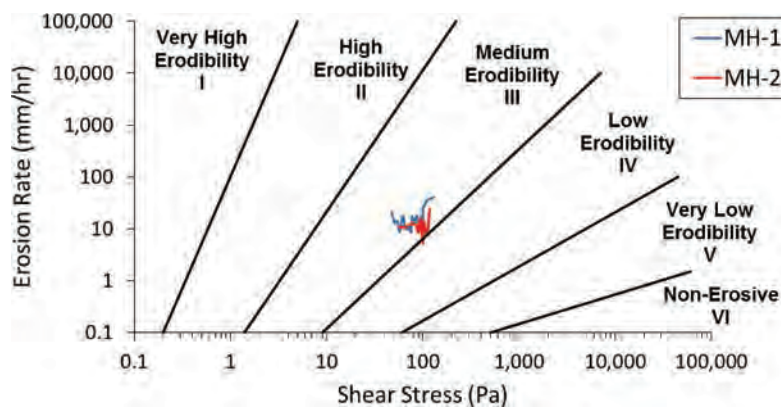


Figure 61. Erosion part of the silt HET curves plotted on the erosion category chart.

## 98 Relationship Between Erodibility and Properties of Soils

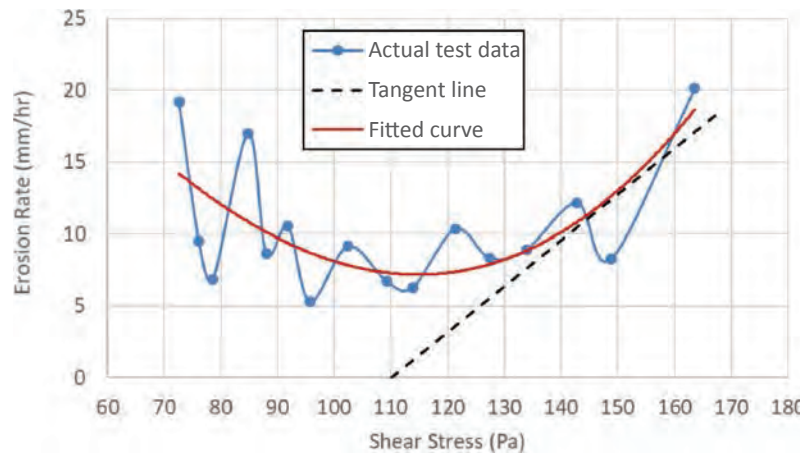


Figure 62. HET result for Sample SH-1.

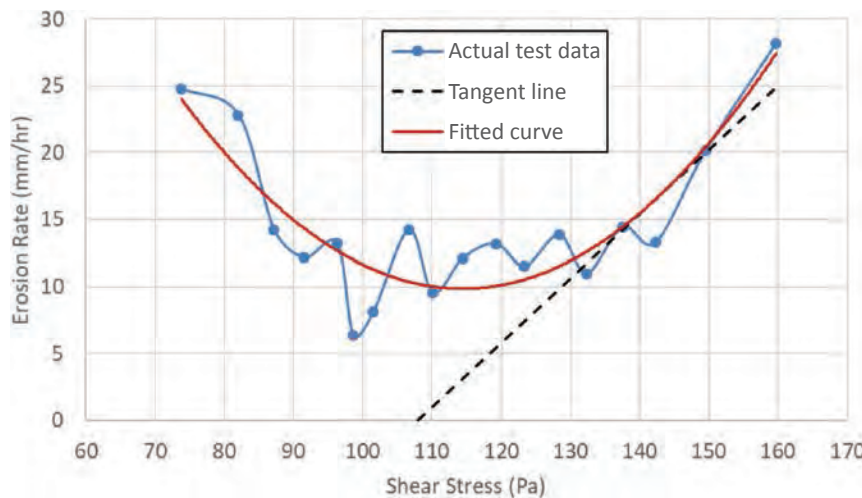


Figure 63. HET result for Sample SH-2.

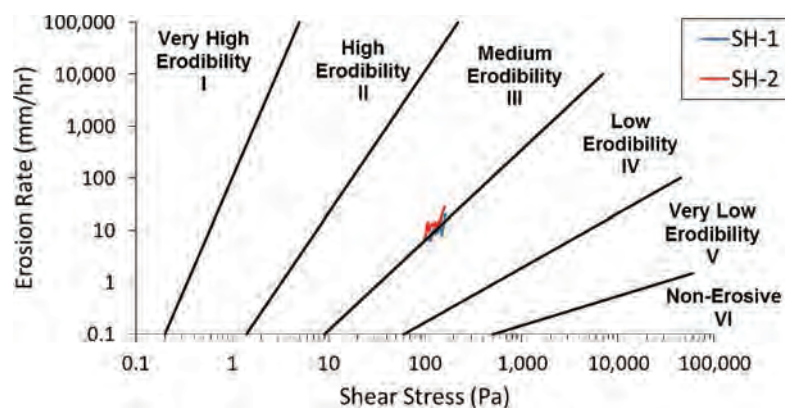


Figure 64. Erosion part of the sand HET curves plotted on the erosion category chart.

#### 4.3.1.4 Ensuring the Repeatability of the JET

As discussed Chapter 2, for every JET the operator records the depth of the hole being created at the center of the sample as a function of time under a constant head condition. The collected data are then backanalyzed to estimate two main erodibility parameters: critical shear stress and erosion rate. Three techniques are used to interpret the JET results: (1) the Blaisdell solution, (2) the iterative solution, and (3) the scour depth solution. Figure 65 shows an example of reading inputs during a JET and a sample JET spreadsheet. Each method gives a different set of erodibility parameters: critical shear stress ( $\tau_c$ ), and detachment coefficient ( $k_d$ ), which is the linear slope of the early part of the erosion curve in the erosion rate–shear stress plot.

It is the test operator's duty to find the best solution for interpreting JET results. In addition, since one of the goals of this research project was to establish relationships between soil erodibility and engineering properties, it was very important to understand each solution well and choose a consistent method of data interpretation for all JET results. The three interpretation techniques are summarized below.

**Blaisdell Solution.** The most established solution in the literature is the Blaisdell solution, which was developed and used by Hanson and Cook (1997, 2004). This technique was created on the basis of a hyperbolic function (Blaisdell et al. 1981) to model the development of the scour hole. The details of this hyperbolic function are not discussed here; however, it is worth noting that this function employs the real-time depth of the scour hole and the velocity of the water jet at the nozzle to predict the maximum depth of erosion, at which the hole stops being eroded. Thereafter, the estimated equilibrium depth is used to measure the critical shear stress (Equation 57):

$$\tau_c = \tau_0 \times \left[ \frac{J_p}{J_e} \right]^2 \quad (57)$$

where

$J_e$  = equilibrium depth,

$J_p$  = potential core length (nozzle diameter  $\times$  6.2), and

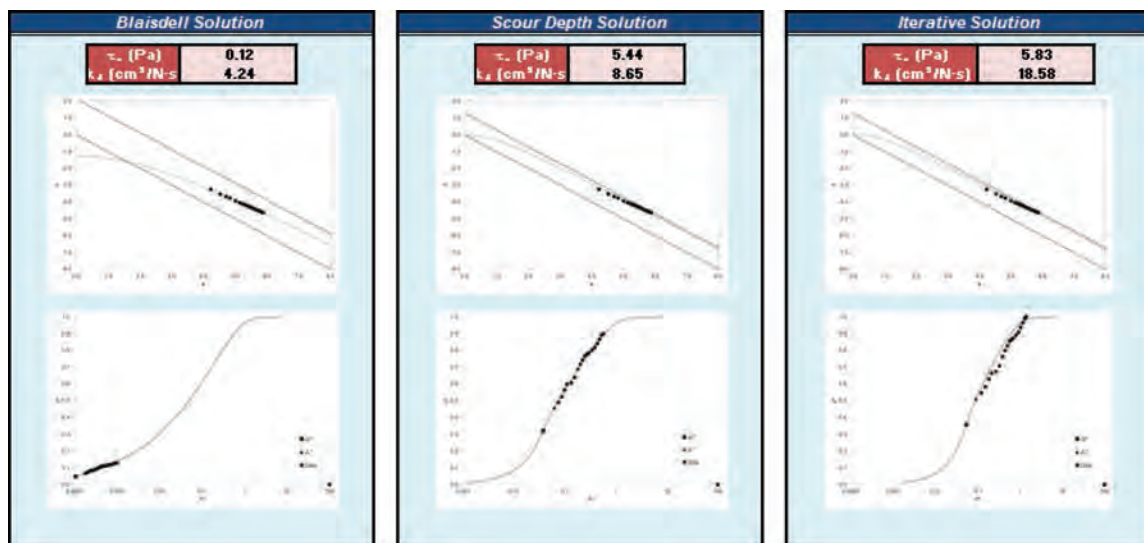
$\tau_0$  = maximum shear stress at the soil–water boundary.

The value of  $k_d$  is then determined by using the least squares derivation between the real time and predicted time. Further information is provided in Chapter 2, Section 2.1.6. It was found in the literature that this technique highly underpredicts the values of  $\tau_c$  and  $k_d$ . After many jet tests were run, letting the sample erode until it reached the equilibrium depth, it was observed that the equilibrium depth estimated with the Blaisdell solution was typically lower than the actual equilibrium depth. This consequently leads to underprediction of the critical shear stress and, subsequently, the detachment coefficient ( $k_d$ ). The other issue with the Blaisdell solution was the high variability of the critical shear stress (Simon et al. 2010; Cossette et al. 2012).

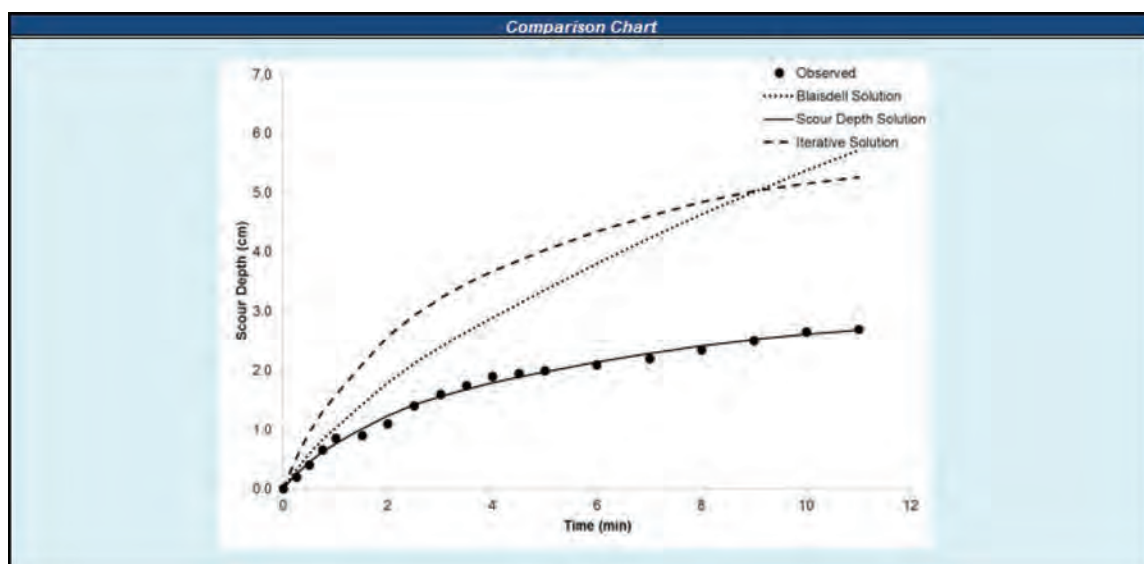
**Iterative Solution.** In an effort to improve the Blaisdell solution and reduce the scatter in  $\tau_c$  versus  $k_d$ , Simon et al. (2010) developed the iterative solution. In this technique, the results of  $\tau_c$  and  $k_d$  from the Blaisdell solution are used for the next iteration to minimize the root mean square deviation between the real time and predicted time; however, many examples showed that the same variation in results was often observed.

**Scour Depth Solution.** The scour depth solution was developed by Daly et al. (2013). The big difference between this technique and the other two is that it solves for  $k_d$  and  $\tau_c$  at the same

Scour Depth Readings						Head Setting	
Time (min)	Diff Time (min)	Pt Gage Reading (mm)	Depth (ft)	Pt Gage Reading (ft)	Maximum Depth of Scour (ft)	Time (min)	Head (in)
0	0	32	0.105	0.895	0.000	0	45.00
0.25	0.25	34	0.112	0.888	0.007	0.25	45.00
0.5	0.25	36	0.118	0.882	0.013	0.5	45.00
0.75	0.25	38.5	0.126	0.874	0.021	0.75	45.00
1	0.25	40.5	0.133	0.867	0.028	1	45.00
1.5	0.5	41	0.135	0.865	0.030	1.5	45.00
2	0.5	43	0.141	0.859	0.036	2	45.00
2.5	0.5	46	0.151	0.849	0.046	2.5	45.00
3	0.5	48	0.157	0.843	0.052	3	45.00
3.5	0.5	49.5	0.162	0.838	0.057	3.5	45.00
4	0.5	51	0.167	0.833	0.062	4	45.00
4.5	0.5	51.5	0.169	0.831	0.064	4.5	45.00
5	0.5	52	0.171	0.829	0.066	5	45.00
6	1	53	0.174	0.826	0.069	6	45.00
7	1	54	0.177	0.823	0.072	7	45.00
8	1	55.5	0.182	0.818	0.077	8	45.00
9	1	57	0.187	0.813	0.082	9	45.00
10	1	58.5	0.192	0.808	0.087	10	45.00
11	1	59	0.194	0.806	0.089	11	45.00



(a)



(b)

Figure 65. Example of (a) reading inputs during a JET, (b) sample JET spreadsheet.

time. As shown in Figure 65, the plot of scour depth versus time is better predicted by the scour depth solution. With this method, the JET should be run until the sample stops eroding in the center (i.e., reaches the equilibrium depth).

To date, JET results are often reported by using the Blaisdell solution technique. However, new studies by Daly et al. (2015) and Khanal et al. (2016) have reported JET results in the form of all three solution techniques. Khanal et al. (2016) have investigated the influence of the operator-dependent variables, such as reading interval, ending time, and pressure head setting on JET results interpreted with all three solutions. It has been partially concluded that the scour depth solution gives the most accurate results in terms of scour depth versus time. This solution also makes fewer assumptions [e.g., assuming the final equilibrium depth ( $J_e$ ) or the predicted time] as compared with the Blaisdell and iterative solutions. Because the scour depth solution makes fewer assumptions than the Blaisdell and iterative solutions, JET results obtained with the scour depth solution were selected for comparison with the erosion results obtained from the HET and the EFA. However, one of the disadvantages of the scour depth solution occurs in the case where the soil is very resistant to erosion. In this case, it is rarely possible to end with the equilibrium depth; therefore, the iterative solution is better for predicting subtle changes in scour depth and obtaining the equilibrium depth, and, consequently the erodibility parameters.

For this project, the JET results are reported according to all three solutions discussed above. For the regression analyses presented in the next chapters, the scour depth solution is used as the primary solution, except in special cases in which use of the iterative solution or Blaisdell solution was more appropriate.

**Clay Samples (CJ-1 and CJ-2).** Table 20 shows the results of the three solutions—Blaisdell, iterative, and scour—for CJ-1 and CJ-2. Reasonable repeatability was observed for all three techniques. The results of all JET tests are presented in the format of a JET result spreadsheet in Appendix 1. Figure 66 shows an example of the JET result spreadsheet for Sample CJ-1.

**Silt Samples (MJ-1 and MJ-2).** Table 21 shows the JET results obtained for Samples MJ-1 and MJ-2. A reasonable repeatability is observed for all three techniques.

**Sand Samples (SJ-1 and SJ-2).** Table 22 shows the JET results obtained for Samples SJ-1 and SJ-2. Except for the iterative solution, reasonable repeatability was observed, especially for the critical shear stress values.

**Gravel Samples (GJ-1 and GJ-2).** Like the HET, the JET can only be performed in fine-grained soils. Therefore, the JET was not conducted for the gravel samples.

#### 4.3.1.5 Field Erosion Device Demonstration

As shown in Table 16, the erosion testing included organizing field demonstration tests of the BET device, the PET, and, possibly, North Carolina State University's ISEEP and FHWA's ISTD. Letters were sent to the appropriate staff at North Carolina State University and FHWA

**Table 20. JET results for Samples CJ-1 and CJ-2.**

Sample	Blaisdell Solution		Iterative Solution		Scour Depth Solution	
	$\tau_c$ (Pa)	$k_d$ (cm <sup>3</sup> /N.s)	$\tau_c$ (Pa)	$k_d$ (cm <sup>3</sup> /N.s)	$\tau_c$ (Pa)	$k_d$ (cm <sup>3</sup> /N.s)
CJ-1	5.79	0.59	5.8	3.82	8.8	2.56
CJ-2	4.81	0.53	4.92	3.76	6.74	1.19

## 102 Relationship Between Erodibility and Properties of Soils

Site:	
Date:	12/15/2016
Test #:	CJ-1
JET #:	1
Operator:	Iman
Test Location:	A&M Erosion Lab
Pt Gage Reading at Nozzle (mm):	4
Ref. Pt Gage Reading at Nozzle (ft):	0.9869
Nozzle Diameter (in):	0.125
Nozzle Height (ft):	0.1378
Initial guess* for $T_c$ (Pa):	1
Initial guess* for $k_e$ ( $\text{cm}^2/\text{N s}$ ):	1

Scour Depth Readings						Head Setting	
Time (min)	Diff Time (min)	Pt Gage Reading (mm)	Depth (ft)	Pt Gage Reading (ft)	Maximum Depth of Scour (ft)		
0	0	46	0.151	0.849	0.000	0	45.00
0.25	0.25	47	0.154	0.846	0.003	0.25	45.00
0.75	0.5	47	0.154	0.846	0.003	0.75	45.00
1.5	0.75	47.5	0.156	0.844	0.005	1.5	45.00
2	0.5	47.5	0.156	0.844	0.005	2	45.00
3	1	48	0.157	0.843	0.007	3	45.00
4	1	48	0.157	0.843	0.007	4	45.00
6	2	48.5	0.159	0.841	0.008	6	45.00
9	3	49	0.161	0.839	0.010	9	45.00
12	3	49	0.161	0.839	0.010	12	45.00
15	3	49	0.161	0.839	0.010	15	45.00
18	3	49.5	0.162	0.838	0.011	18	45.00
23	5	50	0.164	0.836	0.013	23	45.00
28	5	51	0.167	0.833	0.016	28	45.00
33	5	51	0.167	0.833	0.016	33	45.00
38	5	51.5	0.169	0.831	0.018	38	45.00
43	5	52	0.171	0.829	0.020	43	45.00
48	5	52	0.171	0.829	0.020	48	45.00
53	5	52	0.171	0.829	0.020	53	45.00

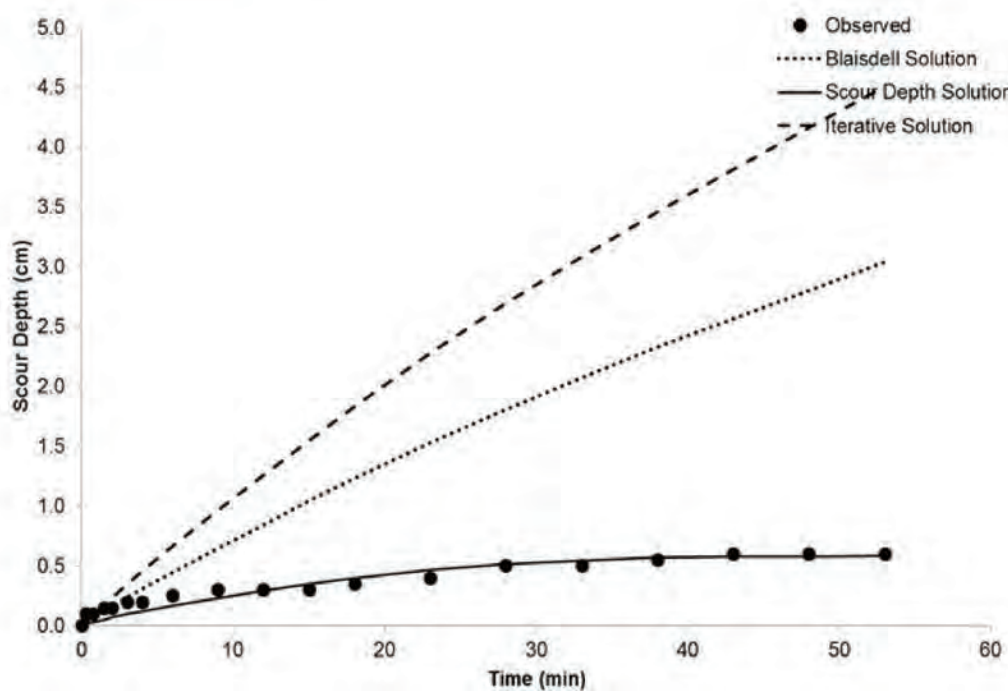


Figure 66. JET result spreadsheet for Sample CJ-1.

**Table 21. JET results for Samples MJ-1 and MJ-2.**

Sample	Blaisdell Solution		Scour Depth Solution		Iterative Solution	
	$\tau_c$ (Pa)	$k_d$ (cm <sup>3</sup> /N.s)	$\tau_c$ (Pa)	$k_d$ (cm <sup>3</sup> /N.s)	$\tau_c$ (Pa)	$k_d$ (cm <sup>3</sup> /N.s)
MJ-1	1.9	1.45	1.74	1.4	4.74	5.22
MJ-2	1.37	1.02	3.89	2.12	3.63	5.2

to invite them to participate in the field demonstration tests. However, North Carolina State University did not have the funds necessary to bring the ISEEP to College Station, and FHWA declined because it was working on improving the ISTD and thus was not ready to contribute to this project.

It was decided to perform the feasible available field tests at the National Geotechnical Experimentation Site at TAMU's RELLIS Campus. These tests include the BET and the PET on both sand and clay sites. Terracon Consultants, Inc., of Conroe, Texas, provided necessary equipment to perform the field demonstration for this project. This section presents the results of the BET in clay and sand sites. The following BET procedure was undertaken at both sites:

1. Sampling was done at from 2 to 5 ft, from 6 to 9 ft, and from 10 to 13 ft in a 14-ft-deep borehole with 3-in. diameter Shelby tubes. Three 3-ft-long Shelby tube samples were taken every 4 ft. A 3-in. drill bit was used if necessary.
2. Insert the mechanical caliper and measure the diameter versus the depth (Figure 67).
3. Circulate the drilling fluid for 1 min to flush the borehole (Figure 68).
4. Insert the mechanical caliper and measure the diameter versus the depth.
5. Withdraw the mechanical caliper.
6. Insert NW drilling rods down to 6 in. above the bottom of the hole and circulate drilling fluid for 15 min at maximum pump velocity.
7. Withdraw the drilling rods.
8. Insert the mechanical caliper and measure the diameter versus the depth.
9. Withdraw the mechanical caliper.
10. Insert NW drilling rods 6 in. above the bottom of the hole and circulate the drilling fluid for 15 min at half the previous rate.
11. Withdraw the drilling rods.
12. Insert mechanical caliper and the measure diameter versus the depth.
13. Withdraw the mechanical caliper.
14. Insert NW drilling rods 6 in. above the bottom of the hole and circulate drilling fluid for 15 min at a flow rate to be decided in the field.
15. Withdraw the drilling rods.
16. Insert the mechanical caliper and measure the diameter versus the depth.
17. Withdraw the mechanical caliper.
18. Plot the data and adjust the procedure.

**Table 22. JET results for Samples SJ-1 and SJ-2.**

Sample	Blaisdell Solution		Scour Depth Solution		Iterative Solution	
	$\tau_c$ (Pa)	$k_d$ (cm <sup>3</sup> /N.s)	$\tau_c$ (Pa)	$k_d$ (cm <sup>3</sup> /N.s)	$\tau_c$ (Pa)	$k_d$ (cm <sup>3</sup> /N.s)
SJ-1	4.10	1.34	8.30	5.56	5.15	10.54
SJ-2	4.06	0.73	8.03	3.59	3.96	5.48

**104** Relationship Between Erodibility and Properties of Soils



**Figure 67.** *Photographs taken from the mechanical caliper (3 arms) in closed-arm and opened-arm conditions.*



**Figure 68.** *Circulating the drilling fluid in the borehole in order to flush.*

A photograph of the pump and the flow meter assembly on the drill rig is shown in Figure 69. One borehole in the sand site and one borehole in the clay site were drilled with 3-in.-diameter hollow stem augers. The drilling rods used to circulate the drilling fluid were 2.75 in. in diameter, which leaves an empty space of almost one-quarter inch between the drilling rods and the borehole wall. During the test, the flow rate is constantly monitored with the in-line flow meter shown in Figure 69; therefore, the velocity of the fluid in the borehole can be obtained by dividing the flow rate by the annular space between the drilling rod and the borehole wall. Results of the BET for clay and sand are discussed in the following sections.

**BET at the Clay Site.** One borehole was drilled to the depth of 14 ft. The borehole was located at the following coordinates: N 30°.38.104', W 096°.29.348'. Soil was classified as CH throughout the borehole. As described earlier for the BET procedure, the zero reading was measured after 1 min of flushing at a flow of 36 gallons per minute (gpm) ( $0.002271 \text{ m}^3/\text{s}$ ). After that, three different flows of 35 gpm ( $0.002208 \text{ m}^3/\text{s}$ ), 21 gpm ( $0.001325 \text{ m}^3/\text{s}$ ), and 33 gpm ( $0.002082 \text{ m}^3/\text{s}$ ) were generated in the borehole and maintained for 10 min each. The mechanical caliper shown in Figure 67 was used to obtain the diameter profile after each flow. Figure 70 shows the caliper readings at five different stages:

1. Before flushing: right after the borehole was drilled and before the 1-min flushing was done.
2. After flushing: after 1 min of flushing.
3. Reading 1: after 10 min of 35-gpm flow.
4. Reading 2: after 10 min of 21-gpm flow.
5. Reading 3: after 10 min of 33-gpm flow.

The caliper readings at each of the aforementioned stages were obtained in two runs to make sure that the readings were repeatable. For all the cases, an acceptable overlay was observed, and the repeatability of the caliper readings was confirmed. The borehole diameter profiles shown in Figure 70 portray the averaged diameter profile between the first and second runs at each stage. Figure 70 clearly shows that, before any calculations of the erosion rate were made, there was a weak sand fissure at the proximity of the depth of 7.5 to 8.5 ft that caused much greater diameter enlargement. This observation is indeed an example of one of the most important advantages of the BET as compared with many other erosion tests in catching a continuous erodibility profile at a site prior to construction of bridges, levees, dams, and so forth.



**Figure 69.** Photograph of the pump and the in-line flow meter assembly on the drill rig.

## 106 Relationship Between Erodibility and Properties of Soils

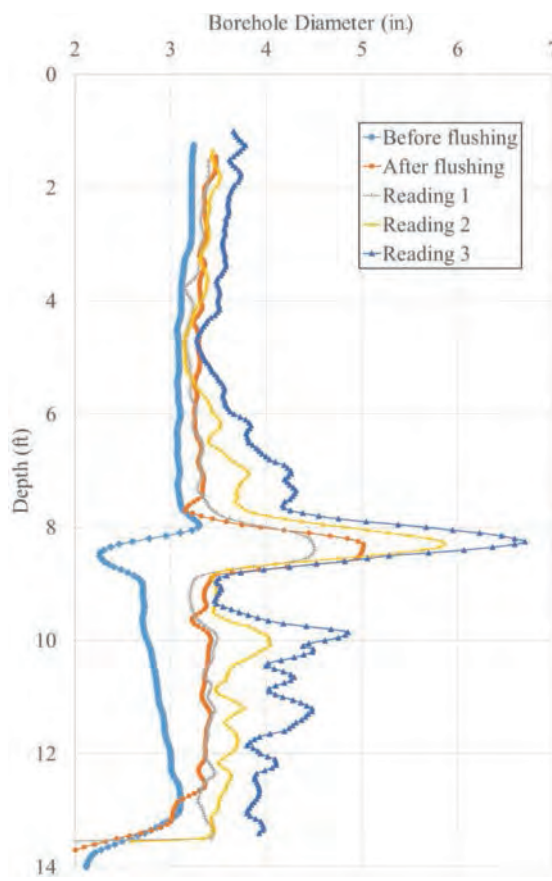


**Figure 70.** *Clay borehole diameter profile at different stages during the BET.*

While Figure 70 shows the borehole diameter profile at different stages during the test, it must be noted that the erosion function curve (i.e., the plot of the average erosion rate versus the fluid velocity) was constructed separately for each 2-ft interval (i.e., 2–4 ft, 4–6 ft, 6–8 ft, 8–10 ft, and 10–12 ft). Table 23 gives the flow rates, velocities, and time of application of each velocity for the BET at the clay site. Figure 71 shows the erosion function curves for each of the 2-ft intervals.

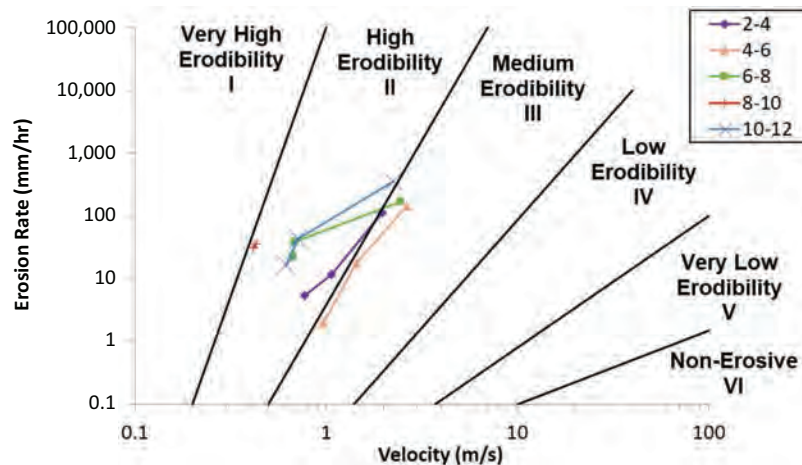
As discussed in Chapter 2, Section 2.2.3, the BET has two component tests: the lateral borehole erosion test (LBET) associated with the increase in diameter of the borehole and the bottom borehole erosion test (BBET) associated with the increase in depth below the bottom of the drilling rods during the flow. The LBET is very similar in concept to the HET but with a larger hole and a vertical flow direction. The BBET is much like an in situ jet erosion test.

The increase in depth at the bottom of the borehole in the BBET was monitored after each stage; however, these measurements did not lead to a reasonable erosion rate at the bottom of the hole. The main reason was that, as the wall of the borehole was being eroded, some eroded materials would settle and remain at the bottom of the borehole; therefore, the measurements of the bottom depth did not necessarily represent the actual erodibility of the soil at that depth. This issue, however, was not confronted during the BET at the sand site. The results of the LBET and BBET are included below in the discussion of the BET at the sand site.

Figure 72 shows the results of some earlier EFA tests performed on samples taken from the same depths at the clay site. These EFA tests were performed about 1 year earlier than the

**Table 23.** Flow, velocity, and time for the BET at clay site.

Flow ( $\text{m}^3/\text{s}$ )	Velocity (m/s)	Duration (min)	Change in Profile (Figure 70)
Depth = 2 to 4 ft			
0.002271	1.967	1	Before flushing to after flushing
0.002208	1.308	10	After flushing to Reading 1
0.001325	0.773	10	Reading 1 to Reading 2
0.002082	1.063	10	Reading 2 to Reading 3
Depth = 4 to 6 ft			
0.002271	2.639	1	Before flushing to after flushing
0.002208	1.444	10	After flushing to Reading 1
0.001325	0.967	10	Reading 1 to Reading 2
0.002082	1.431	10	Reading 2 to Reading 3
Depth = 6 to 8 ft			
0.002271	2.450	1	Before flushing to after flushing
0.002208	1.280	10	After flushing to Reading 1
0.001325	0.669	10	Reading 1 to Reading 2
0.002082	0.687	10	Reading 2 to Reading 3
Depth = 8 to 10 ft			
0.002271	N/A	1	Before flushing to after flushing
0.002208	0.596	10	After flushing to Reading 1
0.001325	0.418	10	Reading 1 to Reading 2
0.002082	0.433	10	Reading 2 to reading 3
Depth = 10 to 12 ft			
0.002271	2.242	1	Before flushing to after flushing
0.002208	1.188	10	After flushing to Reading 1
0.001325	0.621	10	Reading 1 to Reading 2
0.002082	0.712	10	Reading 2 to Reading 3

**Figure 71.** Results of lateral BET: erosion function curves for each 2-ft interval at the clay site.

## 108 Relationship Between Erodibility and Properties of Soils

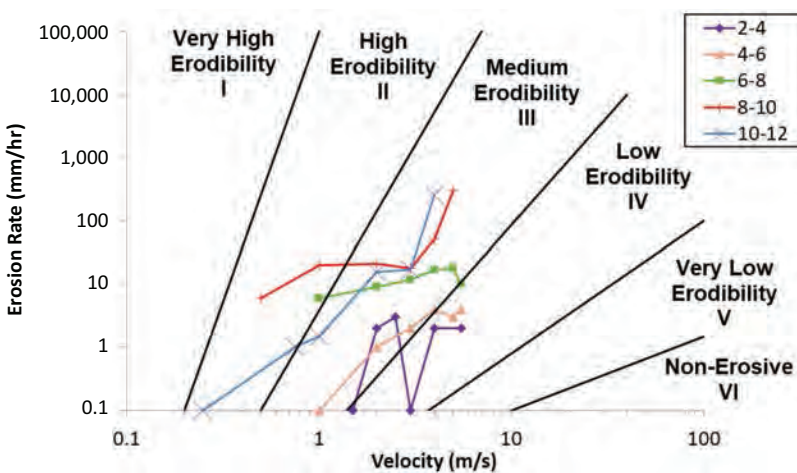


**Figure 72.** EFA results: erosion function curves for each 2-ft interval at the clay site.

BET. Also, the boring from which samples were taken for EFA testing was not the same as or close to the boring done for the BET. These two factors as well as different flow conditions in the EFA and BET could be the main reasons that the EFA and BET results did not match perfectly. Clearly, there is a gap between the results of the two tests; however, in both tests, most erosion was observed in soil layers deeper than 6 ft. Existence of a weak sand fissure in the proximity of 8 ft made a big difference in the erosion resistance of the borehole in the clay site.

**BET at the Sand Site.** One borehole was drilled to the depth of 12 ft. The borehole was located at the following coordinates: N 30°.38.301', W 096°.27.606'. The soil was classified as SC throughout the borehole. Similar to the BET procedure, the borehole was flushed for almost 30 s at a flow of 37 gpm ( $0.002334 \text{ m}^3/\text{s}$ ). After that, flows of 34 gpm ( $0.002145 \text{ m}^3/\text{s}$ ) and 38 gpm ( $0.002397 \text{ m}^3/\text{s}$ ) were generated in the borehole and maintained for 7 min each. The mechanical caliper shown in Figure 67 was used to obtain the borehole diameter profile after each flow. Figure 73 shows the caliper readings at four different stages during the test:

1. Before flushing: right after the borehole was drilled and before the 30-s flushing was done.
2. After flushing: after 30 s of flushing.
3. Reading 1: after 7 min of 34-gpm flow.
4. Reading 2: after 7 min of 38-gpm flow.

As with the BET at the clay site, caliper readings at each of the aforementioned stages were obtained in two runs to ensure that the readings were repeatable. For all the cases, an acceptable overlay was observed, and the repeatability of the caliper readings was confirmed. The borehole diameter profiles shown in Figure 73 portray the averaged diameter profile between the first and second runs at each stage. It is clearly shown that the diameter enlargement at depths closer to the ground surface (0–3 ft) was significantly greater than at other depths. While Figure 73 shows the borehole diameter profile at different stages during the BET, it must be noted that the erosion function curve (i.e., plots of the average erosion rate versus the fluid velocity) was constructed separately for each 2-ft interval (i.e., 1–3 ft, 3–5 ft, 5–7 ft, 7–9 ft, and 9–11 ft). Table 24 gives the flow rates, velocities, and time of application of each velocity for the BET at the sand site. Figure 74 shows the erosion function curves for each of the 2-ft intervals.

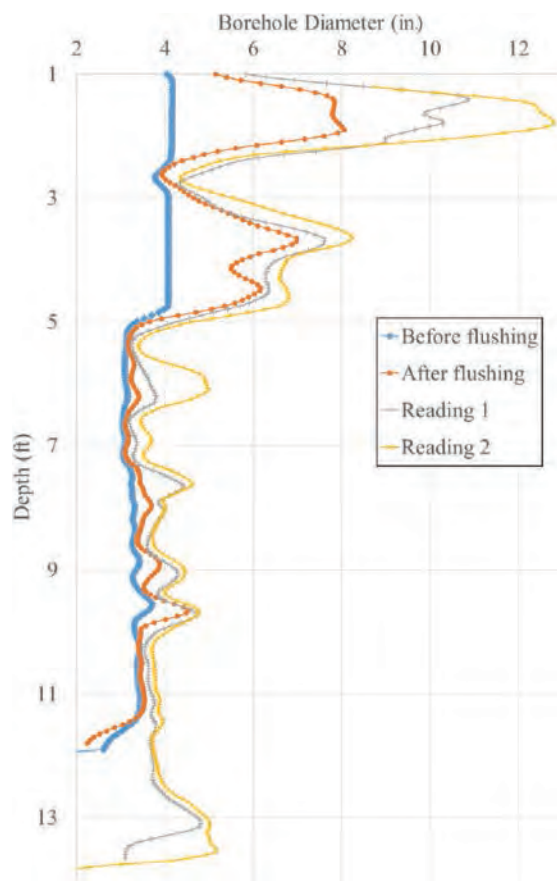


**Figure 73. Sand borehole diameter profile at different stages during the BET.**

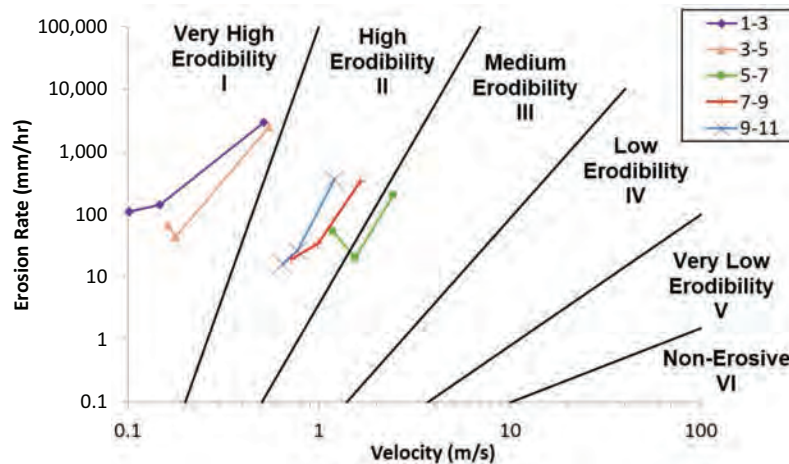
Figure 75 shows the results of some earlier EFA tests performed on the samples from the sand site. The sand samples tested in the EFA were mixed from different depths and constructed in the laboratory to represent a similar condition in the field. The EFA results are acceptably consistent with the BET results, specifically for soil deeper than 5 ft. As mentioned earlier, the first 5 ft showed significant erosion during the BET. One of the reasons for much greater erosion in depths closer to the ground surface was that as the test was being performed, the cohesionless sand wall on top of the borehole became weaker and began to erode more as compared with deeper layers. In the deeper layers, however, more reasonable erosion was observed. One of the reasons that better consistency between the EFA and BET results was observed for the sand samples may be that the borings used for the BET and EFA were close to each other and, therefore, soils from same depth were more similar than was the case with the clay site.

The BET results discussed above are all associated with the increase in the diameter of the borehole (LBET). For the sand borehole, the depth increase at the bottom of the borehole was also monitored (BBET). The erosion function curve for the bottom of the sand borehole is shown in Figure 76. Briaud et al. (2017a) showed that the flow velocity of the jet eroding the borehole was almost equal to the average velocity of the flow in the annular space between the drilling rods and the borehole wall at depths close to the jet nozzle. For this study, the average velocity of the flow for the depth of 9–11 ft was chosen to represent the velocity of the jet at the bottom of the borehole. The BBET results presented in Figure 76 show a higher erosion rate than the LBET result for the depth of 9–11 ft in Figure 74.

## 110 Relationship Between Erodibility and Properties of Soils

**Table 24.** Flow, velocity, and time for the BET at sand site.

Flow ( $\text{m}^3/\text{s}$ )	Velocity (m/s)	Duration (min)	Change in profile (Figure 73)
Depth = 1 to 3 ft			
0.002334	0.518	0.5	Before flushing to after flushing
0.002145	0.147	7	After flushing to Reading 1
0.002397	0.102	7	Reading 1 to Reading 2
Depth = 3 to 5 ft			
0.002334	0.548	0.5	Before flushing to after flushing
0.002145	0.179	7	After flushing to Reading 1
0.002397	0.162	7	Reading 1 to Reading 2
Depth = 5 to 7 ft			
0.002334	2.453	0.5	Before flushing to after flushing
0.002145	1.555	7	After flushing to Reading 1
0.002397	1.191	7	Reading 1 to Reading 2
Depth = 7 to 9 ft			
0.002334	1.652	0.5	Before flushing to after flushing
0.002145	0.988	7	After flushing to Reading 1
0.002397	0.721	7	Reading 1 to Reading 2
Depth = 9 to 11 ft			
0.002334	1.207	0.5	Before flushing to after flushing
0.002145	0.769	7	After flushing to Reading 1
0.002397	0.647	7	Reading 1 to Reading 2

**Figure 74.** LBET results: erosion function curves for each 2-ft interval at the sand site.

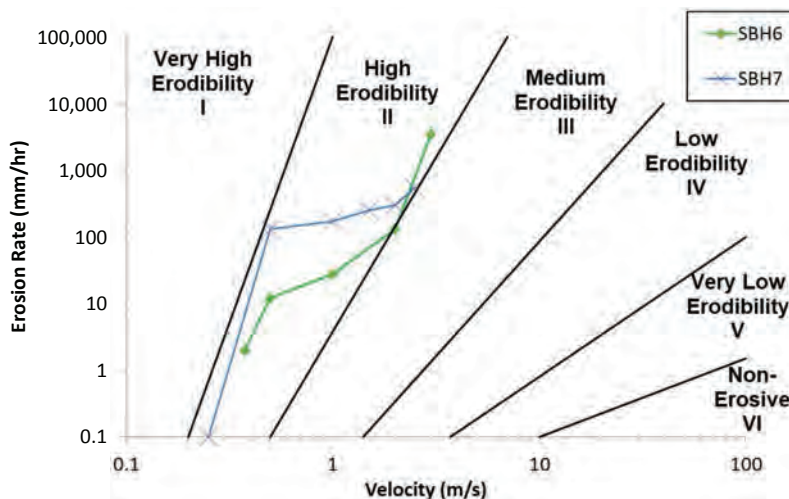


**Figure 75.** EFA results: erosion function curves for each 2-ft interval at the sand site.

#### 4.3.2 Erosion Tests Performed Using Many Different Soils

This section discusses the running of different erosion tests on many natural samples. More than 128 erosion tests (32 EFA, 32 JET, 32 HET, and 32 PET) were performed on 14 natural clay, 8 silt, 6 sand, and 4 gravel samples. Many of these tests were performed on natural samples taken from Terracon's Houston office. Some were collected from the Alcona Dam near Oscoda, Michigan; the Tittabawassee River in Midland, Michigan; Crane Creek in California; and Freeport and Lissie, Texas. After Hurricane Harvey, Iman Shafii, lead engineer on NCHRP Project 24-43, joined the Geotechnical Extreme Events Reconnaissance (GEER) team supported by the National Science Foundation. During this major effort, 15 samples from different locations were obtained and brought to the TAMU Soil Erosion Laboratory for erosion testing (primarily for EFA testing).

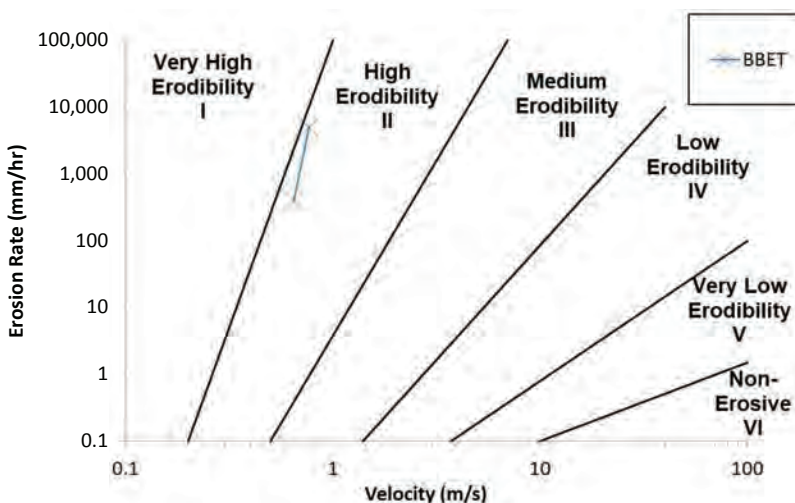


**Figure 76.** BBET results: erosion function associated with the bottom of the sand borehole.

## 112 Relationship Between Erodibility and Properties of Soils

Because of the limitations of each erosion testing device, a few challenges confronted the investigating team during the erosion testing phase. The following revisions were made to the testing plan:

1. **HET testing on clay and silt samples:** The HET was primarily conducted on remolded samples instead of natural samples, following the advice of the panel.
2. **HET testing on sand and gravel (6 tests on sand and 4 tests on gravel):** The HET could not be properly conducted on sand and gravel samples due to the limitations associated with its setup. In all cases, the hole drilled in sand samples collapsed. For gravel samples, this test clearly was not feasible. Therefore, it was decided to increase the number of erosion tests on any other sample (mostly coarse-grained samples) using other erosion tests (i.e., EFA and PET) to make up for the number of erosion tests promised in the proposed testing matrix.
3. **JET testing on gravel (4 tests on gravel):** The JET test also is not designed for gravel samples. Therefore, no JET results were reported for gravel samples.

A summary of the tested samples presented in this section is given in Table 25. The majority of Table 25 is incorporated with intact samples; however, some cohesionless samples were remolded in the laboratory to follow the testing matrix shown in Table 17. Erosion result spreadsheets, as described in earlier sections, were prepared for each tested sample separately. Appendix 1 shows the results of the EFA, JET, and HET for all samples tested in this project. The total number of tests performed during this project turned out to be more than the 168 erosion tests promised in the proposed testing matrix.

**Table 25. Summary list of tested samples.**

Test and Sample Name	Collected From	Date Collected	Site
<b>INTACT SAMPLES</b>			
<b>EFA and PET</b>			
B-1 (23–25 ft)			
B-7 (22–24 ft)	G2 Consulting Group, LLC	Dec. 2016	Tittabawassee River, Midland, Michigan
B-9A (25–27 ft)			
B-9A (29–31ft)			
B-7-16 @ 8.5 ft			
B-7-16 @ 11.6 ft			
B-7-16 @ 13.5 ft			
B-7-16 @ 15.3 ft			
B-9-16 @ 16.1 ft			
B-9-16 @ 17.3 ft			
B-11-16 @ 18 ft			
B-11-16 @ 20.5 ft	Barr Engineering Co.	Nov. 2016	Alcona Dam, Oscoda, Michigan
B-12-16 @ 18.1 ft			
B-12-16 @ 18.9 ft			
B-12-16 @ 20.5 ft			
B-13-16 @ 19 ft			
B-13-16 @ 20.5 ft			
B-13-16 @ 23.5 ft			
B-2 (13–15 ft)			
B-6 (0–2 ft)			
B-1 (4–6 ft)	Terracon, Houston	Oct. 2016	Beaumont Formation, Texas
B-1 (28–30 ft)			
B-8 (2–4 ft) 5694			

**Table 25. (Continued).**

Test and Sample Name	Collected From	Date Collected	Site
B-1 (12.5–14.5 ft)	American Geotechnics	April 2017	Crane Creek, California
GEER Sample #1	Geotechnical Extreme Events Reconnaissance (GEER)	Sept. 2017	Port Aransas Bridge, Texas
GEER Sample #2			Bay City Bridge, Texas
GEER Sample #3			
GEER Sample #4			
GEER Sample #5			
GEER Sample #6			San Louis Pass, Texas
GEER Sample #7			
GEER Sample #8			Levee at Brazos River, Texas
GEER Sample #9			
GEER Sample #10			Rosenberg Culvert Bridge, Texas
<b>JET and PET</b>			
B-1 (2–4 ft)	Terracon, Houston	Oct. 2016	Beaumont Formation, TX
B-1 (4–6 ft)			
B-1 (8–10 ft)			
B-1 (10–12 ft)			
B-1 (13–15 ft)			
B-1 (18–20 ft)			
B-1 (28–30 ft)			
B-2 (2–4 ft)			
B-2 (8–10 ft)			
B-2 (13–15 ft)			
B-3 (8–10 ft)			
B-4 (8–10 ft)			
B-5 (4–6 ft)			
B-5 (6–8 ft)			
B-6 (0–2 ft)			
B-2 (8–10 ft)	Terracon, Houston	Winter 2016	Lissie Formation Texas
B-3 (10–12 ft)			
B-8 (2–4 ft)	Terracon, Houston	Winter 2016	Alluvium, Freeport Texas
B-13 @ 20 ft			
B-13 @ 18 ft			
B-9A @ 26 ft	G2 Consulting Group, LLC	Dec. 2016	Tittabawassee Midland, Michigan
B-9A @ 27 ft			
B-1 (23–25 ft)			
B-7 (22–24 ft)			
GEER Sample #2	GEER	Sept. 2017	Bay City Bridge, Texas

(continued on next page)

## 114 Relationship Between Erodibility and Properties of Soils

**Table 25. (Continued).**

Test and Sample Name	Collected From	Date Collected	Site
<b>REMOLDED SAMPLES</b>			
<b>EFA and PET</b>			
Teton Dam 1			
Teton Dam 2			
Teton Dam 3			
Sample 2 (FHWA)			
S-0-0-0			
Sand #1			
Sand #2			
Gravel #1			
Gravel #2			
Gravel #3			
Gravel #4			
<b>JET and PET</b>			
Teton Dam Core			
S-0-0-0			
Sand #1			
Sand #2			
Sample 2 (FHWA)			
<b>HET and PET</b>			
Clay #1			
Clay #2			
Clay #3			
Clay #4			
Clay #5			
Clay #6			
Clay #7			
Clay #8			
Clay #9			
Clay #10			
Clay #11			
Clay #12			
Clay #13			
Clay #14			
Silt 1			
Silt 2			
Silt 3			
Silt 4			
Silt 5			
Silt 6			
Silt 7			
Teton Dam Core			

Note: Shading indicates not applicable.

## 4.4 Soil Geotechnical Properties

Soil index tests were conducted for all samples tested by any erosion testing device. The geotechnical tests included unit weight (ASTM D7263-09), moisture content (ASTM D2216-10), Atterberg limits (ASTM D4318-17), mini vane shear test (ASTM D4648), pocket penetrometer, sieve analysis (ASTM 422), hydrometer analysis (ASTM D7928-17), USCS (ASTM D2487-17), AASHTO classification, and specific gravity test (ASTM D854-14). Existing relevant geological information such as latitude and longitude, origin, water table data of the samples, and so forth were also recorded for each sample when possible. All this information was compiled in a comprehensive two-page soil properties spreadsheet for each sample. As an illustration, Figure 77 and Figure 78 show the two pages of the completed soil properties spreadsheet for sample B-7-16 (13–15.5 ft). Such spreadsheets were developed for all the soil samples that were tested with different erosion testing devices. Appendix 2 contains all the soil properties spreadsheets developed for this project.

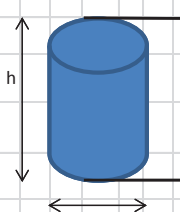
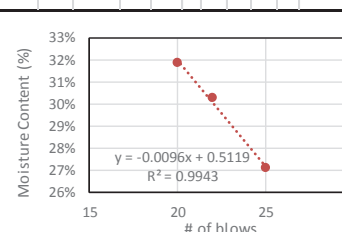
Form # 0916		Sample name	Operator	Bore hole ID	Date	Layer type	Layer depth (ft):	Layer thickness (ft)	Page 1 of 2			
 TEXAS A&M UNIVERSITY	B-7-16 (top)	Iman Shafii	B-7-16	5-Dec	Clay	From : 13	To : 15.5					
							2.5					
<b>Sample Dimensions</b>			Depth of upper side of the core (ft) 13.667  Depth of middle of the core (ft) 13.709  Depth of lower side of the core (ft) 13.750	Notes:  <b>Density Calcs.</b>	Sample Height (ft) 0.083  Sample Diameter (ft) 0.25  Sample Volume (ft³) 0.0041  Sample weight (lb) 0.538  Wet Density (pcf) 131.52	Sample Height (ft) 0.083  Sample Diameter (ft) 0.25  Sample Volume (ft³) 0.0041  Sample weight (lb) 0.538  Wet Density (pcf) 131.52	<b>Wet Density</b>  Wet Density (pcf) 131.5  Dry Density (kg/m³) 1658.2  Dry Density (kN/m³) 16.3  Dry Density (pcf) 104	Wet Density (kN/m³) 20.7  Wet Density (pcf) 131.5  Dry Density (kg/m³) 1658.2  Dry Density (kN/m³) 16.3  Dry Density (pcf) 104				
height (ft)	0.083											
height (mm)	25.315											
<b>Moisture Content</b>		Container #	Weight of Container (gr)	<b>Wet</b>		<b>Dry</b>		Weight of Water (gr)	Weight of Solids (gr)	Moisture (%)		
Sample #	Core depth at middle (ft)			W <sub>c+s</sub> (gr)	W <sub>s</sub> (gr)	W <sub>c+s</sub> (gr)	W <sub>s</sub> (gr)					
1	13.50	45	1	9.9	8.9	8	7	1.9	7	27.14%		
2	13.50	49	1	15.6	14.6	12.5	11.5	3.1	11.5	26.96%		
<b>Liquid Limit</b>		Limits	# of blows (mm)	Container #	Weight of Container (gr)	<b>Wet</b>		WC (%)				
Test #	Core depth at middle (ft)					W <sub>c+s</sub> (gr)*	W <sub>c+s</sub> (gr)					
1	13.50	25-35	25	A1	0.9	9.1	7.35	27.13%	$y = -0.0096x + 0.5119$ $R^2 = 0.9943$			
2		20-30	22	O	1	9.6	7.6	30.30%				
3		15-25	20	46.00	1	10.1	7.9	31.88%				
Liquid Limit (%)		27.19%		Notes:						Notes:  Pocket Penetrometer was 2.32 mm		
<b>Plastic Limit</b>		Test #	Core depth (ft)	Dish #	Weight of Dish (gr)	W <sub>c+s</sub> (gr)*	W <sub>c+s</sub> (gr)	WC (%)				
		1	13.5	45	1	12.7	11.3	13.59%				
		2	13.5	W	1	6.2	5.6	13.04%				
Average Plastic Limit (%)		13.32%		<b>Plasticity Index</b>		13.87%	<b>Liquidity Index</b>	98.99%				
<b>Mini Vane Shear Test</b>		D (mm)	H (mm)	Rotation Rate (°/min)	Su (kPa)	<b>Pocket Penetrometer</b>		Notes:				
		19	29	90	66	Unconfined Strength tsf or kg/cm²		OSHA Category  Type A	Notes:  Pocket Penetrometer was 2.32 mm			
						2.5	239.2					

Figure 77. Page 1 of soil properties spreadsheet for B-7-16 (13–15.5 ft).

## **116 Relationship Between Erodibility and Properties of Soils**

**Figure 78.** Page 2 of soil properties spreadsheet for B-7-16 (13–15.5 ft).



## CHAPTER 5

# Organization and Interpretation of the Data

One of the major problems with analyzing erodibility parameters is that these parameters are derived from different types of tests and are not consistent with one another. While bringing some uniformity to tests results is important, as discussed in Chapter 6, it is equally important to collect existing erodibility data obtained from each test. The first step in collecting such data was to establish an acceptable and consistent fashion for organizing the erosion data collected. To achieve this goal, a global erosion spread sheet called the NCHRP-Erosion spreadsheet was developed. The entire NCHRP-Erosion spreadsheet in .xslm format can be downloaded from the TRB website ([trb.org](http://trb.org)); search for “NCHRP Research Report 915”.

Section 5.1 of this chapter presents how NCHRP-Erosion was organized and developed. Section 5.2 introduces the entries of each column in NCHRP-Erosion. Section 5.3 provides the reader with a manual on how to probe and use NCHRP-Erosion.

## 5.1 Development and Organization of NCHRP-Erosion

During the first phase of this project, nearly 750 erosion tests were collected from the literature review as well as by contacting researchers and organizations working on erosion around the world. Table 26 shows the 34 organizations and people contacted in the first phase of this project. Erosion data were extracted from technical reports, lab test results, field test results, and well-known journal and conference papers. In parallel with the erosion tests, the geotechnical properties of each tested sample, along with any information on the latitude and longitude or origin of the sample, were compiled.

The data collected include the results of commercially used erosion tests such as the erosion function apparatus (EFA) test, the jet erosion test (JET), the hole erosion test (HET), the slot erosion test (SET), the ex situ scour testing device (ESTD), the borehole erosion test (BET), the rotating erosion testing apparatus (RETA), the Sediment Erosion Rate Flume (SERF), the in situ erosion evaluation probe (ISEEP), and some large-scale flume tests.

In addition to the aforementioned erosion tests, around 250 erosion tests were performed during this project. These tests included the EFA, the JET, the HET, the PET, and the BET (see Chapter 4). Tests of all major geotechnical properties were also conducted on each sample that was tested with any erosion device (see Chapter 4, Section 4.4, and Appendix 2), and a soil properties spreadsheet was generated for each sample.

The collected erosion tests and tests performed during this project were gathered in a global spreadsheet consisting of 975 erosion tests. This spreadsheet is called the NCHRP-Erosion spreadsheet. Table 27 is a summary of the number of test results obtained for each erosion

## 118 Relationship Between Erodibility and Properties of Soils

**Table 26. Selected list of contact people and organizations around the world.**

No.	Contact Person	Organization	No.	Contact Person	Organization
1	Stephane Bonelli	IRSTEA, France	18	J. Beard	North Carolina DOT, USA
2	Sherry Hunt	USDA, USA	19	M. Haeri	North Carolina DOT, USA
3	Johannes Wibowo	USACE, USA	20	Kaye Brubaker	University of Maryland, USA
4	Axel Montalvo	USACE, USA	21	Timothy Straub	USGS, USA
5	Anna Shidlovskaya	University of Mines, Russia	22	Tom Over	USGS, USA
6	Tony Wahl	U.S. Bureau of Reclamation	23	Derrick Dasenbrock	Minnesota DOT, USA
7	Maurice Morvant	Fugro, USA	24	Abdelkrim	ESTP, France
8	John Delphia	Texas DOT, USA	25	Marie-Jo Goedert	ESTP, France
9	Jeff Locke	Fugro, USA	26	Michael Heibaum	BAW, Germany
10	M. A. Gabr	NCSU, USA	27	Chenzuyu (Tsinghua)	Beijing, China
11	Beatrice Hunt	AECOM, USA	28	Gijs Hoffmans	Deltares, Netherlands
12	Richard Whitehouse	HR Wallingford, UK	29	Stephen Benedict	USGS, USA
13	Kiseok Kwak	KICT, Korea	30	Christophe Chevalier	IFSTTAR, France
14	Brian Anderson	Auburn, USA	31	Garey Fox	NCSU, USA
15	Robbin Fell	UNSW, Australia	32	Peter Allen	Baylor University, USA
16	Kornel Kerenyi	FHWA, USA	33	Lin Wang	China Institute of Water Resources
17	D. Henderson	North Carolina DOT, USA	34	Mike C. Lin and Scott Shewbridge	USACE, USA

Note: IRSTEA = Institut National de Recherche en Sciences et Technologies pour l'Environnement et l'Agriculture [National Research Institute of Science and Technology for Environment and Agriculture]; USDA = U.S. Department of Agriculture; USACE = U.S. Army Corps of Engineers; NCSU = North Carolina State University; KICT = Korea Institute of Construction Technology; UNSW = University of New South Wales; FHWA = Federal Highway Administration; ESTP = École Spéciale des Travaux Publics; BAW = Bundesanstalt für Wasserbau (Federal Waterways Engineering and Research Institute); USGS = U.S. Geological Survey; IFSTTAR = Institut Français des Sciences et Technologies des Transports, de l'Aménagement et des Réseaux (Institute of Science and Technology for Transport, Development and Networks).

**Table 27. Summary of erosion test data in NCHRP-Erosion.**

Erosion Test Type	Number of Test Result Data Collected
EFA	346
HET	233
SET	84
ESTD	17
ISEEP	6
SERF	13
JET	147
BET	17
RETA	14
PET	95
Large-scale widening test	3
Total	975

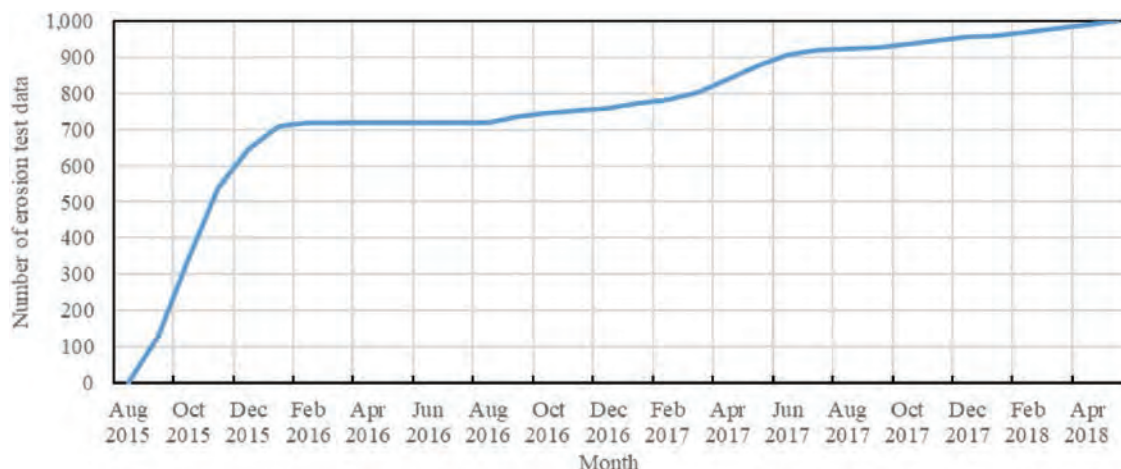


**Figure 79. Summary chart of data compiled for NCHRP-Erosion since the start of the project.**

device. Figure 79 is a summary chart of the data compiled for NCHRP-Erosion since the start of the project.

The important characteristic of NCHRP-Erosion is its ability to bring a wide range of erodibility parameters together and compare them in a consistent fashion, as proposed by Briaud (2008). The following erodibility parameters were selected to represent the erosion characteristics of a soil:

- Critical shear stress,  $\tau_c$ ;
- Critical velocity,  $v_c$ ;
- Initial slope,  $E_v$ , of the  $\dot{z}$  versus  $v$  curve; and
- Initial slope,  $E_\tau$ , of the  $\dot{z}$  versus  $\tau$  curve.

In addition, the erosion category (EC) in the Briaud erosion chart (2013) was considered as an additional parameter for describing the erosion characteristics of a soil and was added as a parameter for the erosion correlations study. Figure 3 in Chapter 1 shows the erosion categories based on velocity and shear stress, respectively.

In NCHRP-Erosion, all the erosion data are analyzed according to the procedures described below for the five erodibility parameters:  $v_c$ ,  $\tau_c$ ,  $E_v$ ,  $E_\tau$ , and EC.

1. **Critical velocity,  $v_c$ .** All the data points of the velocity erosion curve are plotted on the erosion chart (Chapter 1, Figure 3). This plot is on a logarithmic scale for both the  $x$ -axis and the  $y$ -axis. The zero on the  $y$ -axis (logarithmic scale) is set at an arbitrarily low erosion rate of 0.1 mm/hour. The reasons for choosing an arbitrarily low erosion rate of 0.1 mm/h are that (1) a log-log scale plot cannot take a zero value and (2) 0.1 mm/h is practically the same as 0 mm/h. If the erosion curve intercepts the horizontal axis at any point, that point is the critical velocity. If there is no data point on that axis, the line between the first two points of the erosion curve is extrapolated linearly and the point at which this extrapolated line crosses the horizontal axis is selected as the critical velocity value.
2. **Critical shear stress,  $\tau_c$ .** All the data points of the shear stress erosion curve are plotted on the erosion chart (Chapter 1, Figure 3). This plot is on logarithmic scale for both the  $x$ - and the  $y$ -axes. The zero on the  $y$ -axis (logarithmic scale) is set at an arbitrarily low erosion rate of 0.1 mm/hour. If the erosion curve intercepts the horizontal axis at any point, that point is the critical shear stress. If there is no data point on that axis, the line between the first two

## 120 Relationship Between Erodibility and Properties of Soils

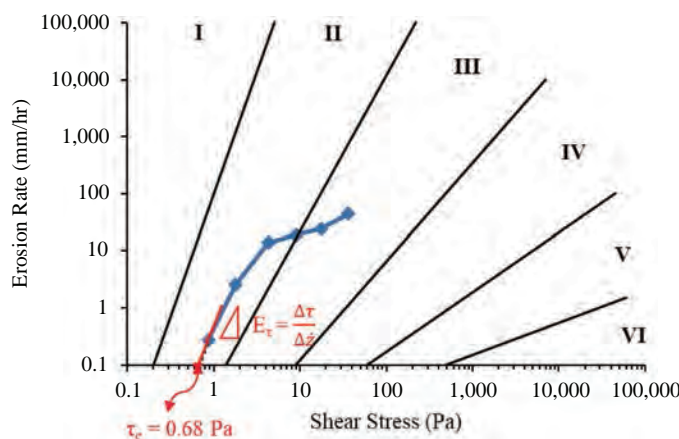


**Figure 80.** Example showing how critical shear stress is obtained when erosion curve itself does not cross the horizontal axis.

points of the erosion curve is extrapolated linearly and the point at which this extrapolated line crosses the horizontal axis is selected as the critical shear stress value. Figure 80 shows an example of how the critical shear stress is calculated for a case where the line has to be extended to cross the horizontal axis.

3. **Initial slope,  $E_v$ , of the  $\dot{z}$  versus  $v$  plot.**  $E_v$  is obtained by fitting a straight line through the initial points of the curve.
4. **Initial slope,  $E_\tau$ , of the  $\dot{z}$  versus  $\tau$  plot.**  $E_\tau$  is obtained by fitting a straight line through the initial points of the curve.
5. **Erosion category, EC.** The median point in the erosion curve is considered as the representative point for EC. Therefore, EC depends on the location of the median point on the erosion curve. The number of points on the erosion function can therefore have an impact on the choice of EC; it is recommended that many points be obtained to define EC. As mentioned earlier, the erosion function is not a single number but a curve. EC translates this curve into a single number that gives useful information about the range of erosion rate for a sample at a given water velocity or hydraulic shear stress. Figure 81 illustrates

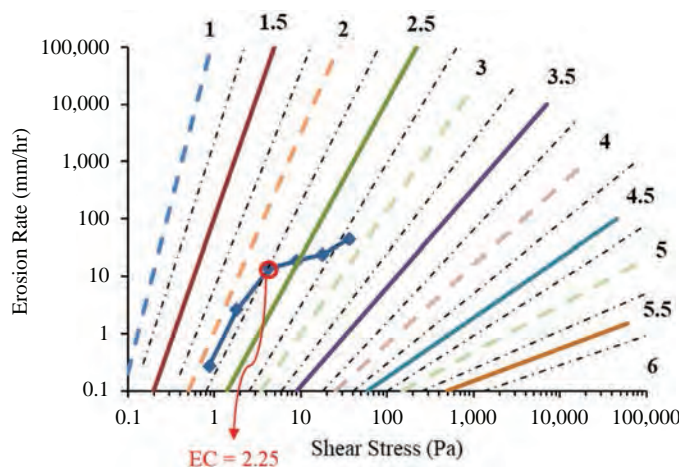


**Figure 81.** Example showing how EC is obtained for a sample erosion curve; the EC for this example is 2.25.

how EC is determined. EC for this particular example was obtained as 2.25. Note that the dashed lines on Figure 81 represent the EC values corresponding to 1.25, 1.75, 2.25, 2.75, and so on.

## 5.2 Column Contents in NCHRP-Erosion

As discussed in the previous section, NCHRP-Erosion includes 975 erosion tests, that is, 975 rows. Each row in NCHRP-Erosion consists of 49 columns. The entries for the columns are listed in Table 28.

All test results are presented in the same format of erosion rate versus velocity or versus shear stress, or both. Furthermore, they are all plotted on the erosion categories proposed by Briaud (2013). In several cases, the data collected had to be digitized. Now, all plots of erosion functions in the erosion function column have embedded spread sheets of their own. That way the user can click on the plot and obtain the point-by-point data. A manual on how to use NCHRP-Erosion is presented in Section 5.3. A comments column for each erosion test gives pertinent details about any special treatment or condition during the erosion test or in

**Table 28. List of entries in NCHRP-Erosion.**

Part 1	Part 3, Section 1 ( <i>continued</i> )
1. Record numbers	25. Pocket penetrometer strength (kPa)
2. Contact/credit	26. Tensile strength (kPa)
3. Data conducted/sampled	27. UCS (kPa)
4. Project title/sponsor	28. Vane shear strength, $S_u$ (kPa)
5. Sample name	29. Percentage of fines (%)
6. Sample depth	30. SPT $N$ -value
7. Soil type	31. D50 (mm)
8. USCS classification	32. D10 (mm)
9. AASHTO classification	33. D30 (mm)
10. Natural/man-made	34. D60 (mm)
Part 2	35. $C_c$
11. Erosion test type	36. $C_u$
12. Erosion function curve	Part 3, Section 2
13. Erosion category	37. Void ratio, $e$ (%)
14. Slope of velocity curve ( $E_v$ )	38. Degree of saturation, $S_r$ (%)
15. Slope of shear stress curve ( $E$ )	39. Percentage of compaction (%)
16. Critical velocity ( $V_c$ )	40. Specific gravity ( $G_s$ )
17. Critical shear stress ( $\tau_c$ )	41. Dispersion ratio (%)
18. Remarks on erosion test	42. pH
Part 3, Section 1	43. Electrical conductivity (microsiemens)
19. General comments	44. Fluid temperature (°C)
20. Liquid limit, LL (%)	45. Salinity (ppm)
21. Plastic limit, PL (%)	46. Percentage of clay (%)
22. Plasticity index, PI (%)	47. Percentage of silt (%)
23. Wet unit weight, $\gamma$ (kN/m <sup>3</sup> )	48. Organic content (%)
24. Water content (%)	49. Soil activity

Note: USCS = Unified Soil Classification System; UCS = unconfined compressive strength;  
SPT = standard penetration test.

## 122 Relationship Between Erodibility and Properties of Soils

interpretation of the results. Also, a column for general comments about the sample provides related special information about the sample, if applicable. Figure 82 shows a general view of NCHRP-Erosion, including its three parts:

- Part 1: Record Information,
- Part 2: Erosion Information, and
- Part 3: Soil Properties Information
  - Section 1: Most-common geotechnical soil properties, and
  - Section 2: Less-common properties.

The entries of each aforementioned part are described in the following sections. It is very important to note that many cells in NCHRP-Erosion are empty because of the lack of information for each sample.

### 5.2.1 Part 1: Record Information

Part 1 of NCHRP-Erosion presents the general record information of the soil sample. Figure 83 shows this information for one sample in NCHRP-Erosion as an illustration. There are 10 columns:

1. Record Number: the row number associated with the sample in NCHRP-Erosion.
2. Contact/Credit: information about the person or entity that owns the data associated with this sample.
3. Date Conducted/Sampled: the date the test was conducted or, in the case of natural samples, the date the sample was obtained from the field.
4. Project Title/Sponsor: the title of the project or, when applicable, the sponsor, that led to the measurement of this sample's test results.
5. Sample Name: the name associated with the sample.
6. Sample Depth: the depth of a natural sample in either meters or feet, depending on the original data.
7. Soil Type.
8. USCS Classification.
9. AASHTO Classification.
10. Natural/Man-made. Identifies whether the sample is remolded (man-made) or natural (intact).

### 5.2.2 Part 2: Erosion Information

Part 2 of NCHRP-Erosion presents the erosion test results for the sample. Figure 84 shows these data for the sample presented in Figure 83. The first column, “Erosion Test Type,” identifies the type of erosion test conducted on the sample. In this example, the sample was tested in the EFA. In NCHRP-Erosion, each erosion test type is designated with a specific color. The colors used to designate each erosion test are shown in Table 29. These colors help the user identify each test more easily in a big-picture view of the spreadsheet.

The second column, “Erosion Function,” plots the erosion test results on the erosion category chart proposed by Briaud (2008). As mentioned earlier, all plots of erosion functions in the erosion function column have embedded spreadsheets of their own. That way the user can click on the plot and obtain the point-by-point data. A manual on how to use NCHRP-Erosion is presented later in Section 5.3. The next five columns—Erosion Category,  $E_c$ ,  $E_v$ ,  $V_c$ , and  $\tau_c$ —present the five erodibility parameters obtained after each erosion test. It should be noted that not all erosion tests can produce all five erodibility parameters. For instance, the JET and the HET can report only three of these five erodibility parameters (Erosion Category,  $E_v$ , and  $\tau_c$ ),

Record Number	Current J-Credit	Date recorded	Depth (in.)	Sample Name	Soil Type	Land Ownership	Natural / Manmade	Condition of the area (esp)	Soil texture type	EROSION PARAMETERS						SEDITIONAL PROPERTIES																																																																																																																																																																																																																																																																																																																																																																																																																																																																																																																																																																																																																																																																																																																																																																																																																											
Number of Tests	Index Coefficient	%	M. (in)	T. (in)	Constituent	n	m	n	r (slope)	R<sub>c</sub> (in)	R<sub>s</sub> (in)	R<sub>d</sub> (in)	R<sub>g</sub> (in)	R<sub>h</sub> (in)	R<sub>l</sub> (in)	R<sub>m</sub> (in)	R<sub>o</sub> (in)	R<sub>p</sub> (in)	R<sub>q</sub> (in)	R<sub>r</sub> (in)	R<sub>s</sub> (in)	R<sub>t</sub> (in)	R<sub>u</sub> (in)	R<sub>v</sub> (in)	R<sub>w</sub> (in)	R<sub>x</sub> (in)	R<sub>y</sub> (in)	R<sub>z</sub> (in)	U<sub>1</sub>	U<sub>2</sub>	U<sub>3</sub>	U<sub>4</sub>	U<sub>5</sub>	U<sub>6</sub>	U<sub>7</sub>	U<sub>8</sub>	U<sub>9</sub>	U<sub>10</sub>	U<sub>11</sub>	U<sub>12</sub>	U<sub>13</sub>	U<sub>14</sub>	U<sub>15</sub>	U<sub>16</sub>	U<sub>17</sub>	U<sub>18</sub>	U<sub>19</sub>	U<sub>20</sub>	U<sub>21</sub>	U<sub>22</sub>	U<sub>23</sub>	U<sub>24</sub>	U<sub>25</sub>	U<sub>26</sub>	U<sub>27</sub>	U<sub>28</sub>	U<sub>29</sub>	U<sub>30</sub>	U<sub>31</sub>	U<sub>32</sub>	U<sub>33</sub>	U<sub>34</sub>	U<sub>35</sub>	U<sub>36</sub>	U<sub>37</sub>	U<sub>38</sub>	U<sub>39</sub>	U<sub>40</sub>	U<sub>41</sub>	U<sub>42</sub>	U<sub>43</sub>	U<sub>44</sub>	U<sub>45</sub>	U<sub>46</sub>	U<sub>47</sub>	U<sub>48</sub>	U<sub>49</sub>	U<sub>50</sub>	U<sub>51</sub>	U<sub>52</sub>	U<sub>53</sub>	U<sub>54</sub>	U<sub>55</sub>	U<sub>56</sub>	U<sub>57</sub>	U<sub>58</sub>	U<sub>59</sub>	U<sub>60</sub>	U<sub>61</sub>	U<sub>62</sub>	U<sub>63</sub>	U<sub>64</sub>	U<sub>65</sub>	U<sub>66</sub>	U<sub>67</sub>	U<sub>68</sub>	U<sub>69</sub>	U<sub>70</sub>	U<sub>71</sub>	U<sub>72</sub>	U<sub>73</sub>	U<sub>74</sub>	U<sub>75</sub>	U<sub>76</sub>	U<sub>77</sub>	U<sub>78</sub>	U<sub>79</sub>	U<sub>80</sub>	U<sub>81</sub>	U<sub>82</sub>	U<sub>83</sub>	U<sub>84</sub>	U<sub>85</sub>	U<sub>86</sub>	U<sub>87</sub>	U<sub>88</sub>	U<sub>89</sub>	U<sub>90</sub>	U<sub>91</sub>	U<sub>92</sub>	U<sub>93</sub>	U<sub>94</sub>	U<sub>95</sub>	U<sub>96</sub>	U<sub>97</sub>	U<sub>98</sub>	U<sub>99</sub>	U<sub>100</sub>	U<sub>101</sub>	U<sub>102</sub>	U<sub>103</sub>	U<sub>104</sub>	U<sub>105</sub>	U<sub>106</sub>	U<sub>107</sub>	U<sub>108</sub>	U<sub>109</sub>	U<sub>110</sub>	U<sub>111</sub>	U<sub>112</sub>	U<sub>113</sub>	U<sub>114</sub>	U<sub>115</sub>	U<sub>116</sub>	U<sub>117</sub>	U<sub>118</sub>	U<sub>119</sub>	U<sub>120</sub>	U<sub>121</sub>	U<sub>122</sub>	U<sub>123</sub>	U<sub>124</sub>	U<sub>125</sub>	U<sub>126</sub>	U<sub>127</sub>	U<sub>128</sub>	U<sub>129</sub>	U<sub>130</sub>	U<sub>131</sub>	U<sub>132</sub>	U<sub>133</sub>	U<sub>134</sub>	U<sub>135</sub>	U<sub>136</sub>	U<sub>137</sub>	U<sub>138</sub>	U<sub>139</sub>	U<sub>140</sub>	U<sub>141</sub>	U<sub>142</sub>	U<sub>143</sub>	U<sub>144</sub>	U<sub>145</sub>	U<sub>146</sub>	U<sub>147</sub>	U<sub>148</sub>	U<sub>149</sub>	U<sub>150</sub>	U<sub>151</sub>	U<sub>152</sub>	U<sub>153</sub>	U<sub>154</sub>	U<sub>155</sub>	U<sub>156</sub>	U<sub>157</sub>	U<sub>158</sub>	U<sub>159</sub>	U<sub>160</sub>	U<sub>161</sub>	U<sub>162</sub>	U<sub>163</sub>	U<sub>164</sub>	U<sub>165</sub>	U<sub>166</sub>	U<sub>167</sub>	U<sub>168</sub>	U<sub>169</sub>	U<sub>170</sub>	U<sub>171</sub>	U<sub>172</sub>	U<sub>173</sub>	U<sub>174</sub>	U<sub>175</sub>	U<sub>176</sub>	U<sub>177</sub>	U<sub>178</sub>	U<sub>179</sub>	U<sub>180</sub>	U<sub>181</sub>	U<sub>182</sub>	U<sub>183</sub>	U<sub>184</sub>	U<sub>185</sub>	U<sub>186</sub>	U<sub>187</sub>	U<sub>188</sub>	U<sub>189</sub>	U<sub>190</sub>	U<sub>191</sub>	U<sub>192</sub>	U<sub>193</sub>	U<sub>194</sub>	U<sub>195</sub>	U<sub>196</sub>	U<sub>197</sub>	U<sub>198</sub>	U<sub>199</sub>	U<sub>200</sub>	U<sub>201</sub>	U<sub>202</sub>	U<sub>203</sub>	U<sub>204</sub>	U<sub>205</sub>	U<sub>206</sub>	U<sub>207</sub>	U<sub>208</sub>	U<sub>209</sub>	U<sub>210</sub>	U<sub>211</sub>	U<sub>212</sub>	U<sub>213</sub>	U<sub>214</sub>	U<sub>215</sub>	U<sub>216</sub>	U<sub>217</sub>	U<sub>218</sub>	U<sub>219</sub>	U<sub>220</sub>	U<sub>221</sub>	U<sub>222</sub>	U<sub>223</sub>	U<sub>224</sub>	U<sub>225</sub>	U<sub>226</sub>	U<sub>227</sub>	U<sub>228</sub>	U<sub>229</sub>	U<sub>230</sub>	U<sub>231</sub>	U<sub>232</sub>	U<sub>233</sub>	U<sub>234</sub>	U<sub>235</sub>	U<sub>236</sub>	U<sub>237</sub>	U<sub>238</sub>	U<sub>239</sub>	U<sub>240</sub>	U<sub>241</sub>	U<sub>242</sub>	U<sub>243</sub>	U<sub>244</sub>	U<sub>245</sub>	U<sub>246</sub>	U<sub>247</sub>	U<sub>248</sub>	U<sub>249</sub>	U<sub>250</sub>	U<sub>251</sub>	U<sub>252</sub>	U<sub>253</sub>	U<sub>254</sub>	U<sub>255</sub>	U<sub>256</sub>	U<sub>257</sub>	U<sub>258</sub>	U<sub>259</sub>	U<sub>260</sub>	U<sub>261</sub>	U<sub>262</sub>	U<sub>263</sub>	U<sub>264</sub>	U<sub>265</sub>	U<sub>266</sub>	U<sub>267</sub>	U<sub>268</sub>	U<sub>269</sub>	U<sub>270</sub>	U<sub>271</sub>	U<sub>272</sub>	U<sub>273</sub>	U<sub>274</sub>	U<sub>275</sub>	U<sub>276</sub>	U<sub>277</sub>	U<sub>278</sub>	U<sub>279</sub>	U<sub>280</sub>	U<sub>281</sub>	U<sub>282</sub>	U<sub>283</sub>	U<sub>284</sub>	U<sub>285</sub>	U<sub>286</sub>	U<sub>287</sub>	U<sub>288</sub>	U<sub>289</sub>	U<sub>290</sub>	U<sub>291</sub>	U<sub>292</sub>	U<sub>293</sub>	U<sub>294</sub>	U<sub>295</sub>	U<sub>296</sub>	U<sub>297</sub>	U<sub>298</sub>	U<sub>299</sub>	U<sub>300</sub>	U<sub>301</sub>	U<sub>302</sub>	U<sub>303</sub>	U<sub>304</sub>	U<sub>305</sub>	U<sub>306</sub>	U<sub>307</sub>	U<sub>308</sub>	U<sub>309</sub>	U<sub>310</sub>	U<sub>311</sub>	U<sub>312</sub>	U<sub>313</sub>	U<sub>314</sub>	U<sub>315</sub>	U<sub>316</sub>	U<sub>317</sub>	U<sub>318</sub>	U<sub>319</sub>	U<sub>320</sub>	U<sub>321</sub>	U<sub>322</sub>	U<sub>323</sub>	U<sub>324</sub>	U<sub>325</sub>	U<sub>326</sub>	U<sub>327</sub>	U<sub>328</sub>	U<sub>329</sub>	U<sub>330</sub>	U<sub>331</sub>	U<sub>332</sub>	U<sub>333</sub>	U<sub>334</sub>	U<sub>335</sub>	U<sub>336</sub>	U<sub>337</sub>	U<sub>338</sub>	U<sub>339</sub>	U<sub>340</sub>	U<sub>341</sub>	U<sub>342</sub>	U<sub>343</sub>	U<sub>344</sub>	U<sub>345</sub>	U<sub>346</sub>	U<sub>347</sub>	U<sub>348</sub>	U<sub>349</sub>	U<sub>350</sub>	U<sub>351</sub>	U<sub>352</sub>	U<sub>353</sub>	U<sub>354</sub>	U<sub>355</sub>	U<sub>356</sub>	U<sub>357</sub>	U<sub>358</sub>	U<sub>359</sub>	U<sub>360</sub>	U<sub>361</sub>	U<sub>362</sub>	U<sub>363</sub>	U<sub>364</sub>	U<sub>365</sub>	U<sub>366</sub>	U<sub>367</sub>	U<sub>368</sub>	U<sub>369</sub>	U<sub>370</sub>	U<sub>371</sub>	U<sub>372</sub>	U<sub>373</sub>	U<sub>374</sub>	U<sub>375</sub>	U<sub>376</sub>	U<sub>377</sub>	U<sub>378</sub>	U<sub>379</sub>	U<sub>380</sub>	U<sub>381</sub>	U<sub>382</sub>	U<sub>383</sub>	U<sub>384</sub>	U<sub>385</sub>	U<sub>386</sub>	U<sub>387</sub>	U<sub>388</sub>	U<sub>389</sub>	U<sub>390</sub>	U<sub>391</sub>	U<sub>392</sub>	U<sub>393</sub>	U<sub>394</sub>	U<sub>395</sub>	U<sub>396</sub>	U<sub>397</sub>	U<sub>398</sub>	U<sub>399</sub>	U<sub>400</sub>	U<sub>401</sub>	U<sub>402</sub>	U<sub>403</sub>	U<sub>404</sub>	U<sub>405</sub>	U<sub>406</sub>	U<sub>407</sub>	U<sub>408</sub>	U<sub>409</sub>	U<sub>410</sub>	U<sub>411</sub>	U<sub>412</sub>	U<sub>413</sub>	U<sub>414</sub>	U<sub>415</sub>	U<sub>416</sub>	U<sub>417</sub>	U<sub>418</sub>	U<sub>419</sub>	U<sub>420</sub>	U<sub>421</sub>	U<sub>422</sub>	U<sub>423</sub>	U<sub>424</sub>	U<sub>425</sub>	U<sub>426</sub>	U<sub>427</sub>	U<sub>428</sub>	U<sub>429</sub>	U<sub>430</sub>	U<sub>431</sub>	U<sub>432</sub>	U<sub>433</sub>	U<sub>434</sub>	U<sub>435</sub>	U<sub>436</sub>	U<sub>437</sub>	U<sub>438</sub>	U<sub>439</sub>	U<sub>440</sub>	U<sub>441</sub>	U<sub>442</sub>	U<sub>443</sub>	U<sub>444</sub>	U<sub>445</sub>	U<sub>446</sub>	U<sub>447</sub>	U<sub>448</sub>	U<sub>449</sub>	U<sub>450</sub>	U<sub>451</sub>	U<sub>452</sub>	U<sub>453</sub>	U<sub>454</sub>	U<sub>455</sub>	U<sub>456</sub>	U<sub>457</sub>	U<sub>458</sub>	U<sub>459</sub>	U<sub>460</sub>	U<sub>461</sub>	U<sub>462</sub>	U<sub>463</sub>	U<sub>464</sub>	U<sub>465</sub>	U<sub>466</sub>	U<sub>467</sub>	U<sub>468</sub>	U<sub>469</sub>	U<sub>470</sub>	U<sub>471</sub>	U<sub>472</sub>	U<sub>473</sub>	U<sub>474</sub>	U<sub>475</sub>	U<sub>476</sub>	U<sub>477</sub>	U<sub>478</sub>	U<sub>479</sub>	U<sub>480</sub>	U<sub>481</sub>	U<sub>482</sub>	U<sub>483</sub>	U<sub>484</sub>	U<sub>485</sub>	U<sub>486</sub>	U<sub>487</sub>	U<sub>488</sub>	U<sub>489</sub>	U<sub>490</sub>	U<sub>491</sub>	U<sub>492</sub>	U<sub>493</sub>	U<sub>494</sub>	U<sub>495</sub>	U<sub>496</sub>	U<sub>497</sub>	U<sub>498</sub>	U<sub>499</sub>	U<sub>500</sub>	U<sub>501</sub>	U<sub>502</sub>	U<sub>503</sub>	U<sub>504</sub>	U<sub>505</sub>	U<sub>506</sub>	U<sub>507</sub>	U<sub>508</sub>	U<sub>509</sub>	U<sub>510</sub>	U<sub>511</sub>	U<sub>512</sub>	U<sub>513</sub>	U<sub>514</sub>	U<sub>515</sub>	U<sub>516</sub>	U<sub>517</sub>	U<sub>518</sub>	U<sub>519</sub>	U<sub>520</sub>	U<sub>521</sub>	U<sub>522</sub>	U<sub>523</sub>	U<sub>524</sub>	U<sub>525</sub>	U<sub>526</sub>	U<sub>527</sub>	U<sub>528</sub>	U<sub>529</sub>	U<sub>530</sub>	U<sub>531</sub>	U<sub>532</sub>	U<sub>533</sub>	U<sub>534</sub>	U<sub>535</sub>	U<sub>536</sub>	U<sub>537</sub>	U<sub>538</sub>	U<sub>539</sub>	U<sub>540</sub>	U<sub>541</sub>	U<sub>542</sub>	U<sub>543</sub>	U<sub>544</sub>	U<sub>545</sub>	U<sub>546</sub>	U<sub>547</sub>	U<sub>548</sub>	U<sub>549</sub>	U<sub>550</sub>	U<sub>551</sub>	U<sub>552</sub>	U<sub>553</sub>	U<sub>554</sub>	U<sub>555</sub>	U<sub>556</sub>	U<sub>557</sub>	U<sub>558</sub>	U<sub>559</sub>	U<sub>560</sub>	U<sub>561</sub>	U<sub>562</sub>	U<sub>563</sub>	U<sub>564</sub>	U<sub>565</sub>	U<sub>566</sub>	U<sub>567</sub>	U<sub>568</sub>	U<sub>569</sub>	U<sub>570</sub>	U<sub>571</sub>	U<sub>572</sub>	U<sub>573</sub>	U<sub>574</sub>	U<sub>575</sub>	U<sub>576</sub>	U<sub>577</sub>	U<sub>578</sub>	U<sub>579</sub>	U<sub>580</sub>	U<sub>581</sub>	U<sub>582</sub>	U<sub>583</sub>	U<sub>584</sub>	U<sub>585</sub>	U<sub>586</sub>	U<sub>587</sub>	U<sub>588</sub>	U<sub>589</sub>	U<sub>590</sub>	U<sub>591</sub>	U<sub>592</sub>	U<sub>593</sub>	U<sub>594</sub>	U<sub>595</sub>	U<sub>596</sub>	U<sub>597</sub>	U<sub>598</sub>	U<sub>599</sub>	U<sub>600</sub>	U<sub>601</sub>	U<sub>602</sub>	U<sub>603</sub>	U<sub>604</sub>	U<sub>605</sub>	U<sub>606</sub>	U<sub>607</sub>	U<sub>608</sub>	U<sub>609</sub>	U<sub>610</sub>	U<sub>611</sub>	U<sub>612</sub>	U<sub>613</sub>	U<sub>614</sub>	U<sub>615</sub>	U<sub>616</sub>	U<sub>617</sub>	U<sub>618</sub>	U<sub>619</sub>	U<sub>620</sub>	U<sub>621</sub>	U<sub>622</sub>	U<sub>623</sub>	U<sub>624</sub>	U<sub>625</sub>	U<sub>626</sub>	U<sub>627</sub>	U<sub>628</sub>	U<sub>629</sub>	U<sub>630</sub>	U<sub>631</sub>	U<sub>632</sub>	U<sub>633</sub>	U<sub>634</sub>	U<sub>635</sub>	U<sub>636</sub>	U<sub>637</sub>	U<sub>638</sub>	U<sub>639</sub>	U<sub>640</sub>	U<sub>641</sub>	U<sub>642</sub>	U<sub>643</sub>	U<sub>644</sub>	U<sub>645</sub>	U<sub>646</sub>	U<sub>647</sub>	U<sub>648</sub>	U<sub>649</sub>	U<sub>650</sub>	U<sub>651</sub>	U<sub>652</sub>	U<sub>653</sub>	U<sub>654</sub>	U<sub>655</sub>	U<sub>656</sub>	U<sub>657</sub>	U<sub>658</sub>	U<sub>659</sub>	U<sub>660</sub>	U<sub>661</sub>	U<sub>662</sub>	U<sub>663</sub>	U<sub>664</sub>	U<sub>665</sub>	U<sub>666</sub>	U<sub>667</sub>	U<sub>668</sub>	U<sub>669</sub>	U<sub>670</sub>	U<sub>671</sub>	U<sub>672</sub>	U<sub>673</sub>	U<sub>674</sub>	U<sub>675</sub>	U<sub>676</sub>	U<sub>677</sub>	U<sub>678</sub>	U<sub>679</sub>	U<sub>680</sub>	U<sub>681</sub>	U<sub>682</sub>	U<sub>683</sub>	U<sub>684</sub>	U<sub>685</sub>	U<sub>686</sub>	U<sub>687</sub>	U<sub>688</sub>	U<sub>689</sub>	U<sub>690</sub>	U<sub>691</sub>	U<sub>692</sub>	U<sub>693</sub>	U<sub>694</sub>	U<sub>695</sub>	U<sub>696</sub>	U<sub>697</sub>	U<sub>698</sub>	U<sub>699</sub>	U<sub>700</sub>	U<sub>701</sub>	U<sub>702</sub>	U<sub>703</sub>	U<sub>704</sub>	U<sub>705</sub>	U<sub>706</sub>	U<sub>707</sub>	U<sub>708</sub>	U<sub>709</sub>	U<sub>710</sub>	U<sub>711</sub>	U<sub>712</sub>	U<sub>713</sub>	U<sub>714</sub>	U<sub>715</sub>	U<sub>716</sub>	U<sub>717</sub>	U<sub>718</sub>	U<sub>719</sub>	U<sub>720</sub>	U<sub>721</sub>	U<sub>722</sub>	U<sub>723</sub>	U<sub>724</sub>	U<sub>725</sub>	U<sub>726</sub>	U<sub>727</sub>	U<sub>728</sub>	U<sub>729</sub>	U<sub>730</sub>	U<sub>731</sub>	U<sub>732</sub>	U<sub>733</sub>	U<sub>734</sub>	U<sub>735</sub>	U<sub>736</sub>	U<sub>737</sub>	U<sub>738</sub>	U<sub>739</sub>	U<sub>740</sub>	U<sub>741</sub>	U<sub>742</sub>	U<sub>743</sub>	U<sub>744</sub>	U<sub>745</sub>	U<sub>746</sub>	U<sub>747</sub>	U<sub>748</sub>	U<sub>749</sub>	U<sub>750</sub>	U<sub>751</sub>	U<sub>752</sub>	U<sub>753</sub>	U<sub>754</sub>	U<sub>755</sub>	U<sub>756</sub>	U<sub>757</sub>	U<sub>758</sub>	U<sub>759</sub>	U<sub>760</sub>	U<sub>761</sub>	U<sub>762</sub>	U<sub>763</sub>	U<sub>764</sub>	U<sub>765</sub>	U<sub>766</sub>	U<sub>767</sub>	U<sub>768</sub>	U<sub>769</sub>	U<sub>770</sub>	U<sub>771</sub>	U<sub>772</sub>	U<sub>773</sub>	U<sub>774</sub>	U<sub>775</sub>	U<sub>776</sub>	U<sub>777</sub>	U<sub>778</sub>	U<sub>779</sub>	U<sub>780</sub>	U<sub>781</sub>	U<sub>782</sub>	U<sub>783</sub></

## 124 Relationship Between Erodibility and Properties of Soils

Record Number	Contact / Credit	Date Conducted / Sampled	Project Title / Sponsor	Sample Name	Sample Depth	Soil Type	USCS Classification	AASHTO Classification	Natural / Man-made
786	Jean Louis Braud / TAMU, US	1/17/2017	NCHRP 24-43	B-12-16 (18'-20.5') @18.95'	18.95'	Clay	CL	A-7-6 (23.6)	Natural

Figure 83. Example of record information recorded in Part 1 in NCHRP-Erosion.

EROSION PARAMETERS																												
Erosion Test Type	Erosion Function	Erosion Category	$E_v$ (mm/hr-m/s)	$E_\tau$ (mm/hr-pa)	$V_c$ (m/s)	$\tau_c$ (Pa)	Remarks on Erosion Test																					
EFA	<p>The table below provides estimated data points from the erosion function plots:</p> <table border="1"> <thead> <tr> <th>Velocity (m/s)</th> <th>Erosion Rate (mm/hr) - EFA (Top Plot)</th> <th>Erosion Rate (mm/hr) - EFA (Bottom Plot)</th> </tr> </thead> <tbody> <tr> <td>0.1</td> <td>~0.1</td> <td>~0.1</td> </tr> <tr> <td>1</td> <td>~1</td> <td>~1</td> </tr> <tr> <td>10</td> <td>~10</td> <td>~5</td> </tr> <tr> <td>100</td> <td>~100</td> <td>~10</td> </tr> <tr> <td>1000</td> <td>~1000</td> <td>~100</td> </tr> <tr> <td>10000</td> <td>~10000</td> <td>~1000</td> </tr> </tbody> </table>	Velocity (m/s)	Erosion Rate (mm/hr) - EFA (Top Plot)	Erosion Rate (mm/hr) - EFA (Bottom Plot)	0.1	~0.1	~0.1	1	~1	~1	10	~10	~5	100	~100	~10	1000	~1000	~100	10000	~10000	~1000	2.5	4.66	1.22	0.57	0.92	
Velocity (m/s)	Erosion Rate (mm/hr) - EFA (Top Plot)	Erosion Rate (mm/hr) - EFA (Bottom Plot)																										
0.1	~0.1	~0.1																										
1	~1	~1																										
10	~10	~5																										
100	~100	~10																										
1000	~1000	~100																										
10000	~10000	~1000																										

Figure 84. Erosion information (Part 2) recorded in NCHRP-Erosion.

**Table 29. List of colors used to designate erosion tests in NCHRP-Erosion.**

Erosion Test Type	Associated Color
EFA	Pink
JET	Light Blue
HET	Gray
PET	Orange
SET	Lavender
SERF	Yellow
ESTD	Green
ISEEP	Dark Blue
BET	Dark Orange
RETA	Red
Large-scale flume	White

while the EFA can generate all five. Finally, the last column in Part 2, “Remarks on Erosion Test,” presents any special treatment or necessary comment regarding the test.

### 5.2.3 Part 3: Soil Properties Information

#### 5.2.3.1 Section 1: More Typically Obtained Geotechnical Properties

Section 1 of Part 3: Soil Properties Information in NCHRP-Erosion presents the geotechnical index properties of the sample that are more typically obtained by engineers. Figure 85 shows the data in Section 1 of Part 3 for the sample presented in Figures 83 and 84. The first column provides general information about the location of the sample, longitude/latitude coordinates, color, and any special treatment of the sample, where applicable. The other columns include mostly the more typically obtained geotechnical properties.

#### 5.2.3.2 Section 2: Less Typically Obtained Geotechnical Properties

Section 2 of Part 3: Soil Properties Information in NCHRP-Erosion presents the geotechnical index properties of the sample that are less typically obtained by the engineers. Figure 86 shows the data in Section 2 of Part 3 for the sample presented in Figures 83 and 84.

## 5.3 NCHRP-Erosion Manual

One of the most important features of NCHRP-Erosion is its ability to be filtered with regard to any column entry. In other words, NCHRP-Erosion is a relational spreadsheet that allows the user to perform multiconditional inquiries. Table 28 lists all 49 entries for one test record in NCHRP-Erosion. The remainder of this section describes the embedded sheets in NCHRP-Erosion and presents the manual for sample inquiry operation in the 2016 Windows version of Microsoft Excel.

#### 5.3.1 Description of Embedded Sheets in NCHRP-Erosion

The first tab in NCHRP-Erosion, “About” (Figure 87), opens to a sheet that provides all the information about the spreadsheet, including what it is called, when it was developed, who the

## 126 Relationship Between Erodibility and Properties of Soils

General Comments	GEOTECHNICAL PROPERTIES																
	LL	PL	PI	$\gamma$ (kN/m <sup>3</sup> )	Water Content (%)	Pocket Penet. (kPa)	Tensile Strength (kPa)	UCS (kPa)	VST Su (kPa)	Percent Fines (%)	SPT N-value	D <sub>50</sub> (mm)	D <sub>10</sub> (mm)	D <sub>30</sub> (mm)	D <sub>60</sub> (mm)	C <sub>u</sub>	C <sub>c</sub>
1- Alcona Dam 2- Cemented 3-Light Brown 4- Undrained shear strength is predicted from Pocket Penetrometer (=0.3*Compression Strength)	42.1	18.6	23.5	18.2	20.51	354		106.2	95.5		0.0028		0.0040				

**Figure 85.** Geotechnical properties recorded in Part 3, Section 1 in NCHRP-Erosion.

authors are, the organization that performed the research, and the organization for which the spreadsheet was developed. This sheet also includes the responses to three basic questions:

- What is NCHRP-Erosion?
- What does NCHRP-Erosion incorporate?
- What does NCHRP-Erosion do?

The second tab, “Inquiry Operation Manual,” directs the user to Section 5.3 of this report, which provides instruction on how to filter and search within NCHRP-Erosion. The tab includes a link to a PDF of the report on the TRB website. The instructions presented in Section 5.3 below are according to Microsoft Excel for Windows 2016. Although the macOS version of Microsoft Excel might be slightly different in appearance, it is similar to the Windows version in terms of the procedure.

The third tab opens to the entire NCHRP-Erosion spreadsheet, which is explained in the previous Sections 5.1 and 5.2 of this chapter. The fourth to the final tabs are sheets that contain the

GEOTECHNICAL PROPERTIES														
Void Ratio	Degree of Saturation	Percent Compaction (%)	G <sub>s</sub>	Dispersion Ratio	pH	Electrical Conductivity (micro siemens)	Fluid Temp. (°C)	Salinity (ppm)	Percent Clay (%)	Percent Silt (%)	Organic Content (%)	Soil Activity	Relative Density (%)	
			2.7017						47.66	47.84		0.492		

**Figure 86.** Geotechnical properties recorded in Part 3, Section 2 in NCHRP-Erosion.



**NCHRP** NATIONAL COOPERATIVE HIGHWAY RESEARCH PROGRAM

PROGRAM	NCHRP-Erosion
VERSION	BETA 1.0
DATE	August 2018
AUTHORS	Jean-Louis Braud, Iman Shafii
PERFORMING ORGANIZATION	Texas A&M Transportation Institute (TTI)
SPONSOR	National Cooperative Highway Research Program

**What Is NCHRP-Erosion?**  
NCHRP-Erosion is a relational spreadsheet that allows the user to perform multiconditional inquiries between erodibility parameters and soil geotechnical properties.

**What Does NCHRP-Erosion Incorporate?**  
NCHRP-Erosion consists of nearly 1,000 erosion tests. Around 750 erosion tests were collected from the literature review as well as by contacting researchers and organizations working on erosion around the entire world. Erosion data were extracted from technical reports, lab test results, field test results, and well-known journal/conference papers. In parallel with the erosion tests, the geotechnical properties of each tested sample, along with any information on the latitude and longitude or origin of the sample were compiled. The data collected include the results of commercially used erosion tests such as the erosion function apparatus test (EFA), the jet erosion test (JET), the hole erosion test (HET), the slot erosion test (SET), the ex-situ scour testing device (ESTD), the borehole erosion test (BET), the rotating erosion testing apparatus (RETA), the Sediment Erosion Rate Flume (SERF), the in-situ erosion evaluation probe (ISEEP), and some large-scale flume tests. In addition to the aforementioned compiled data, around 250 erosion tests were performed during this project (NCHRP Project 24-43). These tests included the EFA, the JET, the HET, the PET, and the BET. Tests of all major geotechnical properties were also conducted on each sample that was tested with any erosion device, and soil properties spreadsheets were generated for each sample.

**What Does NCHRP-Erosion Do?**  
The important characteristic of NCHRP-Erosion is its ability to bring a wide range of erodibility parameters together and compare them in a consistent fashion as proposed by Braud (2008). The erodibility parameters selected to represent the erosion characteristics of a soil are the critical shear stress ( $\tau_c$ ), the critical velocity ( $v_c$ ), the initial slope ( $E_v$ ) of the  $z'$  versus  $v$  curve, the initial slope ( $E_t$ ) of the  $z'$  versus  $t$  curve, and the erosion category (EC).

**Figure 87.** Image of the first sheet, “About,” in NCHRP-Erosion.

original test data used to plot the erosion functions for each erosion test. Each of these sheets is named in the format of a three-word title that consists of the abbreviated or summarized project name, the contact organization, and the erosion test type. For example, the embedded sheet named “ALDOT-Auburn-EFA Data” provides the EFA test data corresponding to an Alabama Department of Transportation project, and the contact organization is Auburn University. It should be noted that the detailed information on the title of the project and person to contact are stated in the corresponding row in NCHRP-Erosion. It should be noted that the names of some embedded sheets are in the format of a two-word title consisting of the contact organization and erosion test type. Figure 88 shows an image of a small part of NCHRP-Erosion that focuses on the embedded sheets.

### 5.3.2 Inquiry Operation Manual

The operation manual in this section is presented with an example inquiry within NCHRP-Erosion. The procedure explained here can be used in any other application regardless of the number of the filters that the user desires to incorporate to search the spreadsheet. The list of choices that the user can opt to use to filter each column entry are also described within this example inquiry.

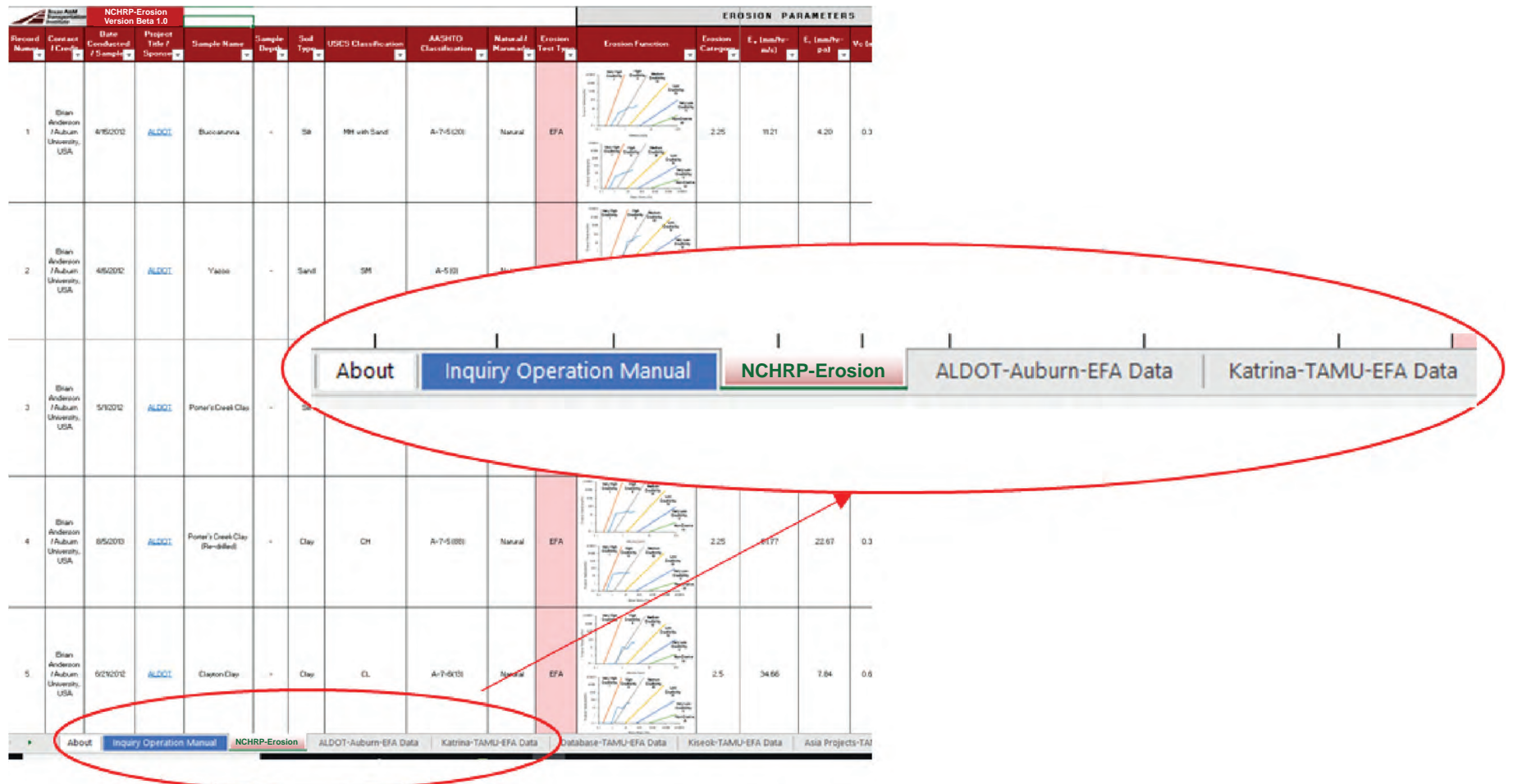


Figure 88. Image of a small part of NCHRP-Erosion that focuses on the embedded sheets.

As shown in Figure 89, the bottom-right corner of each column's header shows a small arrow that can be expanded by clicking on it. After clicking on the arrow, the list of choices that the user can select from is shown. Depending on the column entry, the list can include the names of the contact people, project titles, sample names, soil type, USCS, and so forth. For example, Figure 89 shows the list of contact people/organizations that have contributed to NCHRP-Erosion. The user has the option to filter the NCHRP-Erosion data to the data associated with one, two, or a few of the contact people by checking only the box near the desired contact person/organization and unchecking all other choices. In this example inquiry, the entire data set is filtered to show only erosion test data from "Jean-Louis Briaud/TAMU, USA." As shown in Figure 89, the user also has the option to enter any name in the small search box instead of scrolling through all the choices to find the desired person.

In this example inquiry, the next goal is to filter the Briaud data to show only the data for clay samples. Figure 90 shows the list of choices available to select from in the soil type column. Similarly, all the boxes should be unchecked except for the box for clay. As shown in Figure 90, user has the following options from which to select: cemented sand, clay, gatorock, gravel, limestone, sand, silt, and silt-clay. Some data do not have any entries in the soil type column; these are indicated with a dash (-) in the list of choices.

In this example inquiry, the next goal is to further filter the clay data into only low plastic clay (CL) soils. Figure 91 shows the list of USCS classifications that the user can select from. As with previous columns, some entries might be missing; these are indicated with a dash (-). The user has the option to select from "USCS classification," "AASHTO classification," or both. It is very important to mention that Figure 91 shows all possible choices for the USCS entry, while if the user selects only "clay," as in the example inquiry, the USCS choices are limited to the clay symbols only (see Figure 92). As shown in Figure 92, after the data have been filtered to show clay soils only, the USCS options are also narrowed down to a list of CH, CH with sand, CL, CL/CH, CL with sand, CL with sand/SC, and OH with sand.

It should be noted that at each step, the user can clear the filter by selecting the "Data" tab from the Microsoft Excel toolbar and then clicking on the "Clear" command on the toolbar (i.e., Select: Data → Clear). Figure 93 illustrates this process.

The next step in this example inquiry is to further filter the selected data to show only EFA test data. Figure 94 shows the process of checking the EFA box and unchecking all other choices. As shown in Figure 94, the choices adjust themselves and update as the prior filters are applied to the search. In this example, the choices are narrowed down to the list of BET, EFA, ESTD, HET, JET, large-scaled widening test, PET, and SET.

The next step in this example inquiry is to filter the data further to show the data that have a liquid limit (LL) between 5% and 30%. Figure 95 shows how the selected data can be filtered with regard to the LL. Note that more filters on each column entry can be applied and added to the search criteria. In this example inquiry, only the filter process with regard to LL is shown. The same procedure can be applied to all other column entries.

As shown in Figure 95, Microsoft Excel itself has some predefined boundaries that can be selected, such as "greater than . . ." or "between." However, the custom filter allows the user to choose any arbitrary boundary for filtering the data. After "Custom Filter . . ." is selected, as shown in Figure 95, the Custom AutoFilter window pops up (Figure 96). This window allows the user to select from a wide range of choices to define a custom boundary to filter the data. As described earlier, the example inquiry in this section narrows the data to those that have a liquid limit between 5% and 30%. Figure 96 shows how this range is define in the Custom AutoFilter window in Microsoft Excel (2016).

NCHRP-Erosion Version Beta 1.0												EROSION	
Record Number	Contact / Credit	Date Conducted / Sample	Project Title / Sponsor	Sample Name	Sample Depth	Soil Type	USCS Classification	AASHTO Classification	Natural / Manmade	Erosion Test Type	Erosion Function	Erosion Category	E. C.
1	Brian Anderson / Auburn University, USA	5/1/2012	ALDOI	Porter's Creek Clay	-	Silt	MH with Sand	A-7-5(20)	Natural	EFA		2.25	
2	Brian Anderson / Auburn University, USA	5/1/2012	ALDOI	Porter's Creek Clay	-	Sand	SM	A-5(0)	Natural	EFA		2.5	
3	Brian Anderson / Auburn University, USA	5/1/2012	ALDOI	Porter's Creek Clay	-	Silt	MH	A-5(16)	Natural	EFA		2.25	

Figure 89. Filtering the data with regard to contact person/organization. In this example inquiry, Steps 1 and 2 show how to filter data to show only the data from Jean-Louis Briaud.

NCHRP-Erosion Version Beta 1.0												EROSI
Record Number	Contact / Credit	Date Conducted / Sample	Project Title / Response	Sample Name	Sample Depth	Soil Type	AASHTO Classification	Natural / Manmade	Erosion Test Type	Erosion Function	Erosion Category	E.
1	Brian Anderson / Auburn University, USA	4/15/2012	ALDOT	Buccatunna	-	Silt	<div style="border: 1px solid #ccc; padding: 5px; width: fit-content;"> <span style="color: red;">1</span> <ul style="list-style-type: none"> <li><a href="#">Sort A to Z</a></li> <li><a href="#">Sort Z to A</a></li> <li><a href="#">Sort by Color</a></li> <li><a href="#">Clear Filter From "Soil Type"</a></li> <li><a href="#">Filter by Color</a></li> <li><a href="#">Text Filters</a></li> </ul> <div style="border: 1px solid #ccc; padding: 5px; margin-top: 5px;"> <span style="font-size: small;">Search</span> <input type="text"/> </div> <div style="border: 1px solid #ccc; padding: 5px; margin-top: 5px;"> <input checked="" type="checkbox"/> (Select All)       <ul style="list-style-type: none"> <li><input checked="" type="checkbox"/> -</li> <li><input checked="" type="checkbox"/> Cemented Sand</li> <li><input checked="" type="checkbox"/> Clay</li> <li><input checked="" type="checkbox"/> Gatorock</li> <li><input checked="" type="checkbox"/> Gravel</li> <li><input checked="" type="checkbox"/> Limestone</li> <li><input checked="" type="checkbox"/> Sand</li> <li><input checked="" type="checkbox"/> Silt</li> <li><input checked="" type="checkbox"/> Silt-Clay</li> </ul> </div> <div style="text-align: right; margin-top: 10px;"> <span style="border: 1px solid #0070C0; padding: 2px 10px; color: #0070C0; border-radius: 5px;">OK</span> <span style="margin-left: 10px;">Cancel</span> </div> </div>	Natural	EFA		2.25	
2	Brian Anderson / Auburn University, USA	4/6/2012	ALDOT	Yazoo	-	Sand	<div style="border: 1px solid #ccc; padding: 5px; width: fit-content;"> <span style="color: red;">2</span> <ul style="list-style-type: none"> <li><a href="#">Sort A to Z</a></li> <li><a href="#">Sort Z to A</a></li> <li><a href="#">Sort by Color</a></li> <li><a href="#">Clear Filter From "Soil Type"</a></li> <li><a href="#">Filter by Color</a></li> <li><a href="#">Text Filters</a></li> </ul> <div style="border: 1px solid #ccc; padding: 5px; margin-top: 5px;"> <span style="font-size: small;">Search</span> <input type="text"/> </div> <div style="border: 1px solid #ccc; padding: 5px; margin-top: 5px;"> <input checked="" type="checkbox"/> (Select All)       <ul style="list-style-type: none"> <li><input checked="" type="checkbox"/> -</li> <li><input checked="" type="checkbox"/> Cemented Sand</li> <li><input checked="" type="checkbox"/> Clay</li> <li><input checked="" type="checkbox"/> Gatorock</li> <li><input checked="" type="checkbox"/> Gravel</li> <li><input checked="" type="checkbox"/> Limestone</li> <li><input checked="" type="checkbox"/> Sand</li> <li><input checked="" type="checkbox"/> Silt</li> <li><input checked="" type="checkbox"/> Silt-Clay</li> </ul> </div> <div style="text-align: right; margin-top: 10px;"> <span style="border: 1px solid #0070C0; padding: 2px 10px; color: #0070C0; border-radius: 5px;">OK</span> <span style="margin-left: 10px;">Cancel</span> </div> </div>	Natural	EFA		2.5	
	Brian Anderson											

Figure 90. Filtering the data with regard to the soil type.

NCHRP-Erosion Version Beta 1.0												
Record Number	Contact / Credit	Date Conducted / Sample	Project Title / Sponsor	Sample Name	Sample Depth	Soil Type	USCS Classification	AASHTO Classification	Natural / Manmade	Erosion Test Type	Erosion Function	Erosion Date
1	Brian Anderson / Auburn University, USA	4/15/2012	<a href="#">ADD!</a>	Buccatunna	-	Silt	MH with Sand					2.2
2	Brian Anderson / Auburn University, USA	4/6/2012	<a href="#">ADD!</a>	Yazoo	-	Sand	SM					2.1
3	Brian Anderson / Auburn University, USA	5/1/2012	<a href="#">ADD!</a>	Porter's Creek Clay	-	Silt	MH					2.2
	Brian											

Figure 91. Filtering the data with regard to the USCS.

Copyright National Academy of Sciences. All rights reserved.

NCHRP-Erosion Version Beta 1.0											
Record Number	Contact / Credit	Date Conducted / Sample	Project Title / Sponse	Sample Name	Sample Depth	Soil Type	USCS Classification	AASHTO Classification	Natural / Manmade	Erosion Test Type	Erosion
231	Jean-Louis Briaud / TAMU, USA		TxDOT	EFA-2	5-10ft	Clay	CL				
232	Jean-Louis Briaud / TAMU, USA		TxDOT	EFA-3	5-10ft	Clay	CL				

1

2

[Sort A to Z](#)  
[Sort Z to A](#)  
[Sort by Color](#)  
[Clear Filter From "USCS Classification"](#)  
[Filter by Color](#)  
[Text Filters](#)  
  

(Select All)  
 -  
 CH  
 CH with Sand  
 CL  
 CL / CH  
 CL with Sand  
 CL with sand / SC  
 OH with Sand

OK
Cancel

Figure 92. Filtering the data with regard to the USCS. In this example inquiry, Steps 1 and 2 show how to filter data to show only low plastic clay (CL) soils out of all clay data.

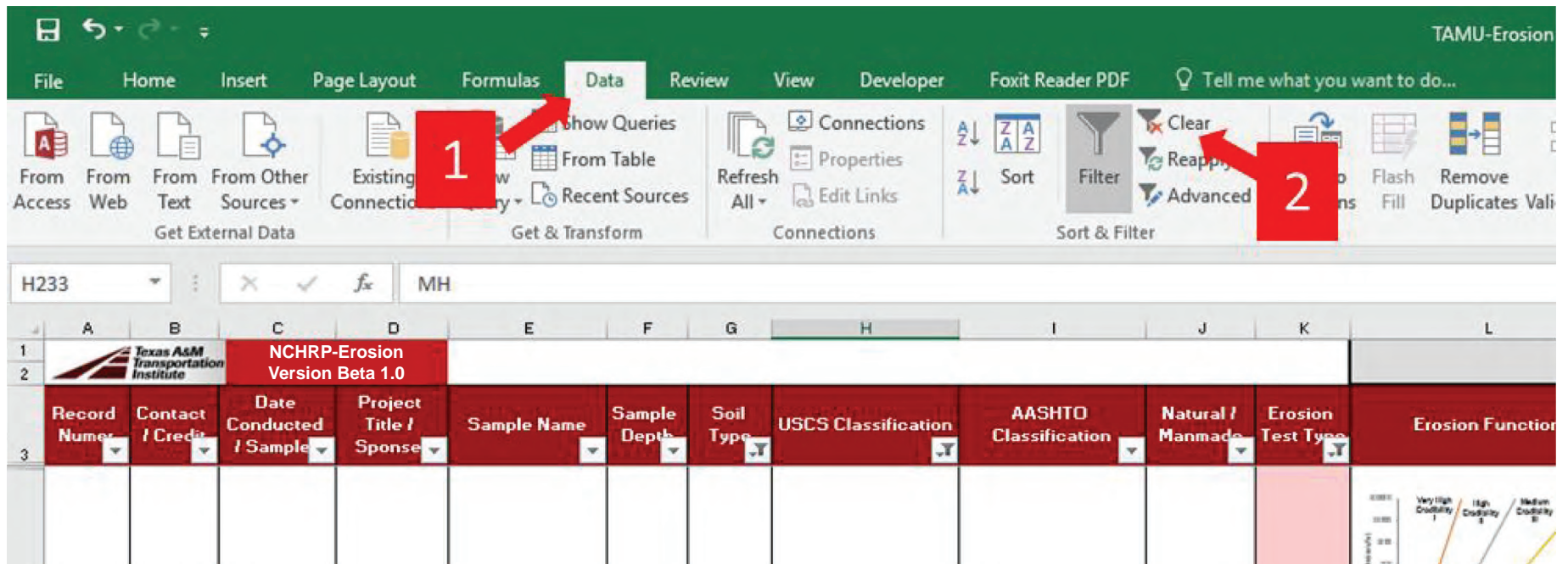
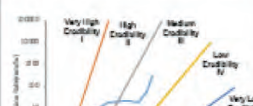


Figure 93. Clearing the filters.

NCHRP-Erosion Version Beta 1.0													EROSION PARA		
Record Number	Contact / Credit	Date Conducted / Sample	Project Title / Sponsor	Sample Name	Sample Depth	Soil Type	USCS Classification	AASHTO Classification	Natural / Manmade	Erosion Test Type	Erosion Function	Erosion Category	E <sub>r</sub> (mm/hr-m/s)	E <sub>r</sub>	
190	Jean-Louis Briaud / TAMU, USA	7/1/2015	Riverside	CBH3-24	2-4 ft	Clay	CL	A-7-6(23.5)	Natural	EFA	1	Sort A to Z Sort Z to A Sort by Color Clear Filter From "Erosion Test Type" Filter by Color Text Filters	3.80		
192	Jean-Louis Briaud / TAMU, USA	7/1/2015	Riverside	CBH3-68	6-8 ft	Clay	CL	A-6(19.2)	Natural	EFA	2	(Select All) BET EFA ESTD HET JET Large-scaled Widening test PET SET	8.94		

Figure 94. Filtering the data with regard to erosion test type. In this example inquiry, Steps 1 and 2 show how to filter data to show only the EFA data.



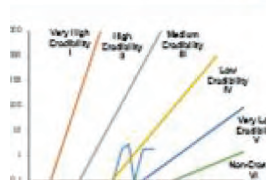
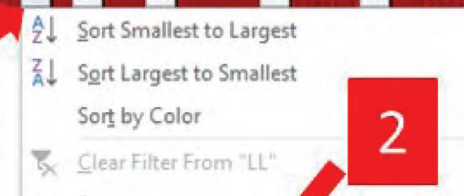
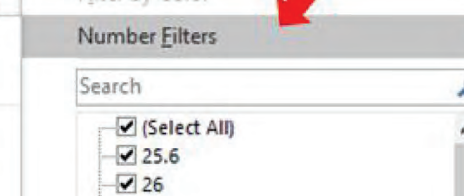
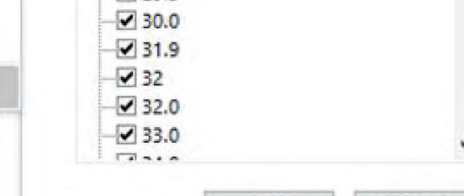
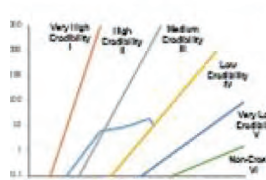
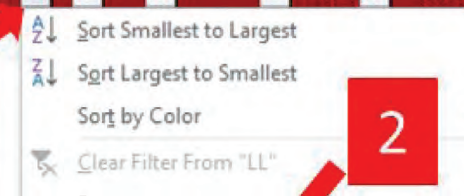
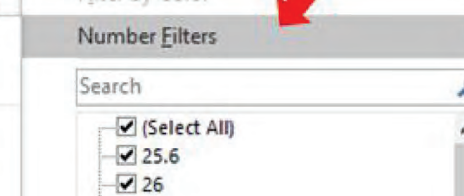
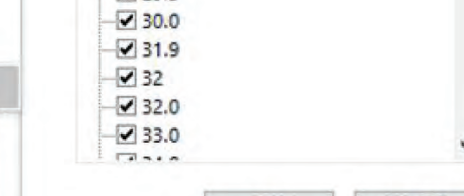
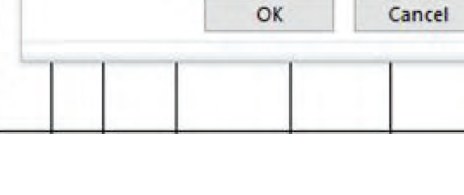
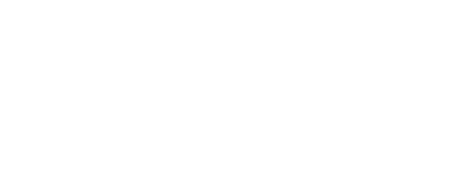
EROSION PARAMETERS							General Comments	LL	PL	PI	$\gamma$ (kN/m <sup>3</sup> )	Water Content (%)	Pocket Penet. (kPa)	Tens. Strt. (kPa)
Erosion Function	Erosion Category	$E_s$ (mm/hr-m/s)	$E_t$ (mm/hr-pa)	$V_c$ (m/s)	$\tau_c$ (Pa)	Remarks on Erosion Test		LL	PL	PI	$\gamma$ (kN/m <sup>3</sup> )	Water Content (%)	Pocket Penet. (kPa)	Tens. Strt. (kPa)
	3.5	3.80	0.20	150	12.38	<p>1</p> <p>1. DILUTE densities of the clay were measured at the time the U-tube tests were performed, the water contents at that time were thus different than those in the table.</p>								
	2.5	8.94	1.16	0.34	0.40	<p>2</p> <p>2- The degree of saturation was calculated based on the bulk densities and the water content measured before performing the triaxial tests.</p>								

Figure 95. Filtering data with regard to the liquid limit.

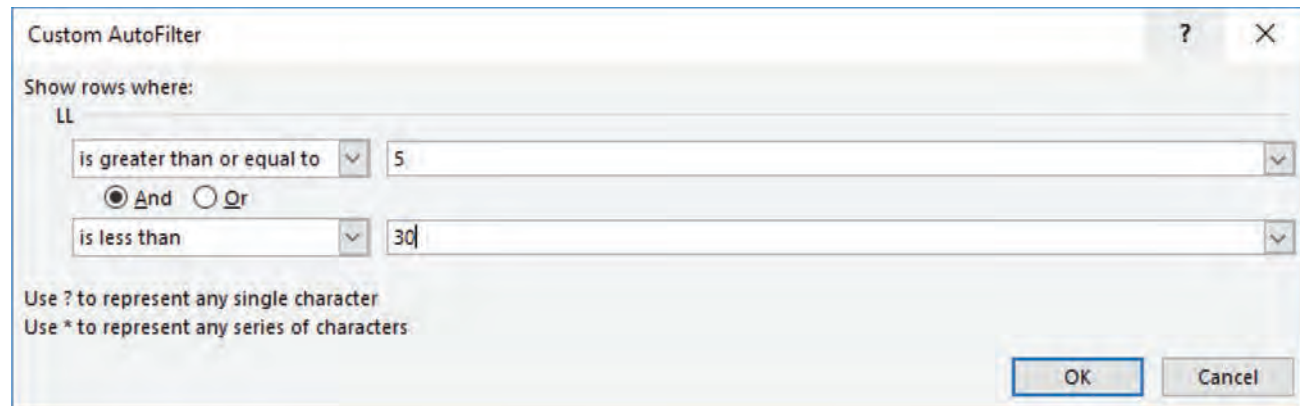


Figure 96. Custom AutoFilter window in Microsoft Excel. In this example inquiry, the data are filtered to show only those for which the liquid limit is between 5% and 30%.



## CHAPTER 6

# Comparison of Selected Soil Erosion Tests by Numerical Simulation

As discussed in Chapters 1 and 2, one of the critical issues associated with all erosion test devices is that they do not give the same erosion parameters and, therefore, do not lead to the same type of results. To overcome this issue, all tests need to be studied in the same fashion. In Chapter 2, all available erosion tests, their applications, test results, and physical specifications are discussed in detail. Table 4 (Chapter 2) lists all the types of erosion tests discussed in this report. Performing numerical studies for all tests would be cost prohibitive; therefore, the investigators decided to study a selected number of the most common tests: erosion function apparatus (EFA), jet erosion test (JET), hole erosion test (HET), and borehole erosion test (BET).

The numerical simulations presented in this chapter are divided into two sections:

1. The evolution of the hydraulic shear stress at the soil–water interface in nonerodible soils and
2. Monitoring the variation in shear stress at the soil–water interface including the erosion process.

Section 6.1 presents the results of numerical simulations for the JET, EFA, HET, and BET prior to erosion. Section 6.2 presents a novel technique using numerical simulations to compare the results of the EFA with those of the JET, BET, and HET, including the erosion process.

## 6.1 Results of Numerical Simulation for Nonerodible Soils

### 6.1.1 CHEN4D Code

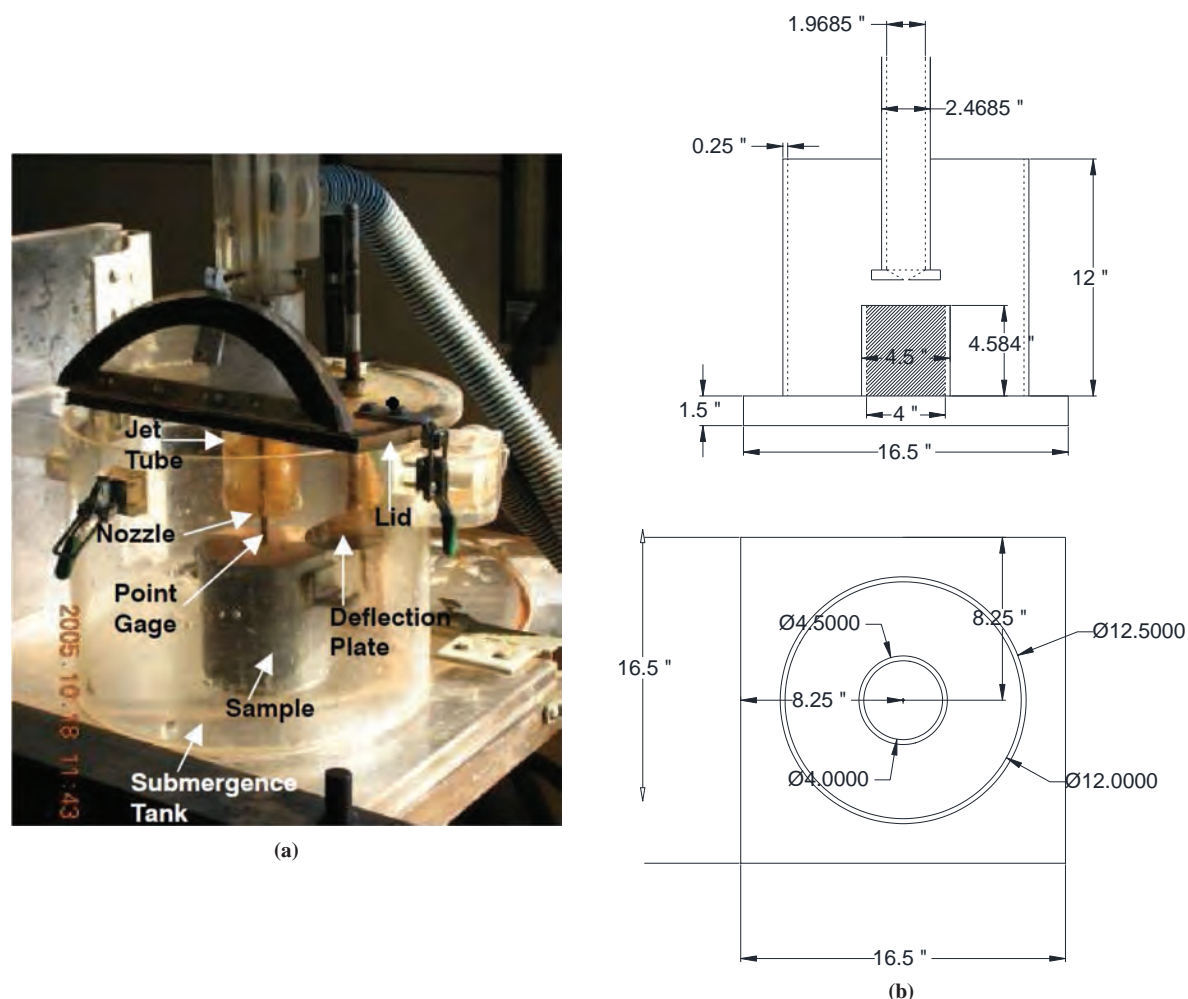
For this task, computational fluid dynamics (CFD) is used together with a code called Computational Hydraulic Engineering in 4 Dimensions (CHEN4D), which was developed by H. C. Chen (Chen et al. 1990). The goal is to simulate each erosion test and develop data reduction techniques that will give the same soil erosion information from these tests without changing the test. CHEN4D is used to perform CFD simulations of the JET, the HET, and the BET and backcalculate the erosion function, which leads to proper matching of the results of these tests with the erosion function from the EFA. These simulations are expected to lead to a common data reduction process of erosion tests and a common output of all erosion tests, to bring uniformity in erosion studies, and to keep all soil erosion testing options open for the engineer.

The CHEN4D code solves unsteady three-dimensional Navier–Stokes equations together with advanced near-wall turbulence closure and sediment transport models for fluid–structure interaction problems around complex configurations. A moving overset (chimera) grid approach is implemented to accommodate time domain simulation of arbitrary body motions and grid

deformations such as those encountered in multiple-ship and floating pier interactions; green water and slamming impact of ships in random waves; vortex-induced motion of offshore platforms; and pier scour, abutment scour, and bridge scour, including overtopping. Both the soil roughness and bed load transport models are incorporated in CHEN4D for the simulation of erosion and accretion of deformable soils. The industry standard CFD models such as FLUENT and CD-adapco's (2016) STAR Computational Continuum Mechanics (STAR-CCM+) have limited capability in dealing with arbitrary multiple-body motions or large grid deformations (Chen et al. 2013).

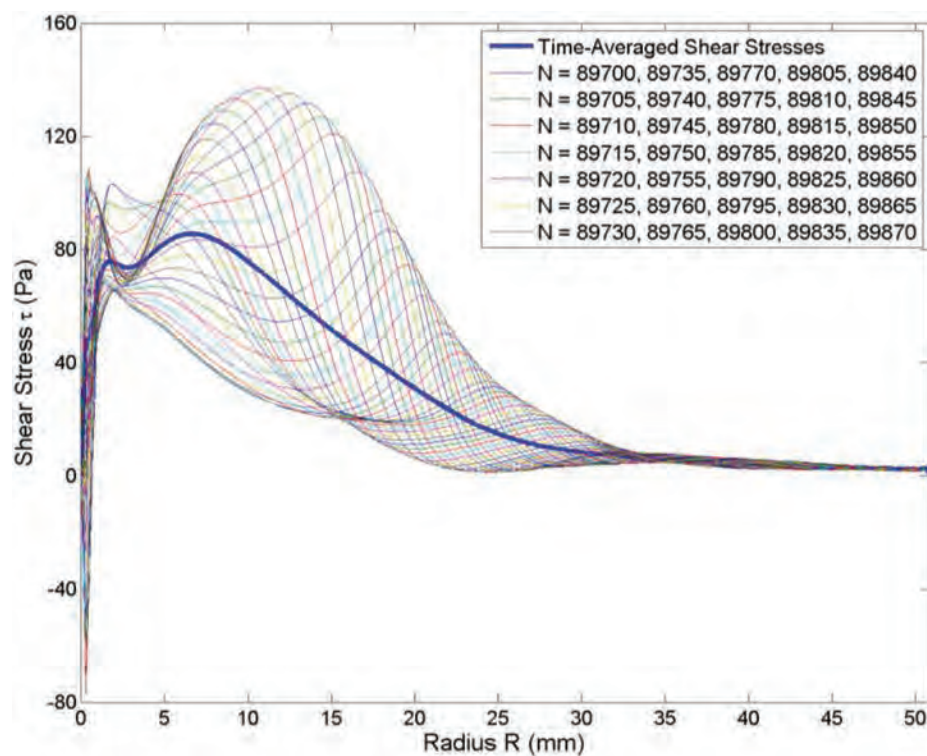
### 6.1.2 JET Simulations

This section discusses the results of numerical simulations of the JET. The simulations were based on the large laboratory JET device developed by Hanson and Hunt (2007) (Figure 97). The goal for this phase of the work was to simulate the submerged jet test with the CHEN4D code to obtain the hydraulic shear stress distribution on the surface of the sample prior to any erosion of the soil. Therefore, the soil was assumed to be nonerodible, and the distribution of jet flow velocity and shear stress on the surface of the soil were obtained. Two cases were assumed for the surface of the soil: (1) a smooth surface to represent a clayey soil and



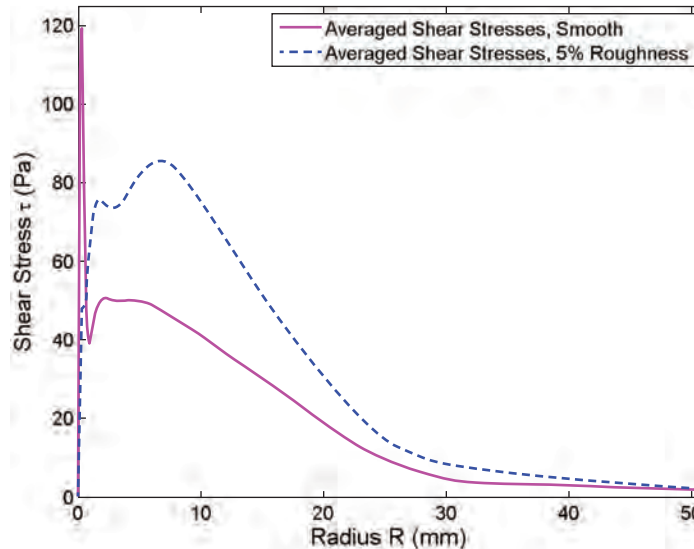
**Figure 97.** Large laboratory JET device used in the numerical simulations: (a) photograph and (b) schematic diagram with dimensions in inches (Hanson and Hunt 2007).

## 140 Relationship Between Erodibility and Properties of Soils



**Figure 98.** Shear stress distribution on the soil surface from the center of the surface to the sides in different time steps.

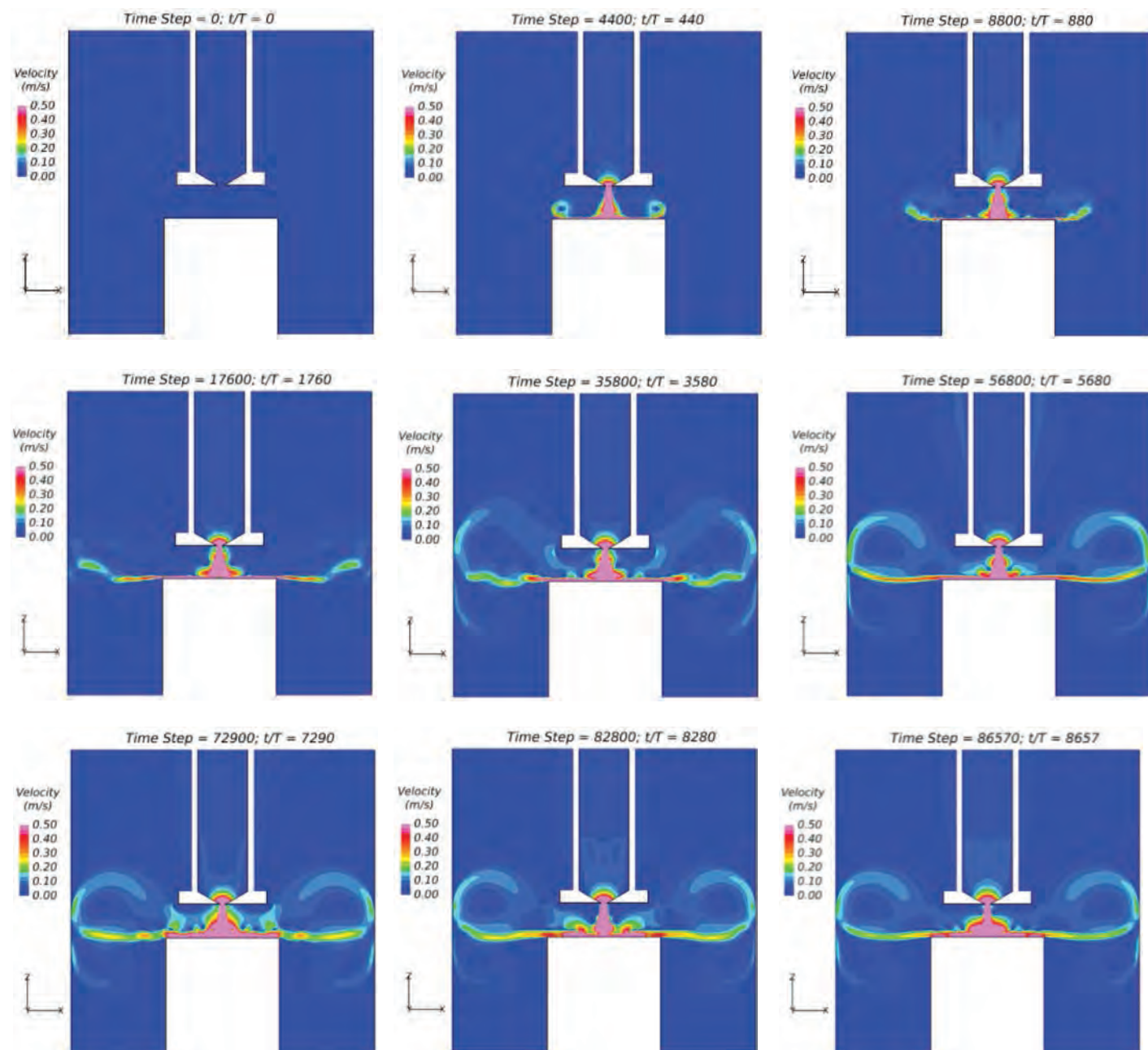
(2) a surface with 5% roughness to represent coarse sand and gravel. Figure 98 shows the distribution of shear stress versus the distance away from the centerline of the soil surface for the smooth case (clayey soils) and the shear stress distributions in different time steps, as well as the time-averaged shear stress. The time-averaged shear stress distribution for the smooth and 5% roughness surfaces are shown in Figure 99. The results are in general agreement with the shape of Hanson's shear stress distribution shown in Figure 11 (Chapter 2). The shear stress



**Figure 99.** Average time shear stress distribution for smooth surfaces and surfaces with 5% roughness.

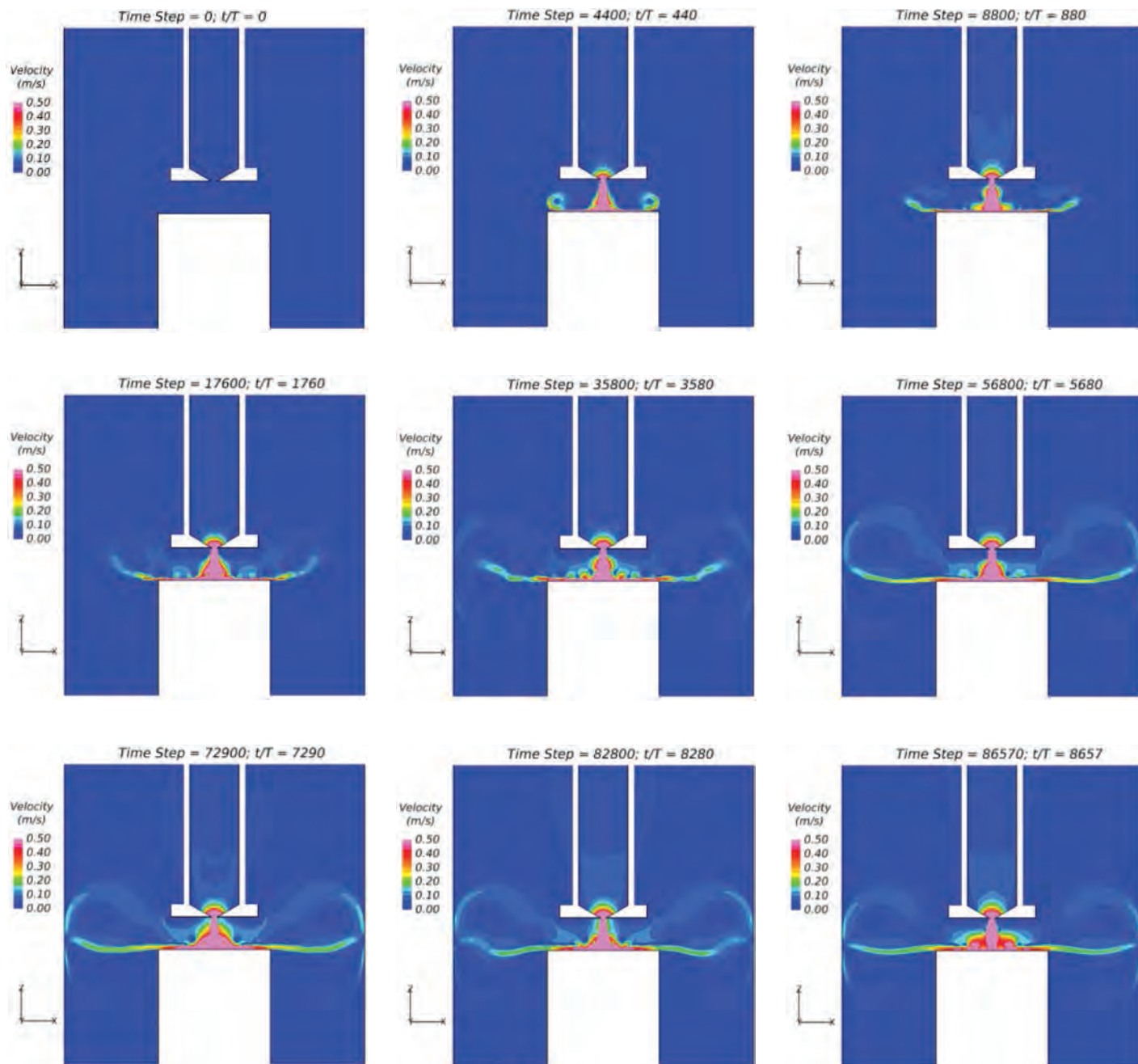
on the point of impingement is zero, while the maximum shear stress occurs at a short distance from the center. Figure 99 shows that for soil with a smooth surface (clayey soil), the maximum is less as compared with the case where the soil surface is rough. Also, it is observed that the maximum shear stress happens farther from the center for the rough soil surface than for the smooth one.

Figure 100 shows the evolution of the jet on the smooth surface as the steady state jet condition develops. Figure 101 shows the evolution of the jet on the rough surface as the steady state jet condition develops. The next step is to replace the soil (white block) with an erodible surface to obtain the erodibility parameters of different soils for different hydraulic conditions.



**Figure 100.** Velocity results of submerged jet evolution in different time steps for the smooth surface (from top left to bottom right).

## 142 Relationship Between Erodibility and Properties of Soils



**Figure 101.** Velocity results of submerged jet evolution in different time steps for the rough surface (from top left to bottom right).

### 6.1.3 HET Simulations

CFD numerical simulations were performed for the Wan and Fell (2002) HET. Figure 102 shows the geometry of the HET used in the numerical simulations. The HET is discussed in greater detail in Chapters 1 and 2 of this report.

As in the case of the JET simulations, the soil was assumed to be nonerodible. The water flow velocity and shear stress distributions through the HET hole were obtained. The initial stresses were evaluated for the 6-mm-diameter hole in the center of the sample at an average

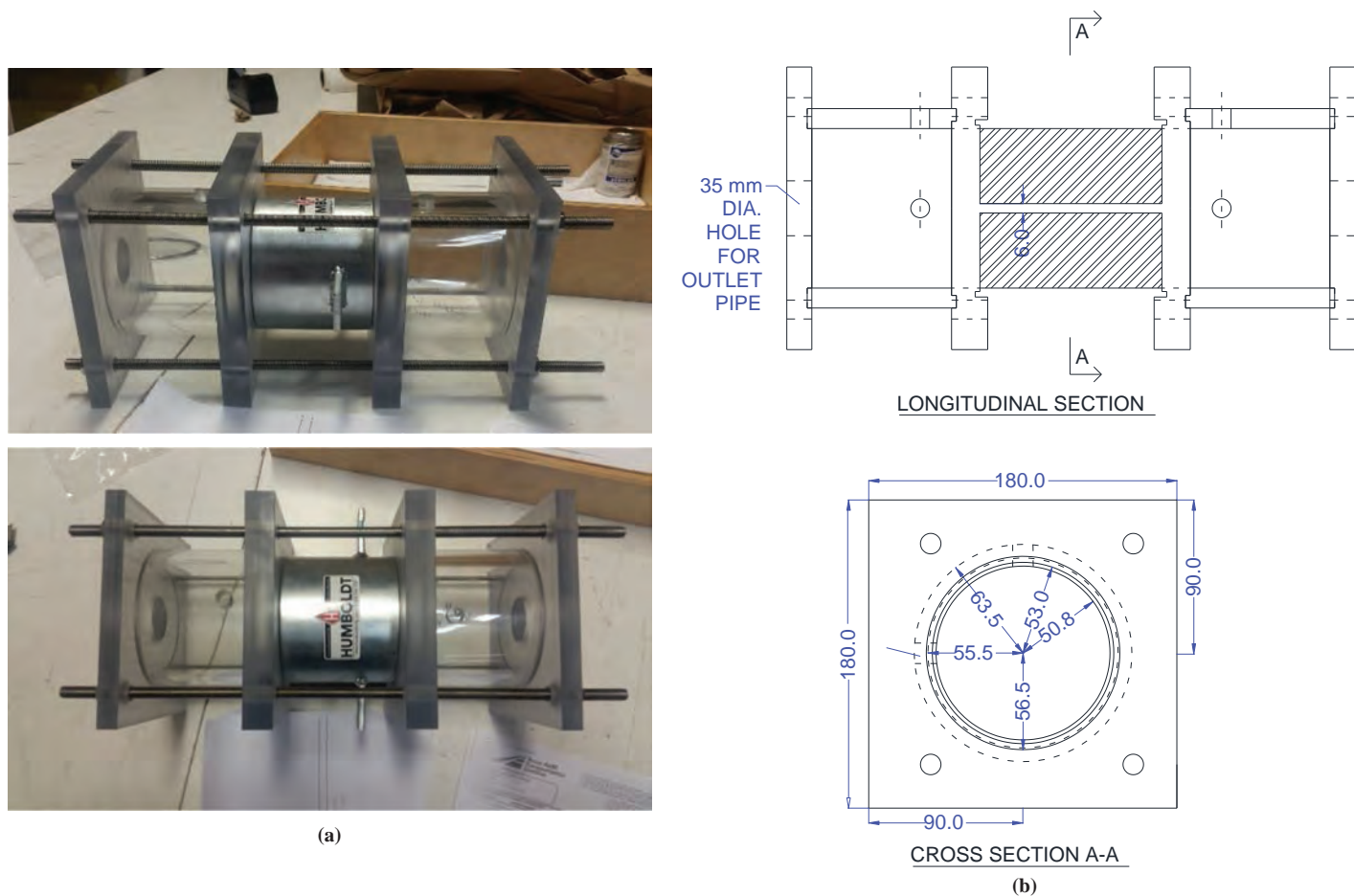


**Figure 102.** HET used in numerical simulations at Texas A&M University: (a) photographs and (b) schematic diagram with dimensions in millimeters (Wan and Fell 2002).

velocity (in the hole) of 2.5 m/s. For the HET simulations, the same two cases as considered in the JET were tested: (1) smooth soil representing clayey soils and (2) a surface with 5% roughness, representing sandy soils. It is worth mentioning that in the HET, the soil is compacted in a compaction mold with an inner diameter of 4 in. (101.6 mm), and a 6-mm hole is drilled in the center of the sample. The time-averaged shear stress distribution through the 6-mm hole along the 101.6-mm length of the sample was obtained. Figure 103 shows that the shear stress along the hole was approximately 30 Pa for the coarser surface (sandy soils). As expected, the shear stress was less when the surface was smooth (clayey soils).

The flow condition at the beginning of the hole is not constant. The existence of negative shear stress at the beginning is due to a small region of recirculation right where flow impinges on the hole. Due to this separate region, contraction occurs and, consequently, flow starts recirculating to get into the hole.

The shear stress along the drilled hole can also be estimated by using Moody charts (Figure 104). Assuming a flow velocity of 2.5 m/s and diameter of 6 mm, the discharge is  $7.1 \times 10^{-5} \text{ m}^3/\text{s}$ . Reynolds number (Re) is calculated to be 14,670 by using Equation 58.

$$\text{Re} = \frac{\rho_w v D}{\mu} \quad (58)$$

## 144 Relationship Between Erodibility and Properties of Soils

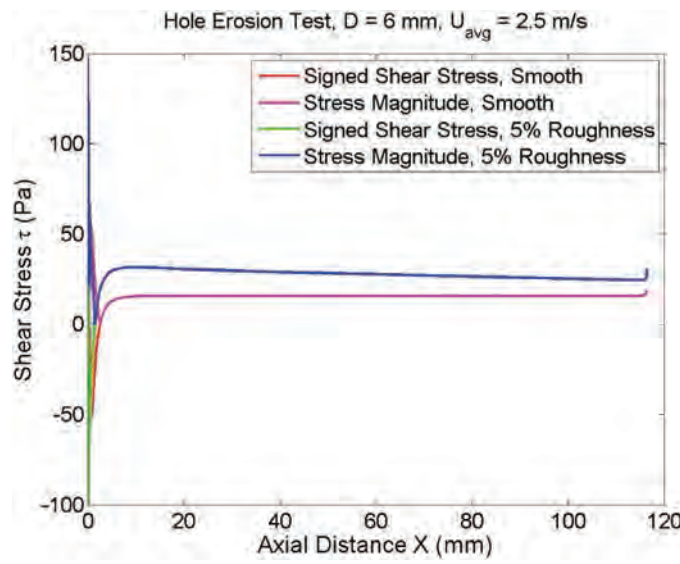


**Figure 103.** Shear stress distribution through the drilled hole along the length of the sample for both smooth and 5% rough surfaces, considering an average velocity of 2.5 m/s in the hole.

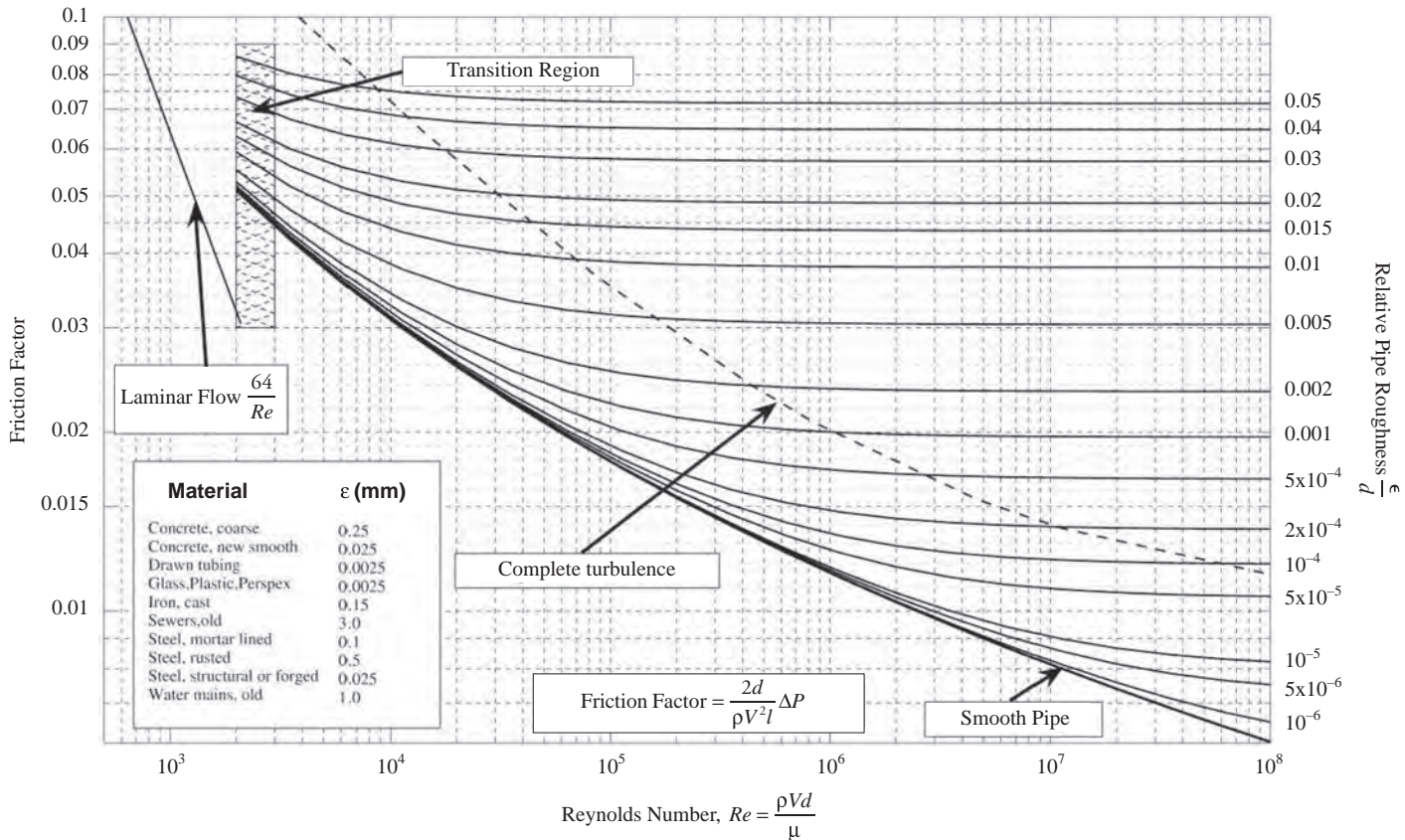


**Figure 104.** Moody diagram (Moody 1944).

where

$\rho_w$  = density of water ( $\text{kg}/\text{m}^3$ ),  
 $v$  = flow velocity ( $\text{m}/\text{s}$ ),  
 $D$  = diameter of flow channel ( $\text{m}$ ), and  
 $\mu$  = viscosity of water ( $1.027 \times 10^{-3} \text{ kg}/\text{m}\cdot\text{s}$ ).

On the basis of the knowledge that the surface roughness is 5%, the friction factor is obtained as approximately 0.075 from the Moody diagram.

By using Equation 7 (Chapter 2), the shear stress is calculated to be 50 Pa, which is greater than the 25 Pa obtained through the numerical analysis results shown in Figure 103. The difference shows that there is a discrepancy between the Moody chart predictions and the numerical simulations and that the Moody charts overestimated the shear stress by 100% in this case. For the case of a smooth pipe, on the basis of the knowledge that  $\text{Re} = 14,670$ , the friction factor is 0.028 on the basis of the Moody chart (see Figure 104). By using Equation 7, the shear stress is calculated as 21.875 Pa, which is larger than the 10 Pa obtained through the numerical simulation shown in Figure 103. Again, the Moody diagram gives a higher value. The evolution of the velocity for the smooth case is shown in Figure 105.

#### 6.1.4 EFA Simulations

The EFA geometry used in the simulations is described in Chapter 2. As mentioned earlier, the EFA comprises a rectangular channel approximately 1.24 m long. On the bottom surface, a sample the size of a Shelby tube with an outer diameter of 76.2 mm is extruded. The surface of the conduit is assumed to be smooth. Three target velocities ( $U = 1 \text{ m}/\text{s}$ ,  $3 \text{ m}/\text{s}$ , and  $6 \text{ m}/\text{s}$ ) are considered in the results. The channel height is used as the characteristic length in the simulations instead of the channel hydraulic diameter ( $D_h = 67.33 \text{ mm}$ ). The roughness of the soil surface is 5% (of the channel height) in all cases.

Figure 106 to Figure 108 show the shear stress distribution on both the top and bottom surfaces of the channel for  $U = 1 \text{ m}/\text{s}$ ,  $3 \text{ m}/\text{s}$ , and  $6 \text{ m}/\text{s}$ , respectively. In these figures, both the smooth (upper half) and rough (lower half) results on the same figure are plotted to facilitate a direct comparison of the effect of surface roughness.

The shear stresses were also calculated by using the Moody chart (Figure 104).  $\text{Re}$  can be calculated by using  $\rho_w = 1,000 \text{ kg}/\text{m}^3$ ,  $D = 0.00508 \text{ m}$ , and  $\mu_w = 1.027 \times 10^{-3} \text{ kg}/\text{m}\cdot\text{s}$ . The friction factors for the case of 5% roughness were then obtained as 0.079, 0.075, and 0.073 for  $U = 1 \text{ m}/\text{s}$ ,  $3 \text{ m}/\text{s}$ , and  $6 \text{ m}/\text{s}$ , respectively. Equation 7 was then used to measure the shear stresses for each velocity. The resulting shear stresses from the Moody chart are 9.875 Pa, 84.375 Pa, and 324 Pa for  $U = 1 \text{ m}/\text{s}$ ,  $3 \text{ m}/\text{s}$ , and  $6 \text{ m}/\text{s}$ , respectively. Comparison of the shear stress results obtained from the numerical simulations with the Moody chart shows that as in the case of the HET results, the Moody chart overestimates the shear stress values by about 25%.

Figure 109 to Figure 111 show the shear stress evolution when the velocity is  $1 \text{ m}/\text{s}$ ,  $3 \text{ m}/\text{s}$ , and  $6 \text{ m}/\text{s}$ , respectively. The soil surface roughness is 5% in all cases.

#### 6.1.5 BET Simulations

Numerical simulations were also performed for the BET, assuming a nonerodible soil for the purpose of obtaining the shear stress distribution at the soil surface. The geometry of the BET is described in Chapter 2. For the following simulations, two flow rates—23 gallons per minute (gpm) and 90 gpm—were considered. Also, three distances between the jet orifice and the bottom surface of the borehole were considered (1 in., 3 in., and 6 in.). Figure 27 (Chapter 2)

## 146 Relationship Between Erodibility and Properties of Soils

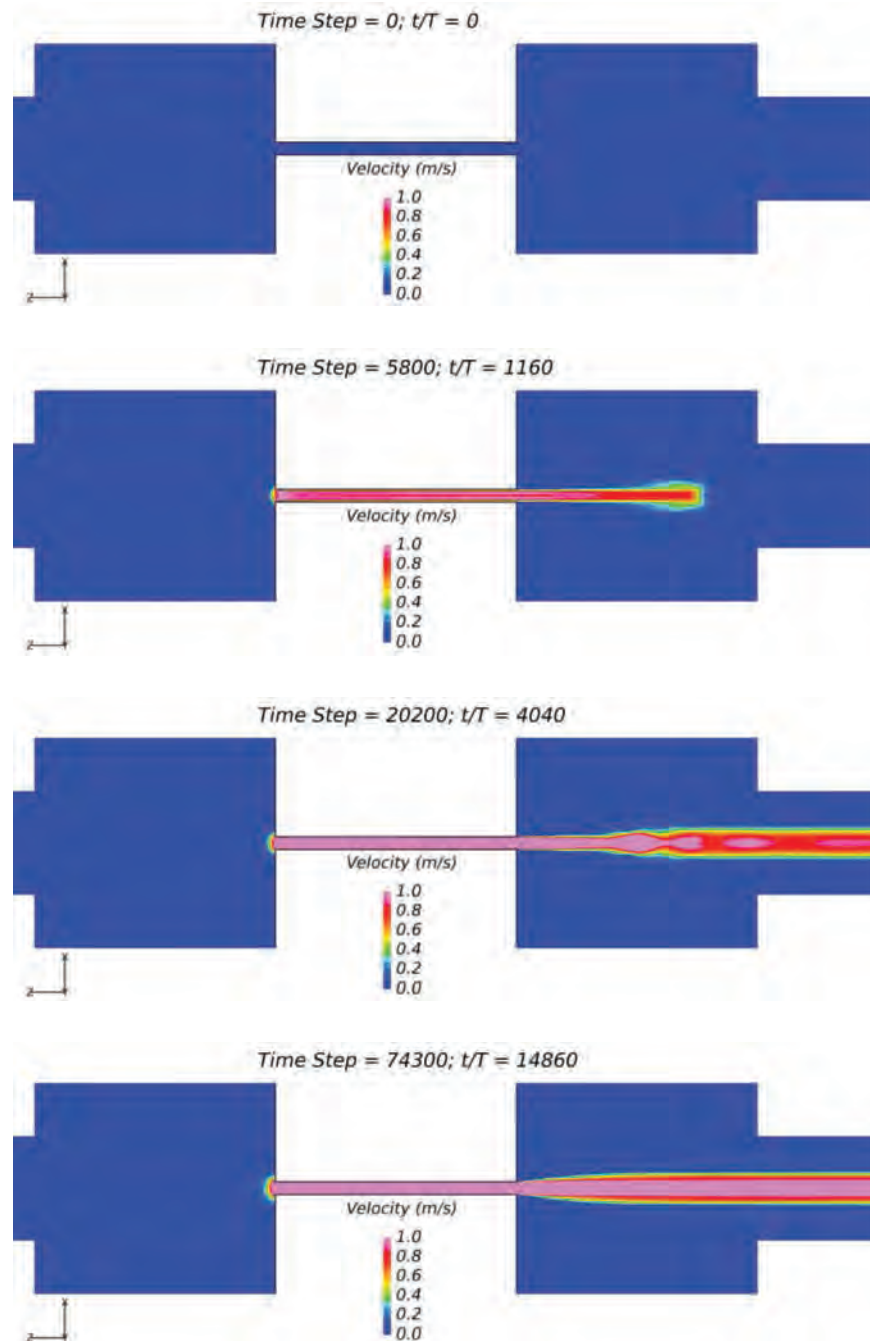
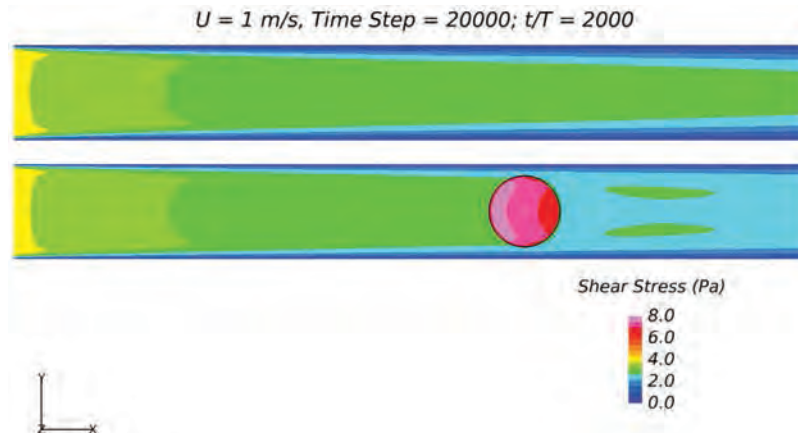
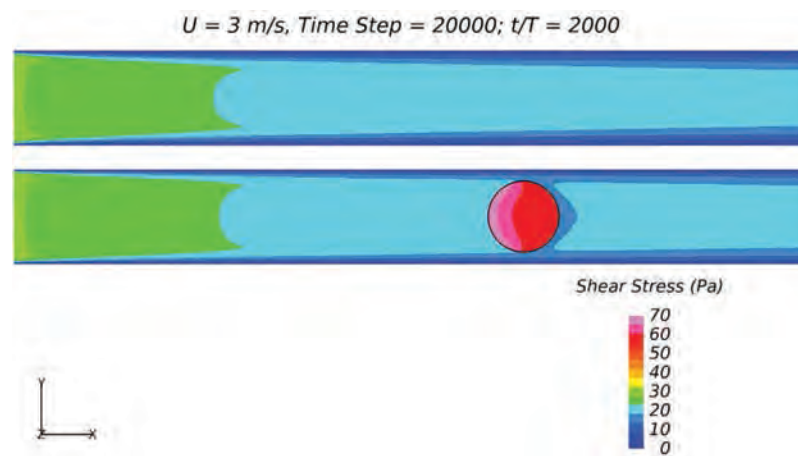


Figure 105. Velocity evolution for the smooth case.



**Figure 106.** *Shear stress distribution on both top surface (which is smooth) and bottom surface (which encompasses the rough soil surface) for  $U = 1 \text{ m/s}$ .*



**Figure 107.** *Shear stress distribution on both top surface (which is smooth) and bottom surface (which encompasses the rough soil surface) for  $U = 3 \text{ m/s}$ .*

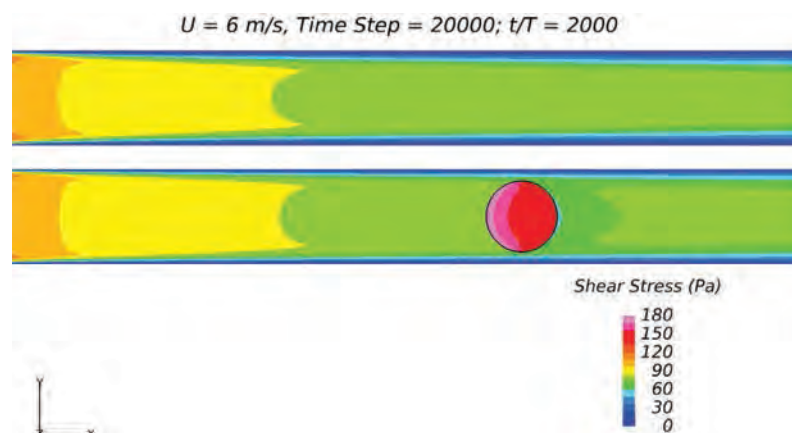


**Figure 108.** *Shear stress distribution on both top surface (which is smooth) and bottom surface (which encompasses the rough soil surface) for  $U = 6 \text{ m/s}$ .*

## 148 Relationship Between Erodibility and Properties of Soils

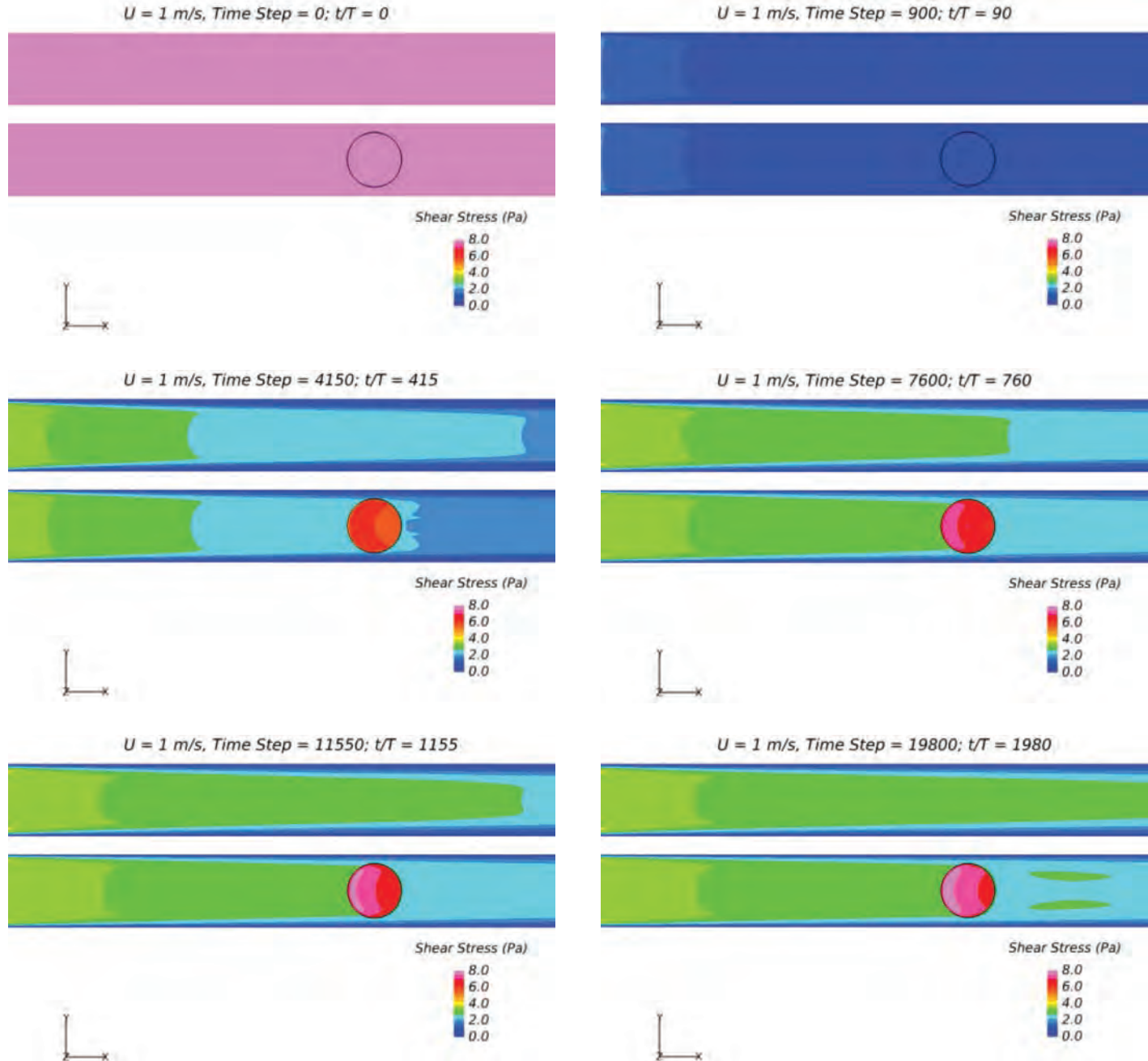


Figure 109. Shear stress evolution captured in six time steps when the flow velocity in the conduit is 1 m/s (from top left to bottom right).

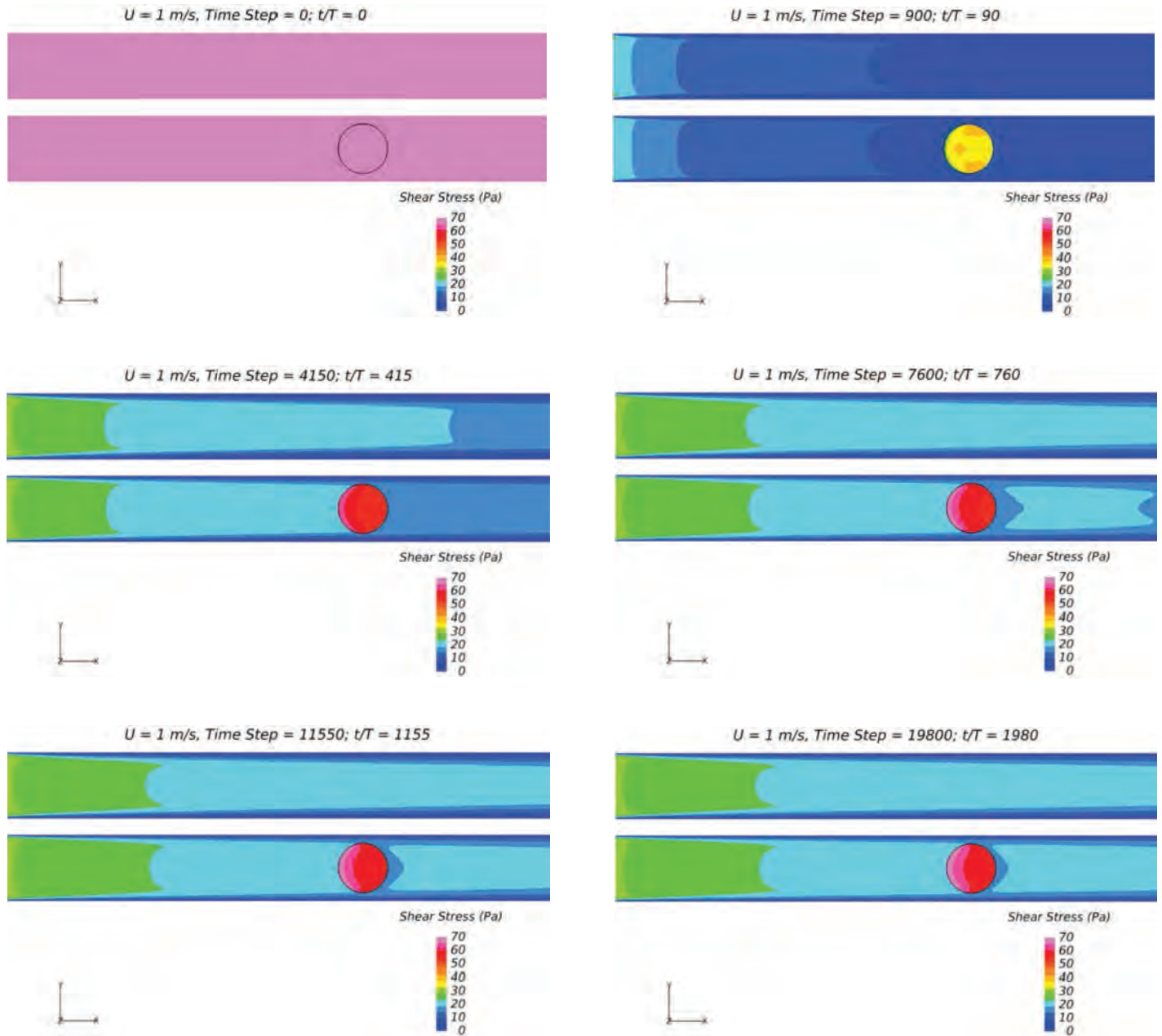
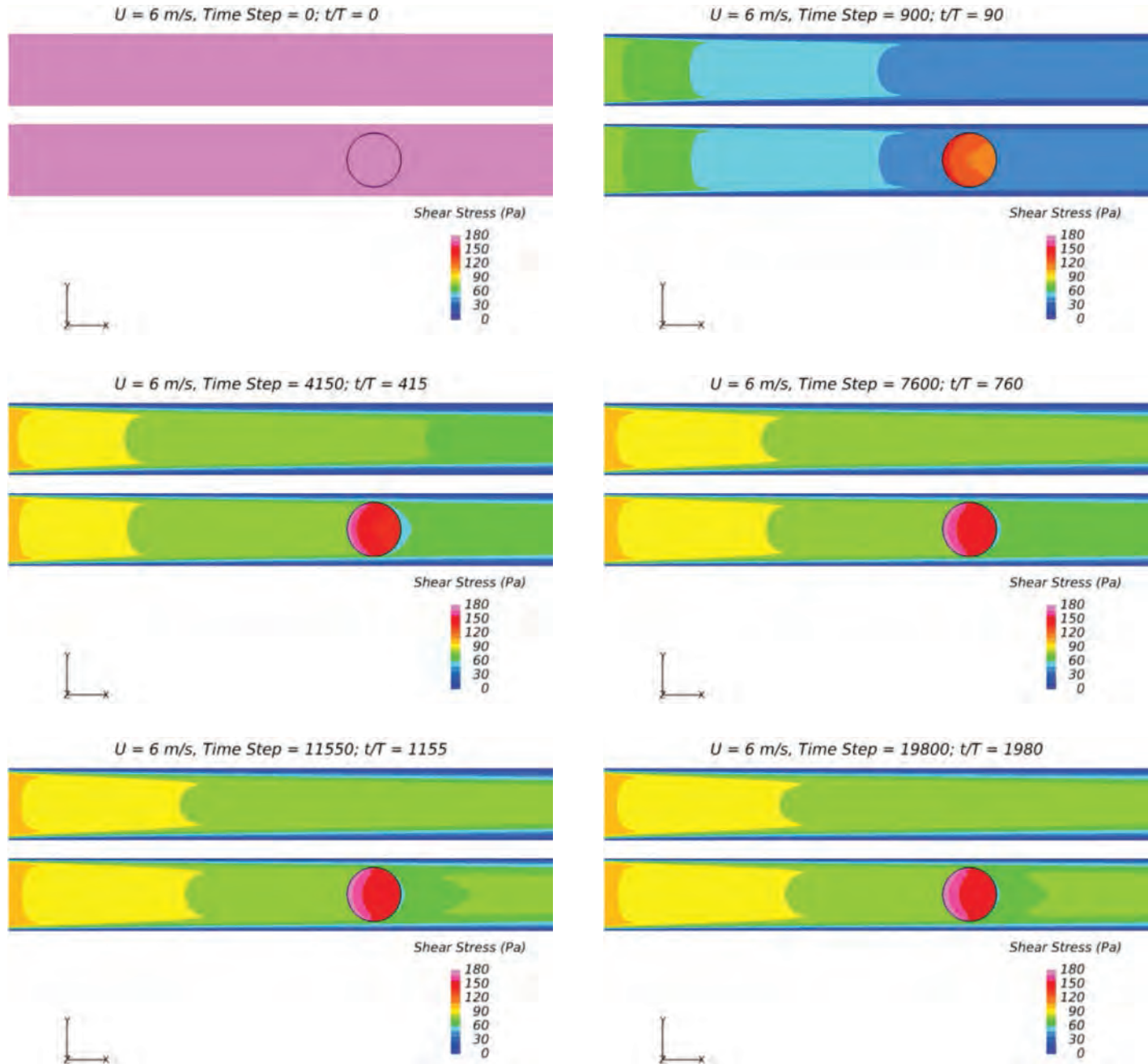


Figure 110. Shear stress evolution captured in six time steps when the flow velocity in the conduit is 3 m/s (from top left to bottom right).

## 150 Relationship Between Erodibility and Properties of Soils



**Figure 111.** Shear stress evolution captured in six time steps when the flow velocity in the conduit is 6 m/s (from top left to bottom right).

shows the schematic diagram of the BET: the jet induces shear stress both at the circular bottom surface and along the side walls in the z-direction. Shear stress results for both regions are presented below for the two aforementioned flow rates.

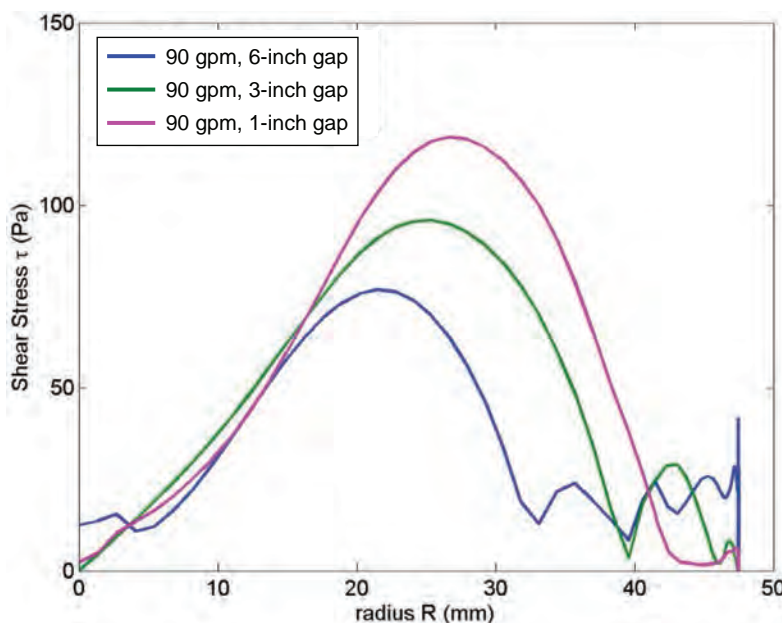
Figure 112 shows the shear stress distribution along the radius of the circular bottom surface of the borehole when the flow rate is 90 gpm. When the gap between the jet orifice and the bottom surface is smaller, the maximum induced shear stress will be larger and farther from the jet's impingement point.

Figure 113 shows the shear stress distribution along the side wall of the drilled hole for the same three gap intervals when the flow rate is 90 gpm. The maximum shear stress is largest when the gap between the discharge orifice and the bottom surface is 3 in.

The same approach was used for a flow rate of 23 gpm. Figure 114 and Figure 115 show the results for the shear stress on the circular bottom surface and on the side wall, respectively. In these figures, the effect of a 2% roughness is shown only when the gap between the discharge orifice and the bottom surface is 1 in. It should be noted that zero elevations are set as the bottom of the borehole in Figure 113 and Figure 115.

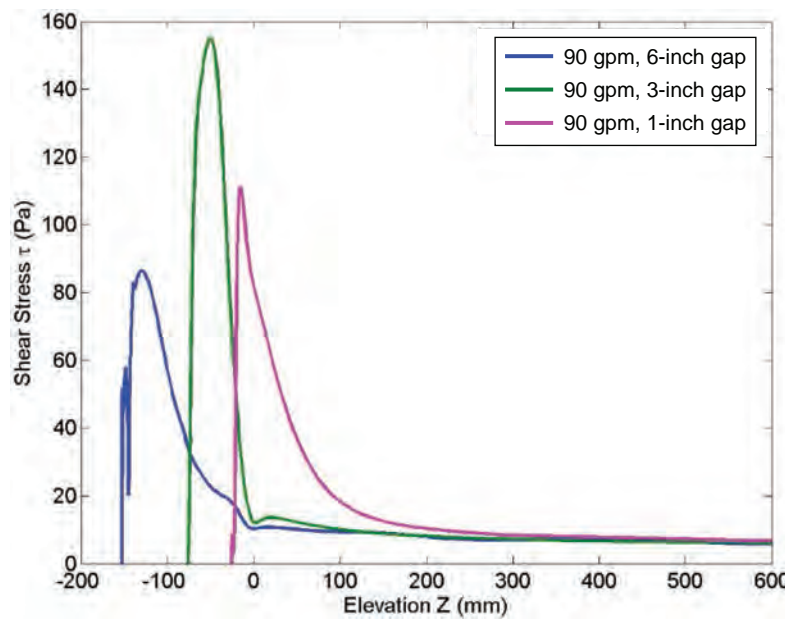
Figure 114 shows that the shear stress is higher when the gap is small (1 in.), and decreases when the gap increases. Also, the shear stress distribution is slightly different when a 2% roughness is considered for the bottom surface (coarser soils). Comparison of Figure 114 and Figure 112 shows that the shear stress distribution is smoother at higher flow rates.

Figure 115 shows the measured shear stress along the side wall of the borehole. The maximum shear stress, similar to the case in which the flow rate was 90 gpm, occurred when the gap between the jet orifice and bottom of the borehole was 3 in. It is also observed that 2% roughness on the sides results in a slightly higher shear stress value as compared with the smooth side. Figure 115 also shows that after about 0.5 m above the bottom discharge, the shear stress on the borehole wall has become constant.



**Figure 112. Shear stress distribution within the circular bottom surface of the drilled hole with 1-in., 3-in., and 6-in. gap between the jet orifice and borehole bottom surface when the flow rate is 90 gpm.**

## 152 Relationship Between Erodibility and Properties of Soils



**Figure 113.** Shear stress distribution along the side wall surface of the drilled hole with 1-in., 3-in., and 6-in. gap between the jet orifice and borehole bottom surface when the flow rate is 90 gpm.

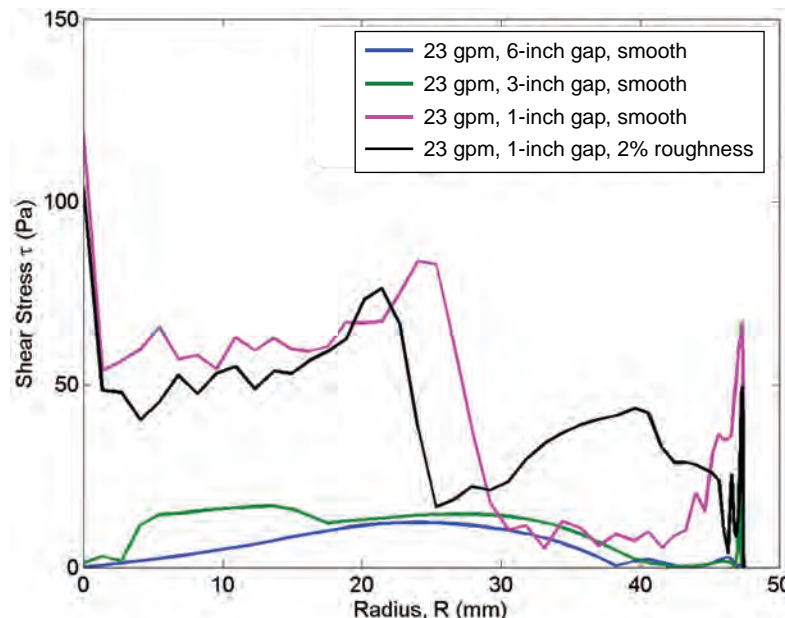


**Figure 114.** Shear stress distribution within the circular bottom surface of the drilled hole with 1-in., 3-in., and 6-in. gap between the jet orifice and borehole bottom surface when the flow rate is 23 gpm.

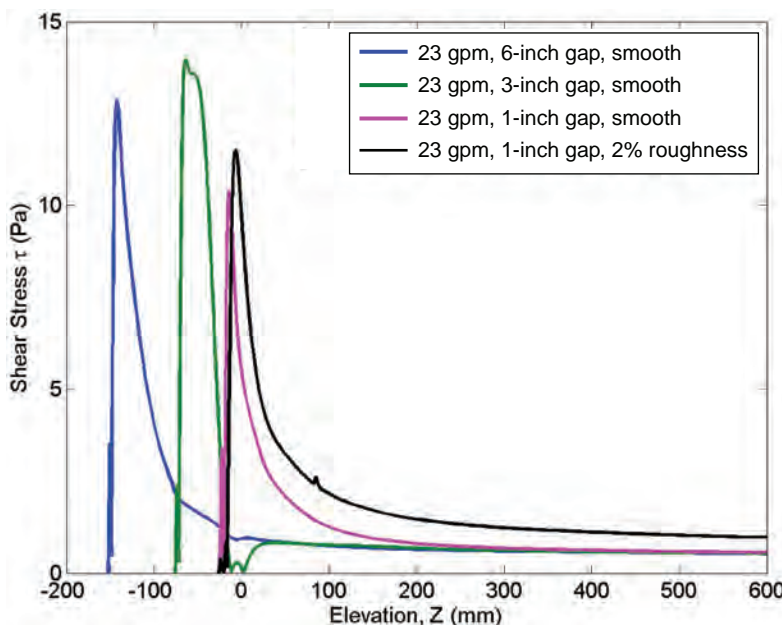


**Figure 115.** Shear stress distribution along the side wall surface of the drilled hole with 1-in., 3-in., and 6-in. gap between the jet orifice and borehole bottom surface when the flow rate is 23 gpm.

Figure 116 shows an example of the numerical simulations in four different time steps. In this example, the gap between the discharge orifice and the bottom of the borehole is 1 in. and the flow rate is 23 gpm. Velocities range from 0 to 6 m/s at the bottom of the borehole and from 0 to 2 m/s on the sides.

## 6.2 Results of Numerical Simulation Including Erosion

### 6.2.1 Methodology

In the previous section, the development of shear stress on the soil–water interface was simulated and discussed for the EFA, JET, HET, and BET on the basis of the assumption that the soil was not erodible. This section presents the results of numerical simulations including the erosion process. The STAR-CCM+ was used for this purpose. The STAR-CCM+ can generate the CFD in soil–fluid interaction problems such as the erosion process.

The primary goal of using numerical simulations was to compare the results of the four erosion testing methods (EFA, HET, JET, and BET) in similar soil samples. As discussed in Chapter 1, the results of each erosion test can be translated into a relationship between the shear stress/velocity and the erosion rate. In fact, the erosion rate ( $\dot{z}$ ) is a function of shear stress/velocity (see Chapter 1, Equations 1 and 2). The relationship between the erosion rate and the shear stress (or velocity) is called the erosion function.

The numerical simulations were concentrated on finding out how the JET, the HET, and the BET would react to the erosion function obtained from the EFA on one common soil sample. The results of the numerical simulations were compared with the actual test results obtained through experiments. The soil surface in the JET, the HET, and the BET was defined as a moving boundary. The erosion process was simulated by using the movement of these boundaries. This movement develops according to the erosion function equation that is obtained from the EFA

## 154 Relationship Between Erodibility and Properties of Soils

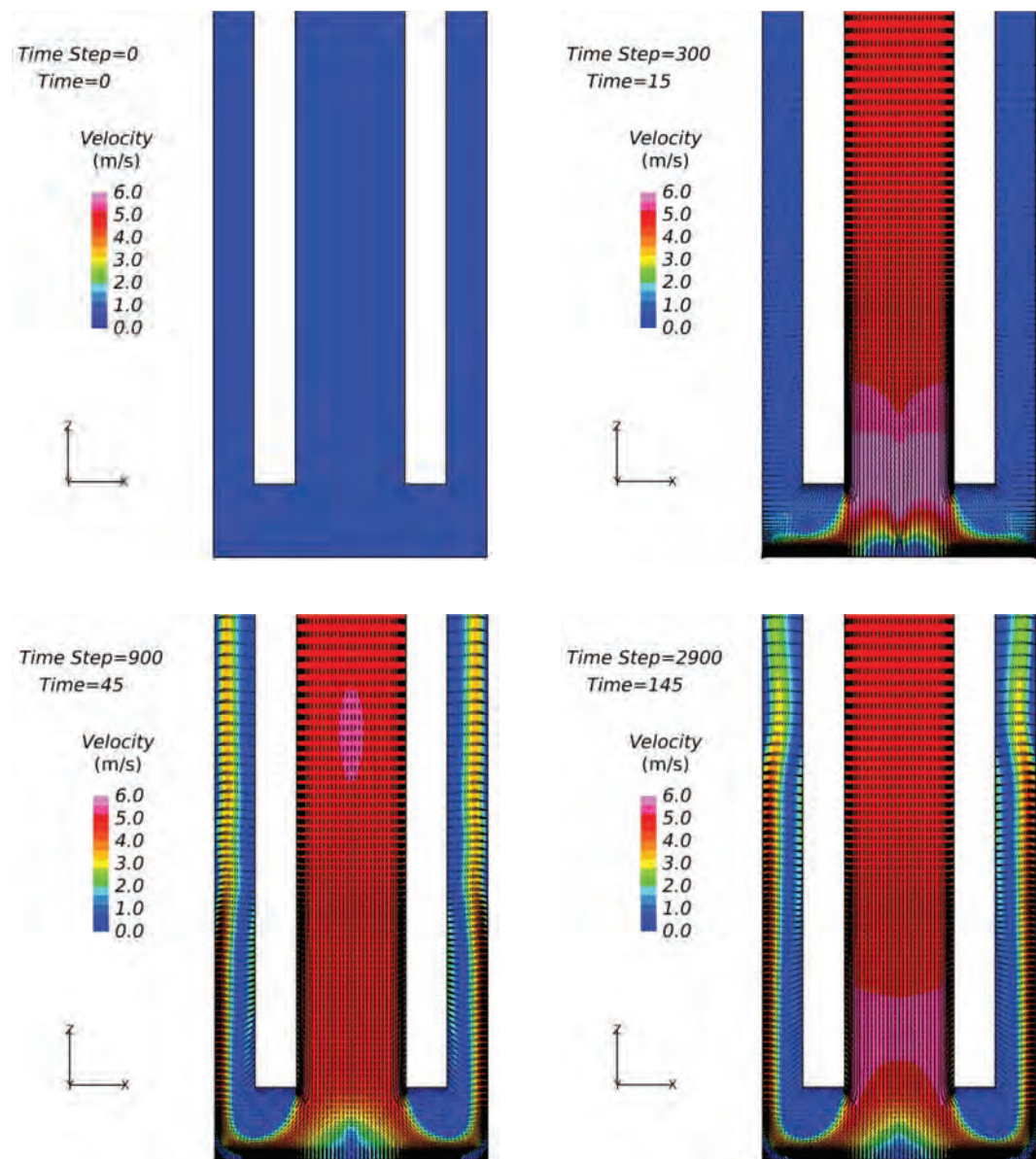


**Figure 116.** Example of velocity results of jet evolution in different time steps for the rough surface when the gap between the orifice and bottom surface is 1 in. (from top left to bottom right).

test performed on the same soil sample. Figure 117 shows a flowchart describing the procedure for each numerical simulation.

The numerical simulations according to the procedure shown in Figure 117 are presented in the following three forms:

1. EFA's erosion function on the JET,
2. EFA's erosion function on the HET, and
3. EFA's erosion function on the BET.

Before the results of these comparisons are discussed, the details of the mesh created for the JET, the HET, and the BET in STAR-CCM+ are presented.

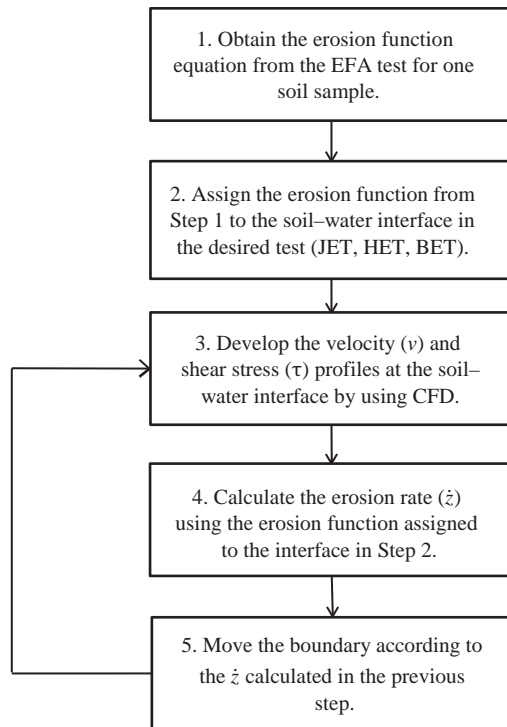


**Figure 117. Procedure for numerical simulations conducted to compare the results of the EFA with the results of the JET, HET, and BET.**

### 6.2.2 Mesh Geometry and Soil-Water Interface

For all three erosion tests (JET, HET, and BET), two-dimensional axisymmetric models were created. The mesh used in these models was quadrilateral. Detailed information on the mesh used for each erosion test is presented in Table 30 below. Figure 118, Figure 119, and Figure 120 show the axisymmetric models created for the JET, the HET, and the BET, respectively. The dimensions used for the models are in accordance with the dimensions of these testing devices in the Soil Erosion Laboratory at Texas A&M University. For detailed information on dimensions of each test device, see Chapter 4, Section 4.1 of this report.

One of the important laws in the fluid dynamics is the law of the wall. This law states that in turbulent flow, the mean velocity at a specific point and the logarithm of the distance between that point and the fluid region boundary (or wall) are proportional. The effect of this law is very significant, especially for those parts of the flow that are closer than 20% of the flow height to the

**Table 30. Detailed information on mesh created for each erosion test.**

Erosion Test	Type of Mesh	Number of Cells	Number of Faces	Number of Vertices
JET	Quadrilateral	8,809	17,501	9,115
HET	Quadrilateral	22,918	45,151	23,673
BET	Quadrilateral	31,765	62,244	33,054

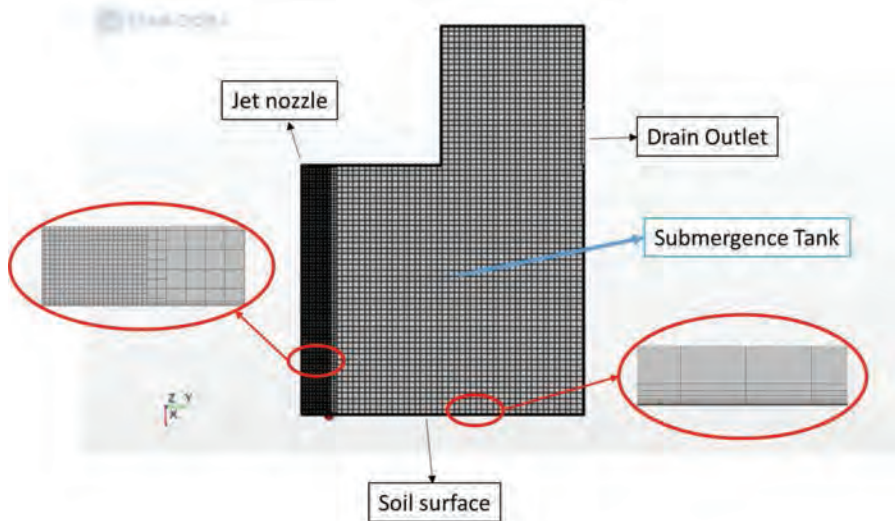


Figure 118. Axisymmetric model for the JET.

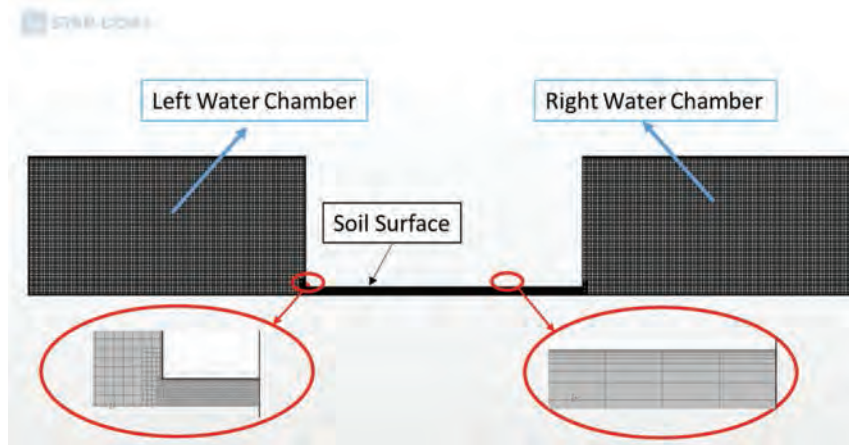


Figure 119. Axisymmetric model for the HET.

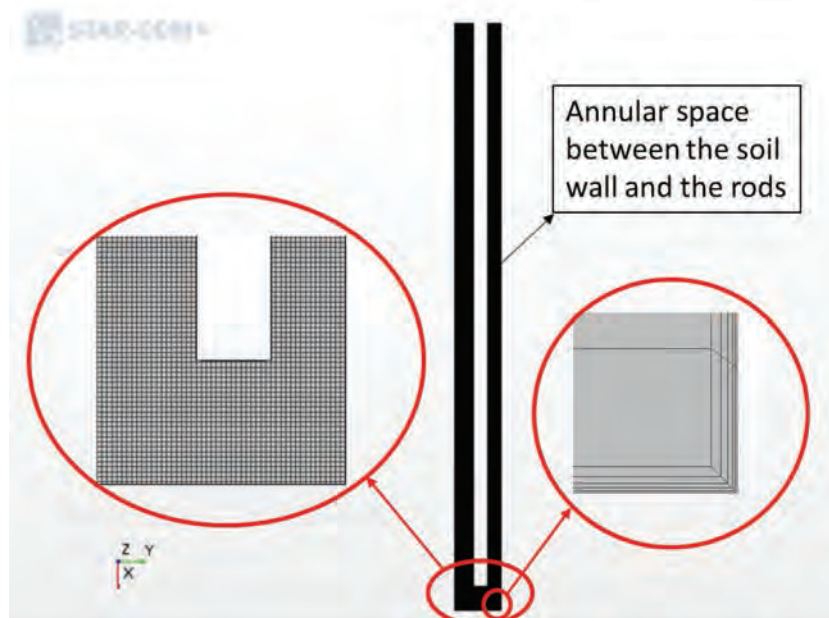


Figure 120. Axisymmetric model for the BET.

wall. The general formulation of the law of the wall (Equation 59) solves for the average velocity parallel to the wall in turbulent flows (high Reynolds numbers).

$$u^+ = \frac{1}{\kappa} \ln y^+ + C^+ \quad (59)$$

where

$u^+$  = dimensionless velocity parameter =  $u$  (average velocity parallel to the wall) ÷ the  $u_T$  (friction velocity);

$y^+$  = dimensionless wall coordinate, obtained by using Equation 60;

$\kappa$  and  $C^+$  = constants equal to 0.41 and 0.5, respectively, for a smooth wall according to Schlichting and Gersten (2000).

$$y^+ = \frac{y + u_T}{v} \quad (60)$$

where

$v$  = local kinematic viscosity of the fluid,

$u_T$  = friction velocity at closest fluid region boundary, and

$y$  = distance of the point to the nearest wall.

The parameter  $y^+$  is one of the most important parameters in defining the law of the wall and conducting the fluid mechanics numerical simulations. For this study, the value of  $y^+$  was designed to be <1 to achieve a very small cell distance between the wall and the point of flow ( $y < 10^{-6}$  m).

### 6.2.3 Model Development

Numerical simulations were performed for the JET, HET, and BET as explained in the previous sections (Figure 117). The results of comparisons between the EFA test and the other erosion tests are presented separately in the following sections.

#### 6.2.3.1 EFA's Erosion Function on the JET

As discussed in Section 6.2.1, the erosion rate can be written as a function of shear stress. For the purpose of comparing the EFA test results with the JET results, the procedure described in Figure 117 was followed for four samples: two sand, one silt, and one clay. The name of these samples are Sand #1 and Sand #2 (sand samples), FHWA Sample 2 (silt sample), and B-1 (4–6 ft) Beaumont (clay sample).

As presented in Figure 117, the first step was to obtain the relationship between the erosion rate,  $\dot{z}$ , and the shear stress for each sample in the EFA. This relationship, also called the erosion function, was obtained after testing each of the four samples in the EFA and then assigned to the soil–water interface in the JET simulation, which is defined in the form of a moving boundary. Once the shear stress was developed on the soil–water interface, the erosion rate at the boundary was calculated by using the assigned erosion function and the boundary moves accordingly. This process repeats itself and the boundary keeps moving until the developed shear stress on the interface becomes equal to or less than the critical shear stress for the tested soil.

To distinguish between smooth clay and rough sand surface, the roughness height (RH) was defined in STAR-CCM+. RH is the height of the roughness of the soil particles (equivalent

## 158 Relationship Between Erodibility and Properties of Soils

to  $\varepsilon$  defined in the Moody diagram shown in Figure 104). For each simulation in this study, whether the sample was clay, silt, or sand, four RH values were considered:

1. RH = 0 mm, or smooth surface;
2. RH = 0.5 mm;
3. RH = 1 mm; and
4. RH = 3 mm.

Figure 121 shows the results of the numerical simulations for the Sand #1 sample when the erosion function obtained from the EFA test on the exact same sample was used at the soil–water interface in the JET model. The observed JET results (black circles) were slightly overestimated through STAR-CCM+ when their erosion function obtained from the EFA was assigned to the soil–water interface. This overestimation was less pronounced when the RH was close to 0 mm (smooth surface). The actual average roughness height ( $D_{50}/2$ ) for Sample SE-1 was about 0.14 mm; therefore, smooth surface results would be a relatively reasonable assumption.

Figure 122 shows an example of the numerical simulations in four different time steps for the Sand #1 sample. In this example, the soil–water interface was defined as a moving boundary. The velocity profile of the flow is shown for each time step. Velocity for this example ranged from 0 to 3.2 m/s. The highest velocity was at the jet nozzle, and when the water reached the soil surface, its velocity became less. This process continued until the shear stress induced on the boundary (i.e., the soil–water interface) became less than the measured critical shear stress from the EFA’s erosion function.

Figure 123 shows the results of the numerical simulations for the Sand #2 sample when the erosion function obtained from the EFA test on the exact same sample was used at the soil–water interface in the JET model. The observed JET results (black circles) were slightly underestimated through STAR-CCM+ when their erosion function obtained from the EFA was assigned to the

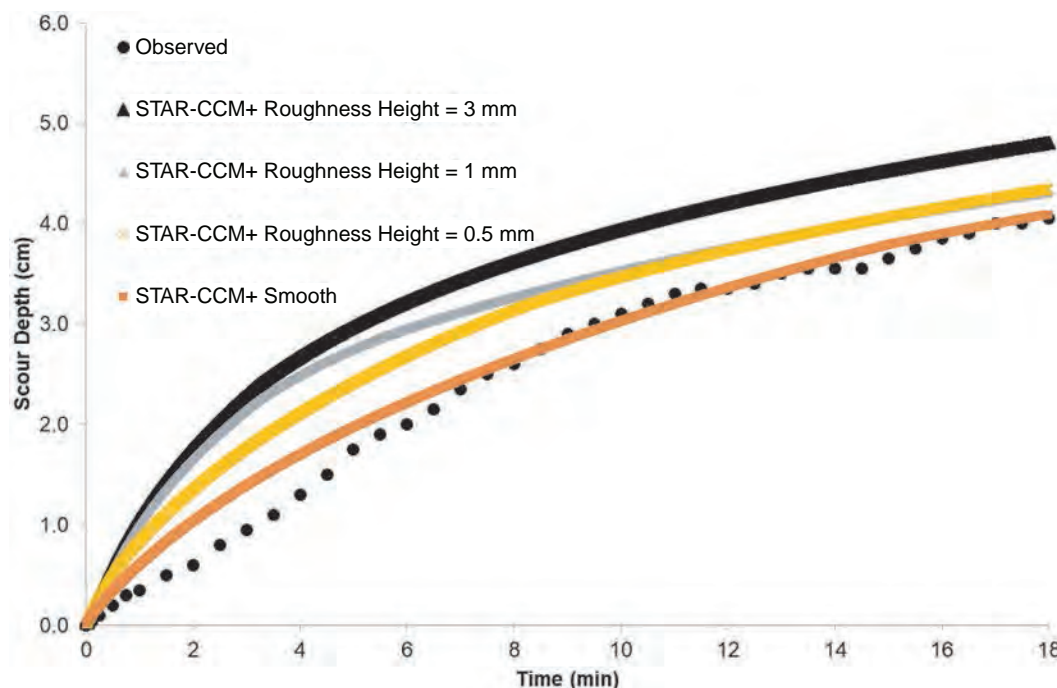


Figure 121. Scour depth versus time for observed JET and simulated JET for Sand #1.

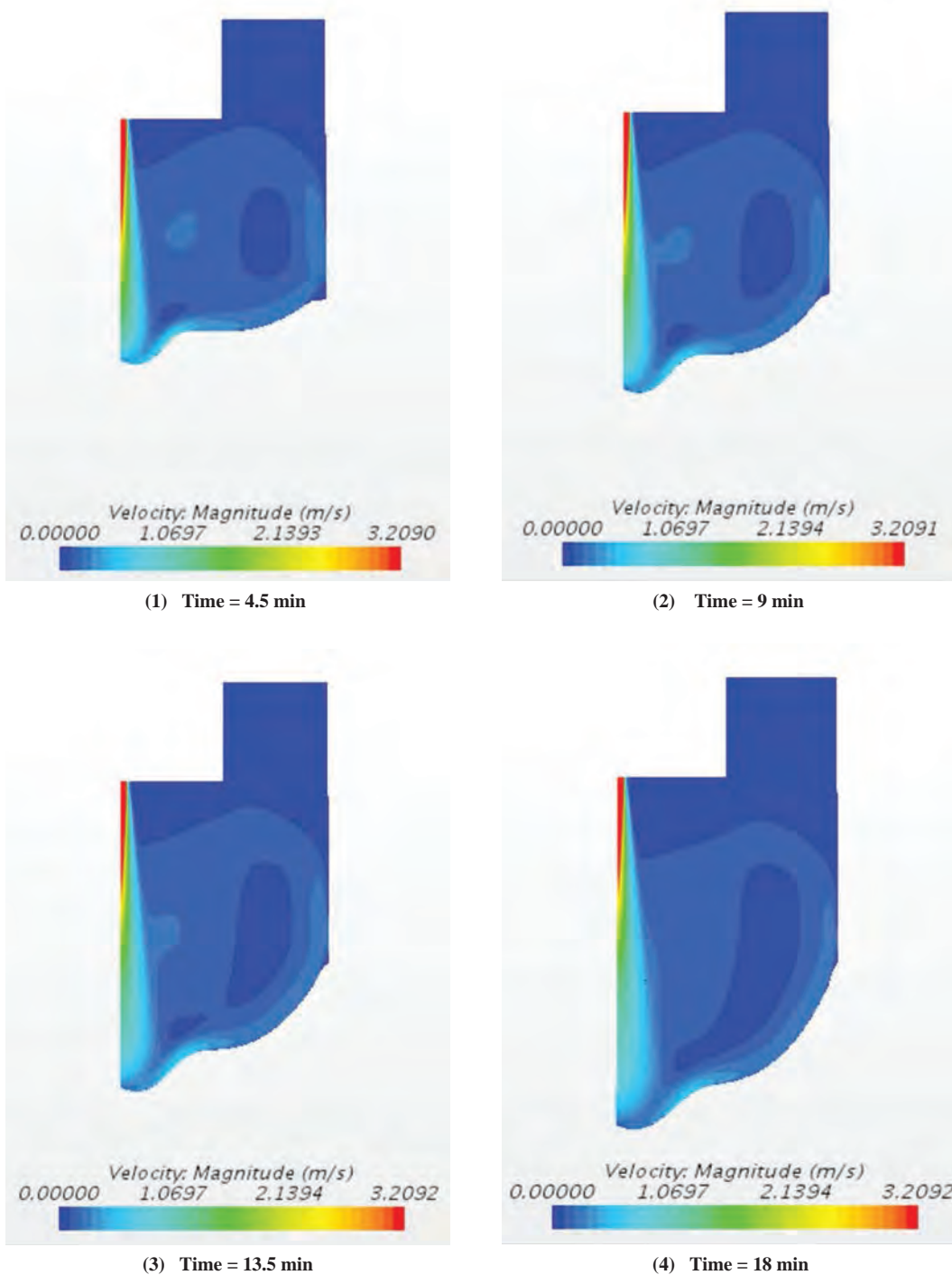
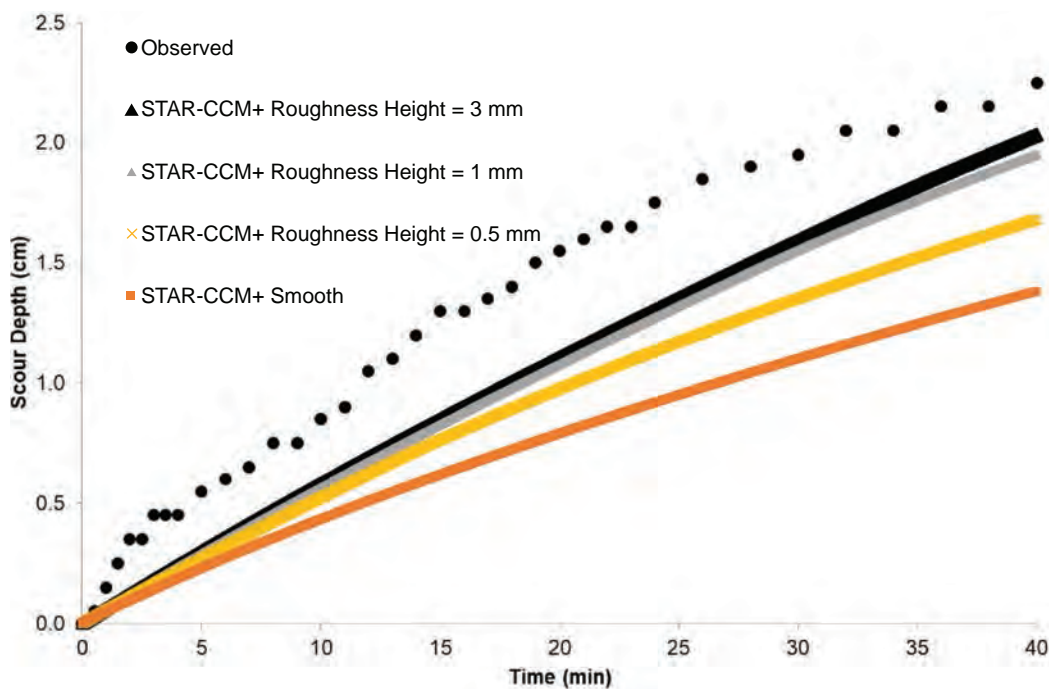


Figure 122. Example of moving boundary for Sand #1 with RH = 0.5 mm.



**Figure 123.** Scour depth versus time for observed JET and simulated JET for Sand #2.

soil–water interface. This underestimation was more pronounced when the RH was close to 0 mm (smooth surface). The actual average RH ( $D_{50}/2$ ) for Sample SE-2 was about 0.122 mm. At the end of the 40-min JET, the observed scour hole was 2.2 cm, while the STAR-CCM+ simulations (using the EFA erosion function assigned to the soil–water interface) resulted in an almost 1.4-cm scour hole in the smooth surface case. Figure 123 also shows that for higher RHs (near 3 mm), the results of the numerical simulations tended to be closer to the observation for Sample SE-2.

Figure 124 shows the results of the numerical simulations for Sample B-1 (4–6 ft) when the erosion function obtained from the EFA test on the exact same sample was used at the soil–water interface in the JET model. The observed JET results (black circles) were slightly overestimated through STAR-CCM+ when their erosion function obtained from the EFA was assigned to the soil–water interface. This overestimation was more pronounced when the RH was greater. The actual average RH ( $D_{50}/2$ ) for B-1 (4–6 ft) was about 0.0024 mm. At the end of the 40-min JET, the observed scour hole was 0.62 cm, while the STAR-CCM+ simulations (using the EFA erosion function assigned to the soil–water interface) resulted in an almost 1.0-cm scour hole in the smooth surface case.

Figure 125 shows the results of the numerical simulations for FHWA Sample 2 when the erosion function obtained from the EFA test on the exact same sample was used at the soil–water interface in the JET model. The observed JET results (black circles) were slightly underestimated through STAR-CCM+ when their erosion function obtained from the EFA was assigned to the soil–water interface. This underestimation was less observed when the RH was greater. The actual average RH ( $D_{50}/2$ ) for FHWA Sample 2 was about 0.0031 mm. At the end of the 40-min JET, the observed scour hole was 1.6 cm, while the STAR-CCM+ simulations (using the EFA erosion function assigned to the soil–water interface) resulted in an almost 0.8-cm scour hole in the case of a smooth surface.

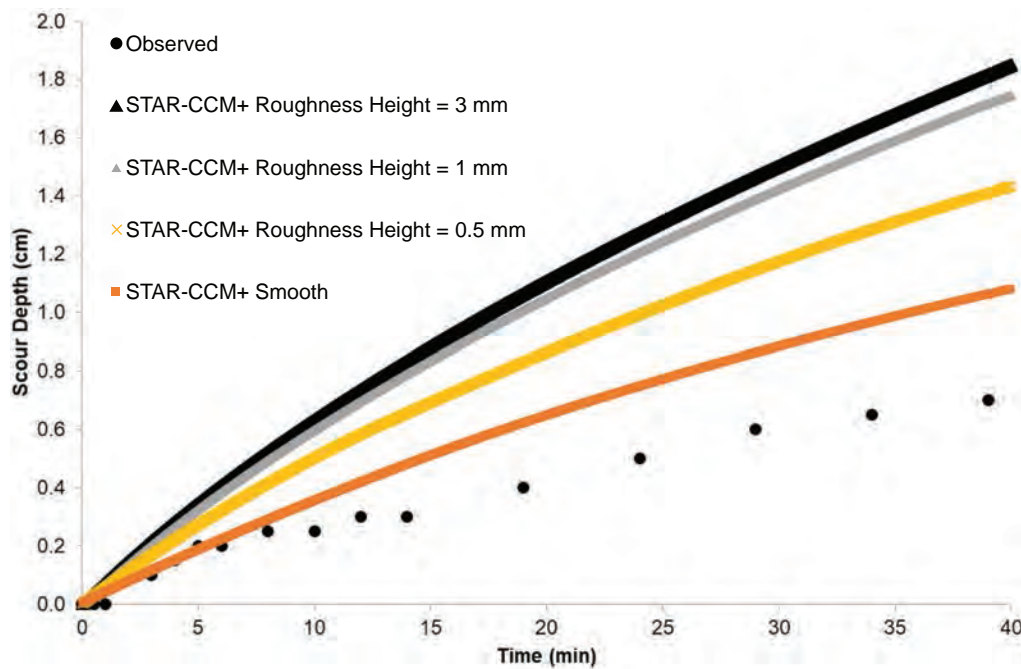


Figure 124. Scour depth versus time for observed JET and simulated JET for B-1 (4-6 ft).

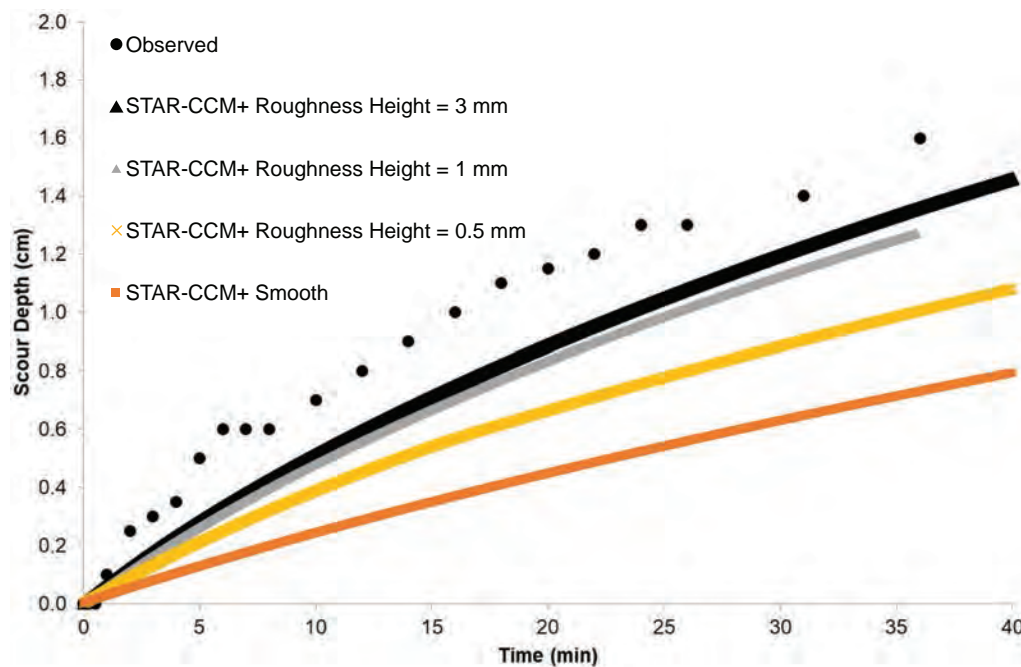


Figure 125. Scour depth versus time for observed JET and simulated JET for FHWA Sample 2.

### 6.2.3.2 EFA's Erosion Function on the HET

The approach outlined in Figure 117 was used to compare the results of the EFA with the HET on the same soil samples. The erosion process for two samples (one silt and one clayey sand) was simulated by using STAR-CCM+ after the EFA erosion function was assigned to the soil–water interface in the HET model. The name of these samples are SH-1 (sand sample) and Teton Sample (silt sample). The results of the numerical simulations were compared with the observations of the enlargement of the hole diameter during the HET for the same samples. As in the EFA–JET comparison, four different RHs were considered for each simulation: smooth, 0.5 mm, 1 mm, and 3 mm.

Figure 126 shows the results of the numerical simulations for SH-1 when the erosion function obtained from the EFA test on the exact same sample was used at the soil–water interface in the HET model. It was shown that the observed evolution of the average hole diameter during the HET would lie between the results of the STAR-CCM+ numerical simulations for the smooth to 0.5-mm RH surface. The actual average RH ( $D_{50}/2$ ) for SH-1 was about 0.1 mm. At the end of the 1,500-s (25-min) HET, the average diameter of the initial hole had become around 13 mm. The STAR-CCM+ simulations (using the EFA erosion function assigned to the soil–water interface) also resulted in an almost average 13-mm hole diameter in the case of an RH of 0.5 mm. It is worth mentioning that at the beginning of the test, when the longitudinal wall of the hole was smoother, the observed evolution of the hole’s diameter tended to better match the results of the numerical simulations for the case of a smooth surface.

Figure 127 shows an example of the numerical simulations in three time steps for SH-1. In this example, the soil–water interface was defined as a moving boundary. The velocity profile of the flow is also shown for each time step. The velocity for this example ranged between 0 and 3.75 m/s.

Figure 128 shows the results of the numerical simulations for the Teton sample when the erosion function obtained from the EFA test on the exact same sample was used at the soil–water interface in the HET model. The observed HET results (black circles) were underestimated through STAR-CCM+ when their erosion function obtained from the EFA was assigned to the

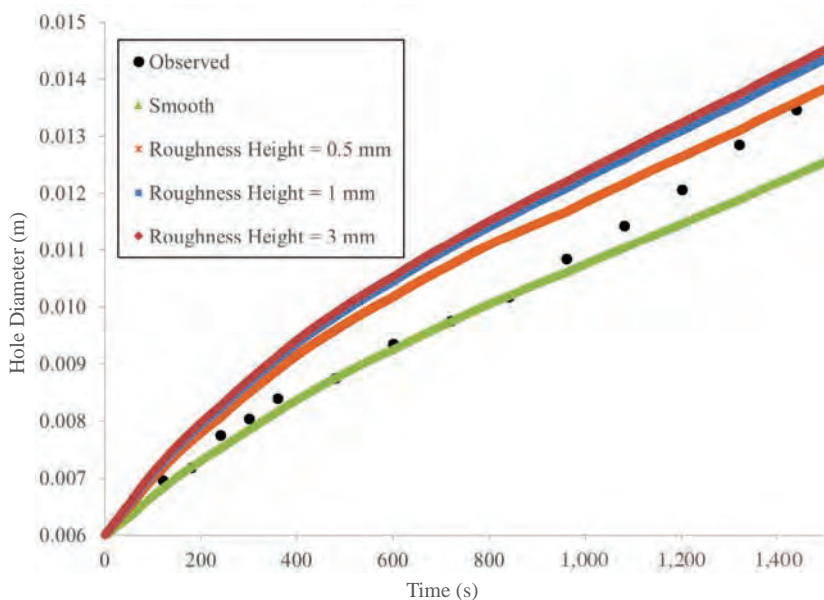


**Figure 126. Average hole diameter versus time for observed HET and simulated HET for SH-1.**

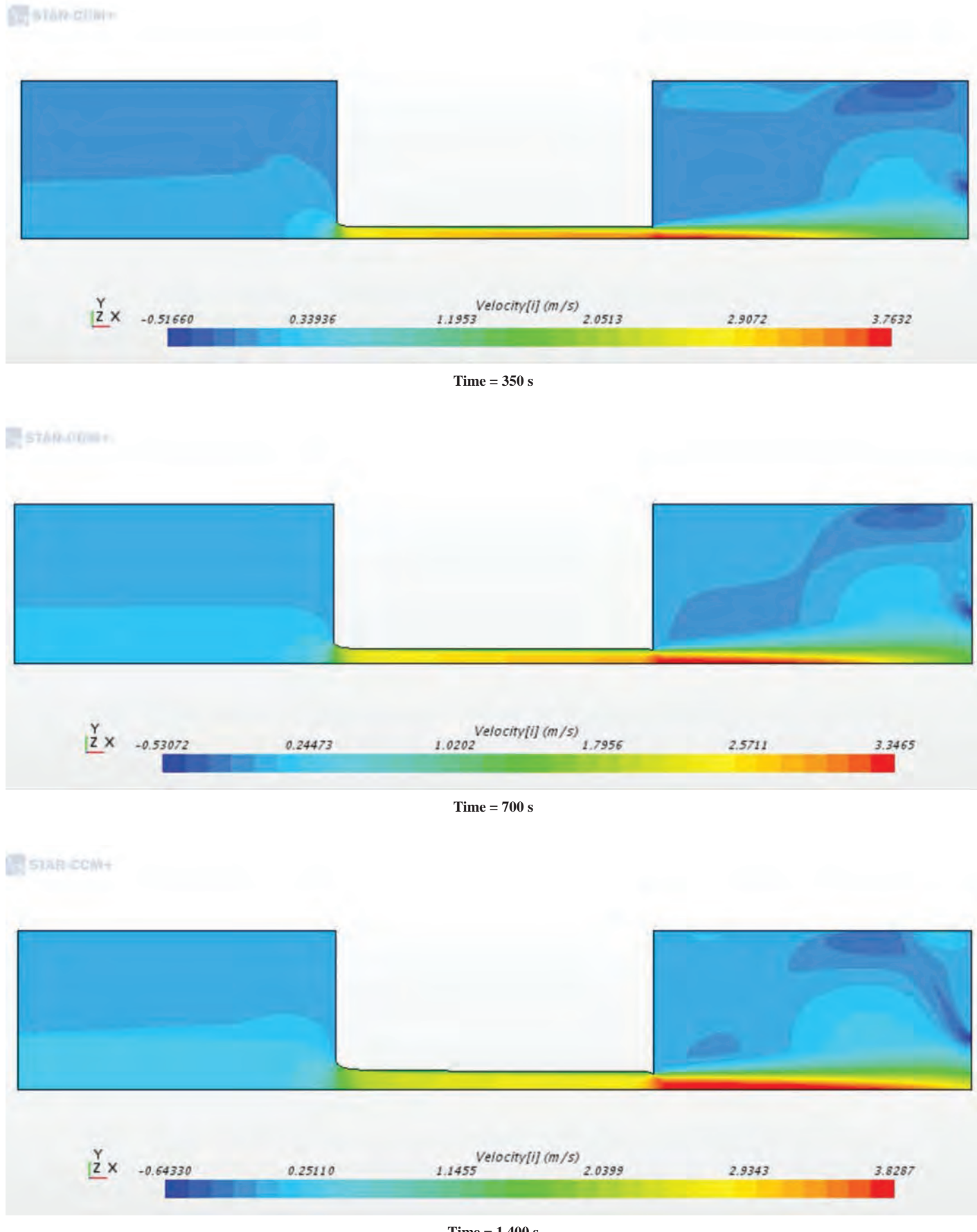
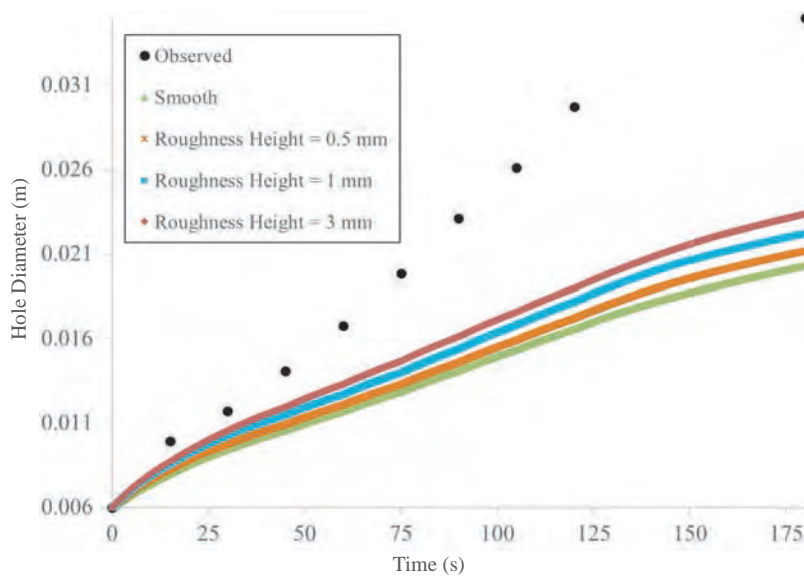


Figure 127. Example of moving boundary for SH-1 with RH = 0.5 mm.

## 164 Relationship Between Erodibility and Properties of Soils



**Figure 128.** Average hole diameter versus time for observed HET and simulated HET for the Teton sample.

soil–water interface. This underestimation was even more pronounced when the surface was smoother. The actual average RH ( $D_{50}/2$ ) for SH-1 was about 0.015 mm. At the end of the 175 (almost 3-min) HET, the diameter of the initial hole had become around 32 mm. However, the STAR-CCM+ simulations (using the EFA erosion function assigned to the soil–water interface) resulted in almost half of the enlargement in the hole diameter for the case of a smooth surface.

#### 6.2.3.3 EFA's Erosion Function on the BET

The approach outlined in Figure 117 was used to compare the results of the EFA with the BET on the same soil samples. The erosion process for one clay sample (CBH3) was simulated by using STAR-CCM+ after the EFA erosion function was assigned to the soil–water interface in the BET model. The results of the numerical simulations were compared with the observations of the borehole diameter enlargement at the depth of 8 to 10 ft during the BET for the same samples. Three different RHs were considered for each simulation: smooth, 0.5 mm, and 1 mm.

Figure 129 shows the results of the numerical simulations for CBH3 when the erosion function obtained from the EFA test on the exact same sample was used at the soil–water interface. Change in the RH did not make a noticeable difference in the diameter enlargement profile; therefore, only one line represents the scour profile in the three cases. In the numerical simulations, the initial borehole profile had to be considered as a straight vertical line (dashed line in Figure 129), whereas in reality, the borehole profile was very irregular. The difference between the initial borehole profiles in the numerical simulations and the actual BET field measurement resulted in different scour profiles after 20 min of testing; however, both results confirmed two common observations: (1) the maximum scour happens close to the bottom of the borehole ( $z = 9.8$  ft) and (2) the maximum diameter enlargement is close to 2 cm.

Figure 130 shows an example of the numerical simulations in three different time steps for the Riverside sample. In this example, the soil–water interface was defined as a moving boundary. The velocity profile of the flow is shown for each time step. The velocity for this example ranged between 0 and 3.75 m/s.

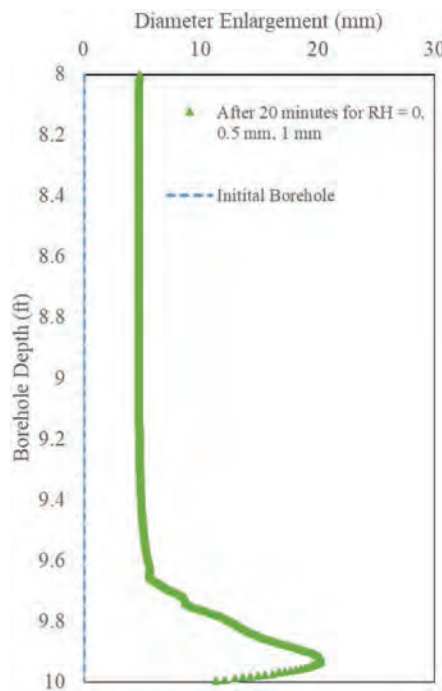


**Figure 129.** Results of BET numerical simulation after 20 min using the EFA's erosion function.

#### 6.2.4 Comparison and Uniformity

The results of the numerical simulations of the JET, HET, and BET are presented in the previous section. The goal, as discussed earlier, was to investigate how the JET, the HET, and the BET would react if the erosion function equation obtained from the EFA test on the same soil were assigned to the soil–water interface. Consequently, the results of numerical simulations were compared with the actual observations for each test. This section presents a summary of the findings.

Table 31 summarizes the numerical simulation results presented in Section 6.2.3. The findings show that the erosion function obtained from the EFA test for each sample can reasonably be used to produce a scour-versus-time plot similar to what the results of the JET, the HET, and the BET experiments would produce. However, the variety of interpretation techniques used in each test to obtain the shear stress in the soil–water interface leads to different erosion functions. Therefore, one must be aware of the interpretation techniques that each test uses to obtain the erosion function (erosion rate versus shear stress). It is also worth noting that, in the case of the HET results, the scour values actually refer to the average diameter of the drilled hole in the center of the sample.

## 166 Relationship Between Erodibility and Properties of Soils

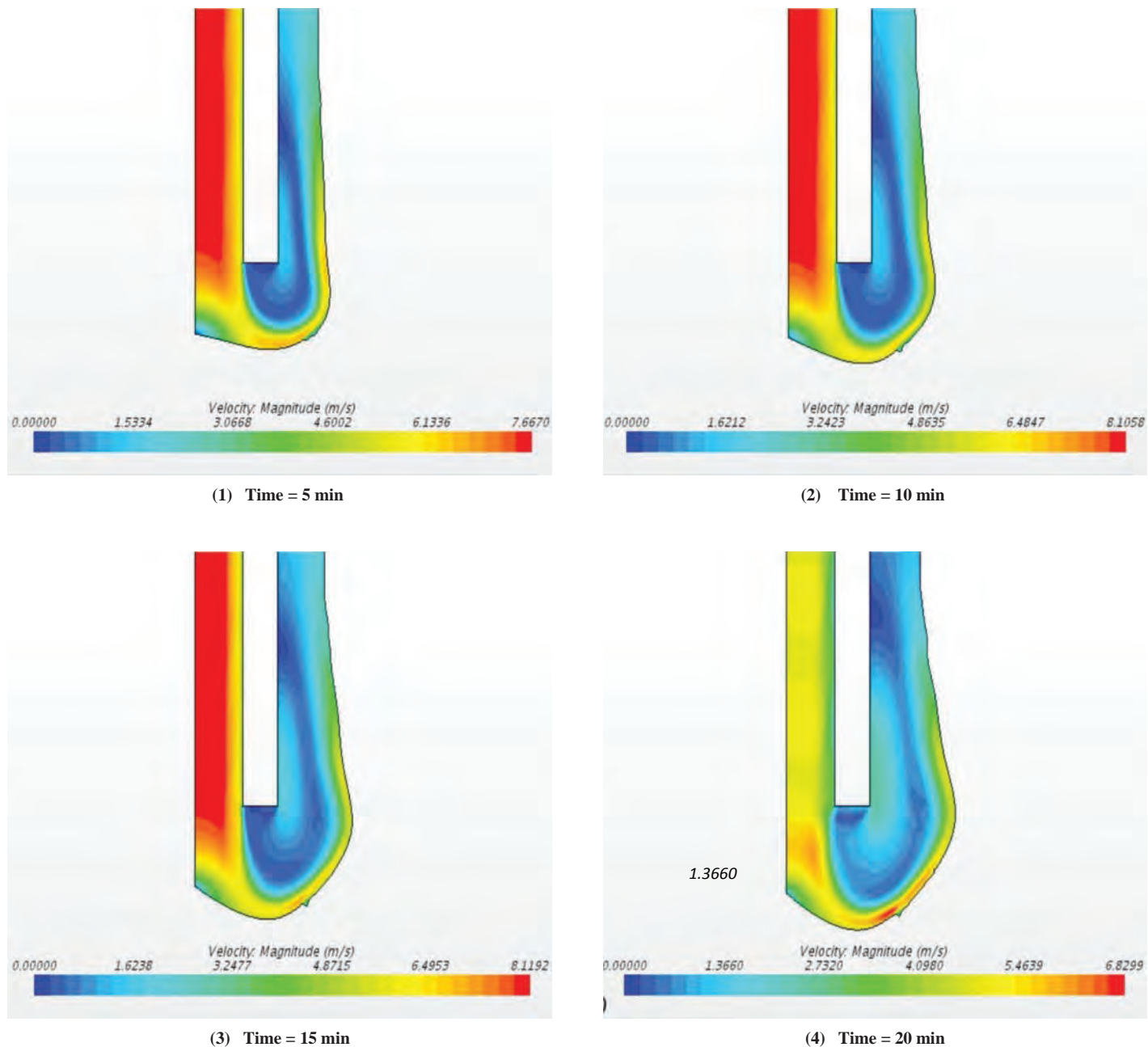


Figure 130. Example of moving boundary for the Riverside sample with RH = 0.5 mm.

**Table 31. Summary of the numerical simulation results.**

Sample Name	RH (mm)	Final Observed Scour (mm)	Final Scour Calculated Using EFA Erosion Function (mm)				Figure No.
			RH = 0 mm	RH = 0.5 mm	RH = 1 mm	RH = 3 mm	
<b>JET</b>							
Sand #1	0.14	40	40.8	43.5	43.1	48	121
Sand #2	0.122	23	13.8	16.8	20	20.3	123
B-1 (4-6)	0.0024	7	10.8	14.3	17.5	18.5	124
FHWA S2	0.0031	17	8	10.8	12.8	14.6	125
<b>HET</b>							
SH-1	0.1	13.4	12.5	13.5	14	14.2	126
Teton	0.015	35	19	20	21	22.5	128
<b>BET</b>							
Riverside	0.00038	20 <sup>a</sup>	20.31	20.35	20.40	-	129

<sup>a</sup>Scour values shown for BET are the maximum diameter enlargements in the 8- to 10-ft depth of the borehole.



## CHAPTER 7

# Development of Correlation Equations

The main goal of this research was to develop equations correlating soil erosion parameters defined in previous chapters (i.e., EC,  $E_v$ ,  $E_t$ ,  $v_c$ , and  $\tau_c$ ) with the common soil engineering properties. Since the majority of the erosion test data compiled in NCHRP-Erosion consists of data obtained from the erosion function apparatus (EFA), jet erosion test (JET), and hole erosion test (HET), and given that these tests are the main erosion tests, the regression analyses were focused on these three tests.

Section 7.1 of this chapter presents the quickest method to estimate the erosion resistance of a soil using the Unified Soil Classification System (USCS). In section 7.2, the plots of critical shear stress/velocity versus mean particle size (Chapter 3, Figure 31) are populated with the hundreds of EFA test data compiled in the NCHRP-Erosion spreadsheet, and new equations are developed. The final phase of this project consisted of two parallel statistical approaches: deterministic frequentist regression analysis and probabilistic (Bayesian) analysis. The goal was to reach the best potential fit between erodibility parameters and geotechnical properties of soils. The experimental design, optimization, model selection, and final results of the deterministic frequentist regression approach are comprehensively presented in Section 7.3. The results of the probabilistic (Bayesian) approach are presented in Section 7.4.

### 7.1 Determining Erosion Resistance Using the USCS

As discussed in Chapter 1, the erosion function charts are charts that show erosion categories in the  $\dot{z}$  versus  $v$  and the  $\dot{z}$  versus  $\tau$  space (see Chapter 1, Figure 3). These charts were conceptually designed to eliminate the need for site-specific erosion testing in the case of preliminary investigations and first order erosion analyses. The erosion function charts were first developed on the basis of EFA tests performed at Texas A&M University after Hurricane Katrina in 2005. The categories in the charts are zoned according to boundaries that originate at the critical velocity of the corresponding erosion category. Table 1 (Chapter 1) shows the values of  $\tau_c$  and  $v_c$  according to the erosion categories.

This section discusses the introduction of zones that represent different soil types on the erosion charts. These zones are characterized by using the USCS categories. The erodibility of coarse-grained soils is influenced mostly by gravity forces and, therefore, by the grain size. Since the USCS soil classification for coarse-grained soils is based primarily on grain size distribution, it is thought to have good potential for distinguishing between erosion categories of coarse-grained soils. For fine-grained soils, parameters such as soil structure, orientation of clay particles, and aging may be important in characterizing erodibility (Lefebvre et al. 1985; Partheniades 2009). It was also observed that plasticity, clay content, and soil activity play the most dominant roles in the erosion resistance of fine-grained soils. Plasticity parameters form

the basis of the USCS classification for fine-grained soils, and it is reasonable to think that the USCS categories therefore have good potential for distinguishing between erosion categories for fine-grained soils as well.

As discussed in the previous chapters, nearly 330 EFA test results compiled in the NCHRP-Erosion spreadsheet were divided into different USCS classification groups. Table 32 lists the USCS classification groups along with the number of EFA tests in each group.

Figure 131 through Figure 144 show the erosion functions of the samples plotted according to their USCS category in velocity space. The highlighted zones and the dashed red lines in each figure are proposed after consideration of the two following criteria:

1. The highlighted zone contains nearly 90% of the EFA test data for that specific USCS category.
2. The zone is adjusted (especially in cases in which there are not enough EFA data to make an inclusive conclusion) so that it is reasonably consistent with the previously proposed version of this chart by Briaud (2008).

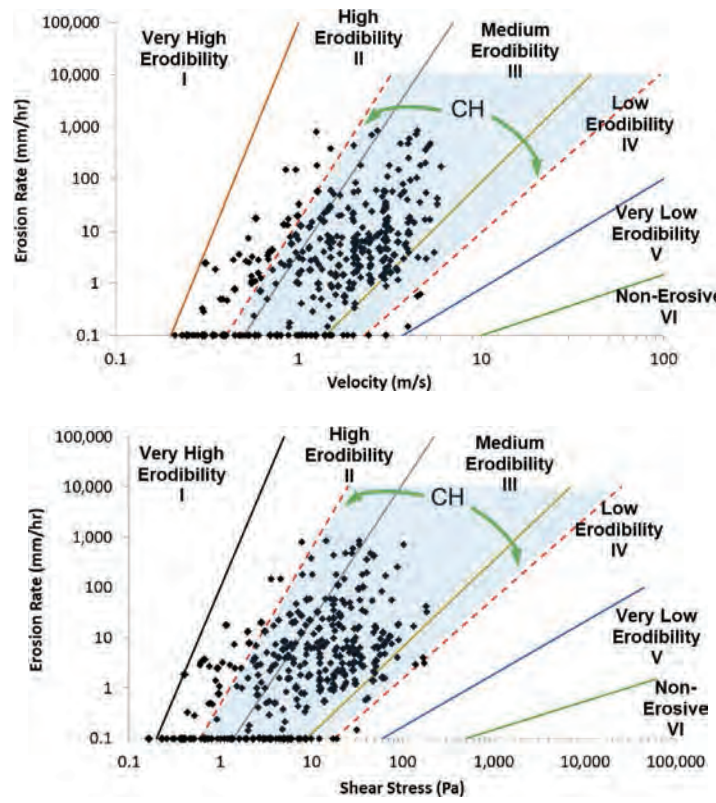
The erosion functions for soils with a given USCS category do not generally fall distinctly into a single erosion category but rather seem to plot approximately across two categories. Figure 145 summarizes all results into the two erosion category charts shown in Chapter 1, Figure 3.

Figure 145 can be used as a preliminary step to estimate the erodibility of any sample, using the USCS. The width of each box, which is associated with a USCS category, represents the zone in which 90% of the EFA results performed on such samples would fall in the erosion category chart. For instance, if the soil type of a location in an arbitrary geotechnical site is classified as SM (silty sand) according to the USCS, it would most likely (with close to 90% confidence based on the EFA results compiled in NCHRP-Erosion) fall into the Category II (high erodibility) on Figure 145. Similarly, a soil classified as CH (fat clay) would most likely fall into the Category III (medium erodibility), and a SP (poorly graded sand) would fall within the Categories I and II (very high to high erodibility). Evidently, the wider the box is for a USCS category, the more the variability of the erodibility is for that particular soil type. It must be noted that the boxes shown in Figure 145 apply solely to the erosion category and are not shown with respect to the erosion rate.

**Table 32. List of the USCS categories associated with the 329 samples.**

USCS Categories	Number of Samples
Fat clay (CH)	63
Lean clay (CL)	131
Poorly graded gravel (GP)	7
Clayey gravel (GC)	1
High-plasticity silt (MH)	14
Low-plasticity silt (ML)	24
Low-plasticity silty clay (ML-CL)	14
Clayey sand (SC)	28
Clayey silty sand (SC-SM)	8
Silty sand (SM)	17
Poorly graded sand (SP)	16
Poorly graded sand with clay (SP-SC)	3
Poorly graded sand with silt (SP-SM)	2
Well graded sand with silt (SW-SM)	1

## 170 Relationship Between Erodibility and Properties of Soils



**Figure 131.** Velocity–erosion rate and shear stress–erosion rate plots for fat clay (CH) soils.

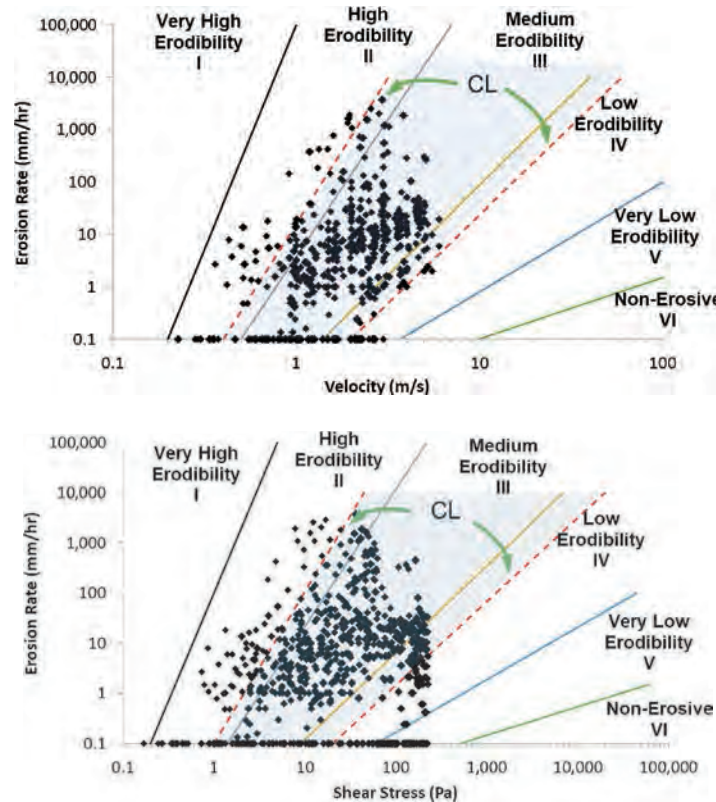


**Figure 132.** Velocity–erosion rate and shear stress–erosion rate plots for lean clay (CL) soils.

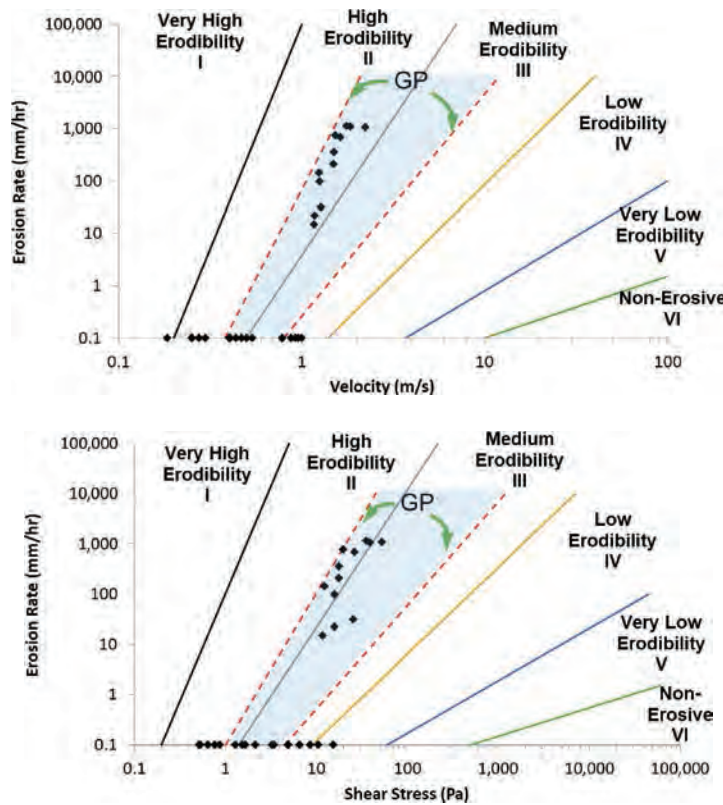


**Figure 133.** Velocity–erosion rate and shear stress–erosion rate plots for poorly graded gravel (GP) soils.

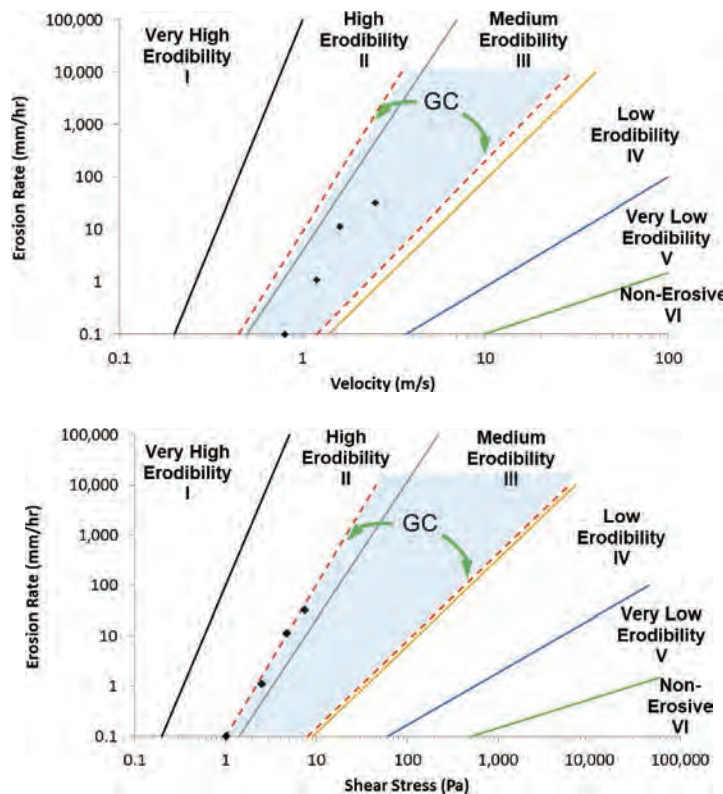


**Figure 134.** Velocity–erosion rate and shear stress–erosion rate plots for clayey gravel (GC) soils.

## 172 Relationship Between Erodibility and Properties of Soils

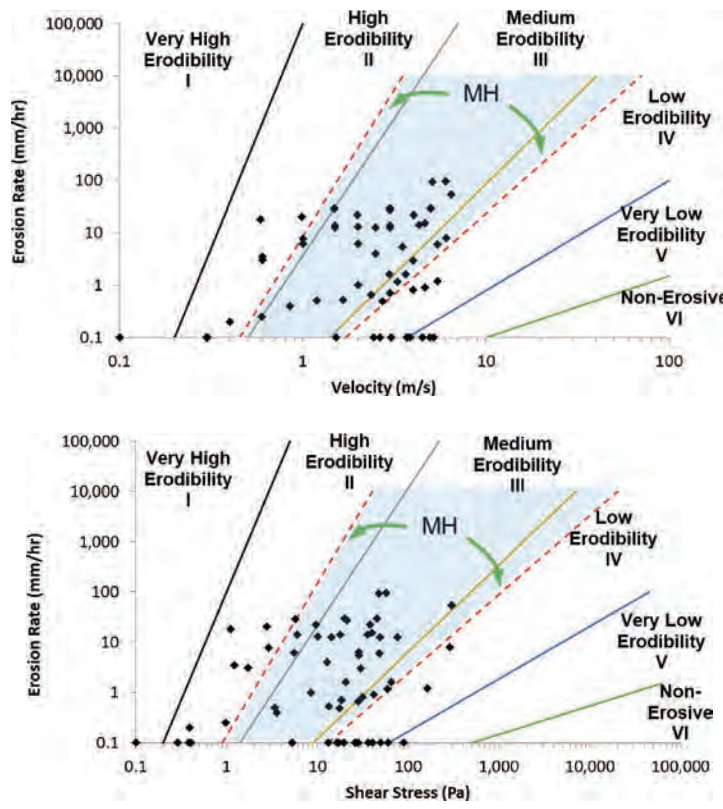


**Figure 135.** Velocity–erosion rate and shear stress–erosion rate plots for high-plasticity silt (MH) soils.

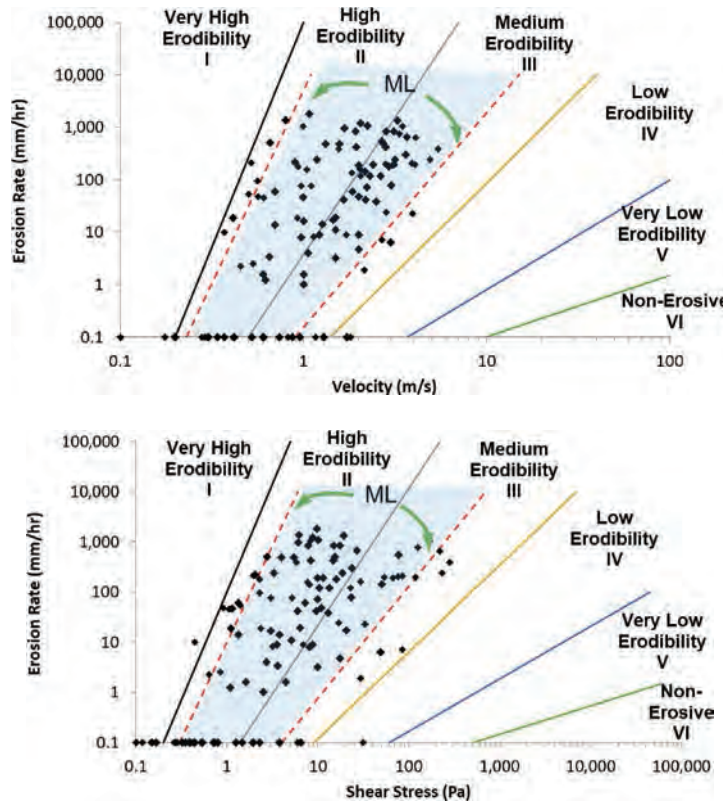


**Figure 136.** Velocity–erosion rate and shear stress–erosion rate plots for low-plasticity silt (ML) soils.

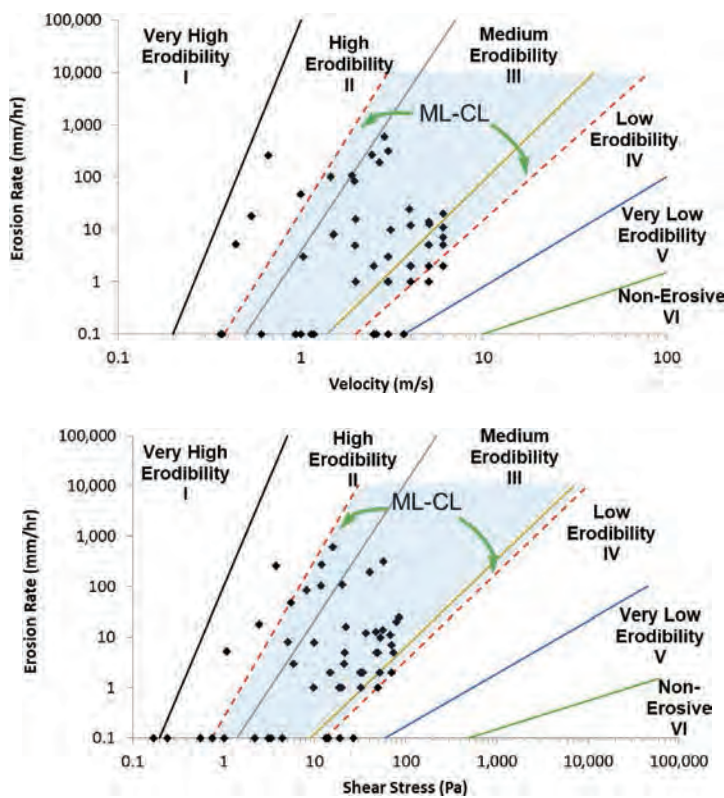


**Figure 137.** Velocity–erosion rate and shear stress–erosion rate plots for low-plasticity silty clay (ML-CL) soils.

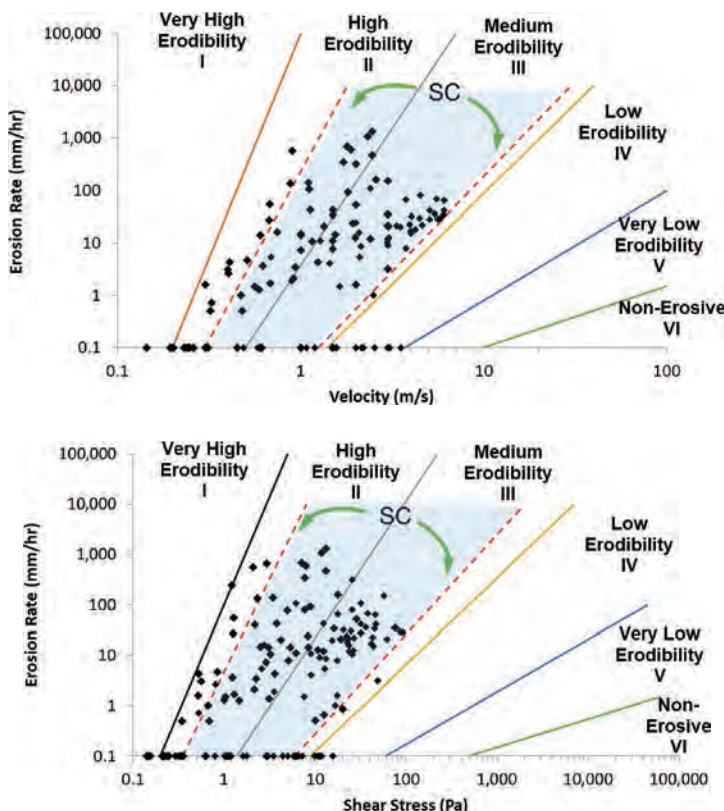


**Figure 138.** Velocity–erosion rate and shear stress–erosion rate plots for clayey sand (SC) soils.

## 174 Relationship Between Erodibility and Properties of Soils

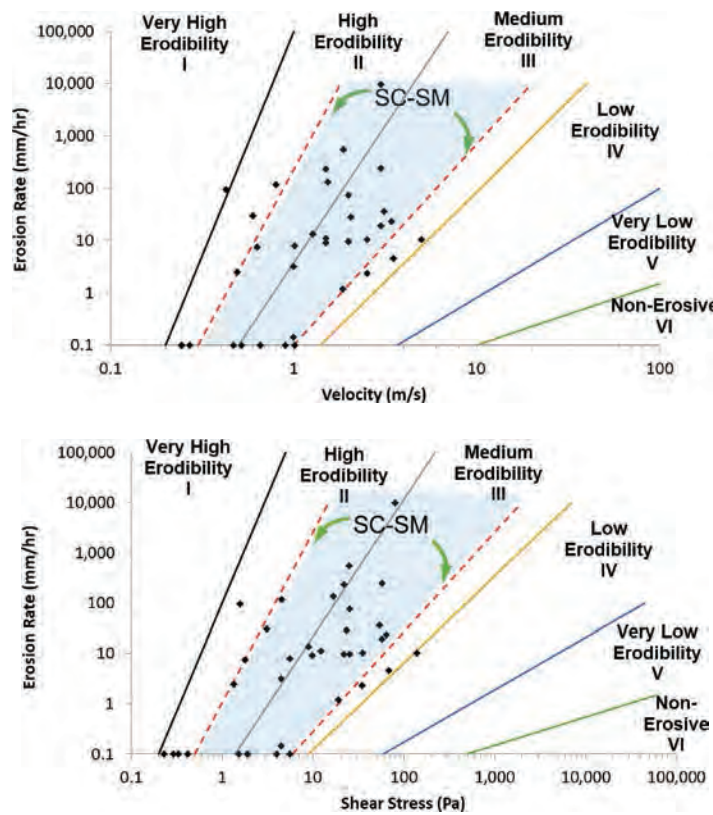


**Figure 139.** Velocity–erosion rate and shear stress–erosion rate plots for clayey silty sand (SC-SM) soils.

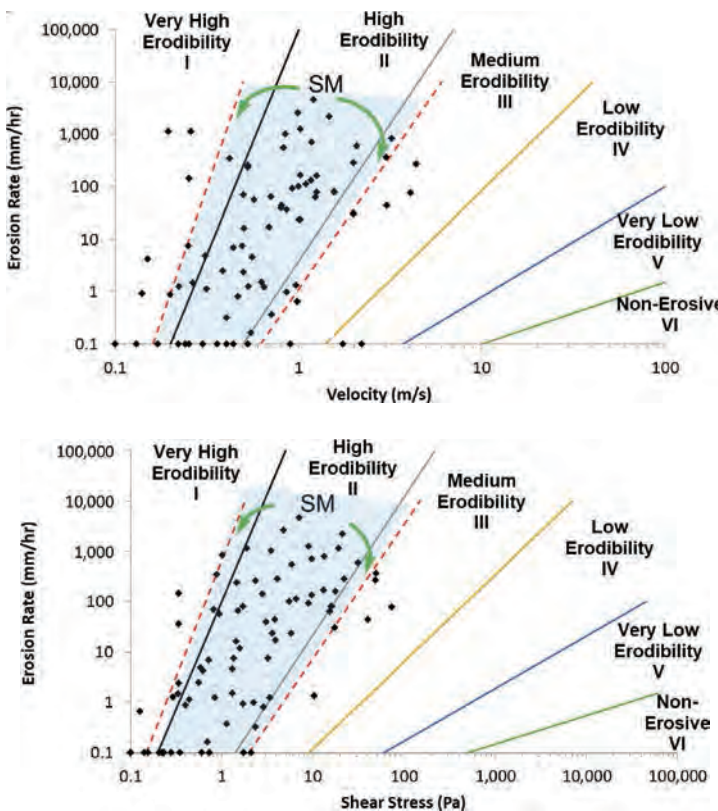


**Figure 140.** Velocity–erosion rate and shear stress–erosion rate plots for silty sand (SM) soils.

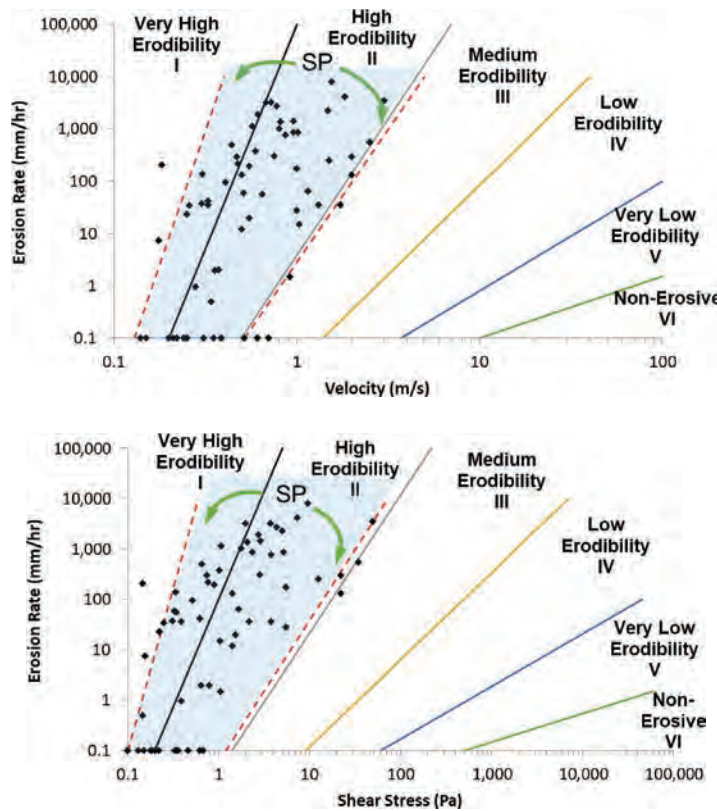


**Figure 141.** Velocity–erosion rate and shear stress–erosion rate plots for poorly graded sand (SP) soils.

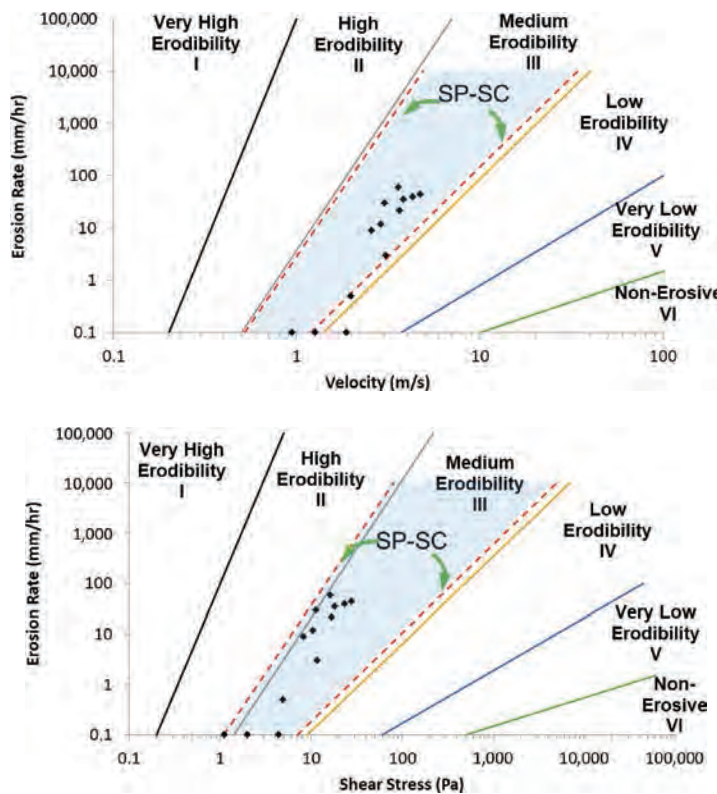


**Figure 142.** Velocity–erosion rate and shear stress–erosion rate plots for poorly graded sand with clay (SP-SC) soils.

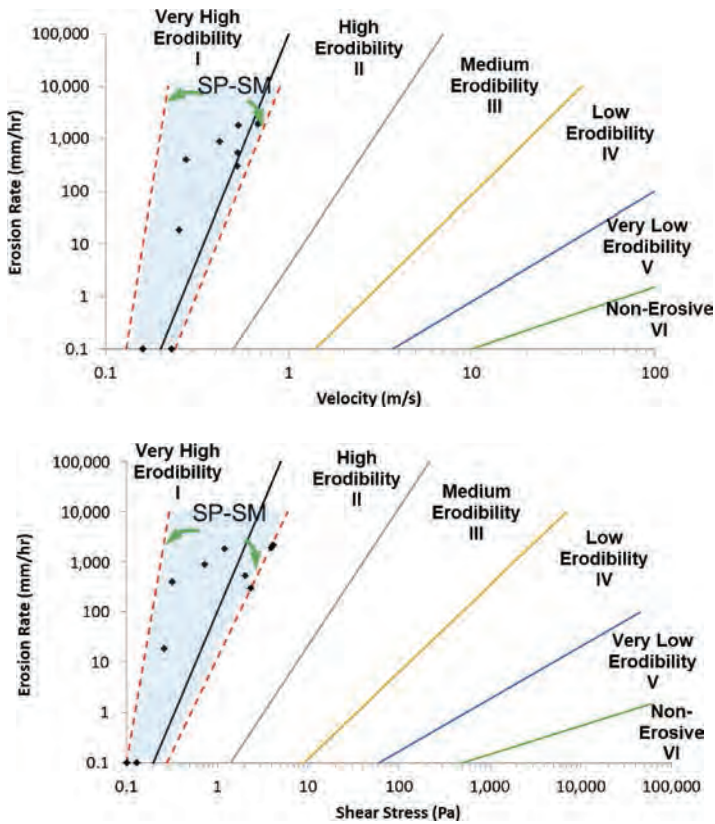


**Figure 143.** Velocity–erosion rate and shear stress–erosion rate plots for poorly graded sand with silt (SP-SM) soils.

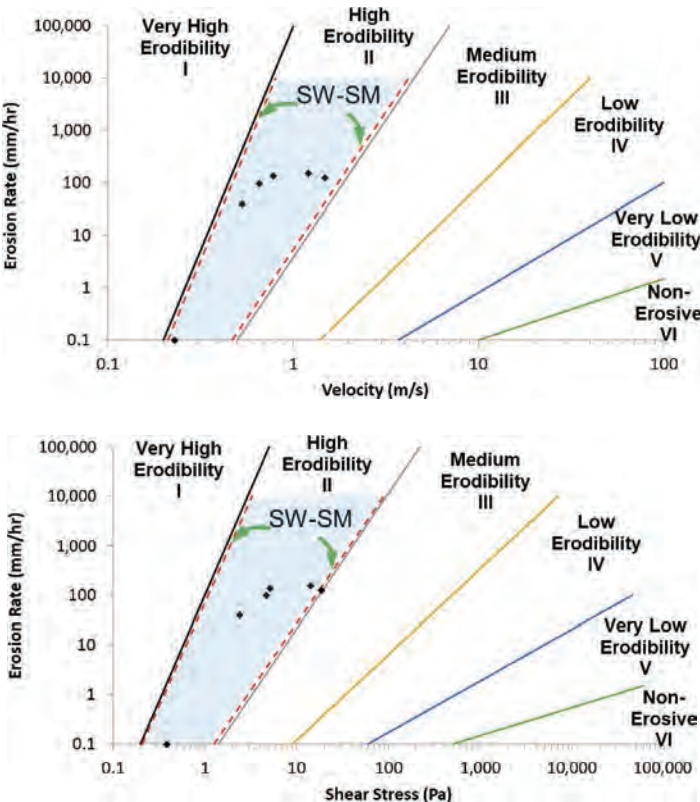


**Figure 144.** Velocity–erosion rate and shear stress–erosion rate plots for well-graded sand with silt (SW-SM) soils.

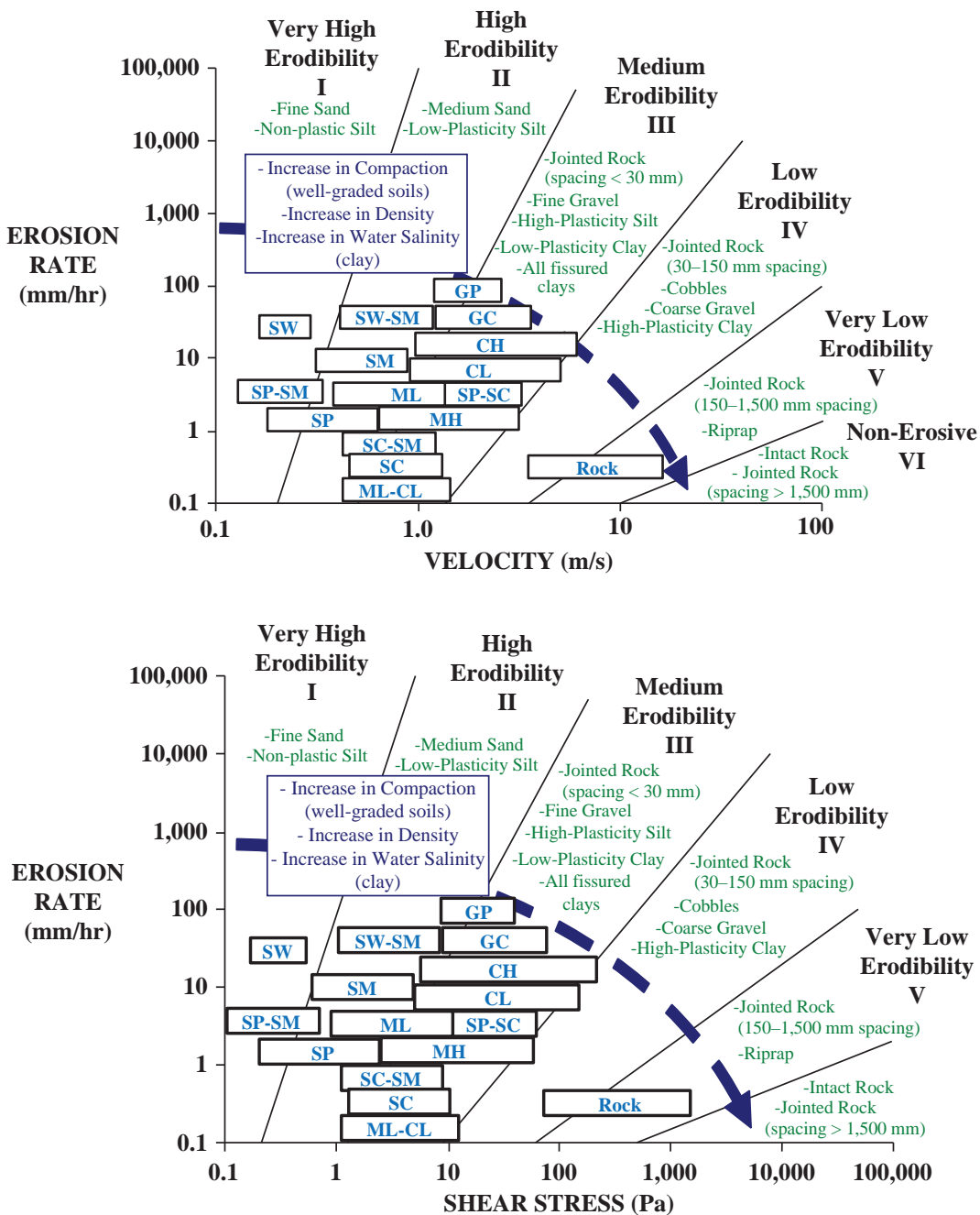


Figure 145. Erosion category charts with USCS symbols.

## 7.2 Plots of Critical Velocity and Shear Stress Versus Mean Particle Size

Briaud et al. (2001a) and Briaud et al. (2017b) proposed a set of equations to predict the critical velocity and critical shear stress of coarse-grained soils based on many EFA erosion tests performed at Texas A&M University. The number of data points used to generate the equations and corresponding plots were limited to few erosion test results. One of the goals of this NCHRP project was to update and possibly modify the older plots and equations using hundreds of new test results compiled in the NCHRP-Erosion spreadsheet.

It was observed that for soils with mean particle size larger than 0.3 mm, following relationships exist between the critical velocity/shear stress and mean particle size (Equations 61 and 62).

$$v_c (\text{m/s}) = 0.315(D_{50} (\text{mm}))^{-0.5} \quad (61)$$

$$\tau_c (\text{Pa}) = D_{50} (\text{mm}) \quad (62)$$

It was also concluded that for fine-grained soils there is no direct relationship between critical velocity/shear stress and the mean particle size. However, the data can be bracketed with an upper bound and a lower bound equation as follows (Equations 63 to 66).

$$\text{Upper bound: } v_c (\text{m/s}) = 0.07(D_{50} (\text{mm}))^{-1.45} \quad (63)$$

$$\text{Lower bound: } v_c (\text{m/s}) = 0.1(D_{50} (\text{mm}))^{-0.12} \quad (64)$$

$$\text{Upper bound: } \tau_c (\text{Pa}) = 0.06(D_{50} (\text{mm}))^{-2.3} \quad (65)$$

$$\text{Lower bound: } \tau_c (\text{Pa}) = 0.05(D_{50} (\text{mm}))^{-0.25} \quad (66)$$

One major difference of the updated plots with earlier versions (Figure 31) is that the boundary in which Equations 61 and 62 are valid is shifted to  $D_{50} = 0.3$  mm. In earlier versions of these plots, there was this wrong notion that for soils that are categorized as coarse-grained soils according to USCS classification system ( $D_{50} > 0.074$  mm), direct relationships between critical velocity/shear stress and  $D_{50}$  exist.

Figure 146 and Figure 147 show the scattered data for fine-grained soils with the defined upper and lower bound, as well as for the coarse-grained soils. These figures show clearly that mean particle size is not a sufficient parameter for soils that have a  $D_{50}$  smaller than 0.3 mm. Therefore, more parameters that specifically involve the plasticity behavior of fine-grained soils affect the critical velocity and critical shear stress of the soils. On the other hand, it is evident that once the soil has a relatively larger mean particle size ( $D_{50} > 0.3$  mm), the mean particle size becomes the predominant parameter in showing the erosion resistance. Equations 61 and 62 are strong equations for predicting the values of the critical velocity and the critical shear stress, respectively, for coarse sand to very large gravels.

## 7.3 Deterministic (Frequentist) Regression Analysis

As discussed in Chapter 1, the final phase of this project consisted of performing two parallel statistical approaches—frequentist regression and Bayesian inference—with the goal of reaching the best potential fits between erodibility parameters and geotechnical properties of soils.

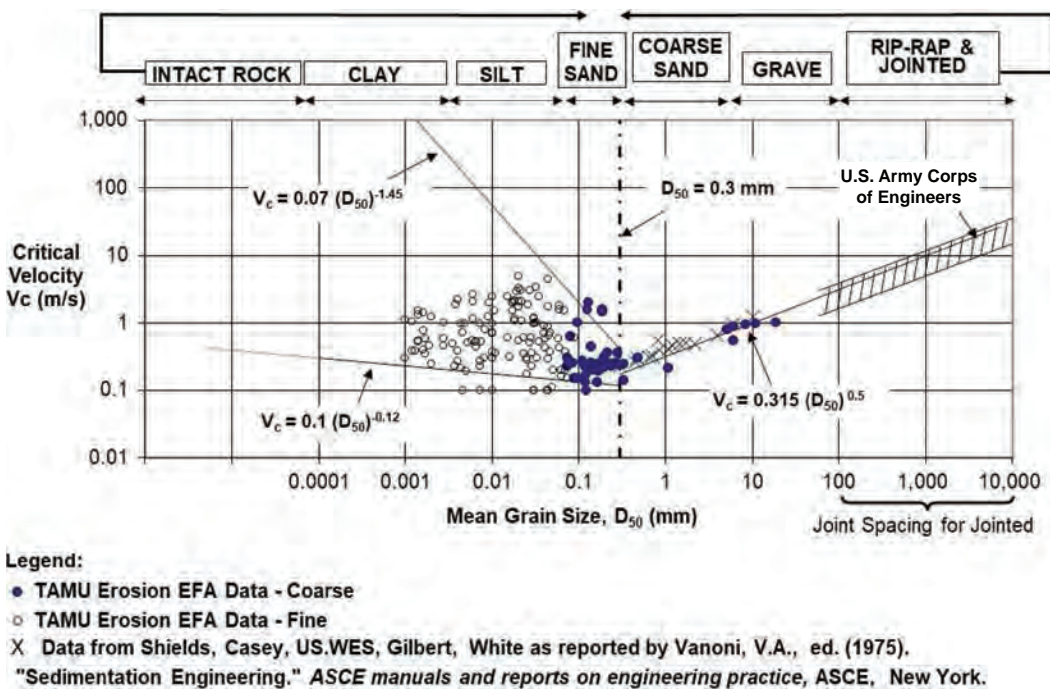


Figure 146. Mean particle size versus critical velocity.

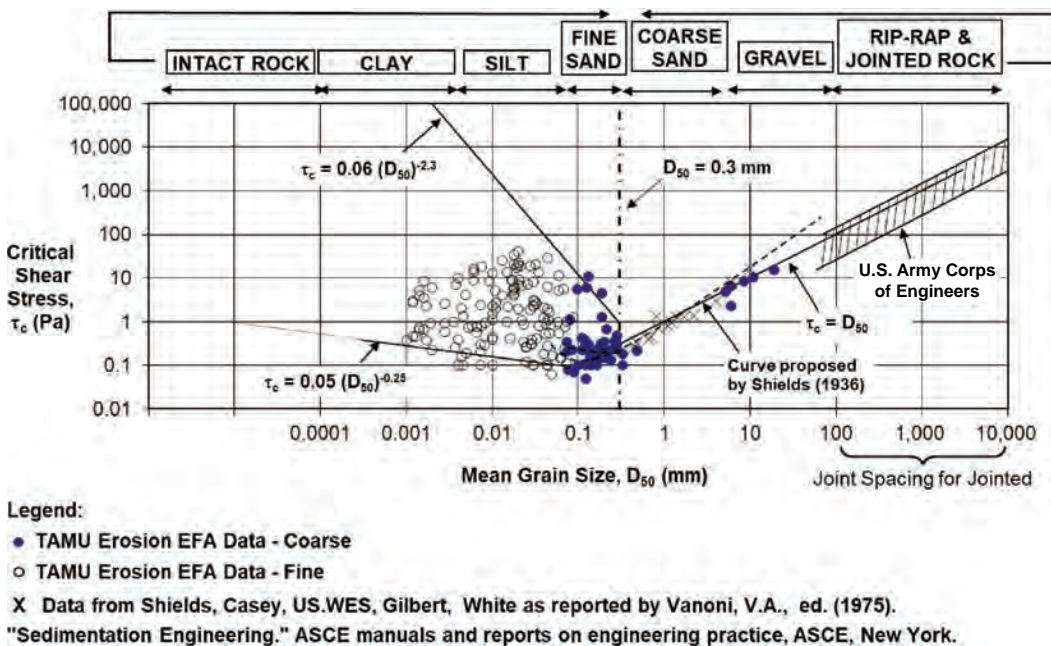


Figure 147. Mean particle size versus critical shear stress.

## 180 Relationship Between Erodibility and Properties of Soils

This section is dedicated to the step-by-step process of frequentist regression. This approach was implemented in three major steps:

1. First order statistical analysis,
2. Second order statistical analysis, and
3. Regression, optimization, and model selection.

### 7.3.1 First Order Statistical Analysis

The first step was to develop the first order statistical features. This step in statistics is known as a very crucial step to learn about all the details and complexities within the raw data themselves, before making any effort to generate relationships among them. The programming language of Python is used as the primary tool for this project and the software Stata and SPSS are used as alternative tools for overseeing the results. This step consisted of obtaining the primary statistical measures of our database (i.e., number of data points, range, quartiles, mean, median, mode, standard deviation, histograms, probability density functions, empirical cumulative density functions, etc.). As discussed earlier in Chapter 5, overall, there are 5 erodibility parameters (function variables). These parameters are the critical shear stress  $\tau_c$ , the critical velocity  $v_c$ , the initial slope  $E_v$  of the  $\dot{z}$  versus  $v$  curve, the initial slope  $E_\tau$  of the  $\dot{z}$  versus  $\tau$  curve, and the erosion category (EC) in the Briaud erosion chart (2013). Up to 16 geotechnical engineering parameters (model variables) were also collected for each sample. These parameters include

- Liquid limit, LL;
- Plastic limit, PL;
- Plasticity index, PI;
- Water content, WC;
- Undrained shear strength,  $S_u$ ;
- Total unit weight,  $\gamma$ ;
- Particle size at which 10% of the particles are finer than this size,  $D_{10}$ ;
- Particle size at which 30% of the particles are finer than this size,  $D_{30}$ ;
- Mean particle size,  $D_{50}$ ;
- Particle size at which 10% of the particles are finer than this size,  $D_{60}$ ;
- Coefficient of curvature,  $C_c$ ;
- Coefficient of uniformity,  $C_u$ ;
- Percentage finer than #200 sieve, PF;
- Specific gravity,  $G_s$ ;
- Percentage of clay (PC); and
- Soil activity (A).

Nearly 1,000 erosion tests compiled in NCHRP-Erosion were studied in different groups. Chapter 5 showed that NCHRP-Erosion incorporates more than 10 different erosion tests; however, the three major erosion tests—EFA, HET, and JET—were chosen to investigate the potential relationships further.

The study of the first order statistical features was started with the global data set (including all different tests and all soil types all together). Next, the data were divided on the basis of their erosion test type, and the first order statistical features for each subgroup were developed. Next, the data for each subgroup were again divided with regard to their soil type (coarse or fine) according to the USCS. The aforementioned groups are labeled and listed below:

1. TAMU/Global data set,
2. TAMU/Fine data set,

3. TAMU/Coarse data set,
4. EFA/Global data set,
5. EFA/Fine data set,
6. EFA/Coarse data set,
7. JET/Global data set,
8. JET/Fine data set,
9. JET/Coarse data set,
10. HET/Global data set,
11. HET/Fine data set, and
12. HET/Coarse data set.

A flowchart diagram of the grouping procedure is shown in Figure 148 below.

As shown in Figure 148, 12 data sets were obtained, and the first order statistics analyses were performed on each data set separately. The first order statistical features of all function and model variables were obtained for the aforementioned groups. Table 33 to Table 44 show these results.

As part of the first order statistical analyses of the parameters, and in order to learn about the statistical traits of each parameter, the histograms, probability density functions (PDFs) and empirical cumulative density functions (ECDFs) were plotted for each parameter. After that, multiple statistical distribution models were fitted to the actual data with the goal of finding the best representative distribution for each parameter in each group. Figure 149 shows an example of a histogram and PDF and ECDF plots for the critical velocities of the TAMU/Global group in the NCHRP-Erosion spreadsheet, which are fitted with many statistical distribution models, namely, normal, lognormal, exponential, Rayleigh, alpha, gamma, and beta. Figure 150 and Figure 151 show the same set of plots for the TAMU/Coarse and TAMU/Fine, respectively.

Results show that the critical velocity ( $v_c$ ) can be well represented by exponential distribution. The same approach was taken for all erodibility parameters (i.e.,  $v_c$ ,  $\tau_c$ ,  $E_v$ ,  $E_r$ , and EC) as well as all 12 major geotechnical properties (i.e., LL, PL, PI,  $\gamma$ , WC,  $S_u$ , PF,  $D_{50}$ ,  $C_u$ ,  $C_c$ , PC, and A). The goal was to identify the best statistical distribution models to best represent each parameter. The findings of this effort are not only very important to understanding each erodibility parameter and the geotechnical properties but are also a vital tool in performing frequentist regression and Bayesian inference.

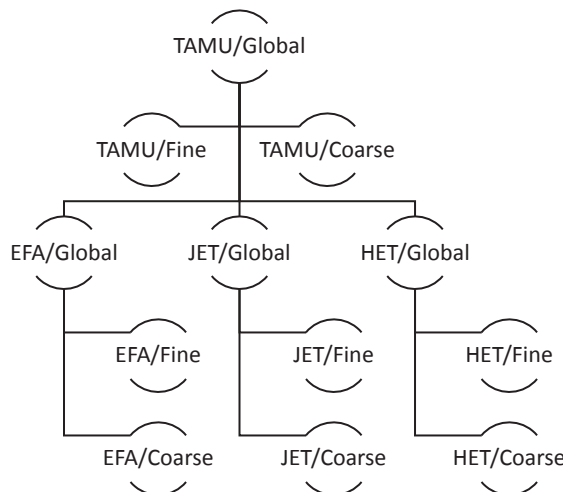


**Figure 148.** Flowchart diagram of the grouping procedure.

**Table 33.** First order statistics results for NCHRP-Erosion spreadsheet: TAMU/Global data set.

	<b>EC</b>	<b><math>E_v</math> (mm-s/ m-h)</b>	<b><math>E_\tau</math> (mm/ h-Pa)</b>	<b><math>v_c</math> (m/s)</b>	<b><math>\tau_c</math> (Pa)</b>	<b>LL (%)</b>	<b>PL (%)</b>	<b>PI (%)</b>	<b><math>\gamma</math> (kN/m<sup>3</sup>)</b>	<b>WC (%)</b>	<b><math>S_u</math> (kPa)</b>	<b>PF (%)</b>	<b><math>D_{50}</math> (mm)</b>	<b><math>C_u</math></b>	<b><math>C_c</math></b>	<b>PC (%)</b>
Count	831	314	810	319	807	675	674	676	729	729	244	683	483	172	172	584
Mean	2.86	129.07	88.18	0.90	64.33	43.14	19.93	23.17	19.17	22.15	51.97	66.24	0.21	64.85	4.07	26.58
SD	0.78	565.28	522.91	0.87	153.28	22.48	7.46	19.41	2.13	17.87	39.65	26.72	1.18	102.68	8.85	19.50
Min.	0.75	0.07	0	0.1	0.0001	14.5	6.3	1.5	11.4	1.02	2	0	0.0009	1.29	0.11	0
25%	2.5	3.2875	0.3425	0.29	0.56	30	15	11.8	18.1	14.2	20	42.95	0.0058	4.7949	1.0641	13
50%	3	8.885	1.425	0.6	5.7	37.6	19	21.9	19.2	18.5	38	75	0.0302	30	1.95541	20
75%	3.25	29.27	7.2275	1.065	32.255	48.2	23	30	20.3	26.88	76.05	87.165	0.13	49	3.4087	39.925
Max.	5.5	6300	6690.26	5.2	1158	264.1	77	238.8	25.13	286.7	150.7	100	19	850	82	96.39

**Table 34.** First order statistics results for NCHRP-Erosion spreadsheet: TAMU/Fine data set.

	<b>EC</b>	<b><math>E_v</math> (mm-s/ m-h)</b>	<b><math>E_\tau</math> (mm/ h-Pa)</b>	<b><math>v_c</math> (m/s)</b>	<b><math>\tau_c</math> (Pa)</b>	<b>LL (%)</b>	<b>PL (%)</b>	<b>PI (%)</b>	<b><math>\gamma</math> (kN/m<sup>3</sup>)</b>	<b>WC (%)</b>	<b><math>S_u</math> (kPa)</b>	<b>PF (%)</b>	<b><math>D_{50}</math> (mm)</b>	<b><math>C_u</math></b>	<b><math>C_c</math></b>	<b>PC (%)</b>
Count	612	239	595	243	594	570	570	572	537	556	211	502	328	91	91	421
Mean	3.03	29.86	16.64	0.95	81.25	44.53	19.91	24.61	19.08	24.83	53.34	80.23	0.02	38.27	3.30	32.58
SD	0.74	87.38	105.43	0.87	173.24	23.28	7.48	20.19	2.15	19.06	40.12	13.25	0.02	90.46	8.64	19.66
Min.	0.75	0.07	0	0.1	0.01	15.2	6.3	1.5	11.4	7.51	3.3	48	0.0009	1.29	0.28	0
25%	2.5	2.775	0.22	0.34	0.9225	30	15	13	17.9	16.625	20	75	0.0025	5.41026	0.96	18.3
50%	3	6.56	0.79	0.7	6.125	39	18.8	22	19	20.75	39.2	81	0.016	30	1.57035	29.7
75%	3.5	16.915	3.005	1.155	64.8225	51	23	31	20.2	29.215	77.5	90.075	0.031	49	2.04082	48
Max.	5.5	761.8	1718.02	5.2	1158	264.1	77	238.8	25.13	286.7	150.7	100	0.075	850	82	96.39

**Table 35.** First order statistics results for NCHRP-Erosion spreadsheet: TAMU/Coarse data set.

EC	$E_v$ (mm-s/ m-h)	$E_\tau$ (mm/ h-Pa)	$v_c$ (m/s)	$\tau_c$ (Pa)	LL (%)	PL (%)	PI (%)	$\gamma$ (kN/m <sup>3</sup> )	WC (%)	$S_u$ (kPa)	PF (%)	$D_{50}$ (mm)	$C_u$	$C_c$	PC (%)	
Count	219	75	215	76	213	105	104	104	192	173	33	181	155	81	81	163
Mean	2.37	445.21	286.18	0.73	17.16	35.55	20.07	15.28	19.42	13.52	43.22	27.44	0.62	94.72	4.93	11.09
SD	0.67	1092.66	974.27	0.85	48.34	15.49	7.42	11.69	2.05	9.06	35.84	12.54	2.03	107.80	9.05	5.69
Min.	1	0.35	0.05	0.1	0.0001	14.5	7.7	2	12.3	1.02	2	0	0.074	1.42857	0.11	0
25%	2	8.13	2.46	0.23	0.23	24.5	16	5.7	18.63	9.7	22	22	0.13	3.88235	1.125	7
50%	2.5	30.79	9	0.325	3.46	36	19	15.05	19.6	11.6	32	29	0.22	38	3.4087	13
75%	2.75	296.67	109.05	0.9075	13.8	39	22.975	21.25	20.5	15.8	45.49	35.14	0.29	230	6.94901	15
Max.	4.25	6300	6690.26	4	513	90.6	43	56.8	24.29	82	132	65	19	500	57.12	29

**Table 36.** First order statistics results for NCHRP-Erosion spreadsheet: EFA/Global data set.

EC	$E_v$ (mm-s/ m-h)	$E_\tau$ (mm/ h-Pa)	$v_c$ (m/s)	$\tau_c$ (Pa)	LL (%)	PL (%)	PI (%)	$\gamma$ (kN/m <sup>3</sup> )	WC (%)	$S_u$ (kPa)	PF (%)	$D_{50}$ (mm)	$C_u$	$C_c$	PC (%)	
Count	333	307	330	312	331	275	274	274	256	267	190	274	193	66	66	145
Mean	2.60	105.67	46.45	0.92	4.25	47.70	20.82	26.85	19.20	27.01	46.24	69.48	0.38	44.42	3.65	21.15
SD	0.70	476.80	285.49	0.87	7.92	27.67	9.34	24.62	2.77	14.41	37.20	31.72	1.85	125.83	12.20	19.74
Min.	0.75	0.07	0.01	0.1	0.05	14.5	6.3	1.5	12.3	1.02	2	0	0.001	1.32	0.11	0
25%	2.25	3.205	0.44	0.3	0.335	32.1	14.3	13	17.55	17.945	19	46.55	0.0082	3.2867	0.86595	5
50%	2.5	8.02	1.615	0.615	1.6	40.9	18.5	22.9	18.91	25.25	32.6	84.3	0.029	5.66536	1.11743	18.06
75%	3	26.725	5.74	1.0925	5.045	58.9	24.4	34.3	20.425	31.2	63.125	95.23	0.088	15	1.47322	28.88
Max.	5.5	6300	4470.97	5.2	88.35	264.1	77	238.8	25.13	88.1	143.5	100	19	850	82	96.39

**Table 37.** First order statistics results for NCHRP-Erosion spreadsheet: EFA/Fine data set.

	<b>EC</b>	$E_v$ (mm-s/ m-h)	$E_\tau$ (mm/ h-Pa)	$v_c$ (m/s)	$\tau_c$ (Pa)	LL (%)	PL (%)	PI (%)	$\gamma$ (kN/m <sup>3</sup> )	WC (%)	$S_u$ (kPa)	PF (%)	$D_{50}$ (mm)	$C_u$	$C_c$	PC (%)
Count	256	235	253	239	254	232	231	231	192	213	161	203	140	35	35	104
Mean	2.71	30.21	11.18	0.97	4.73	48.89	20.70	28.16	19.47	29.66	47.42	86.24	0.02	36.54	3.49	26.02
SD	0.65	88.10	46.26	0.87	8.68	28.56	9.14	25.80	2.81	13.36	37.73	13.78	0.02	143.54	13.67	20.92
Min.	0.75	0.07	0.01	0.1	0.06	15.2	6.3	1.5	13.87	9.8	3.3	48	0.001	1.32	0.44462	0
25%	2.5	2.665	0.36	0.34	0.435	34.225	14.4	15.35	17.6975	21.7	19	78.9	0.00567	3.97077	0.89663	7.5
50%	2.75	6.17	1.15	0.7	1.89	41	18.2	23.2	19.1	27.75	33.8	90.5	0.0172	5.71429	1.06786	21.98
75%	3	16.915	3.7	1.165	5.1075	59.25	24.2	35	20.625	32.9	67	97.3	0.03155	8.06818	1.35425	33.775
Max.	5.5	761.8	478	5.2	88.35	264.1	77	238.8	25.13	88.1	143.5	100	0.088	850	82	96.39

**Table 38.** First order statistics results for NCHRP-Erosion spreadsheet: EFA/Coarse data set.

	<b>EC</b>	$E_v$ (mm-s/ m-h)	$E_\tau$ (mm/ h-Pa)	$v_c$ (m/s)	$\tau_c$ (Pa)	LL (%)	PL (%)	PI (%)	$\gamma$ (kN/m <sup>3</sup> )	WC (%)	$S_u$ (kPa)	PF (%)	$D_{50}$ (mm)	$C_u$	$C_c$	PC (%)
Count	77	72	77	73	77	43	43	43	64	54	29	71	53	31	31	41
Mean	2.22	351.95	162.34	0.75	2.69	41.29	21.49	19.81	18.39	16.54	39.72	21.58	1.32	53.32	3.83	8.77
SD	0.75	934.81	572.69	0.86	4.32	21.40	10.45	15.34	2.50	13.72	34.00	15.31	3.37	103.93	10.51	7.57
Min.	1	0.35	0.08	0.1	0.05	14.5	7.7	2	12.3	1.02	2	0	0.074	1.63	0.11	0
25%	1.75	7.155	1.81	0.23	0.21	24.5	13	6.1	16.67	9.6775	15.7	8.5	0.12	2.455	0.85932	1
50%	2	24.455	4.8	0.34	0.34	38	19.3	15.1	18.63	15.6	31.4	20	0.17	4.87805	1.125	8.5
75%	2.5	247.048	20.97	0.93	4.4	54.6	28.5	32.45	20.2	19.75	45.49	35.07	0.28	57.725	1.64528	15
Max.	4	6300	4470.97	4	20.03	90.6	43	56.8	23.3	82	132	50.36	19	500	57.12	25

**Table 39.** First order statistics results for NCHRP-Erosion spreadsheet: HET/Global data set.

EC	$E_v$ (mm-s/ m-h)	$E_\tau$ (mm/ h-Pa)	$v_c$ (m/s)	$\tau_c$ (Pa)	LL (%)	PL (%)	PI (%)	$\gamma$ (kN/m <sup>3</sup> )	WC (%)	$S_u$ (kPa)	PF (%)	$D_{50}$ (mm)	$C_u$	$C_c$	PC (%)	
Count	232	0	231	0	231	185	185	185	233	233	21	221	154	53	53	221
Mean	3.40	na	28.49	na	194.50	41.58	19.59	21.99	19.14	18.43	61.10	63.18	0.10	91.86	4.25	28.41
SD	0.70	na	132.72	na	237.10	18.41	6.00	15.17	1.56	8.32	38.76	21.99	0.11	92.71	2.33	18.91
Min.	1	na	0	na	0.1	20	11	2.9	13.9	7.5	4.3	22	0.001	1.29	0.48	2
25%	3	na	0.13	na	15.305	30	15	15	18.3	12.56	43.1	42	0.0025	30	2.04082	13
50%	3.5	na	0.64	na	89.75	36	19	20	19.3	16.2	57.4	73.4	0.038	38	3.4087	24.84
75%	4	na	3.31	na	314.98	42	22	24	20.1	21.2	71.8	80.06	0.22	230	6.80272	44.75
max	4.75	na	1684.04	na	1158	148.1	33	125.8	22.9	44	143.5	100	0.29	230	7.74	77

Note: na = not applicable.

**Table 40.** First order statistics results for NCHRP-Erosion spreadsheet: HET/Fine data set.

EC	$E_v$ (mm-s/ m-h)	$E_\tau$ (mm/ h-Pa)	$v_c$ (m/s)	$\tau_c$ (Pa)	LL (%)	PL (%)	PI (%)	$\gamma$ (kN/m <sup>3</sup> )	WC (%)	$S_u$ (kPa)	PF (%)	$D_{50}$ (mm)	$C_u$	$C_c$	PC (%)	
Count	169	0	168	0	168	169	169	169	170	170	21	158	92	25	25	158
Mean	3.68	n/a	2.10	n/a	254.35	42.12	19.64	22.48	18.73	20.91	61.10	75.44	0.02	29.30	3.49	34.76
SD	0.58	n/a	7.81	n/a	248.77	19.18	6.27	15.79	1.46	8.28	38.76	11.24	0.02	19.33	2.66	18.84
Min.	1	n/a	0	n/a	4.65	20	11	2.9	13.9	7.51	4.3	51	0.001	1.29	0.48	2
25%	3.25	n/a	0.0775	n/a	57.795	30	15	12	18	15.085	43.1	68.8	0.002	2.9	1.14	18.9
50%	3.75	n/a	0.29	n/a	192.93	36	19	22	18.87	18.5	57.4	79	0.0111	30	2.04082	30.9
75%	4	n/a	0.96	n/a	379.525	44	22	24	19.8	23.3235	71.8	84	0.0312	49	6.80272	49.5
Max.	4.75	n/a	70.81	n/a	1158	148.1	33	125.8	21.8	44	143.5	100	0.075	49	7.74	77

**Table 41.** First order statistics results for NCHRP-Erosion spreadsheet: HET/Coarse data set.

EC	$E_v$ (mm-s/ m-h)	$E_\tau$ (mm/ h-Pa)	$v_c$ (m/s)	$\tau_c$ (Pa)	LL (%)	PL (%)	PI (%)	$\gamma$ (kN/m <sup>3</sup> )	WC (%)	$S_u$ (kPa)	PF (%)	$D_{50}$ (mm)	$C_u$	$C_c$	PC (%)	
Count	63	0	63	0	63	16	16	16	63	63	0	63	62	28	28	63
Mean	2.67	na	98.85	na	34.92	35.94	19.06	16.88	20.24	11.72	na	32.44	0.22	147.71	4.93	12.51
SD	0.41	na	241.37	na	79.15	0.25	0.25	0.50	1.27	3.07	na	7.22	0.06	96.76	1.78	3.10
Min.	2	na	0.05	na	0.1	35	19	15	17.8	7.5	na	22	0.13	38	3.4087	7
25%	2.25	na	2.895	na	8.73	36	19	17	19.35	9.6	na	29	0.1525	38	3.4087	13
50%	2.75	na	12.82	na	13.35	36	19	17	19.9	10.8	na	34	0.23	230	3.4087	13
75%	3	na	85.355	na	23.815	36	19	17	21.3	14	na	42	0.29	230	6.94901	14
Max.	4.25	na	1684.04	na	513	36	20	17	22.9	18.9	na	46.5	0.29	230	6.94901	23.9

**Table 42.** First order statistics results for NCHRP-Erosion spreadsheet: JET/Global data set.

EC	$E_v$ (mm-s/ m-h)	$E_\tau$ (mm/ h-Pa)	$v_c$ (m/s)	$\tau_c$ (Pa)	LL (%)	PL (%)	PI (%)	$\gamma$ (kN/m <sup>3</sup> )	WC (%)	$S_u$ (kPa)	PF (%)	$D_{50}$ (mm)	$C_u$	$C_c$	PC (%)	
Count	145	0	145	0	144	122	122	123	118	108	28	76	29	6	6	108
Mean	2.47	na	272.67	na	5.35	36.09	17.65	18.43	19.43	20.11	88.45	63.89	0.05	83.71	14.94	21.36
SD	0.67	na	1082.02	na	9.44	12.63	4.90	12.17	1.86	36.46	39.37	25.31	0.07	77.59	21.88	12.54
Min.	1.25	na	0.03	na	0.0001	14.5	7.7	2.9	11.4	7.16526	22.2	17.12	0.0009	7.14	0.98	1.5
25%	2	na	1.29	na	0.18	27.725	14.3	6	18.7	11.8145	52.375	41.125	0.0053	43.3625	1.87	11.1575
50%	2.5	na	4.92	na	1.12	36	16.55	19.1	19.45	14.4	79.6	68.8	0.0165	69.64	4.805	20
75%	3	na	29.53	na	7.2675	42	21.975	24	20.4	17.385	129.2	84	0.0625	85.83	16.995	29.7
Max.	3.75	na	6690.26	na	60.72	79.5	34.1	50.3	24.29	286.7	150.7	100	0.28	230	57.12	64.66

**Table 43.** First order statistics results for NCHRP-Erosion spreadsheet: JET/Fine data set.

EC	$E_v$ (mm-s/ m-h)	$E_\tau$ (mm/ h-Pa)	$v_c$ (m/s)	$\tau_c$ (Pa)	LL (%)	PL (%)	PI (%)	$\gamma$ (kN/m <sup>3</sup> )	WC (%)	$S_u$ (kPa)	PF (%)	$D_{50}$ (mm)	$C_u$	$C_c$	PC (%)	
Count	97	0	97	0	96	85	85	86	80	80	56	25	3	3	73	
Mean	2.63	na	58.39	na	6.38	39.38	17.14	22.18	19.43	23.18	91.77	77.29	0.02	70.55	3.83	26.38
SD	0.63	na	238.47	na	10.40	13.10	4.83	11.99	1.89	41.98	38.55	13.04	0.03	26.46	3.39	11.42
Min.	1.25	na	0.03	na	0.01	15.2	9.9	2.9	11.4	7.55	22.2	51.5	0.0009	40	1.87	5.3
25%	2.25	na	0.86	na	0.31	29	13	11.325	18.8225	13.6925	55.375	68.8	0.0049	62.915	1.87	18.9
50%	2.75	na	2.92	na	1.78	36.7	16	22.2	19.64	15.935	83.15	79.8	0.0082	85.83	1.87	28
75%	3.25	na	11.59	na	8.32	47	21	31	20.35	18.68	129.4	87.3025	0.0461	85.83	4.805	30
Max.	3.75	na	1718.02	na	60.72	79.5	34.1	50.3	23.05	286.7	150.7	100	0.0733	85.83	7.74	64.66

**Table 44.** First order statistics results for NCHRP-Erosion spreadsheet: JET/Coarse data set.

EC	$E_v$ (mm-s/ m-h)	$E_\tau$ (mm/ h-Pa)	$v_c$ (m/s)	$\tau_c$ (Pa)	LL (%)	PL (%)	PI (%)	$\gamma$ (kN/m <sup>3</sup> )	WC (%)	$S_u$ (kPa)	PF (%)	$D_{50}$ (mm)	$C_u$	$C_c$	PC (%)	
Count	48	0	48	0	48	37	37	37	38	28	4	20	4	3	3	35
Mean	2.13	na	705.68	na	3.29	28.52	18.84	9.69	19.43	11.33	68.55	26.38	0.21	96.86	26.06	10.87
SD	0.63	na	1784.55	na	6.78	7.20	4.94	7.08	1.81	2.37	44.03	5.14	0.07	117.60	28.54	7.15
Min.	1.25	na	0.41	na	0.0001	14.5	7.7	3.9	15.8	7.16526	30.1	17.12	0.1351	7.14	0.98	1.5
25%	1.6875	na	4.0325	na	0.115	22	16	5	18.475	10	39.85	25.1	0.15603	30.295	10.53	6.83
50%	2	na	20.875	na	0.45	30	17	6	19.4	11.2	57.45	25.1	0.204	53.45	20.08	8
75%	2.5625	na	208.705	na	2.8025	30	25	14	20.4	11.9804	86.15	25.1	0.25375	141.725	38.6	20
Max.	3.5	na	6690.26	na	28.92	39	25	22	24.29	17.8787	129.2	42.5	0.28	230	57.12	29

## 188 Relationship Between Erodibility and Properties of Soils

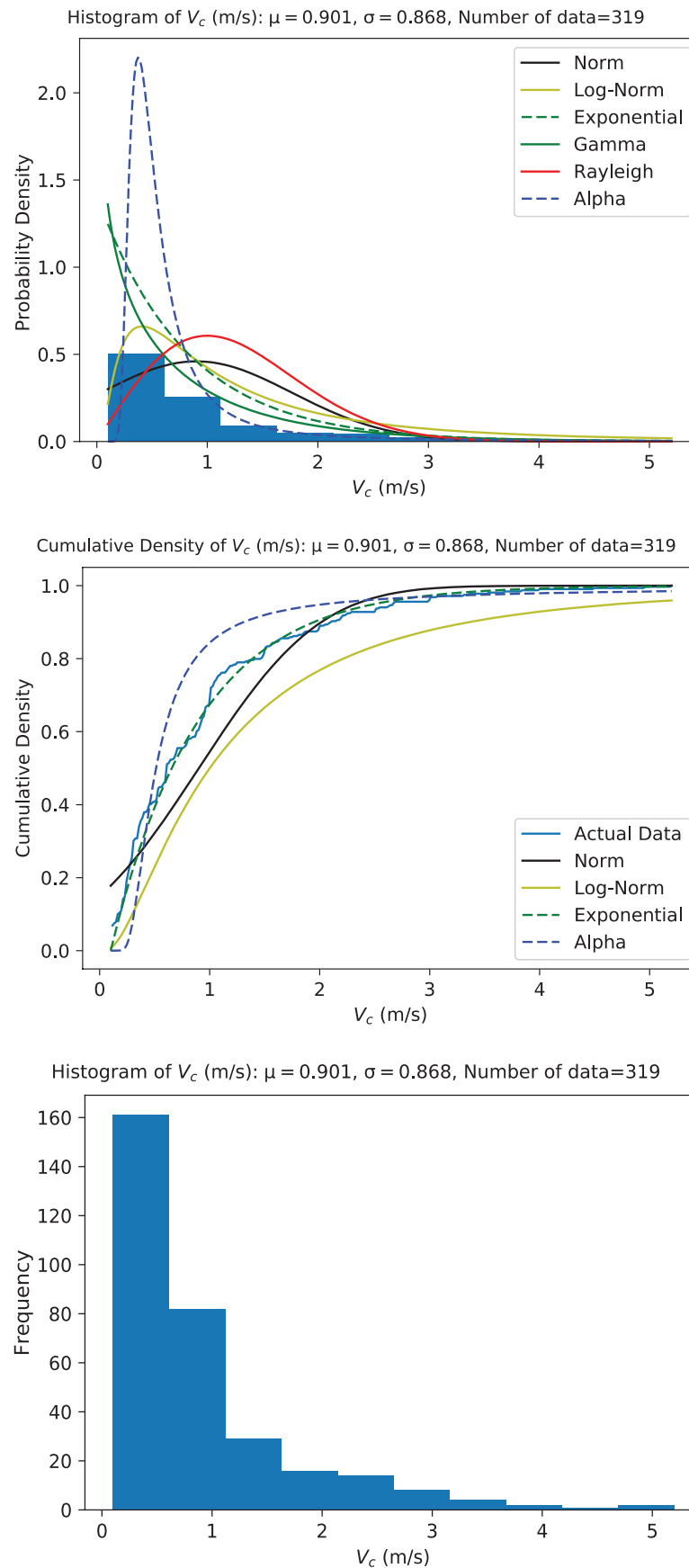


**Figure 149.** PDF, ECDF, and histogram plots for critical velocity in TAMU/Global data set.

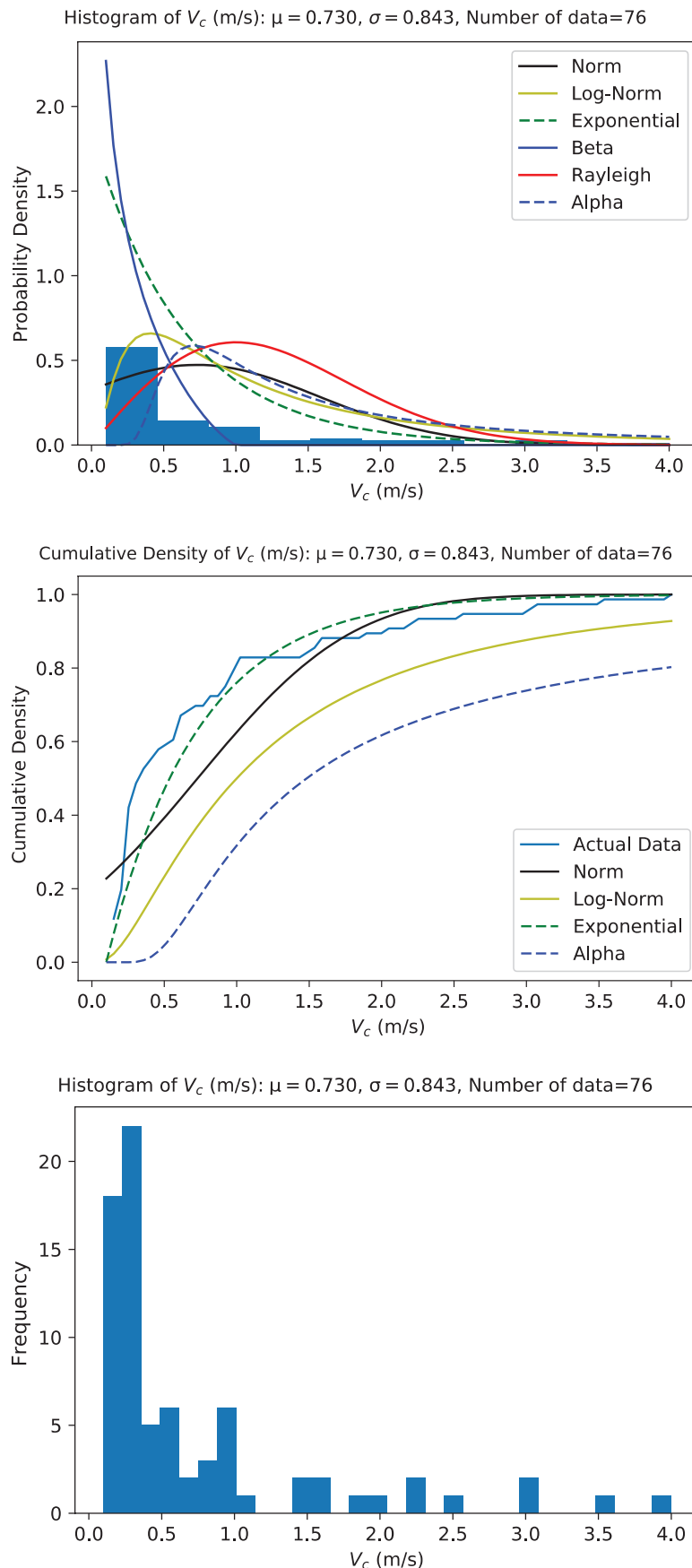


**Figure 150.** PDF, ECDF, and histogram plots for critical velocity in the TAMU/Coarse data set.

## 190 Relationship Between Erodibility and Properties of Soils

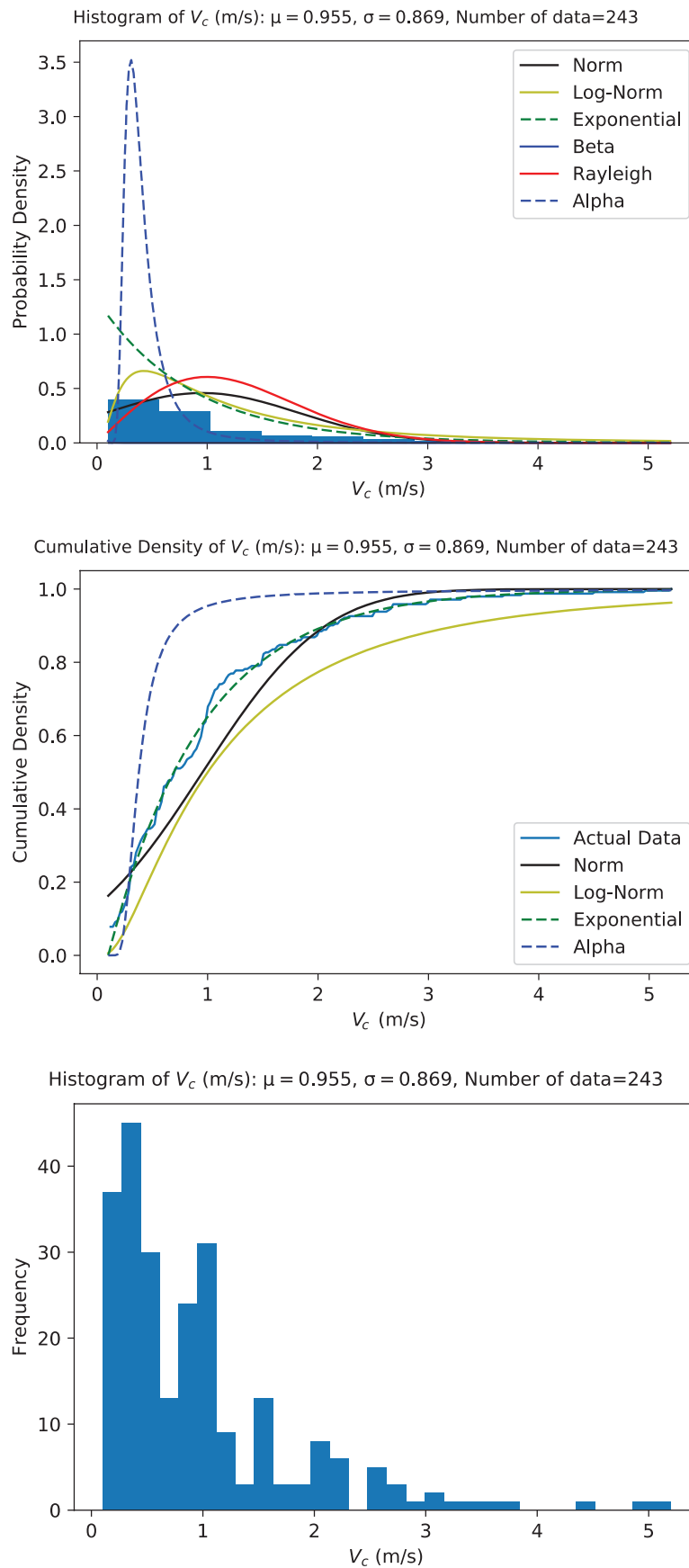


**Figure 151.** PDF, ECDF, and histogram plots for critical velocity in the TAMU/Fine data set.

**Table 45. Best simplest statistical model to represent erodibility parameters.**

No.	Subgroup	Best Simplest Statistical Model to Represent Each Parameter				
		EC	$E_v$	$E_\tau$	$v_c$	$\tau_c$
1	TAMU/Global	Normal	Exp.	ln	Exp.	Exp.
2	TAMU/Fine	Normal	Exp.	ln	Exp.	Exp.
3	TAMU/Coarse	Normal	Exp.	Exp.	Exp.	Exp.
4	EFA/Global	Normal	Exp.	ln	Exp.	Exp.
5	EFA/Fine	Normal	Exp.	ln	Exp.	Exp.
6	EFA/Coarse	Normal	Exp.	Exp.	Exp.	ln
7	JET/Global	Normal	na	ln	na	ln
8	JET/Fine	Normal	ns	ln	na	ln
9	JET/Coarse	Normal	na	ln	na	Alpha
10	HET/Global	Normal	na	ln	na	Normal
11	HET/Fine	Normal	na	Exp.	na	Normal
12	HET/Coarse	Normal	na	Normal	na	ln

Note: Exp. = exponential; ln = lognormal; na = not applicable.

Similar figures are included in Appendix 3 for all five erodibility parameters as well as the 12 major geotechnical properties for each subgroup (see Figure 148). The results of the best simplest statistical model for each parameter and in each subgroup are obtained and shown in Table 45 and Table 46. Table 45 shows the best models to represent each erodibility parameter ( $v_c$ ,  $\tau_c$ ,  $E_v$ ,  $E_\tau$ , and EC) in each subgroup. Table 46 shows the best models to represent each major geotechnical property (i.e., LL, PL, PI,  $\gamma$ , WC,  $S_u$ , PF,  $D_{50}$ ,  $C_u$ ,  $C_c$ , and PC) in each subgroup.

**Table 46. Best simplest statistical model to represent geotechnical properties.**

No.	Subgroup	Best Simplest Statistical Model to Represent Each Parameter										
		LL	PL	PI	$\gamma$	WC	$S_u$	PF	$D_{50}$	$C_u$	$C_c$	PC
1	TAMU/Global	Normal	Normal	Normal	Normal	Normal	Exp.	Normal	Gamma	Exp.	Exp.	Normal
2	TAMU/Fine	Normal	Normal	Normal	Normal	Normal	Exp.	Normal	Normal	Exp.	Exp.	Normal
3	TAMU/Coarse	Normal	Normal	Normal	Normal	Normal	Exp.	Normal	Gamma	Normal	Exp.	Normal
4	EFA/Global	Normal	Normal	Normal	Normal	Normal	Exp.	Normal	Gamma	Exp.	ln	Exp.
5	EFA/Fine	Normal	Normal	Normal	Normal	Normal	Exp.	Normal	Exp.	Exp.	ln	Normal
6	EFA/Coarse	Normal	Exp.	Exp.	Normal	Normal	Exp.	Normal	ln	Exp.	ln	Normal
7	JET/Global	Normal	Normal	Normal	Normal	Normal	Normal	Normal	Gamma	Normal	Normal	Normal
8	JET/Fine	Normal	Normal	Normal	Normal	Exp.	Normal	Normal	Normal	Normal	Normal	Normal
9	JET/Coarse	na	na	na	Normal	Normal	na	Normal	na	na	na	Normal
10	HET/Global	Normal	Normal	Normal	Normal	Normal	Normal	Normal	Normal	Normal	Normal	Normal
11	HET/Fine	Normal	Normal	Normal	Normal	Normal	Normal	Normal	Normal	Alpha	Normal	Normal
12	HET/Coarse	Normal	Normal	Normal	Normal	Normal	na	Normal	Normal	Alpha	Normal	Normal

Note: Exp. = exponential; ln = lognormal; na = not applicable.

### 7.3.2 Second Order Statistical Analysis

The second order statistical analysis dealt with constructing correlation matrices for the different parameters defined in each group and discussed in the previous step. Before the regression relationships could be generated, it was necessary to learn about any potential inter-parameter relationships between the model variables (geotechnical parameters) and the function variables (erosion parameters). To do that, correlation matrices were formed between the parameters, and Pearson's correlation coefficient was obtained for each matrix. Pearson's correlation coefficient is defined as the covariance of the two variables divided by the product of their standard deviations. It ranges from  $-1$  to  $+1$  and reflects the linear dependency between two variables, with  $+1$  indicating a strong positive relationship,  $-1$  indicating a solid negative relationship, and  $0$  indicating no relationship at all. Figure 152 shows an example of the results of the second order statistical analysis for EFA/Fine data. Such plots were created for all aforementioned groups explained in Figure 148 and compiled in Appendix 3. The knowledge developed after the second order statistical analysis is very important for implementing the Bayesian inference approach.

### 7.3.3 Experimental Design

#### 7.3.3.1 Model Expression

The next step in the process dealt with generating the relationship equations between the erosion parameters and the geotechnical engineering parameters.

Two models were used in this research: the linear model and the power model. The power model was the multiple nonlinear model shown in Equation 67.

$$Y = A \times (P_1)^{\alpha_1} \times (P_2)^{\alpha_2} \times (P_3)^{\alpha_3} \times (P_4)^{\alpha_4} \times \dots \quad (67)$$

where

$Y$  = dependent variable, which in this case includes  $\tau_c$ ,  $v_c$ ,  $E_v$ ,  $E_v$ , and EC;

$P_i$  = soil geotechnical properties used in the regressions; and

$A$  and  $\alpha_i$  = constant parameters defined in the model expression.

The linear model, on the other hand, was the simple first-degree linear model, as described in Equation 68.

$$Y = [\alpha_1 \times (P_1) + \alpha_2 \times (P_2) + \alpha_3 \times (P_3) + \dots] + \beta \quad (68)$$

where

$Y$  = dependent variable, which in this case includes  $\tau_c$ ,  $v_c$ ,  $E_v$ ,  $E_v$ , and EC;

$P_i$  = soil geotechnical properties used in the regressions; and

$\alpha_i$  and  $\beta$  = constant parameters defined in the model expression.

Several combinations between a function variable, say,  $\tau_c$ , and model variables (e.g., LL, PL, PI, water content, unit weight, etc.) can be selected to generate regression equations. To obtain the best fits, the investigators decided to study nearly all possible combinations and evaluate the goodness of each fit. Therefore, 135 regression combination groups were constructed for each function variable in each subgroup shown in Figure 148. In addition, the two model expressions (Equations 67 and 68) were used to develop the equations. That is, the total number of regression equations was  $2 \times 5 \times 135$  ( $2$  model expressions  $\times$   $5$  function parameters  $\times$   $135$  combination groups) = 1,350 regression equations for each subgroup shown in Figure 148.

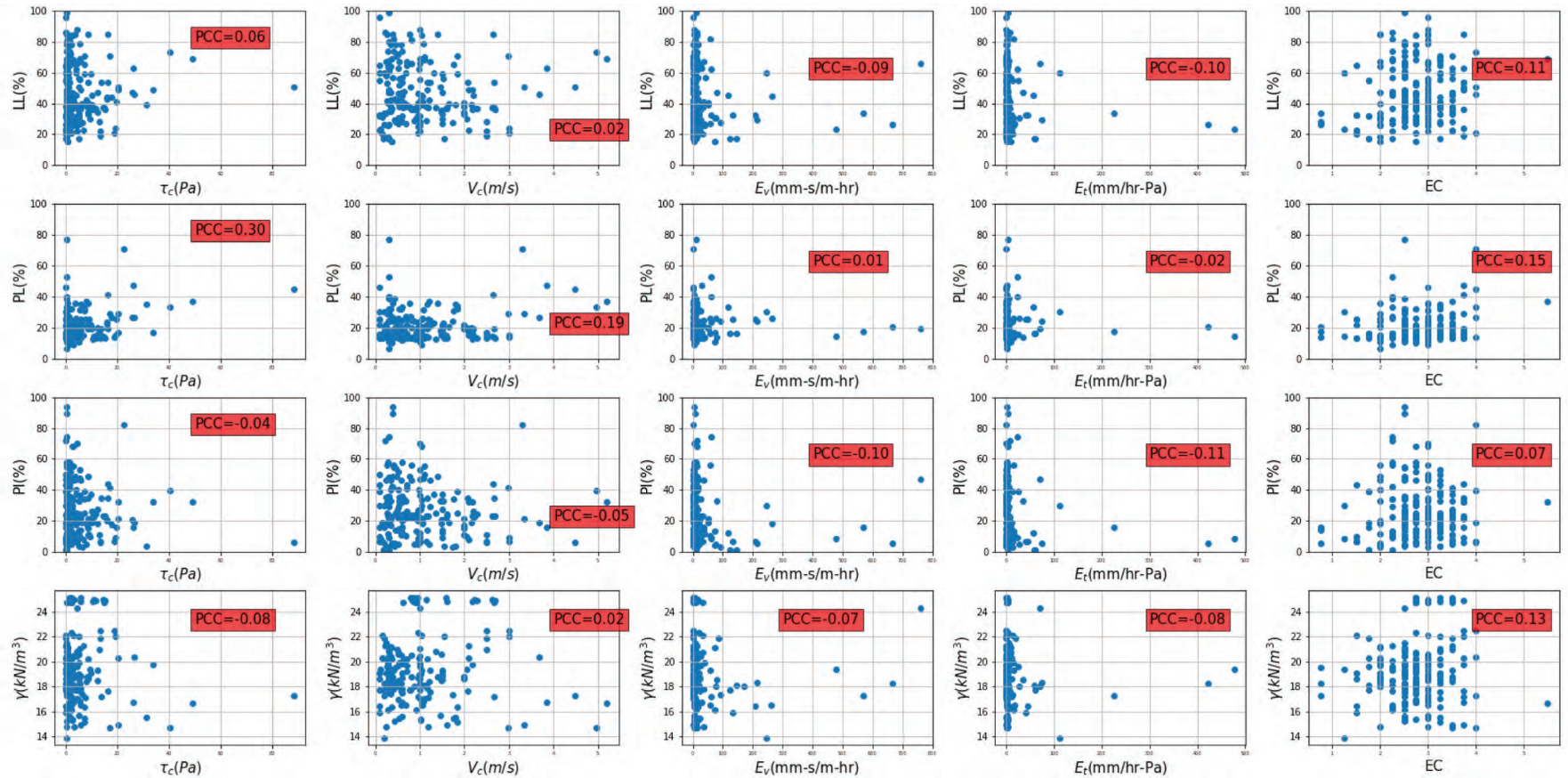


**Figure 152. Correlation matrix for EFA/Fine data.**  
(continued on next page)

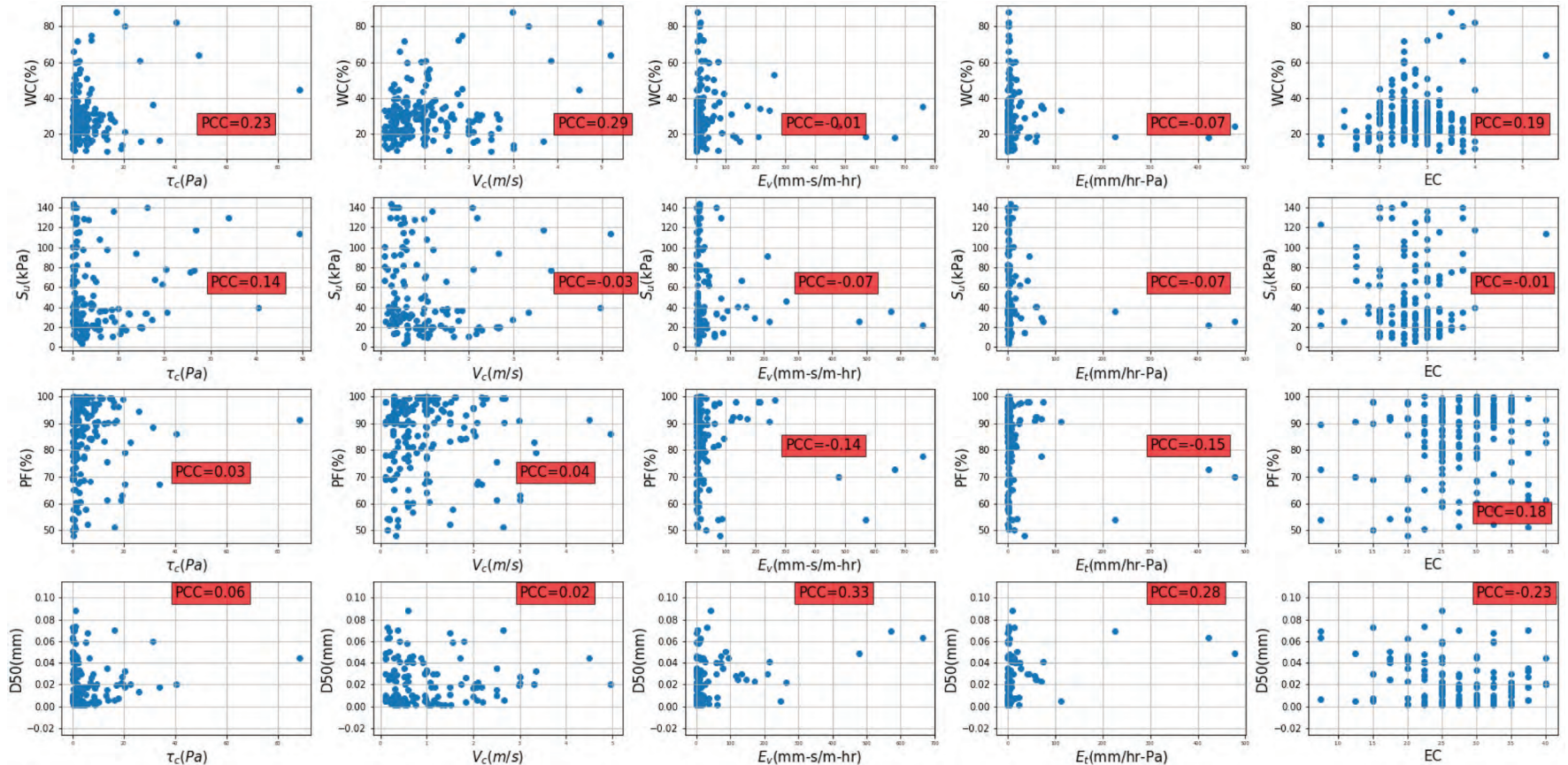


Figure 152. (Continued).

### 7.3.3.2 Measures of Statistical Significance

The best models were selected after passing through a four-filter process:

- Filter 1.  $R^2$ ,
- Filter 2. Mean square error (MSE),
- Filter 3. F-value/F-statistic, and
- Filter 4. Cross-validation score.

Each model generated was checked with Filters 1 to 4, one after another. Each model that did not meet the requirements of a given specific filter was not further studied with the subsequent filters and thus was eliminated from the best model sets.

$R^2$ , also called the coefficient of determination, is one of the most well-known statistical measures of fit. It represents how far the actual data stands from the fitted regression model. The mathematical definition of  $R^2$  is as follows:

$$R^2 = 1 - \frac{\sum(y_i - f_i)^2}{\sum(y_i - \bar{y})^2} \quad (69)$$

where

- $y_i$  = the data,
- $\bar{y}$  = mean value of the data set, and
- $f_i$  = predicted values using the fitted regression model.

This study reports  $R^2$  values for each regression.  $R^2$  ranges from 1.0 (absolute fit), to 0 (no relationship).  $R^2$  can also sometimes be negative. Generally speaking,  $R^2$  values greater than 0.6 can be considered as potential correlations in many engineering applications. However, in many sources, even  $R^2$  values greater than 0.4 are accepted by researchers.

The MSE is another statistical measure for evaluating the quality of a predictive model. MSE is also sometimes called the mean square deviation. It always gets a nonnegative value and reflects the average of the squared difference between the predicted value and the actual value. The mathematical definition of MSE is shown below:

$$MSE = \frac{1}{n} \sum(Y_i - \hat{Y}_i)^2 \quad (70)$$

where

- $Y_i$  = the data,
- $\hat{Y}_i$  = predicted value using the estimator, and
- $n$  = number of predicted data points.

The main concern with  $R^2$  and MSE is that they cannot completely represent the statistical significance of an estimator; therefore, an additional statistical measure is used in this study. The main problem with  $R^2$  is that it is highly dependent on the number of variables involved in the regression model. For example, if there is only one parameter to predict, and the data set includes only one data point, any regression model can lead to an  $R^2$  of 1.

The F-value can be used to reject the null hypothesis in a regression model. The F-value is obtained from Equation 71:

$$F_{\text{value}} = \frac{SSE(\text{reg})}{SSE(\text{res})} \times \left( \frac{D}{V} - 1 \right) \quad (71)$$

## 196 Relationship Between Erodibility and Properties of Soils

where

$SSE(\text{reg})$  = sum of square errors for the regression values,

$SSE(\text{res})$  = sum of square errors for the residual values,

$D$  = number of data points, and

$V$  = number of variables.

As can be seen from the equations, if the regression model has a lot of error [i.e.,  $SSE(\text{res})$  is large] then  $F$  will be small. Also, if the number of data points is close to the number of variables, then  $F$  will be small again. The goal is to maximize the value of  $F$  and in any case to make it higher than the  $F$ -statistic ( $F$ -stat), a target value given in statistical tables.

The  $R^2$  and MSE values represent the goodness of fit evaluation, while the  $F$ -test, which compares the  $F$ -value with the  $F$ -stat, indicates whether there are enough data to propose the equation. The probability level for the  $F$ -test in this study was chosen as 5%.

After the first three filters ( $R^2$ , MSE,  $F$ -value/ $F$ -stat) were successfully met, the cross-validation score of the selected models was examined. Overfitting is a common problem in many similar statistical analyses conducted in different fields of engineering. Overfitting may occur when the equation is generated on the basis of all the data points available in the data set. In this case, the proposed model is not necessarily designed for yet unseen data. As a result, adding a few data points to the existing data set or removing some data from it can sometimes dramatically change the goodness of fit of the model. One approach to evaluate whether this is a problem is to divide the data set into two random subsets and call them training and testing subsets (i.e., 85% and 15% of the data, respectively). After that, the model is trained using the training subset, and validated through the testing subset. One issue with this approach is that the analysis is very dependent on the random training and testing subsets chosen in the beginning.

Cross-validation is a technique used to assess the estimator performance by folding the data set into  $k$  random folds. The model is trained using the  $k-1$  fold and then validated with the remaining folds. The final score of the cross-validation is the average of all scores for each time that the model is trained and validated (the average of  $k$  scores). Cross-validation was used to further sieve the best models to obtain the most robust equations.

This four-filter model selection process was performed for each subgroup as shown in Figure 148. This process incorporates studying thousands of generated models in the first step and narrowing down to a smaller number of models after each filter is passed. By the end of the fourth filter, the best models for correlating erodibility parameters with geotechnical properties were supposedly achieved.

For the coarse data sets (subgroups of TAMU/Coarse, EFA/Coarse, HET/Coarse, and JET/Coarse), 105 soil parameter combination groups were chosen for each function variable; however, for the Global and Fine data sets (subgroups of TAMU/Global, TAMU/Fine, EFA/Global, EFA/Fine, HET/Global, HET/Fine, JET/Global, JET/Fine), 135 soil parameter combination groups were selected for each function variable. Units of the parameters used in the regression analyses as well as list of these combination groups are presented in Appendix 4.

After the requirements of all four filters were met successfully, the best-fitting models were selected. If more than one fitting model met the filter requirements, the authors' engineering judgement helped narrow down the choices to one or at most two equations. More regarding the selected models is discussed in Chapter 8.

### 7.3.3.3 Probability of Over- or Underpredicting

The best correlation equations that can estimate each erodibility parameter (i.e.,  $\tau_c$ ,  $v_c$ ,  $E_r$ ,  $E_v$ , and EC) were selected according to the four-filter process discussed in the previous section.

These equations were obtained through a deterministic statistical analysis, meaning that they reflect the predicted value as a single number, with no quantification of the possible error associated with predicting the future event.

One of the major goals of this study was to provide the engineer with a reliability-based approach to also assess whether the predicted values are conservative enough for the purpose of engineering design. This approach is called the probability of underpredicting (POU)/probability of overpredicting (POO) approach. As an instance, the engineer needs to know the probability that the predicted  $\tau_c$  is smaller than the actual  $\tau_c$  to be on the safe side in the design problem. Similarly, critical velocity,  $v_c$ , and erosion category, EC, are among those erodibility parameters that require the POU. On the other hand, the engineer needs to know the probability that the predicted  $E_c$  or  $E_v$  is larger than the actual  $E_c$  or  $E_v$ , in order to be on the safe side in the design problem. Therefore in such cases, the POO is presented.

Equation 72 shows the probabilistic model, which consists of the selected deterministic predicted erodibility parameter and a correction factor,  $\theta$ .

$$Z_{\text{new}} = \theta \times Z_{\text{det}} \quad (72)$$

where

$Z_{\text{new}}$  = new value for erodibility parameter,

$\theta$  = correction factor, and

$Z_{\text{det}}$  = deterministically predicted erodibility parameter.

$\theta$  can also be inferred as the ratio of  $Z_{\text{new}}$  over  $Z_{\text{det}}$ .

Depending on the erodibility parameter, the POU versus  $\theta$  or POO versus  $\theta$  plots were developed for the best selected equations, as discussed in the next section. These plots help engineers find the best correction factors associated with a confidence level in design problems. Figure 153 gives an example of how POU is calculated for a function parameter such as EC. POU refers to the probability that the predicted values ( $Z_p$ ) are smaller than the measured values ( $Z_m$ ). The black solid line in Figure 153 represents the case in which  $Z_m = Z_p$ . In this example, two different correction factors ( $\theta = 0.6$  and  $\theta = 1.0$ ) are considered. The data points

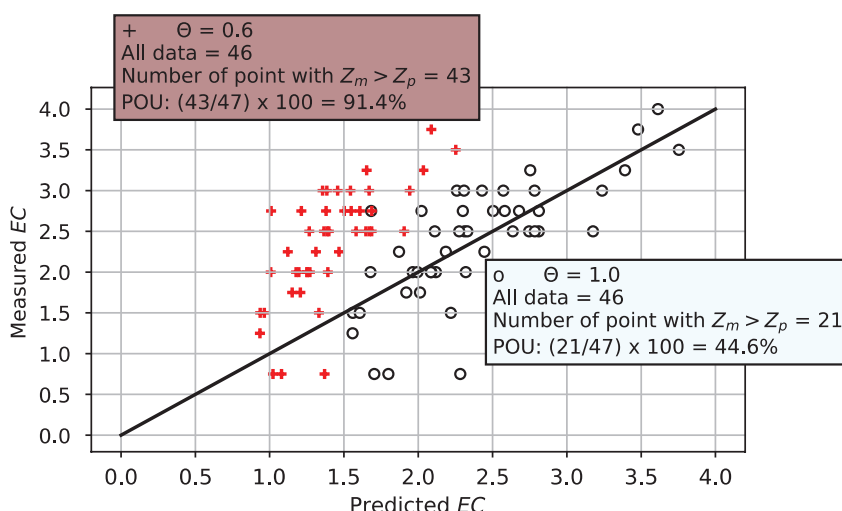


Figure 153. Example of how POU is obtained for two different correction factors.

## 198 Relationship Between Erodibility and Properties of Soils

associated with  $\theta = 1.0$  are shown as black open circles, and the data points associated with  $\theta = 0.6$  are shown as red plus signs. The POU is then calculated by counting the number of data points above the black solid line (the data points in which  $Z_m > Z_p$ ) and dividing that by the total number of data points.

In this report, these plots are often accompanied by an offset value. For example, the POO is calculated as the probability that  $Z_m - Z_p <$  offset value instead of the probability that  $Z_m - Z_p < 0$ . The offset values are small compared with the standard deviation of the parameter and can often be neglected; however, because the  $R^2$  for selected equations were very high and the parameter values were very small in many cases, the lack of an offset value could lead to unrealistic POU or POO values.

The next section presents the process in which the best equations were selected for each erodibility parameter. The POU versus correction factor or POO versus correction factor plots are also presented for the selected equations.

### 7.3.4 Regression, Optimization, and Model Selection

The step-by-step procedure discussed in Section 7.3.3 for selecting the best-fitting models was implemented for each erodibility parameter (i.e.,  $\tau_c$ ,  $v_c$ ,  $E_v$ ,  $E_v$ , EC). The selected correlation equations in this section are repeated in the Chapter 8, and recommendations on how they should be used are provided. The units and description of all the parameters used in the following equations in this section are listed in Table 47, as well as in Appendix 4 of the appendices report.

**Table 47. Units and descriptions of parameters used in regression analyses.**

Parameter	Description	Unit
A	Soil activity	na
$\tau_c$	Critical shear stress	Pa
$C_c$	Coefficient of curvature	na
$C_u$	Coefficient of uniformity	na
$D_{50}$	Mean particle size	mm
EC	Erosion category	na
$E_v$	Slope of velocity–erosion rate	mm·s/m·h
$F_t$	Slope of shear–erosion rate	Mm/h·Pa
LL	Liquid limit	%
PC	Clay percentage (<0.002 mm)	%
PF	Percent finer than sieve #200	%
PI	Plasticity index	%
PL	Plastic limit	%
PP	Pocket penetrometer strength	kPa
$S_u$	Undrained shear strength	kPa
$v_c$	Critical velocity	m/s
VST	Vane shear strength	kPa
WC	Water content	%
$\gamma$	Unit weight	kN/m <sup>3</sup>

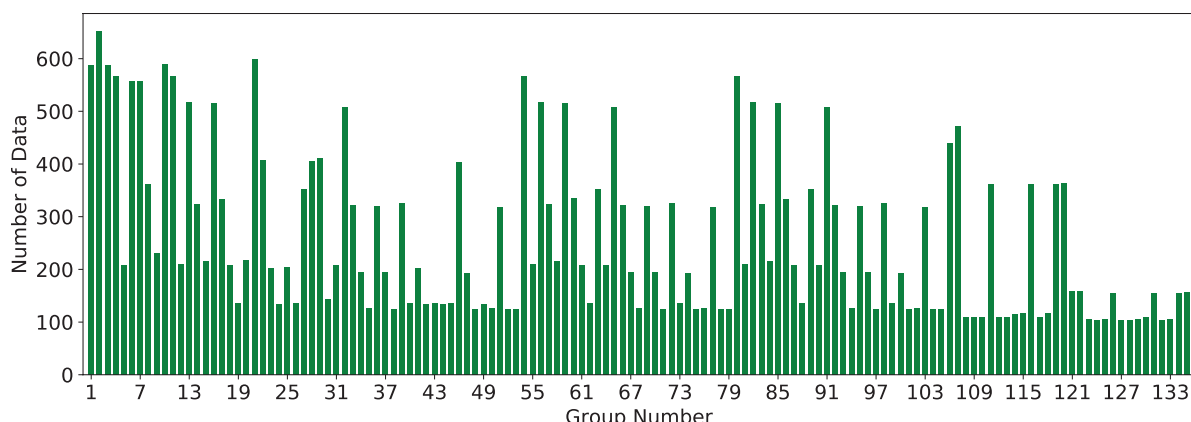


**Figure 154.** Number of data points in each of 135 soil parameter combination groups for TAMU/Global data set: critical shear stress.

#### 7.3.4.1 Critical Shear Stress

The first filter was  $R^2$ . The study began with the first subgroup, TAMU/Global (see Figure 148). This database includes all existing data, regardless of test type or the fine/coarse nature of the samples. Figure 154 shows the number of data points in each of the 135 soil parameter combination groups. Figure 155 and Figure 156 show the results for  $R^2$  for these 135 soil parameter combination groups with the linear model (Equation 68) and power model (Equation 67), respectively.

Figure 155 and Figure 156 show very poor  $R^2$  values ( $<0.2$ ) for critical shear stress,  $\tau_c$ , in the TAMU/Global data set. Therefore, continuing with Filters 2 through 4 was not reasonable for this data set. The same poor results were observed when the data set was changed to TAMU/Fine and TAMU/Coarse. These observations proved that the regression analyses needed to be narrowed down to each test separately and, consecutively, to the coarse or fine nature of the soil. Therefore, the subgroups EFA/Global, EFA/Fine, and EFA/Coarse; JET/Global, JET/Fine, and JET/Coarse; and HET/Global, HET/Fine, and HET/Coarse were used to implement the regression analyses, as described below.

**EFA Data Set.** It was observed that dividing the EFA/Global data set into EFA/Fine and EFA/Coarse led to better results. Figure 157 shows the number of data points in each of the

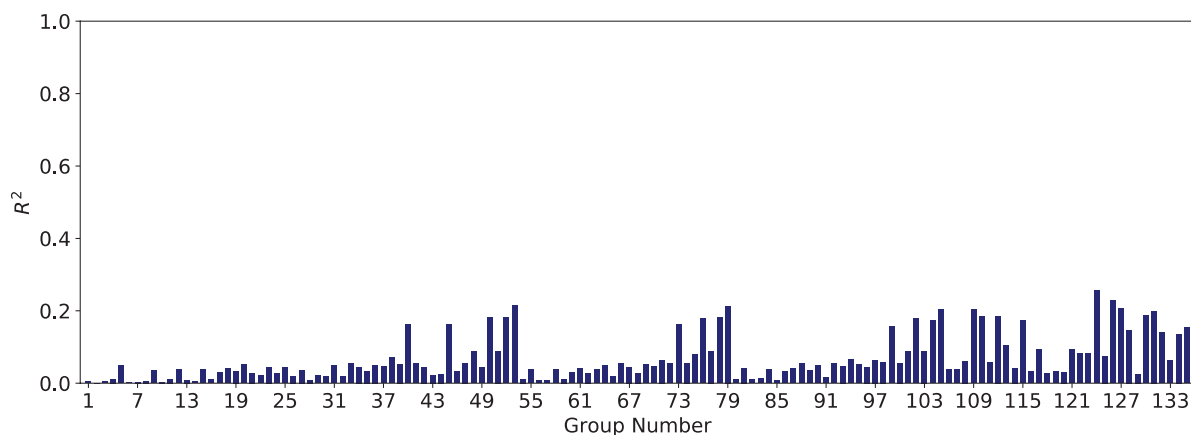


**Figure 155.**  $R^2$  results for linear models in TAMU/Global data set: critical shear stress.

## 200 Relationship Between Erodibility and Properties of Soils

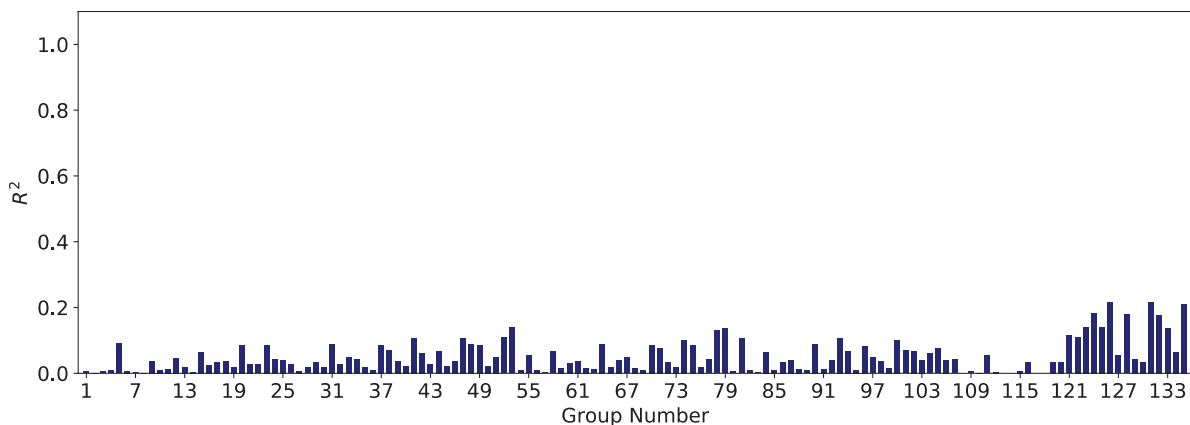


**Figure 156.** *R<sup>2</sup> results for power models in TAMU/Global data set: critical shear stress.*

135 combination groups in the EFA/Fine data set. Figure 158 and Figure 159 show the results for  $R^2$  for each combination group for the linear and power models, respectively.

The  $R^2$  values of Groups 108 to 135 were generally higher than those of the other groups for both the linear and the power models; however, a quick glance shows that the power model was a better fit for the existing data in the case of critical shear stress in the EFA/Fine data set.

The next step was to select the best  $R^2$  values, and move forward with Filter 2 (MSE). Figure 160 and Figure 161 show the values of MSE for the linear and power models, respectively. As expected, the MSE values were generally lower for same group numbers (Groups 108 to 135) in both figures.

After passing through Filters 1 and 2 ( $R^2$  and MSE), the power models associated with Groups 109, 110, 113, 123, 124, 125, and 128 were selected for further analysis. Filter 3,  $F$ -value/ $F$ -stat, was determined for each group. In cases in which  $F$ -value/ $F$ -stat was lower than 1, the model was removed from the selection list. Otherwise, the model remained in the list. Table 48 shows the results of the selected models after the requirements of the first three filters ( $R^2$ , MSE, and  $F$ -value/ $F$ -stat) were met.

Table 48 shows the selected models that met the requirements of the first three filters; however, not all of them performed satisfactorily in the cross-validation test. As mentioned

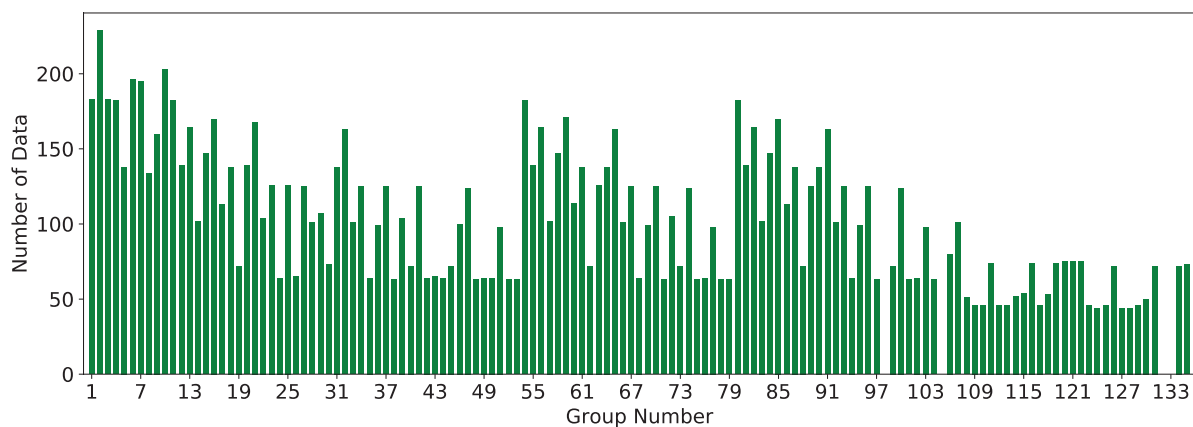


**Figure 157.** *Number of data points in each of 135 combination groups for the EFA/Fine data set: critical shear stress.*

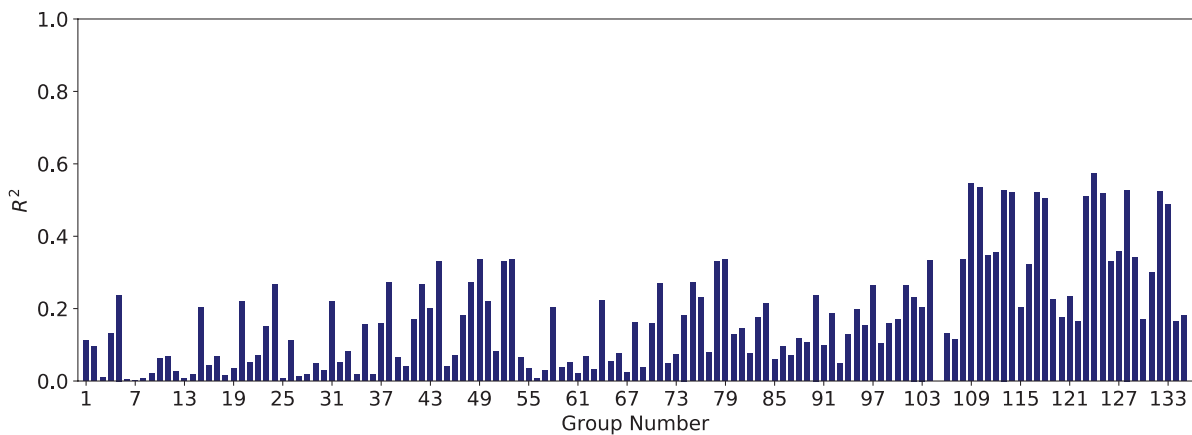


Figure 158.  $R^2$  results for the linear models in EFA/Fine data set: critical shear stress.

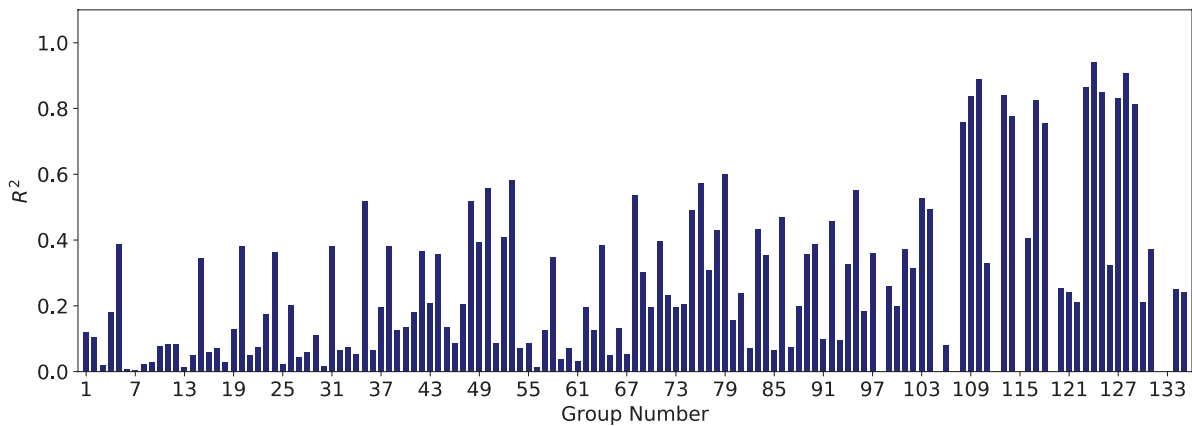


Figure 159.  $R^2$  results for the power models in EFA/Fine data set: critical shear stress.

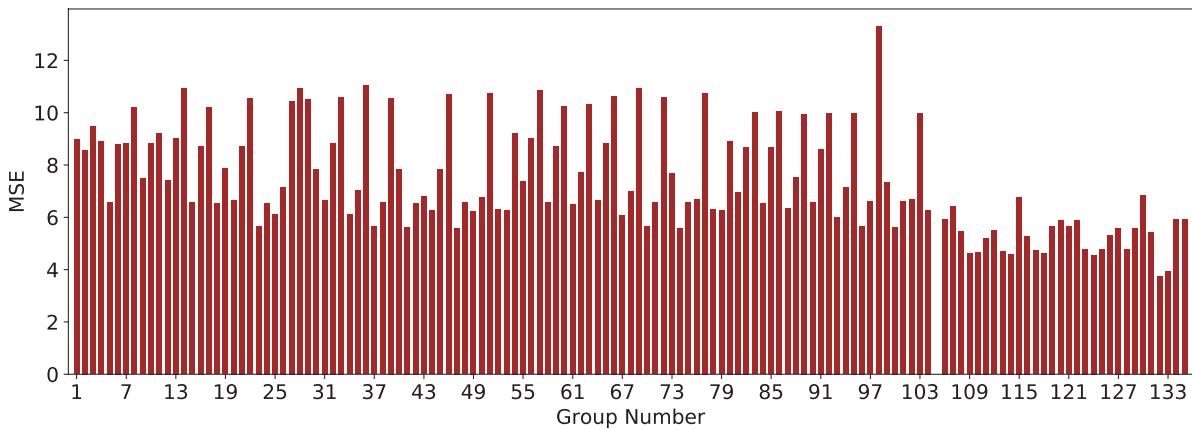


Figure 160. MSE results for linear models in EFA/Fine data set: critical shear stress.

## 202 Relationship Between Erodibility and Properties of Soils

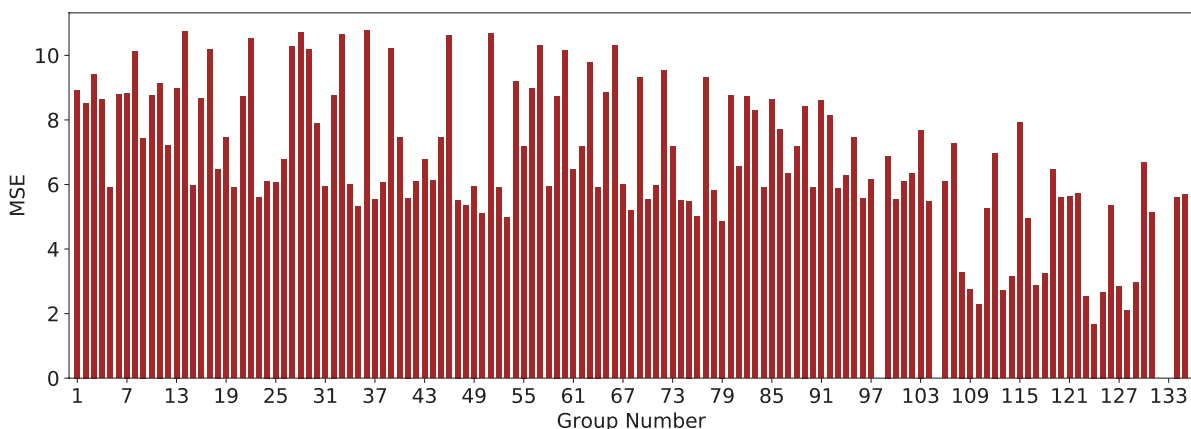


Figure 161. MSE results for power models in EFA/Fine data set: critical shear stress.

earlier, cross-validation is a technique used to assess the estimator performance by folding the data set into  $k$  random folds. The model is trained by using the  $k-1$  fold and then validated by using the remaining folds. The final score of the cross-validation test is the average of all scores for each time that the model is trained and validated (the average of  $k$  scores). Out of the seven selected groups in Table 48, Group 110 and, to some extent, Group 124 (both shaded and highlighted in blue) were the ones that passed all four filters successfully.

Section 7.3.3.3 and Equation 72 discussed the reliability-based approach called the POU approach. The plots of POU versus  $\theta$  are shown in Figure 162 and Figure 163 for Groups 110 and 124, respectively. The vertical axes in these plots represent the probability that, when the selected model is used, the predicted  $\tau_c$  will be smaller than the actual  $\tau_c$ , in percentage (with  $\pm 0.5$  Pa precision). The horizontal axes represent the correction factor ( $\theta$ ) that can be multiplied by the predicted value to reach a certain POU level (See Equation 72). For instance, Figure 162 shows that by using the Group 110 correlation equation (see Table 48), there is near 73% chance that the predicted  $\tau_c$  will be smaller than the actual  $\tau_c$  (with  $\pm 0.5$  Pa precision). However,

Table 48. Selected power models for critical shear stress in EFA/Fine data set.

Group No.	Independent Variables	Model Expression	$R^2$	MSE	F-value/ F-stat	Cross-Validation Score
109	PC, $\gamma$ , WC, $S_u$ , PF, $D_{50}$	$\tau_c = (5.5 \times 10^{-9}) \times \gamma^{-1.03} \times WC^{4.03} \times S_u^{1.57} \times PF^{-0.22} \times D_{50}^{0.68} \times PC^{9.6 \times 10^{-8}}$	0.84	2.76	3.5	0.66
110	PC, WC, $S_u$ , PF, $D_{50}$	$\tau_c = (1.5 \times 10^{-5}) \times WC^{4.37} \times S_u^{1.49} \times PF^{-3.25} \times D_{50}^{-1.1} \times PC^{6.1 \times 10^{-8}}$	0.86	2.50	4.7	0.83
113	PC, $\gamma$ , WC, $S_u$ , $D_{50}$	$\tau_c = (7.9 \times 10^{-7}) \times \gamma^{-2.74} \times WC^{3.74} \times S_u^{1.59} \times D_{50}^{-0.64} \times PC^{1.4 \times 10^{-7}}$	0.84	2.73	4.9	0.65
123	A, PL, $\gamma$ , WC, $S_u$	$\tau_c = (3.56 \times 10^{12}) \times A^{0.77} \times PL^{1.02} \times \gamma^{-16.05} \times WC^{1.04} \times S_u^{2.27}$	0.87	2.53	7.1	0.18
124	$\gamma$ , A, WC, $S_u$ , PF, $D_{50}$	$\tau_c = (158.06) \times \gamma^5 \times A^{-0.46} \times WC^{10.03} \times S_u^{1.83} \times PF^{-18.28} \times D_{50}^{-4.21}$	0.94	1.67	3.9	0.66
125	$\gamma$ , WC, $S_u$ , PF, A	$\tau_c = (3.25 \times 10^{12}) \times \gamma^{-14.93} \times WC^{1.18} \times S_u^{2.34} \times PF^{-0.17} \times A^{1.05}$	0.85	2.67	5.1	0.25
128	$D_{50}$ , $\gamma$ , WC, $S_u$ , A	$\tau_c = (2.2 \times 10^{12}) \times D_{50}^{-0.74} \times \gamma^{-18.99} \times WC^{3.57} \times S_u^{2.43} \times A^{-0.72}$	0.91	2.11	2.9	-0.08

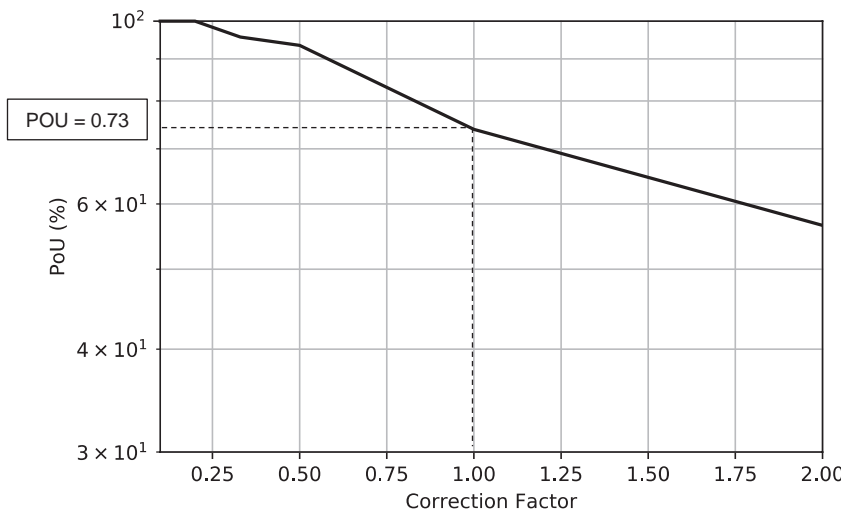


**Figure 162.** Plot of POU versus correction factor for Group 110 (power model):  $\tau_c$  in EFA/Fine data set.

if the engineer desires a higher confidence level, say, near 90%, then he or she needs to multiply the predicted value by 0.6. Figure 163, however, shows that by using the Group 124 correlation equation (see Table 48), there is almost a 90% chance that the predicted value will be smaller than the actual  $\tau_c$  (with 0.5 Pa offset). These plots give the engineers flexibility in choosing the desired correction factors according to the design application.

The same procedure was conducted in the EFA/Coarse data set, and the best models were selected. Figure 164 shows the number of data points in each of the 105 combination groups in the EFA/Coarse data set. Figure 165 and Figure 166 show the results for  $R^2$  for each combination group for the linear and power models, respectively.

Unlike the EFA/Fine data set, both the linear and power models showed a few good groups in terms of  $R^2$  values; however, as shown in Figure 164, the number of data points in most groups

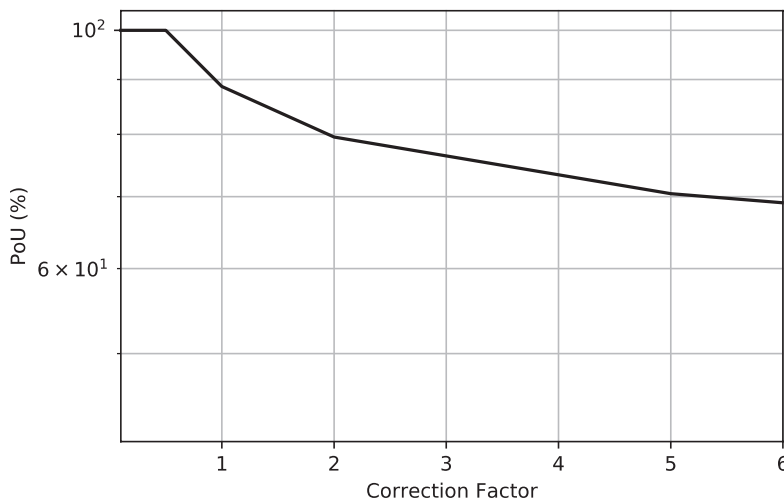


**Figure 163.** Plot of POU versus correction factor for Group 124 (power model):  $\tau_c$  in EFA/Fine data set.

## 204 Relationship Between Erodibility and Properties of Soils

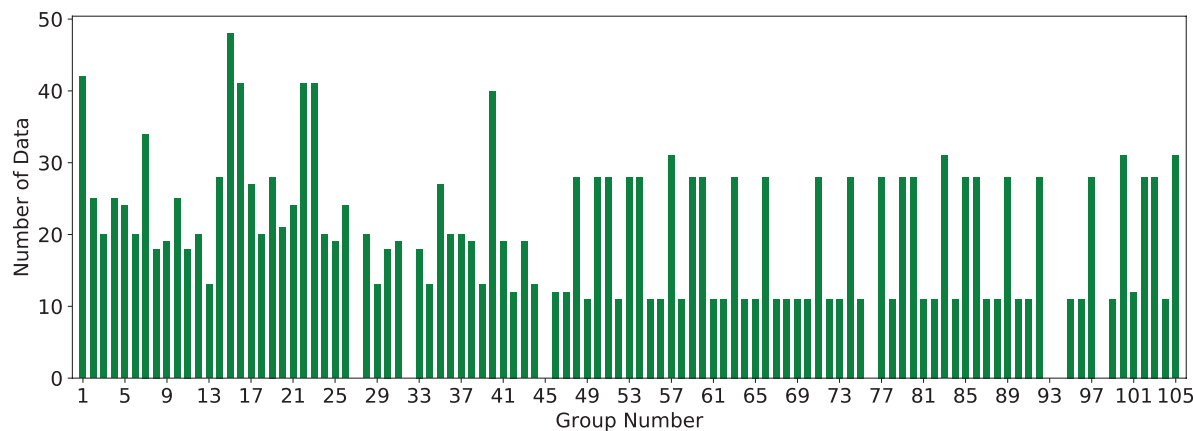


**Figure 164.** Number of data points in each of 105 combination groups for the EFA/Coarse data set: critical shear stress.

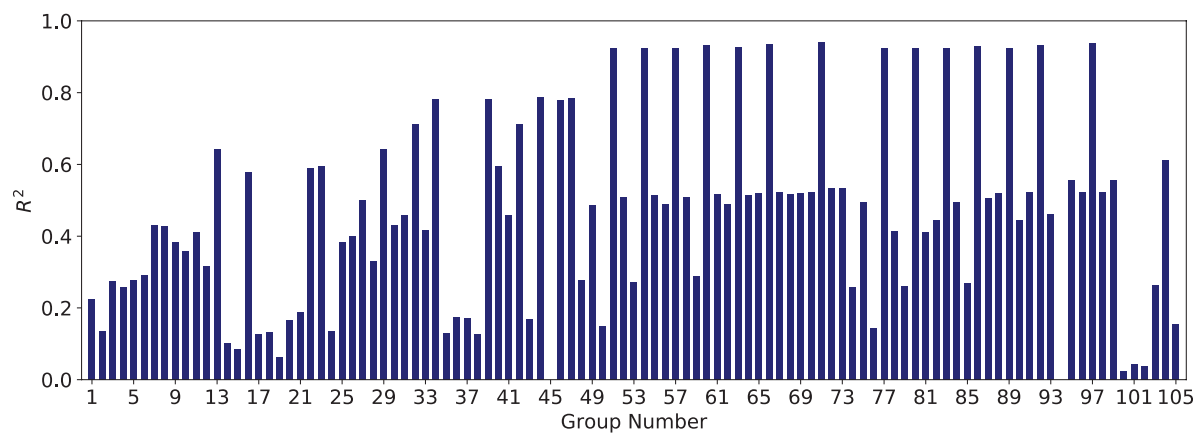


**Figure 165.**  $R^2$  results for linear models in EFA/Coarse data set: critical shear stress.

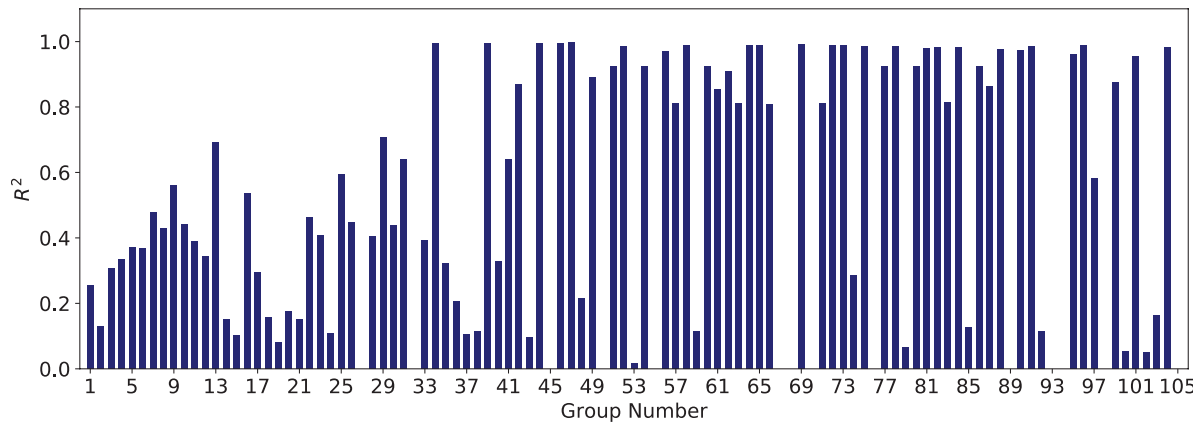


**Figure 166.**  $R^2$  results for the power models in EFA/Coarse data set: critical shear stress.

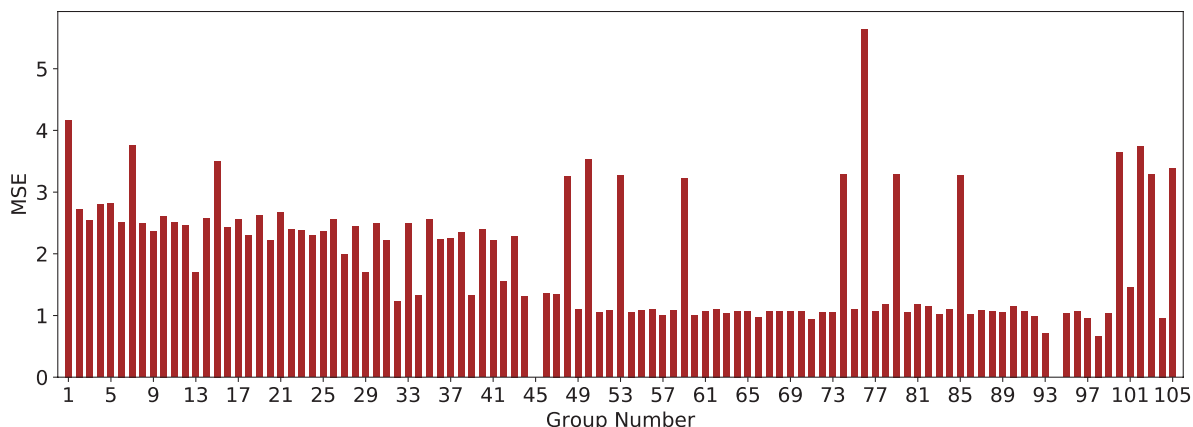


**Figure 167.** MSE results for linear models in EFA/Coarse data set: critical shear stress.

were very low as compared with the EFA/Fine data set. That is, many regression groups might meet the requirements of the first two filters,  $R^2$  and MSE, but only marginally pass through the  $F$ -test. Figure 167 and Figure 168 show the values of MSE for the linear and power models, respectively.

After passing through Filters 1 and 2 ( $R^2$  and MSE), linear models associated with Groups 51, 54, 57, 60, 63, 66, 71, 77, 80, 83, 86, 89, 92, and 97 were selected for further analysis. Power models associated with Groups 34, 44, 46, 47, 51, 52, 54, 58, 60, 64, 77, 78, 80, 86, 88, 95, 101, and 104 were also selected for further analysis.

Filter 3,  $F$ -value/ $F$ -stat, was determined for each group mentioned above. Table 49 shows the results of the selected linear models after the requirements of the first three filters ( $R^2$ , MSE, and  $F$ -value/ $F$ -stat) were met. As shown in Table 49, all selected models performed satisfactorily in the cross-validation test. Table 50 shows the results of the selected power models after the requirements of the first three filters were met. The best models that also had a good cross-validation score are shaded and highlighted in blue in Tables 49 and 50. Out of all the highlighted correlation equations in Table 49 and Table 50, the Group 77 correlation equation in power form was selected as the most promising equation. Figure 169 shows the plot of POU versus  $\theta$  for this model. The vertical axis in Figure 169 represents the probability that, when the selected model is used, the predicted  $\tau_c$  will be smaller than the actual  $\tau_c$ , in percentage

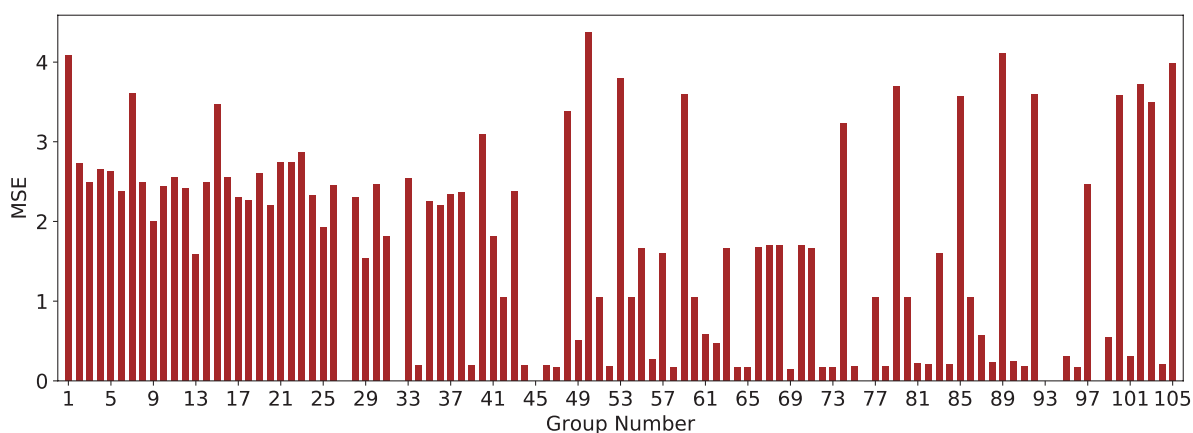


**Figure 168.** MSE results for power models in EFA/Coarse data set: critical shear stress.

## 206 Relationship Between Erodibility and Properties of Soils

**Table 49. Selected linear models for critical shear stress in the EFA/Coarse data set.**

Group No.	Independent Variables	Model Expression	R <sup>2</sup>	MSE	F-value/F-stat	Cross-Validation Score
51	$C_c, \gamma, D_{50}$	$\tau_c = -0.016 \times C_c + 0.09 \times \gamma + 0.86 \times D_{50} - 1.12$	0.92	1.05	5.1	0.89
54	$C_c, WC, D_{50}$	$\tau_c = -0.009 \times C_c - 0.03 \times WC + 0.82 \times D_{50} + 0.83$	0.92	1.06	5.1	0.89
57	$PF, C_c, D_{50}$	$\tau_c = 0.015 \times PF - 0.01 \times C_c + 0.88 \times D_{50} + 0.05$	0.93	1.01	5.4	0.88
60	$C_c, \gamma, WC, PF$	$\tau_c = -0.023 \times C_c + 0.16 \times \gamma - 0.06 \times WC + 0.82 \times D_{50} - 1.6$	0.93	1.00	2.6	0.89
63	$C_c, \gamma, PF, D_{50}$	$\tau_c = -0.015 \times C_c + 0.06 \times \gamma + 0.01 \times PF + 0.88 \times D_{50} - 0.89$	0.93	1.03	2.9	0.87
66	$C_c, WC, PF, D_{50}$	$\tau_c = -0.01349 \times C_c - 0.06 \times WC + 0.03 \times PF + 0.85 \times D_{50} + 0.62$	0.93	0.98	2.9	0.88
71	$C_c, \gamma, WC, PF, D_{50}$	$\tau_c = -0.024 \times C_c + 0.13 \times \gamma - 0.08 \times WC + 0.03 \times PF + 0.84 \times D_{50} - 1.38$	0.94	0.93	2.1	0.88
77	$C_u, \gamma, D_{50}$	$\tau_c = 0.001 \times C_u + 0.06 \times \gamma + 0.86 \times D_{50} - 0.71$	0.92	1.06	5.1	0.9
80	$C_u, WC, D_{50}$	$\tau_c = 0.001 \times C_u - 0.03 \times WC + 0.83 \times D_{50} + 0.72$	0.92	1.05	5.1	0.88
83	$PF, C_u, D_{50}$	$\tau_c = 0.015 \times PF + 0.0007 \times C_u + 0.88 \times D_{50} + 0.02$	0.92	1.01	5.3	0.88
86	$C_u, \gamma, WC, D_{50}$	$\tau_c = 0.001 \times C_u + 0.11 \times \gamma - 0.05 \times WC + 0.83 \times D_{50} - 1.03$	0.93	1.02	3.3	0.89
89	$C_u, \gamma, PF, D_{50}$	$\tau_c = 0.00025 \times C_u + 0.04 \times \gamma + 0.01 \times PF + 0.88 \times D_{50} - 0.55$	0.93	1.05	3.3	0.86
92	$C_u, WC, PF, D_{50}$	$\tau_c = -0.00037 \times C_u - 0.06 \times WC + 0.03 \times PF + 0.85 \times D_{50} + 0.56$	0.93	0.99	3.3	0.87
97	$C_u, \gamma, WC, PF, D_{50}$	$\tau_c = -0.001 \times C_u + 0.09 \times \gamma - 0.07 \times WC + 0.03 \times PF + 0.85 \times D_{50} - 0.88$	0.94	0.96	2.4	0.86

(with 0.3 Pa offset). To reach 90% confidence that the predicted  $\tau_c$  is smaller than the actual  $\tau_c$ , the predicted value should be multiplied by 0.82.

**JET Data Set.** A similar approach was taken to select the best correlation equation for critical shear stress in the JET database. However, there are two important notes to notice about the JET database:

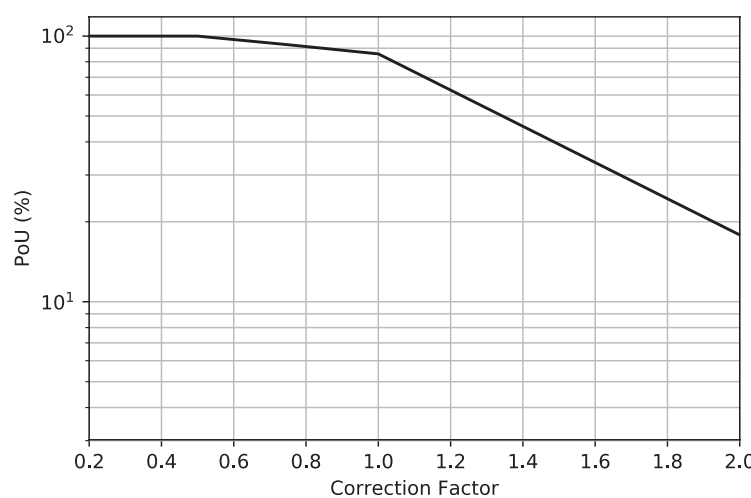
1. The JET was primarily performed on the finer soils ( $D_{50} < 0.3$  mm), and, therefore, the number of data points in the JET/Coarse data set was substantially low compared with the JET/Fine data set. Figure 170 and Figure 171 show the number of data points in each of the 135 combination groups in the JET/Global data set and each of the 105 combination groups in the JET/Coarse data set, respectively.
2. The  $R^2$  values for the JET/Global data set ( $D_{50} < 0.3$  mm), although low themselves, were still better than the  $R^2$  values for the JET/Fine data set. Therefore, the regression results for the JET/Global data set are presented as the best models.

Figure 172 and Figure 173 show the results for  $R^2$  for each combination group in the JET/Global data set, for the linear and power models, respectively. Both plots show relatively poor  $R^2$  for the JET/Global data set. One of the major reasons behind the poor relationships for critical shear stress in the JET database is the variety of methods used to interpret the raw data and obtain the critical shear stress. Section 4.3.1.4 of this report discussed these different methods. More on the JET issues is discussed in Chapter 8.

Figure 174 and Figure 175 show the values of MSE for the linear and power models, respectively.

**Table 50.** Selected power models for critical shear stress in the EFA/Coarse data set.

Group No.	Independent Variables	Model Expression	R <sup>2</sup>	MSE	F-value/F-stat	Cross-Validation Score
34	PI, VST, PF, D <sub>50</sub>	$\tau_c = (32,400.5) \times PI^{-0.27} \times VST^{6.28} \times PF^{-19.79} \times D_{50}^{-15.93}$	0.99	0.191	140	-15.44
44	PI, γ, VST, PF, D <sub>50</sub>	$\tau_c = (7.8 \times 10^{-5}) \times PI^{1.41} \times \gamma^{0.82} \times VST^{4.91} \times PF^{-15.57} \times D_{50}^{-18.06}$	0.99	0.198	88	-1.4
46	PI, WC, VST, PF, D <sub>50</sub>	$\tau_c = (267,267.2) \times PI^{-0.36} \times \gamma^{-0.21} \times VST^{6.24} \times PF^{-20.26} \times D_{50}^{-16.14}$	0.99	0.197	70.5	0.08
47	PI, γ, WC, VST, PF, D <sub>50</sub>	$\tau_c = (35.65) \times PI^{-0.19} \times \gamma^{7.82} \times WC^{-2.91} \times VST^{2.36} \times PF^{-16.46} \times D_{50}^{-14.05}$	0.99	0.169	56.1	0.09
51	C <sub>c</sub> , γ, D <sub>50</sub>	$\tau_c = (2.32) \times C_c^{0.04} \times \gamma^{-0.13} \times D_{50}^{0.77}$	0.93	1.045	36	0.98
52	C <sub>c</sub> , WC, VST	$\tau_c = (1,228,385.72) \times C_c^{-0.31} \times WC^{-11.03} \times VST^{2.35}$	0.98	0.178	38.6	0.1
54	C <sub>c</sub> , WC, D <sub>50</sub>	$\tau_c = (1.67) \times C_c^{0.05} \times WC^{-0.04} \times D_{50}^{0.76}$	0.93	1.043	36.2	0.98
58	C <sub>c</sub> , γ, WC, VST	$(0.22) \times C_c^{-0.55} \times \gamma^{5.95} \times WC^{-10.42} \times VST^{1.6}$	0.99	0.168	24.3	-0.5
60	C <sub>c</sub> , γ, WC, D <sub>50</sub>	$\tau_c = (1.517) \times C_c^{0.06} \times \gamma^{0.04} \times WC^{-0.04} \times D_{50}^{0.76}$	0.93	1.043	29.1	0.97
64	C <sub>c</sub> , WC, VST, PF	$\tau_c = (1.09 \times 10^{-5}) \times C_c^{5.12} \times WC^{-20.76} \times VST^{-12.04} \times PF^{29.64}$	0.98	0.164	25.8	-1.5
77	C <sub>c</sub> , γ, D <sub>50</sub>	$\tau_c = (1.58) \times C_u^{-0.04} \times \gamma^{0.02} \times D_{50}^{0.77}$	0.93	1.044	36.1	0.99
78	C <sub>c</sub> , WC, VST	$\tau_c = (257.02) \times C_u^{-1.73} \times WC^{-8.77} \times VST^{4.76}$	0.98	0.183	33.1	0.04
80	C <sub>c</sub> , WC, D <sub>50</sub>	$\tau_c = (1.66) \times C_u^{-0.04} \times WC^{-0.01} \times D_{50}^{0.78}$	0.93	1.044	36.1	0.98
86	C <sub>c</sub> , γ, WC, D <sub>50</sub>	$\tau_c = (1.378) \times C_u^{-0.04} \times \gamma^{0.07} \times WC^{-0.01} \times D_{50}^{0.78}$	0.93	1.044	29.1	0.96
88	C <sub>c</sub> , γ, VST, D <sub>50</sub>	$\tau_c = (5.845 \times 10^{11}) \times C_u^{-3.07} \times \gamma^{-19.6} \times VST^{10.74} \times D_{50}^{1.62}$	0.97	0.236	21	0.03
95	C <sub>c</sub> , γ, WC, VST, D <sub>50</sub>	$\tau_c = (2.24 \times 10^{11}) \times C_u^{-2.31} \times \gamma^{-16.85} \times WC^{-0.48} \times VST^{8.48} \times D_{50}^{1.18}$	0.96	0.307	19	-11.3
101	C <sub>c</sub> , C <sub>u</sub> , PI	$\tau_c = (2.555 \times 10^{13}) \times C_c^{-4.19} \times C_u^{22.94} \times PI^{-80.26}$	0.95	0.313	26.7	-0.44
104	C <sub>c</sub> , C <sub>u</sub> , VST	$\tau_c = (5.87 \times 10^{-13}) \times C_c^{-0.503} \times C_u^{-2.32} \times VST^{8.47}$	0.98	0.204	25.5	0.01

**Figure 169.** Plot of POU versus correction factor for Group 77 (power):  $\tau_c$  in the EFA/Coarse data set.

## 208 Relationship Between Erodibility and Properties of Soils

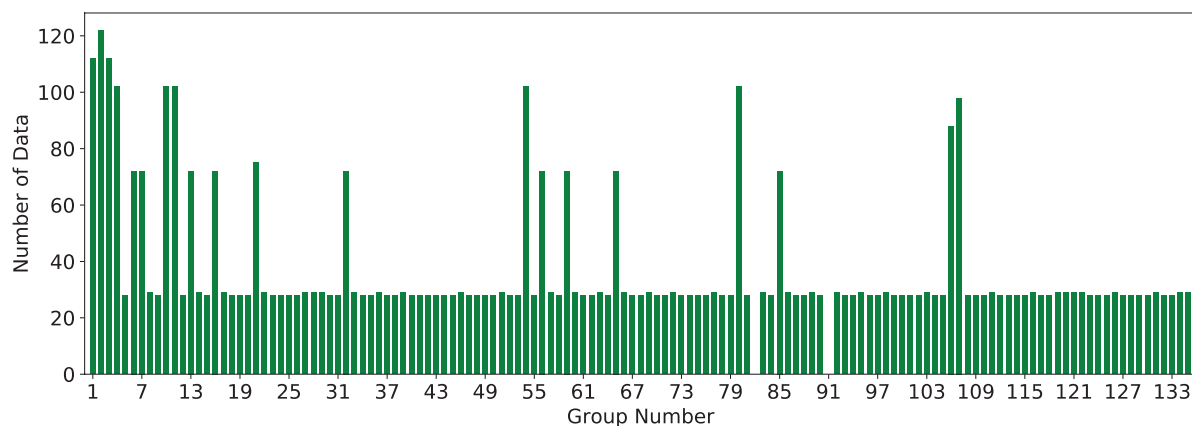


**Figure 170.** Number of data points in each of 135 combination groups for the JET/Global data set: critical shear stress.

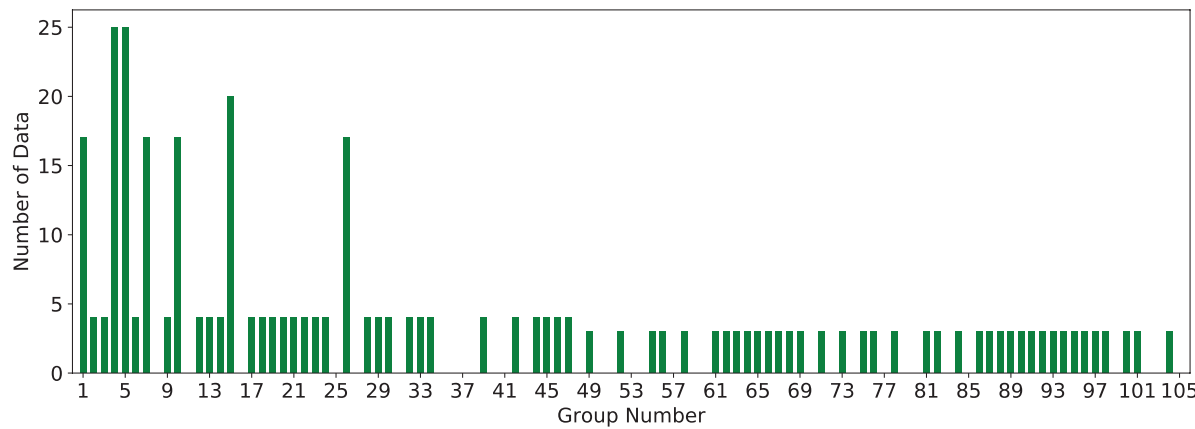


**Figure 171.** Number of data points in each of 105 combination groups for the JET/Coarse data set: critical shear stress.

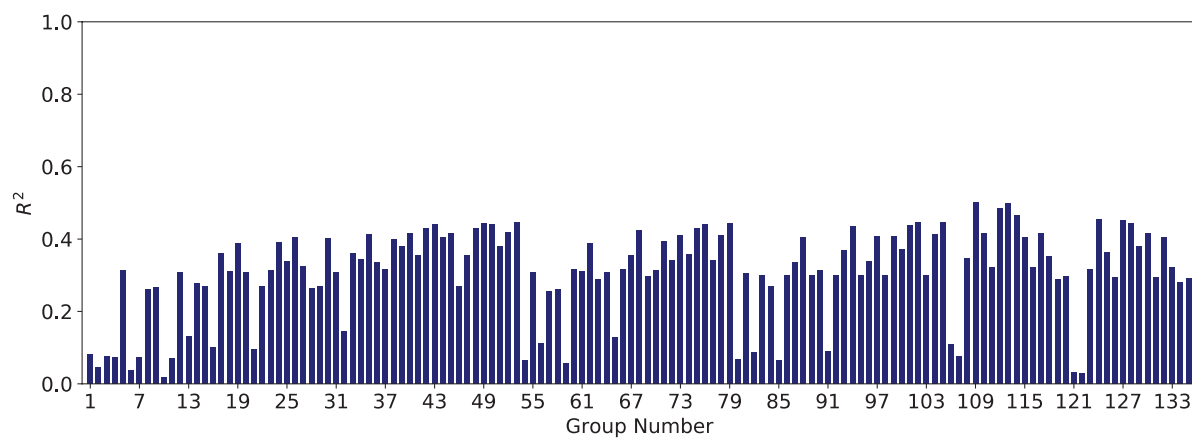


**Figure 172.** R<sup>2</sup> results for the linear model in JET/Global data set: critical shear stress.

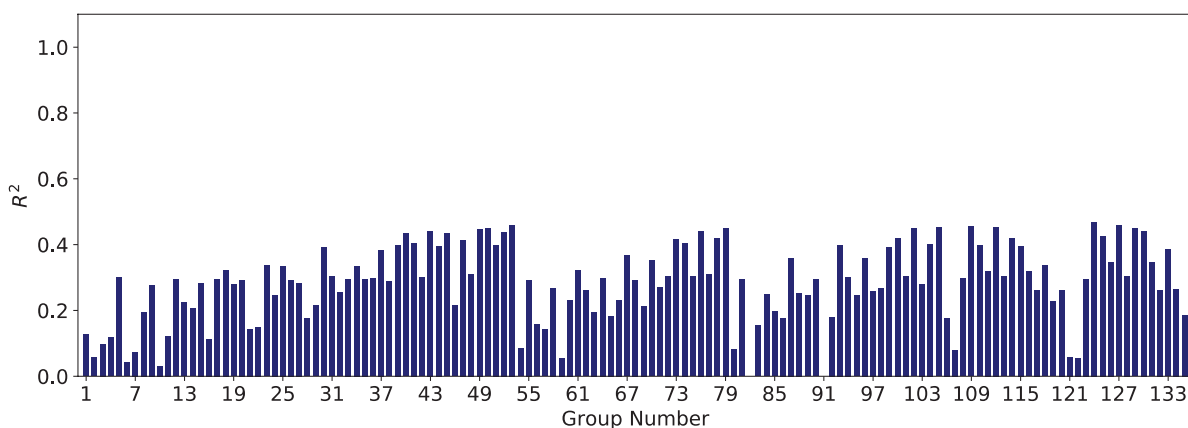


**Figure 173.**  *$R^2$  results for the power models in JET/Global data set: critical shear stress.*

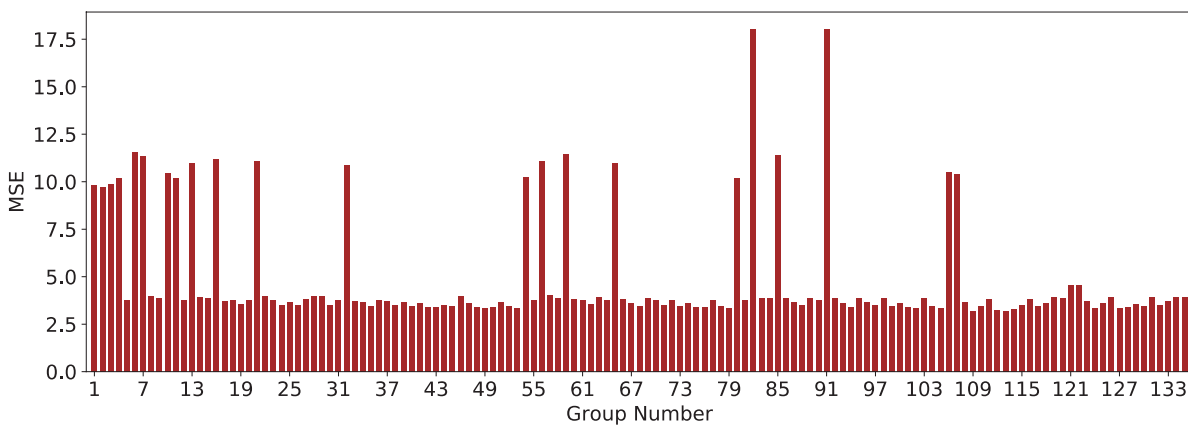


**Figure 174.** *MSE results for linear models in JET/Global data set: critical shear stress.*

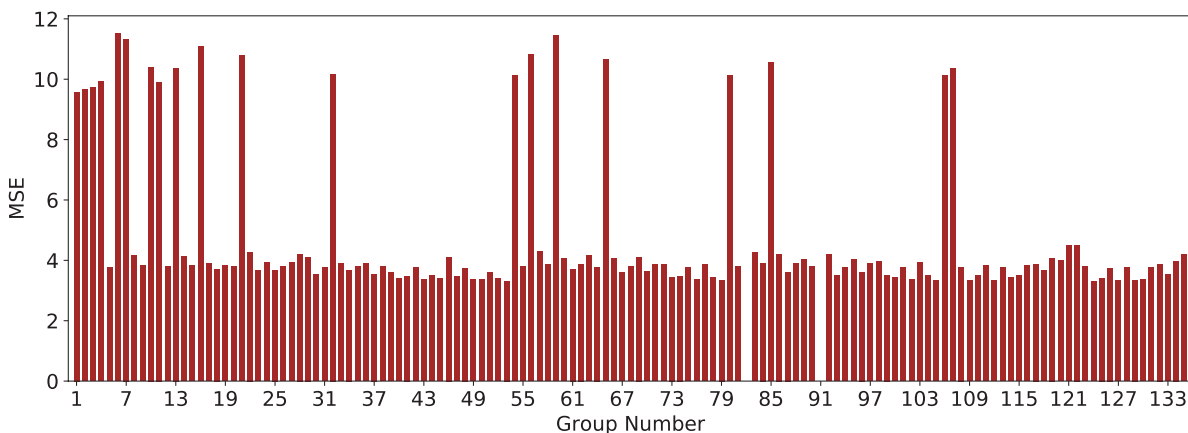


**Figure 175.** *MSE results for power models in JET/Global data set: critical shear stress.*

## 210 Relationship Between Erodibility and Properties of Soils

**Table 51.** Selected linear models for critical shear stress in the JET/Global data set.

Group No.	Independent Variables	Model Expression	R <sup>2</sup>	MSE	F-value/F-stat	Cross-Validation Score
49	$\gamma$ , WC, $S_u$ , PF, $D_{50}$	$\tau_c = -0.769 \times \gamma - 0.08 \times WC + 0.04 \times S_u - 0.07 \times PF - 46.05 \times D_{50} + 28.36$ for $D_{50} < 0.3$ mm	0.44	3.36	1.318	0.05
76	LL, $\gamma$ , $S_u$ , PF, $D_{50}$	$\tau_c = -0.011 \times LL - 0.71 \times \gamma + 0.04 \times S_u - 0.08 \times PF - 46.8 \times D_{50} + 26.56$ for $D_{50} < 0.3$ mm	0.44	3.38	1.299	0.04
109	PC, $\gamma$ , WC, $S_u$ , PF, $D_{50}$	$\tau_c = -0.272 \times PC - 1.28 \times \gamma + 0.22 \times WC + 0.07 \times S_u + 0.03 \times PF - 31.65 \times D_{50} + 31.03$ for $D_{50} < 0.3$ mm	0.50	3.20	1.365	-0.02
112	PC, $\gamma$ , $S_u$ , PF, $D_{50}$	$\tau_c = -0.176 \times PC - 1.24 \times \gamma + 0.06 \times S_u + 0.02 \times PF - 34.03 \times D_{50} + 33.38$ for $D_{50} < 0.3$ mm	0.49	3.24	1.563	0.08
113	PC, $\gamma$ , WC, $S_u$ , $D_{50}$	$\tau_c = -0.248 \times PC - 1.23 \times \gamma + 0.21 \times WC + 0.07 \times S_u - 36.89 \times D_{50} + 31.82$ for $D_{50} < 0.3$ mm	0.50	3.20	1.647	0.1

After passing through Filters 1 and 2 ( $R^2$  and MSE), the linear models associated with Groups 49, 76, 109, 112, and 113 in the JET/Global data set were selected for further analysis. Power models associated with Groups 53, 79, 109, and 124 in the JET/Global data set were also selected for further analysis.

Filter 3, F-value/F-stat, was determined for each group mentioned above. Table 51 shows the results of the selected linear models after the requirements of the first three filters ( $R^2$ , MSE, and F-value/F-stat) were met. Only one of the selected models in Table 51 performed well in the cross-validation test and is shaded and highlighted in blue. Table 52 shows the results of the selected power models after the requirements of the first three filters were met. Out of all the correlation equations in Table 51 and Table 52, the Group 113 correlation equation in linear form was selected as the most promising equation. Figure 176 shows the plot of POU versus  $\theta$  for this model. The vertical axis in Figure 176 represents the probability that, when the selected model is used, the predicted  $\tau_c$  will be smaller than the actual  $\tau_c$ , in percentage (with 1 Pa offset). To reach 90% confidence that the predicted  $\tau_c$  is smaller than the actual  $\tau_c$ , the predicted value should be multiplied by 0.6.

**Table 52.** Selected power models for critical shear stress in the JET/Global data set.

Group No.	Independent Variables	Model Expression	R <sup>2</sup>	MSE	F-value/F-stat	Cross-Validation Score
53	PI, $\gamma$ , WC, $S_u$ , PF, $D_{50}$	$\tau_c = (2.697) \times PI^{0.13} \times \gamma^{2.02} \times WC^{-0.43} \times S_u^{0.43} \times PF^{1.69} \times D_{50}^{0.27}$ for $D_{50} < 0.3$ mm	0.46	3.32	7.155	-1.5
79	LL, $\gamma$ , WC, $S_u$ , PF, $D_{50}$	$\tau_c = (7.412) \times LL^{0.14} \times \gamma^{-2.43} \times WC^{-0.38} \times S_u^{0.47} \times PF^{1.64} \times D_{50}^{0.27}$ for $D_{50} < 0.3$ mm	0.45	3.35	7.005	-0.69
109	PC, $\gamma$ , WC, $S_u$ , PF, $D_{50}$	$\tau_c = (76.49) \times PC^{-0.26} \times \gamma^{-3.17} \times WC^{-0.2} \times S_u^{0.56} \times PF^{1.68} \times D_{50}^{0.23}$ for $D_{50} < 0.3$ mm	0.46	3.33	7.089	-1.62
124	$\gamma$ , A, WC, $S_u$ , PF, $D_{50}$	$\tau_c = (3.86) \times \gamma^{2.1} \times A^{0.19} \times WC^{-0.41} \times S_u^{0.44} \times PF^{1.73} \times D_{50}^{1.26}$ for $D_{50} < 0.3$ mm	0.47	3.30	6.891	-0.77

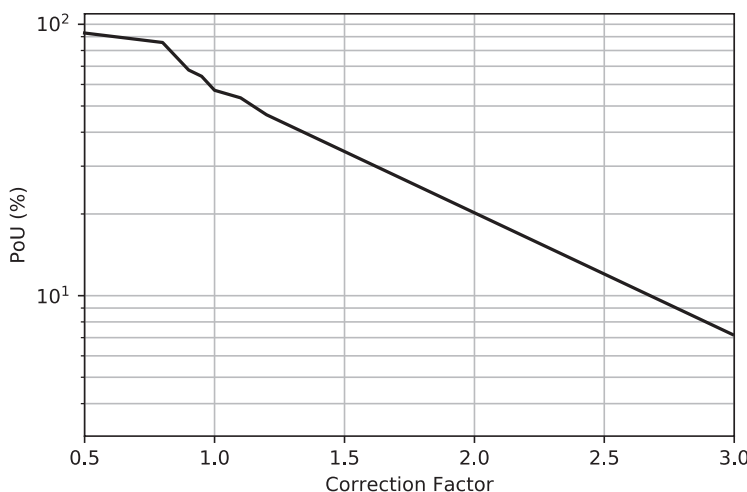


**Figure 176.** Plot of POU versus correction factor for Group 113 (linear):  $\tau_c$  in the JET/Global data set.

**HET Data Set.** A similar approach was taken to select the best correlation equation for critical shear stress in the HET database. In the HET database, there are also two important observations to notice:

1. The HET was primarily performed on finer soils ( $D_{50} < 0.3$  mm), and, therefore, the number of data points in the HET/Coarse data set was substantially low compared with the HET/Fine data set. In fact, many combination groups in the HET/Coarse database had zero data points. Figure 177 and Figure 178 show the number of data points in each of the 135 combination groups in the HET/Global data set and each of the 105 combination groups in the HET/Coarse data set, respectively.
2. The  $R^2$  values for the HET/Global data set ( $D_{50} < 0.3$  mm) were significantly better than the  $R^2$  values for the HET/Coarse and HET/Fine data sets. Therefore the regression results for the HET/Global data set are presented as the best models.

Figure 179 and Figure 180 show the results for  $R^2$  for each combination group in the HET/Global data set, for the linear and power models, respectively. Both plots show that the best  $R^2$  values for the HET/Global data set were around 0.60 to 0.65. One of the major reasons

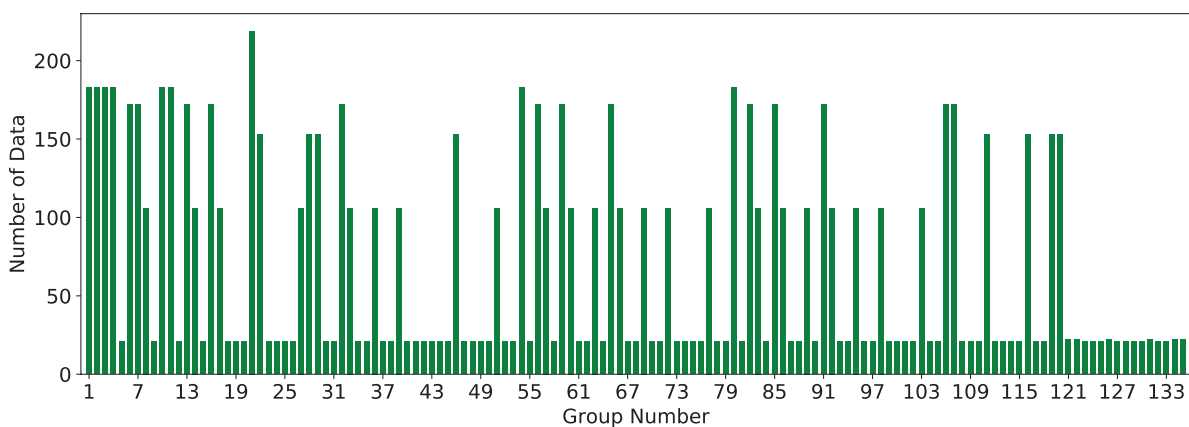


**Figure 177.** Number of data points in each of 135 combination groups for the HET/Global data set: critical shear stress.

## 212 Relationship Between Erodibility and Properties of Soils

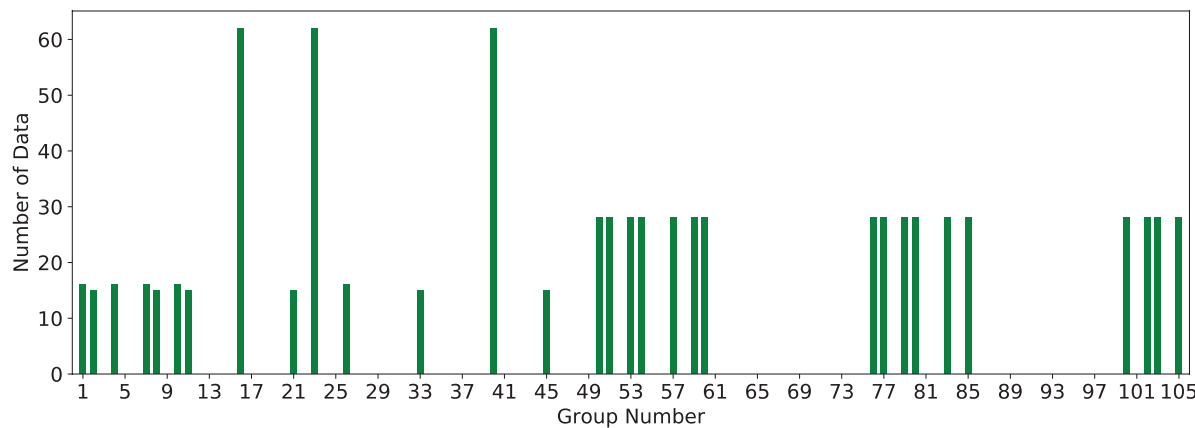


Figure 178. Number of data points in each of 105 combination groups for the HET/Coarse data set: critical shear stress.

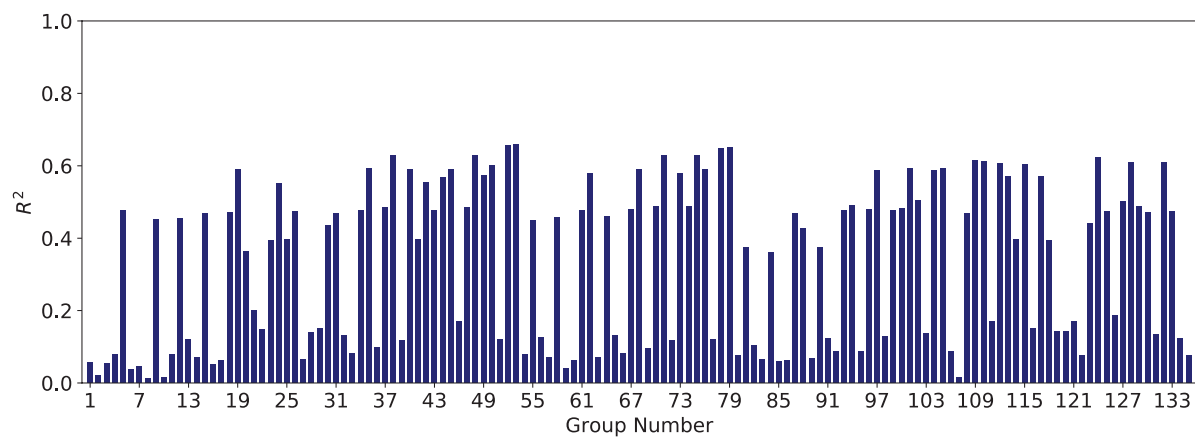


Figure 179.  $R^2$  results for the linear models in HET/Global data set: critical shear stress.

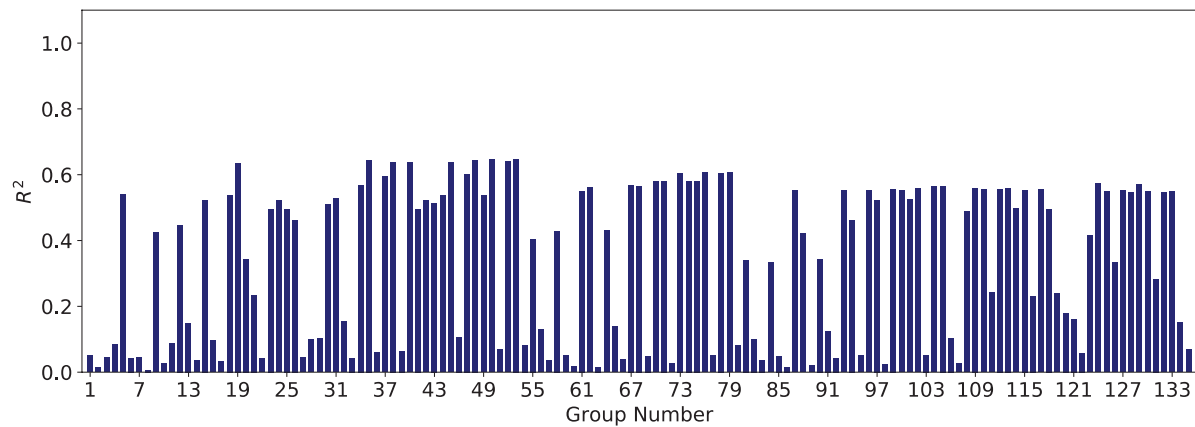


Figure 180.  $R^2$  results for the power models in HET/Global data set: critical shear stress.

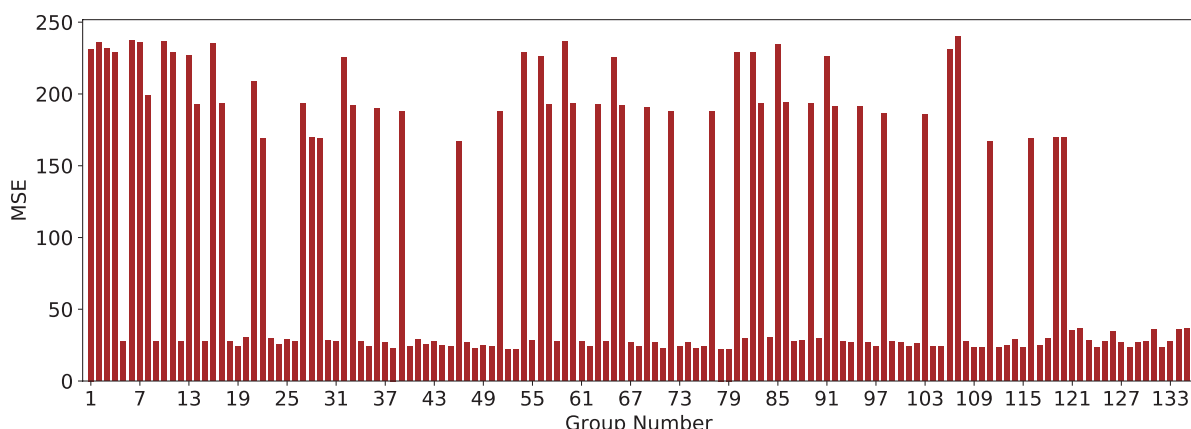


Figure 181. MSE results for linear models in HET/Global data set: critical shear stress.

behind the poor relationships for critical shear stress in the HET database was that the method used to calculate the erodibility parameters in the HET includes many crude judgements. More on the issues affecting the HET is discussed in Chapter 8. Figure 181 and Figure 182 show the values of MSE for the linear and power models, respectively.

After passing through Filters 1 and 2 ( $R^2$  and MSE), linear models associated with Groups 38, 48, 49, 52, 53, 71, 78, 79, 124, and 128 in the HET/Global data set were selected for further analysis. Power models associated with Groups 19, 35, 38, 40, 48, 50, 52, and 53 in the HET/Global data set were also selected for further analysis.

Filter 3,  $F$ -value/ $F$ -stat, was determined for each group mentioned above. Table 53 shows the results of the selected linear models after the requirements of the first three filters ( $R^2$ , MSE, and  $F$ -value/ $F$ -stat) were met. Table 54 shows the results of the selected power models after the requirements of the first three filters were met. Only one of the selected models in Table 54 performed well in the cross-validation test and is shaded and highlighted in blue. Of all the correlation equations in Table 53 and Table 54, the Group 19 correlation equation in power form was selected as the most promising equation. Figure 183 shows the plot of POU versus  $\theta$  for this model. The vertical axis in Figure 183 represents the probability that, when the selected model is used, the predicted  $\tau_c$  will be smaller than the actual  $\tau_c$ , in percentage (with 0.4 Pa offset). To reach 90% confidence that the predicted  $\tau_c$  is smaller than the actual  $\tau_c$ , the predicted value should be multiplied by 0.6.

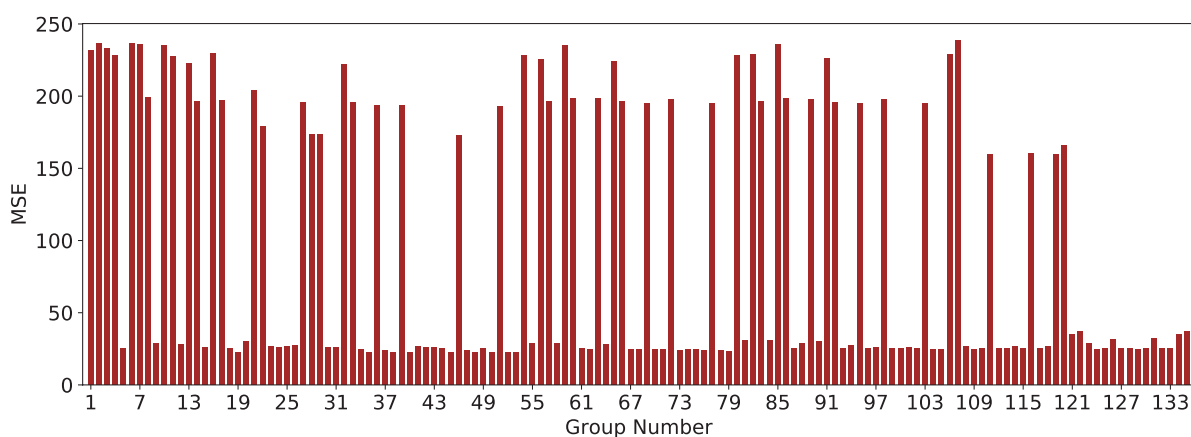


Figure 182. MSE results for power models in HET/Global data set: critical shear stress.

## 214 Relationship Between Erodibility and Properties of Soils

**Table 53.** Selected linear models for critical shear stress in the HET/Global data set.

Group No.	Independent Variables	Model Expression	R <sup>2</sup>	MSE	F-value/F-stat	Cross-Validation Score
38	PI, WC, S <sub>u</sub> , D <sub>50</sub>	$\tau_c = 0.446 \times +3.48 \times WC + 0.82 \times S_u + 2153.5 \times D_{50} - 98.12$	0.63	23.0	1.945	0.01
48	PI, γ, WC, S <sub>u</sub> , D <sub>50</sub>	$\tau_c = 0.45 \times PI - 0.61 \times \gamma + 3.6 \times WC + 0.83 \times S_u + 2,161.4 \times D_{50} - 89.22$	0.63	23.0	1.741	-0.09
49	γ, WC, S <sub>u</sub> , PF, D <sub>50</sub>	$\tau_c = 3.66 \times \gamma + 6.55 \times WC + 0.98 \times S_u + 0.61 \times PF + 3,053.2 \times D_{50} - 281.53$	0.58	24.5	1.397	-0.05
52	PI, WC, S <sub>u</sub> , PF, D <sub>50</sub>	$\tau_c = 0.49 \times PI + 5.26 \times WC + 0.92 \times S_u + 0.7 \times PF + 2,958 \times D_{50} - 201.85$	0.66	22.0	1.977	0.1
53	PI, γ, WC, S <sub>u</sub> , PF, D <sub>50</sub>	$\tau_c = 0.479 \times PI + 1.43 \times \gamma + 5.1 \times WC + 0.91 \times S_u + 0.73 \times PF + 2,979.7 \times D_{50} - 227.85$	0.66	22.0	1.574	-0.13
71	LL, WC, S <sub>u</sub> , D <sub>50</sub>	$\tau_c = 0.416 \times LL + 3.86 \times WC + 0.85 \times S_u + 2216.6 \times D_{50} - 113$	0.63	22.9	2.257	0.11
78	LL, WC, S <sub>u</sub> , PF, D <sub>50</sub>	$\tau_c = 0.423 \times LL + 5.4 \times WC + 0.93 \times S_u + 0.55 \times PF + 2,870.5 \times D_{50} - 198$	0.65	22.3	1.905	0.07
79	LL, γ, WC, S <sub>u</sub> , PF, D <sub>50</sub>	$\tau_c = 0.414 \times LL + 1.63 \times \gamma + 5.19 \times WC + 0.91 \times S_u + 0.6 \times PF + 2,897.1 \times D_{50} - 227.7$	0.65	22.3	1.519	0.01
124	γ, A, WC, S <sub>u</sub> , PF, D <sub>50</sub>	$\tau_c = 2.1 \times \gamma + 8.71 \times A + 7.3 \times WC + 1.03 \times S_u + 0.48 \times PF + 2,808.5 \times D_{50} - 265$	0.63	23.1	1.353	-0.6
128	D <sub>50</sub> , γ, WC, S <sub>u</sub> , A	$\tau_c = 2,257.2 \times D_{50} + 0.57 \times \gamma + 6.34 \times WC + 0.99 \times S_u + 9.34 \times A - 171.52$	0.61	23.5	1.616	0.06

**Table 54.** Selected power models for critical shear stress in the HET/Global data set.

Group No.	Independent Variables	Model Expression	R <sup>2</sup>	MSE	F-value/F-stat	Cross-Validation Score
19	PI, S <sub>u</sub> , D <sub>50</sub>	$\tau_c = (25.07) \times PI^{0.27} \times S_u^{0.55} \times D_{50}^{0.5}$	0.64	22.7	16.049	0.43
35	PI, γ, S <sub>u</sub> , D <sub>50</sub>	$\tau_c = (495.9) \times PI^{0.32} \times \gamma^{-1.1} \times S_u^{0.57} \times D_{50}^{0.49}$	0.65	22.4	12.907	-0.47
38	PI, WC, S <sub>u</sub> , D <sub>50</sub>	$\tau_c = (54.04) \times PI^{0.31} \times WC^{-0.28} \times S_u^{0.5} \times D_{50}^{0.47}$	0.64	22.6	12.650	-0.1
40	PI, S <sub>u</sub> , PF, D <sub>50</sub>	$\tau_c = (38.24) \times PI^{0.26} \times S_u^{0.55} \times PF^{-0.11} \times D_{50}^{0.48}$	0.64	22.7	12.580	-0.19
48	PI, γ, WC, S <sub>u</sub> , D <sub>50</sub>	$\tau_c = (562.6) \times PI^{0.33} \times \gamma^{-1.01} \times WC^{-0.13} \times S_u^{0.54} \times D_{50}^{0.47}$	0.65	22.4	10.322	-0.14
50	PI, γ, S <sub>u</sub> , PF, D <sub>50</sub>	$\tau_c = (1,430.36) \times PI^{0.3} \times \gamma^{-1.2} \times S_u^{0.56} \times PF^{-0.21} \times D_{50}^{0.44}$	0.65	22.4	10.366	-0.48
52	PI, WC, S <sub>u</sub> , PF, D <sub>50</sub>	$\tau_c = (209.5) \times PI^{0.3} \times WC^{-0.41} \times S_u^{0.46} \times PF^{-0.26} \times D_{50}^{0.41}$	0.64	22.6	10.176	-0.41
53	PI, γ, WC, S <sub>u</sub> , PF, D <sub>50</sub>	$\tau_c = (2491.8) \times PI^{0.32} \times \gamma^{-1.04} \times WC^{-0.26} \times S_u^{0.5} \times PF^{-0.28} \times D_{50}^{0.4}$	0.65	22.3	8.410	-0.47

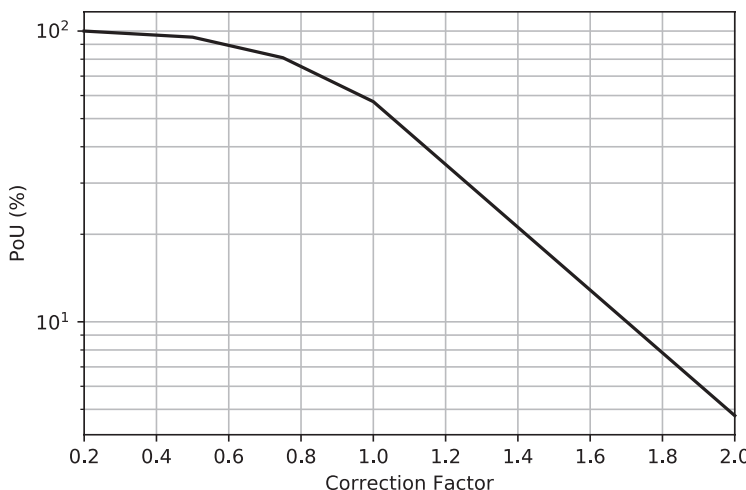


**Figure 183.** Plot of POU versus correction factor for Group 19 (power):  $\tau_c$  in the HET/Global data set.

#### 7.3.4.2 Critical Velocity

The same four-filter process discussed in Section 7.3.3 was implemented to obtain the best models for critical velocity. The first observation was that of the three erosion tests studied in this chapter (EFA, JET, HET), only the EFA test has critical velocity,  $v_c$ , as one of its outputs. That is, the results of the JET and HET consist of only three erodibility parameters (i.e.,  $\tau_c$ ,  $E_v$ , and EC), whereas the EFA results include all five erodibility parameters (i.e.,  $\tau_c$ ,  $v_c$ ,  $E_v$ ,  $E_s$ , and EC). Therefore, regression analysis for critical velocity was limited to the EFA data set.

As in the case of critical shear stress, it was observed that dividing the EFA/Global data set into the EFA/Fine and EFA/Coarse data sets would significantly improve the regression results. Figure 184 shows the number of data points in each of the 135 combination groups in the EFA/Fine data set. Figure 185 and Figure 186 show the results for  $R^2$  for each combination group for the linear and power models, respectively.

The  $R^2$  values of Groups 109 to 135 were generally higher than the rest for both the linear and power models. Figure 187 and Figure 188 show the MSE results for each of the 135 combination groups in the EFA/Fine data set for the linear and power models, respectively.

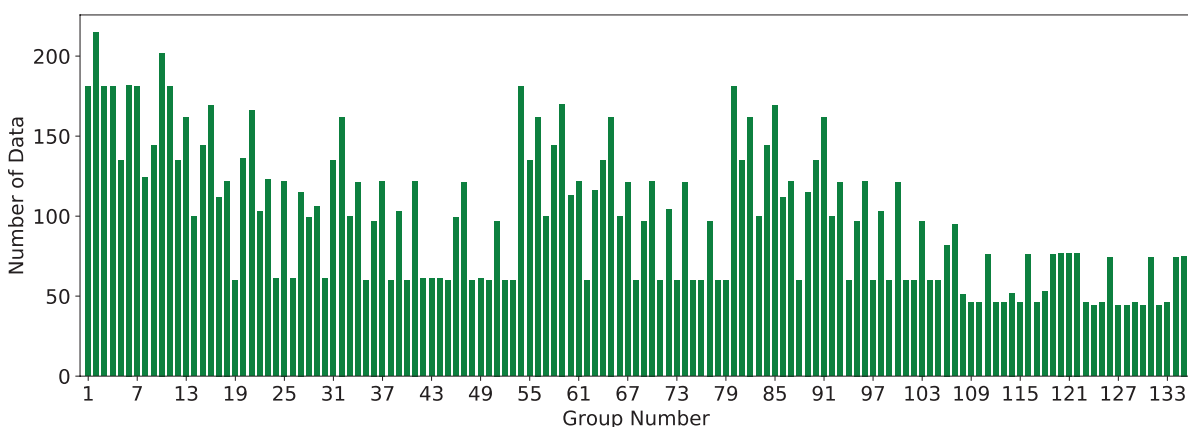


**Figure 184.** Number of data points in each of 135 combination groups for the EFA/Fine data set: critical velocity.

## 216 Relationship Between Erodibility and Properties of Soils

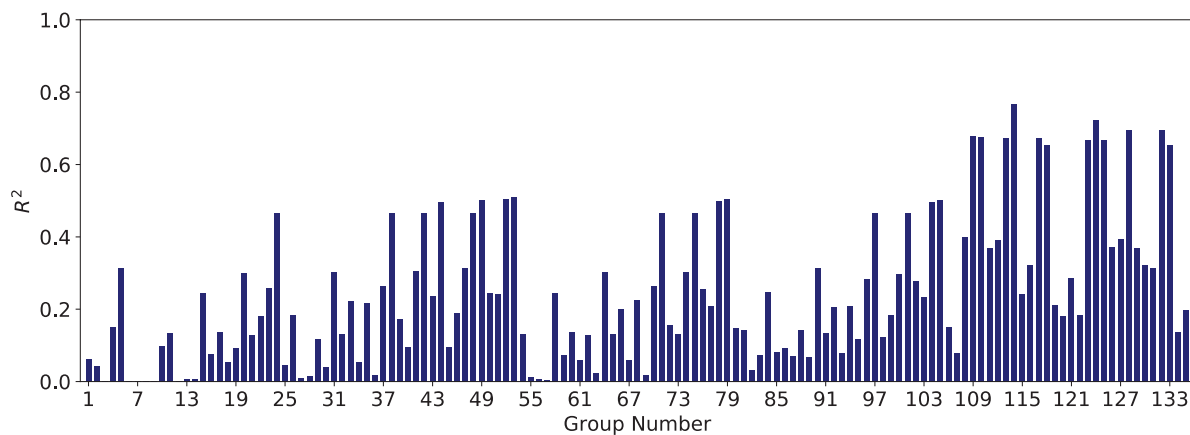


Figure 185.  $R^2$  results for the linear models in EFA/Fine data set: critical velocity.

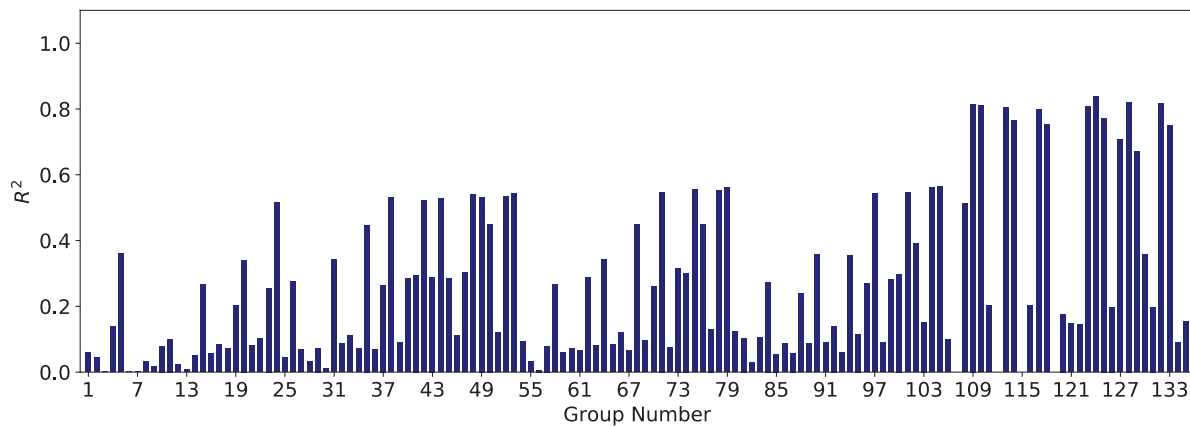


Figure 186.  $R^2$  results for the power models in EFA/Fine data set: critical velocity.

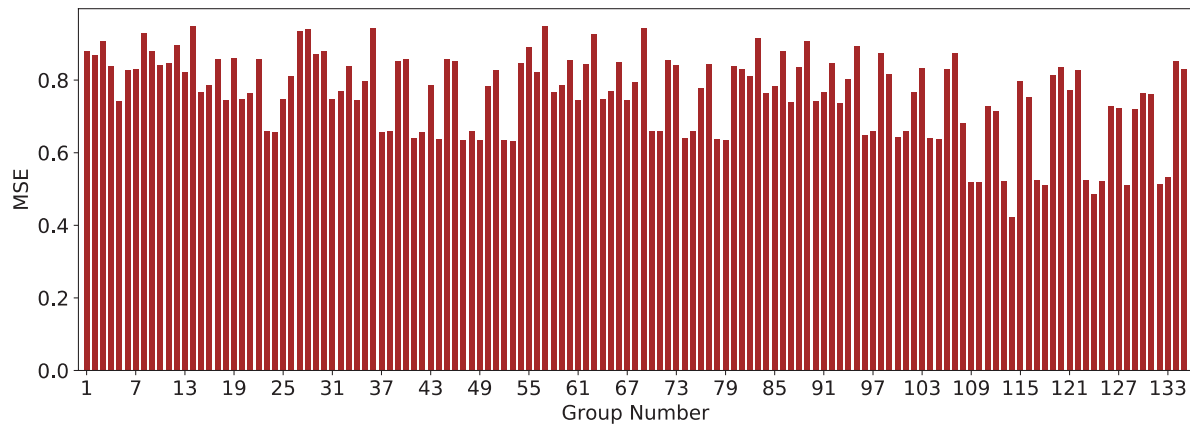
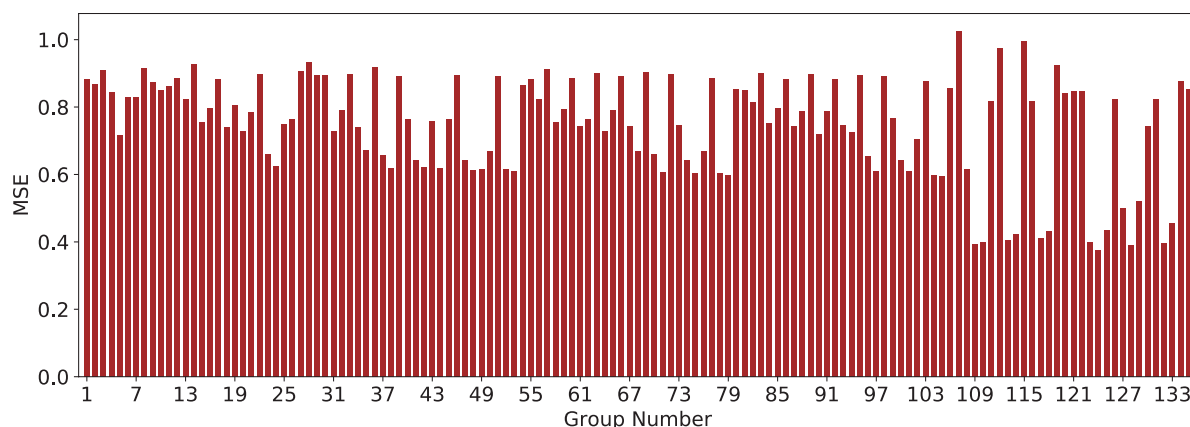


Figure 187. MSE results for linear models in EFA/Fine data set: critical velocity.



**Figure 188.** MSE results for power models in EFA/Fine data set: critical velocity.

After passing through Filters 1 and 2 ( $R^2$  and MSE), the linear models associated with Groups 114, 124, 128, and 132 in the EFA/Fine data set were selected for further analysis. Power models associated with Groups 109, 110, 113, 114, 117, 118, 123, 124, 125, 128, 132, and 133 in the EFA/Fine data set were also selected for further analysis.

Filter 3,  $F$ -value/ $F$ -stat, was determined for each group mentioned above. Table 55 shows the results of the selected linear models after the requirements of the first three filters ( $R^2$ , MSE, and  $F$ -value/ $F$ -stat) were met. As shown in Table 55, all four selected models performed acceptably in the cross-validation test. Table 56 shows the results of the selected power models after the requirements of the first three filters were met. The best models that also had the best cross-validation scores are shaded and highlighted in blue in Tables 55 and 56. Out of all the correlation equations in Table 55 and Table 56, the Group 117 correlation equation in power form was selected as the most promising equation. Figure 189 shows the plot of POU versus  $\theta$  for this model. The vertical axis in Figure 189 represent the probability that, when the selected model is used the predicted  $v_c$  will be smaller than the actual  $v_c$ , in percentage (with 0.2 m/s offset). To reach 90% confidence that the predicted  $v_c$  is smaller than the actual  $v_c$ , the predicted value should be multiplied by 0.8.

The same procedure was conducted in the EFA/Coarse data set, and the best models were selected for critical velocity. Figure 190 shows the number of data points in each of the 105 combination groups in the EFA/Coarse data set. Figure 191 and Figure 192 show the results for  $R^2$  for each combination group for the linear and power models, respectively.

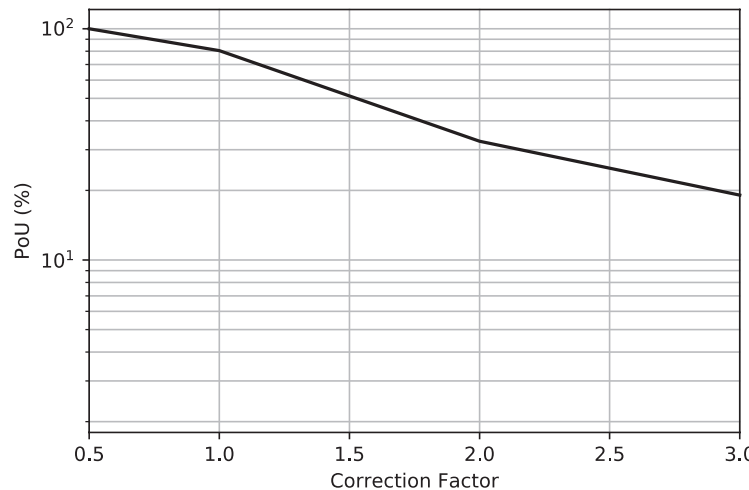
**Table 55.** Selected linear models for critical velocity in the EFA/Fine data set.

Group No.	Independent Variables	Model Expression	$R^2$	MSE	$F$ -value/ $F$ -stat	Cross-Validation Score
114	PC, $\gamma$ , WC, $S_u$ , PF	$v_c = 0.012 \times PC - 0.038 \times \gamma + 0.041 \times WC \pm 0.0042 \times S_u - 0.008 \times PF + 0.328$	0.77	0.42	21.5	0.58
124	$\gamma$ , A, WC, $S_u$ , PF, $D_{50}$	$v_c = -0.075 \times \gamma - 0.171 \times A + 0.05 \times WC + 0.0042 \times S_u - 0.02 \times PF - 11.33 \times D_{50} + 2.41$	0.72	0.49	16.6	0.64
128	$D_{50}$ , $\gamma$ , WC, $S_u$ , A	$v_c = -2.561 \times D_{50} - 0.022 \times \gamma + 0.051 \times WC + 0.005 \times S_u - 0.146 \times A - 0.384$	0.69	0.51	14.9	0.62
132	A, WC, $S_u$ , $D_{50}$	$v_c = -0.142 \times A + 0.051 \times WC + 0.004 \times S_u - 2.674 \times D_{50} - 0.784$	0.69	0.51	15.07	0.62

## 218 Relationship Between Erodibility and Properties of Soils

**Table 56.** Selected power models for critical velocity in the EFA/Fine data set.

Group No.	Independent Variables	Model Expression	R <sup>2</sup>	MSE	F-value/F-stat	Cross-Validation Score
109	PC, $\gamma$ , WC, $S_u$ , PF, $D_{50}$	$v_c = (40.218) \times PC^{0.12} \times \gamma^{-2.23} \times WC^{1.66} \times S_u^{0.48} \times PF^{-1.57} \times D_{50}^{-0.33}$	0.81	0.39	21.16	0.87
110	PC, WC, $S_u$ , PF, $D_{50}$	$v_c = (0.013) \times PC^{0.13} \times WC^{2.13} \times S_u^{0.51} \times PF^{-1.62} \times D_{50}^{-0.36}$	0.81	0.4	23.74	0.87
113	PC, $\gamma$ , WC, $S_u$ , $D_{50}$	$v_c = (0.1085) \times PC^{0.19} \times \gamma^{-2.3} \times WC^{1.6} \times S_u^{0.49} \times D_{50}^{-0.1212}$	0.8	0.41	22.92	0.81
114	PC, $\gamma$ , WC, $S_u$ , PF	$v_c = (2.699) \times PC^{0.39} \times \gamma^{-2.4} \times WC^{1.54} \times S_u^{0.4} \times PF^{-0.51}$	0.77	0.42	23.23	0.83
117	PC, WC, $S_u$ , $D_{50}$	$v_c = (2.518 \times 10^{-5}) \times PC^{0.2} \times WC^{2.06} \times S_u^{0.51} \times D_{50}^{-0.13}$	0.80	0.41	26.05	0.80
118	PC, WC, $S_u$ , PF	$v_c = (1.8 \times 10^{-4}) \times PC^{0.4} \times WC^{2.01} \times S_u^{0.45} \times PF^{-0.31}$	0.75	0.43	25.80	0.77
123	A, PL, $\gamma$ , WC, $S_u$	$v_c = (0.00875) \times A^{-0.24} \times PL^{1.11} \times \gamma^{-2.07} \times WC^{1.38} \times S_u^{0.58}$	0.81	0.40	21.56	0.78
124	$\gamma$ , A, WC, $S_u$ , PF, $D_{50}$	$v_c = (7.299) \times \gamma^{-2.02} \times A^{-0.41} \times WC^{2.25} \times S_u^{0.39} \times PF^{-1.68} \times D_{50}^{-0.41}$	0.84	0.37	18.09	0.74
125	$\gamma$ , WC, $S_u$ , PF, A	$v_c = (57.994) \times \gamma^{-3.76} \times WC^{1.48} \times S_u^{0.54} \times PF^{-0.18} \times A^{-0.23}$	0.77	0.43	19.1	0.68
128	$D_{50}$ , $\gamma$ , WC, $S_u$ , A	$v_c = (0.00728) \times D_{50}^{-0.26} \times \gamma^{-2.05} \times WC^{2.21} \times S_u^{0.46} \times A^{-0.39}$	0.82	0.39	22.9	0.50
132	A, WC, $S_u$ , $D_{50}$	$v_c = (3.92 \times 10^{-6}) \times A^{-0.41} \times WC^{2.65} \times S_u^{0.46} \times D_{50}^{-0.28}$	0.82	0.40	26.11	0.69
133	A, WC, $S_u$ , PF	$v_c = (7 \times 10^{-5}) \times A^{-0.28} \times WC^{2.23} \times S_u^{0.54} \times PF^{-0.12}$	0.75	0.45	23.71	0.67

**Figure 189.** Plot of POU versus correction factor for Group 117 (power):  $v_c$  in the EFA/Fine data set.

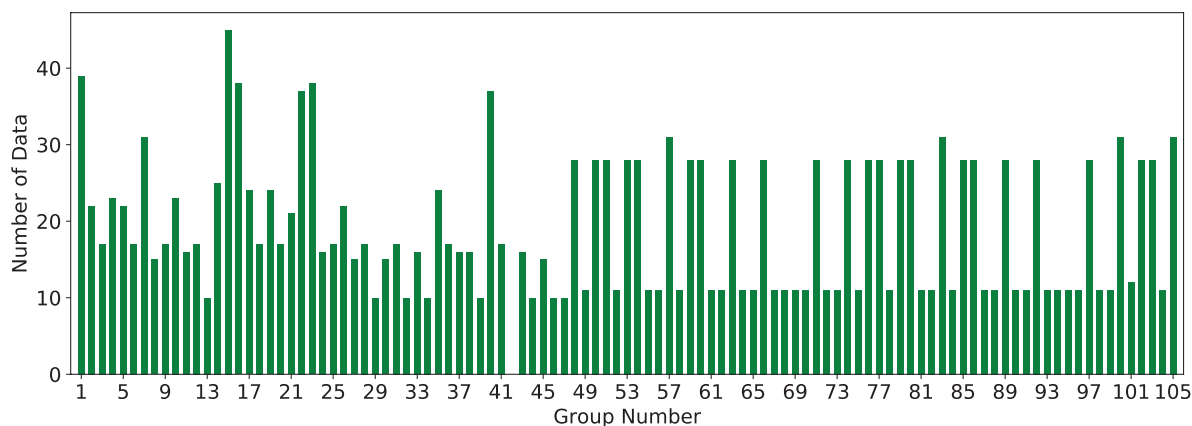


Figure 190. Number of data points in each of 105 combination groups for the EFA/Coarse data set: critical velocity.

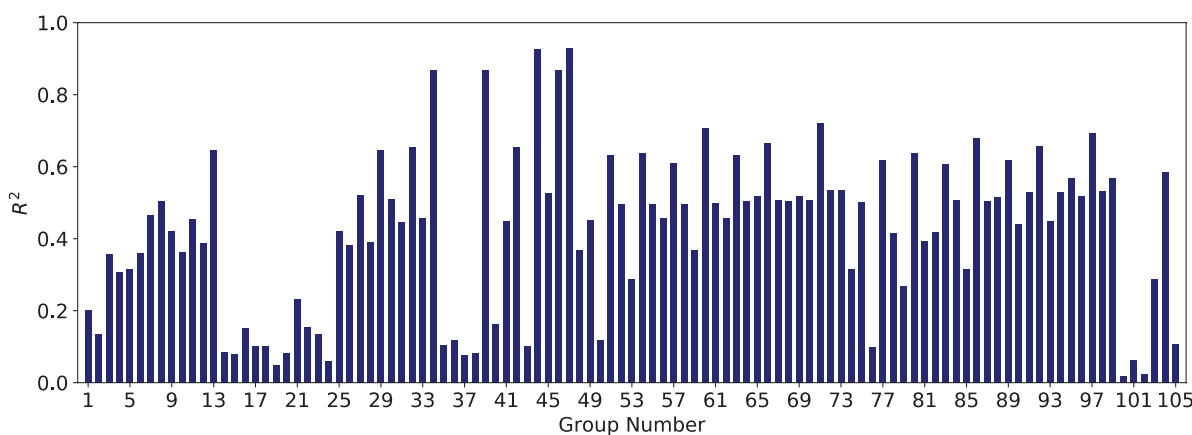


Figure 191.  $R^2$  results for the linear models in EFA/Coarse data set: critical velocity.

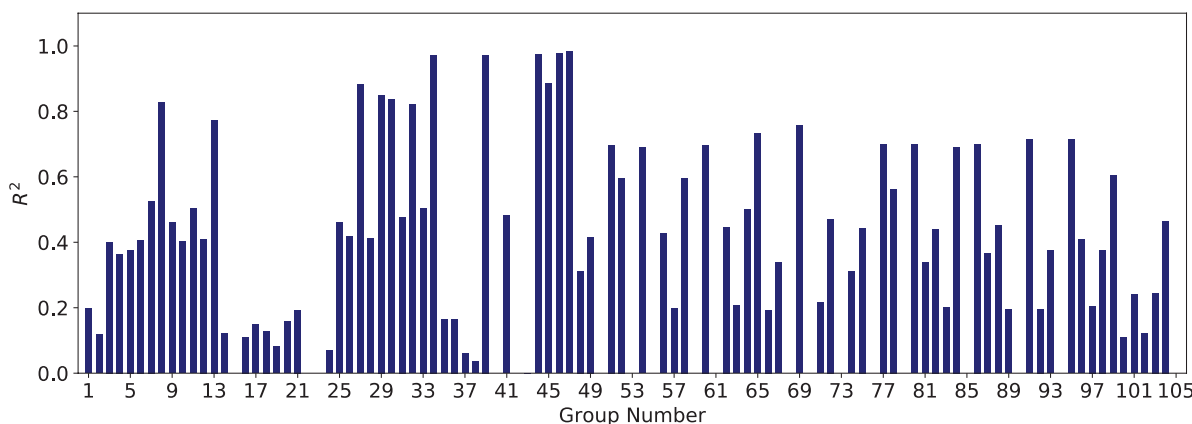
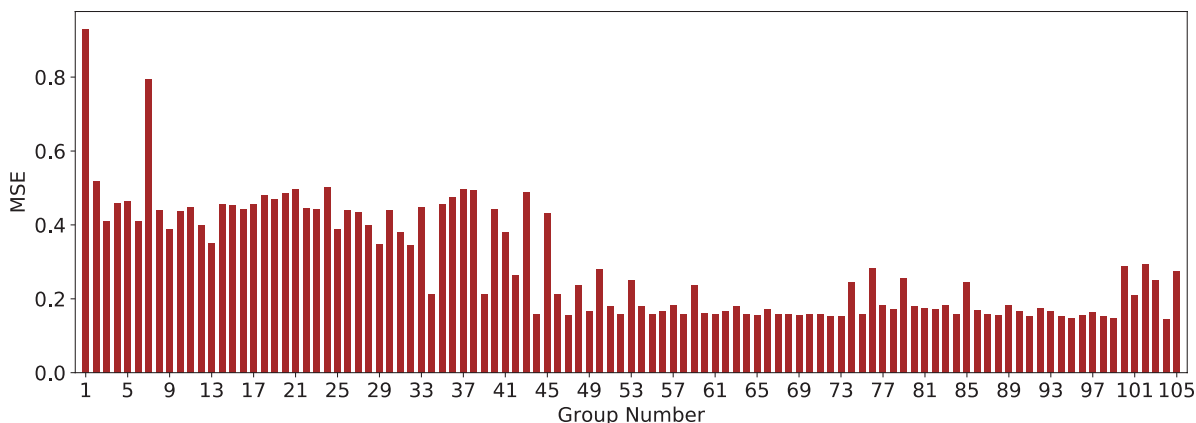


Figure 192.  $R^2$  results for the power models in EFA/Coarse data set: critical velocity.

## 220 Relationship Between Erodibility and Properties of Soils



**Figure 193.** MSE results for linear models in EFA/Coarse data set: critical velocity.

Both the linear and power models showed a few good groups in terms of  $R^2$  values; however, as shown in Figure 190, the number of data points in most groups was lower as compared with the EFA/Fine data set. Figure 193 and Figure 194 show the values of MSE for the linear and power models, respectively.

After passing through Filters 1 and 2 ( $R^2$  and MSE), the linear models associated with Groups 44 and 47 were selected for further analysis. Power models associated with Groups 8, 27, 30, 44, 45, 46, and 47 were also selected for further analysis.

Filter 3,  $F$ -value/ $F$ -stat, was determined for each group mentioned above. Table 57 shows the results of the selected linear models after the requirements of the first three filters ( $R^2$ , MSE, and  $F$ -value/ $F$ -stat) were met. As shown in Table 57, only one selected model performed satisfactorily in the cross-validation test. Table 58 shows the results of the selected power models after the requirements of the first three filters were met. The best models that also had a good cross-validation score are shaded and highlighted in blue in Tables 57 and 58. Out of all the highlighted correlation equations in Table 57 and Table 58, the Group 27 correlation equation in power form was selected as the most promising. Figure 195 shows the plot of POU versus  $\theta$  for this model. The vertical axis in Figure 195 represents the probability that, when the selected model is used, the predicted  $v_c$  will be smaller than the actual  $v_c$ , in percentage (with 0.1 m/s offset). To reach 90% confidence that the predicted  $v_c$  is smaller than the actual  $v_c$ , the predicted value should be multiplied by 0.7.

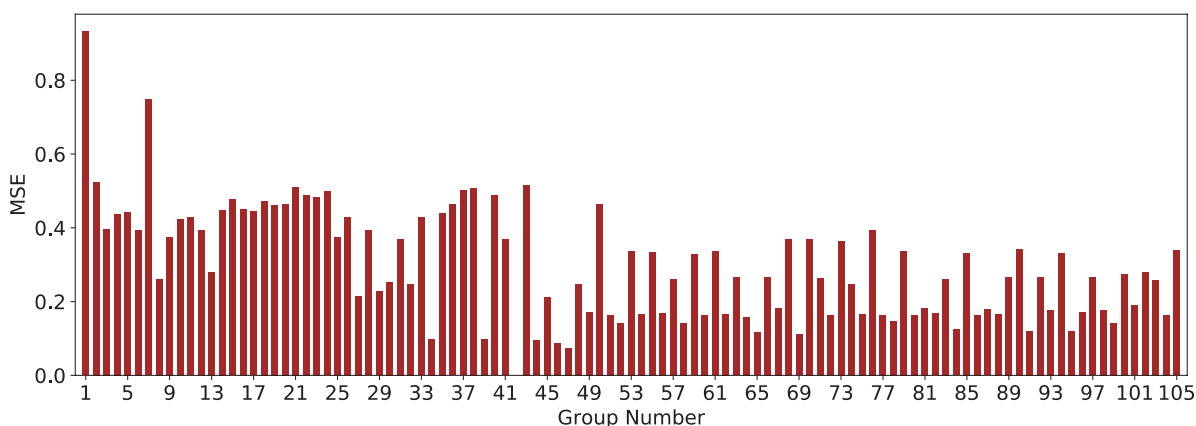


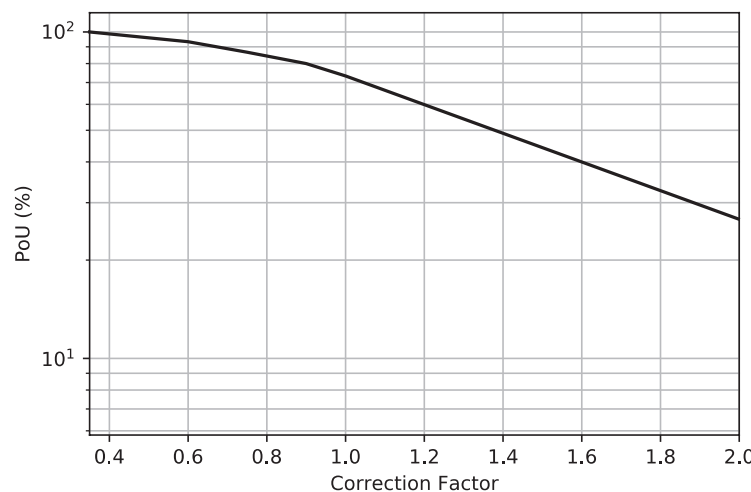
**Figure 194.** MSE results for power models in EFA/Coarse data set: critical velocity.

**Table 57.** Selected linear models for critical velocity in the EFA/Coarse data set.

Group No.	Independent Variables	Model Expression	R <sup>2</sup>	MSE	F-value/F-stat	Cross-Validation Score
44	PI, $\gamma$ , VST, PF, $D_{50}$	$v_c = 0.002 \times PI - 0.1 \times \gamma + 0.01 \times VST - 0.09 \times PF - 13.6 \times D_{50} + 7.21$ for $0.074 < D_{50} < 0.3$	0.93	0.16	2.43	0.67
47	PI, $\gamma$ , WC, VST, PF, $D_{50}$	$v_c = 0.002 \times PI - 0.11 \times \gamma - 0.007 \times WC + 0.009 \times VST - 0.092 \times PF - 13.846 \times D_{50} + 7.46$	0.93	0.16	0.75	-0.75

**Table 58.** Selected power models for critical velocity in the EFA/Coarse data set.

Group No.	Independent Variables	Model Expression	R <sup>2</sup>	MSE	F-value/F-stat	Cross-Validation Score
8	PI, $\gamma$ , $D_{50}$	$v_c = (3 \times 10^{-15}) \times PI^{1.27} \times \gamma^{8.35} \times D_{50}^{-2.75}$ for $0.074 < D_{50} < 0.3$	0.83	0.26	9.56	0.74
27	PI, $\gamma$ , WC, $D_{50}$	$v_c = (3 \times 10^{-15}) \times PI^{1.24} \times \gamma^{8.11} \times WC^{0.54} \times D_{50}^{-2.35}$ for $0.074 < D_{50} < 0.3$	0.88	0.22	10.73	0.72
30	PI, $\gamma$ , PF, $D_{50}$	$v_c = (4 \times 10^{-15}) \times PI^{1.33} \times \gamma^{7.81} \times PF^{0.55} \times D_{50}^{-2.34}$ for $0.074 < D_{50} < 0.3$	0.84	0.25	7.09	0.62
44	PI, $\gamma$ , VST, PF, $D_{50}$	$v_c = (0.027) \times PI^{0.18} \times \gamma^{2.31} \times VST^{1.37} \times PF^{-5.89} \times D_{50}^{-5.22}$ for $0.074 < D_{50} < 0.3$	0.97	0.09	7.10	0.91
45	PI, $\gamma$ , WC, PF, $D_{50}$	$v_c = (4 \times 10^{-15}) \times PI^{1.27} \times \gamma^{7.87} \times WC^{0.51} \times PF^{0.23} \times D_{50}^{-2.24}$ for $0.074 < D_{50} < 0.3$	0.88	0.21	7.97	0.28
46	PI, WC, VST, PF, $D_{50}$	$v_c = (7162.39) \times PI^{-0.12} \times WC^{-0.66} \times VST^{1.33} \times PF^{-7.27} \times D_{50}^{6.05}$ for $0.074 < D_{50} < 0.3$	0.98	0.09	7.86	0.94
47	PI, $\gamma$ , WC, VST, PF, $D_{50}$	$v_c = (2.055) \times PI^{0.03} \times \gamma^{3.11} \times WC^{-0.92} \times VST^1 \times PF^{-7.24} \times D_{50}^{-6.32}$ for $0.074 < D_{50} < 0.3$	0.98	0.08	4.97	0.90

**Figure 195.** Plot of POU versus correction factor for Group 27 (power):  $v_c$  in the EFA/Coarse data set.

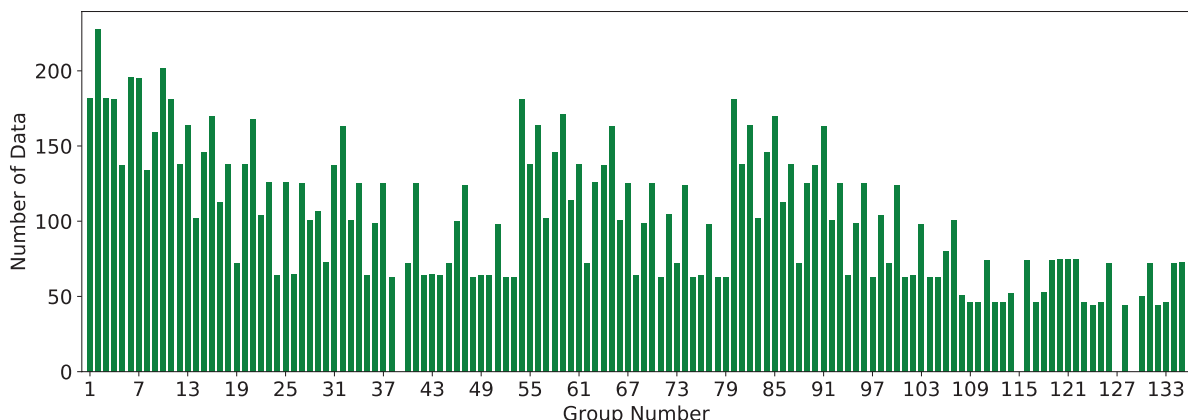


**Figure 196.** Number of data points in each of 135 combination groups for the EFA/Fine data set:  $E_t$ .

#### 7.3.4.3 Initial Slope of Erosion Rate–Shear Stress

The same four-filter process discussed in Section 7.3.3 is implemented in this section to obtain the best models for the initial slope of the erosion rate–shear stress curve,  $E_t$ . Regression analysis for  $E_t$  was performed for the EFA, HET, and JET separately.

**EFA Database.** As with the cases of critical shear stress and critical velocity, it was observed that dividing the EFA/Global data set into the EFA/Fine and the EFA/Coarse data sets would significantly improve the regression results. Figure 196 shows the number of data points in each of the 135 combination groups in the EFA/Fine data set. Figure 197 and Figure 198 show the results for  $R^2$  for each combination group for the linear and power models, respectively.

The  $R^2$  values of the power models were generally higher than those of the linear models. It can be observed that the  $R^2$  values were considerably higher for Groups 123 to 135 in Figure 198. Figure 199 shows the MSE results for the power models for each of the 135 combination groups in the EFA/Fine data set.

After passing through Filters 1 and 2 ( $R^2$  and MSE), the power models associated with Groups 124, 126, 128, 130, 131, 132, and 134 were selected for further analysis. Filter 3,  $F$ -value/ $F$ -stat, was determined for each group mentioned above. Table 59 shows the results of the

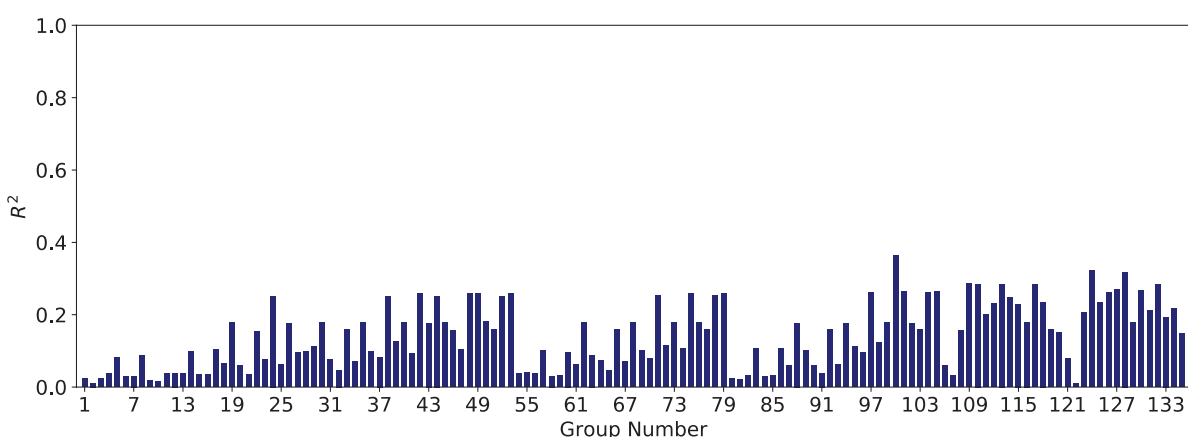


**Figure 197.**  $R^2$  results for the linear models in EFA/Fine data set:  $E_t$ .

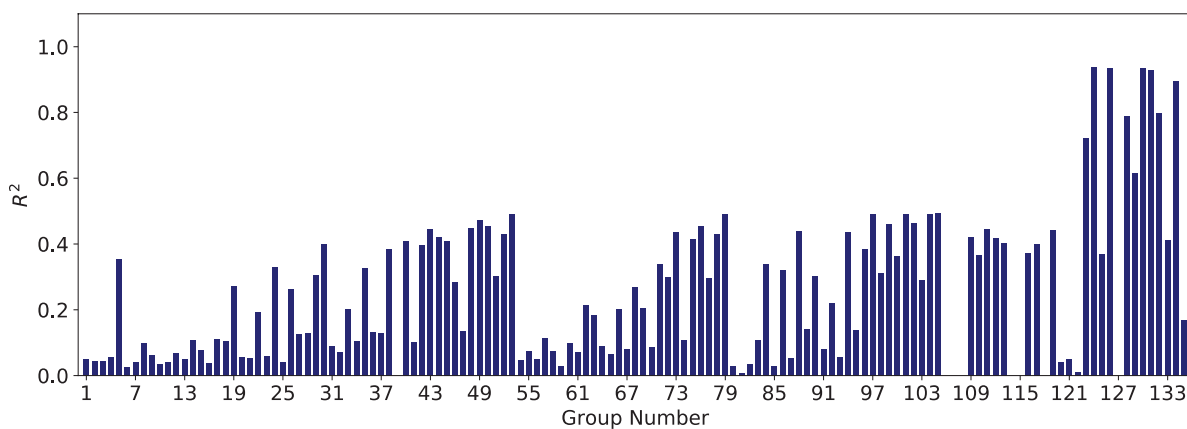


Figure 198.  $R^2$  results for the power models in EFA/Fine data set:  $E_t$ .

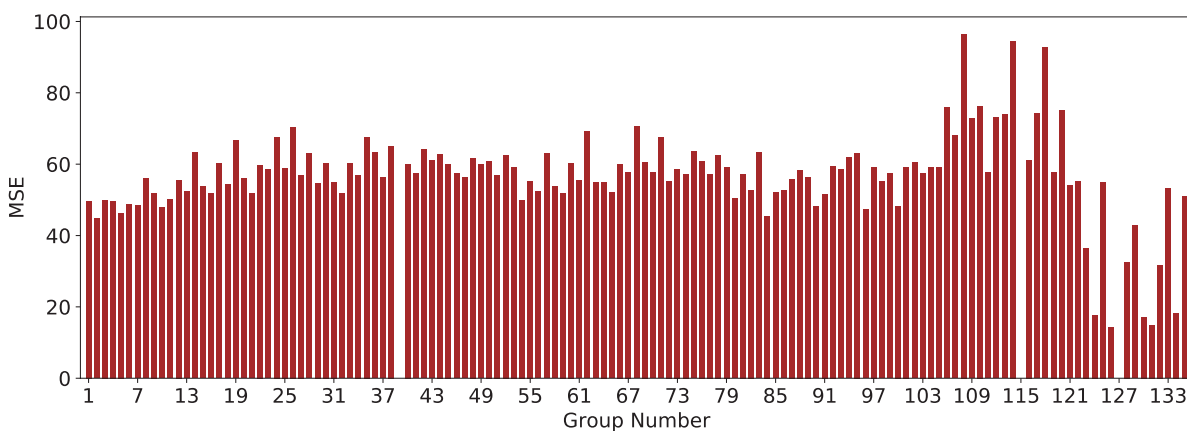
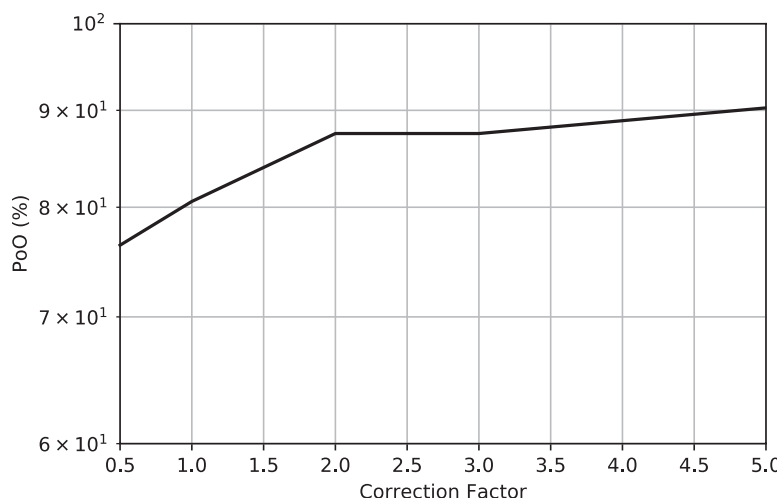


Figure 199. MSE results for the power models in EFA/Fine data set:  $E_t$ .

Table 59. Selected power models for shear stress slope in the EFA/Fine data set.

Group No.	Independent Variables	Model Expression	$R^2$	MSE	F-value/ F-stat	Cross- Validation Score
124	$\gamma, A, WC, S_u, PF, D_{50}$	$E_t = (1.043059638 \times 10^{13}) \times \gamma^{-8.58} \times A^{-0.01} \\ \times WC^{-1.69} \times S_u^{-0.36} \times PF^{5.29} \times D_{50}^{5.69}$	0.94	17.7	9.6	0.04
126	$D_{50}, \gamma, WC, PF, A$	$E_t = (1.208024 \times 10^{13}) \times D_{50}^{7.36} \times \gamma^{-10.09} \times WC^{-1.58} \\ \times PF^{7.04} \times A^{0.05}$	0.94	14.26	21.3	0.51
128	$D_{50}, \gamma, WC, S_u, A$	$E_t = (2.3983097 \times 10^{13}) \times D_{50}^2 \times \gamma^{-3.07} \times WC^{-1.99} \\ \times S_u^{-1.57} \times A^{-0.09}$	0.79	32.56	6.6	0.09
130	$D_{50}, S_u, PF, A$	$E_t = (789314.3) \times D_{50}^{21.14} \times S_u^{-1.13} \times PF^{13.17} \times A^{1.98}$	0.93	17.2	11.7	-0.63
131	$D_{50}, WC, PF, A$	$E_t = (86.707) \times D_{50}^{31} \times WC^{0.1} \times PF^{21} \times A^{2.89}$	0.93	14.9	24.1	-0.21
132	$A, WC, S_u, D_{50}$	$E_t = (2.63681129 \times 10^{13}) \times A^{0.31} \times WC^{-3.85} \\ \times S_u^{-2.57} \times D_{50}^{2.02}$	0.80	31.7	10.3	0.06
134	$A, \gamma, PF, D_{50}$	$E_t = (1.429078 \times 10^{13}) \times A^{-0.47} \times \gamma^{-10.43} \times PF^{6.14} \\ \times D_{50}^{7.52}$	0.90	18.2	22.9	0.53

## 224 Relationship Between Erodibility and Properties of Soils



**Figure 200.** Plot of PoO versus correction factor for Group 134 (power):  $E_t$  in the EFA/Fine data set.

selected power models after the requirements of the first three filters ( $R^2$ , MSE, and F-value/ F-stat) were met. The best models that also had a good cross-validation score are shaded and highlighted in blue. The Group 134 correlation equation in power form was selected as the most promising equation. Figure 200 shows the plot of PoO versus  $\theta$  for this model. The vertical axis in Figure 200 represents the probability that, when the selected model is used, the predicted  $E_t$  will be greater than the actual  $E_v$ , in percentage (with 4 mm/h-Pa offset). To reach an 87% confidence that the predicted  $E_t$  is greater than the actual  $E_v$ , the predicted value should be multiplied by 2.

The same procedure was conducted in the EFA/Coarse data set, and the best models were selected for  $E_t$ . Figure 201 shows the number of data points in each of the 105 combination groups in the EFA/Coarse data set. Figure 202 and Figure 203 show the results for  $R^2$  for each combination group for the linear and power models, respectively.

Both the linear and power models showed a few good groups in terms of  $R^2$  values; however, as seen in Figure 201, the number of data points in most groups was lower as compared with the EFA/Fine data set. Figure 204 and Figure 205 show the values of MSE for the linear and power models, respectively.

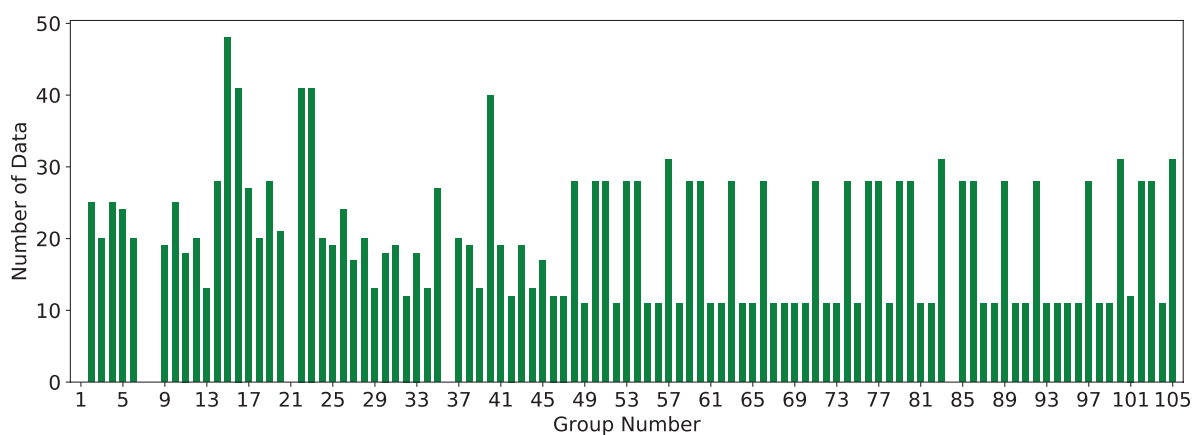


**Figure 201.** Number of data points in each of 105 combination groups for the EFA/Coarse data set:  $E_t$ .

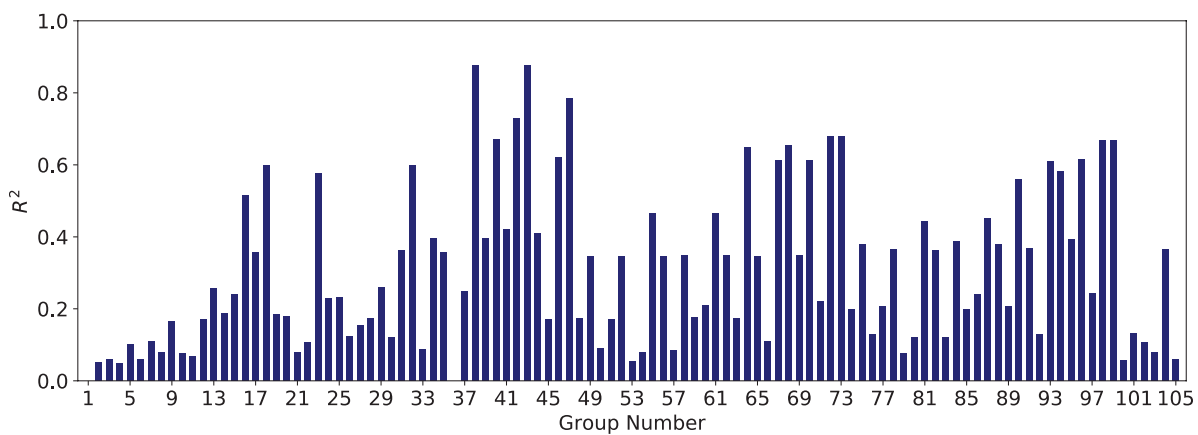


Figure 202.  $R^2$  results for the linear models in EFA/Coarse data set:  $E_r$ .

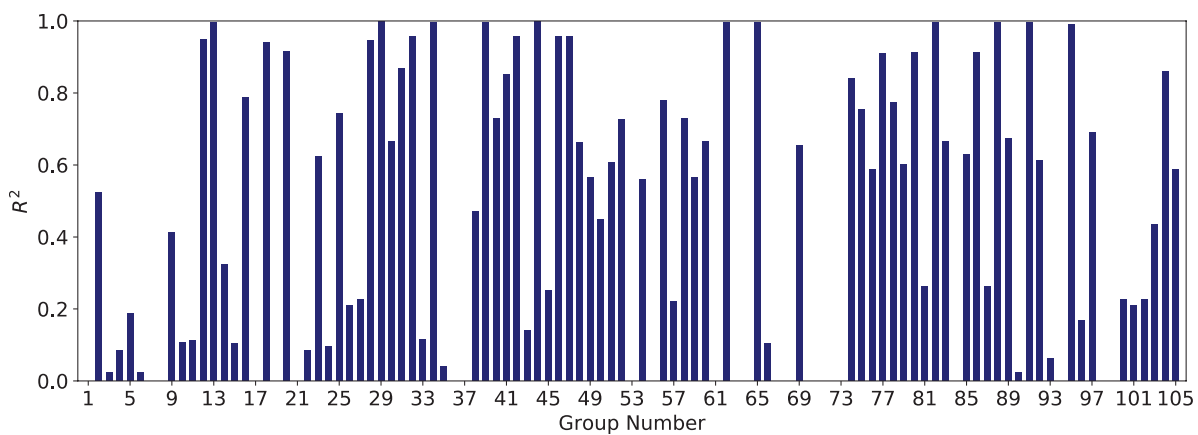


Figure 203.  $R^2$  results for the power models in EFA/Coarse data set:  $E_r$ .

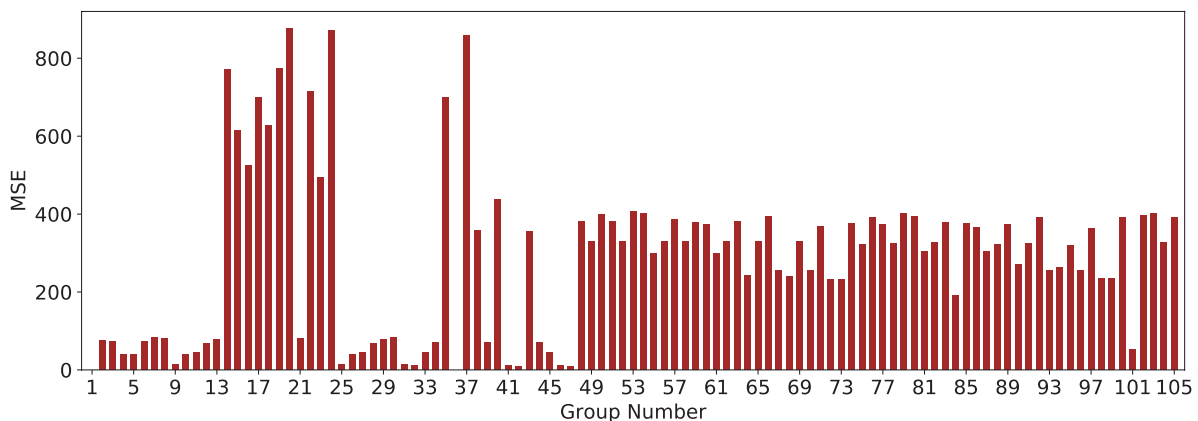
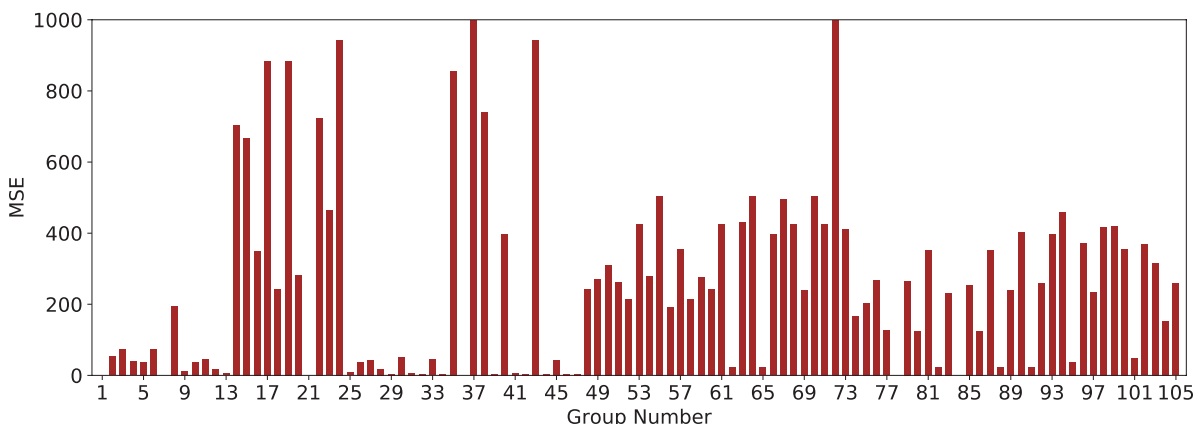


Figure 204. MSE results for the linear models in EFA/Coarse data set:  $E_r$ .

## 226 Relationship Between Erodibility and Properties of Soils

Figure 205. MSE results for the power models in EFA/Coarse data set:  $E_t$ .

After passing through Filters 1 and 2 ( $R^2$  and MSE), linear models associated with Groups 38, 42, 43, and 47 were selected for further analysis. Power models associated with Groups 12, 13, 16, 18, 20, 28, 31, 34, 39, 40, 41, 42, 44, 74, 77, 80, 82, 86, 91, and 95 were also selected for further analysis.

Filter 3,  $F$ -value/ $F$ -stat, was determined for each group mentioned above. Table 60 shows the results of the selected linear models after the requirements of the first three filters ( $R^2$ , MSE, and  $F$ -value/ $F$ -stat) were met. As shown in Table 60, none of the selected models performed satisfactorily in the cross-validation test. Table 61 shows the results of the selected power models after the requirements of the first three filters were met. The Group 77 correlation equation in power form was selected as the most promising equation. Figure 206 shows the plot of POO versus  $\theta$  for this model. The vertical axis in Figure 206 represents the probability that, when the selected model is used, the predicted  $E_t$  will be greater than the actual  $E_t$ , in percentage (with 15 mm/h-Pa offset). To reach 80% confidence that the predicted  $E_t$  is greater than the actual  $E_t$ , the predicted value should be multiplied by 2.5.

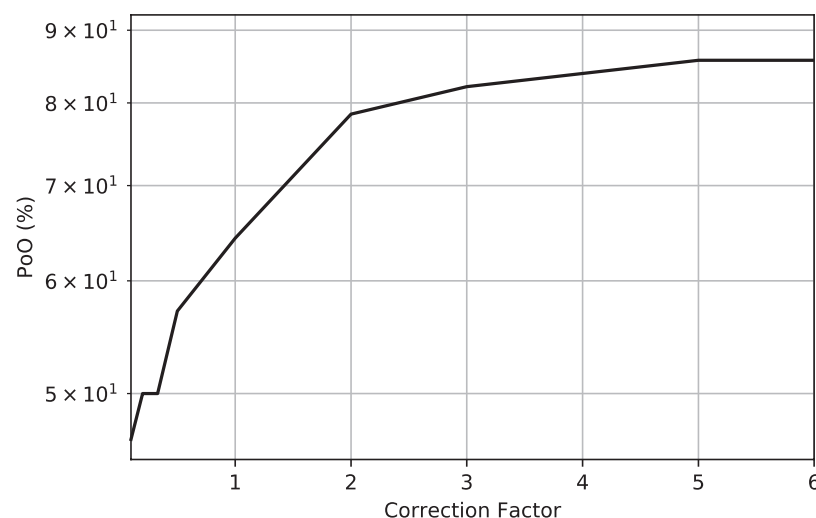
**JET Database.** As with the case of the EFA database, it was observed that dividing the JET/Global data set into the JET/Fine and the JET/Coarse data sets would significantly improve the regression results. Figure 207 shows the number of data points in each of the 135 combination groups in the JET/Fine data set. Figure 208 and Figure 209 show the results for  $R^2$  for each combination group for the linear and power models, respectively.

Table 60. Selected linear models for shear stress slope in the EFA/Coarse data set.

Group No.	Independent Variables	Model Expression	$R^2$	MSE	$F$ -value/ $F$ -stat	Cross-Validation Score
38	WC, VST, PF, $D_{50}$	$E_t = 79.308 \times WC + 7.52 \times VST - 38.22 \times PF + 20.35 \times D_{50} - 374.67$	0.88	359.3	7.71	-8.5
42	PI, $\gamma$ , WC, VST, $D_{50}$	$E_t = -0.669 \times PI - 5.06 \times \gamma - 1.89 \times WC - 0.31 \times VST + 112.8 \times D_{50} + 149.23$	0.73	10.3	0.64	-0.35
43	$\gamma$ , WC, VST, PF, $D_{50}$	$E_t = -31.207 \times \gamma + 78.76 \times WC + 7.86 \times VST - 36.82 \times PF + 39.92 \times D_{50} + 180.81$	0.88	356	5.98	-7.4
47	PI, $\gamma$ , WC, VST, PF, $D_{50}$	$E_t = -0.897 \times PI - 5.82 \times \gamma - 1.5 \times WC - 0.2 \times VST - 1.01 \times PF + 46.15 \times D_{50} + 198.61$	0.78	9.19	0.49	-1.5

**Table 61.** Selected power models for shear stress slope in the EFA/Coarse data set.

Group No.	Independent Variables	Model Expression	R <sup>2</sup>	MSE	F-value/F-stat	Cross-Validation Score
12	PI, VST, PF	$E_\tau = (0.00009) \times PI^{0.33} \times VST^{-10.86} \times PF^{12.46}$	0.95	17.39	26.4	-0.97
13	PI, VST, D <sub>50</sub>	$E_\tau = (1.096668 \times 10^{13}) \times PI^{1.69} \times VST^{-8.13} \times D_{50}^{1.05}$	0.99	5.41	22.2	-0.35
16	$\gamma$ , WC, D <sub>50</sub>	$E_\tau = (93090257.5) \times \gamma^{-7.02} \times WC^{2.04} \times D_{50}^{-0.72}$	0.79	349.1	19.6	-0.14
18	WC, VST, D <sub>50</sub>	$E_\tau = (4112.67) \times WC^{0.01} \times VST^{-2.95} \times D_{50}^{-3.2}$	0.94	243.5	23.9	-4.5
20	VST, $\gamma$ , D <sub>50</sub>	$E_\tau = (604968.99) \times VST^{-3.74} \times \gamma^{-1.52} \times D_{50}^{-3.77}$	0.92	281.8	18.1	-9.01
28	PI, $\gamma$ , VST, PF PF	$E_\tau = (4630.2794 \times 10^8) \times PI^{2.45} \times \gamma^{-20.92} \times VST^{-4.78} \times PF^{12.80}$	0.95	17.58	19.9	-2.5
31	PI, WC, VST, PF	$E_\tau = (2.59644111 \times 10^{13}) \times PI^{-0.87} \times WC^{-5.19} \times VST^{-0.72} \times PF^{-3.65}$	0.87	5.9	18.1	-0.33
34	PI, VST, PF, D <sub>50</sub>	$E_\tau = (7.1386087 \times 10^{12}) \times PI^{1.6} \times VST^{-8.56} \times PF^{1.17} \times D_{50}^{2.04}$	0.99	4.99	9.1	-1.53
39	PI, VST, PF, D <sub>50</sub>	$E_\tau = (7.13860971 \times 10^{12}) \times WC^{1.6} \times VST^{-8.56} \times PF^{1.17} \times D_{50}^{2.04}$	0.99	4.99	8.8	-0.03
40	$\gamma$ , WC, PF, D <sub>50</sub>	$E_\tau = (2.881) \times \gamma^{-1.44} \times WC^{3.32} \times PF^{0.00000002} \times D_{50}^{0.91}$	0.73	398.4	41.1	-0.53
41	PI, $\gamma$ , WC, VST, PF	$E_\tau = (2.99273 \times 10^{13}) \times PI^{-1.06} \times \gamma^{-4.34} \times WC^{-2.08} \times VST^{-0.28} \times PF^{-2.23}$	0.85	6.23	13.3	-0.11
42	PI, $\gamma$ , WC, VST, D <sub>50</sub>	$E_\tau = (1591199925) \times PI^{-1.69} \times \gamma^{-2.09} \times WC^{0.79} \times VST^{-1.39} \times D_{50}^{3.68}$	0.96	4.05	8.3	-7.09
44	PI, $\gamma$ , VST, PF, D <sub>50</sub>	$E_\tau = (127160023) \times PI^{1.75} \times \gamma^{6.82} \times VST^{-10.86} \times PF^{1.11} \times D_{50}^{2.88}$	0.99	4.15	9.6	-0.37
74	C <sub>u</sub> , $\gamma$ , WC	$E_\tau = (3785948678096) \times C_u^{-1.86} \times \gamma^{-10.09} \times WC^{3.01}$	0.84	167.8	16.7	0.58
77	C <sub>u</sub> , $\gamma$ , D <sub>50</sub>	$E_\tau = (3228.7) \times C_u^{-2.8} \times \gamma^{-1.58} \times D_{50}^{-2.91}$	0.91	126.3	28.02	0.64
80	C <sub>u</sub> , WC, D <sub>50</sub>	$E_\tau = (34.62) \times C_u^{-3.6} \times WC^{-0.52} \times D_{50}^{-3.99}$	0.91	124.6	28.9	0.62
82	C <sub>u</sub> , VST, D <sub>50</sub>	$E_\tau = (12.22) \times C_u^{-16.14} \times VST^{-23.44} \times D_{50}^{-43.92}$	0.99	22.6	10.04	-3.76
86	C <sub>u</sub> , $\gamma$ , WC, D <sub>50</sub>	$E_\tau = (0.148) \times C_u^{-4.71} \times \gamma^{1.83} \times WC^{-1.11} \times D_{50}^{-5.42}$	0.91	124.3	23.4	-3.96
91	C <sub>u</sub> , WC, VST, D <sub>50</sub>	$E_\tau = (45.82) \times C_u^{-13.48} \times WC^{0.67} \times VST^{-22.78} \times D_{50}^{-40.08}$	0.99	22.6	9.5	-10.54
95	C <sub>u</sub> , $\gamma$ , WC, VST, D <sub>50</sub>	$E_\tau = (9.2 \times 10^{-15}) \times C_u^{-2.13} \times \gamma^{15.56} \times WC^{-2.7} \times VST^{-7.67} \times D_{50}^{-12.99}$	0.99	37.13	11.1	-10.35

**Figure 206.** Plot of POO versus correction factor for Group 77 (power): E<sub>τ</sub> in the EFA/Coarse data set.

## 228 Relationship Between Erodibility and Properties of Soils

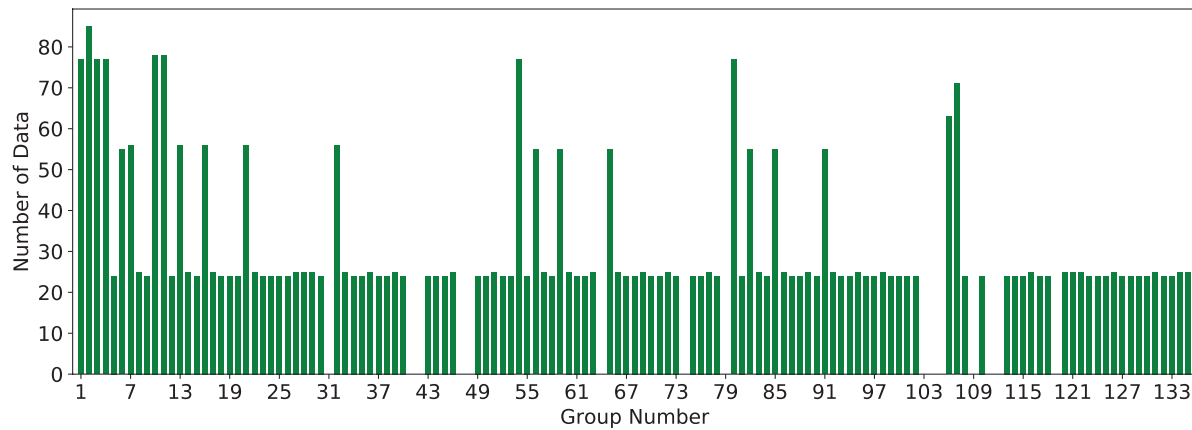


**Figure 207.** Number of data points in each of 135 combination groups for the JET/Fine data set:  $E_t$ .

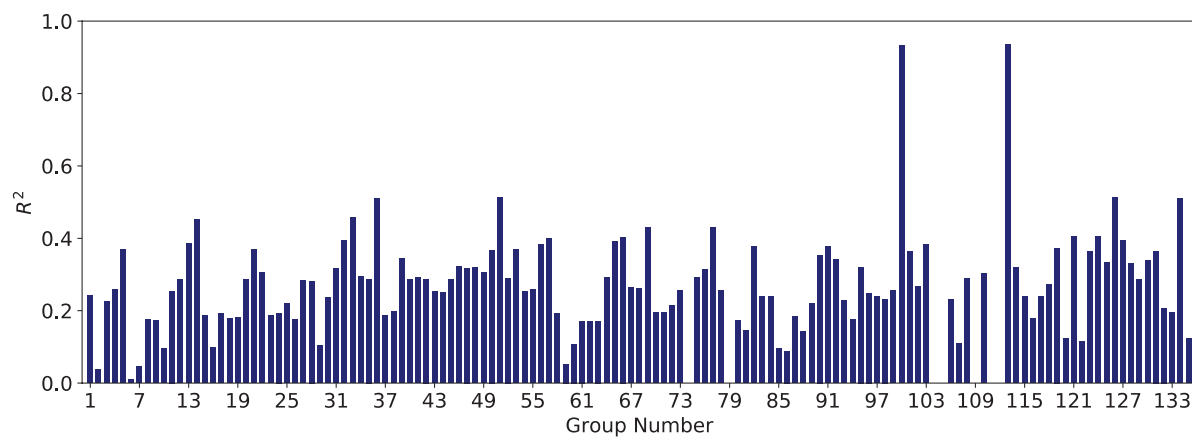


**Figure 208.**  $R^2$  results for the linear models in JET/Fine data set:  $E_t$ .

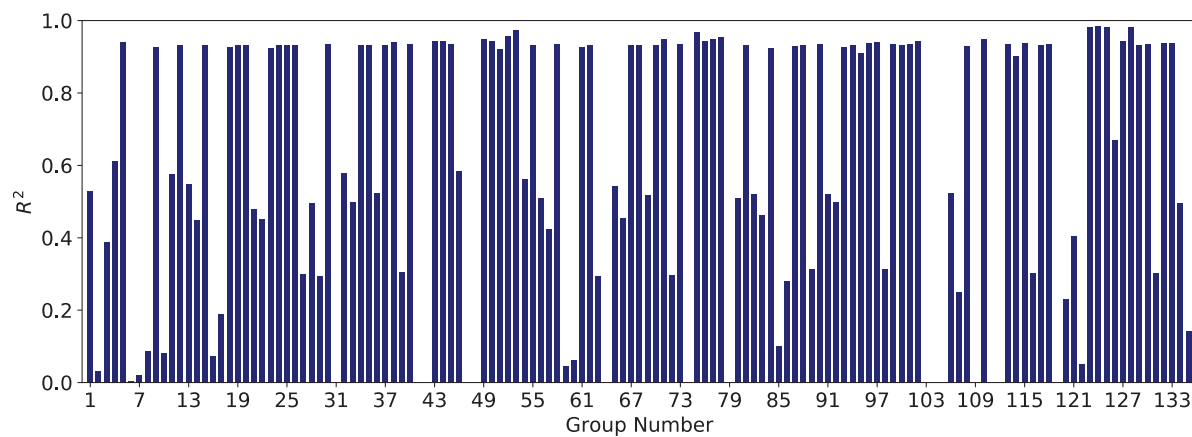


**Figure 209.**  $R^2$  results for the power models in JET/Fine data set:  $E_t$ .

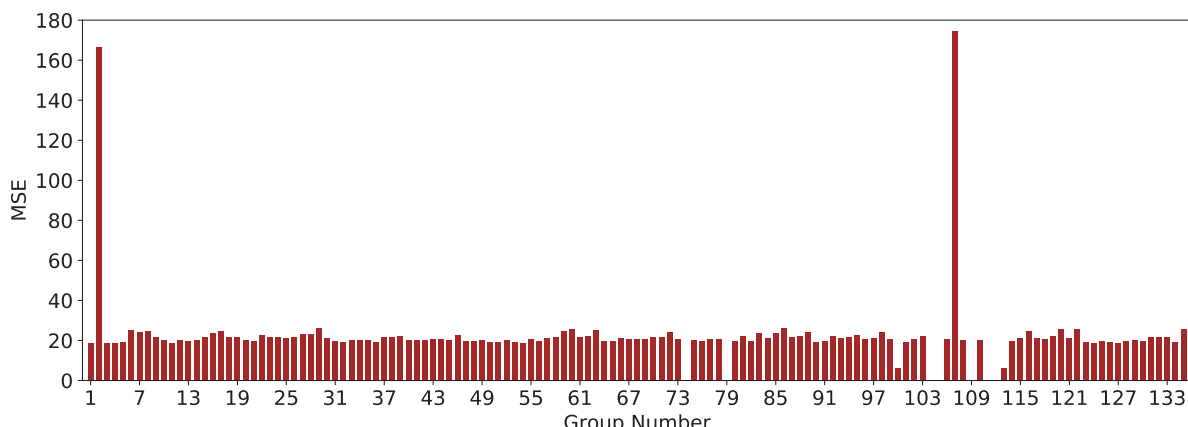


Figure 210. MSE results for the linear models in JET/Fine data set:  $E_t$ .

The  $R^2$  values of the power models were generally higher than those of the linear models. Figure 210 and Figure 211 show the MSE results for each of the 135 combination groups in the EFA/Fine data set for the linear and power models, respectively.

After passing through Filters 1 and 2 ( $R^2$  and MSE), the linear models associated with Groups 100 and 113 were selected for further analysis. Power models associated with Groups 5, 12, 15, 20, 24, 38, 43, 71, 75, 78, 97, 123, 125, 128 were also selected for further analysis.

Filter 3,  $F$ -value/ $F$ -stat, was determined for each group mentioned above. Table 62 shows the results of the selected linear models after the requirements of the first three filters ( $R^2$ , MSE, and  $F$ -value/ $F$ -stat) were met. As shown in Table 62, none of the selected models performed satisfactorily in the cross-validation test. Table 63 shows the results of the selected power models after the requirements of the first three filters were met. The Group 15 correlation equation in power form was selected as the most promising equation. Figure 212 shows the plot of POO versus  $\theta$  for this model. The vertical axis in Figure 212 represents the probability that, when the selected model is used, the predicted  $E_t$  will be greater than the actual  $E_t$ , in percentage (with 6 mm/h-Pa offset). To reach 88% confidence that the predicted  $E_t$  is greater than the actual  $E_t$ , the predicted value should be multiplied by 2.

The same procedure was conducted with the JET/Coarse data set, and the best models were selected for  $E_t$ . Figure 213 shows the number of data points in each of the 105 combination

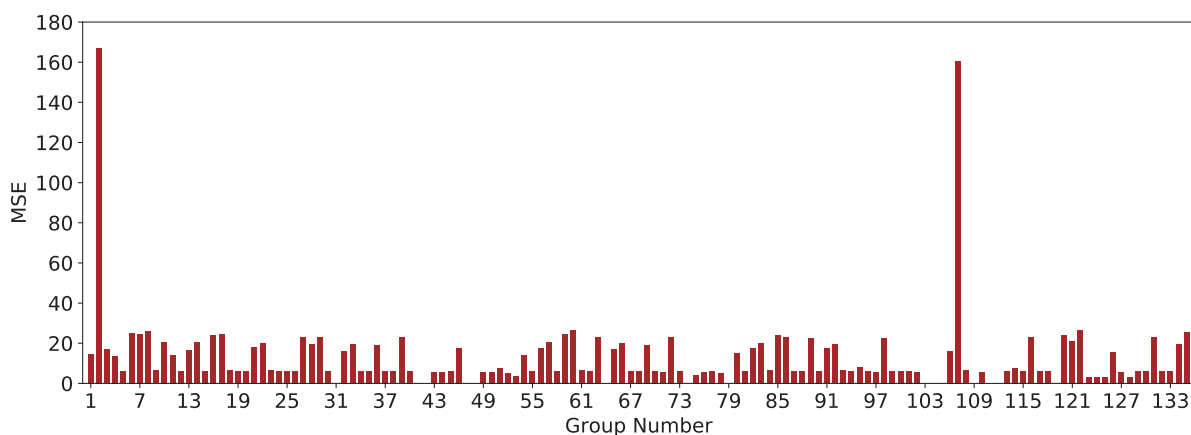


Figure 211. MSE results for the power models in JET/Fine data set:  $E_t$ .

## 230 Relationship Between Erodibility and Properties of Soils

**Table 62.** Selected linear models for shear stress slope in the JET/Fine data set.

Group No.	Independent Variables	Model Expression	R <sup>2</sup>	MSE	F-value/F-stat	Cross-Validation Score
100	PL, γ, WC, S <sub>u</sub> , PF	$E_{\tau} = 2.468 \times PL - 9.40 \times \gamma - 3.30 \times WC - 0.38 \times S_u - 0.39 \times PF + 287.11$	0.93	6.29	2.31	-0.59
113	PC, γ, WC, S <sub>u</sub> , D <sub>50</sub>	$E_{\tau} = 0.707 \times PC - 7.10 \times \gamma - 2.89 \times WC - 0.39 \times S_u + 162.63 \times D_{50} + 218.4$	0.94	6.14	2.54	-0.64

**Table 63.** Selected power models for shear stress slope in the JET/Fine data set.

Group No.	Independent Variables	Model Expression	R <sup>2</sup>	MSE	F-value/F-stat	Cross-Validation Score
5	LL, PL, γ, WC, S <sub>u</sub>	$E_{\tau} = (35,913.13) \times LL^{-9.69} \times PL^{17.77} \times \gamma^{-5.74} \times WC^{5.46} \times S_u^{-7.08}$	0.94	5.94	6.98	-0.79
12	PI, γ, S <sub>u</sub>	$E_{\tau} = (0.085) \times PI^{-0.62} \times \gamma^{8.57} \times S_u^{-5.24}$	0.93	6.29	8.63	-0.95
15	PI, WC, S <sub>u</sub>	$E_{\tau} = (396,599.6) \times PI^{-2.54} \times WC^{4.58} \times S_u^{-4.91}$	0.93	6.30	9.11	0.23
20	γ, WC, S <sub>u</sub>	$E_{\tau} = (4.363 \times 10^{-4}) \times \gamma^{12.07} \times WC^{-1.96} \times S_u^{-5.48}$	0.93	6.27	8.74	-0.52
24	WC, S <sub>u</sub> , D <sub>50</sub>	$E_{\tau} = (1,986,216) \times WC^{2.74} \times S_u^{-4.32} \times D_{50}^{1.22}$	0.93	6.29	10.01	-2.08
38	PI, WC, S <sub>u</sub> , D <sub>50</sub>	$E_{\tau} = (13,854,336,090,024) \times PI^{2.48} \times WC^{-4.79} \times S_u^{-3.95} \times D_{50}^{1.47}$	0.94	5.89	8.21	-1.46
43	γ, S <sub>u</sub> , PF, D <sub>50</sub>	$E_{\tau} = (1.7 \times 10^{-9}) \times \gamma^{-13.49} \times S_u^{-1.21} \times PF^{20.76} \times D_{50}^{5.49}$	0.94	5.74	7.33	-8.18
71	LL, WC, S <sub>u</sub> , D <sub>50</sub>	$E_{\tau} = (21,641,385,785) \times LL^{4.5} \times WC^{-5.05} \times S_u^{-3.92} \times D_{50}^{1.93}$	0.95	5.40	8.14	-1.43
75	LL, γ, WC, S <sub>u</sub> , D <sub>50</sub>	$E_{\tau} = (5.3 \times 10^{-15}) \times LL^{9.24} \times \gamma^{27.26} \times WC^{-14.86} \times S_u^{-8.38} \times D_{50}^{1.49}$	0.97	4.35	7.99	-330
78	LL, WC, S <sub>u</sub> , PF, D <sub>50</sub>	$E_{\tau} = (5.22 \times 10^{-7}) \times LL^{2.07} \times WC^{-4.74} \times S_u^{-3.15} \times PF^{11.19} \times D_{50}^{3.13}$	0.95	5.15	8.1	-2.95
97	PL, WC, S <sub>u</sub> , D <sub>50</sub>	$E_{\tau} = (11,377,689,319) \times PL^{4.36} \times WC^{-5.78} \times S_u^{-3.61} \times D_{50}^{0.61}$	0.94	5.89	7.88	-76.1
123	A, PL, γ, WC, S <sub>u</sub>	$E_{\tau} = (5.8 \times 10^{-9}) \times A^{5.32} \times PL^{1.00} \times \gamma^{31.35} \times WC^{-12.88} \times S_u^{-9.08}$	0.98	3.27	8.90	-7.25
125	γ, WC, S <sub>u</sub> , PF, A	$E_{\tau} = (1.341 \times 10^{-7}) \times \gamma^{32.96} \times WC^{-12.31} \times S_u^{-9.47} \times PF^{-1.21} \times A^{5.72}$	0.98	3.27	8.66	-2.5
128	D <sub>50</sub> , γ, WC, S <sub>u</sub> , A	$E_{\tau} = (1.898 \times 10^{-5}) \times D_{50}^{0.58} \times \gamma^{28.59} \times WC^{-11.37} \times S_u^{-8.88} \times A^{5.55}$	0.98	3.23	8.59	-2.28

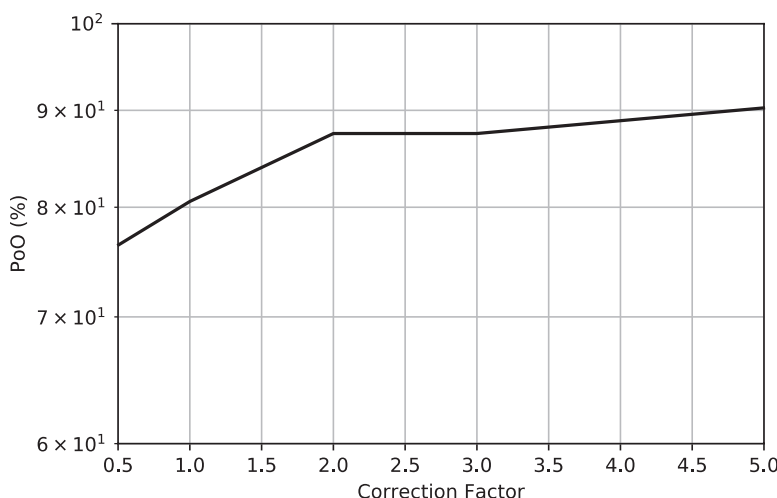


**Figure 212.** Plot of PoO versus correction factor for Group 15 (power):  $E_t$  in the JET/Fine data set.

groups in the EFA/Coarse data set. Figure 214 and Figure 215 show the results for  $R^2$  for each combination group for the linear and power models, respectively.

Both the linear and power models showed many good groups in terms of  $R^2$  values; however, as shown in Figure 213, the number of data points in most groups was extremely low. Only a few combination groups contained sufficient data for regression analysis.

After passing through Filters 1 and 2 ( $R^2$  and MSE), the linear models associated with Groups 5 and 26 were selected for further analysis. Power models associated with Groups 5, 7, and 26 were also selected for further analysis.

Filter 3,  $F$ -value/ $F$ -stat, was determined for each group mentioned above. Table 64 shows the results of the selected linear models after the requirements of the first three filters ( $R^2$ , MSE, and  $F$ -value/ $F$ -stat) were met. As shown in Table 64, none of the selected models performed satisfactorily in the cross-validation test. Table 65 shows the results of the selected power models after the requirements of the first three filters were met. The Group 5 correlation equation in power

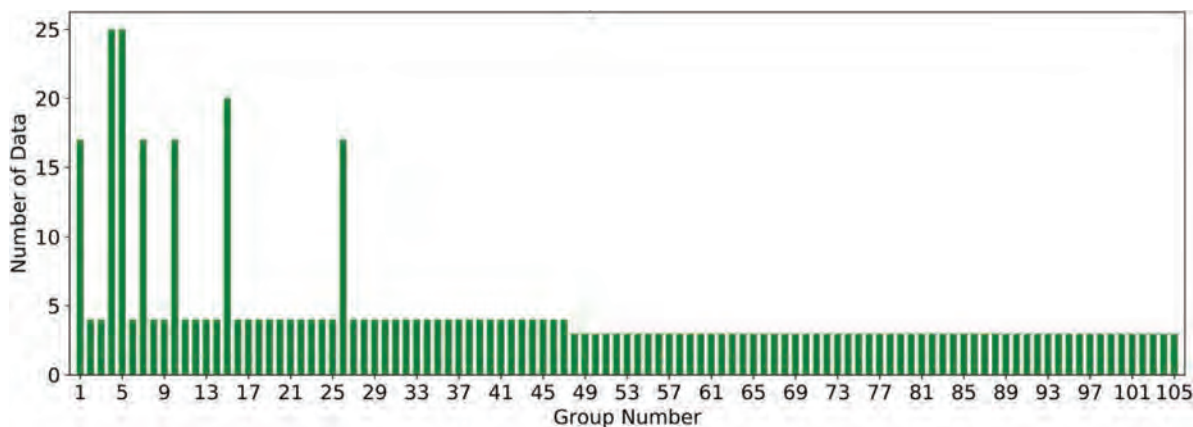


**Figure 213.** Number of data points in each of 105 combination groups for the JET/Coarse data set:  $E_t$ .

## 232 Relationship Between Erodibility and Properties of Soils

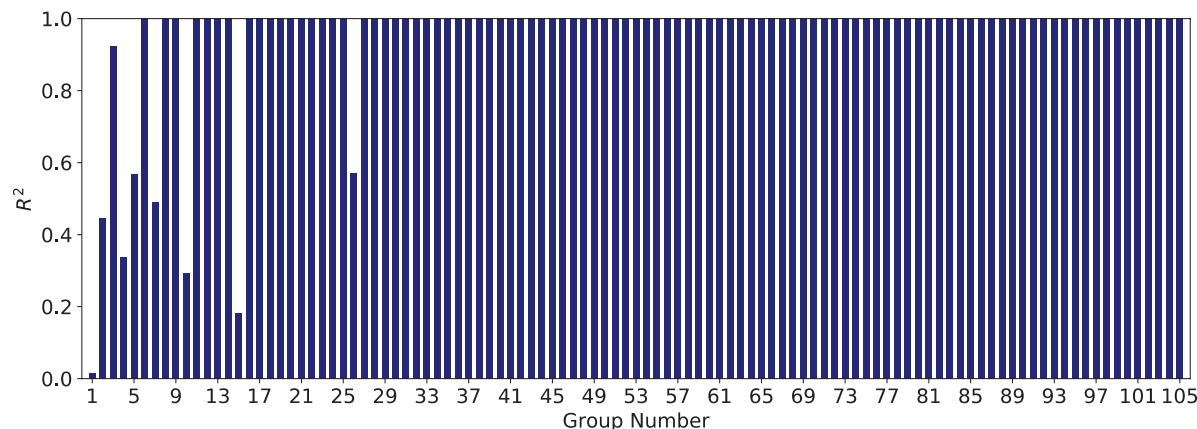
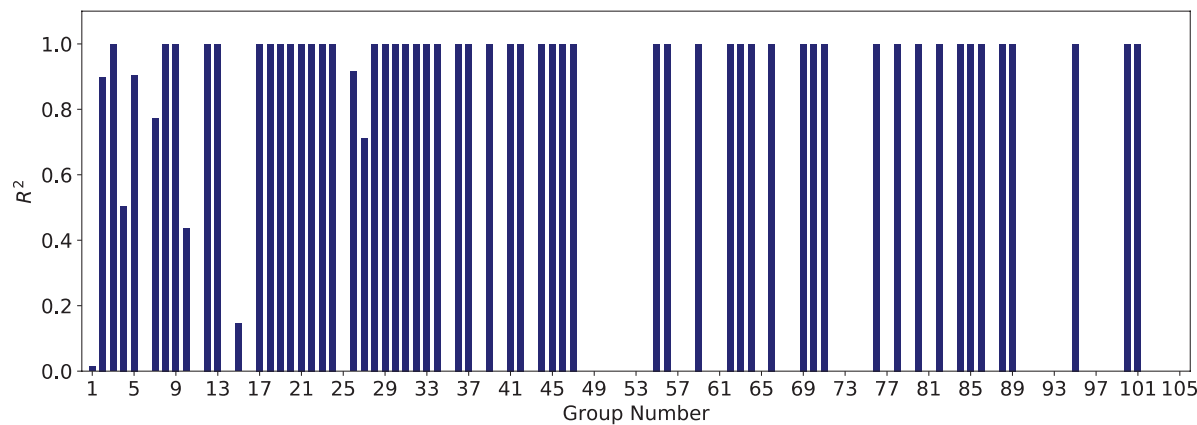
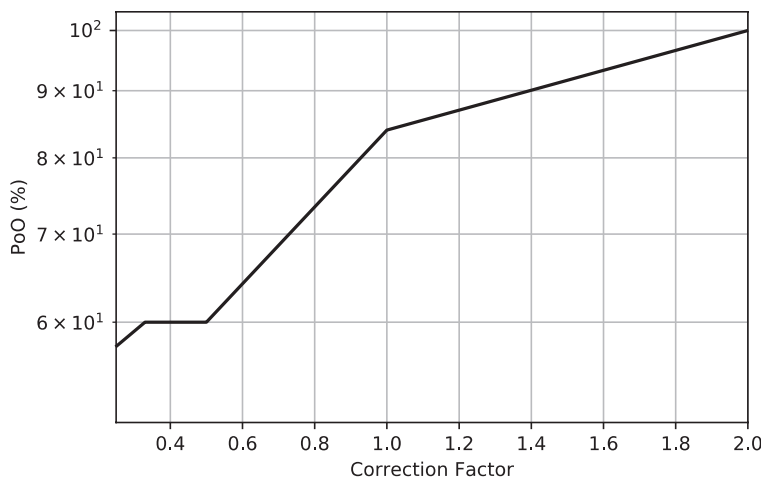
Figure 214. R<sup>2</sup> results for the linear models in JET/Coarse data set: E<sub>r</sub>.Figure 215. R<sup>2</sup> results for the power models in JET/Coarse data set: E<sub>r</sub>.

Table 64. Selected linear models for shear stress slope in the JET/Coarse data set.

Group No.	Independent Variables	Model Expression	R <sup>2</sup>	MSE	F-value/ F-stat	Cross-Validation Score
5	PI, γ, WC	$E_r = -1.827 \times PI - 28.85 \times \gamma - 13.87 \times WC + 797.2$	0.57	63.2	2.99	0.06
26	PI, γ, WC, PF	$E_r = -7 \times PI - 30.85 \times \gamma - 13.85 \times WC + 5.6 \times PF + 722.2$	0.57	70.5	1.22	-86.9

Table 65. Selected power models for shear stress slope in the JET/Coarse data set.

Group No.	Independent Variables	Model Expression	R <sup>2</sup>	MSE	F-value/ F-stat	Cross-Validation Score
5	PI, γ, WC	$E_r = (55,637,006,351,614) \times PI^{-0.19} \times \gamma^{-6.39} \times WC^{-3.67}$	0.90	29.6	8.13	0.67
7	PI, γ, PF	$E_r = (14,284,687,933,437) \times PI^{-1.53} \times \gamma^{-12.16} \times PF^{3.62}$	0.77	51.42	6.56	-0.53
26	PI, γ, WC, PF	$E_r = (17,383,934,656,478) \times PI^{-0.05} \times \gamma^{-7.97} \times WC^{-4.03} \times PF^{1.9}$	0.92	31.3	4.35	0.26



**Figure 216.** Plot of PoO versus correction factor for Group 5 (power):  $E_t$  in the JET/Coarse data set.

form was selected as the most promising equation. Figure 216 shows the plot of PoO versus  $\theta$  for this model. The vertical axis in Figure 216 shows the probability that, when the selected model is used, the predicted  $E_t$  will be greater than the actual  $E_t$ , in percentage (with 5 mm/h-Pa offset). To reach 90% confidence that the predicted  $E_t$  is greater than the actual  $E_t$ , the predicted value should be multiplied by 1.4.

**HET Database.** It was observed that dividing the HET/Global data set into the HET/Fine and the HET/Coarse data sets would not significantly improve the regression results; however, the HET/Coarse database included a few combination groups with acceptable  $R^2$  values. Figure 217 shows the number of data points in each of the 105 combination groups in the HET/Coarse data set. As shown in Figure 217, many combination groups had no data points. Figure 218 and Figure 219 show the results for  $R^2$  for each combination group for the linear and power models, respectively. It is noteworthy that as the HET is limited to finer-grained soils, the HET/Coarse database corresponds to soils with  $D_{50}$  ranging from 0.074 to 0.3 mm.

After passing through Filters 1 and 2 ( $R^2$  and MSE), the power models associated with Groups 40 and 60 were selected for further analysis. Linear models did not lead to  $R^2$  values that were any better; therefore, the study of best-fitting models was limited to power models.

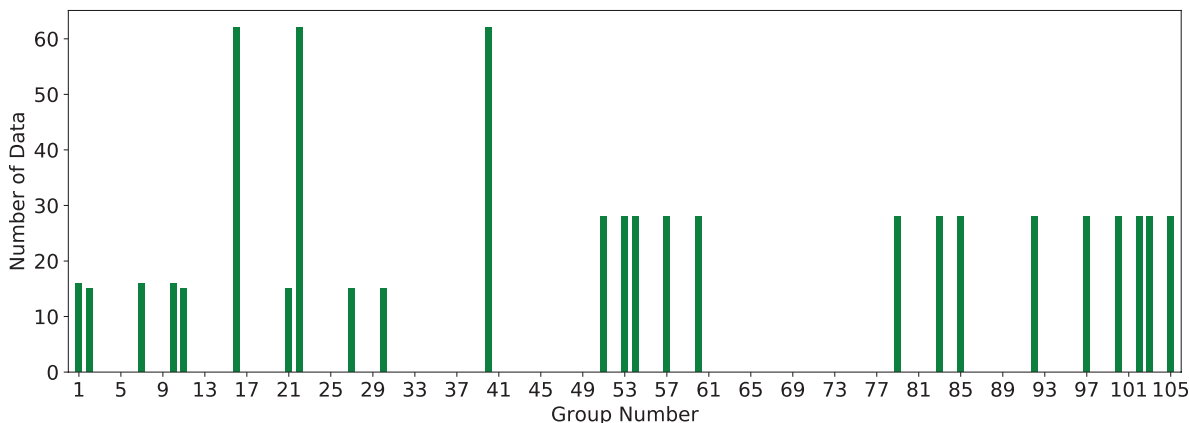


**Figure 217.** Number of data points in each of 105 combination groups for the HET/Coarse data set:  $E_t$ .

## 234 Relationship Between Erodibility and Properties of Soils

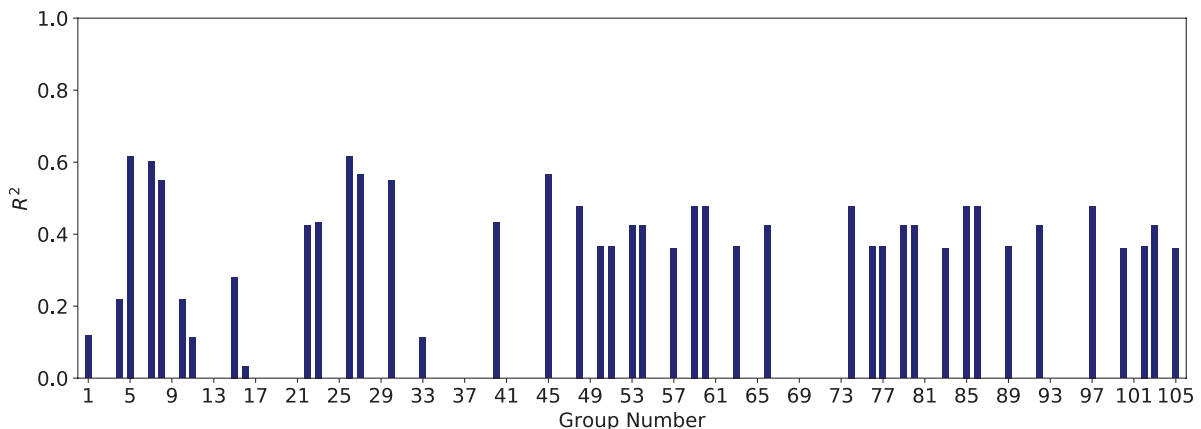


Figure 218. R<sup>2</sup> results for the linear models in HET/Coarse data set: E<sub>r</sub>.

Filter 3, F-value/F-stat, was determined for each group mentioned above. Table 66 shows the results of the selected power models after the requirements of the first three filters (R<sup>2</sup>, MSE, and F-value/F-stat) were met. The Group 40 correlation equation in power form was selected as the most promising equation. Figure 220 shows the plot of POO versus θ for this model. The vertical axis in Figure 220 shows the probability that, when the selected model is used, the predicted E<sub>r</sub> will be greater than the actual E<sub>r</sub>, in percentage (with 10 mm/h-Pa offset). To reach 80% confidence that the predicted E<sub>r</sub> is greater than the actual E<sub>r</sub>, the predicted value should be multiplied by 2. It is important to note that the equation associated with Group 40 should be used for coarse-grained soils with D<sub>50</sub> ranging between 0.074 mm and 0.3 mm.

The same procedure was conducted with the HET/Global data set (soils with D<sub>50</sub> < 0.3 mm), and best models were selected for E<sub>r</sub>. Figure 221 shows the number of data points in each of the 135 combination groups in the HET/Global data set. Figure 222 and Figure 223 show the results for R<sup>2</sup> for each combination group for the linear and power models, respectively. Figure 224 and Figure 225 show the MSE results for each of the 135 combination groups in the HET/Global data set for the linear and power models, respectively. As expected, the combination groups with better R<sup>2</sup> values possess a lower MSE value as well.

After passing through Filters 1 and 2 (R<sup>2</sup> and MSE), linear models associated with Groups 5, 49, 53, 78, 79, 104, 105, 108, 109, 110, 112, 113, 114, 115, 118, and 124 were selected for further analysis. Power models associated with Groups 5, 49, 53, 79, 105, 108, 109, 110, 112, 114, 115, 118, and 124 were also selected for further analysis.

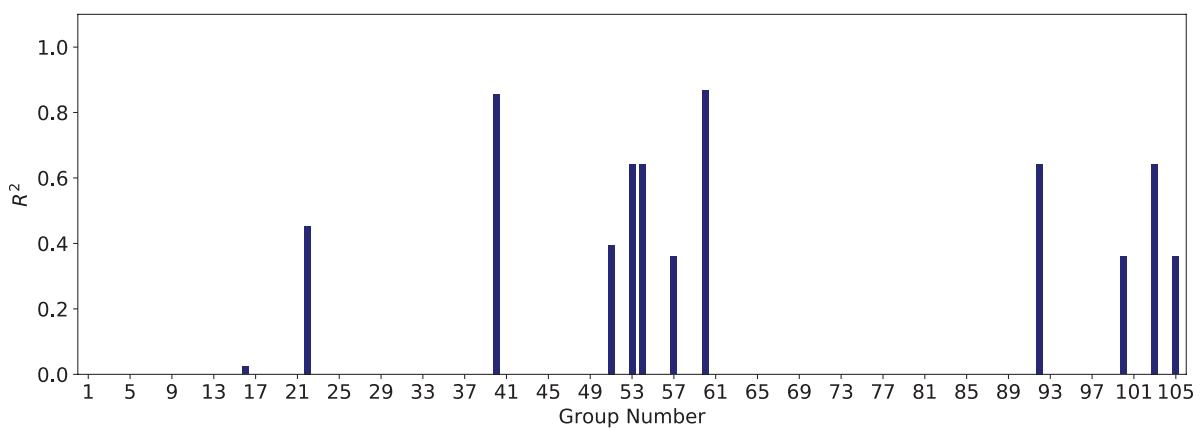
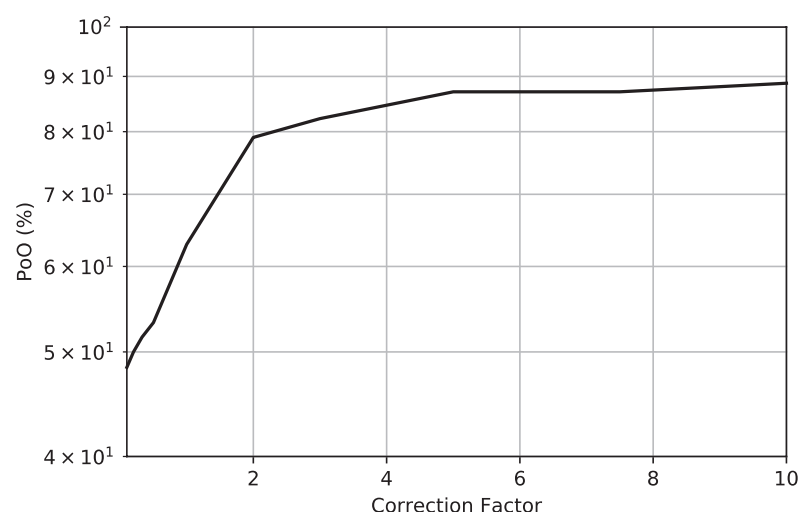
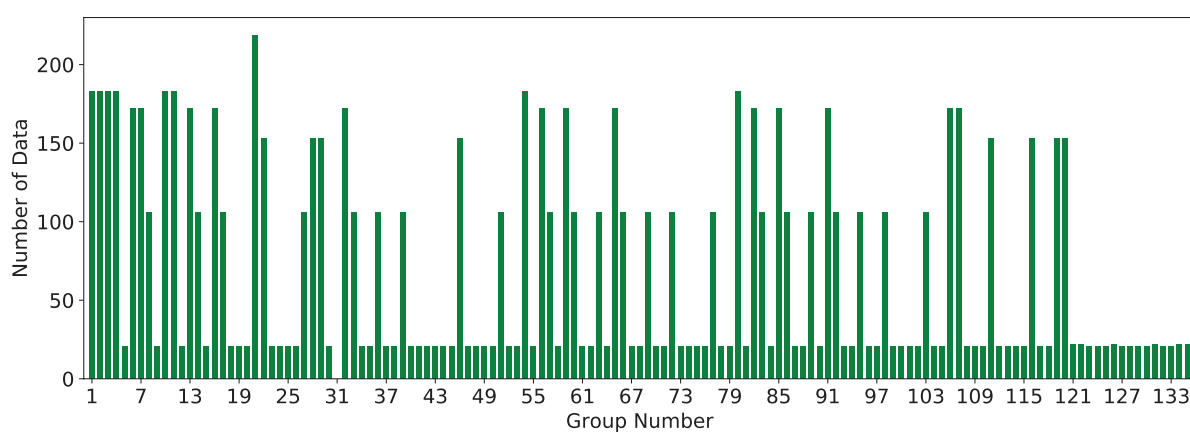


Figure 219. R<sup>2</sup> results for the power models in HET/Coarse data set: E<sub>r</sub>.

**Table 66.** Selected power models for shear stress slope in the HET/Coarse data set.

Group No.	Independent Variables	Model Expression	R <sup>2</sup>	MSE	F-value/F-stat	Cross-Validation Score
40	$\gamma$ , WC, PF, $D_{50}$	$E_t = (2.951) \times \gamma^{26.08} \times WC^{-7.48} \times PF^{-19.96} \times D_{50}^{-5.32}$	0.86	91.04	34.67	0.55
60	$C_c$ , $\gamma$ , WC, $D_{50}$	$E_t = (4.4 \times 10^{-9}) \times C_c^{-3.11} \times \gamma^{26.08} \times WC^{-7.52} \times D_{50}^{19.36}$	0.87	121.8	15.56	0.20

**Figure 220.** Plot of PoO versus correction factor for Group 40 (power):  $E_t$  in the HET/Coarse data set.**Figure 221.** Number of data points in each of 135 combination groups for the HET/Global data set:  $E_t$ .

## 236 Relationship Between Erodibility and Properties of Soils

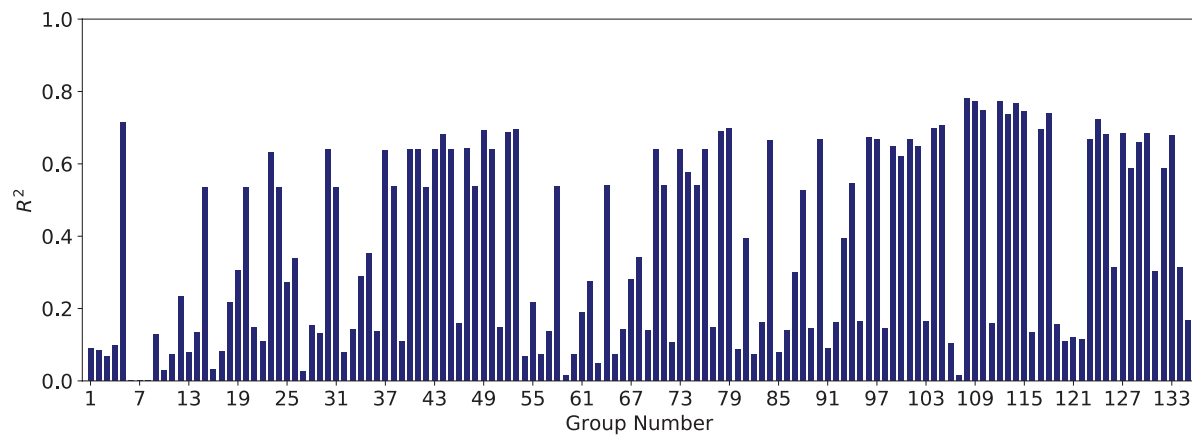


Figure 222.  $R^2$  results for the linear models in HET/Global data set:  $E_t$ .

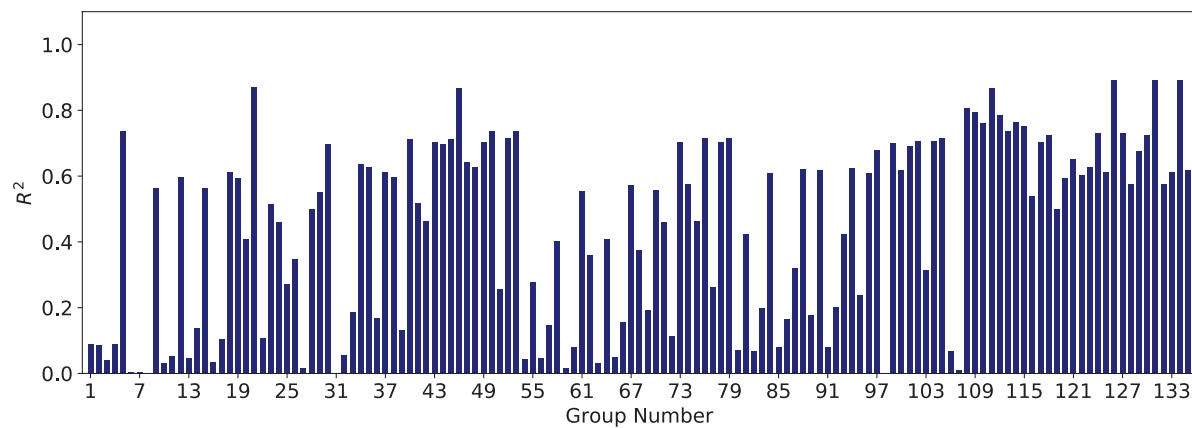


Figure 223.  $R^2$  results for the power models in HET/Global data set:  $E_t$ .

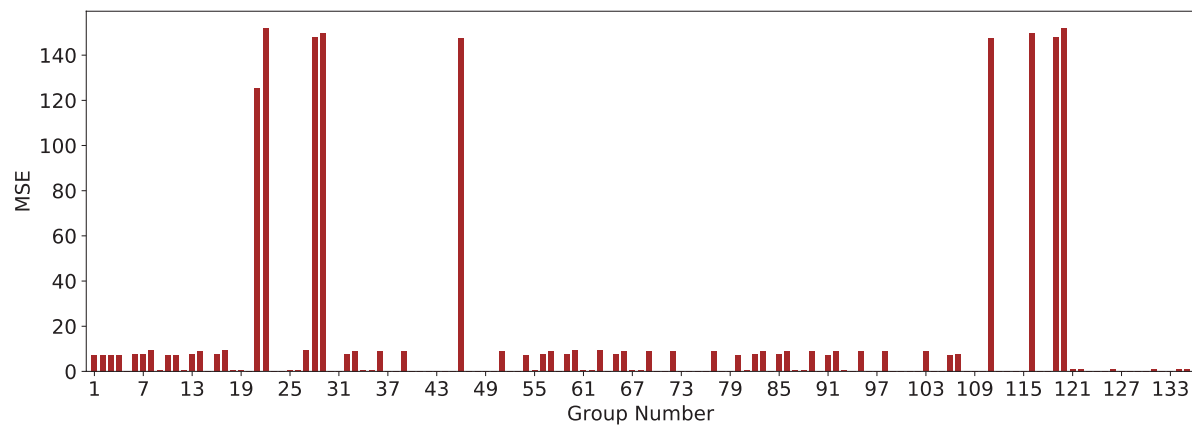


Figure 224. MSE results for the linear models in HET/Global data set:  $E_t$ .

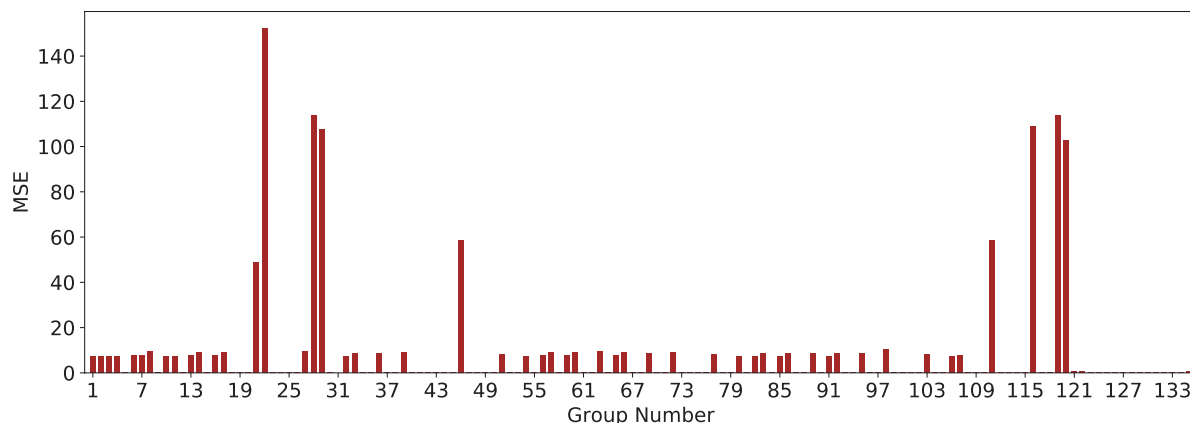


Figure 225. MSE results for the power models in HET/Global data set:  $E_\tau$ .

Filter 3,  $F$ -value/ $F$ -stat, was determined for each group mentioned above. Table 67 shows the results of the selected linear models after the requirements of the first three filters ( $R^2$ , MSE, and  $F$ -value/ $F$ -stat) were met. As shown in Table 67, many of the selected models perform satisfactorily in the cross-validation test. Table 68 shows the results of the selected power models after the requirements of the first three filters were met. The best models that also had a good cross-validation score are shaded and highlighted in blue in Tables 67 and 68. Out of all the highlighted correlation equations, the Group 108 equation in power form was selected as the most promising equation. Figure 226 shows the plot of POO versus  $\theta$  for this model. The vertical axis in Figure 226 represent the probability that, when the selected model is used, the predicted  $E_\tau$  will be greater than the actual  $E_\tau$ , in percentage (with 0 mm/h-Pa offset). To reach 90% confidence that the predicted  $E_\tau$  is greater than the actual  $E_\tau$ , the predicted value should be multiplied by 1.45. It is noteworthy that the equation associated with the combination Group 108 in power form is best to be used for finer-grained soils with  $D_{50}$  smaller than 0.3 mm.

Table 67. Selected linear models for shear stress slope in the HET/Global data set.

Group No.	Independent Variable	Model Expression	$R^2$	MSE	$F$ -value/ $F$ -stat	Cross-Validation Score
5	LL, PL, $\gamma$ , WC, $S_u$	$E_\tau = -0.01 \times LL + 0.07 \times PL + 0.07 \times \gamma - 0.08 \times WC - 0.0045 \times S_u - 0.16$	0.71	0.26	2.581	0.37
49	$\gamma$ , WC, $S_u$ , PF, $D_{50}$	$E_\tau = 0.061 \times \gamma - 0.06 \times WC - 0.004 \times S_u + 0.02 \times PF + 21.73 \times D_{50} - 1.33$	0.69	0.27	2.316	0.32
53	PI, $\gamma$ , WC, $S_u$ , PF, $D_{50}$	$E_\tau = 0.001 \times PI + 0.05 \times \gamma - 0.07 \times WC - 0.004 \times S_u + 0.02 \times PF + 21.58 \times D_{50} - 1.18$	0.70	0.27	1.879	0.31
78	LL, WC, $S_u$ , PF, $D_{50}$	$E_\tau = 0.002 \times LL - 0.06 \times WC - 0.0036 \times S_u + 0.02 \times PF + 20.42 \times D_{50} - 0.17$	0.69	0.27	2.287	0.35
79	LL, $\gamma$ , WC, $S_u$ , PF, $D_{50}$	$E_\tau = 0.001 \times LL + 0.054 \times \gamma - 0.07 \times WC - 0.004 \times S_u + 0.02 \times PF + 21.3 \times D_{50} - 1.16$	0.70	0.27	1.886	0.31
104	PL, WC, $S_u$ , PF, $D_{50}$	$E_\tau = 0.024 \times PL - 0.06 \times WC - 0.0035 \times S_u + 0.01 \times PF + 15.67 \times D_{50} + 0.09$	0.70	0.27	2.386	0.31
105	PL, $\gamma$ , WC, $S_u$ , PF, $D_{50}$	$E_\tau = 0.023 \times PL + 0.054 \times \gamma - 0.07 \times WC - 0.004 \times S_u + 0.02 \times PF + 16.84 \times D_{50} - 0.91$	0.71	0.26	1.971	0.29

(continued on next page)

## 238 Relationship Between Erodibility and Properties of Soils

**Table 67. (Continued).**

Group No.	Independent Variable	Model Expression	R <sup>2</sup>	MSE	F-value/ F-stat	Cross-Validation Score
108	LL, PL, γ, PC, S <sub>u</sub>	$E_{\tau} = -0.005 \times LL + 0.06 \times PL + 0.1 \times \gamma - 0.02 \times PC - 0.0001 \times S_u - 1.47$	0.78	0.23	3.697	0.52
109	PC, γ, WC, S <sub>u</sub> , PF, D <sub>50</sub>	$E_{\tau} = -0.03 \times PC + 0.094 \times \gamma + 0.01 \times WC + 0.0003 \times S_u + 0.02 \times PF + 8.86 \times D_{50} - 2$	0.77	0.23	2.791	0.46
110	PC, WC, S <sub>u</sub> , PF, D <sub>50</sub>	$E_{\tau} = -0.027 \times PC + 0.02 \times WC + 0.0008 \times S_u + 0.01 \times PF + 8.95 \times D_{50} - 0.32$	0.75	0.25	3.068	0.45
112	PC, γ, S <sub>u</sub> , PF, D <sub>50</sub>	$E_{\tau} = -0.028 \times PC + 0.1 \times \gamma - 0.0003 \times S_u + 0.02 \times PF + 8.31 \times D_{50} - 1.86$	0.77	0.23	3.134	0.51
113	PC, γ, WC, S <sub>u</sub> , D <sub>50</sub>	$E_{\tau} = -0.04 \times PC + 0.07 \times \gamma + 0.01 \times WC + 0.0004 \times S_u - 10.12 \times D_{50} + 0.26$	0.74	0.25	2.689	0.48
114	PC, γ, WC, S <sub>u</sub> , PF	$E_{\tau} = -0.034 \times PC + 0.09 \times \gamma + 0.0045 \times WC - 0.00003 \times S_u + 0.01 \times PF - 1.35$	0.77	0.24	3.716	0.63
115	PC, S <sub>u</sub> , PF, D <sub>50</sub>	$E_{\tau} = -0.023 \times PC - 0.0002 \times S_u + 0.01 \times PF + 8.08 \times D_{50} - 0.03$	0.75	0.25	3.679	0.51
118	PC, WC, S <sub>u</sub> , PF	$E_{\tau} = -0.031 \times PC + 0.01 \times WC + 0.0004 \times S_u + 0.01 \times PF + 0.36$	0.74	0.25	3.608	0.62
124	γ, A, WC, S <sub>u</sub> , PF, D <sub>50</sub>	$E_{\tau} = 0.045 \times \gamma + 0.09 \times A - 0.05 \times WC - 0.003 \times S_u + 0.02 \times PF + 19.41 \times D_{50} - 1.16$	0.72	0.26	3.009	0.27

**Table 68. Selected power models for shear stress slope in the HET/Global data set.**

Group No.	Independent Variable	Model Expression	R <sup>2</sup>	MSE	F-value/ F-stat	Cross-Validation Score
5	LL, PL, γ, WC, S <sub>u</sub>	$E_{\tau} = (3.96 \times 10^{-5}) \times LL^{-1.62} \times PL^{2.71} \times \gamma^{3.17} \times WC^{-0.42} \times S_u^{-0.15}$	0.74	0.25	8.578	0.21
49	γ, WC, S <sub>u</sub> , PF, D <sub>50</sub>	$E_{\tau} = (4.1 \times 10^{-5}) \times \gamma^{1.19} \times WC^{-0.25} \times S_u^{-0.02} \times PF^{2.67} \times D_{50}^{1.21}$	0.71	0.27	7.968	0.08
53	PL, γ, WC, S <sub>u</sub> , PF, D <sub>50</sub>	$E_{\tau} = (10^{-5}) \times PL^{-0.4} \times \gamma^{2.11} \times WC^{0.16} \times S_u^{0.03} \times PF^{2.12} \times D_{50}^{1.01}$	0.74	0.25	8.012	-1.53
79	LL, γ, WC, S <sub>u</sub> , PF, D <sub>50</sub>	$E_{\tau} = (1.7 \times 10^{-5}) \times LL^{-0.61} \times \gamma^{1.52} \times WC^{0.11} \times S_u^{0.03} \times PF^{2.85} \times D_{50}^{1.20}$	0.72	0.26	5.568	-0.16
105	PL, γ, WC, S <sub>u</sub> , PF, D <sub>50</sub>	$E_{\tau} = (3.16 \times 10^{-4}) \times PL^{0.82} \times \gamma^{1.41} \times WC^{-0.58} \times S_u^{-0.08} \times PF^{1.63} \times D_{50}^{1.04}$	0.72	0.26	5.960	-2.92
108	LL, PL, γ, PC, S <sub>u</sub>	$E_{\tau} = (9 \times 10^{-6}) \times LL^{-0.35} \times PL^{1.59} \times \gamma^{3.3} \times PC^{-0.48} \times S_u^{-0.19}$	0.81	0.21	9.238	0.51
109	PC, γ, WC, S <sub>u</sub> , PF, D <sub>50</sub>	$E_{\tau} = (4 \times 10^{-6}) \times PC^{-0.48} \times \gamma^{2.34} \times WC^{-0.71} \times S_u^{0.08} \times PF^{1.52} \times D_{50}^{0.71}$	0.80	0.22	5.466	0.32
110	PC, WC, S <sub>u</sub> , PF, D <sub>50</sub>	$E_{\tau} = (0.006) \times PC^{-0.38} \times WC^{0.57} \times S_u^{0.15} \times PF^{1.40} \times D_{50}^{0.7}$	0.76	0.24	8.259	0.48
112	PC, γ, S <sub>u</sub> , PF, D <sub>50</sub>	$E_{\tau} = (8.5 \times 10^{-5}) \times PC^{-0.39} \times \gamma^{2.1} \times S_u^{-0.04} \times PF^{1.43} \times D_{50}^{0.64}$	0.78	0.23	9.017	0.48
114	PC, γ, WC, S <sub>u</sub> , PF	$E_{\tau} = (2 \times 10^{-5}) \times PC^{-0.66} \times \gamma^{2.28} \times WC^{0.43} \times S_u^{-0.06} \times PF^{0.97}$	0.76	0.24	8.881	-2.16
115	PC, S <sub>u</sub> , PF, D <sub>50</sub>	$E_{\tau} = (0.031) \times PC^{-0.3} \times S_u^{0.02} \times PF^{1.41} \times D_{50}^{0.67}$	0.75	0.24	6.363	0.34
118	PC, WC, S <sub>u</sub> , PF	$E_{\tau} = (0.016) \times PC^{-0.56} \times WC^{0.37} \times S_u^{0.04} \times PF^{0.86}$	0.72	0.26	7.113	0.48
124	γ, A, WC, S <sub>u</sub> , PF, D <sub>50</sub>	$E_{\tau} = (1.84 \times 10^{-4}) \times \gamma^{1.06} \times A^{0.26} \times WC^{-0.12} \times S_u^{-0.02} \times PF^{2.28} \times D_{50}^{1.18}$	0.73	0.25	5.349	-0.24

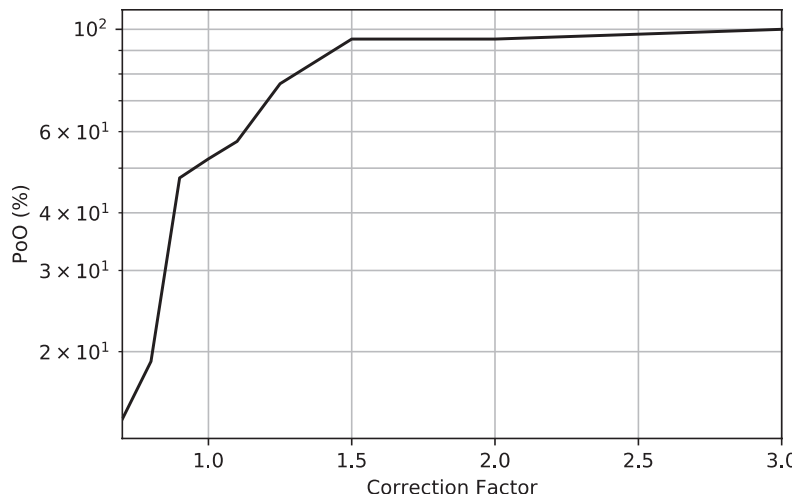


**Figure 226.** Plot of POO versus correction factor for Group 108 (power):  $E_v$  in the HET/Global data set.

#### 7.3.4.4 Initial Slope of Erosion Rate–Velocity

The same four-filter process discussed in Section 7.3.3 is implemented in this section to obtain the best models for  $E_v$ . Similar to the case of critical velocity,  $v_c$ , among the three erosion tests studied in this chapter (EFA, JET, HET), only the EFA test can reflect the initial slope of the erosion rate,  $E_v$ , as one of its outputs. In other words, results of JET and HET consist of only three erodibility parameters (i.e.,  $\tau_c$ ,  $E_v$ , and EC) in contrary with the EFA results which include all five erodibility parameters (i.e.,  $\tau_c$ ,  $v_c$ ,  $E_v$ ,  $E_t$ , and EC). Therefore, regression analysis for  $E_v$  is limited to only the EFA data set.

**EFA Data Set.** Similar to the case of  $E_t$ , it was observed that dividing the EFA/Global data set into the EFA/Fine and the EFA/Coarse data sets would significantly improve the regression results for  $E_v$ . Figure 227 shows the number of data points in each of the 135 combination groups in the EFA/Fine data set. Figure 228 and Figure 229 show the results for  $R^2$  for each combination group for the linear and power models, respectively.

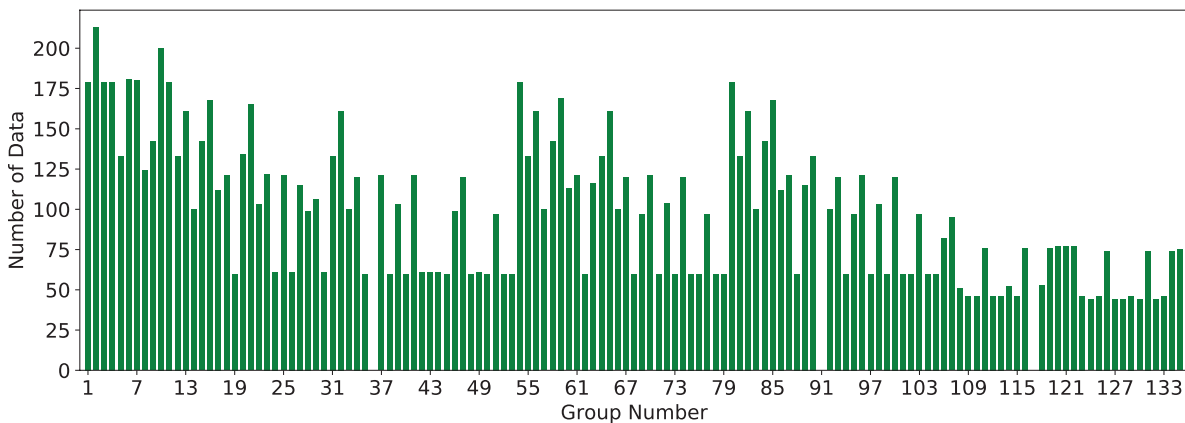


**Figure 227.** Number of data points in each of 135 combination groups for the EFA/Fine data set:  $E_v$ .

## 240 Relationship Between Erodibility and Properties of Soils

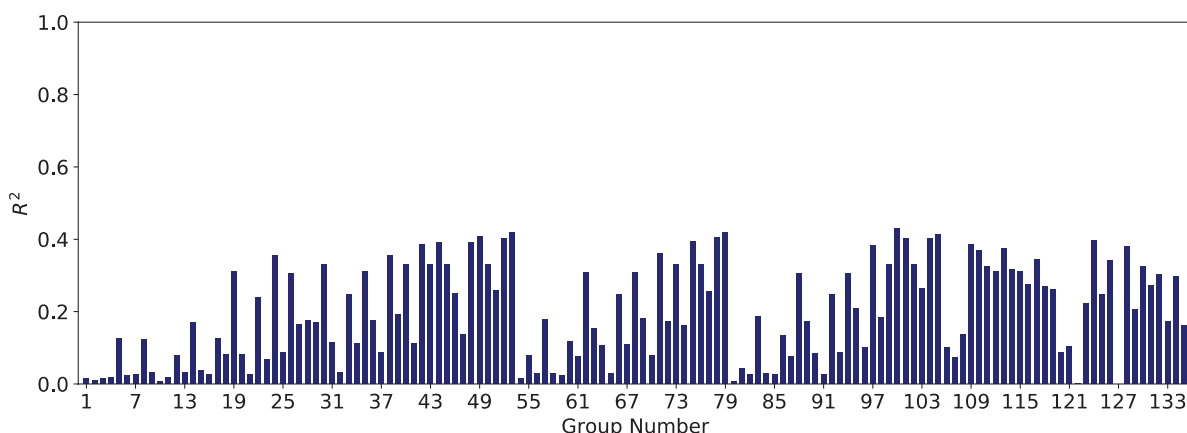


**Figure 228.** *R<sup>2</sup> results for the linear models in EFA/Fine data set: E<sub>v</sub>.*

Results show that power models in general perform better than the linear models.  $R^2$  values of Groups 109 to 135 are generally higher than the rest for both power models. Figure 230 and Figure 231 show the MSE results for each of the 135 combination groups in the EFA/Fine data set for linear and power models, respectively.

After passing through Filters 1 and 2 ( $R^2$  and MSE), the power models associated with Groups 53, 79, 101, 105, 124, 126, 127, 131, and 134 were selected for further analysis. The linear models did not lead to  $R^2$  values that were any better; therefore, the study of best-fitting models was limited to power models.

Filter 3, *F*-value/*F*-stat, was determined for each group mentioned above. Table 69 shows the results of the selected power models after the requirements of the first three filters ( $R^2$ , MSE, and *F*-value/*F*-stat) were met. The Group 126 equation in power form was selected as the most promising equation. Figure 232 shows the plot of POO versus  $\theta$  for this model. The vertical axis in Figure 232 shows the probability that, when the selected model is used, the predicted  $E_v$  will be greater than the actual  $E_v$ , in percentage (with 10 mm-s/m-h offset). To reach 80% confidence that the predicted  $E_v$  is greater than the actual  $E_v$ , the predicted value should be multiplied by 2.

The same procedure was conducted with the EFA/Coarse data set, and the best models were selected for  $E_v$ . Figure 233 shows the number of data points in each of the 105 combination groups in the EFA/Coarse data set. Figure 234 and Figure 235 show the results for  $R^2$  for each combination group for the linear and power models, respectively.

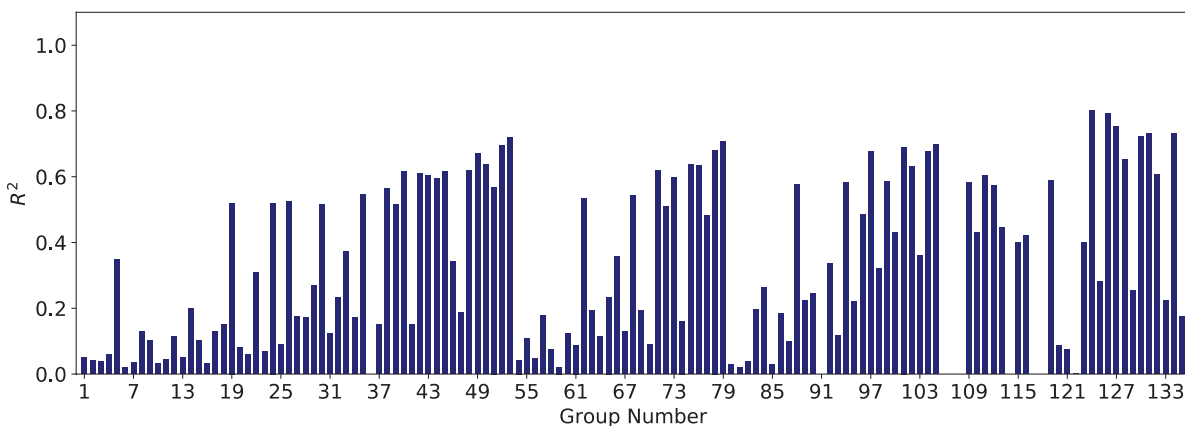


**Figure 229.** *R<sup>2</sup> results for the power models in EFA/Fine data set: E<sub>v</sub>.*

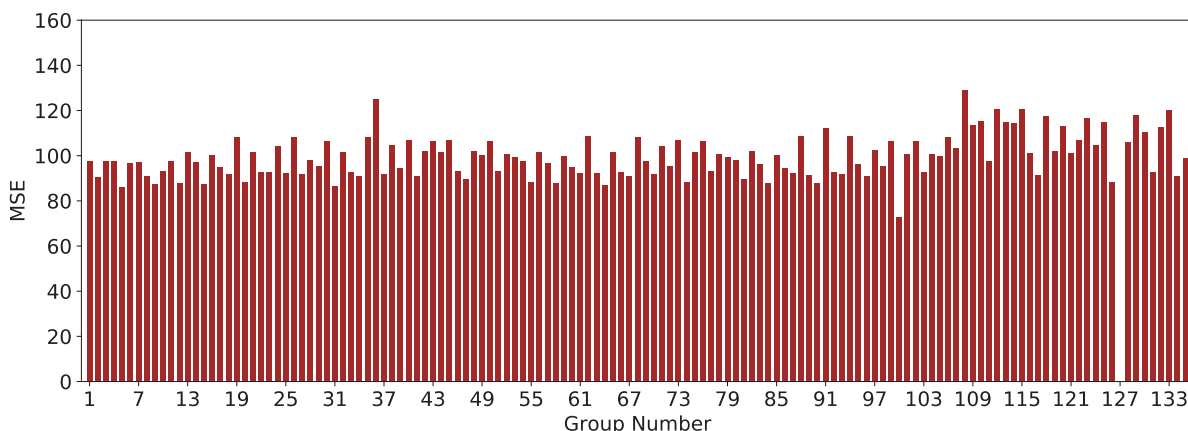


Figure 230. MSE results for the linear models in EFA/Fine data set: E<sub>v</sub>.

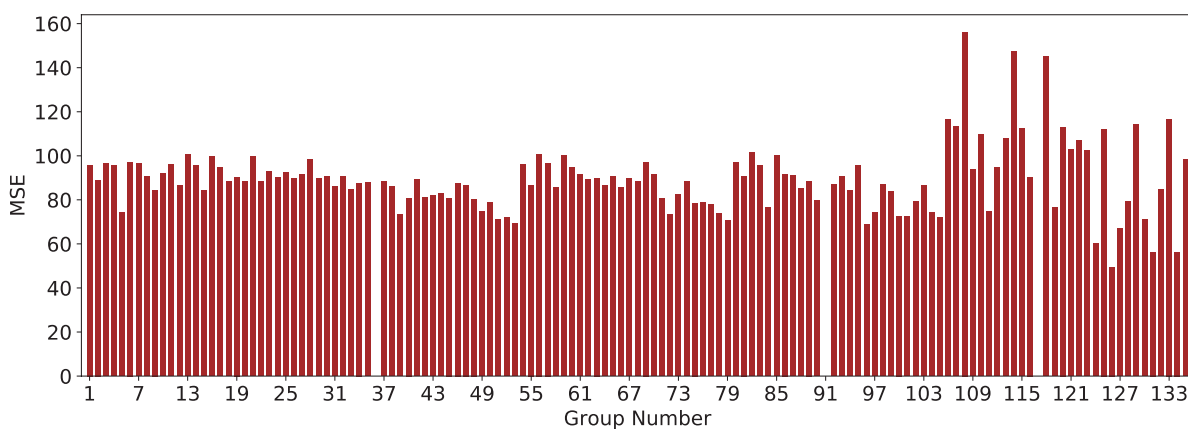


Figure 231. MSE results for the power models in EFA/Fine data set: E<sub>v</sub>.

Table 69. Selected power models for velocity slope in the EFA/Fine data set.

Group No.	Independent Variable	Model Expression	R <sup>2</sup>	MSE	F-value/F-stat	Cross-Validation Score
53	PI, γ, WC, S <sub>u</sub> , PF, D <sub>50</sub>	$E_v = (9,785,577.4) \times PI^{0.61} \times \gamma^{-4.16} \times WC^{-1.62}$ $\times S_u^{-0.54} \times PF^{4.04} \times D_{50}^{3.45}$	0.72	69.2	324.6	-5.9
79	LL, γ, WC, S <sub>u</sub> , PF, D <sub>50</sub>	$E_v = (142,233,608) \times LL^{0.92} \times \gamma^{-4.48} \times WC^{-1.42}$ $\times S_u^{-0.38} \times PF^{2.83} \times D_{50}^{3.30}$	0.71	70.6	320.1	-0.55
101	PL, γ, WC, S <sub>u</sub> , D <sub>50</sub>	$E_v = (662,947,356) \times PL^{2.07} \times \gamma^{-2.93} \times WC^{-1.58}$ $\times S_u^{-0.35} \times D_{50}^{2.14}$	0.70	72.6	318.5	-0.43
105	PL, γ, WC, S <sub>u</sub> , PF, D <sub>50</sub>	$E_v = (3.12869 \times 10^{10}) \times PL^1 \times \gamma^{-5.09} \times WC^{-1.26}$ $\times S_u^{-0.29} \times PF^{1.63} \times D_{50}^{3.04}$	0.70	71.8	316.3	-0.05
124	γ, A, WC, S <sub>u</sub> , PF, D <sub>50</sub>	$E_v = (1.4227 \times 10^{13}) \times \gamma^{-8.45} \times A^{0.04} \times WC^{-1.18}$ $\times S_u^{-0.06} \times PF^{4.12} \times D_{50}^{4.81}$	0.80	60.1	221.2	-2.33
126	D <sub>50</sub> , γ, WC, PF, A	$E_v = (1.682339 \times 10^{13}) \times D_{50}^{5.10} \times \gamma^{-9.20} \times WC^{-1.13}$ $\times PF^{4.69} \times A^{-0.01}$	0.79	49.5	384.3	0.52
127	D <sub>50</sub> , γ, S <sub>u</sub> , PF, A	$E_v = (1.429 \times 10^{13}) \times D_{50}^{6.09} \times \gamma^{-10.23} \times S_u^{0.58}$ $\times PF^{4.79} \times A^{-0.4}$	0.75	66.8	361.5	0.4
131	D <sub>50</sub> , WC, PF, A	$E_v = (4610.15) \times D_{50}^{28.67} \times WC^{0.52} \times PF^{18.36} \times A^{2.76}$	0.73	56.4	355.6	-0.98
134	A, γ, PF, D <sub>50</sub>	$E_v = (2.0788 \times 10^{13}) \times A^{-0.3} \times \gamma^{-9.71} \times PF^{4.48}$ $\times D_{50}^{5.61}$	0.73	56.3	329.9	0.05

## 242 Relationship Between Erodibility and Properties of Soils

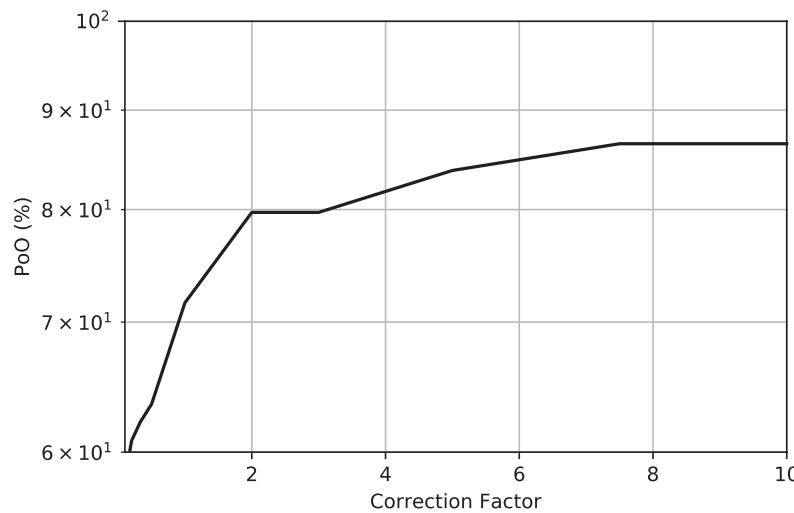


Figure 232. Plot of PoO versus correction factor for Group 126  
(power):  $E_v$  in the EFA/Fine data set.

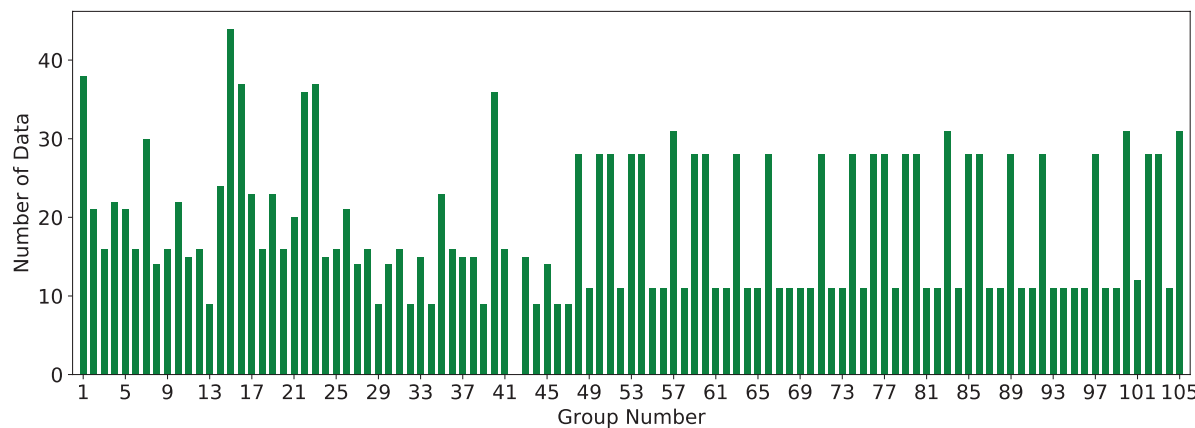


Figure 233. Number of data points in each of 105 combination groups for the EFA/Coarse data set:  $E_v$ .

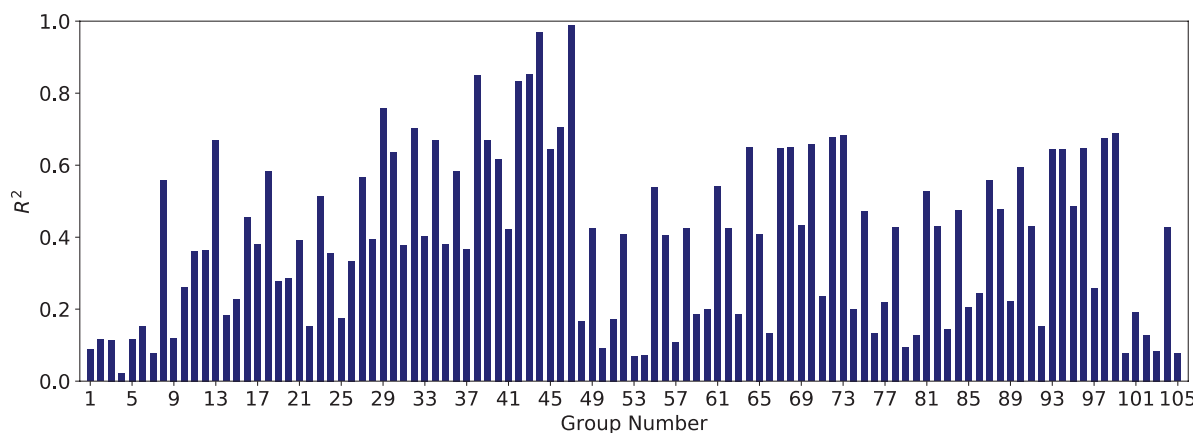
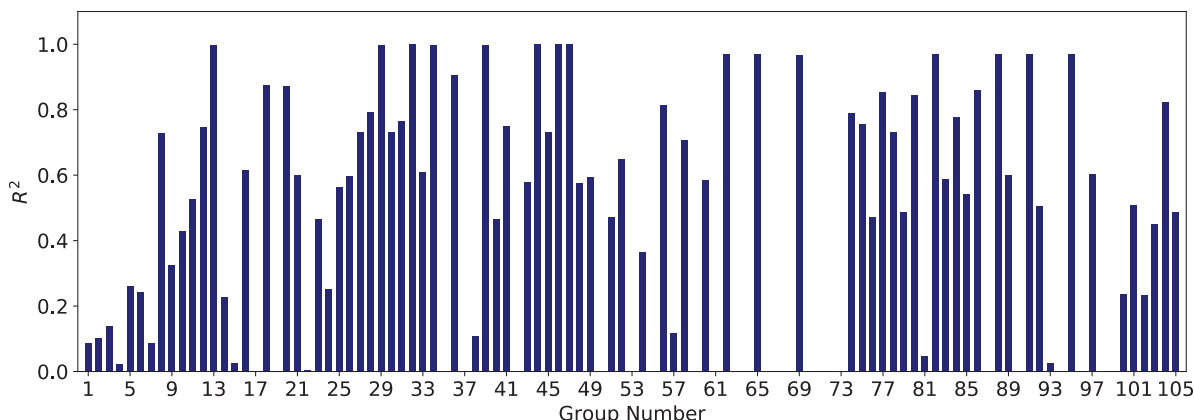


Figure 234.  $R^2$  results for the linear models in EFA/Coarse data set:  $E_v$ .



**Figure 235. R<sup>2</sup> results for the power models in EFA/Coarse data set: E<sub>v</sub>.**

Both the linear and power models showed some good groups in terms of  $R^2$  values; however, as shown in Figure 233, the number of data points in most groups was very low.

After passing through Filters 1 and 2 ( $R^2$  and MSE), the linear models associated with Groups 38, 42, 43, and 45 were selected for further analysis. Power models associated with Groups 18, 20, 28, 34, 36, 44, 46, 56, 65, 74, 77, 80, 82, 86, and 88 were also selected for further analysis.

Filter 3, F-value/F-stat, was determined for each group mentioned above. Table 70 shows the results of the selected linear models after the requirements of the first three filters ( $R^2$ , MSE, and F-value/F-stat) were met. As shown in Table 70, none of the selected models performed satisfactorily in the cross-validation test. Table 71 shows the results of the selected power models after the requirements of the first three filters were met. The Group 86 correlation equation in power form was selected as the most promising equation. Figure 236 shows the plot of POO versus  $\theta$  for this model. The vertical axis in Figure 236 shows the probability that, when the selected model is used, the predicted  $E_v$  will be greater than the actual  $E_v$ , in percentage (with 10 mm-s/m-h offset). To reach 80% confidence that the predicted  $E_v$  is greater than the actual  $E_v$ , the predicted value should be multiplied by 5.

#### 7.3.4.5 Erosion Category

The four-filter process discussed in Section 7.3.3 was implemented to obtain the best models for erosion category, EC. Regression analysis for EC was performed for the EFA, HET, and JET separately.

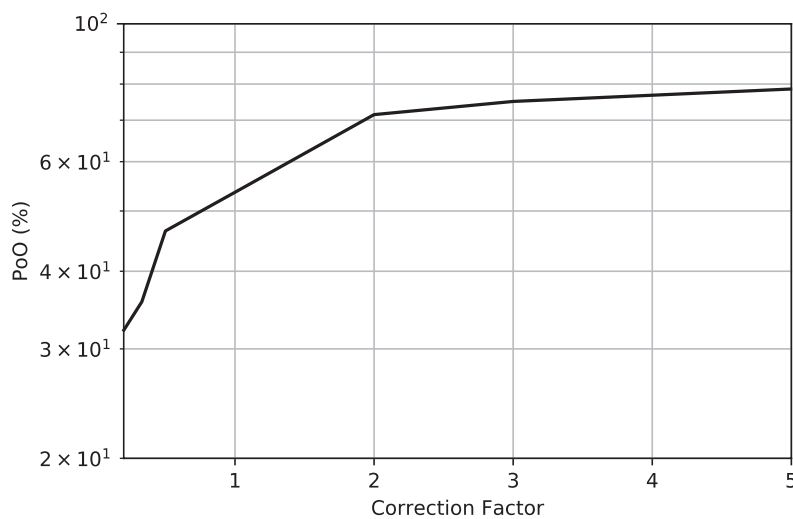
**Table 70. Selected linear models for velocity slope in the EFA/Coarse data set.**

Group No.	Independent Variable	Model Expression	R <sup>2</sup>	MSE	F-value/F-stat	Cross-Validation Score
38	WC, VST, PF, D <sub>50</sub>	$E_v = 101.665 \times WC + 4.65 \times VST - 55.46 \times PF - 85.9 \times D_{50} + 355.9$	0.85	643.1	5.46	-2.3
42	PI, γ, WC, VST, D <sub>50</sub>	$E_v = -4.543 \times PI - 35.21 \times \gamma - 9.16 \times WC - 2.03 \times VST + 1277.9 \times D_{50} + 901.4$	0.83	49.23	5.11	-4.6
43	γ, WC, VST, PF, D <sub>50</sub>	$E_v = -59.184 \times \gamma + 101.11 \times WC + 5.77 \times VST - 54.22 \times PF - 45 \times D_{50} + 1,391$	0.85	635.7	2.09	-22.4
45	PI, γ, WC, PF, D <sub>50</sub>	$E_v = -6.62 \times PI - 48.82 \times \gamma - 2.92 \times WC - 10.46 \times PF + 216.18 \times D_{50} + 1,497$	0.65	88.3	0.96	-0.03

## 244 Relationship Between Erodibility and Properties of Soils

**Table 71.** Selected power models for velocity slope in the EFA/Coarse data set.

Group No.	Independent Variable	Model Expression	R <sup>2</sup>	MSE	F-value/F-stat	Cross-Validation Score
18	WC, VST, D <sub>50</sub>	$E_v = (9,280.99) \times WC^{-0.13} \times VST^{-2.35} \times D_{50}^{-2.58}$	0.87	570	8.62	-2.8
20	VST, γ, D <sub>50</sub>	$E_v = (1,481.13) \times VST^{-2.18} \times \gamma^{0.5} \times D_{50}^{-2.36}$	0.87	577	8.40	-0.58
28	PI, γ, VST, PF	$E_v = (2.991 \times 10^{13}) \times PI^{-1.03} \times \gamma^{-5} \times VST^{0.48} \times PF^{-3.56}$	0.79	58.0	4.9	-0.7
34	PI, VST, PF, D <sub>50</sub>	$E_v = (805,281.14 \times 10^7) \times PI^{-1.52} \times VST^{-0.42} \times PF^{-8.05} \times D_{50}^{2.93}$	0.99	4.85	0.93	-0.57
36	γ, WC, VST, D <sub>50</sub>	$E_v = (2 \times 10^{-5}) \times \gamma^{8.94} \times WC^{-1.11} \times VST^{-5.3} \times D_{50}^{-5.08}$	0.91	491	8.8	-5.02
44	PI, γ, VST, PF, D <sub>50</sub>	$E_v = (820,969.5 \times 10^6) \times PI^{-1.06} \times \gamma^{-3.54} \times VST^{-1.6} \times PF^{-2.2} \times D_{50}^{1.15}$	0.99	2.02	0.89	0.82
46	PI, WC, VST, PF, D <sub>50</sub>	$E_v = (84,388,620) \times PI^{-0.73} \times WC^{1.28} \times VST^{-1.6} \times PF^{-1.63} \times D_{50}^{2.76}$	0.99	3.21	0.91	-0.51
56	C <sub>c</sub> , VST, D <sub>50</sub>	$E_v = (5,401.92) \times C_c^{-1.54} \times VST^{-3.54} \times D_{50}^{-4.73}$	0.81	399	2.98	-0.25
65	C <sub>c</sub> , WC, VST, D <sub>50</sub>	$E_v = (10,199,544.5) \times C_c^{-5.65} \times WC^{4.51} \times VST^{-31.3} \times D_{50}^{-35.32}$	0.97	155.6	13.4	-1.98
74	C <sub>c</sub> , γ, WC	$E_v = (23,300,967,450) \times C_u^{-1.32} \times \gamma^{-7.26} \times WC^{2.04}$	0.79	389.2	9.9	0.29
77	C <sub>c</sub> , γ, D <sub>50</sub>	$E_v = (4,489.56) \times C_u^{-2.97} \times \gamma^{-1.18} \times D_{50}^{-2.25}$	0.86	323.5	19.2	0.37
80	C <sub>c</sub> , WC, D <sub>50</sub>	$E_v = (152.16) \times C_u^{-2.53} \times WC^{-0.32} \times D_{50}^{-2.92}$	0.85	324	17.9	0.01
82	C <sub>c</sub> , VST, D <sub>50</sub>	$E_v = (95.18) \times C_u^{-13.21} \times VST^{-20.14} \times D_{50}^{-37.13}$	0.97	155.9	21.7	0.03
86	C <sub>u</sub> , γ, WC, D <sub>50</sub>	$E_v = (8,8969.4) \times C_u^{-1.77} \times \gamma^{-2.26} \times WC^{0.34} \times D_{50}^{-1.69}$	0.86	319.4	15.9	0.64
88	C <sub>c</sub> , γ, VST, D <sub>50</sub>	$E_v = (7.6 \times 10^{-5}) \times C_u^{-3.28} \times \gamma^{7.23} \times VST^{-14.04} \times D_{50}^{-20.09}$	0.97	155.6	13.43	-1.28

**Figure 236.** Plot of POO versus correction factor for Group 86 (power): E<sub>v</sub> in the EFA/Coarse data set.

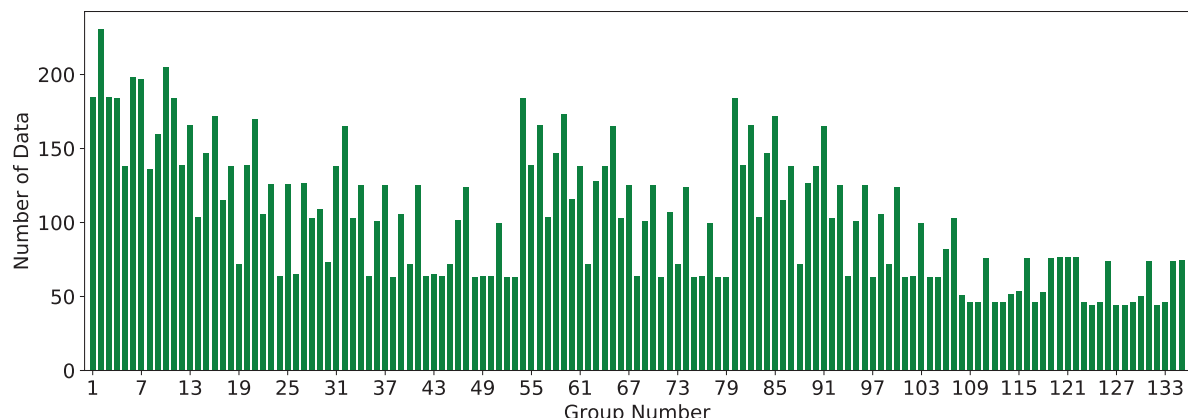


**Figure 237.** Number of data points in each of 135 combination groups for the EFA/Fine data set: EC.

**EFA Database.** It was observed that dividing the EFA/Global data set into the EFA/Fine and the EFA/Coarse data sets would improve the regression results. Figure 237 shows the number of data points in each of the 135 combination groups in the EFA/Fine data set. Figure 238 and Figure 239 show the results for  $R^2$  for each combination group for the linear and power models, respectively.

The  $R^2$  values for both the linear and power models were not very high (up to 0.6). It can be observed that the better  $R^2$  values were observed in Combination Groups 109 to 135. Figure 240 and Figure 241 show the MSE results for each of the 135 combination groups in the EFA/Fine data set, for linear and power models, respectively. In general, the power and linear models were not noticeably different.

After passing through Filters 1 and 2 ( $R^2$  and MSE), the linear models associated with Groups 109, 110, 113, 117, and 124 were selected for further analysis. Power models associated with Groups 124, 128, and 132 were also selected for further analysis.

Filter 3,  $F$ -value/ $F$ -stat, was determined for each group mentioned above. Table 72 shows the results of the selected linear models after the requirements of the first three filters ( $R^2$ , MSE, and  $F$ -value/ $F$ -stat) were met. As shown in Table 72, most of the selected models performed satisfactorily in the cross-validation test. Table 73 shows the results of the selected power models after the requirements of the first three filters were met. The Group 132 correlation equation in power form was selected as the most promising equation. Figure 242 shows the plot of POU

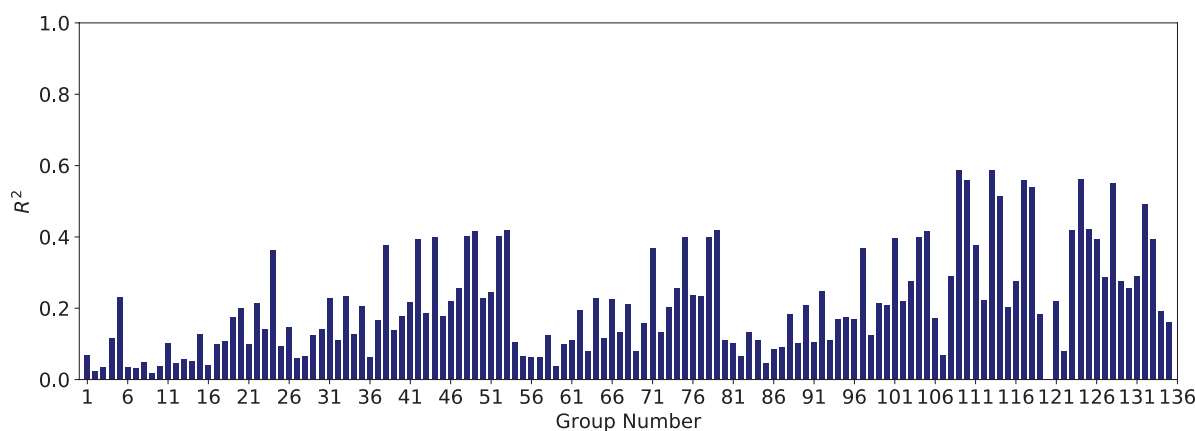


**Figure 238.**  $R^2$  results for the linear models in EFA/Fine data set: EC.

## 246 Relationship Between Erodibility and Properties of Soils

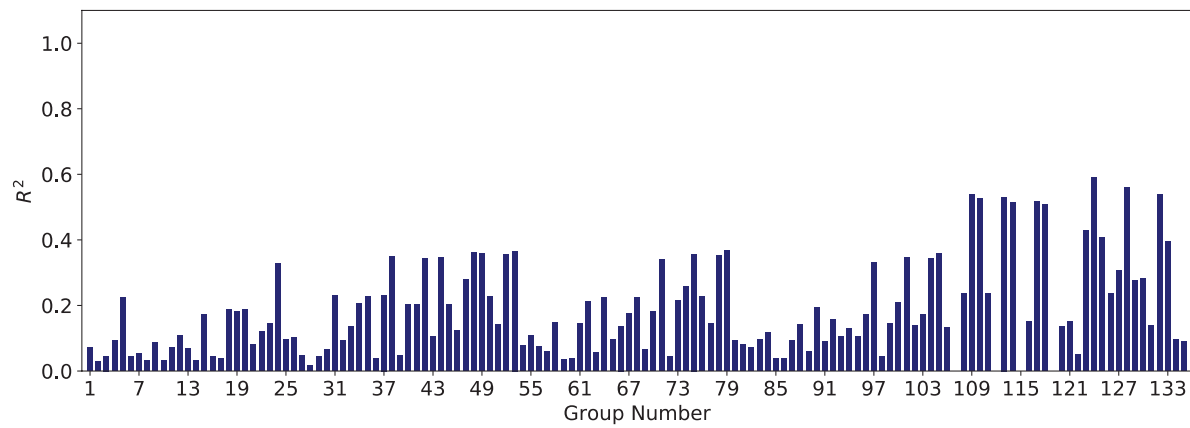


**Figure 239.**  $R^2$  results for the power models in EFA/Fine data set: EC.

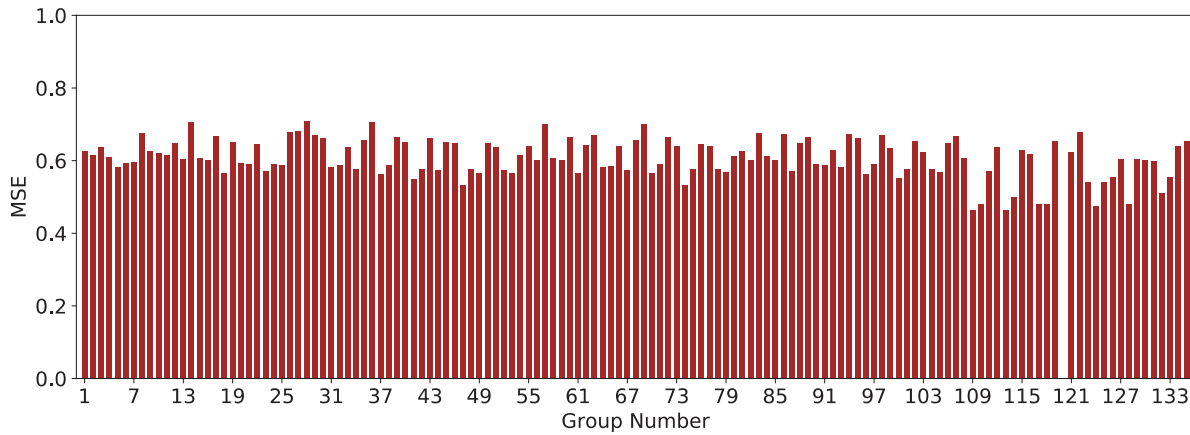


**Figure 240.** MSE results for the linear models in EFA/Fine data set: EC.

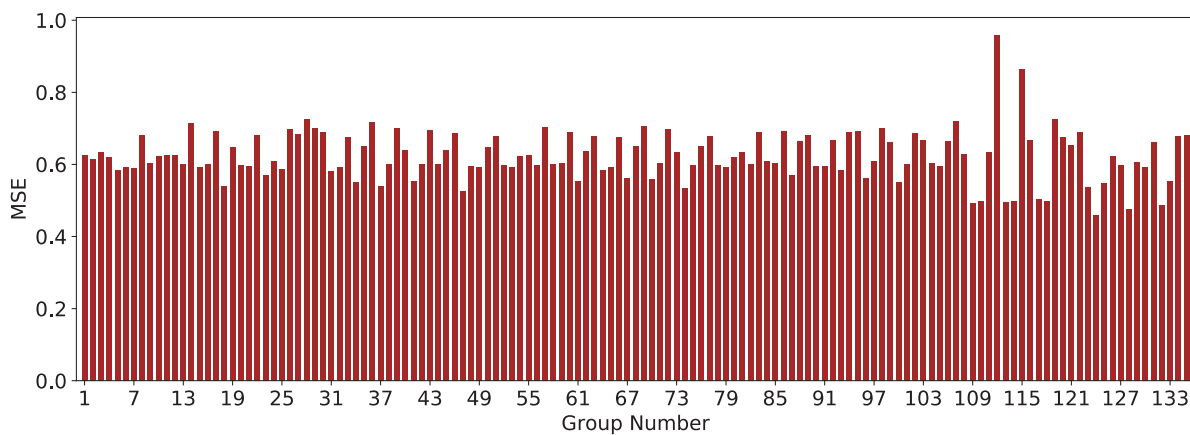


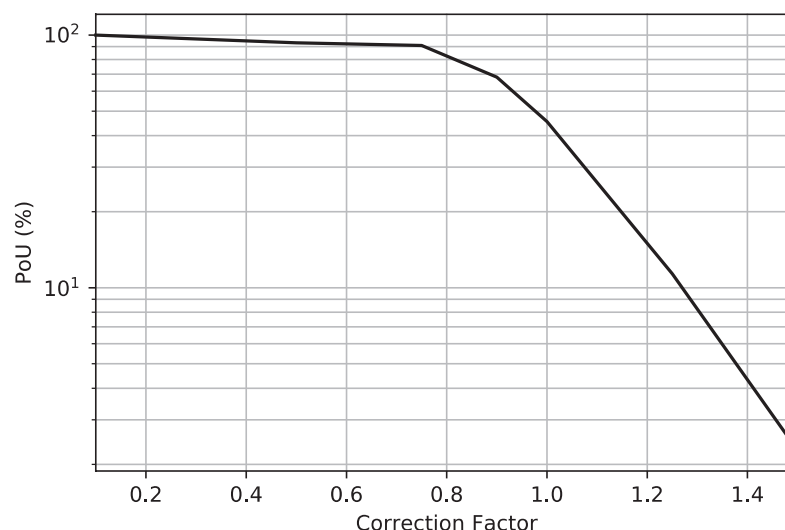
**Figure 241.** MSE results for the power models in EFA/Fine data set: EC.

**Table 72.** Selected linear models for erosion category in the EFA/Fine data set.

Group No.	Independent Variable	Model Expression	R <sup>2</sup>	MSE	F-value/ F-stat	Cross-Validation Score
109	PC, $\gamma$ , WC, $S_u$ , PF, $D_{50}$	EC = 0.02 × PC + 0.112 × $\gamma$ + 0.04 × WC + 0.0005 × $S_u$ + 0.0012 × PF - 3.09 × $D_{50}$ - 1.27	0.59	0.47	3.96	0.33
110	PC, WC, $S_u$ , PF, $D_{50}$	EC = 0.022 × PC + 0.03 × WC + 0.0016 × $S_u$ - 0.0029 × PF - 3.85 × $D_{50}$ + 1.2	0.56	0.48	4.13	0.35
113	PC, $\gamma$ , WC, $S_u$ , $D_{50}$	EC = 0.02 × PC + 0.11 × $\gamma$ + 0.04 × WC + 0.0005 × $S_u$ - 3.853 × $D_{50}$ - 1.088	0.59	0.46	4.64	0.43
117	PC, WC, $S_u$ , $D_{50}$	EC = 0.023 × PC + 0.03 × WC + 0.0017 × $S_u$ - 1.845 × $D_{50}$ + 0.8566	0.56	0.48	4.97	0.43
124	$\gamma$ , A, WC, $S_u$ , PF, $D_{50}$	EC = 0.125 × $\gamma$ - 0.072 × A + 0.04 × WC + 0.0001 × $S_u$ - 0.0086 × PF - 16.12 × $D_{50}$ + 0.259	0.56	0.47	3.34	0.33

**Table 73.** Selected power models for erosion category in the EFA/Fine data set.

Group No.	Independent Variable	Model Expression	R <sup>2</sup>	MSE	F-value/ F-stat	Cross-Validation Score
124	$\gamma$ , A, WC, $S_u$ , PF, $D_{50}$	EC = (0.193) × $\gamma^{0.53} × A^{-0.07} × WC^{0.64} × S_u^{0.08} × PF^{-0.47} × D_{50}^{-0.16}$	0.59	0.46	6.09	0.58
128	$D_{50}$ , $\gamma$ , WC, $S_u$ , A	EC = (0.0237) × $D_{50}^{-0.11} × \gamma^{0.65} × WC^{0.59} × S_u^{0.08} × A^{-0.06}$	0.56	0.48	8.23	0.53
132	A, WC, $S_u$ , $D_{50}$	EC = (0.1933) × $A^{-0.06} × WC^{0.51} × S_u^{0.09} × D_{50}^{-0.12}$	0.55	0.49	7.99	0.53

**Figure 242.** Plot of POU versus correction factor for Group 132 (power): EC in the EFA/Fine data set.

## 248 Relationship Between Erodibility and Properties of Soils

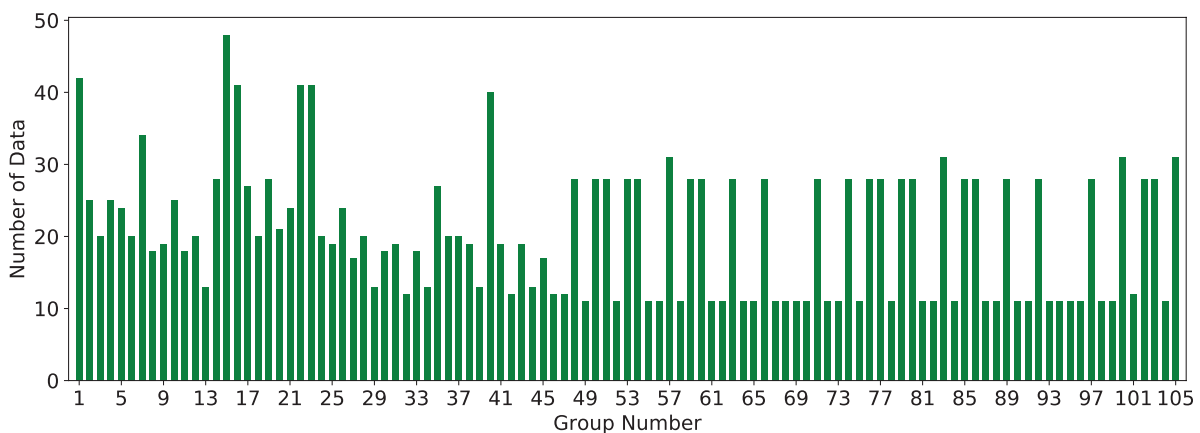


**Figure 243.** Number of data points in each of 105 combination groups for the EFA/Coarse data set: EC.

versus  $\theta$  for this model. The vertical axis in Figure 242 shows the probability that, when the selected model is used, the predicted EC will be smaller than the actual EC, in percentage. To reach 90% confidence that the predicted EC is smaller than the actual EC, the predicted value should be multiplied by 0.75.

The same procedure was conducted with the EFA/Coarse data set, and the best models were selected for the EC. Figure 243 shows the number of data points in each of the 105 combination groups in the EFA/Coarse data set. Figure 244 and Figure 245 show the results for  $R^2$  for each combination group for the linear and power models, respectively.

Both the linear and power models showed some good groups in terms of  $R^2$  values; however, as shown in Figure 243, the number of data points was very low in many combination groups.

After passing through Filters 1 and 2 ( $R^2$  and MSE), the linear models associated with Groups 42, 46, 47, 55, 61, 64, 67, 68, 70, 72, 73, 87, 90, 94, 98, and 99 were selected for further analysis. Power models associated with Groups 32, 42, 46, 47, 65, 69, 91, and 95 were also selected for further analysis.

Filter 3,  $F$ -value/ $F$ -stat, was determined for each group mentioned above. Table 74 shows the results of the selected linear models after the requirements of the first three filters ( $R^2$ , MSE, and  $F$ -value/ $F$ -stat) were met. Table 75 shows the results of the selected power models after the

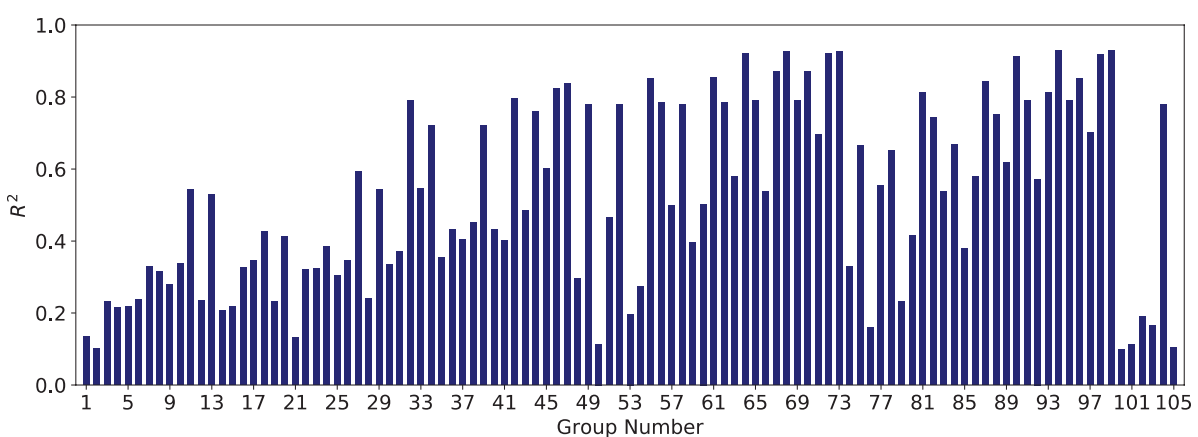


**Figure 244.**  $R^2$  results for the linear models in EFA/Coarse data set: EC.

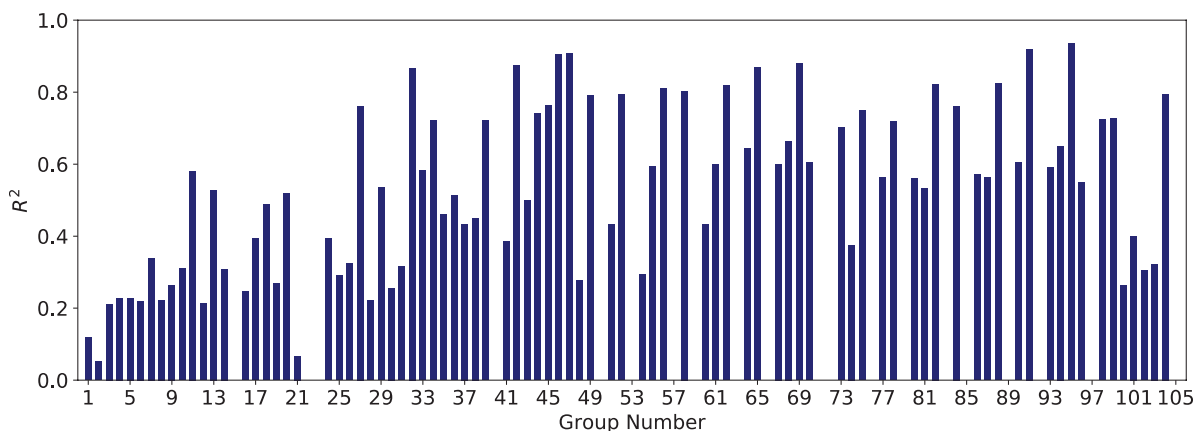


Figure 245.  $R^2$  results for the power models in EFA/Coarse data set: EC.

Table 74. Selected linear models for erosion category in the EFA/Coarse data set.

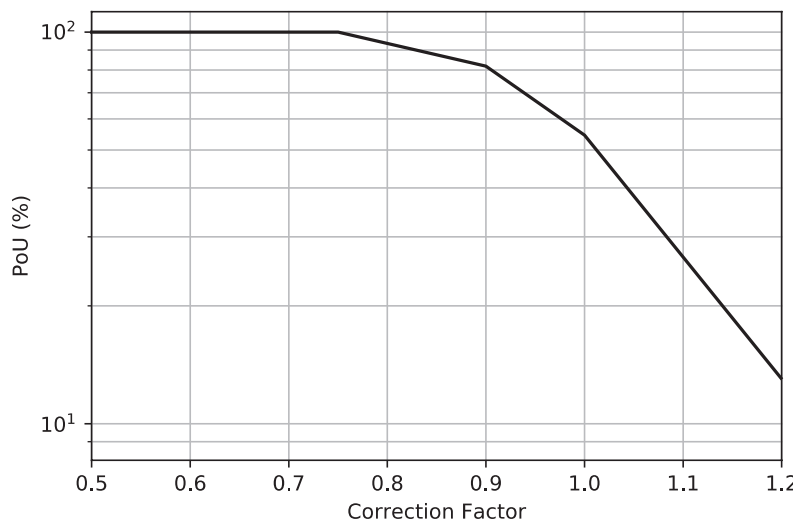
Group No.	Independent Variable	Model Expression	$R^2$	MSE	F-value/F-stat	Cross-Validation Score
42	PI, $\gamma$ , WC, VST, $D_{50}$	$EC = 0.02 \times PI - 0.03 \times \gamma - 0.02 \times WC + 0.0027 \times VST - 5.586 \times D_{50} + 3.917$	0.80	0.27	0.93	0.08
46	PI, WC, VST, PF, $D_{50}$	$EC = 0.017 \times PI - 0.01 \times WC + 0.0049 \times VST - 0.023 \times PF - 7.27 \times D_{50} + 4.01$	0.82	0.25	1.11	-0.5
47	PI, $\gamma$ , WC, VST, PF, $D_{50}$	$EC = 0.014 \times PI - 0.05 \times \gamma - 0.01 \times WC + 0.006 \times VST - 0.027 \times PF - 7.36 \times D_{50} + 5.231$	0.84	0.24	0.70	-2.12
55	$C_c$ , VST, PF	$EC = -0.01 \times C_c + 0.0094 \times VST + 0.0137 \times PF + 1.105$	0.85	0.24	2.78	0.33
61	$C_c$ , $\gamma$ , VST, PF	$EC = -0.009 \times C_c - 0.02 \times \gamma + 0.0095 \times VST + 0.0145 \times PF + 1.458$	0.85	0.24	1.68	0.01
64	$C_c$ , $\gamma$ , PF, $D_{50}$	$EC = -0.0047 \times C_c - 0.03 \times WC + 0.0031 \times VST + 0.028 \times PF + 1.524$	0.92	0.18	1.59	0.55
67	$C_c$ , VST, PF, $D_{50}$	$EC = -0.015 \times C_c + 0.0092 \times VST + 0.02 \times PF + 2.69 \times D_{50} + 0.534$	0.87	0.23	1.94	-0.16
68	$C_c$ , $\gamma$ , WC, VST, PF	$EC = -0.003 \times C_c - 0.03 \times \gamma - 0.03 \times WC + 0.0032 \times VST + 0.03 \times PF + 1.995$	0.93	0.17	2.00	0.61
70	$C_c$ , $\gamma$ , VST, PF, $D_{50}$	$EC = -0.014 \times C_c - 0.01 \times \gamma + 0.0092 \times VST + 0.021 \times PF + 2.578 \times D_{50} + 0.75$	0.87	0.22	1.07	-0.5
72	$C_c$ , WC, VST, PF, $D_{50}$	$EC = -0.0041 \times C_c - 0.04 \times WC + 0.003 \times VST + 0.028 \times PF - 0.23 \times D_{50} + 1.58$	0.92	0.18	1.85	-0.13
73	$C_c$ , $\gamma$ , WC, VST, PF, $D_{50}$	$EC = -0.0009 \times C_c - 0.03 \times \gamma - 0.04 \times WC + 0.0027 \times VST + 0.029 \times PF - 0.74 \times D_{50} + 2.24$	0.93	0.17	0.94	0.14
87	$C_c$ , $\gamma$ , VST, PF	$EC = -0.001 \times C_u - 0.07 \times \gamma + 0.01 \times VST + 0.02 \times PF + 2.2$	0.84	0.25	1.56	-0.76
90	$C_c$ , WC, VST, PF	$EC = -0.0001 \times C_u - 0.04 \times WC + 0.0015 \times VST + 0.032 \times PF + 1.55$	0.91	0.18	3.04	0.27
94	$C_c$ , $\gamma$ , WC, VST, PF	$EC = -0.0005 \times C_u - 0.047 \times \gamma - 0.036 \times WC + 0.004 \times VST + 0.032 \times PF + 2.338$	0.93	0.17	2.10	0.35
98	$C_c$ , WC, VST, PF, $D_{50}$	$EC = 0.00006 \times C_u - 0.04 \times WC + 0.002 \times VST + 0.029 \times PF - 1.2 \times D_{50} + 1.85$	0.92	0.18	1.79	0.14
99	$C_c$ , $\gamma$ , WC, VST, PF, $D_{50}$	$EC = -0.0004 \times C_u - 0.044 \times \gamma - 0.036 \times WC + 0.003 \times VST + 0.031 \times PF - 0.32 \times D_{50} + 2.37$	0.93	0.17	0.98	-1.55

## 250 Relationship Between Erodibility and Properties of Soils

**Table 75.** Selected power models for erosion category in the EFA/Coarse data set.

Group No.	Independent Variable	Model Expression	R <sup>2</sup>	MSE	F-value/F-stat	Cross-Validation Score
32	PI, WC, VST, D <sub>50</sub>	EC = (0.722) × PI <sup>0.21</sup> × WC <sup>-0.16</sup> × VST <sup>0.05</sup> × D <sub>50</sub> <sup>-0.5</sup> for 0.074 < D <sub>50</sub> < 0.3	0.87	0.22	40.8	0.49
42	PI, γ, WC, VST, D <sub>50</sub>	EC = (0.1685) × PI <sup>0.24</sup> × γ <sup>0.42</sup> × WC <sup>-0.13</sup> × VST <sup>0.05</sup> × D <sub>50</sub> <sup>-0.53</sup> for 0.074 < D <sub>50</sub> < 0.3	0.87	0.21	27.5	0.54
46	PI, WC, VST, PF, D <sub>50</sub>	EC = (1.055) × PI <sup>0.15</sup> × WC <sup>-0.04</sup> × VST <sup>0.17</sup> × PF <sup>-0.36</sup> × D <sub>50</sub> <sup>0.61</sup> for 0.074 < D <sub>50</sub> < 0.3	0.90	0.19	36.2	0.22
47	PI, γ, WC, VST, PF, D <sub>50</sub>	EC = (0.44) × PI <sup>0.17</sup> × γ <sup>0.26</sup> × WC <sup>-0.04</sup> × VST <sup>0.16</sup> × PF <sup>-0.34</sup> × D <sub>50</sub> <sup>-0.62</sup> for 0.074 < D <sub>50</sub> < 0.3	0.91	0.18	21.8	-0.16
65	C <sub>c</sub> , WC, VST, D <sub>50</sub>	EC = (0.7423) × C <sub>c</sub> <sup>0.03</sup> × WC <sup>-0.25</sup> × VST <sup>0.21</sup> × D <sub>50</sub> <sup>-0.41</sup> for 0.074 < D <sub>50</sub> < 0.3	0.87	0.23	18.1	0.65
69	C <sub>c</sub> , γ, WC, VST, D <sub>50</sub>	EC = (2.22) × C <sub>c</sub> <sup>0.04</sup> × γ <sup>-0.41</sup> × WC <sup>-0.24</sup> × VST <sup>0.24</sup> × D <sub>50</sub> <sup>0.4</sup>	0.88	0.22	11.3	-0.08
91	C <sub>u</sub> , WC, VST, D <sub>50</sub>	EC = (1.12) × C <sub>u</sub> <sup>0.1</sup> × WC <sup>-0.28</sup> × VST <sup>0.02</sup> × D <sub>50</sub> <sup>-0.44</sup> for 0.074 < D <sub>50</sub> < 0.3	0.92	0.18	29.9	0.80
95	C <sub>u</sub> , γ, WC, VST, D <sub>50</sub>	EC = (0.222) × C <sub>u</sub> <sup>0.17</sup> × γ <sup>0.72</sup> × WC <sup>-0.36</sup> × VST <sup>-0.17</sup> × D <sub>50</sub> <sup>-0.54</sup> for 0.074 < D <sub>50</sub> < 0.3	0.94	0.16	21.2	0.79

requirements of the first three filters were met. The Group 91 correlation equation in power form was selected as the most promising equation. Figure 246 shows the plot of POU versus θ for this model. The vertical axis in Figure 246 shows the probability that, when the selected model is used, the predicted EC will be smaller than the actual EC, in percentage. To reach 90% confidence that the predicted EC is smaller than the actual EC, the predicted value should be multiplied by 0.84. It is also noteworthy that the equation associated with Group 91 is the best one to use for soils with D<sub>50</sub> ranging between 0.074 and 0.3 mm.

**Figure 246.** Plot of POU versus correction factor for Group 91 (power): EC in the EFA/Coarse data set.

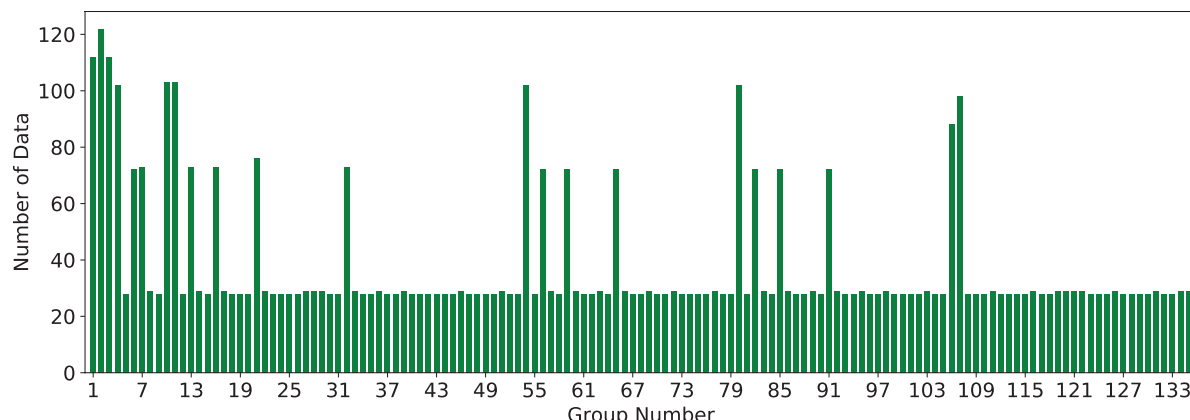


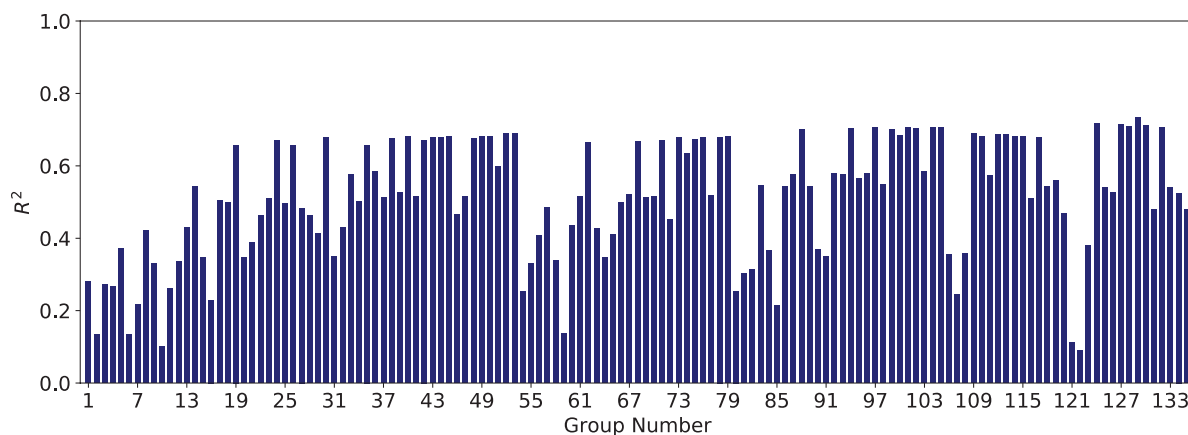
**Figure 247.** Number of data points in each of 135 combination groups for the JET/Global data set: EC.

**JET Data Set.** A similar approach was taken to select the best correlation equation for EC in the JET database. In the JET database, there are two important observations:

1. The JET was performed primarily on the finer soils ( $D_{50} < 0.3$  mm), and, therefore, the number of data points in the JET/Coarse data set is substantially low compared with the JET/Fine data set. In fact, many combination groups in the JET/Coarse database have zero data points.
2. The  $R^2$  values for the JET/Global data set ( $D_{50} < 0.3$  mm) are significantly better than those for the JET/Coarse and JET/Fine data sets. Therefore, the regression results for the JET/Global data set are presented as the best models.

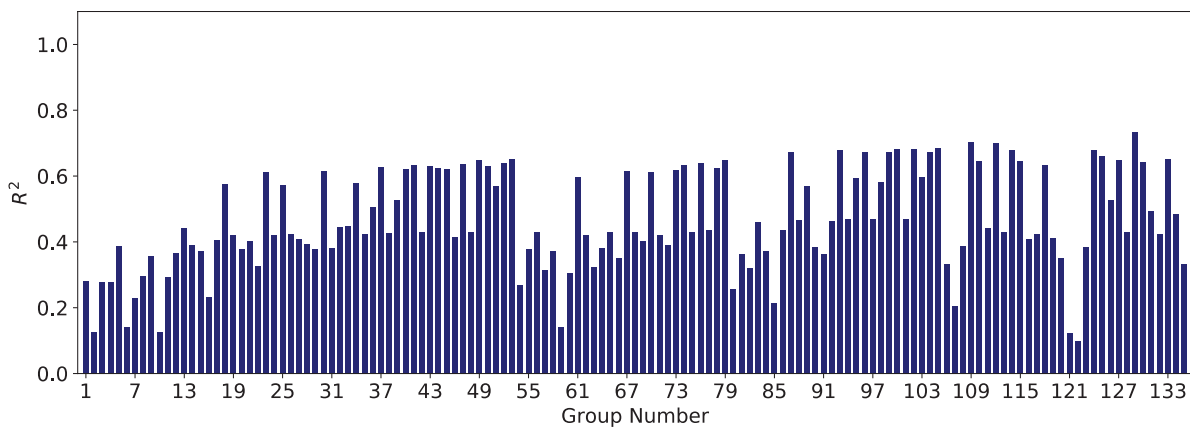
Figure 247 shows the number of data points in each of the 135 combination groups in the JET/Global data set. Figure 248 and Figure 249 show the results for  $R^2$  for each combination group for the linear and power models, respectively. Both the linear and power models show some reasonable groups in terms of  $R^2$  values.

After passing through Filters 1 and 2 ( $R^2$  and MSE), linear models associated with Groups 30, 40, 49, 50, 52, 53, 88, 94, 97, 104, 124, and 129 were selected for further analysis. Power models associated with Groups 87, 93, 100, 102, 109, 112, and 129 were also selected for further analysis.



**Figure 248.**  $R^2$  results for the linear models in JET/Global data set: EC.

## 252 Relationship Between Erodibility and Properties of Soils

**Figure 249.** R<sup>2</sup> results for the power models in JET/Global data set: EC.

Filter 3, F-value/F-stat, was determined for each group mentioned above. Table 76 shows the results of the selected linear models after the requirements of the first three filters ( $R^2$ , MSE, and F-value/F-stat) were met. As shown in Table 76, almost all of the selected models performed satisfactorily in the cross-validation test. Table 77 shows the results of the selected power models after the requirements of the first three filters were met. The best models that also had a good cross-validation score are shaded and highlighted in blue in Tables 76 and 77. Out of all of the highlighted correlation equations in Table 76 and Table 77, the Group 88 correlation equation in

**Table 76.** Selected linear models for erosion category in the JET/Global data set.

Group No.	Independent Variable	Model Expression	R <sup>2</sup>	MSE	F-value/F-stat	Cross-Validation Score
30	PF, $S_u$ , $D_{50}$	EC = -0.007 × PF + 0.003 × $S_u$ - 6.48 × $D_{50}$ + 3.5	0.68	0.26	5.58	0.58
40	PI, $S_u$ , PF, $D_{50}$	EC = 0.003 × PI + 0.0029 × $S_u$ - 0.009 × PF - 6.73 × $D_{50}$ + 3.6	0.68	0.26	4.39	0.58
49	$\gamma$ , WC, $S_u$ , PF, $D_{50}$	EC = -0.019 × $\gamma$ - 0.01 × WC + 0.003 × $S_u$ - 0.006 × PF - 6.37 × $D_{50}$ + 3.95	0.68	0.26	3.52	0.28
50	PI, $\gamma$ , $S_u$ , PF, $D_{50}$	EC = 0.003 × PI - 0.0004 × $\gamma$ + 0.003 × $S_u$ - 0.009 × $S_u$ - 6.73 × $D_{50}$ + 3.61	0.68	0.26	3.54	0.47
52	PI, WC, $S_u$ , PF, $D_{50}$	EC = 0.006 × PI - 0.013 × WC + 0.002 × $S_u$ - 0.007 × PF - 6.65 × $D_{50}$ + 3.72	0.69	0.25	3.55	0.52
53	PI, $\gamma$ , WC, $S_u$ , PF, $D_{50}$	EC = 0.006 × PI - 0.01 × $\gamma$ - 0.013 × WC + 0.002 × $S_u$ - 0.007 × PF - 6.37 × $D_{50}$ + 3.83	0.69	0.25	3.00	0.42
88	PL, $S_u$ , $D_{50}$	EC = -0.022 × PL + 0.0031 × $S_u$ - 5.5 × $D_{50}$ + 3.34	0.70	0.25	6.23	0.58
94	PL, $\gamma$ , $S_u$ , $D_{50}$	EC = -0.023 × PL - 0.01 × $\gamma$ + 0.003 × $S_u$ - 5.4 × $D_{50}$ + 3.64	0.70	0.25	4.96	0.33
97	PL, WC, $S_u$ , $D_{50}$	EC = -0.029 × PL + 0.009 × WC + 0.0037 × $S_u$ - 5.25 × $D_{50}$ + 3.23	0.71	0.25	5.11	0.58
104	PL, WC, $S_u$ , PF, $D_{50}$	EC = -0.027 × PL + 0.011 × WC + 0.0038 × $S_u$ - 0.002 × PF - 5.74 × $D_{50}$ + 3.35	0.71	0.24	5.13	0.24
124	$\gamma$ , A, WC, $S_u$ , PF, $D_{50}$	EC = -0.017 × $\gamma$ + 0.2 × A - 0.008 × WC + 0.003 × $S_u$ - 0.005 × PF - 6.54 × $D_{50}$ + 3.75	0.72	0.24	3.96	0.47
129	LL, $\gamma$ , A, $S_u$ , PF	EC = -0.013 × LL - 0.05 × $\gamma$ + 0.31 × A + 0.0054 × $S_u$ + 0.018 × PF + 2.6	0.73	0.23	5.03	0.20

**Table 77.** Selected power models for erosion category in the JET/Global data set.

Group No.	Independent Variable	Model Expression	R <sup>2</sup>	MSE	F-value/F-stat	Cross-Validation Score
87	PL, S <sub>u</sub> , PF	EC = (0.8) × PL <sup>-0.25</sup> × S <sub>u</sub> <sup>0.09</sup> × PF <sup>0.38</sup>	0.67	0.26	286.6	0.40
93	PL, γ, S <sub>u</sub> , PF	EC = (1.639) × PL <sup>-0.26</sup> × γ <sup>-0.22</sup> × S <sub>u</sub> <sup>0.1</sup> × PF <sup>0.37</sup>	0.68	0.26	235.2	0.05
100	PL, γ, WC, S <sub>u</sub> , PF	EC = (2.33) × PL <sup>-0.23</sup> × γ <sup>-0.32</sup> × WC <sup>-0.06</sup> × S <sub>u</sub> <sup>0.09</sup> × PF <sup>0.38</sup>	0.68	0.26	195.7	0.10
102	PL, γ, S <sub>u</sub> , PF, D <sub>50</sub>	EC = (1.644) × PL <sup>-0.23</sup> × γ <sup>-0.29</sup> × S <sub>u</sub> <sup>0.11</sup> × PF <sup>0.4</sup> × D <sub>50</sub> <sup>0.02</sup>	0.68	0.26	196.3	0.05
109	PC, γ, WC, S <sub>u</sub> , PF, D <sub>50</sub>	EC = (4.345) × PC <sup>-0.13</sup> × γ <sup>-0.79</sup> × WC <sup>-0.05</sup> × S <sub>u</sub> <sup>0.13</sup> × PF <sup>0.52</sup> × D <sub>50</sub> <sup>0.04</sup>	0.70	0.25	163.8	0.14
112	PC, γ, S <sub>u</sub> , PF, D <sub>50</sub>	EC = (3.282) × PC <sup>-0.14</sup> × γ <sup>-0.75</sup> × S <sub>u</sub> <sup>0.14</sup> × PF <sup>0.52</sup> × D <sub>50</sub> <sup>0.05</sup>	0.70	0.25	165.7	0.17
129	LL, γ, A, S <sub>u</sub> , PF	EC = (4.35) × LL <sup>-0.34</sup> × γ <sup>-0.61</sup> × A <sup>0.14</sup> × S <sub>u</sub> <sup>0.13</sup> × PF <sup>0.51</sup>	0.73	0.23	190.4	0.25

linear form was selected as the most promising equation. Figure 250 shows the plot of POU versus θ for this model. The vertical axis in Figure 250 represents the probability that, when the selected model is used, the predicted EC will be smaller than the actual EC, in percentage. To reach 90% confidence that the predicted EC is smaller than the actual EC, the predicted value should be multiplied by 0.85. The proposed equations are best for soils with D<sub>50</sub> smaller than 0.3 mm.

**HET Database.** Although the number of data points in the HET/Coarse combination groups was very low in most cases, it was observed that dividing the HET/Global data set into the HET/Fine and the HET/Coarse data sets would improve the regression results. Figure 251 shows the number of data points in each of the 135 combination groups in the HET/Fine data set. Figure 252 and Figure 253 show the results for R<sup>2</sup> for each combination group for the linear and power models, respectively.

The R<sup>2</sup> values for both the linear and power models were not very high (up to 0.7). Figure 254 and Figure 255 show the MSE results for each of the 135 combination groups in the HET/Fine data set for the linear and power models, respectively. In general, the power and linear models were not noticeably different.

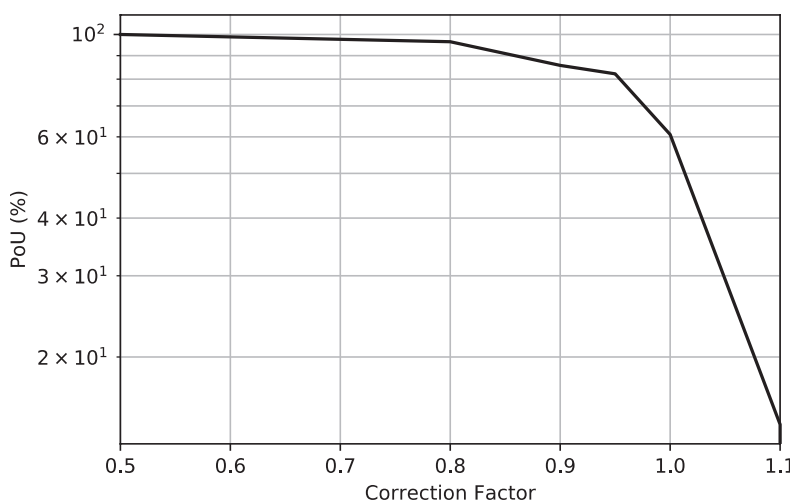


**Figure 250.** Plot of POU versus correction factor for Group 88 (linear): EC in the JET/Global data set.

## 254 Relationship Between Erodibility and Properties of Soils

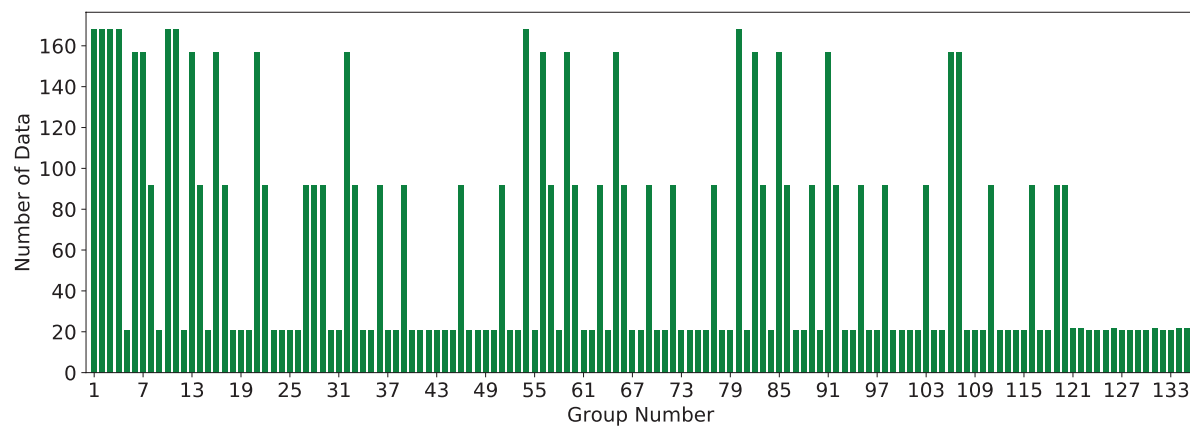


Figure 251. Number of data points in each of 135 combination groups for the HET/Fine data set: EC.

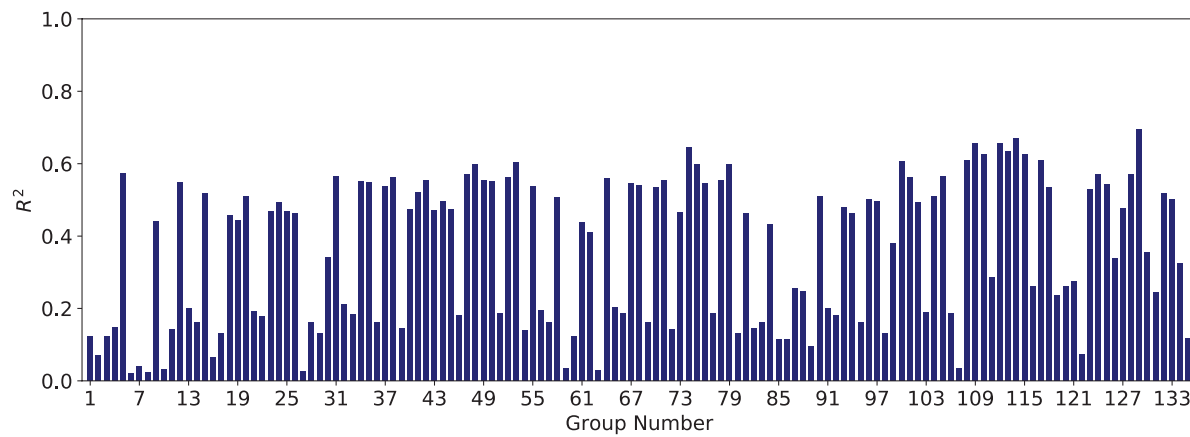


Figure 252.  $R^2$  results for the linear models in HET/Fine data set: EC.

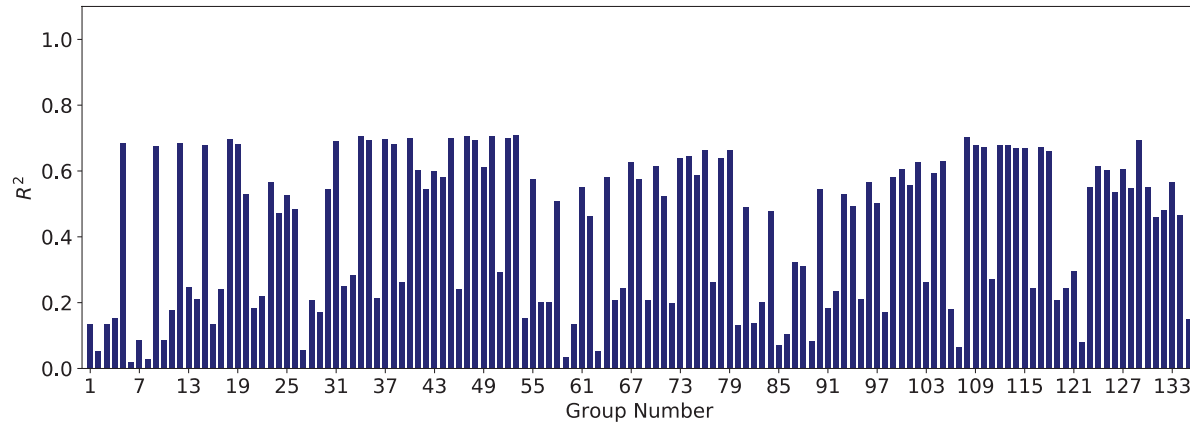
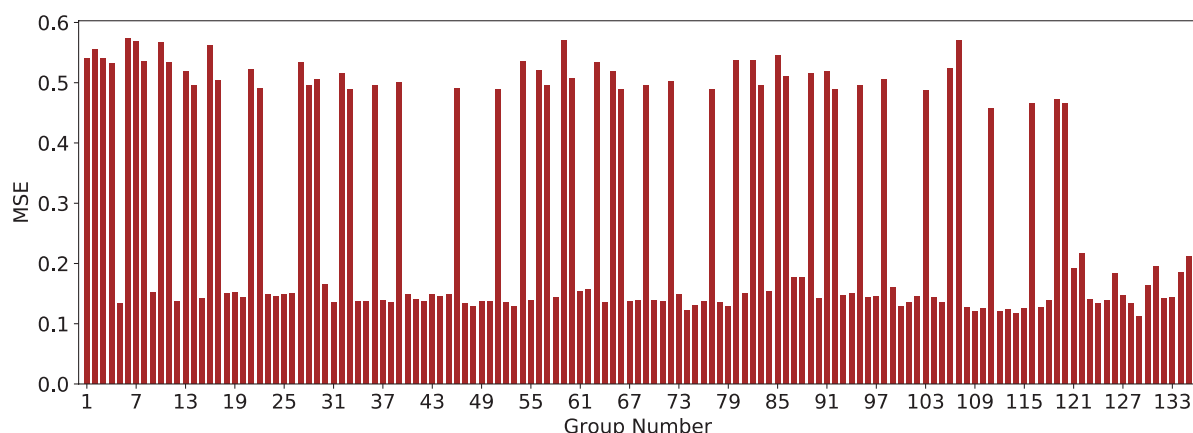


Figure 253.  $R^2$  results for the power models in HET/Fine data set: EC.



**Figure 254.** MSE results for the linear models in HET/Fine data set: EC.

After passing through Filters 1 and 2 ( $R^2$  and MSE), the linear models associated with Groups 48, 53, 74, 79, 100, 109, 112, 114, and 129 were selected for further analysis. Power models associated with Groups 5, 12, 18, 19, 31, 34, 35, 37, 40, 47, 50, 52, 53, 108, 109, 112, 113, and 129 were also selected for further analysis.

Filter 3,  $F$ -value/ $F$ -stat, was determined for each group mentioned above. Table 78 shows the results of the selected linear models after the requirements of the first three filters ( $R^2$ , MSE, and  $F$ -value/ $F$ -stat) were met. Table 79 shows the results of the selected power models after the requirements of the first three filters were met. The best models that also had a good cross-validation score are shaded and highlighted in blue in Tables 78 and 79. The Group 12 correlation equation in power form was selected as the most promising equation. Figure 256 shows the plot of POU versus  $\theta$  for this model. The vertical axis in Figure 256 represents the probability that, when the selected model is used, the predicted EC will be smaller than the actual EC, in percentage. To reach 100% confidence that the predicted EC is smaller than the actual EC, the predicted value should be multiplied by 0.95.

The same procedure was conducted with the HET/Coarse data set, and the best models were selected for EC. Figure 257 shows the number of data points in each of the 105 combination groups in the EFA/Coarse data set. Figure 258 and Figure 259 show the results for  $R^2$  for each combination group for the linear and power models, respectively.

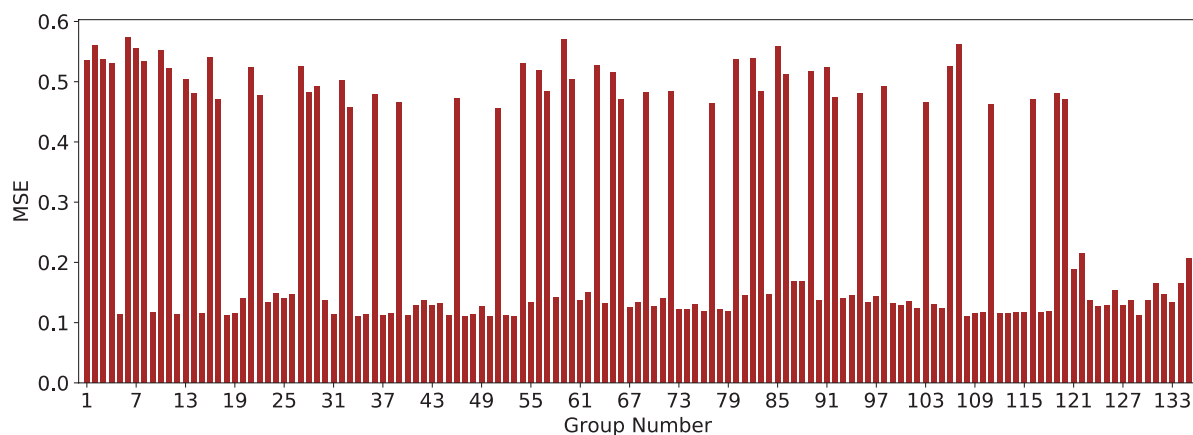


**Figure 255.** MSE results for the power models in HET/Fine data set: EC.

## 256 Relationship Between Erodibility and Properties of Soils

**Table 78.** Selected linear models for erosion category in the HET/Fine data set.

Group No.	Independent Variable	Model Expression	R <sup>2</sup>	MSE	F-value/ F-stat	Cross-Validation Score
48	PI, γ, WC, S <sub>u</sub> , D <sub>50</sub>	EC = 0.002 × PI + 0.05 × γ + 0.02 × WC + 0.004 × S <sub>u</sub> + 5.43 × D <sub>50</sub> + 1.59	0.60	0.13	1.548	-0.18
53	PI, γ, WC, S <sub>u</sub> , PF, D <sub>50</sub>	EC = 0.002 × PI + 0.05 × γ + 0.03 × WC + 0.0037 × S <sub>u</sub> + 0.001 × PF + 6.82 × D <sub>50</sub> + 1.36	0.60	0.13	1.242	-0.39
74	LL, γ, WC, S <sub>u</sub> , PF	EC = 0.002 × LL + 0.05 × γ + 0.01 × WC + 0.0029 × S <sub>u</sub> - 0.002 × PF + 2.05	0.64	0.12	2.097	-0.50
79	LL, γ, WC, S <sub>u</sub> , PF, D <sub>50</sub>	EC = 0.002 × LL + 0.051 × γ + 0.03 × WC + 0.0037 × S <sub>u</sub> + 0.0007 × PF + 6.48 × D <sub>50</sub> + 1.36	0.60	0.13	1.220	-0.52
100	PL, γ, WC, S <sub>u</sub> , PF	EC = 0.012 × PL + 0.05 × γ + 0.02 × WC + 0.0033 × S <sub>u</sub> - 0.0045 × PF + 1.82	0.61	0.13	1.929	0.12
109	PC, γ, WC, S <sub>u</sub> , PF, D <sub>50</sub>	EC = 0.014 × PC + 0.044 × γ - 0.0015 × WC + 0.002 × S <sub>u</sub> + 0.0038 × PF + 13.1 × D <sub>50</sub> + 1.46	0.66	0.12	2.416	0.25
112	PC, γ, S <sub>u</sub> , PF, D <sub>50</sub>	EC = 0.014 × PC + 0.04 × γ + 0.0021 × S <sub>u</sub> + 0.0038 × PF + 13.17 × D <sub>50</sub> + 1.44	0.66	0.12	3.018	0.32
114	PC, γ, WC, S <sub>u</sub> , PF	EC = 0.008 × PC + 0.04 × γ - 0.01 × WC + 0.0015 × S <sub>u</sub> - 0.0016 × PF + 2.44	0.67	0.12	2.052	0.09
129	LL, γ, A, S <sub>u</sub> , PF	EC = 0.003 × LL + 0.05 × γ - 0.04 × A + 0.0021 × S <sub>u</sub> - 0.0014 × PF + 2.17	0.69	0.11	1.623	-0.42

**Table 79.** Selected power models for erosion category in the HET/Fine data set.

Group No.	Independent Variable	Model Expression	R <sup>2</sup>	MSE	F-value/ F-stat	Cross-Validation Score
5	LL, PL, γ, WC, S <sub>u</sub>	EC = (1.87) × LL <sup>0.08</sup> × PL <sup>-0.12</sup> × γ <sup>0.16</sup> × WC <sup>-0.005</sup> × S <sub>u</sub> <sup>0.03</sup>	0.69	0.12	796.3	0.26
12	PI, γ, S <sub>u</sub>	EC = (1.67) × PI <sup>0.04</sup> × γ <sup>0.15</sup> × S <sub>u</sub> <sup>0.03</sup>	0.70	0.11	1,172.2	0.54
18	PI, S <sub>u</sub> , PF	EC = (3.23) × PI <sup>0.05</sup> × S <sub>u</sub> <sup>0.03</sup> × PF <sup>-0.06</sup>	0.70	0.11	1,172.3	0.57
19	PI, S <sub>u</sub> , D <sub>50</sub>	EC = (2.57) × PI <sup>0.05</sup> × S <sub>u</sub> <sup>0.03</sup> × D <sub>50</sub> <sup>0.01</sup>	0.68	0.12	917.4	0.54
31	PI, γ, WC, S <sub>u</sub>	EC = (1.74) × PI <sup>0.05</sup> × γ <sup>0.17</sup> × WC <sup>-0.03</sup> × S <sub>u</sub> <sup>0.03</sup>	0.69	0.11	911.5	0.38
34	PI, γ, S <sub>u</sub> , PF	EC = (2.221) × PI <sup>0.04</sup> × γ <sup>0.13</sup> × S <sub>u</sub> <sup>0.03</sup> × PF <sup>-0.06</sup>	0.71	0.11	968.3	0.40
35	PI, γ, S <sub>u</sub> , D <sub>50</sub>	EC = (1.68) × PI <sup>0.05</sup> × γ <sup>0.15</sup> × S <sub>u</sub> <sup>0.03</sup> × D <sub>50</sub> <sup>0.01</sup>	0.69	0.11	968.6	0.24
37	PI, WC, S <sub>u</sub> , PF	EC = (3.221) × PI <sup>0.05</sup> × WC <sup>0.0016</sup> × S <sub>u</sub> <sup>0.035</sup> × PF <sup>-0.06</sup>	0.70	0.11	963.5	0.39
40	PI, S <sub>u</sub> , PF, D <sub>50</sub>	EC = (3.47) × PI <sup>0.04</sup> × S <sub>u</sub> <sup>0.03</sup> × PF <sup>-0.08</sup> × D <sub>50</sub> <sup>0.01</sup>	0.70	0.11	963.5	0.33
47	PI, γ, WC, S <sub>u</sub> , PF	EC = (2.211) × PI <sup>0.04</sup> × γ <sup>0.13</sup> × WC <sup>-0.01</sup> × S <sub>u</sub> <sup>0.03</sup> × PF <sup>-0.05</sup>	0.71	0.11	781.6	0.24
50	PI, γ, S <sub>u</sub> , PF, D <sub>50</sub>	EC = (2.4) × PI <sup>0.04</sup> × γ <sup>0.12</sup> × S <sub>u</sub> <sup>0.03</sup> × PF <sup>-0.07</sup> × D <sub>50</sub> <sup>-0.01</sup>	0.71	0.11	780.2	0.15
52	PI, WC, S <sub>u</sub> , PF, D <sub>50</sub>	EC = (3.708) × PI <sup>0.04</sup> × WC <sup>-0.02</sup> × S <sub>u</sub> <sup>0.03</sup> × PF <sup>-0.09</sup> × D <sub>50</sub> <sup>-0.01</sup>	0.70	0.11	771.9	-0.26
53	PI, γ, WC, S <sub>u</sub> , PF, D <sub>50</sub>	EC = (2.547) × PI <sup>0.04</sup> × γ <sup>0.13</sup> × WC <sup>-0.03</sup> × S <sub>u</sub> <sup>0.03</sup> × PF <sup>-0.08</sup> × D <sub>50</sub> <sup>-0.01</sup>	0.71	0.11	638.6	-0.11
108	LL, PL, γ, PC, S <sub>u</sub>	EC = (2.064) × LL <sup>0.06</sup> × PL <sup>-0.06</sup> × γ <sup>0.09</sup> × PC <sup>0.02</sup> × S <sub>u</sub> <sup>0.03</sup>	0.70	0.11	622.9	0.32
109	PC, γ, WC, S <sub>u</sub> , PF, D <sub>50</sub>	EC = (1.861) × PC <sup>0.04</sup> × γ <sup>0.12</sup> × WC <sup>0.02</sup> × S <sub>u</sub> <sup>0.04</sup> × PF <sup>-0.0011</sup> × D <sub>50</sub> <sup>0.02</sup>	0.68	0.12	608.8	0.39
112	PC, γ, S <sub>u</sub> , PF, D <sub>50</sub>	EC = (1.919) × PC <sup>0.04</sup> × γ <sup>0.13</sup> × S <sub>u</sub> <sup>0.04</sup> × PF <sup>-0.005</sup> × D <sub>50</sub> <sup>0.02</sup>	0.68	0.12	778.3	0.51
113	PC, γ, WC, S <sub>u</sub> , D <sub>50</sub>	EC = (1.854) × PC <sup>0.04</sup> × γ <sup>0.12</sup> × WC <sup>-0.02</sup> × S <sub>u</sub> <sup>0.04</sup> × D <sub>50</sub> <sup>0.02</sup>	0.68	0.12	778.1	0.44
129	LL, γ, A, S <sub>u</sub> , PF	EC = (2.123) × LL <sup>0.07</sup> × γ <sup>0.15</sup> × A <sup>-0.03</sup> × S <sub>u</sub> <sup>0.04</sup> × PF <sup>-0.09</sup>	0.69	0.11	779.6	0.19

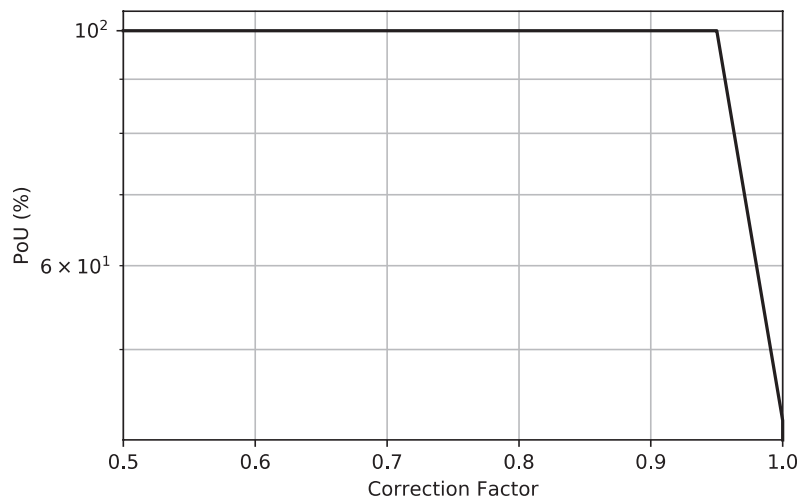


**Figure 256.** Plot of POU versus correction factor for Group 12 (power): EC in the HET/Fine data set.

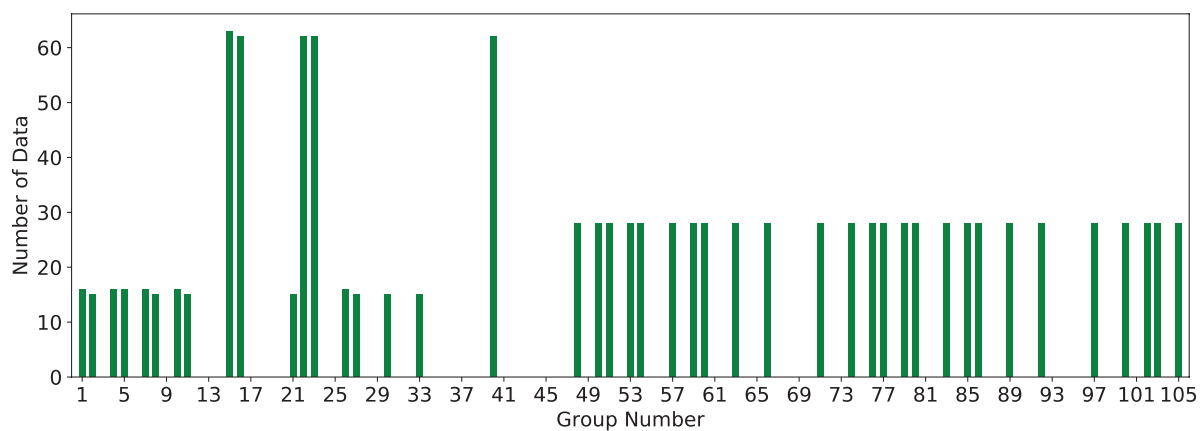


**Figure 257.** Number of data points in each of 105 combination groups for the HET/Coarse data set: EC.

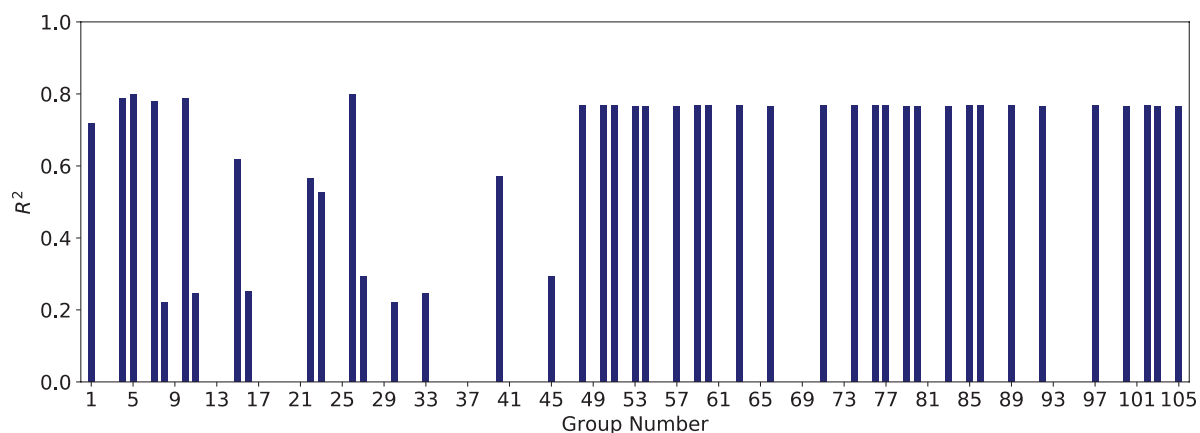


**Figure 258.** R<sup>2</sup> results for the linear models in HET/Coarse data set: EC.

## 258 Relationship Between Erodibility and Properties of Soils

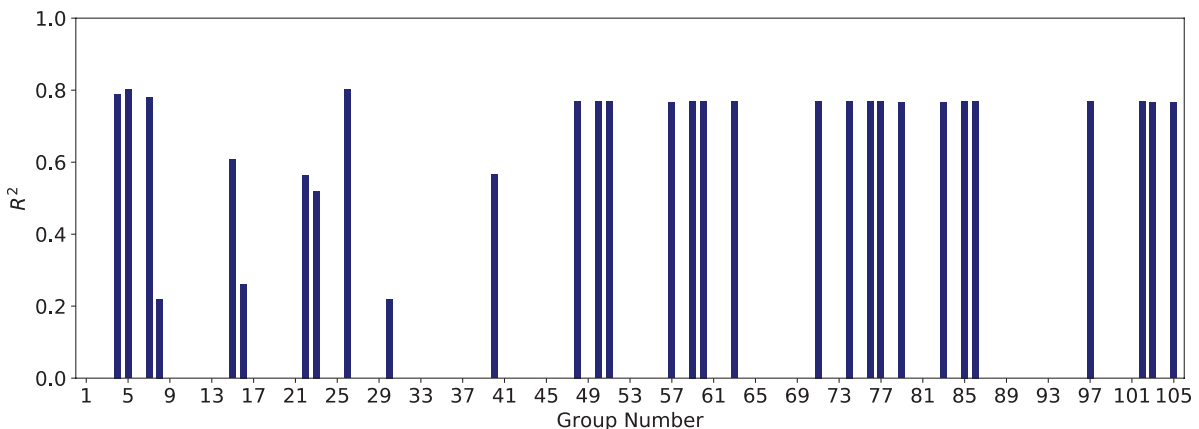


**Figure 259.** *R<sup>2</sup> results for the power models in HET/Coarse data set: EC.*

Both the linear and power models showed some good groups in terms of  $R^2$  values; however, as shown in Figure 257, the number of data points was very low in most combination groups. In fact, close to half of the combination groups did not have any data points.

After passing through Filters 1 and 2 ( $R^2$  and MSE), the linear models associated with Groups 4, 5, 7, 10, 15, 26, 48, 50, 51, 53, 54, 57, 59, 60, 63, 66, 71, 74, 76, 79, 85, 100, 102, and 103 were selected for further analysis. Power models associated with Groups 4, 5, 7, 15, 26, 48, 50, 51, 57, 59, 60, 71, 74, 76, 77, 79, 83, 85, 86, 97, 102, 103, and 105 were also selected for further analysis.

Filter 3, *F*-value/*F*-stat, was determined for each group mentioned above. Table 80 shows the results of the selected linear models after the requirements of the first three filters ( $R^2$ , MSE, and *F*-value/*F*-stat) were met. Table 81 shows the results of the selected power models after the requirements of the first three filters were met. The best models that also had a good cross-validation score are shaded and highlighted in blue in Tables 80 and 81. The Group 48 correlation equation in power form was selected as the most promising equation. Figure 260 shows the plot of POU versus  $\theta$  for this model. The vertical axis in Figure 260 represents the probability that, when the selected model is used, the predicted EC will be smaller than the actual EC, in percentage. To reach 90% confidence that the predicted EC is smaller than the actual EC, the predicted value should be multiplied by 0.85. It is very important to note that the proposed equation associated with Group 48 should be used for soils with  $D_{50}$  ranging from 0.074 to 0.3 mm.

## 7.4 Probabilistic (Bayesian) Analysis

The preceding section focused on selecting the optimal vector of model parameters that maximizes the likelihood of fitting experimental observations. This section introduces a series of Bayesian probabilistic calibrations carried out on a set of regression (empirical) models proposed as optimal to capture only the model's first order statistics (expected or mean behavior). The Bayesian regression analysis introduces a methodology to fully assess both first and second order statistics (expected or mean and variance and covariance, respectively) generated by the same erosion tests presented in the deterministic regression analysis discussed in the previous section. That is, Bayesian regression allows quantification of varying uncertainty scenarios resulting from different sources of evidence (i.e., varying experimental observations, varying model complexity, and varying expert judgment), providing further inferences to better understand the performance of a given regression model. This is achieved by providing a full

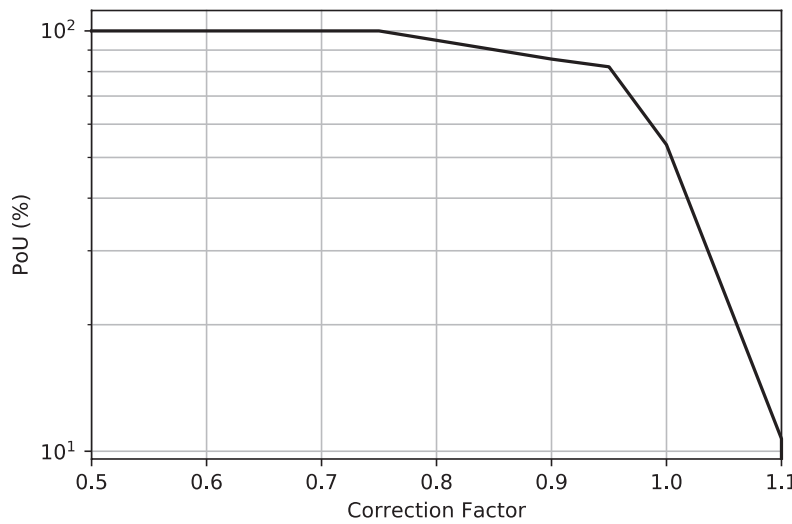
**Table 80.** Selected linear models for erosion category in the HET/Coarse data set.

Group No.	Independent Variable	Model Expression	R <sup>2</sup>	MSE	F-value/F-stat	Cross-Validation Score
4	PI, WC	EC = -0.569 × PI + 0.07 × WC + 11.94	0.79	0.17	6.29	0.04
5	PI, γ, WC	EC = -0.557 × PI + 0.12 × γ + 0.05 × WC + 9.41	0.80	0.16	4.58	0.11
7	PI, γ, PF	EC = -0.014 × PI + 0.21 × γ + 0.09 × PF - 3.6	0.78	0.17	6.29	0.13
10	PI, WC, PF	EC = -0.015 × PI + 0.07 × WC + 0.09 × PF - 1.1	0.79	0.17	4.6	0.04
15	γ, WC, PF	EC = -0.128 × γ + 0.02 × WC + 0.05 × PF + 3.38	0.62	0.25	4.59	0.55
26	PI, γ, WC, PF	EC = -0.014 × PI + 0.12 × γ + 0.05 × WC + 0.09 × PF - 2.78	0.80	0.16	3.11	0.10
48	C <sub>c</sub> , γ, WC	EC = -0.138 × C <sub>c</sub> + 0.05 × γ - 0.0037 × WC + 2.35	0.77	0.17	4.58	0.70
50	C <sub>c</sub> , γ, PF	EC = -0.004 × C <sub>c</sub> + 0.04 × γ + 0.02 × PF + 0.92	0.77	0.17	4.59	0.73
51	C <sub>c</sub> , γ, D <sub>50</sub>	EC = -0.145 × C <sub>c</sub> + 0.04 × γ - 0.0045 × D <sub>50</sub> + 2.5	0.77	0.17	4.59	0.73
53	C <sub>c</sub> , WC, PF	EC = -0.005 × C <sub>c</sub> + 0.004 × WC + 0.04 × PF + 1.55	0.77	0.17	4.56	0.71
54	C <sub>c</sub> , WC, D <sub>50</sub>	EC = -0.177 × C <sub>c</sub> + 0.004 × WC - 0.0055 × D <sub>50</sub> + 3.41	0.77	0.17	4.57	0.71
57	PF, C <sub>c</sub> , D <sub>50</sub>	EC = 0.03 × PF - 0.01 × C <sub>c</sub> - 0.0002 × D <sub>50</sub> + 1.61	0.77	0.17	4.59	0.74
59	C <sub>c</sub> , γ, WC, PF	EC = -0.004 × C <sub>c</sub> + 0.05 × γ - 0.0037 × WC + 0.02 × PF + 0.89	0.77	0.17	3.13	0.69
60	C <sub>c</sub> , γ, WC, D <sub>50</sub>	EC = -0.138 × C <sub>c</sub> + 0.05 × γ - 0.0037 × WC - 0.0043 × D <sub>50</sub> + 2.35	0.78	0.16	3.08	0.69
63	C <sub>c</sub> , γ, PF, D <sub>50</sub>	EC = -0.0044 × C <sub>c</sub> + 0.04 × γ + 0.02 × PF - 0.0001 × D <sub>50</sub> + 0.92	0.77	0.16	3.11	0.73
66	C <sub>c</sub> , WC, PF, D <sub>50</sub>	EC = -0.0054 × C <sub>c</sub> + 0.004 × WC + 0.03 × PF - 0.0002 × D <sub>50</sub> + 1.55	0.76	0.17	3.06	0.71
71	C <sub>c</sub> , γ, WC, PF, D <sub>50</sub>	EC = -0.004 × C <sub>c</sub> + 0.05 × γ - 0.0037 × WC + 0.024 × PF - 0.0001 × D <sub>50</sub> + 0.9	0.77	0.17	2.84	0.69
74	C <sub>u</sub> , γ, WC	EC = 0.003 × C <sub>u</sub> + 0.05 × γ - 0.0037 × WC + 1.3	0.77	0.17	4.58	0.64
76	C <sub>u</sub> , γ, PF	EC = 0.003 × C <sub>u</sub> + 0.04 × γ × 0.0003 × PF + 1.33	0.77	0.17	4.59	0.73
79	C <sub>u</sub> , WC, PF	EC = 0.003 × C <sub>u</sub> + 0.004 × WC + 0.0003 × PF + 2.1	0.77	0.17	4.56	0.71
85	C <sub>u</sub> , γ, WC, PF	EC = 0.003 × C <sub>u</sub> + 0.05 × γ - 0.0037 × WC + 0.0003 × PF + 1.28	0.77	0.16	3.10	0.64
100	C <sub>c</sub> , C <sub>u</sub>	EC = -0.00006 × C <sub>c</sub> + 0.003 × C <sub>u</sub> + 2.11	0.76	0.16	6.3	0.68
102	C <sub>c</sub> , C <sub>u</sub> , γ	EC = -0.00005 × C <sub>c</sub> + 0.003 × C <sub>u</sub> + 0.04 × γ + 1.34	0.77	0.16	4.45	0.67
103	C <sub>c</sub> , C <sub>u</sub> , WC	EC = -0.0006 × C <sub>c</sub> + 0.003 × C <sub>u</sub> + 0.004 × WC + 2.1	0.76	0.17	4.40	0.66

## 260 Relationship Between Erodibility and Properties of Soils

**Table 81.** Selected power models for erosion category in the HET/Coarse data set.

Group No.	Independent Variable	Model Expression	R <sup>2</sup>	MSE	F-value/F-stat	Cross-Validation Score
4	PI, WC	EC = (1675.1) × PI <sup>-2.62</sup> × WC <sup>0.4</sup>	0.79	0.17	419.5	0.51
5	PI, γ, WC	EC = (151.5) × PI <sup>-2.42</sup> × γ <sup>0.74</sup> × WC <sup>0.27</sup>	0.80	0.16	329.3	-0.10
7	PI, γ, PF	EC = (7.31) × PI <sup>-1.92</sup> × γ <sup>1.32</sup> × PF <sup>0.19</sup>	0.78	0.17	330.1	-0.20
15	γ, WC, PF	EC = (3.47) × γ <sup>-0.84</sup> × WC <sup>0.07</sup> × PF <sup>0.61</sup>	0.61	0.26	321.8	0.51
26	PI, γ, WC, PF	EC = (1.848) × PI <sup>-1.39</sup> × γ <sup>0.74</sup> × WC <sup>0.27</sup> × PF <sup>0.42</sup>	0.80	0.16	294.5	-1.19
48	C <sub>c</sub> , γ, WC	EC = (1.045) × C <sub>c</sub> <sup>-0.25</sup> × γ <sup>0.45</sup> × WC <sup>-0.04</sup>	0.77	0.17	328.6	0.78
50	C <sub>c</sub> , γ, PF	EC = (27.15) × C <sub>c</sub> <sup>-0.84</sup> × γ <sup>0.34</sup> × PF <sup>-0.61</sup>	0.77	0.17	328.6	0.75
51	C <sub>c</sub> , γ, D <sub>50</sub>	EC = (1.23) × C <sub>c</sub> <sup>-0.25</sup> × γ <sup>0.34</sup> × D <sub>50</sub> <sup>-0.04</sup>	0.77	0.17	328.8	-22.7
57	PF, C <sub>c</sub> , D <sub>50</sub>	EC = (0.272) × PF <sup>0.65</sup> × C <sub>c</sub> <sup>0.14</sup> × D <sub>50</sub> <sup>0.13</sup>	0.76	0.17	323.5	0.65
59	C <sub>c</sub> , γ, WC, PF	EC = (5.834) × C <sub>c</sub> <sup>-0.57</sup> × γ <sup>0.45</sup> × WC <sup>-0.04</sup> × PF <sup>-0.35</sup>	0.77	0.16	291.5	0.67
60	C <sub>c</sub> , γ, WC, D <sub>50</sub>	EC = (1.16) × LL <sup>-0.28</sup> × γ <sup>0.45</sup> × WC <sup>-0.04</sup> × D <sub>50</sub> <sup>0.03</sup>	0.77	0.17	292.6	-18.62
71	C <sub>c</sub> , γ, WC, PF, D <sub>50</sub>	EC = (0.06) × C <sub>c</sub> <sup>0.09</sup> × γ <sup>0.45</sup> × WC <sup>-0.04</sup> × PF <sup>1.01</sup> × D <sub>50</sub> <sup>0.67</sup>	0.77	0.17	266.4	0.12
74	C <sub>u</sub> , γ, WC	EC = (0.45) × C <sub>u</sub> <sup>0.1</sup> × γ <sup>0.45</sup> × WC <sup>-0.04</sup>	0.77	0.17	329.5	0.66
76	C <sub>u</sub> , γ, PF	EC = (0.98) × C <sub>u</sub> <sup>0.23</sup> × γ <sup>0.34</sup> × PF <sup>-0.33</sup>	0.77	0.17	328.3	0.55
77	C <sub>u</sub> , γ, D <sub>50</sub>	EC = (0.02) × C <sub>u</sub> <sup>-6.07</sup> × γ <sup>0.34</sup> × D <sub>50</sub> <sup>18.16</sup>	0.77	0.17	330.1	0.62
79	C <sub>u</sub> , WC, PF	EC = (34.54) × C <sub>u</sub> <sup>0.78</sup> × WC <sup>-0.004</sup> × PF <sup>-1.8</sup>	0.76	0.17	330.1	0.54
83	PF, C <sub>u</sub> , D <sub>50</sub>	EC = (0.21) × PF <sup>1.87</sup> × C <sub>u</sub> <sup>2.11</sup> × D <sub>50</sub> <sup>7.77</sup>	0.76	0.17	326.6	-8.3
85	C <sub>u</sub> , γ, WC, PF	EC = (9.902) × C <sub>u</sub> <sup>0.72</sup> × γ <sup>0.45</sup> × WC <sup>-0.04</sup> × PF <sup>-1.73</sup>	0.77	0.17	329.5	0.65
86	C <sub>u</sub> , γ, WC, D <sub>50</sub>	EC = (3.97) × C <sub>u</sub> <sup>4.03</sup> × γ <sup>0.45</sup> × WC <sup>-0.04</sup> × D <sub>50</sub> <sup>11.56</sup>	0.77	0.16	295.6	0.55
97	C <sub>u</sub> , γ, WC, PF, D <sub>50</sub>	EC = (0.19) × C <sub>u</sub> <sup>0.67</sup> × γ <sup>0.45</sup> × WC <sup>-0.04</sup> × PF <sup>0.74</sup> × D <sub>50</sub> <sup>2.44</sup>	0.77	0.17	258.1	0.55
102	C <sub>c</sub> , C <sub>u</sub> , γ	EC = (0.006) × C <sub>c</sub> <sup>1.35</sup> × C <sub>u</sub> <sup>0.65</sup> × γ <sup>0.34</sup>	0.77	0.17	328.9	0.53
103	C <sub>c</sub> , C <sub>u</sub> , WC	EC = (3.42) × C <sub>c</sub> <sup>-0.27</sup> × C <sub>u</sub> <sup>0.03</sup> × WC <sup>-0.004</sup>	0.76	0.17	329.5	0.57
105	C <sub>c</sub> , C <sub>u</sub> , PF	EC = (0.0032) × C <sub>c</sub> <sup>1.57</sup> × C <sub>u</sub> <sup>0.6</sup> × PF <sup>0.43</sup>	0.76	0.17	329.5	-9.5

**Figure 260.** Plot of POU versus correction factor for Group 48 (power): EC in the HET/Coarse data set.

characterization of all possible solutions of the model parameters and their relative probabilities while simultaneously providing a systematic and transparent approach to assess the performance of the proposed regression model.

The major difference between Bayesian analysis and deterministic frequentist regression is in how each approach interprets the observed data and model parameters. Frequentist regression assumes that the model parameters are, in fact, fixed unknown parameters and the observed data are random repeatable samples. However, the Bayesian inference approach assumes that the observed data are fixed values, while the model parameters are random parameters. Therefore, a frequentist regression approach results in fixed values attributed to the model parameters, whereas the Bayesian approach results in posterior probability distributions for each model parameter rather than a fixed value.

The main benefit of the use of the Bayesian inference approach is the definition of a metric of confidence on the model predictions. This permits assessment of both the performance of competing models given a set of experimental observations based on a given experimental method and the performance of competing experimental methods given a predictive model. The Bayesian approach departs from standard deterministic calibrations (i.e., least squares) by populating “all” the likely combinations of parameters of a predictive model suitable to represent the mean of the process of interest (i.e., the fit of a given set of experimental observations), as opposed to proposing a combination of single parameters (i.e., the optimal, which may not be unique). As a result, it is then possible to generate a full probabilistic description of the model parameters in the form of marginal probability density functions (PDFs)—that is, each model parameter is represented by its own PDF—and a full probabilistic description of the parameters’ correlation structure (when taken two at a time).

It should also be noted that the concepts of the confidence interval and hypothesis testing in frequentist regression and Bayesian inference are different. As an illustration, when, in the interpretation of the results of a frequentist regression approach, the confidence interval for a parameter is reported as 90%, this means that if the exact same experiment is repeated several times, and for each time the confidence interval is obtained, then 90% of the obtained intervals include the parameter. It does not mean that there is 90% chance that the parameter is within the confidence interval. On the other hand, when a Bayesian approach reports a 90% confidence interval (or, as it is typically called in Bayesian inference, the “credible interval”) for a parameter, this means that there is 90% chance that the credible interval contains the parameter.

#### 7.4.1 Motivation

One main objective of the NCHRP-Erosion spreadsheet (see Chapter 5) is to assimilate information collected from a broad range of erodibility tests and correlate those results with the geotechnical properties of primary soil by means of statistical modeling. However, regardless of the level of model sophistication, broadness of experimental observations, or accuracy of expert judgement, there is a finite amount of uncertainty associated with every mathematical representation—none of the modeling results can predict the property of interest with complete confidence. This is due to several practical limitations:

- Missing data from the database may introduce bias into the proper model calibration.
- The proposed empirical models do not capture the mean of the process of interest or do not show a proper correlation between erodibility and geotechnical parameters.
- One single model selection, the optimal, may represent only one single fit of possibly millions of likely combinations that may produce the same degree of curve fitting (i.e., the regression analysis is an ill-posed problem).

Understanding this varying evidence condition motivates a specialized calibration that points to systematic and transparent assessment of prediction confidence based on all available evidence.

### 7.4.2 Hypotheses

The foregoing regression analysis selected several groups of experimental observations and corresponding statistical models that showed satisfying model/observation comparisons. The proposed probabilistic (Bayesian) calibration method (Medina-Cetina 2006) is introduced here to complement the previous deterministic regression approach. Several hypotheses are proposed and are thoroughly discussed in Chapter 8:

- The probabilistic approach allows a full characterization of sources and propagation of model uncertainty and relative probabilities through systematic assimilation of available evidence (i.e., experimental observations, model prediction, and expert judgment).
- Varying estimation confidence levels of parameters can exhibit in the parametric space.
- Varying correlation structures among parameters can be shown in the calibration results, which will help reveal the model nature.
- The probabilistic characteristics of the proposed models will be depicted in multidimensional “physical domains” (composed of model independent variables); the goodness of the modeling depends not only on capturing each available observation (erodibility test results), but also on the confidence level of the estimation.

### 7.4.3 Methodology

#### 7.4.3.1 Uncertainty Quantification Framework

The uncertainty quantification of an inverse problem aims to identify, characterize, and simulate the various sources of uncertainty inherently participating in the physical process of interest (Medina-Cetina 2006). The expected output of the true process is represented by a set of random vectors,  $d$ , which is based on the definition of the physical process at prescribed control points. In practice, experimental observations,  $d_{\text{obs}}$ , can be retrieved from lab or field measurements and compared with predicting outcomes of the same process,  $d_{\text{pred}}$ . These are quantifiable vectors formed as a priori information used to approximate the true process,  $d$ . Accordingly, the uncertainty quantification framework in terms of  $d$ ,  $d_{\text{obs}}$  and  $d_{\text{pred}}$  can be summarized as follows:

$$\begin{aligned} d &= d_{\text{obs}} + \Delta d_{\text{obs}} \\ d &= d_{\text{pred}} + \Delta d_{\text{pred}} \\ d_{\text{obs}} - d_{\text{pred}} &= \Delta d_{\text{obs}} - \Delta d_{\text{pred}} \end{aligned} \tag{73}$$

Equation 73 illustrates the tradeoff between the scientific evidence  $d_{\text{obs}}$  and  $d_{\text{pred}}$  through the gradients,  $\Delta d$ . The involved uncertainty incorporates random vectors both in experimental observations and theoretical predictions. Herein,  $d_{\text{pred}}$  comprises mathematical predictions stemming from a forward model,  $g(\theta)$ , which is governed or characterized by a set of parameters,  $\theta$ . Notice that  $\theta$  can represent geometric and statistical properties, such as shape parameters or, in this case, linear/power parameters. Similarly, the uncertainty involved in the calibration of vectors,  $\theta$ , can be defined as

$$\theta = \hat{\theta} + \Delta \theta \tag{74}$$

where  $\hat{\theta}$  denotes mean of parameters and  $\Delta\theta$  represents the uncertainty component. Other than the deterministic methodology, the probabilistic calibration allows for an exhaustive exploration of all potential combinations of the model parameters that best resemble the experimental observations. As a result, the correlation structures of model parameters are populated, which ultimately can be translated into a better understanding of uncertainty inherent to model nature ( $\Delta d_{\text{pred}}$ ) with respect to the experimental observations. Notice that in this work, the model prediction is assumed to be unbiased with respect to the process of interest, which implies  $E(\Delta d_{\text{obs}} - \Delta d_{\text{pred}}) = 0$ .

#### 7.4.3.2 Bayesian Probabilistic Calibration

The proposed uncertainty quantification framework requires assessment of plausible solutions of model parameters  $\theta$  conditioned on the data,  $d_{\text{obs}}$ , which generates the need of mathematical mapping regarding this inverse problem. From a deterministic standpoint, this can be accomplished by selecting an optimal set of model parameters that maximize the likelihood of fitting  $d_{\text{obs}}$ . However, the proposed calibration can be an ill-posed inverse problem, since many combinations of the model parameters can lead to the same experimental response. To tackle this problem, the proposed probabilistic calibration method follows a Bayesian approach, which accounts for the full probabilistic description of the model parameters through probability maps. This starts from an expert's belief setting up the prior  $[\pi(\theta)]$  about model parameters  $\theta$  before the experimental evidence is presented to the mechanical model (forward model). This prior knowledge ideally facilitates calibration of model parameters by limiting and defining plausible values in the form of probability distribution, which is later updated systematically via quantifying the likelihood ( $p(d_{\text{obs}}|\theta)$ ) between available observations  $d_{\text{obs}}$  and model parameters  $\theta$ . From the basic definition of Bayes theorem:

$$\pi(\theta|d_{\text{obs}}) = \frac{p(d_{\text{obs}}|g(\theta), \theta)\pi(\theta)}{\int_{\Theta} p(d_{\text{obs}}|g(\theta), \theta)\pi(\theta)d\theta} \propto p(d_{\text{obs}}|g(\theta), \theta)\pi(\theta) \quad (75)$$

The posterior  $\pi(\theta|d_{\text{obs}})$  is the probability proportional to the prior  $\pi(\theta)$  and the likelihood,  $p(d_{\text{obs}}|\theta)$ . This is because the integral of the denominator is a normalizing constant over the parametric space  $\Theta$  so that the integral of the posterior  $\pi(\theta|d_{\text{obs}})$  can be 1.

One important note about implementing Bayesian inference is that the computations often involve very complex integrations that cannot be handled analytically. Also, the posterior distribution hardly is in explicit form and requires simulations in order to be achieved. Markov Chain Monte Carlo (MCMC) sampling methods are typically used to solve for complex posterior models. The most typical MCMC sampling method is the Metropolis–Hastings (Metropolis et al. 1953; Hastings 1970). This sampling method follows an algorithm that generates values from a posterior distribution and converges to a predetermined target distribution. Further information on MCMC and its algorithm can be found in Hastings (1970). When any MCMC sampling method is used to approximate the posterior distributions, verifying its convergence becomes a vital step in the Bayesian inference approach. In this study, the sampling of the posterior is based on an MCMC approach coupled with Metropolis–Hastings criteria, which makes it possible to draw samples from a proposing distribution to infer the target posterior distributions.

#### 7.4.4 Probabilistic Calibration for Varying Data Scenarios

The probabilistic calibrations discussed in this section were conducted on the proposed model/data scenarios produced by the deterministic regression results populated in the previous section. Table 82 to Table 86 list deterministic regression calibrations with the highest

## 264 Relationship Between Erodibility and Properties of Soils

**Table 82.** Selected models for critical shear stress,  $\tau_c$ .

Group No.	Independent Variables	Data Set <sup>a</sup>	Model Expression <sup>b</sup>	$R^2$	Cross-Validation Score
124	$\gamma, A, WC, S_u, PF, D_{50}$	EFA/Fine ( $n = 44$ )	$\tau_c = (158.06) \times \gamma^5 \times A^{-0.46} \times WC^{10.03} \times S_u^{1.83} \times PF^{-18.28} \times D_{50}^{-4.21}$	0.94	0.66
77	$C_u, \gamma, D_{50}$	EFA/Coarse ( $n = 28$ )	$\tau_c = (1.58) \times C_u^{-0.04} \times \gamma^{0.02} \times D_{50}^{0.77}$	0.93	0.99
113	PC, $\gamma, WC, S_u, D_{50}$	JET/Global ( $n = 28$ )	$\tau_c = -0.248 \times PC - 1.23 \times \gamma + 0.21 \times WC + 0.07 \times S_u - 36.89 \times D_{50} + 31.82$ for $D_{50} < 0.3$ mm	0.50	0.10
19	PI, $S_u, D_{50}$	HET/Global ( $n = 21$ )	$\tau_c = (25.07) \times PI^{0.27} \times S_u^{0.55} \times D_{50}^{0.5}$ for $D_{50} < 0.3$ mm	0.64	0.43

<sup>a</sup> $n$  = number of data points.<sup>b</sup>Parameter values given by deterministic regression.**Table 83.** Selected models for critical velocity,  $v_c$ .

Group No.	Independent Variables	Data Set <sup>a</sup>	Model Expression <sup>b</sup>	$R^2$	Cross-Validation Score
117	PC, WC, $S_u, D_{50}$	EFA/Fine ( $n = 46$ )	$v_c = (2.518 \times 10^{-5}) \times PC^{0.2} \times WC^{2.06} \times S_u^{0.51} \times D_{50}^{-0.13}$	0.80	0.80
44	PI, $\gamma, VST, PF, D_{50}$	EFA/Coarse ( $n = 10$ )	$v_c = 0.002 \times PI - 0.1 \times \gamma + 0.01 \times VST - 0.09 \times PF - 13.6 \times D_{50} + 7.21$ for $0.074 < D_{50} < 0.3$	0.93	0.67

<sup>a</sup> $n$  = number of data points.<sup>b</sup>Parameter values given by deterministic regression.**Table 84.** Selected models for erosion category, EC.

Group No.	Independent Variables	Data Set <sup>a</sup>	Model Expression <sup>b</sup>	$R^2$	Cross-Validation Score
132	$A, WC, S_u, D_{50}$	EFA/Fine ( $n = 44$ )	$EC = (0.1933) \times A^{-0.06} \times WC^{0.51} \times S_u^{0.09} \times D_{50}^{-0.12}$	0.55	0.53
117	PC, WC, $S_u, D_{50}$	EFA/Fine ( $n = 44$ )	$EC = 0.023 \times PC + 0.03 \times WC + 0.0017 \times S_u - 1.845 \times D_{50} + 0.8566$	0.56	0.43
91	$C_u, WC, VST, D_{50}$	EFA/Coarse ( $n = 11$ )	$EC = (1.12) \times C_u^{0.1} \times WC^{-0.28} \times VST^{0.02} \times D_{50}^{-0.44}$ for $0.074 < D_{50} < 0.3$	0.92	0.80
13	PI, $\gamma, PF$	JET/Fine ( $n = 56$ )	$EC = (0.00375) \times PI^{0.12} \times \gamma^{1.81} \times PF^{0.21}$	0.51	0.47
88	PL, $S_u, D_{50}$	JET/Global ( $n = 28$ )	$EC = -0.022 \times PL + 0.0031 \times S_u - 5.5 \times D_{50} + 3.34$ for $D_{50} < 0.3$ mm	0.70	0.58
12	PI, $\gamma, S_u$	HET/Fine ( $n = 21$ )	$EC = (1.67) \times PI^{0.04} \times \gamma^{0.15} \times S_u^{0.03}$	0.70	0.54

<sup>a</sup> $n$  = number of data points.<sup>b</sup>Parameter values given by deterministic regression.

**Table 85.** Selected model for velocity slope,  $E_v$ .

Group No.	Independent Variables	Data Set <sup>a</sup>	Model Expression <sup>b</sup>	$R^2$	Cross-Validation Score
86	$C_u, \gamma, WC, D_{50}$	EFA/Coarse ( $n = 28$ )	$E_v = (88,969.4) \times C_u^{-1.77} \times \gamma^{-2.26} \times WC^{0.34} \times D_{50}^{-1.69}$	0.86	0.64

goodness of fit for each erodibility variable (i.e., critical shear stress,  $\tau_c$ ; critical velocity,  $v_c$ ; erosion category, EC; velocity slope,  $E_v$ ; and shear stress slope,  $E_\tau$ , respectively). It must be noted that not all of the selected equations in the previous section could be converged in the probabilistic calibration. Tables 82 to 86 show only the equations that were successfully calibrated.

The results of the probabilistic calibrations for all of the equations presented in Tables 82 to 86 are presented in Appendix 5 of the appendices report. However, in this section, one case is discussed to illustrate the applicability of the method, labeled with Group 132 (See Table 84). In Appendix 5, the same type of results as the ones described in this section are generated for all of the selected equations.

#### 7.4.4.1 Power Model for Erosion Category, EC, EFA/Fine Data Set

The selected case is the power model created to predict the erodibility parameter, EC, for the EFA/Fine data set (Group 132). Four independent variables are considered: soil activity,  $A$ ; water content, WC; undrained shear strength,  $S_u$ ; and mean particle size,  $D_{50}$ . A total of 44 data observations were available, each consisting of four geotechnical properties as input and EC as the erodibility property or output. Table 84 provides the optimization result of model parameters through nonlinear regression. Taking these parameter values, the generated model predictions, along with the observed data plotted along each variable domain, are as shown in Figure 261. It is shown that the vector of experimental observations is scattered along each variable domain and that the proposed model overall captures the mean of the process.

**Step 1. Optimization.** In the proposed probabilistic calibration framework, the optimization results are able not only to provide the initial guess of random parameter values (as presented in Figure 261), but also to retrieve the shape of the error between model predictions and observations, which leads to the selection of the probability function to be considered for the likelihood. Figure 262a shows a histogram and kernel density estimate of residuals of model prediction, a nominal Gaussian distribution of the mean around zero, seemingly a reasonable fit of empirical

**Table 86.** Selected models for shear stress slope,  $E_\tau$ .

Group No.	Independent Variables	Data Set <sup>a</sup>	Model Expression <sup>b</sup>	$R^2$	Cross-Validation Score
77	$C_u, \gamma, D_{50}$	EFA/Coarse ( $n = 28$ )	$E_\tau = (3,228.7) \times C_u^{-2.8} \times \gamma^{-1.58} \times D_{50}^{-2.91}$	0.91	0.64
40	$\gamma, WC, PF, D_{50}$	HET/Coarse ( $n = 62$ )	$E_\tau = (2.951) \times \gamma^{26.08} \times WC^{-7.48} \times PF^{-19.96} \times D_{50}^{-5.32}$	0.86	0.55

<sup>a</sup> $n$  = number of data points.<sup>b</sup>Parameter values given by deterministic regression.

## 266 Relationship Between Erodibility and Properties of Soils

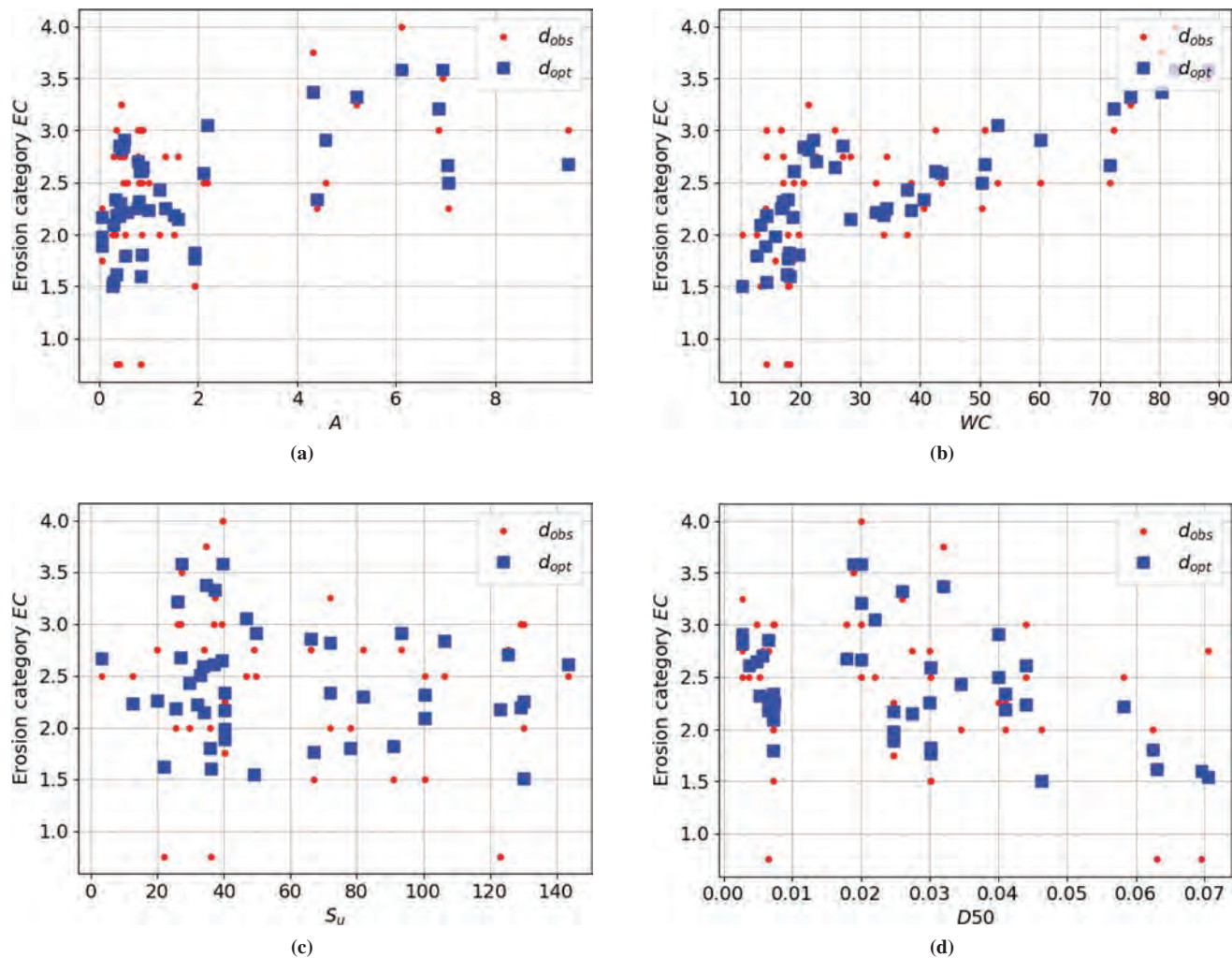


**Figure 261.** Experimental observations and model predictions along variable domains: (a) soil activity, (b) water content, (c) undrained shear strength, and (d) mean particle size ( $d_{obs}$  = experimental observations;  $d_{opt}$  =  $d$  optimized).

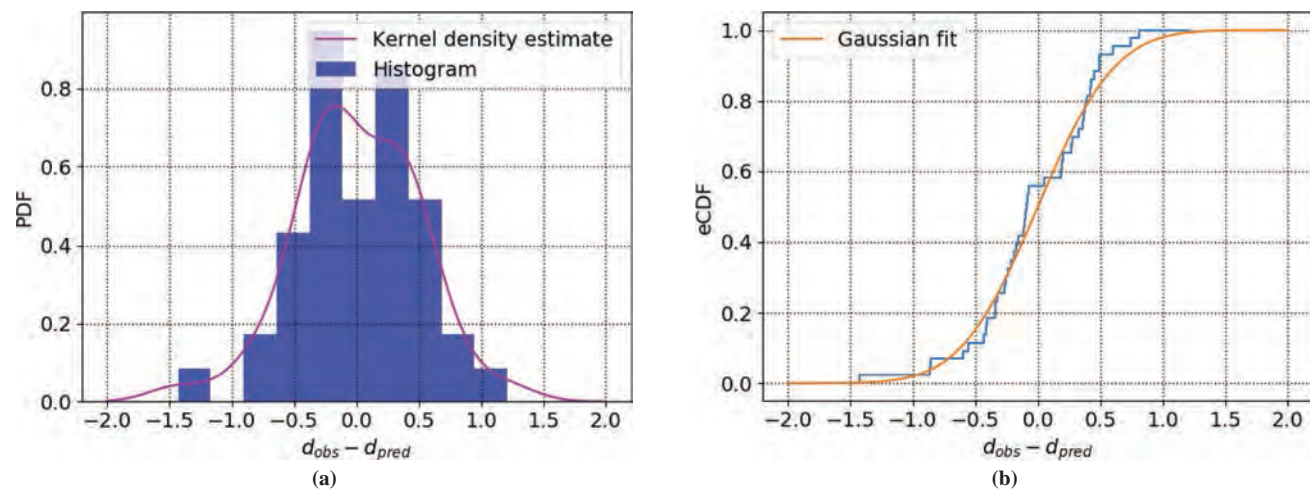


**Figure 262.** (a) Histogram and kernel density estimate of error and (b) ECDF and Gaussian fit of error.

distribution, which indicates also the unbiased character of the proposed model. However, the change of bin size and starting position of the histogram may result in a variation to its shape. Even though the kernel density estimate can eliminate the effect of the starting position of the plot, one still needs to determine the kernel width, which is generally difficult in practice. Figure 262b indicates a better solution to the problem. Plotting the ECDF of error allows a monotonic increase of probability to provide a unique description of error distribution. A Gaussian distribution presents a suitable approximation of error distribution; thus, it is adopted as the likelihood function and used in the Bayesian formulation. A noninformative distribution is considered as a prior for the Bayesian formulation.

**Step 2. Probabilistic Calibration and Convergence Diagnosis.** For the sake of a better presentation of the calibration results for Group 132 (Table 84), each model parameter was named following the variable it serves, that is,  $\beta_0$ ,  $\beta_A$ ,  $\beta_{WC}$ , and  $\beta_{S_u}$ , where  $\beta_0$  refers to the scaling factor at the beginning of the equation. The selected prior for all parameters is a vague Gaussian prior with the mean equal to zero and a standard deviation of  $10^6$ .

Figure 263 presents MCMC sample sequences of each parameter for 100,000 iterations. A stationary state was achieved for each parameter as illustrated by Figure 264 and Figure 265 are cumulative mean and cumulative standard deviations of sample sequences for each parameter. These plots are used to validate the convergence of MCMC achieved at a stationary condition and to define the burn-in point after which statistics about the model performance are computed. The principle of stationary should be achieved for both cumulative mean and standard deviation plots. In this case, the burn-in point is set as 40,000.

**Step 3. Posterior Statistics.** Once the MCMC posterior sampling reaches a stationary state, statistical inferences can be generated. Figure 266 shows a depiction of the joint relative frequency histograms across all model parameters as well as the marginal PDFs of each parameter presented along the figures' matrix diagonal. Most probability distributions indicate an asymptotic normality in its shape. The validity of this rests on the central limit theorem. Table 87 gives posterior statistics in terms of mean, standard deviation (SD), coefficient of variation (CV), mode, and 95% highest posterior density (HPD) region. The mean values are close to what has been obtained from regression analysis, but one should adopt these with caution. For instance, the distribution of  $\beta_0$  is not symmetric and skews to the right (i.e., positive skewness), which yields its mean value greater than the mode. A more rational choice would be the latter, as it represents higher probability by the probabilistic calibration. Lower triangular plots in Figure 266 are the parameters' cross-correlation investigations, with two at a time. Since the PDF of  $\beta_0$  is asymmetric, nonlinear correlation structure is observed between  $\beta_0$  and other parameters. A significant negative correlation is shown between  $\beta_A$  and  $\beta_{WC}$ , indicating the strong association of soil's water content and activity in predicting erosion category. Scatter plots of posterior samples and Pearson correlation coefficients are given in the upper triangular matrix, which provides direct delineations of correlation type and degree among various parameter combinations.

It is worth noting that in Table 87, the CVs are given as complementary information of parameter variability. Additionally, a 95% HPD region, which denotes the credible range where a given parameter exhibits higher probability of occurrence, is given for each parameter.

**Step 4. Probabilistic Realizations and Assessment of Model Performance.** Finally, the probabilistic calibration approach allows production of a metric of the model performance. Once the posterior distribution is populated, likely realizations of the model predictions can be computed by sampling random parameter combinations from it. These model responses provide numerical evidence to estimate first and second order statistics in regard to model performance.

## 268 Relationship Between Erodibility and Properties of Soils

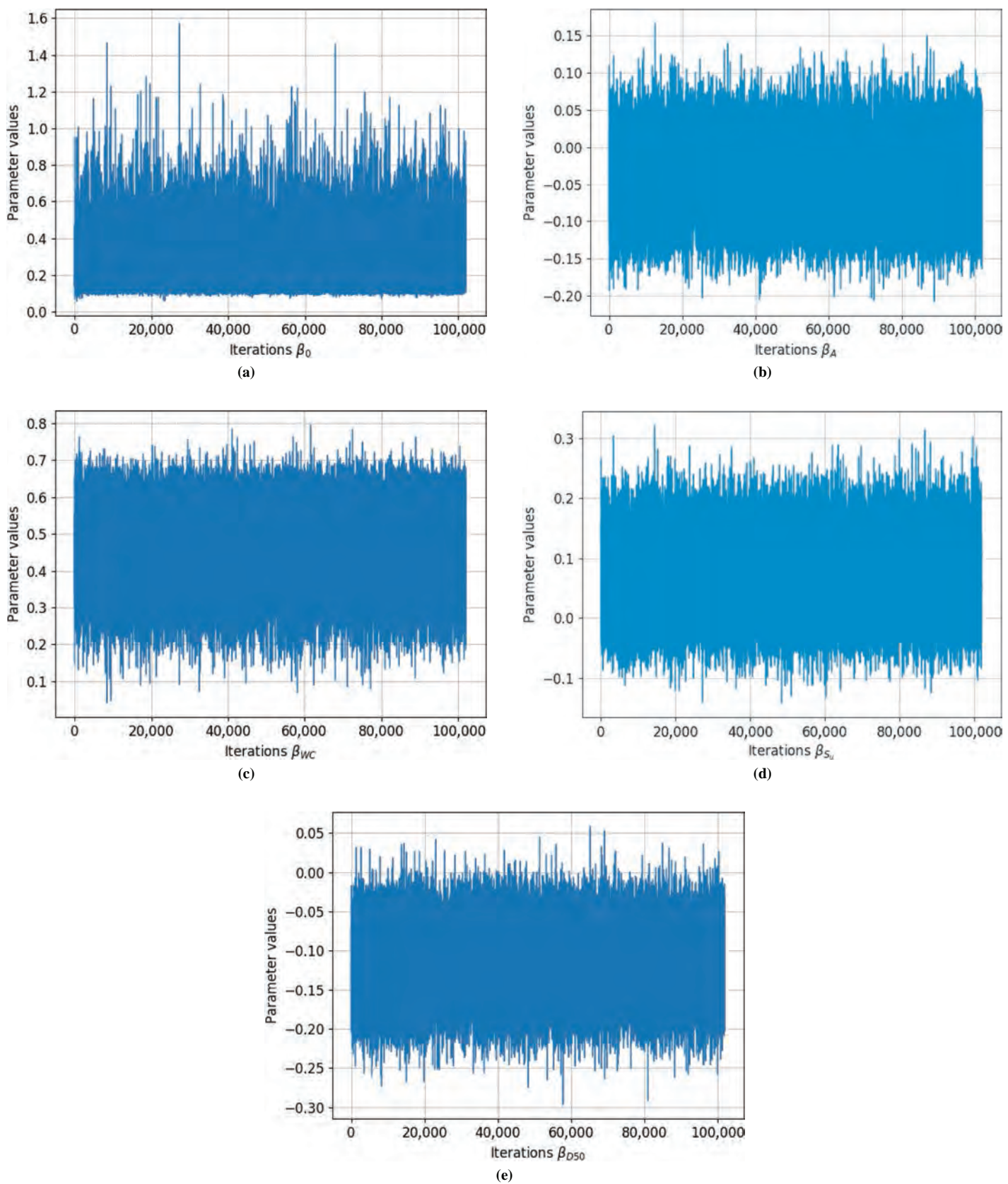


**Figure 263.** Random samples of model parameters: (a)  $\beta_0$ , (b)  $\beta_A$ , (c)  $\beta_{WC}$ , (d)  $\beta_{Su}$ , and (e)  $\beta_{D50}$ .

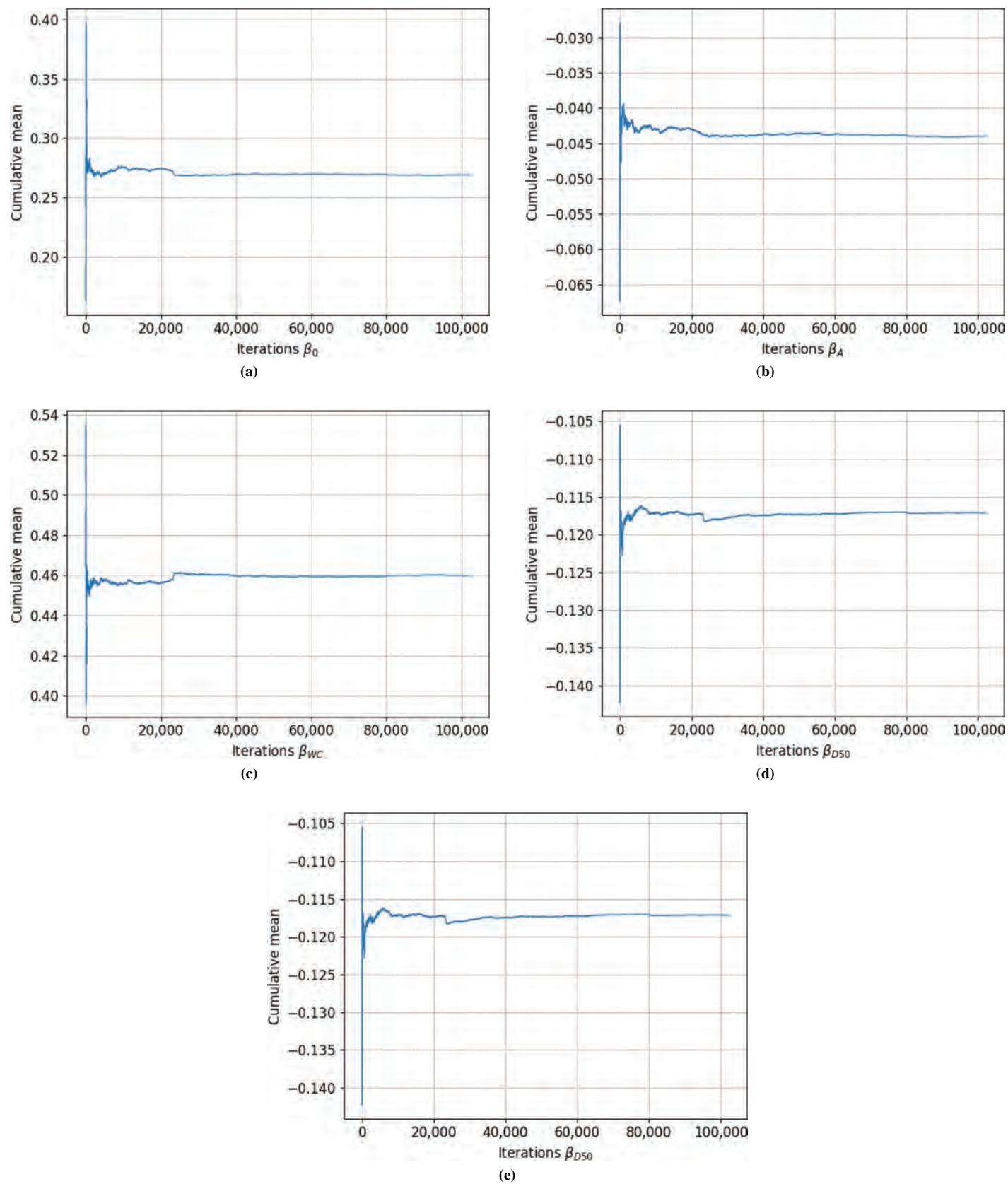
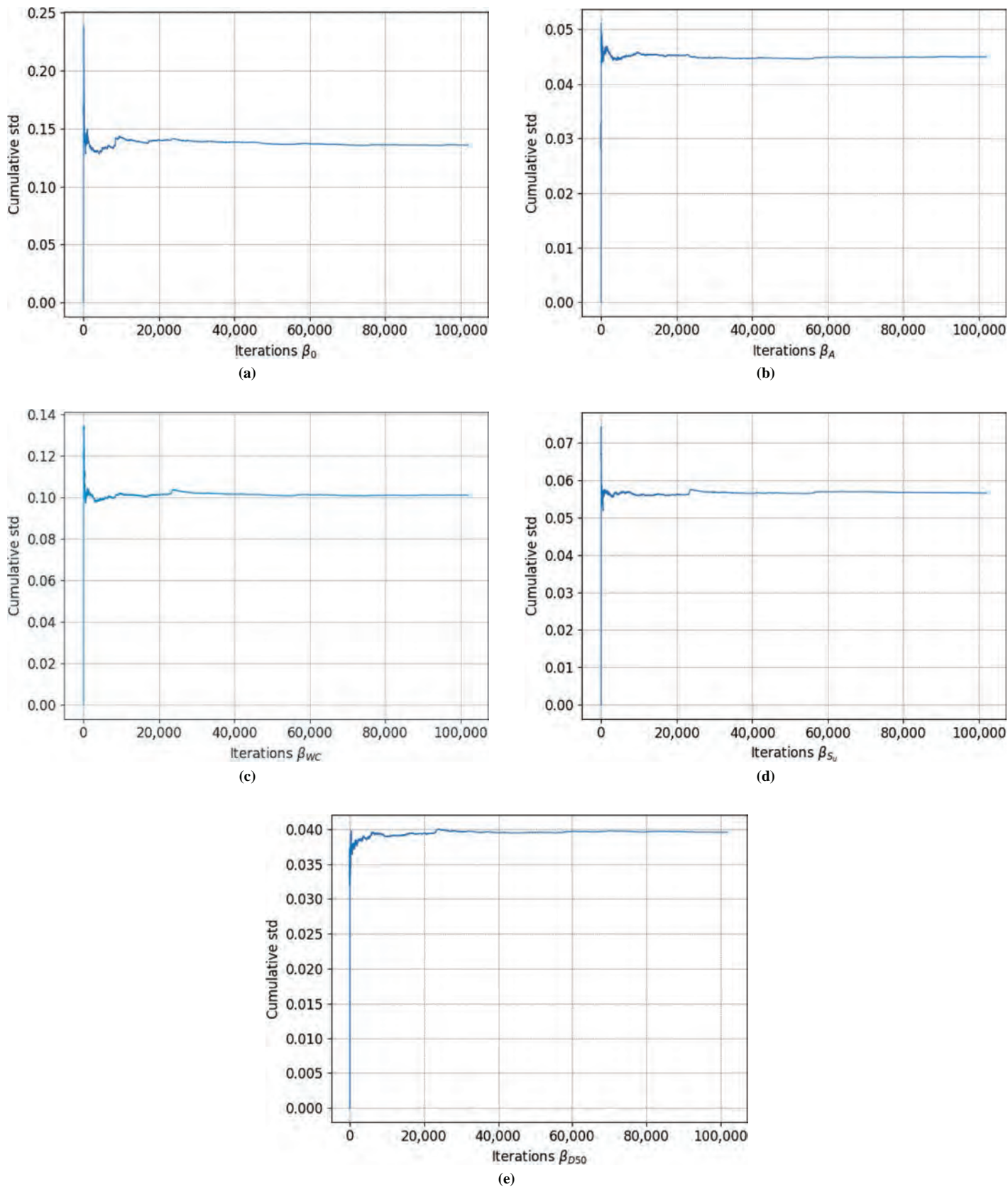


Figure 264. Cumulative mean of sample sequences for each parameter: (a)  $\beta_0$ , (b)  $\beta_A$ , (c)  $\beta_{WC}$ , (d)  $\beta_{Su}$ , and (e)  $\beta_{D50}$ .

## 270 Relationship Between Erodibility and Properties of Soils



**Figure 265.** Cumulative standard deviation of sample sequences for each parameter: (a)  $\beta_0$ , (b)  $\beta_A$ , (c)  $\beta_{WC}$ , (d)  $\beta_{Su}$ , and (e)  $\beta_{D50}$ .

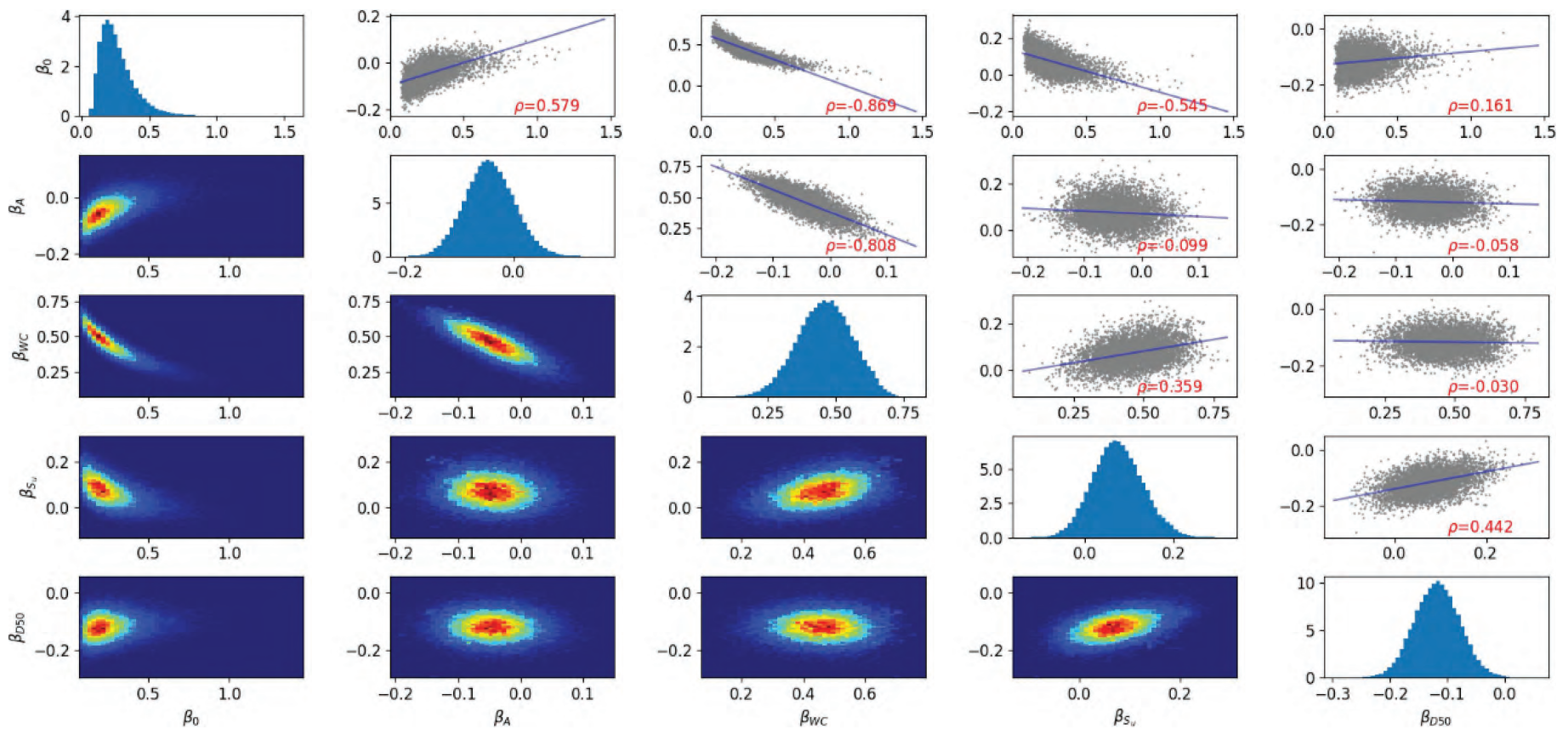


Figure 266. Joint relative frequency histogram of model parameters, two at a time.

**Table 87. Statistics of probabilistic calibrated model parameters.**

Parameter	Mean	SD	CV	Mode	95% HPD region	
					Lower Bound	Upper Bound
$\beta_0$	0.27	0.13	0.50	0.19	0.07	0.53
$\beta_A$	-0.04	0.05	-1.02	-0.04	-0.13	0.05
$\beta_{WC}$	0.46	0.10	0.22	0.49	0.27	0.66
$\beta_{S_u}$	0.07	0.06	0.77	0.07	-0.03	0.19
$\beta_{D_{50}}$	-0.12	0.04	-0.34	-0.12	-0.19	-0.04

To achieve this goal, composition of a multidimensional mesh grid retrieved across all independent variables is required, enabling the assessment of the model prediction along each domain of all independent variables versus the dependent variable or erodibility parameter. Each domain range is decided by minimum and maximum values retrieved from experimental observations; additionally, 10 uniform discretization steps were chosen for each variable to ensure computational efficiency and sufficiency of the inferences at the same time. For example, in the case of Group 132, there are four independent variables, and the mesh grid is discretized with 10 steps, meaning  $10^4 = 10,000$  points where the hypersurface produced by the model will be repeatedly evaluated for different parameters' combinations. That is, from the posterior, 1,000 random parameter samples are taken after the burn-in point; these produce the ensemble of model predictions ( $10^7$  model predictions along the mesh grid).

Probabilistic and deterministic model realizations along each independent variable domain are shown in Figure 267. Once the ensemble of model predictions is plotted along each variable domain, a one-to-one mapping is then possible where multiple model outputs can correspond to one prescribed variable value, as it shown in Figure 267. This shows 1,000 probabilistic realizations as opposed to 1 deterministic realization. The progress of model realizations along the  $A$  and  $D_{50}$  domains shows a distinct trend compared with WC and  $S_u$ . This is due to the mean of the parameters retrieved from the posterior being positive for  $\beta_{WC}$  and  $\beta_{S_u}$  but negative for  $\beta_A$  and  $\beta_{D_{50}}$ .

First order statistics for this model can be computed along the domain of each independent variable (physical domain) as presented in Figure 268, which shows that the mean computed from the ensemble of simulations produced by the posterior converges to the optimal estimate produced by the deterministic calibration. However, a heteroscedastic condition is shown, or variance variability along each domain of all independent variables. This is a reflection of the non-Gaussian nature of the variation of the mean of the EC process. Figure 268 shows larger HPD interval areas above the mean of the model predictions, which indicates that the EC predictions are skewed to the upper side for all independent variables. It is very important to notice that these first and second order statistics correspond to the given model realizations (Group 132), which represent the credibility of the mean, not of the whole population. The yellow and red curves represent the mean of the probabilistic calibration and optimal model predictions at each independent variable. The mean produced from the probabilistic calibration stemmed from an exhaustive sampling process across all the parametric space (MCMC) as opposed to a limited sampling to assess the deterministic calibration to produce the optimal vector of the model parameters. Figure 268b presents the least overall uncertainty among the four independent variables, which shows WC as the best predictor for this group number.

As with the POU/POO analyses performed on the basis of the deterministic regression results, it is also possible to associate the correction factors with confidence levels with respect to the probabilistic results. Figure 269 presents the measured EC versus predicted EC in an

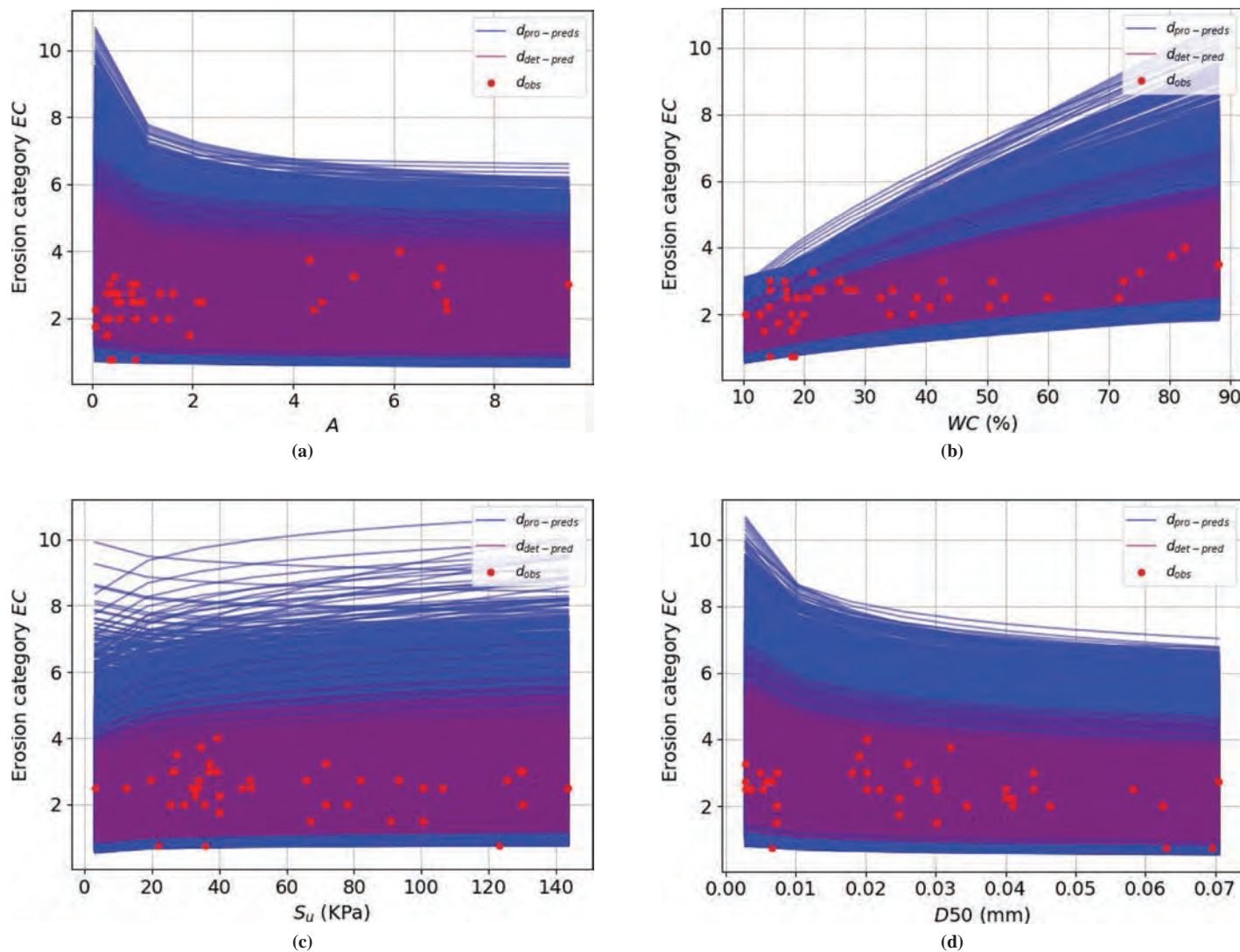


**Figure 267.** Model realizations coupled with observed data set along each variable domain: (a) soil activity, (b) water content, (c) undrained shear strength, and (d) mean particle size ( $d_{pro-pred} = d$  probabilistically predicted;  $d_{det-pred} = d$  deterministically predicted).

equal aspect ratio context, where results lying along the  $45^\circ$  line indicate a perfect fit. Similar to the 1,000 posterior ensemble of realizations, this figure shows 1,000 model predictions at the same location of the available experimental EC observations. Box plots at each of these points are presented to indicate the model variation or variation of the mean of the EC process. From the same 1,000 realizations, the correction factors ( $\theta$ ) are computed to produce POU levels, as shown in Figure 270a. Figure 270b presents the mean and HPD intervals for the same realizations, showing a growing uncertainty inherent in POU with the increase of the correction factor. This is a significant improvement over the previous deterministic plots, since these add a confidence metric on the assessment of the correction factors associated with every POU value.

#### 7.4.4.2 Linear Model for Erosion Category, EC, EFA/Fine Data Set

A second probabilistic calibration is presented for the linear model for erodibility parameter EC, EFA/Fine data set (Group 117). The main difference between the two cases discussed here is the proposed regression model used to predict EC. Both first and second order statistics for each model parameter are evaluated. Only results after Step 2 of the probabilistic calibration

## 274 Relationship Between Erodibility and Properties of Soils

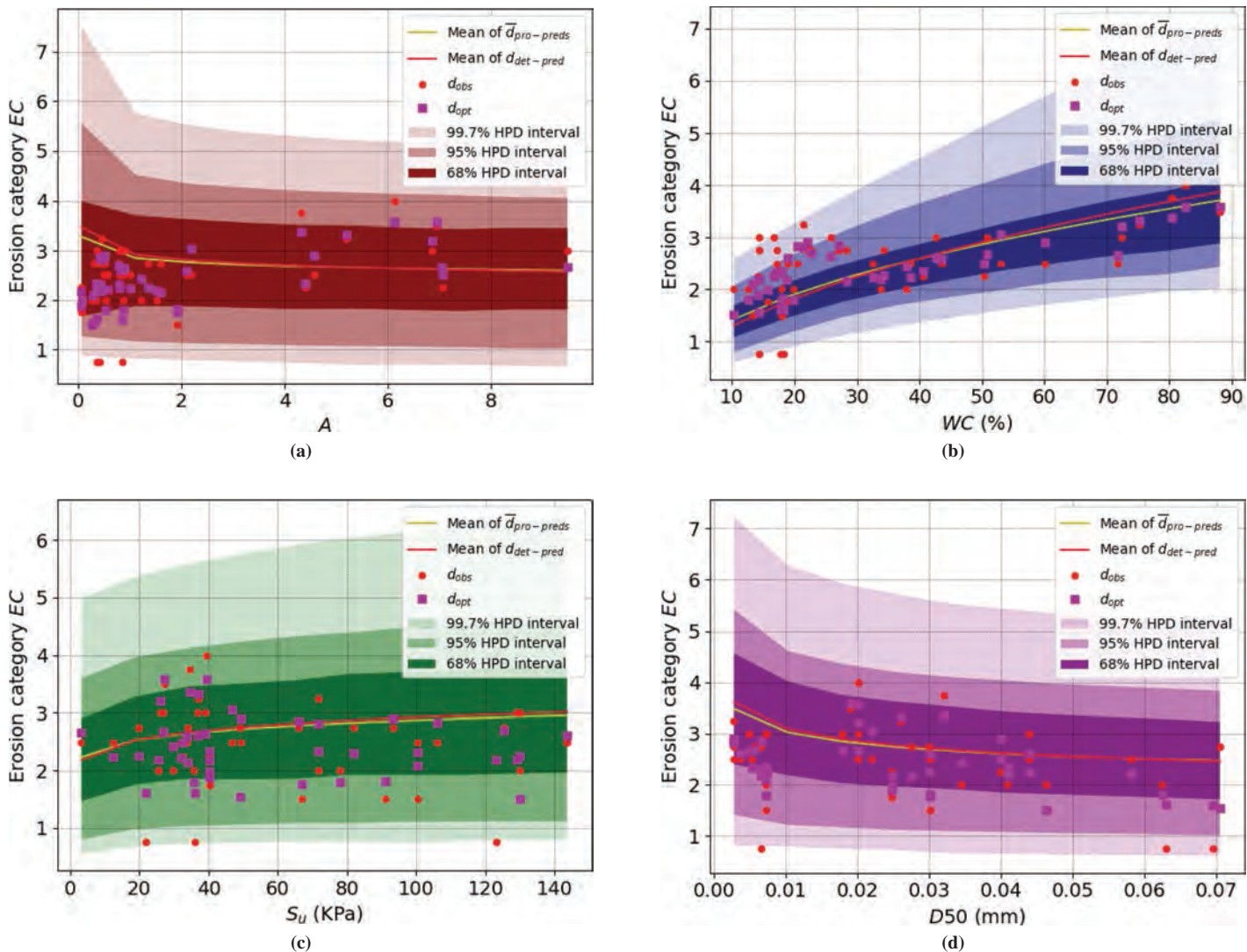


**Figure 268.** Mean and standard deviations of model predictions versus observed data: (a) soil activity, (b) water content, (c) undrained shear strength, and (d) mean particle size.

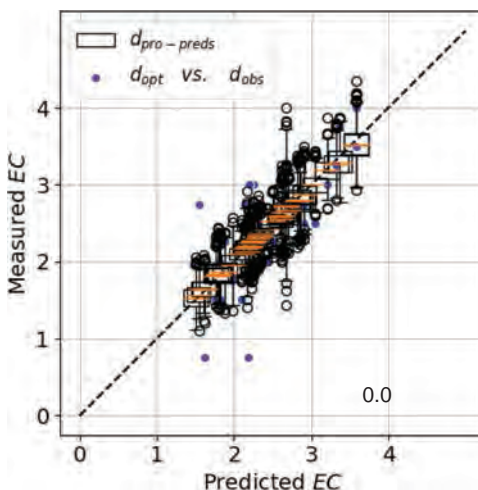


**Figure 269.** Measured EC versus predicted EC based on optimization and probabilistic calibration results.

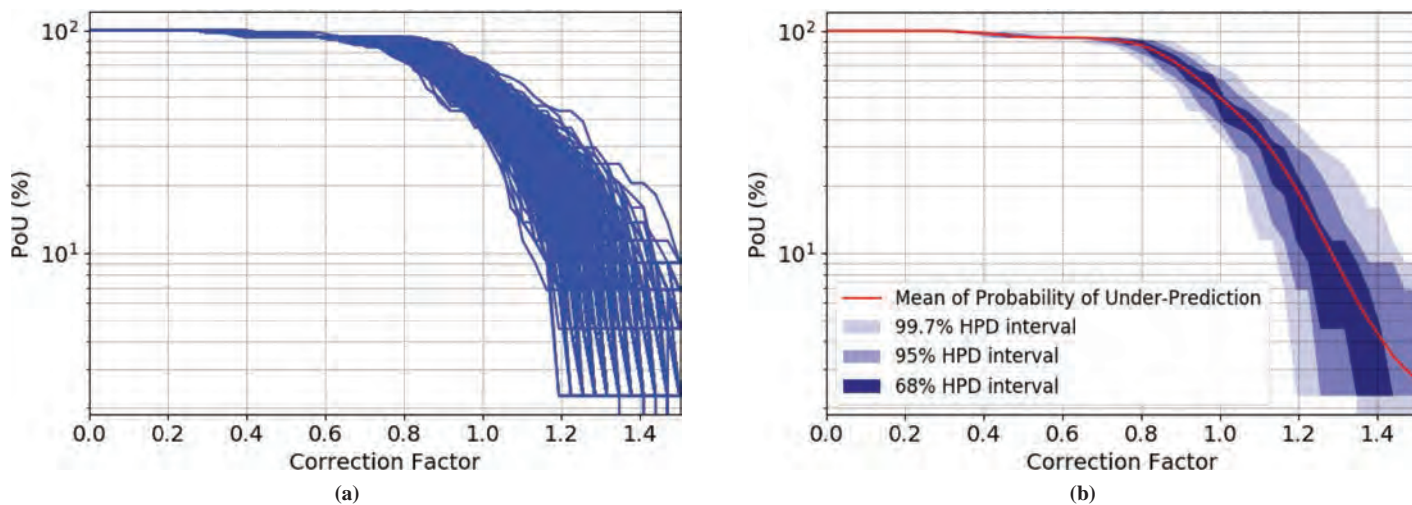


**Figure 270.** Probability of underprediction: (a) 1,000 realizations of POU versus correction factor and (b) mean and HPD intervals of POU.

are presented for this model, as convergence of the MCMC posterior sample was also achieved. The matrix of plots presenting the posterior's joint relative frequency histograms of this model's parameters is introduced in Figure 271. A uniform negative correlation between intercept  $\beta_0$  and other parameters is presented in the bottom row, with correlation coefficients ranging from  $-0.491$  to  $-0.841$ . In contrast with the power model, all marginal PDFs along the diagonal follow a Gaussian shape without skewness, which results from the free boundary of possible EC parameter values in the linear model (negative values of  $\beta_0$  in the power model are by default not sampled during MCMC). Higher CV values of  $\beta_{D_{50}}$  and  $\beta_{S_u}$  are expected to cause bigger variations along the  $D_{50}$  and  $S_u$  domains, which will be examined through realizations and statistical analysis in each variable domain.

Table 88 shows the model characteristics and optimization result on the basis of the deterministic approach. Table 89 gives posterior statistics for the same group of parameters in terms of the mean, standard deviation, coefficient of variation, mode, and 95% highest posterior density (HPD) region.

Figure 272 and Figure 273 display 1,000 model realizations from the sampling of the posterior and its corresponding first and second order statistics along each domain of the independent variables. The mean of the EC process produced by the probabilistic calibration and the optimal realization produced by the deterministic regression show significant agreement. In addition, comparison of HPD intervals for the linear and power models indicates uncertainty is more uniformly distributed in both domains and codomains for the former and also quantitatively smaller. However, it is worth noticing that using the linear model may yield negative values of EC that might not make sense in reality. A rational choice in such a case would be a power model instead or to further restrict the variation of EC during the MCMC sampling process of the posterior.

Finally, a reliability-based analysis is conducted to assess the model performance. Even though both linear and power models show a good capacity to capture the mean of the EC process, a more uniform prediction variation is presented for the linear model (Figure 274), which is consistent with the findings in Figure 273. In regard to the plots of POU versus  $\theta$  (see Figure 275), the results are similar for both models. For instance, seeking 90% confidence that the predicted EC is smaller than the actual EC, the predicted value should be multiplied by a correction factor equal to 0.80 for both scenarios.

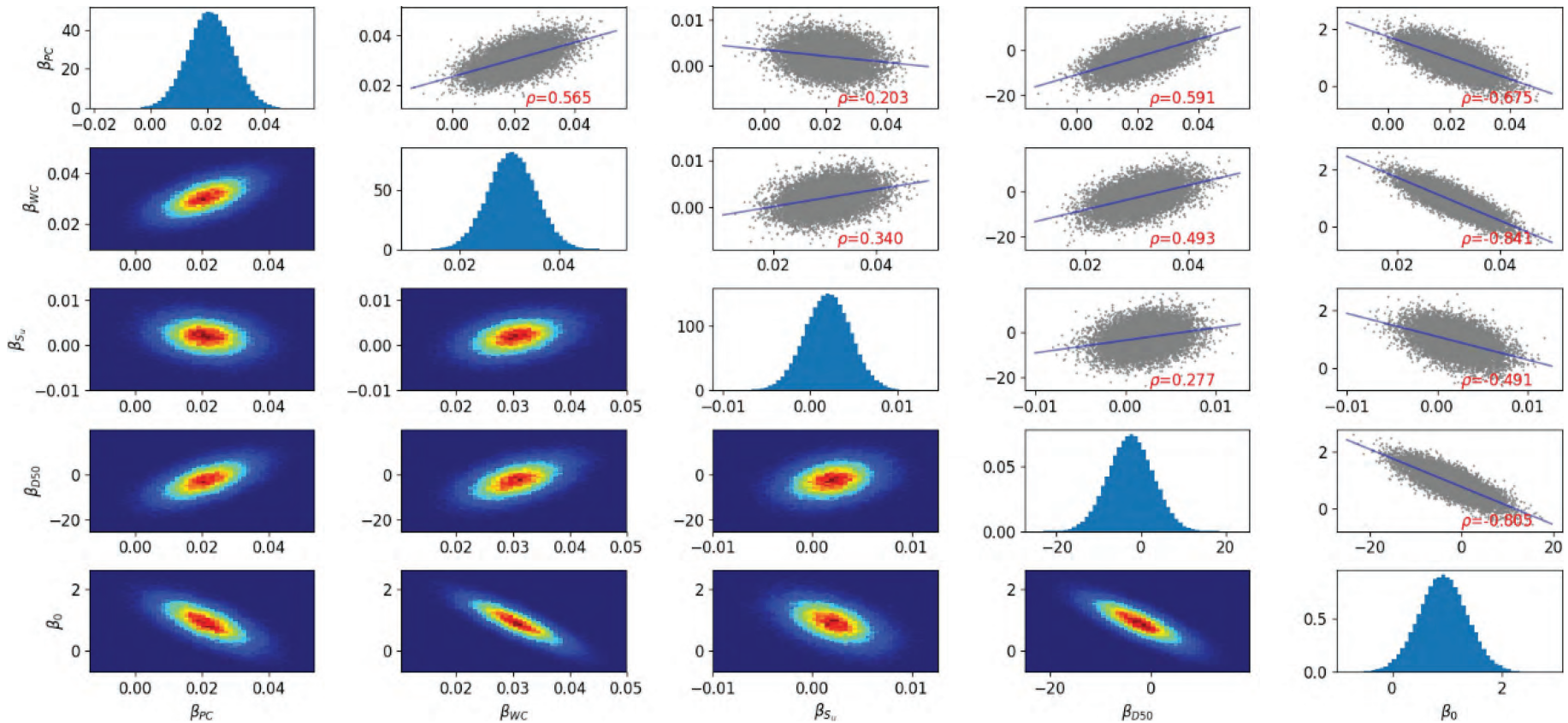


Figure 271. Joint relative frequency histogram of model parameters, two at a time.

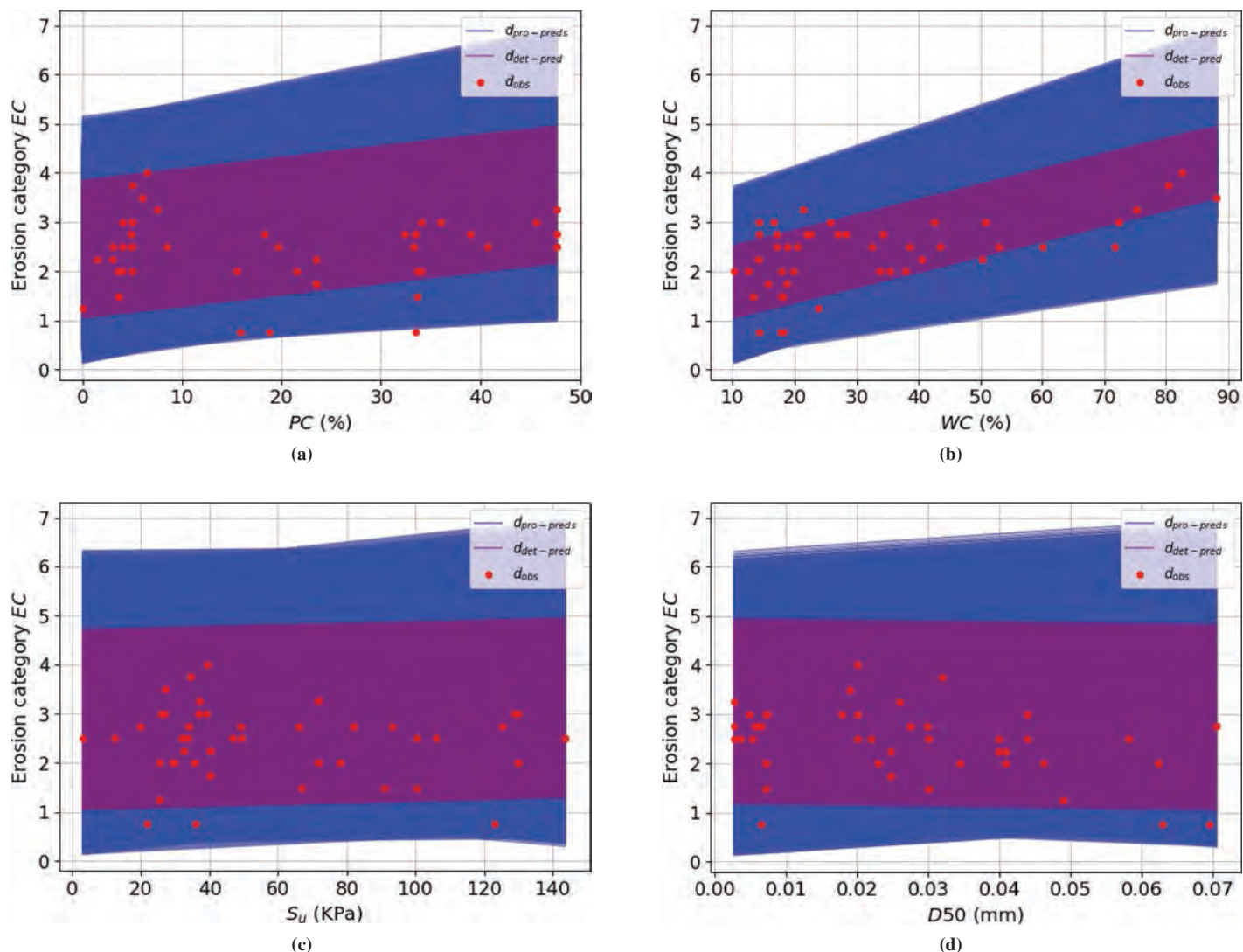
**Table 88.** Model characteristics and optimization result.

Group No.	Independent Variables	Data Set <sup>a</sup>	Model Expression (parameter values given by deterministic regression)	R <sup>2</sup>	Cross-Validation Score
117	PC, WC, S <sub>u</sub> , D <sub>50</sub>	EFA/Fine (n = 44)	EC = 0.023 × PC + 0.03 × WC + 0.0017 × S <sub>u</sub> - 1.845 × D <sub>50</sub> + 0.8566	0.56	0.43

<sup>a</sup>n = number of data points.

**Table 89.** Statistics of probabilistic calibrated model parameters.

Parameter	Mean	SD	CV	Mode	95% HPD region	
					Lower Bound	Upper Bound
β <sub>PC</sub>	0.021	0.008	0.378	0.021	0.006	0.037
β <sub>WC</sub>	0.031	0.005	0.160	0.030	0.021	0.040
β <sub>S<sub>u</sub></sub>	0.002	0.003	1.313	0.002	-0.003	0.007
β <sub>D<sub>50</sub></sub>	-2.396	5.349	-2.232	-1.137	-12.858	8.083
β <sub>0</sub>	0.922	0.440	0.477	1.004	0.053	1.770

**Figure 272.** Model realizations coupled with observed data set along each variable domain: (a) percentage of clay, (b) water content, (c) undrained shear strength, and (d) mean particle size.

## 278 Relationship Between Erodibility and Properties of Soils

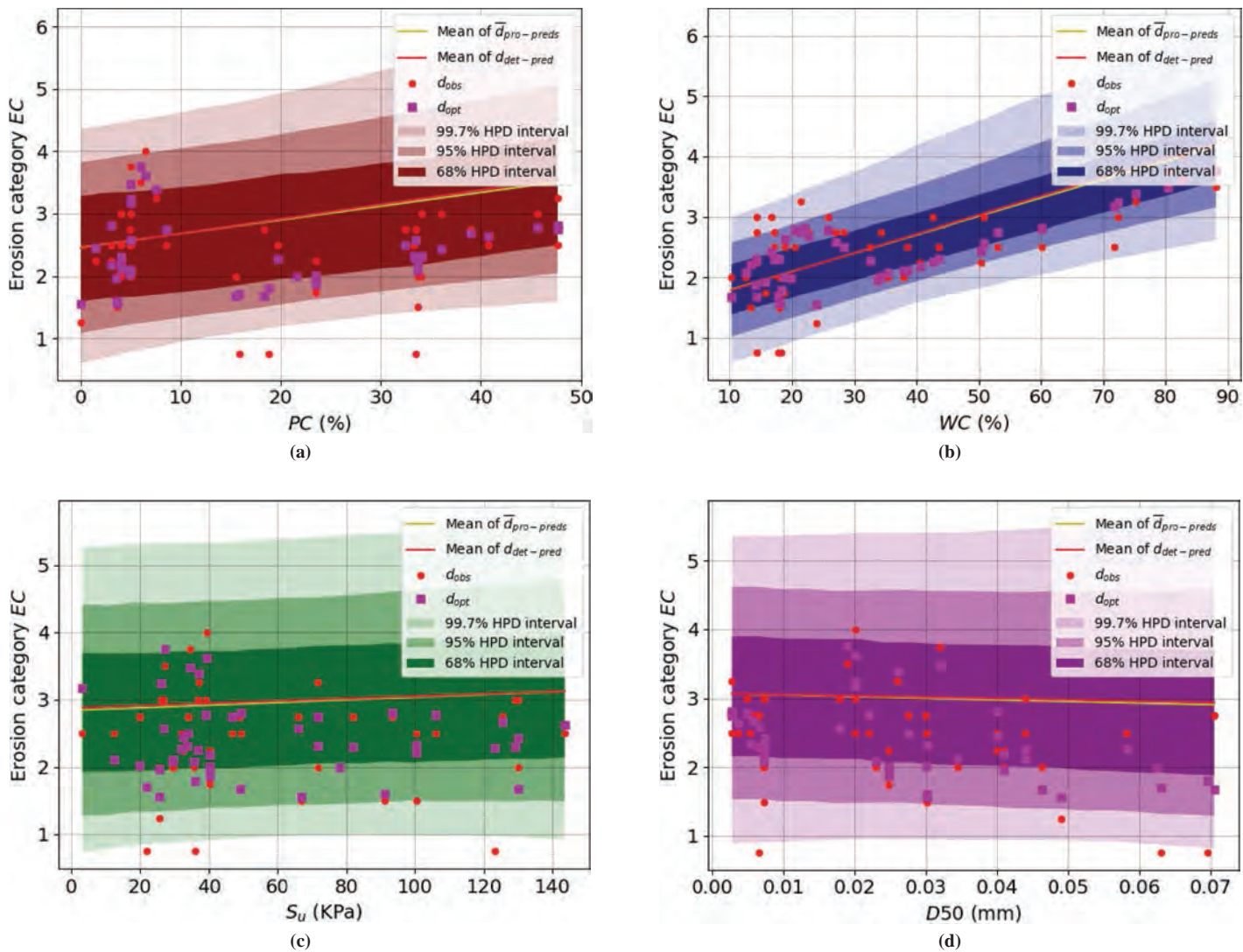


**Figure 273.** Mean and standard deviations of model predictions versus observed data: (a) percentage of clay, (b) water content, (c) undrained shear strength, and (d) mean particle size.

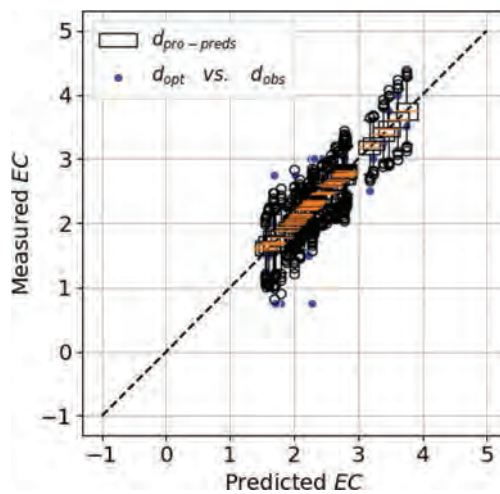


**Figure 274.** Measured EC versus predicted EC, based on optimization and probabilistic calibration results.

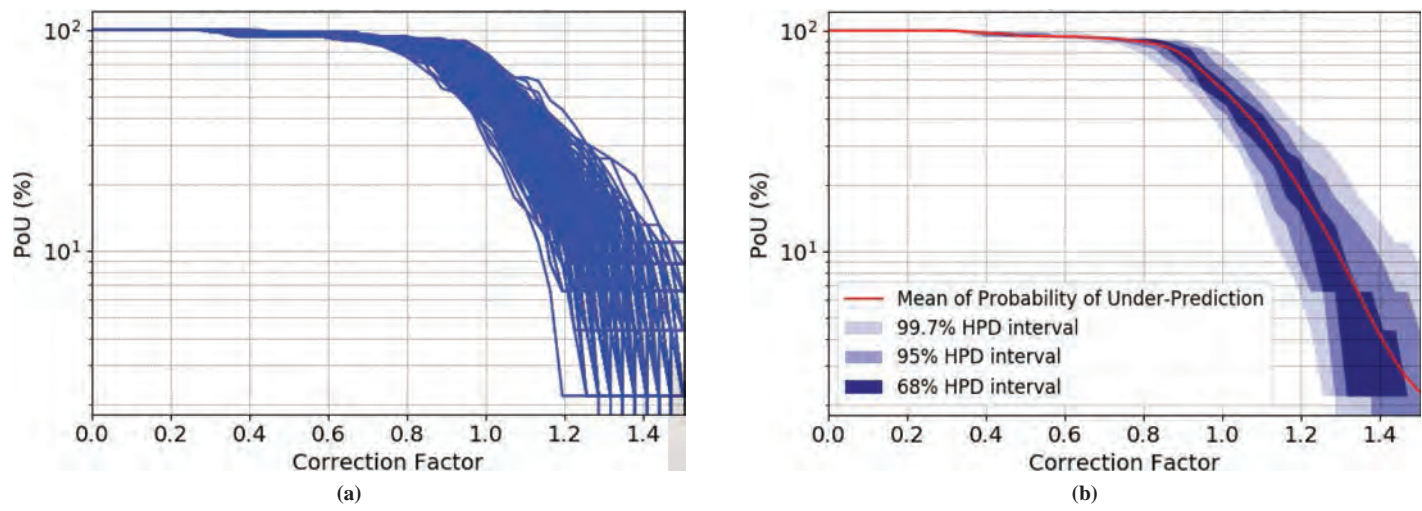


Figure 275. Probability of underprediction: (a) 1,000 realizations of POU versus correction factor and (b) mean and HPD intervals of POU.



## CHAPTER 8

# Most Robust Correlation Equations

As discussed in Chapter 7, two statistical approaches—deterministic frequentist regression and probabilistic (Bayesian) inference—were carried out to identify the best correlation equations between erodibility parameters and geotechnical properties. In this chapter, the selected models are repeated and tabulated in order to make it easier for practitioners to use them. It should be noted that the erodibility parameters are predicted using different equations, depending on which erosion test data—erosion function apparatus (EFA), jet erosion test (JET), or hole erosion test (HET)—were used to develop them. Therefore, knowledge of the strength points and limitations of each test is a vital step prior to choosing an equation. Before the most robust correlation equations are presented, the advantages and disadvantages of each test are presented in Section 8.1. Section 8.1 helps readers identify and understand the differences between the erosion tests. The engineer is free to select the best equation according to his or her objective and considering the differences between the equations. Section 8.2 presents the selected correlation equations generated using the deterministic frequentist regression approach in a tabulated format.

### 8.1 Differences Between the EFA, JET, and HET

Table 90 presents a list of advantages and disadvantages associated with the EFA, JET, and HET as well as the applications of each erosion test. The information provided here constitutes recommendations made by the authors on the basis of decades of experience in erosion testing and according to the various challenges confronted in conducting hundreds of erosion tests during this project. The development of the equations proposed in Section 8.2 was based on the data obtained in different erosion tests; therefore, a good knowledge of each test is very useful in choosing the best equation. The content of Table 90 should be studied carefully before the equations proposed in Section 8.2 are used. Chapter 2 discusses all major differences between erosion tests.

### 8.2 Deterministic Analysis (Frequentist Regression)

The best models discussed in Chapter 7 were selected for each erodibility parameter and for each erosion test. The results are shown in Table 91 through Table 101. In each table, the first column gives the accepted range of mean particle size ( $D_{50}$ ) for the proposed equations. The second column shows the model, a plot of the probability of under- or overpredicting (POU/POO) for the model, and a plot of predicted versus measured values. Such plots provide great insight into using each equation. For further information on the use of these plots, see Chapter 7, Section 7.3.3.3. The third column gives the value of  $R^2$  and the cross-validation (C.V.) score,

**Table 90. Comparison of EFA, JET, and HET.**

Advantages	Drawbacks	Applications
<b>EFA</b>		
<p>1. Minimizes the sample disturbance effect, as it takes the unextruded Shelby tube sample directly from the field.</p> <p>2. Can be used on natural samples as well as man-made samples</p> <p>3. Gives all five erodibility parameters (i.e., <math>v_c</math>, <math>\tau_c</math>, <math>E_v</math>, <math>E_t</math>, and EC). Can give the erosion function directly.</p> <p>4. Can monitor the erosion rate in real time rather than by interpolating or extrapolating using indirect equations.</p> <p>5. EFA test results are directly used as input to the TAMU-SCOUR method for bridge scour depth predictions (Arneson et al. 2012, Chapter 6).</p> <p>6. EFA can test the erodibility of the soil at any depth as long as a sample can be recovered.</p> <p>7. Gives the erosion function, which is a fundamental measure of erodibility at the element level.</p> <p>8. Can be used to test very soft to hard soils. Very broad applications. The velocity range is from 0.2 to 6 m/s.</p>	<p>1. Shear stress is indirectly measured from velocity using Moody charts, which might not be accurate. Also, the average flow velocity is used in the calculation.</p> <p>2. In some cases, obtaining samples is difficult and costly. The test needs to be done on the sample before the sample is affected by long periods of storage.</p> <p>3. Particles larger than about 40 mm cannot be tested with confidence, as the diameter of the sampling tube is 75 mm.</p> <p>4. The EFA device is fairly expensive (around \$50,000 in 2018).</p>	<p>1. Bridge scour.</p> <p>2. Meander migration.</p> <p>3. Levee overtopping.</p> <p>4. Soil improvement.</p> <p>5. Internal erosion of dams.</p>
<b>JET</b>		
<p>1. Can be run both in the field and in the lab.</p> <p>2. The latest version of the JET, the mini-JET, is simple, quick, and inexpensive compared with other types of erosion tests.</p> <p>3. Can be performed on any surface—vertical, horizontal, or inclined.</p> <p>4. Very good as an index erodibility test.</p>	<p>1. Particles larger than 30 mm cannot be tested with confidence because of the small size of the sample.</p> <p>2. Coarse-grained soils (i.e., noncohesive sand and gravel) tend to fall back into the open hole during the jet erosion process, thereby making the readings dubious.</p> <p>3. Very small-scale test application.</p> <p>4. Typically used for man-made samples. Natural samples are more difficult to test.</p> <p>5. The flow within the eroded hole and at the soil boundary is complex and difficult to analyze.</p> <p>6. Gives only three of the five possible erodibility parameters (<math>\tau_c</math>, <math>E_t</math>, and EC).</p> <p>7. The elements of erosion are inferred rather than measured directly.</p> <p>8. There are multiple interpretation techniques for predicting the critical shear stress, and these give significantly different results.</p>	<p>1. Agriculture erosion.</p> <p>2. Levees.</p>
<b>HET</b>		
<p>1. Direct similitude with piping erosion in earth dams.</p> <p>2. Can apply to a wide range of pressure heads and therefore a wide range of hydraulic shear stress at the soil–water interface.</p>	<p>1. The sample needs to be cohesive and strong enough to stand under its own weight. Therefore, the test cannot be run on loose cohesionless soils or soft cohesive soils.</p> <p>2. Very difficult to run on intact samples in Shelby tubes from the field. Only good for remolded, recompacted samples in the lab.</p> <p>3. Preparation of the test is difficult and time consuming.</p> <p>4. No direct monitoring of the erosion process. The erosion rate needs to be inferred and extrapolated.</p> <p>5. The hydraulic shear stress is inferred rather than directly measured.</p> <p>6. The data reduction process is quite subjective.</p> <p>7. Gives only three of the five possible erodibility parameters (<math>\tau_c</math>, <math>E_t</math>, and EC).</p> <p>8. The flow within the eroded hole and at the soil boundary is complex.</p>	<p>1. Internal erosion of earth dams.</p> <p>2. Suffusion.</p> <p>3. Levee breach.</p> <p>4. Soil improvement.</p>

## 282 Relationship Between Erodibility and Properties of Soils

**Table 91.** Proposed equations for critical shear stress ( $\tau_c$ ) based on the EFA test data.

$D_{50} > 0.3 \text{ mm}$	$\tau_c = D_{50}$	Refer to Figure 147
$0.074 \text{ mm} < D_{50} < 0.3 \text{ mm}$	$\tau_c = (1.58) \times C_u^{-0.04} \times \gamma^{0.02} \times D_{50}^{0.77}$ <b>Group 77: <math>\tau = f(C_u, \gamma, D_{50})</math></b>	<b>Remarks</b> <p><math>R^2 = 0.93</math> C.V. score = 0.99</p> <ol style="list-style-type: none"> <li>Refer to Group 77 in Table 50 for further information on the statistical significance of the proposed equation.</li> <li>The POU versus correction factor plot is based on the data used to develop the proposed equation.</li> <li>To reach 90% confidence that the predicted <math>\tau_c</math> is less than the actual <math>\tau_c</math>, the predicted value should be multiplied by 0.82. (with 0.3 Pa offset).</li> </ol>

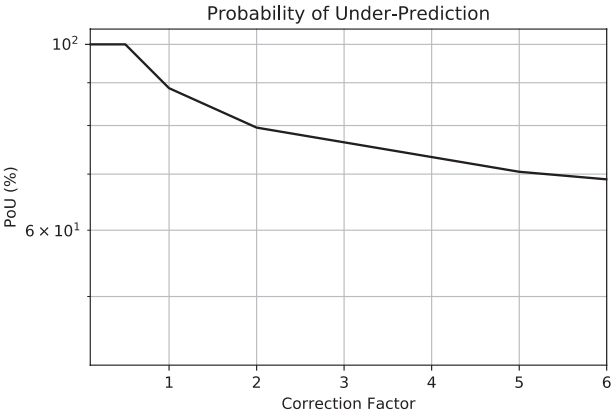
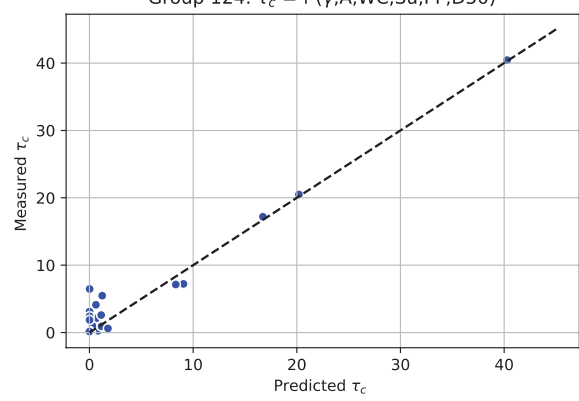
presents remarks on the proposed equation, and gives the correction factor needed to reach 90% confidence in under- or overpredicting the measured erodibility parameter. The units used for each parameter are indicated in Table 47 (Chapter 7) and also in Appendix 4.

Table 91 shows the proposed correlation equations for predicting the critical shear stress ( $\tau_c$ ) based on the EFA test. This table presents the recommended correlation equations for predicting critical shear stress in different  $D_{50}$  ranges. Table 92 and Table 93 show the proposed correlation equations for predicting the critical shear stress ( $\tau_c$ ) based on the JET and HET, respectively.

Table 94 shows the proposed correlation equations for predicting the critical velocity ( $v_c$ ) based on the EFA test. Because the HET and the JET do not report critical velocity as an output erodibility parameter, the critical velocity equations are proposed based on the EFA test alone.

Table 95 shows the proposed correlation equations for predicting the initial linear slope of the shear stress–erosion rate plot ( $E_v$ ) based on the EFA test. Table 96 and Table 97 show the proposed correlation equations for predicting  $E_v$  based on the JET and HET, respectively. It must be noted that the proposed equation for  $D_{50} < 0.074 \text{ mm}$  is based on Group 108 in the HET/Global data set (see Table 68 in Chapter 7). The reason for this selection is that the

**Table 91. (Continued).**

$D_{50} > 0.3 \text{ mm}$	$\tau_c = D_{50}$	Refer to Figure 147
$D_{50} < 0.074 \text{ mm}$	$\tau_c = (158.06) \times \gamma^5 \times A^{-0.46} \times WC^{10.03} \times S_u^{1.83} \times PF^{-18.28} \times D_{50}^{-4.21}$  <p style="text-align: center;">Probability of Under-Prediction</p> <p style="text-align: center;">POU (%)</p> <p style="text-align: center;">Correction Factor</p>  <p style="text-align: center;">Group 124: <math>\tau_c = f (\gamma, A, WC, Su, PF, D50)</math></p> <p style="text-align: center;">Measured <math>\tau_c</math></p> <p style="text-align: center;">Predicted <math>\tau_c</math></p>	<p><math>R^2 = 0.94</math> C.V. score = 0.66</p> <ol style="list-style-type: none"> <li>Refer to Group 124 in Table 48 for further information on the statistical significance of the proposed equation.</li> <li>The POU versus correction factor plot is based on the data used to develop the proposed equation.</li> <li>There is almost 90% chance that the predicted value is less than the actual <math>\tau_c</math> (with 0.5 Pa offset).</li> </ol>

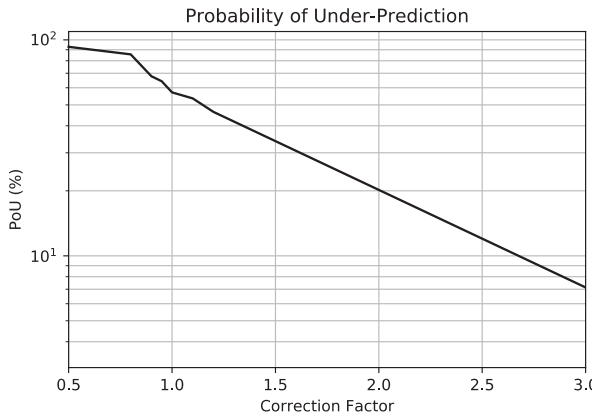
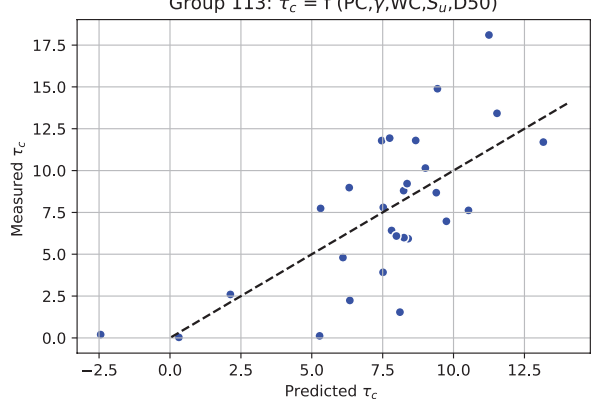
data used in Group 108 were all related to soils with mean particle size less than 0.074 mm. That is, Group 108 in both HET/Global and HET/Fine would lead to the same selected equation.

Table 98 shows the proposed correlation equations for predicting the initial linear slope of the velocity–erosion rate plot ( $E_v$ ) based on the EFA test. Because the HET and the JET do not report  $E_v$  as an output erodibility parameter, the proposed equations are based on the EFA test alone.

Table 99 shows the proposed correlation equations for predicting the erosion category (EC) based on the EFA test. Table 100 and Table 101 show the proposed correlation equations for predicting EC based on the JET and HET, respectively.

## 284 Relationship Between Erodibility and Properties of Soils

**Table 92.** Proposed equation for critical shear stress ( $\tau_c$ ) based on the JET data.

$D_{50} < 0.3 \text{ mm}$	$\tau_c = -0.248 \times PC - 1.23 \times \gamma + 0.21 \times WC + 0.07 \times S_u - 36.89 \times D_{50} + 31.82$  <p>Probability of Under-Prediction</p> <p>PoU (%)</p> <p>Correction Factor</p>  <p>Group 113: <math>\tau_c = f(PC, \gamma, WC, S_u, D50)</math></p> <p>Measured <math>\tau_c</math></p> <p>Predicted <math>\tau_c</math></p>	Remarks
	<p><math>R^2 = 0.50</math></p> <p>C.V. score = 0.10</p> <ol style="list-style-type: none"> <li>Refer to Group 113 in Table 51 for further information on the statistical significance of the proposed equation.</li> <li>The POU versus correction factor plot is based on the data used to develop the proposed equation.</li> <li>To reach 90% confidence that the predicted <math>\tau_c</math> is less than the actual <math>\tau_c</math>, the predicted value should be multiplied by 0.6 (with 1 Pa offset).</li> </ol>	

**Table 93.** Proposed equation for critical shear stress ( $\tau_c$ ) based on the HET data.

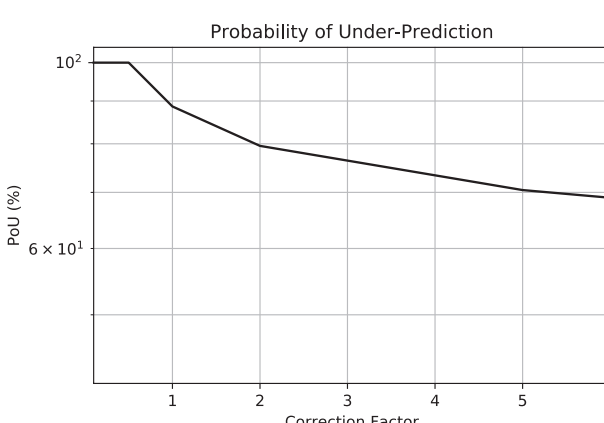
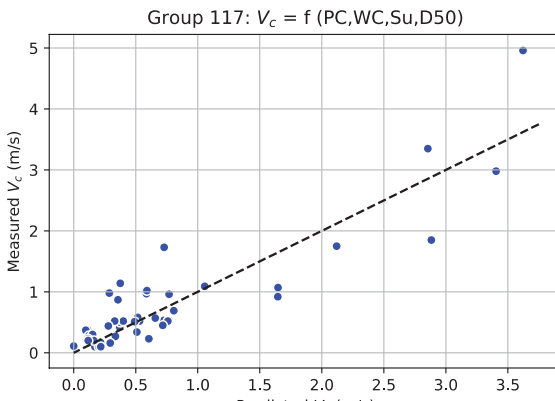
$D_{50} < 0.3 \text{ mm}$	<p><math>\tau_c = (25.07) \times \text{PI}^{0.27} \times S_u^{0.55} \times D_{50}^{0.5}</math></p> <p>Probability of Under-Prediction</p> <p>POU (%)</p> <p>Correction Factor</p> <p>Group 19: <math>\tau = f(\text{PI}, \text{Su}, D_{50})</math></p> <p>Measured <math>\tau</math> (Pa)</p> <p>Predicted <math>\tau</math> (Pa)</p>	<p><b>Remarks</b></p> <p><math>R^2 = 0.64</math> C.V. score = 0.43</p> <ol style="list-style-type: none"> <li>Refer to Group 19 in Table 54 for further information on the statistical significance of the proposed equation.</li> <li>The POU versus correction factor plot is based on the data used to develop the proposed equation.</li> <li>To reach 90% confidence that the predicted <math>\tau_c</math> is less than the actual <math>\tau_c</math>, the predicted value should be multiplied by 0.6 (with 1 Pa offset).</li> </ol>
---------------------------	--	--

## 286 Relationship Between Erodibility and Properties of Soils

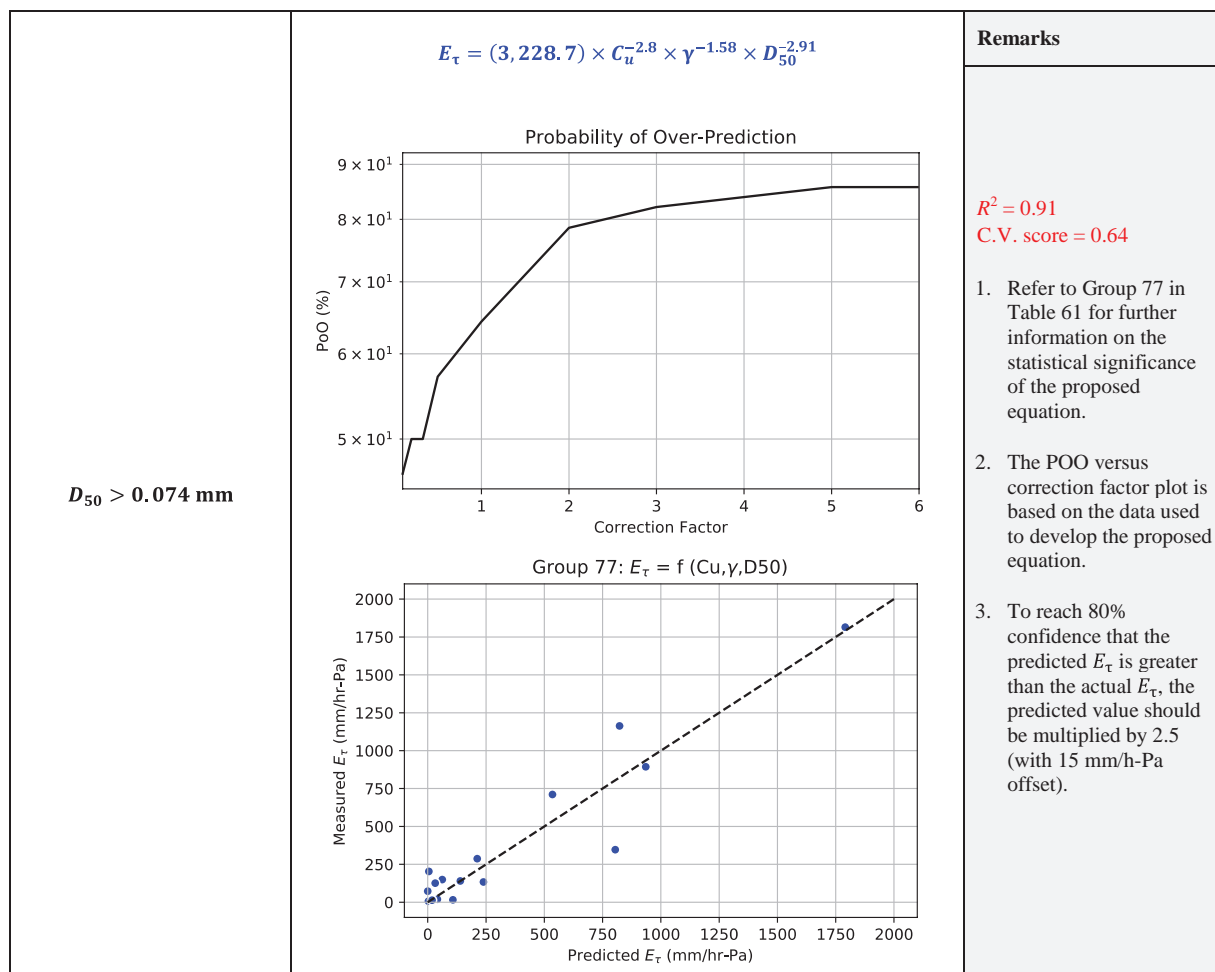
**Table 94.** Proposed equations for critical velocity ( $v_c$ ) based on the EFA test data.

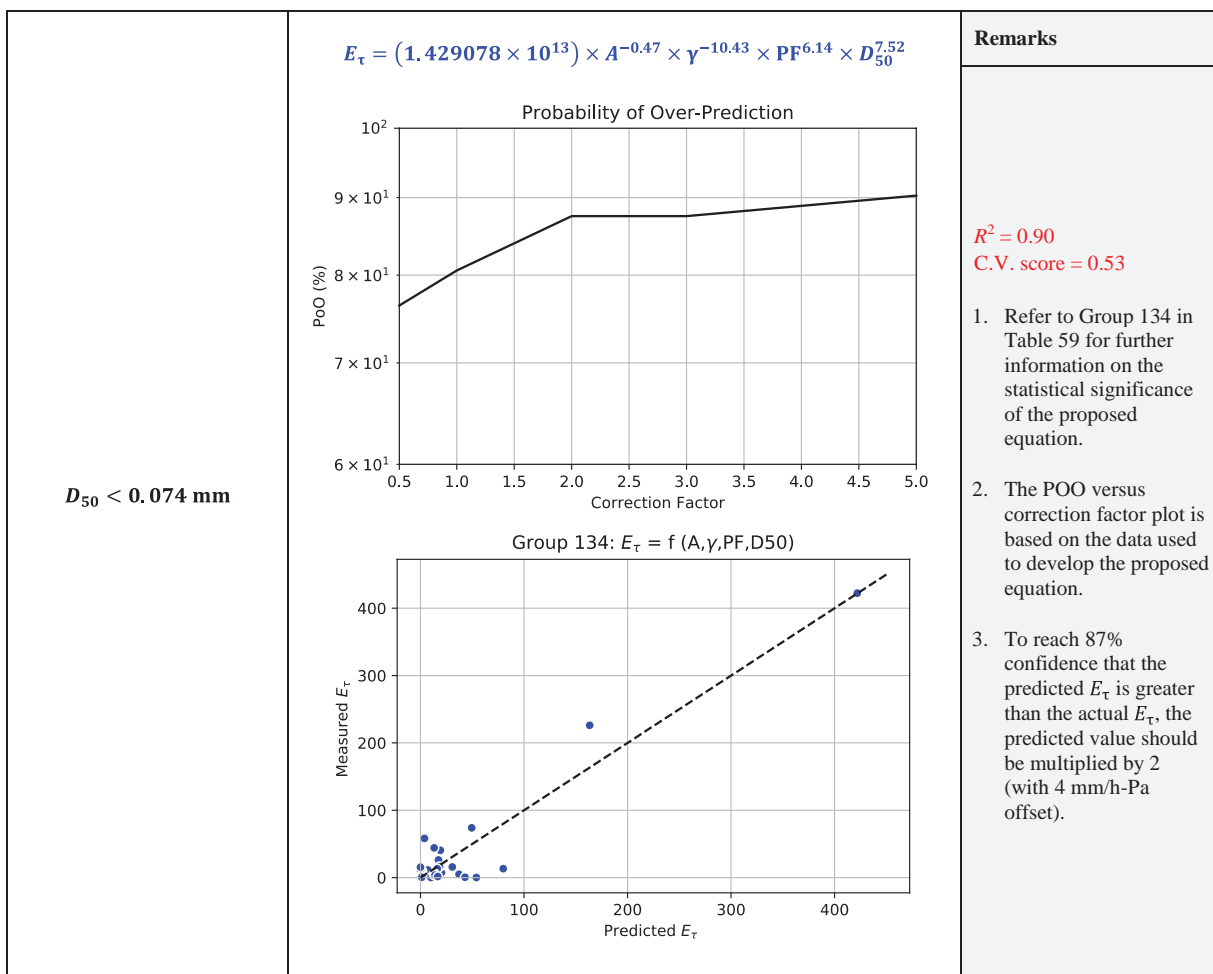
$D_{50} > 0.3 \text{ mm}$	$v_c = 0.315 \times (D_{50})^{0.5}$	Refer to Figure 146
$0.074 \text{ mm} < D_{50}$	$v_c = (3 \times 10^{-15}) \times PI^{1.24} \times \gamma^{8.11} \times WC^{0.54} \times D_{50}^{2.35}$ <b>Group 27: <math>V_c = f(PI, \gamma, WC, D50)</math></b>	<p><b>Remarks</b></p> <p><math>R^2 = 0.88</math> C.V. score = 0.72</p> <ol style="list-style-type: none"> <li>Refer to Group 27 in Table 58 for further information on the statistical significance of the proposed equation.</li> <li>The POU versus correction factor plot is based on the data used to develop the proposed equation.</li> <li>To reach 90% confidence that the predicted <math>v_c</math> is less than the actual <math>v_c</math>, the predicted value should be multiplied by 0.7 (with 0.1 m/s offset).</li> </ol>

**Table 94. (Continued).**

$D_{50} > 0.3 \text{ mm}$	$v_c = 0.315 \times (D_{50})^{0.5}$	Refer to Figure 146
$D_{50} < 0.074 \text{ mm}$	$v_c = (2.518 \times 10^{-5}) \times PC^{0.2} \times WC^{2.06} \times Su^{0.51} \times D_{50}^{-0.13}$  <p>Probability of Under-Prediction</p> <p>POU (%)</p> <p>Correction Factor</p>  <p>Measured <math>V_c</math> (m/s)</p> <p>Predicted <math>V_c</math> (m/s)</p>	<b>Remarks</b> <p><math>R^2 = 0.80</math> C.V. score = 0.80</p> <ol style="list-style-type: none"> <li>Refer to Group 117 in Table 56 for further information on the statistical significance of the proposed equation.</li> <li>The POU versus correction factor plot is based on the data used to develop the proposed equation.</li> <li>To reach 90% confidence that the predicted <math>v_c</math> is less than the actual <math>v_c</math>, the predicted value should be multiplied by 0.8 (with 0.2 m/s offset).</li> </ol>

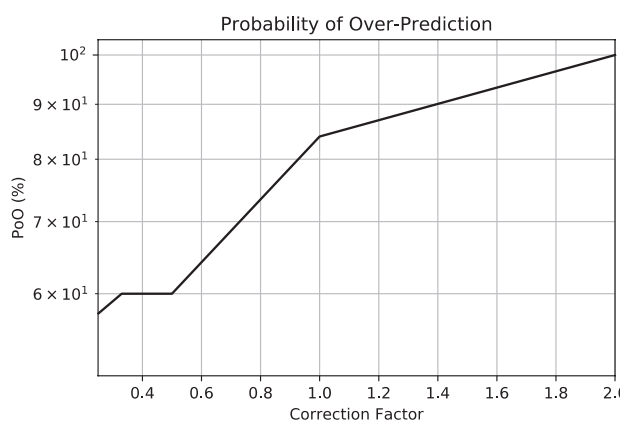
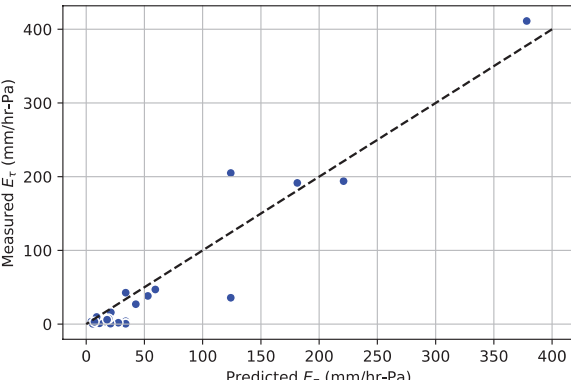
## 288 Relationship Between Erodibility and Properties of Soils

**Table 95.** Proposed equations for shear stress slope ( $E_\tau$ ) based on the EFA test data.

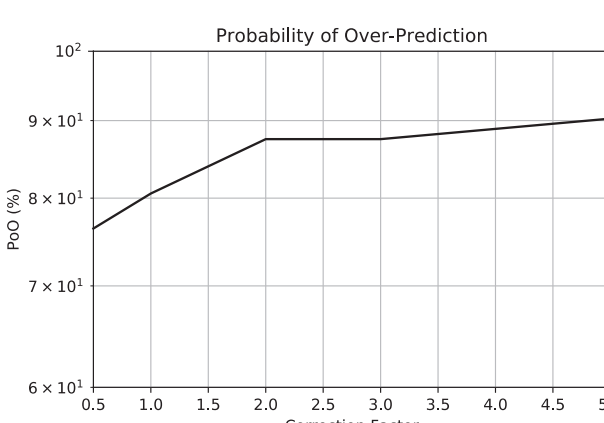
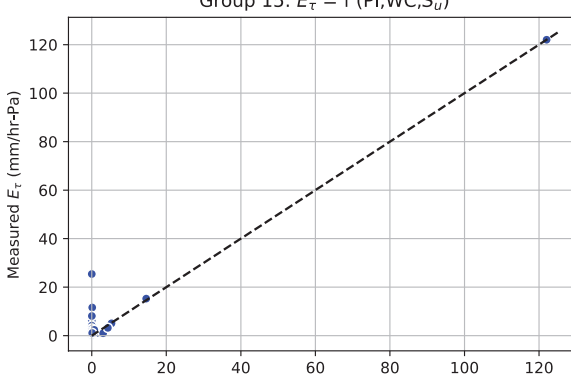
**Table 95. (Continued).**

## 290 Relationship Between Erodibility and Properties of Soils

**Table 96.** Proposed equations for shear stress slope ( $E_\tau$ ) based on the JET data.

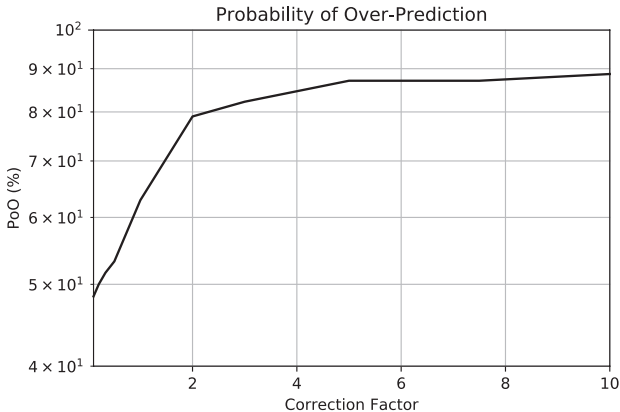
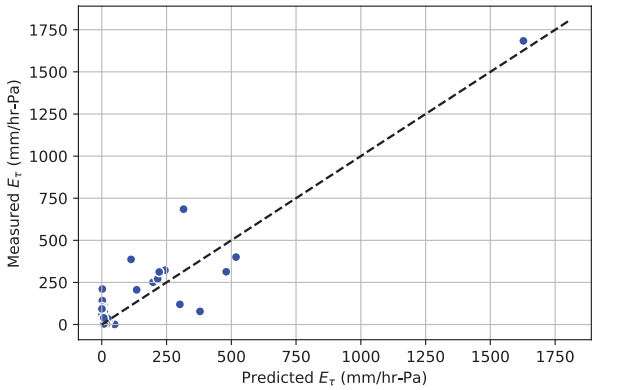
$D_{50} > 0.074 \text{ mm}$	$E_\tau = (55,637,006,351,614) \times PI^{-0.19} \times \gamma^{-6.39} \times WC^{-3.67}$  <b>Group 5: <math>E_\tau = f(PI, \gamma, WC)</math></b> 	<b>Remarks</b>
	<p><math>R^2 = 0.90</math>  <math>C.V. \text{ score} = 0.67</math></p> <ol style="list-style-type: none"> <li>Refer to Group 5 in Table 65 for further information on the statistical significance of the proposed equation.</li> <li>The POO versus correction factor plot is based on the data used to develop the proposed equation.</li> <li>To reach 90% confidence that the predicted <math>E_\tau</math> is greater than the actual <math>E_\tau</math>, the predicted value should be multiplied by 1.4 (with 5 mm/h-Pa offset).</li> </ol>	

**Table 96. (Continued).**

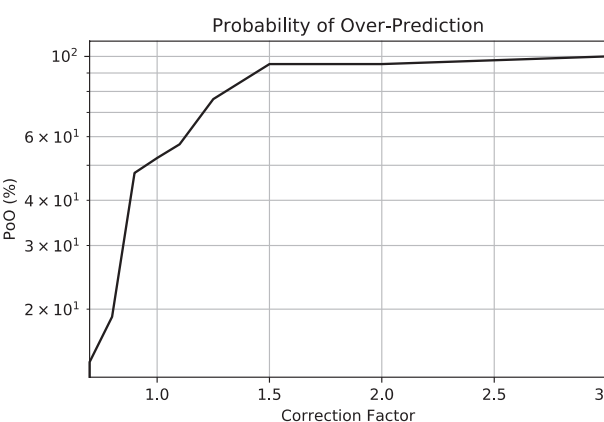
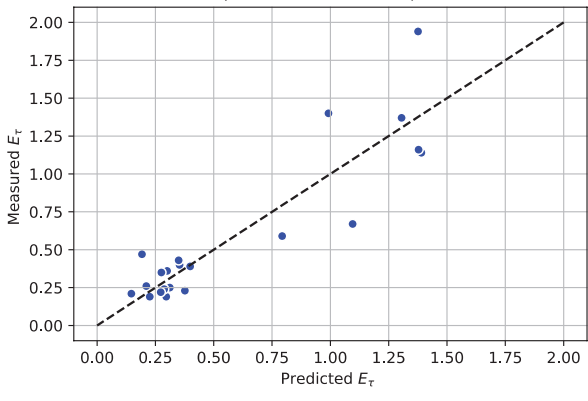
$D_{50} < 0.074 \text{ mm}$	$E_\tau = (396,599.6) \times \text{PI}^{-2.54} \times \text{WC}^{4.58} \times S_u^{-4.91}$  <b>Group 15: <math>E_\tau = f(\text{PI}, \text{WC}, S_u)</math></b> 	Remarks
	<p style="text-align: right;"><math>R^2 = 0.93</math> C.V. score = 0.23</p> <ol style="list-style-type: none"> <li>Refer to Group 15 in Table 63 for further information on the statistical significance of the proposed equation.</li> <li>The POO versus correction factor plot is based on the data used to develop the proposed equation.</li> <li>To reach 88% confidence that the predicted <math>E_\tau</math> is greater than the actual <math>E_\tau</math>, the predicted value should be multiplied by 2 (with 6 mm/h-Pa offset).</li> </ol>	

## 292 Relationship Between Erodibility and Properties of Soils

**Table 97. Proposed equations for shear stress slope ( $E_\tau$ ) based on the HET data.**

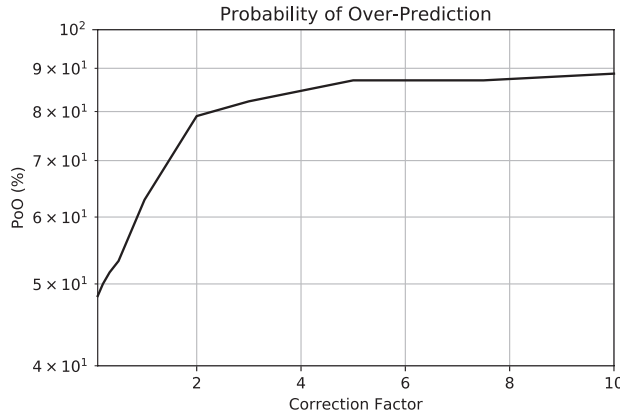
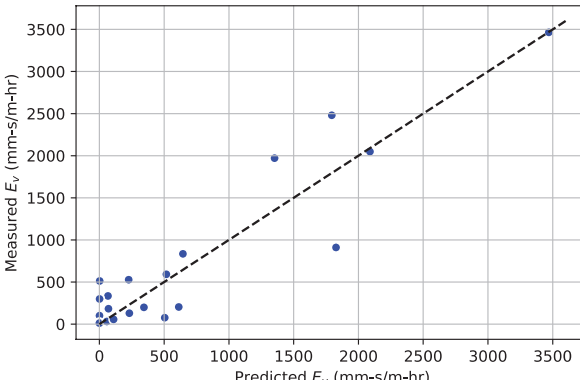
	$E_\tau = (2.951) \times \gamma^{26.08} \times WC^{-7.48} \times PF^{-19.96} \times D_{50}^{-5.32}$  <p style="text-align: center;">Probability of Over-Prediction</p>  <p style="text-align: center;">Group 40: <math>E_\tau = f (\gamma, WC, PF, D50)</math></p>	<b>Remarks</b> $R^2 = 0.86$ C.V. score = 0.55 <ul style="list-style-type: none"> <li>1. Refer to Group 40 in Table 66 for further information on the statistical significance of the proposed equation.</li> <li>2. The POO versus correction factor plot is based on the data used to develop the proposed equation.</li> <li>3. To reach 80% confidence that the predicted <math>E_\tau</math> is greater than the actual <math>E_\tau</math>, the predicted value should be multiplied by 2 (with 10 mm/h-Pa offset).</li> </ul>
<b>0.3 mm &gt; <math>D_{50}</math> &gt; 0.074 mm</b> Use this equation when PF > 30%.		

**Table 97. (Continued).**

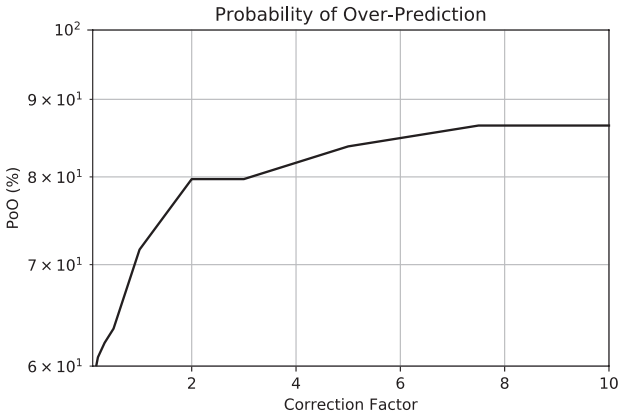
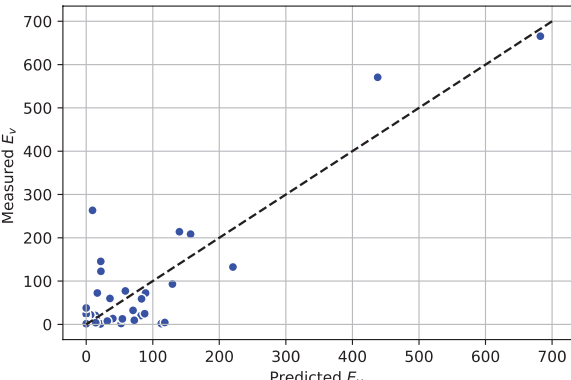
$D_{50} < 0.074 \text{ mm}$	$E_\tau = (9 \times 10^{-6}) \times LL^{-0.35} \times PL^{1.59} \times \gamma^{3.3} \times PC^{-0.48} \times S_u^{-0.19}$  <b>Group 108: <math>E_\tau = f(LL, PL, \gamma, PC, S_u)</math></b> 	<b>Remarks</b>
	$R^2 = 0.81$ $C.V. \text{ score} = 0.531$ <ul style="list-style-type: none"> <li>1. Refer to Group 108 in Table 68 for further information on the statistical significance of the proposed equation.</li> <li>2. The POO versus correction factor plot is based on the data used to develop the proposed equation.</li> <li>3. To reach 90% confidence that the predicted <math>E_\tau</math> is greater than the actual <math>E_\tau</math>, the predicted value should be multiplied by 1.45 (with 0 mm/h-Pa offset).</li> </ul>	

## 294 Relationship Between Erodibility and Properties of Soils

**Table 98. Proposed equations for velocity slope ( $E_v$ ) based on the EFA test data.**

$D_{50} > 0.074 \text{ mm}$	$E_v = (88,969.4) \times C_u^{-1.77} \times \gamma^{-2.26} \times WC^{0.34} \times D_{50}^{-1.69}$  <b>Group 86: <math>E_v = f(C_u, \gamma, WC, D_{50})</math></b> 	Remarks
		<p><math>R^2 = 0.86</math>  <math>C.V.</math> score = 0.64</p> <ol style="list-style-type: none"> <li>Refer to Group 86 in Table 71 for further information on the statistical significance of the proposed equation.</li> <li>The POO versus correction factor plot is based on the data used to develop the proposed equation.</li> <li>To reach 80% confidence that the predicted <math>E_v</math> is greater than the actual <math>E_v</math>, the predicted value should be multiplied by 5 (with 10 mm-s/m-h offset).</li> </ol>

**Table 98. (Continued).**

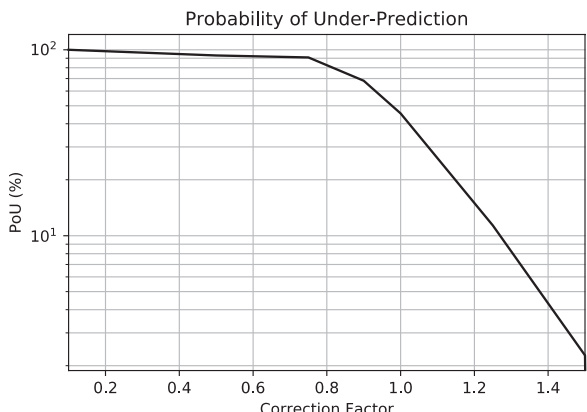
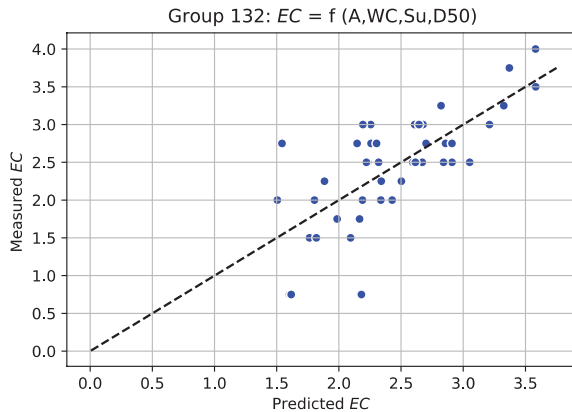
	$E_v = (1.682339 \times 10^{13}) \times D_{50}^{5.10} \times \gamma^{-9.20} \times WC^{-1.13} \times PF^{4.69} \times A^{-0.01}$  <b>Group 126: <math>E_v = f(D_{50}, \gamma, WC, PF, A)</math></b> 	Remarks
$D_{50} < 0.074 \text{ mm}$	<p style="text-align: right;"><math>R^2 = 0.79</math> <math>C.V. \text{ score} = 0.52</math></p> <ol style="list-style-type: none"> <li>Refer to Group 126 in Table 69 for further information on the statistical significance of the proposed equation.</li> <li>The POO versus correction factor plot is based on the data used to develop the proposed equation.</li> <li>To reach 80% confidence that the predicted <math>E_v</math> is greater than the actual <math>E_v</math>, the predicted value should be multiplied by 2 (with 10 mm-s/m-h offset).</li> </ol>	

## 296 Relationship Between Erodibility and Properties of Soils

**Table 99. Proposed equations for erosion category (EC) based on the EFA test data.**

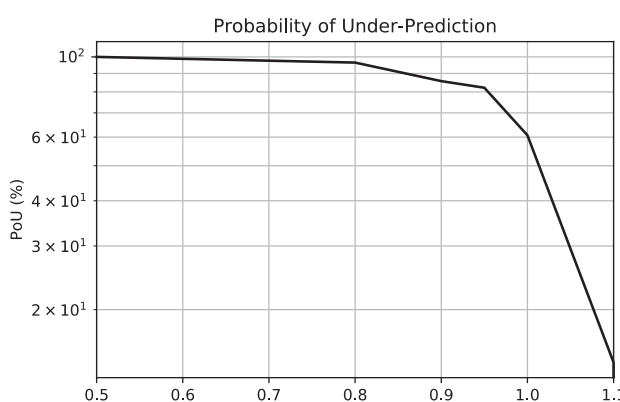
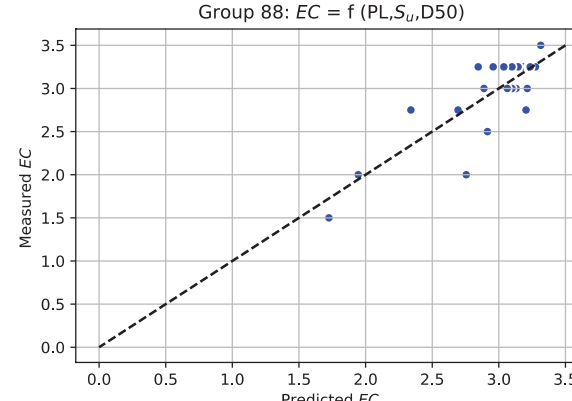
	Remarks
<p><b>0.3 mm &gt; <math>D_{50}</math> &gt; 0.074 mm</b></p> <p><math>EC = (1.12) \times C_u^{0.1} \times WC^{-0.28} \times VST^{0.02} \times D_{50}^{-0.44}</math></p> <p>Probability of Under-Prediction</p> <p>POU (%)</p> <p>Correction Factor</p> <p><b>Group 91: <math>EC = f(Cu, WC, VST, D50)</math></b></p> <p>Measured EC</p> <p>Predicted EC</p>	<p><math>R^2 = 0.92</math> C.V. score = 0.80</p> <ol style="list-style-type: none"> <li>Refer to Group 91 in Table 75 for further information on the statistical significance of the proposed equation.</li> <li>The POU versus correction factor plot is based on the data used to develop the proposed equation.</li> <li>To reach 90% confidence that the predicted EC is less than the actual EC, the predicted value should be multiplied by 0.84.</li> </ol>

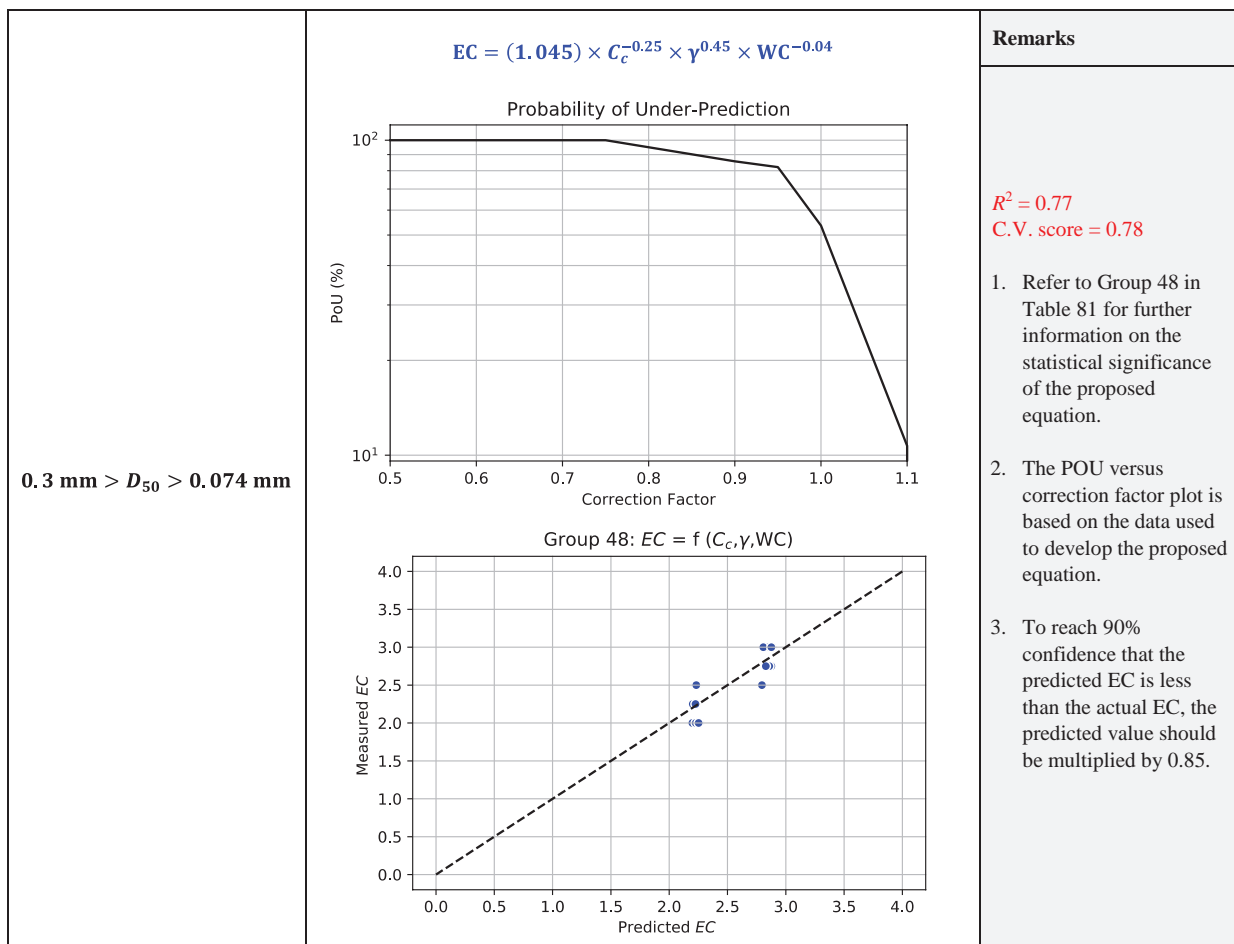
**Table 99. (Continued).**

$D_{50} < 0.074 \text{ mm}$	$\text{EC} = (0.1933) \times A^{-0.06} \times \text{WC}^{0.51} \times S_u^{0.09} \times D_{50}^{-0.12}$ 	<b>Remarks</b> $R^2 = 0.55$ $\text{C.V. score} = 0.53$ <ol style="list-style-type: none"> <li>Refer to Group 132 in Table 73 for further information on the statistical significance of the proposed equation.</li> <li>The POU versus correction factor plot is based on the data used to develop the proposed equation.</li> <li>To reach 90% confidence that the predicted EC is less than the actual EC, the predicted value should be multiplied by 0.75.</li> </ol>
		

## 298 Relationship Between Erodibility and Properties of Soils

**Table 100.** Proposed equation for erosion category (EC) based on the JET data.

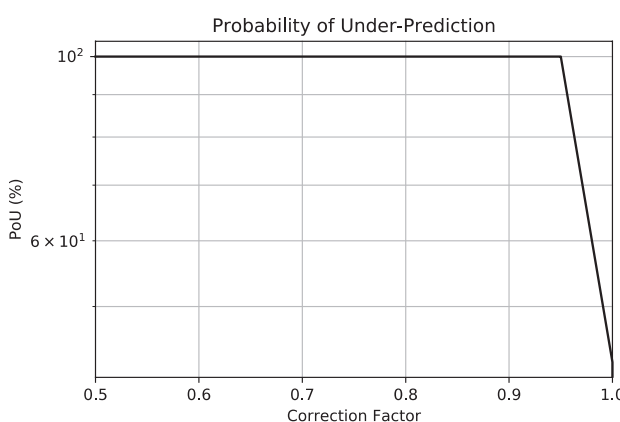
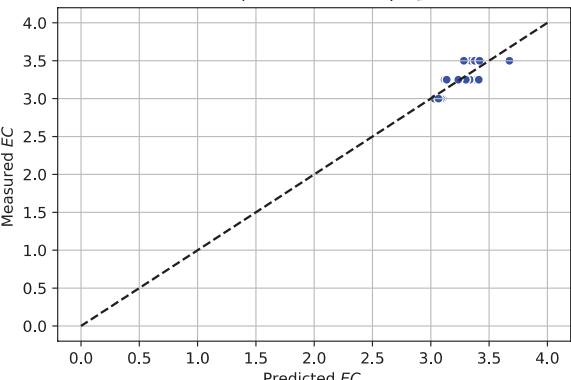
$D_{50} < 0.3 \text{ mm}$	$\text{EC} = -0.022 \times \text{PL} + 0.0031 \times S_u - 5.5 \times D_{50} + 3.34$  <b>Group 88: <math>EC = f(\text{PL}, S_u, D_{50})</math></b> 	Remarks
	$R^2 = 0.70$ $\text{C.V. score} = 0.58$ <ul style="list-style-type: none"> <li>1. Refer to Group 88 in Table 76 for further information on the statistical significance of the proposed equation.</li> <li>2. The POU versus correction factor plot is based on the data used to develop the proposed equation.</li> <li>3. To reach 90% confidence that the predicted EC is less than the actual EC, the predicted value should be multiplied by 0.85.</li> </ul>	

**Table 101.** Proposed equations for erosion category (EC) based on the HET data.

(continued on next page)

## 300 Relationship Between Erodibility and Properties of Soils

**Table 101. (Continued).**

$D_{50} < 0.074 \text{ mm}$	$\text{EC} = (1.67) \times \text{PI}^{0.04} \times \gamma^{0.15} \times S_u^{0.03}$  <b>Group 12: <math>\text{EC} = f(\text{PI}, \gamma, S_u)</math></b> 	<b>Remarks</b>
	$R^2 = 0.70$ C.V. score = 0.54 <ul style="list-style-type: none"> <li>1. Refer to Group 12 in Table 79 for further information on the statistical significance of the proposed equation.</li> <li>2. The POU versus correction factor plot is based on the data used to develop the proposed equation.</li> <li>3. To reach 100% confidence that the predicted EC is less than the actual EC, the predicted value should be multiplied by 0.95.</li> </ul>	



## CHAPTER 9

# Conclusions and Recommendations

The goal of this project was to develop reliable and simple equations quantifying the erodibility of soils on the basis of soil properties. The reliability must take into account the accuracy required for erosion-related projects, while the simplicity must consider the economic aspects of erosion-related projects. Different soils exhibit different erodibility (e.g., sand, clay); therefore, erodibility is tied to soil properties. However, many researchers have attempted to develop such equations without much success. One problem is that erodibility is not a single number, but a relationship between the erosion rate and the water velocity or the hydraulic shear stress. This erosion function is a curve, and it is difficult to correlate a curve to soil properties.

Another problem that needs to be solved is associated with the availability of several erosion testing devices. In the laboratory, these include the pinhole test, the hole erosion test (HET), the jet erosion test (JET), the rotating cylinder test, and the erosion function apparatus (EFA) test. In the field, they include the JET, the North Carolina State University in situ scour evaluation probe test, the Texas A&M University (TAMU) borehole erosion test (BET) and pocket erodometer test, and others. All these tests measure the soil erodibility but give different results. It is important to give engineers options so that they can choose one test or another. Therefore, it would be helpful if all these tests could give the same answer. Indeed, the soil does not know the difference between erosion tests, and the erosion function is a fundamental property of the soil. Experimental and numerical efforts were made to advance in this direction. The findings for each chapter are summarized below.

### 9.1 Summary of Chapters 1 Through 8

#### 9.1.1 Chapter 1: Introduction

Chapter 1 is divided into two parts. The first part presented a definition for the erosion phenomenon and introduced different types of erosion. The general parameters for quantifying soil erodibility and the constitutive models for erosion were briefly discussed. The second part of the chapter presented the research approach. The project tasks were described, and a summary of how and where within the report each one of the tasks is addressed was provided.

#### 9.1.2 Chapter 2: Existing Erosion Tests

Chapter 2 presented a comprehensive literature review on different soil erosion tests. Tests developed all over the world in the past few decades were discussed in terms of their application in the lab or in the field and their application in surface erosion or internal erosion problems. The advantages and disadvantages of the most important tests were explained, and a table summarizing selected tests was provided at the end of the chapter. The advantages, drawbacks, and

**302 Relationship Between Erodibility and Properties of Soils**

applications of the three major erosion tests (EFA, JET, and HET) used in this study are presented in Table 90 (Chapter 8).

### **9.1.3 Chapter 3: Existing Correlations Between Soil Erodibility and Soil Properties**

Chapter 3 provided a literature review of the existing correlations between soil erodibility and soil properties. The observations and correlation equations proposed by various researchers in the past century were summarized. The factors that influence erosion, including the less easily obtained engineering properties, were presented and discussed in detail. Table 10 (Chapter 3) summarizes these parameters.

### **9.1.4 Chapter 4: Erosion Experiments**

Chapter 4 began with a description of the Soil Erosion Laboratory at TAMU. The erosion testing devices built as part of this research project, as well as the refurnished and armored EFA, were presented. The test plan matrix proposed for this project was presented and discussed. Next, the results of the hundreds of erosion tests performed during this project were presented and discussed. The chapter concludes with a discussion of how the geotechnical engineering properties associated with each tested sample were obtained at TAMU and presented in the form of a spreadsheet of soil geotechnical properties for each sample. The erosion spreadsheets and geotechnical properties spreadsheets for all samples tested in this project are available in Appendices 1 and 2.

### **9.1.5 Chapter 5: Organization and Interpretation of the Data**

Chapter 5 introduced NCHRP-Erosion, the erosion spreadsheet developed for this project. NCHRP-Erosion includes records of the geotechnical properties of each sample from nearly 1,000 erosion tests: approximately 750 tests collected from literature review and from contacts with researchers and organizations around the world and the approximately 250 erosion tests performed during this project. The chapter explained the process of collecting and compiling the worldwide data and lists the people and organizations who helped gather the information.

In NCHRP-Erosion, all the erosion data are analyzed according to the procedures described in the report for five erodibility parameters:

1. Critical shear stress,  $\tau_c$ ,
2. Critical velocity,  $v_c$ ,
3. Initial slope of velocity,  $E_v$ ,
4. Initial slope of shear stress,  $E_\tau$ , and
5. Erosion category, EC.

NCHRP-Erosion includes 50 columns and nearly 1,000 rows. Chapter 5 discussed the column contents in detail. The chapter also included the Inquiry Operation Manual that explains how to search for specific data within NCHRP-Erosion.

### **9.1.6 Chapter 6: Comparison of Selected Soil Erosion Tests by Numerical Simulation**

Chapter 6 presented a comparison of selected soil erosion tests (EFA, HET, JET, and BET) with results obtained with numerical simulation software. This chapter was divided into two sections: (1) numerical simulations on nonerodible soils and (2) numerical simulations including

the erosion process. The first part of the chapter dealt with the evolution of hydraulic shear stress and the velocity profile with the assumption that the soil was not erodible. A discrepancy was observed between the Moody chart predictions and the numerical simulations, and the Moody charts were found generally to overestimate shear stress. This discrepancy was more pronounced in higher shear stress values (up to 100% difference between the Moody chart prediction and the numerical simulation in one case). In the second part of the chapter, the erosion function was assigned to the soil–water interface, and the erosion was numerically simulated with a moving boundary for selected erosion tests. The results of the numerical simulations were compared with the actual observations for each test. The findings showed that the erosion function obtained from the EFA test for each sample can reasonably be used to produce a scour versus time plot similar to what the JET, the HET, and the BET experiments would produce. However, the variety of interpretation techniques used for each test to obtain the shear stress in the soil–water interface leads to different erosion functions. Therefore, one must be aware of the interpretation techniques that each test uses to obtain the erosion function (erosion rate versus shear stress).

### **9.1.7 Chapter 7: Development of Correlation Equations**

Chapter 7 was dedicated to the main goal of this study: the development of correlation equations. The chapter was divided into four major parts. The first part presented a preliminary and quick method for determining the erosion resistance of a soil using only the Unified Soil Classification System (USCS) of the soil and associated erosion categories. The plot of erosion rate versus velocity based on the USCS categories is shown in Figure 145 (Chapter 7). In the figure, the width of each box is associated with a USCS category represents the zone in which 90% of the EFA results performed on such samples would fall in the Erosion Category Chart. For instance, if the soil type of a location in an arbitrary geotechnical site were classified as SM (silty sand) according to the USCS, it would most likely (with close to 90% confidence based on the EFA results compiled in NCHRP-Erosion) fall within Category II (high erodibility).

The second part of Chapter 7 dealt with improving existing plots of critical velocity/critical shear stress versus mean particle size. It was observed that for soils with mean particle size greater than 0.3 mm, the following relationships exist between the critical velocity/shear stress and mean particle size:  $v_c$  (m/s) = 0.315( $D_{50}$  (mm))<sup>0.5</sup> and  $\tau_c$  (Pa) =  $D_{50}$  (mm). It was also concluded that for fine-grained soils, there is no direct relationship between critical velocity/shear stress and mean particle size. However, the data could be bracketed with an upper bound and a lower bound equation.

The third part of this chapter presented the frequentist regression technique. The step-by-step procedure for implementing the frequentist regression technique, the experimental design, and the model selection process were discussed, and the results of the regressions were presented. The best correlation equations were selected after passing through a four-filter process including

1.  $R^2$ ,
2. Mean square error (MSE),
3. Statistical  $F$ -test, and
4. Cross-validation test.

POO and POU plots were also presented for the selected equations. Table 102 to Table 106 show the selected equations for each erodibility parameter and for each data set.

The last part of this chapter dealt with a probabilistic approach as opposed to the deterministic approach presented in the previous section. The probabilistic approach was based on the Bayesian inference method. The methodology of the Bayesian inference method and its results were presented in Section 7.4 and are also given in Appendix 5.

## 304 Relationship Between Erodibility and Properties of Soils

**Table 102.** Selected models for critical shear stress,  $\tau_c$ .

Group No.	Independent Variables <sup>a</sup>	Data Set <sup>b</sup>	Model Expression <sup>c</sup>	$R^2$	Cross-Validation Score
124	$\gamma, A, WC, S_u, PF, D_{50}$	EFA/Fine ( $n = 44$ )	$\tau_c = (158.06) \times \gamma^5 \times A^{-0.46} \times WC^{10.03} \times S_u^{1.83} \times PF^{-18.28} \times D_{50}^{-4.21}$	0.94	0.66
77	$C_u, \gamma, D_{50}$	EFA/Coarse ( $n = 28$ )	$\tau_c = (1.58) \times C_u^{-0.04} \times \gamma^{0.02} \times D_{50}^{0.77}$	0.93	0.99
113	PC, $\gamma, WC, S_u, D_{50}$	JET/Global ( $n = 28$ )	$\tau_c = -0.248 \times PC - 1.23 \times \gamma + 0.21 \times WC + 0.07 \times S_u - 36.89 \times D_{50} + 31.82$	0.50	0.10
19	PI, $S_u, D_{50}$	HET/Global ( $n = 21$ )	$\tau_c = (25.07) \times PI^{0.27} \times S_u^{0.55} \times D_{50}^{0.5}$	0.64	0.43

<sup>a</sup>See Chapter 7, Section 7.3.1.<sup>b</sup> $n$  = number of data points.<sup>c</sup>Parameter values given by deterministic regression.**Table 103.** Selected models for critical velocity,  $v_c$ .

Group No.	Independent Variables <sup>a</sup>	Data Set <sup>b</sup>	Model Expression <sup>c</sup>	$R^2$	Cross-Validation Score
117	PC, WC, $S_u, D_{50}$	EFA/Fine ( $n = 46$ )	$v_c = (2.518 \times 10^{-5}) \times PC^{0.2} \times WC^{2.06} \times S_u^{0.51} \times D_{50}^{-0.13}$	0.80	0.80
27	PI, $\gamma, WC, D_{50}$	EFA/Coarse ( $n = 15$ )	$v_c = (3 \times 10^{-15}) \times PI^{1.24} \times \gamma^{8.11} \times WC^{0.54} \times D_{50}^{-2.35}$	0.88	0.72

<sup>a</sup>See Chapter 7, Section 7.3.1.<sup>b</sup> $n$  = number of data points.<sup>c</sup>Parameter values given by deterministic regression.**Table 104.** Selected models for erosion category, EC.

Group No.	Independent Variables <sup>a</sup>	Data Set <sup>b</sup>	Model Expression <sup>c</sup>	$R^2$	Cross-Validation Score
132	$A, WC, S_u, D_{50}$	EFA/Fine ( $n = 44$ )	$EC = (0.1933) \times A^{-0.06} \times WC^{0.51} \times S_u^{0.09} \times D_{50}^{-0.12}$	0.55	0.53
91	$C_u, WC, VST, D_{50}$	EFA/Coarse ( $n = 11$ )	$EC = (1.12) \times C_u^{0.1} \times WC^{-0.28} \times VST^{0.02} \times D_{50}^{-0.44}$ for $0.074 < D_{50} < 0.3$	0.92	0.80
88	PL, $S_u, D_{50}$	JET/Global ( $n = 28$ )	$EC = -0.022 \times PL + 0.0031 \times S_u - 5.5 \times D_{50} + 3.34$	0.70	0.58
12	PI, $\gamma, S_u$	HET/Fine ( $n = 21$ )	$EC = (1.67) \times PI^{0.04} \times \gamma^{0.15} \times S_u^{0.03}$	0.70	0.54
48	$C_u, \gamma, WC$	HET/Coarse ( $n = 28$ )	$EC = (1.045) \times C_u^{-0.25} \times \gamma^{0.45} \times WC^{-0.04}$	0.77	0.78

<sup>a</sup>See Chapter 7, Section 7.3.1.<sup>b</sup> $n$  = number of data points.<sup>c</sup>Parameter values given by deterministic regression.

**Table 105. Selected models for velocity slope,  $E_v$ .**

Group No.	Independent Variables <sup>a</sup>	Data Set <sup>b</sup>	Model Expression <sup>c</sup>	$R^2$	Cross-Validation Score
86	$C_u, \gamma, WC, D_{50}$	EFA/Coarse ( $n = 28$ )	$E_v = (88,969.4) \times C_u^{-1.77} \times \gamma^{-2.26} \times WC^{0.34} \times D_{50}^{-1.69}$	0.86	0.64
126	$D_{50}, \gamma, WC, PF, A$	EFA/Fine ( $n = 74$ )	$E_v = (1.682339 \times 10^{13}) \times D_{50}^{5.10} \times \gamma^{-9.20} \times WC^{-1.13} \times PF^{4.69} \times A^{-0.01}$	0.79	0.52

<sup>a</sup>See Chapter 7, Section 7.3.1.<sup>b</sup> $n$  = number of data points.<sup>c</sup>Parameter values given by deterministic regression.

### 9.1.8 Chapter 8: Most Robust Correlation Equations

Chapter 8 began with a summary of the advantages, disadvantages, and applications of the three major erosion tests used in this study—the EFA, the JET, and the HET [see Table 90 (Chapter 8)]. The chapter then presented correlation equations recommended on the basis of the work discussed in Chapter 7 (see Tables 102 to 106) and provided instructions on how best to use them. Table 100 (Chapter 8) shows an example of the proposed equation chart for erosion category based on the JET data. This table presents the recommended correlation equation for predicting the erosion category in for  $D_{50} < 0.3$  mm. Along with each proposed equation, the tables in Chapter 8 that present proposed equations give one or two plots showing the probability of underpredicting (POU)—or, where applicable, the probability of overpredicting (POO)—versus a correction factor, as well as a plot of predicted versus measured values. Such plots provide great insight into the use of each equation. A column to the right of each equation offers a few remarks on the proposed equation, the value of  $R^2$ , and the cross-validation score.

**Table 106. Selected models for shear stress slope,  $E_\tau$ .**

Group No.	Independent Variables <sup>a</sup>	Data Set <sup>b</sup>	Model Expression <sup>c</sup>	$R^2$	Cross-Validation Score
77	$C_u, \gamma, D_{50}$	EFA/Coarse ( $n = 28$ )	$E_\tau = (3,228.7) \times C_u^{-2.8} \times \gamma^{-1.58} \times D_{50}^{-2.91}$	0.91	0.64
134	$A, \gamma, PF, D_{50}$	EFA/Fine ( $n = 72$ )	$E_\tau = (1.429078 \times 10^{13}) \times A^{-0.47} \times \gamma^{-10.43} \times PF^{6.14} \times D_{50}^{7.52}$	0.90	0.51
40	$\gamma, WC, PF, D_{50}$	HET/Coarse ( $n = 62$ )	$E_\tau = (2.951) \times \gamma^{25.08} \times WC^{-7.48} \times PF^{-19.96} \times D_{50}^{-5.32}$	0.86	0.55
108	$LL, PL, \gamma, PC, S_u$	HET/Fine ( $n = 21$ )	$E_\tau = (9 \times 10^{-6}) \times LL^{-0.35} \times PL^{1.59} \times \gamma^{3.3} \times PC^{-0.48} \times S_u^{-0.19}$	0.81	0.51
5	$PI, \gamma, WC$	JET/Coarse ( $n = 25$ )	$E_\tau = (55,637,006,351,614) \times PI^{-0.19} \times \gamma^{-6.39} \times WC^{-3.67}$	0.90	0.67
15	$PI, WC, S_u$	JET/Fine ( $n = 24$ )	$E_\tau = (396,599.6) \times PI^{-2.54} \times WC^{4.58} \times S_u^{-4.91}$	0.93	0.23

<sup>a</sup>See Chapter 7, Section 7.3.1.<sup>b</sup> $n$  = number of data points.<sup>c</sup>Parameter values given by deterministic regression.

## 9.2 Recommendations on How to Approach Erosion-Related Design Problems

One of the key missions of this project was to provide engineers in charge of erosion problems with a set of correlation equations for predicting erosion parameters without the need to perform multiple and costly erosion tests. In this section, a step-by-step approach is presented. It must be noted that each step can stand alone by itself and help solve the problem; however, the combination of all four steps would lead to the most accurate results. While Steps 1 and 2 yield more preliminary estimates of the erodibility parameters, Steps 3 and 4 provide more detailed insights in obtaining the erodibility parameters. It is recommended that the engineer consider all four steps prior to making a final decision.

### 9.2.1 Step 1. Probe NCHRP-Erosion

Chapter 5 of this report discussed the development of the NCHRP-Erosion database. This global spreadsheet is a searchable tool and allows the engineer to filter the data according to multiple criteria. The first preliminary approach to evaluating the erodibility of a desired site is through probing NCHRP-Erosion. The engineer can use information on as many geotechnical properties as possible from the site (i.e., USCS category, AASHTO classification, Atterberg limits, unit weight, and so forth), and filter NCHRP-Erosion on the basis of those criteria with the goal of finding soil samples that are similar to the target soil. After the filtering, the soil samples obtained might be tested with more than one erosion test (e.g., EFA, BET, JET, HET). The engineer then can see for himself or herself what erodibility parameters he or she must expect from the soil without having to conduct different erosion tests. Probing the NCHRP-Erosion database can also help the engineer to compare the results of these different erosion tests on similar soil samples.

### 9.2.2 Step 2. Use the USCS Erosion Charts to Estimate Erosion Resistance

Chapter 7, Section 7.1, showed that the erosion functions for soils with a given USCS category do not generally fall distinctly into a single erosion category but rather seem to plot approximately across two categories. Figure 145 (Chapter 7) summarizes all results into erosion category charts. Figure 145 can be used as another preliminary tool for estimating the erodibility of any sample by using only the USCS category. In this figure, the width of each box associated with a USCS category represents the zone in which the results of 90% of the EFA tests performed on such samples would fall in the erosion category chart. For instance, if the soil type of a location in an arbitrary geotechnical site is classified as SM (silty sand) according to the USCS, it would most likely (with close to 90% confidence based on the EFA results compiled in NCHRP-Erosion) fall into Category II (high erodibility) in Figure 145. Similarly, a soil classified as CH (fat clay) would most likely fall into Category III (medium erodibility), and an SP (poorly graded sand) would fall within Categories I and II (very high to high erodibility). The wider the box is for a USCS category, the greater the variability of the erosion category (EC) is for that particular soil type. Knowledge of the erosion category of a soil can lead to much useful information about the erosion resistance of that soil; however, it should be noted that such results are not accurate enough for design purposes.

### 9.2.3 Step 3. Use the Deterministic Regression Results

Chapter 7, Section 7.3, presented a comprehensive deterministic approach to selecting the best correlation equations between the geotechnical properties and the erodibility parameters.

The most robust equations were repeated in Chapter 8, Section 8.2. The proposed equations were developed on the basis of data obtained in different erosion tests (i.e., EFA, JET, and HET); therefore, advance knowledge of each test is extremely useful in choosing the best equation. Table 90 (Chapter 8) shows a list of advantages, disadvantages, and applications for the EFA, JET, and HET. The content of this table should be studied carefully before the proposed equations in Section 8.2 are used. POU/POO plots are presented with the best equations. These plots help the engineer find the correction factor needed to reach a certain confidence that the predicted value is under- or overpredicted. The POU/POO plots can be very useful for design purposes.

### 9.2.4 Step 4. Use the Bayesian Inference Results

One of the issues with conventional deterministic approaches is that they fail to capture uncertainty by accounting only for the mean value of the unknown parameter. Therefore, Chapter 7, Section 7.4, was dedicated to performing a probabilistic analysis using the Bayesian inference approach. The comprehensive deterministic frequentist regression analysis performed in Section 7.3 was the foundation of the Bayesian inference analysis performed in Section 7.4. The selected correlation equations using the deterministic approach were analyzed using Bayesian inference. The engineer can evaluate the sensitivity of the predicted value with regard to one or more model parameters. All possible values that an erodibility parameter can get for each selected equation are presented in the form of a probability distribution. Examples of the Bayesian inference analysis are presented in Section 7.4. Appendix 5 presents the complete results of the Bayesian inference analysis.

## 9.3 Example Applications

This section consists of generic examples illustrating the use of the approach to evaluating soil erosion resistance presented in Section 9.2. Four geotechnical sites (gravel, sand, silt, and clay sites) were studied to examine their resistance to potential surface erosion caused by an arbitrary upcoming flood. In these examples, earlier geotechnical explorations have included sieve and hydrometer analysis, unit weight test, and, where applicable, Atterberg limit tests and unconsolidated undrained tests. Table 107 shows selected geotechnical properties of the upper soil layer (first 2 m) in each site. In these examples, the use of the first three steps discussed in Section 9.2 are illustrated. For Step 4 (Bayesian inference), the user is referred to Section 7.4.

The geotechnical properties shown in Table 107 help the user search NCHRP-Erosion and find soil samples that are very similar to the existing soil for each site. Using NCHRP-Erosion, the user can see the results of different erosion tests performed on similar samples

**Table 107. Selected geotechnical properties of upper soil layer at each site.**

Site	USCS Category	Unit		PL (%)	PI (%)	Percent Finer Than #200	Mean Particle Size (mm)	Vane Shear Test		WC (%)	$C_u$	Clay Percentage (< 0.002 mm) (%)
		Weight (kN/m <sup>3</sup> )	PL (%)					(kPa)	(%)			
Gravel	GP	18.5	na	na	na	0	14	na	6	0.4	0	0
Sand	SP-SM	16	25	4	na	11	0.2	12	11	4.5	na	1.5
Silt	ML	20	23	7	na	60	0.037	29	30	na	na	15
Clay	CH	18	25	26	na	100	0.001	75	23	na	na	42

Note: na = not applicable.

## 308 Relationship Between Erodibility and Properties of Soils

from different projects. (Chapter 5 of this report includes the Inquiry Operation Manual for NCHRP-Erosion.) The user is then referred to Chapter 2 of this report and to Table 90 (Chapter 8) to study the advantages, drawbacks, and applications of each test. The user can then use his or her engineering judgment to decide which results would be an appropriate match to the existing problem.

It is recommended that the engineer carry out all four steps to confirm his or her findings in Step 1 and also have a more thorough examination of the erodibility of the existing soil, in case there are not enough samples in NCHRP-Erosion for that particular soil. The second step is to use the USCS erosion charts (Figure 145, Chapter 7) as a preliminary estimate of the erosion category at each site. Section 9.2.2 gives a few examples of how to use these charts. In this example application, the gravel site soil is classified as GP. Figure 145 (Chapter 7) shows that this soil would most likely fall into a zone in the vicinity of the boundary between Category II and Category III (high to medium erodibility). In addition to the erosion category, the user can use the plot to determine approximately the erosion rate he or she should expect at the site given the flow conditions (i.e., velocity) of the upcoming flood. For example, Figure 145 shows that, assuming the GP soil in this example would fall very close to the boundary between Category II and Category III, for a flow velocity of 2 m/s, an erosion rate of approximately 100 mm/h erosion rate would be expected. Similarly, Figure 145 shows that the example sand site (SP-SM), silt site (ML), and clay site (CH) would likely fall into Category I (very high erodibility), Categories II to III (high to medium erodibility), and Category III (medium erodibility), respectively. The erosion rate expected for each site can then be determined in a manner similar to that of the case of the gravel site (GP), by considering an average line in the appropriate zone and the flow conditions of the upcoming flood.

In Step 3, the user is recommended to use the selected correlation equations to evaluate his or her findings during the first two steps and improve his or her decision, where applicable. Different equations are used to predict the erodibility parameters, depending on the erosion test data (EFA, JET, or HET) used to develop them (see Tables 102 to 106 and Chapter 8). Therefore, knowledge of the strength points and limitations of each test is a vital step prior to choosing an equation. Table 90 (Chapter 8) helps readers identify and understand the differences between the erosion tests. The user is free to select the best equation according to his or her objective and consideration of the differences between the equations.

### 9.3.1 Gravel Site

Table 91 (Chapter 8) shows that for soils with  $D_{50}$  greater than 0.3 mm, the recommended equation for obtaining the critical shear stress is  $\tau_c = D_{50}$ . Therefore, for the case of this example site, critical shear stress is  $\tau_c = 14$  Pa.

The critical velocity can be defined from equations shown in Table 94 (Chapter 8). For soils with  $D_{50}$  greater than 0.3 mm, it is recommended to use

$$v_c = 0.315 \times (D_{50})^{0.5}$$

Therefore, for the case of this example site, the critical velocity is

$$v_c = 0.315 \times (14)^{0.5} = 1.18 \text{ m/s}$$

Table 95 (Chapter 8) shows the recommended equations for the slope of the shear stress–erosion rate plot ( $E_\tau$ ) according to the EFA test data. For soils with  $D_{50}$  greater than 0.074 mm,

$$E_\tau = (3,228.7) \times C_u^{-2.8} \times \gamma^{-1.58} \times D_{50}^{-2.91}$$

Therefore,

$$E_t = (3,228.7) \times (0.4)^{-2.8} \times (18.5)^{-1.58} \times (14)^{-2.91} = 0.19 \text{ mm/h-Pa}$$

The POO plot in Table 95 shows that to reach 80% confidence that the predicted  $E_t$  is greater than the actual  $E_t$ , the predicted value should be multiplied by 2.5 ( $2.5 \times 0.19 = 0.475 \text{ mm/h-Pa}$ ). Tables 96 and 97 (Chapter 8) show the recommended equations for the slope of the shear stress–erosion rate plot ( $E_t$ ) according to the JET and HET data, respectively. However, because performing the JET and HET on gravel is not feasible, the equations given in Tables 96 and 97 cannot be used for this example site.

Table 98 (Chapter 8) shows the recommended equations for the slope of velocity–erosion rate plot ( $E_v$ ) according to the EFA test data. For soils with  $D_{50}$  greater than 0.074 mm,

$$E_v = (88,969.4) \times C_u^{-1.77} \times \gamma^{-2.26} \times WC^{0.34} \times D_{50}^{-1.69}$$

Therefore,

$$E_v = (88,969.4) \times 0.4^{-1.77} \times 19.5^{-2.26} \times 6^{0.34} \times 14^{-1.69} = 11.6 \text{ mm-s/m-h}$$

The POO plot in Table 98 shows that to reach 80% confidence that the predicted  $E_t$  is greater than the actual  $E_t$ , the predicted value should be multiplied by 5 ( $5 \times 11.6 = 58 \text{ mm-s/m-h}$ ).

Tables 99, 100, and 101 (Chapter 8) show that there is no strong equation for obtaining the erosion category (EC) for soils with  $D_{50}$  greater than 0.3 mm.

### 9.3.2 Sand Site

Table 107 shows that the upper soil layer in the example sand site has an average mean particle size of 0.2 mm. In this example, the erodibility parameters are calculated using the equations developed on the basis of the EFA, JET, and HET data; however, as noted above, the user is referred to Table 90 to select the best equation according to his or her objective and with regard to the differences between the equations.

Table 91 shows the recommended equations for critical shear stress ( $\tau_c$ ) according to the EFA test data. For soils with  $D_{50}$  between 0.074 mm and 0.3 mm,

$$\tau_c = (1.58) \times C_u^{-0.04} \times \gamma^{0.02} \times D_{50}^{0.77}$$

Therefore,

$$\tau_c = (1.58) \times 4.5^{-0.04} \times 16^{0.02} \times 0.2^{0.77} = 0.46 \text{ Pa}$$

The POU plot in Table 91 shows that to reach 90% confidence that the predicted  $\tau_c$  is less than the actual  $\tau_c$ , the predicted value should be multiplied by 0.82 ( $0.82 \times 0.46 = 0.38 \text{ Pa}$ ).

Table 92 (Chapter 8) shows the recommended equations for critical shear stress ( $\tau_c$ ) according to the JET data. For soils with  $D_{50}$  less than 0.3 mm,

$$\tau_c = -0.248 \times PC - 1.23 \times \gamma + 0.21 \times WC + 0.07 \times S_u - 36.89 \times D_{50} + 31.82$$

Therefore,

$$\tau_c = -0.248 \times 1.5 - 1.23 \times 16 + 0.21 \times 11 + 0.07 \times 12 - 36.89 \times 0.2 + 31.82 = 7.54 \text{ Pa}$$

### 310 Relationship Between Erodibility and Properties of Soils

The POU plot in Table 92 shows that to reach 90% confidence that the predicted  $\tau_c$  is less than the actual  $\tau_c$ , the predicted value should be multiplied by 0.6 ( $0.6 \times 7.54 = 4.54$  Pa). Performing the HET on SP-SM samples is typically not feasible; therefore, the equation in Table 93 cannot be used for this site.

Table 94 shows the recommended equations for critical velocity ( $v_c$ ) according to the EFA test data. For soils with  $D_{50}$  greater than 0.074 mm,

$$v_c = (3 \times 10^{-15}) \times PI^{1.24} \times \gamma^{8.11} \times WC^{0.54} \times D_{50}^{-2.35}$$

Therefore,

$$v_c = (3 \times 10^{-15}) \times 4^{1.24} \times 16^{8.11} \times 11^{0.54} \times 0.2^{-2.35} = 0.016 \text{ m/s}$$

The POU plot in Table 94 shows that to reach 90% confidence that the predicted  $v_c$  is less than the actual  $v_c$ , the predicted value should be multiplied by 0.7 ( $0.7 \times 0.016 = 0.01$  m/s). This very low critical velocity implies that this site's resistance to initiation of erosion is significantly low.

Table 95 shows the recommended equations for the slope of shear stress–erosion rate plot ( $E_\tau$ ) according to the EFA test data. For soils with  $D_{50}$  greater than 0.074 mm,

$$E_\tau = (3,228.7) \times C_u^{-2.8} \times \gamma^{-1.58} \times D_{50}^{-2.91}$$

Therefore,

$$E_\tau = (3,228.7) \times (4.5)^{-2.8} \times (16)^{-1.58} \times (0.2)^{-2.91} = 64.8 \text{ mm/h-Pa}$$

The POO plot in Table 95 shows that to reach 80% confidence that the predicted  $E_\tau$  is greater than the actual  $E_\tau$ , the predicted value should be multiplied by 2.5 ( $2.5 \times 64.8 = 162$  mm/h-Pa).

Table 96 shows the recommended equations for the slope of shear stress–erosion rate plot ( $E_\tau$ ) according to the JET data. For soils with  $D_{50}$  greater than 0.074 mm,

$$E_\tau = (55,637,006,351,614) \times PI^{-0.19} \times \gamma^{-6.39} \times WC^{-3.67}$$

Therefore,

$$E_\tau = (55,637,006,351,614) \times 4^{-0.19} \times 16^{-6.39} \times 11^{-3.67} = 130.2 \text{ mm/h-Pa}$$

The POO plot in Table 96 shows that to reach 90% confidence that the predicted  $E_\tau$  is greater than the actual  $E_\tau$ , the predicted value should be multiplied by 1.4 ( $1.4 \times 130.2 = 184.8$  mm/h-Pa). Due to the low fine content of the upper soil in this example site, the equation in Table 97 cannot be used.

Table 98 shows the recommended equations for the slope of velocity–erosion rate plot ( $E_v$ ) according to the EFA test data. For soils with  $D_{50}$  greater than 0.074 mm,

$$E_v = (88,969.4) \times C_u^{-1.77} \times \gamma^{-2.26} \times WC^{0.34} \times D_{50}^{-1.69}$$

Therefore,

$$E_v = (88,969.4) \times 4.5^{-1.77} \times 16^{-2.26} \times 11^{0.34} \times 0.2^{-1.69} = 404.6 \text{ mm-s/m-h}$$

The POO plot in Table 98 shows that to reach 80% confidence that the predicted  $E_v$  is greater than the actual  $E_v$ , the predicted value should be multiplied by 5 ( $5 \times 404.6 = 2,023$  mm-s/m-h).

Table 99 shows the recommended equations for the erosion category (EC) according to the EFA test data. For soils with  $D_{50}$  between 0.074 mm and 0.3 mm,

$$EC = (1.12) \times C_u^{0.1} \times WC^{-0.28} \times VST^{0.02} \times D_{50}^{-0.44}$$

Therefore,

$$EC = (1.12) \times 4.5^{0.1} \times 11^{-0.28} \times 12^{0.02} \times 0.2^{-0.44} = 1.42$$

The POU plot in Table 99 shows that to reach 90% confidence that the predicted EC is less than the actual EC, the predicted value should be multiplied by 0.84 ( $0.84 \times 1.42 = 1.19$ ).

Table 100 shows the recommended equations for the erosion category (EC) according to the JET data. For soils with  $D_{50}$  less than 0.3 mm,

$$EC = -0.022 \times PL + 0.0031 \times S_u - 5.5 \times D_{50} + 3.34$$

Therefore,

$$EC = -0.022 \times 25 + 0.0031 \times 12 - 5.5 \times 0.2 + 3.34 = 1.73$$

The POU plot in Table 100 shows that to reach 90% confidence that the predicted EC is less than the actual EC, the predicted value should be multiplied by 0.85 ( $0.85 \times 1.73 = 1.47$ ). The equation in Table 101 is based on the HET data, and because performing the HET is not feasible on SP-SM, use of this equation is not recommended.

### 9.3.3 Silt Site

Table 107 shows that the upper soil layer in the example silt site has an average mean particle size of 0.037 mm. In this example, the erodibility parameters are calculated using the equations developed on the basis of the EFA, JET, and HET data; however, as also mentioned above, the user is referred to Table 90 to select the best equation according to his or her objective.

Table 91 shows the recommended equations for critical shear stress ( $\tau_c$ ) according to the EFA test data. For soils with  $D_{50}$  less than 0.074 mm,

$$\tau_c = (158.06) \times \gamma^5 \times A^{-0.46} \times WC^{10.03} \times S_u^{1.83} \times PF^{-18.28} \times D_{50}^{-4.21}$$

Soil activity ( $A$ ) is obtained as PI/PC. Therefore,

$$\tau_c = (158.06) \times 20^5 \times 0.47^{-0.46} \times 30^{10.03} \times 29^{1.83} \times 60^{-18.28} \times 0.037^{-4.21} = 0.74 \text{ Pa}$$

The POU plot in Table 91 shows that there is a 90% chance that the predicted  $\tau_c$  is less than the actual  $\tau_c$ .

Table 92 shows the recommended equations for critical shear stress ( $\tau_c$ ) according to the JET data. For soils with  $D_{50}$  less than 0.3 mm,

$$\tau_c = -0.248 \times PC - 1.23 \times \gamma + 0.21 \times WC + 0.07 \times S_u - 36.89 \times D_{50} + 31.82$$

Therefore,

$$\tau_c = -0.248 \times 15 - 1.23 \times 20 + 0.21 \times 30 + 0.07 \times 29 - 36.89 \times 0.037 + 31.82 = 10.47 \text{ Pa}$$

The POU plot in Table 92 shows that to reach 90% confidence that the predicted  $\tau_c$  is less than the actual  $\tau_c$ , the predicted value should be multiplied by 0.6 ( $0.6 \times 10.47 = 6.28 \text{ Pa}$ ).

### 312 Relationship Between Erodibility and Properties of Soils

Table 93 shows the recommended equations for critical shear stress ( $\tau_c$ ) according to the HET data. For soils with  $D_{50}$  less than 0.3 mm,

$$\tau_c = (25.07) \times PI^{0.27} \times S_u^{0.55} \times D_{50}^{0.5}$$

Therefore,

$$\tau_c = (25.07) \times 7^{0.27} \times 29^{0.55} \times 0.037^{0.5} = 51.9$$

The POU plot in Table 93 shows that to reach 90% confidence that the predicted  $\tau_c$  is less than the actual  $\tau_c$ , the predicted value should be multiplied by 0.6 ( $0.6 \times 51.9 = 31.1 \text{ Pa}$ ).

Table 94 shows the recommended equations for critical velocity ( $v_c$ ) according to the EFA test data. For soils with  $D_{50}$  less than 0.074 mm,

$$v_c = (2.518 \times 10^{-5}) \times PC^{0.2} \times WC^{2.06} \times S_u^{0.51} \times D_{50}^{-0.13}$$

Therefore,

$$v_c = (2.518 \times 10^{-5}) \times 15^{0.2} \times 30^{2.06} \times 29^{0.51} \times 0.037^{-0.13} = 0.41 \text{ m/s}$$

The POU plot in Table 94 shows that to reach 90% confidence that the predicted  $v_c$  is less than the actual  $v_c$ , the predicted value should be multiplied by 0.8 ( $0.8 \times 0.41 = 0.33 \text{ m/s}$ ).

Table 95 shows the recommended equations for the slope of shear stress–erosion rate plot ( $E_\tau$ ) according to the EFA test data. For soils with  $D_{50}$  less than 0.074 mm,

$$E_\tau = (1.429078 \times 10^{13}) \times A^{-0.47} \times \gamma^{-10.43} \times PF^{6.14} \times D_{50}^{7.52}$$

Therefore,

$$E_\tau = (1.429078 \times 10^{13}) \times 0.47^{-0.47} \times 20^{-10.43} \times 60^{6.14} \times 0.037^{7.52} = 0.78 \text{ mm/h-Pa}$$

The POO plot in Table 95 shows that to reach 87% confidence that the predicted  $E_\tau$  is greater than the actual  $E_\tau$ , the predicted value should be multiplied by 2 ( $2 \times 0.78 = 1.56 \text{ mm/h-Pa}$ ).

Table 96 shows the recommended equations for the slope of shear stress–erosion rate plot ( $E_\tau$ ) according to the JET data. For soils with  $D_{50}$  less than 0.074 mm,

$$E_\tau = (396,599.6) \times PI^{-2.54} \times WC^{4.58} \times S_u^{-4.91}$$

Therefore,

$$E_\tau = (396,599.6) \times 7^{-2.54} \times 30^{4.58} \times 29^{-4.91} = 1088 \text{ mm/h-Pa}$$

The POO plot in Table 96 shows that to reach 88% confidence that the predicted  $E_\tau$  is greater than the actual  $E_\tau$ , the predicted value should be multiplied by 2 ( $2 \times 1,088 = 2,176 \text{ mm/h-Pa}$ ).

Table 97 shows the recommended equations for the slope of shear stress–erosion rate plot ( $E_\tau$ ) according to the HET data. For soils with  $D_{50}$  less than 0.074 mm,

$$E_\tau = (9 \times 10^{-6}) \times LL^{-0.35} \times PL^{1.59} \times \gamma^{3.3} \times PC^{-0.48} \times S_u^{-0.19}$$

Therefore,

$$E_\tau = (9 \times 10^{-6}) \times 30^{-0.35} \times 23^{1.59} \times 20^{3.3} \times 15^{-0.48} \times 29^{-0.19} = 1.13 \text{ mm/h-Pa}$$

The POO plot in Table 97 shows that to reach 90% confidence that the predicted  $E_v$  is greater than the actual  $E_v$ , the predicted value should be multiplied by 1.45 ( $1.45 \times 1.13 = 1.64$  mm/h-Pa).

Table 98 shows the recommended equations for the slope of velocity–erosion rate plot ( $E_v$ ) according to the EFA test data. For soils with  $D_{50}$  less than 0.074 mm,

$$E_v = (1.682339 \times 10^{13}) \times D_{50}^{5.1} \times \gamma^{-9.2} \times WC^{-1.13} \times PF^{4.69} \times A^{-0.01}$$

Therefore,

$$E_v = (1.682339 \times 10^{13}) \times 0.037^{5.1} \times 20^{-9.2} \times 30^{-1.13} \times 60^{4.69} \times 0.47^{-0.01} = 4.3 \text{ mm-s/m-h}$$

The POO plot in Table 98 shows that to reach 80% confidence that the predicted  $E_v$  is greater than the actual  $E_v$ , the predicted value should be multiplied by 2 ( $2 \times 4.3 = 8.6$  mm-s/m-h).

Table 99 shows the recommended equations for the erosion category (EC) according to the EFA test data. For soils with  $D_{50}$  less than 0.074 mm,

$$EC = (0.1933) \times A^{-0.06} \times WC^{0.51} \times S_u^{0.09} \times D_{50}^{-0.12}$$

Therefore,

$$EC = (0.1933) \times 0.47^{-0.06} \times 30^{0.51} \times 29^{0.09} \times 0.037^{-0.12} = 2.3$$

The POU plot in Table 99 shows that to reach 90% confidence that the predicted EC is less than the actual EC, the predicted value should be multiplied by 0.75 ( $0.75 \times 2.3 = 1.73$ ).

Table 100 shows the recommended equations for the erosion category (EC) according to the JET data. For soils with  $D_{50}$  less than 0.3 mm,

$$EC = -0.022 \times PL + 0.0031 \times S_u - 5.5 \times D_{50} + 3.34$$

Therefore,

$$EC = -0.022 \times 23 + 0.0031 \times 29 - 5.5 \times 0.037 + 3.34 = 2.72$$

The POU plot in Table 100 shows that to reach 90% confidence that the predicted EC is less than the actual EC, the predicted value should be multiplied by 0.85 ( $0.85 \times 2.72 = 2.31$ ).

Table 101 shows the recommended equations for the erosion category (EC) according to the HET data. For soils with  $D_{50}$  less than 0.074 mm,

$$EC = (1.67) \times PI^{0.04} \times \gamma^{0.15} \times S_u^{0.03}$$

Therefore,

$$EC = (1.67) \times 7^{0.04} \times 20^{0.15} \times 29^{0.03} = 3.1$$

The POU plot in Table 101 shows that to reach 100% confidence that the predicted EC is less than the actual EC, the predicted value should be multiplied by 0.95 ( $0.95 \times 3.1 = 2.95$ ).

### 9.3.4 Clay Site

Table 107 shows that the upper soil layer in this site has an average mean particle size of 0.001 mm. In this example, the erodibility parameters are calculated using the equations

### 314 Relationship Between Erodibility and Properties of Soils

developed on the basis of the EFA, JET, and HET data; however, as also mentioned previously, the user is referred to Table 90 to select the best equation according to his or her objective.

Table 91 shows the recommended equations for critical shear stress ( $\tau_c$ ) according to the EFA test data. For soils with  $D_{50}$  less than 0.074 mm,

$$\tau_c = (158.06) \times \gamma^5 \times A^{-0.46} \times WC^{10.03} \times S_u^{1.83} \times PF^{-18.28} \times D_{50}^{-4.21}$$

Soil activity (A) is obtained as PI/PC. Therefore,

$$\tau_c = (158.06) \times 18^5 \times 0.62^{-0.46} \times 23^{10.03} \times 75^{1.83} \times 100^{-18.28} \times 0.001^{-4.21} = 53.7 \text{ Pa}$$

The POU plot given in Table 91 shows that there is an almost 90% chance that the predicted  $\tau_c$  is less than the actual  $\tau_c$ .

Table 92 shows the recommended equations for critical shear stress ( $\tau_c$ ) according to the JET data. For soils with  $D_{50}$  less than 0.3 mm,

$$\tau_c = -0.248 \times PC - 1.23 \times \gamma + 0.21 \times WC + 0.07 \times S_u - 36.89 \times D_{50} + 31.82$$

Therefore,

$$\tau_c = -0.248 \times 42 - 1.23 \times 18 + 0.21 \times 23 + 0.07 \times 75 - 36.89 \times 0.001 + 31.82 = 9.3 \text{ Pa}$$

The POU plot in Table 92 shows that to reach 90% confidence that the predicted  $\tau_c$  is less than the actual  $\tau_c$ , the predicted value should be multiplied by 0.6 ( $0.6 \times 9.3 = 5.6 \text{ Pa}$ ).

Table 93 shows the recommended equations for critical shear stress ( $\tau_c$ ) according to the HET data. For soils with  $D_{50}$  less than 0.3 mm,

$$\tau_c = (25.07) \times PI^{0.27} \times S_u^{0.55} \times D_{50}^{0.5}.$$

Therefore,

$$\tau_c = (25.07) \times 26^{0.27} \times 75^{0.55} \times 0.001^{0.5} = 20.5 \text{ Pa}$$

The POU plot in Table 93 shows that to reach 90% confidence that the predicted  $\tau_c$  is less than the actual  $\tau_c$ , the predicted value should be multiplied by 0.6 ( $0.6 \times 20.5 = 12.3 \text{ Pa}$ ).

Table 94 shows the recommended equations for critical velocity ( $v_c$ ) according to the EFA test data. For soils with  $D_{50}$  less than 0.074 mm,

$$v_c = (2.518 \times 10^{-5}) \times PC^{0.2} \times WC^{2.06} \times S_u^{0.51} \times D_{50}^{-0.13}$$

Therefore,

$$v_c = (2.518 \times 10^{-5}) \times 42^{0.2} \times 23^{2.06} \times 75^{0.51} \times 0.001^{-0.13} = 0.75 \text{ m/s}$$

The POU plot in Table 94 shows that to reach 90% confidence that the predicted  $v_c$  is less than the actual  $v_c$ , the predicted value should be multiplied by 0.8 ( $0.8 \times 0.75 = 0.6 \text{ m/s}$ ).

Table 95 shows the recommended equations for the slope of shear stress–erosion rate plot ( $E_\tau$ ) according to the EFA test data. For soils with  $D_{50}$  less than 0.074 mm,

$$E_\tau = (1.429078 \times 10^{13}) \times A^{-0.47} \times \gamma^{-10.43} \times PF^{6.14} \times D_{50}^{7.52}$$

Therefore,

$$E_\tau = (1.429078 \times 10^{13}) \times 0.62^{-0.47} \times 18^{-10.43} \times 100^{6.14} \times 0.001^{7.52} = 7 \times 10^{-11} \text{ mm/h-Pa}$$

The POO plot in Table 95 shows that to reach 87% confidence that the predicted  $E_\tau$  is greater than the actual  $E_\tau$ , the predicted value should be multiplied by 2 ( $2 \times 7 \times 10^{-11} = 14 \times 10^{-11} \text{ mm/h-Pa}$ ). This very low  $E_\tau$  implies the fact that once the erosion is initiated, the erosion rate increases at a significantly low rate with increase in velocity/shear stress.

Table 96 shows the recommended equations for the slope of shear stress–erosion rate plot ( $E_\tau$ ) according to the JET data. For soils with  $D_{50}$  less than 0.074 mm,

$$E_\tau = (396,599.6) \times PI^{-2.54} \times WC^{4.58} \times S_u^{-4.91}$$

Therefore,

$$E_\tau = (396,599.6) \times 26^{-2.54} \times 23^{4.58} \times 75^{-4.91} = 0.1 \text{ mm/h-Pa}$$

The POO plot in Table 96 shows that to reach 88% confidence that the predicted  $E_\tau$  is greater than the actual  $E_\tau$ , the predicted value should be multiplied by 2 ( $2 \times 0.1 = 0.2 \text{ mm/h-Pa}$ ).

Table 97 shows the recommended equations for the slope of shear stress–erosion rate plot ( $E_\tau$ ) according to the HET data. For soils with  $D_{50}$  less than 0.074 mm,

$$E_\tau = (9 \times 10^{-6}) \times LL^{-0.35} \times PL^{1.59} \times \gamma^{3.3} \times PC^{-0.48} \times S_u^{-0.19}$$

Therefore,

$$E_\tau = (9 \times 10^{-6}) \times 51^{-0.35} \times 25^{1.59} \times 18^{3.3} \times 42^{-0.48} \times 75^{-0.19} = 0.39 \text{ mm/h-Pa}$$

The POO plot in Table 97 shows that to reach 90% confidence that the predicted  $E_\tau$  is greater than the actual  $E_\tau$ , the predicted value should be multiplied by 1.45 ( $1.45 \times 0.39 = 0.57 \text{ mm/h-Pa}$ ).

Table 98 shows the recommended equations for the slope of velocity–erosion rate plot ( $E_v$ ) according to the EFA test data. For soils with  $D_{50}$  less than 0.074 mm,

$$E_v = (1.682339 \times 10^{13}) \times D_{50}^{5.1} \times \gamma^{-9.20} \times WC^{-1.13} \times PF^{4.69} \times A^{-0.01}$$

Therefore,

$$E_v = (1.682339 \times 10^{13}) \times 0.001^{5.1} \times 18^{-9.20} \times 23^{-1.13} \times 100^{4.69} \times 0.62^{-0.01} = 1.6 \times 10^{-6} \text{ mm-s/m-h}$$

The POO plot in Table 98 shows that to reach 80% confidence that the predicted  $E_v$  is greater than the actual  $E_v$ , the predicted value should be multiplied by 2 ( $2 \times 1.6 \times 10^{-6} = 3.2 \times 10^{-6} \text{ mm-s/m-h}$ ). This low  $E_v$  is consistent with the very low  $E_\tau$  for this site.

Table 99 shows the recommended equations for the erosion category (EC) according to the EFA test data. For soils with  $D_{50}$  less than 0.074 mm,

$$EC = (0.1933) \times A^{-0.06} \times WC^{0.51} \times S_u^{0.09} \times D_{50}^{-0.12}$$

Therefore,

$$EC = (0.1933) \times 0.62^{-0.06} \times 23^{0.51} \times 75^{0.09} \times 0.001^{-0.12} = 3.3$$

### 316 Relationship Between Erodibility and Properties of Soils

The POU plot in Table 99 shows that to reach 90% confidence that the predicted EC is less than the actual EC, the predicted value should be multiplied by 0.75 ( $0.75 \times 3.3 = 2.48$ ).

Table 100 shows the recommended equations for the erosion category (EC) according to the JET data. For soils with  $D_{50}$  less than 0.3 mm,

$$EC = -0.022 \times PL + 0.0031 \times S_u - 5.5 \times D_{50} + 3.34$$

Therefore,

$$EC = -0.022 \times 25 + 0.0031 \times 75 - 5.5 \times 0.001 + 3.34 = 3.0$$

The POU plot in Table 100 shows that to reach 90% confidence that the predicted EC is less than the actual EC, the predicted value should be multiplied by 0.85 ( $0.85 \times 3.0 = 2.6$ ).

Table 101 shows the recommended equations for the erosion category (EC) according to the HET data. For soils with  $D_{50}$  less than 0.074 mm,

$$EC = (1.67) \times PI^{0.04} \times \gamma^{0.15} \times S_u^{0.03}$$

Therefore,

$$EC = (1.67) \times 26^{0.04} \times 18^{0.15} \times 75^{0.03} = 3.34$$

The POU plot in Table 101 shows that to reach 100% confidence that the predicted EC is less than the actual EC, the predicted value should be multiplied by 0.95 ( $0.95 \times 3.34 = 3.17$ ).

## 9.4 General Observations on the Effect of Geotechnical Properties on Soil Erodibility

Out of all the findings of this study, the correlation matrices [such as Figure 152 (Chapter 7)], along with the equations proposed in Chapter 8, may be the best measures for understanding the effect of each geotechnical property on each soil erodibility parameter. Appendix 3 presents all correlation matrices for the 12 groups shown in Figure 148 (Chapter 7). As discussed in Chapter 7, Section 7.3.2, the correlation matrices also show the Pearson correlation coefficient for each plot. The Pearson correlation coefficient was used to reflect the linear dependency between two variables, with +1 indicating a strong positive relationship, -1 indicating a solid negative relationship, and 0 indicating no relationship at all.

In general, the geotechnical properties that, by increasing, lead to an increase of the critical shear stress ( $\tau_c$ ), the critical velocity ( $v_c$ ), and the erosion category (EC) and to a decrease in the shear stress slope ( $E_\tau$ ) and the velocity slope ( $E_v$ ) are considered to be parameters that have a positive impact on erosion resistance. However, those geotechnical properties that, by increasing, lead to a decrease of  $\tau_c$ ,  $v_c$ , and EC and to an increase in  $E_\tau$  and  $E_v$  are considered to be parameters that have a negative impact on soil erosion resistance. The following observations were made regarding the effect of each soil property on the erodibility of soils:

- An increase in mean particle size ( $D_{50}$ ) leads to an increase in the erosion resistance of soils with  $D_{50}$  greater than 0.3 mm. However, regardless of the erosion test type, an increase in  $D_{50}$  leads to a decrease in the erosion resistance of soils with  $D_{50}$  less than 0.3 mm.
- In fine-grained soils ( $D_{50} < 0.074$  mm), a decrease in the coefficient of curvature or coefficient of uniformity ( $C_c$  and  $C_u$ ) leads to an increase in soil erosion resistance.
- In both fine- and coarse-grained soils, an increase in the percentage of clay leads to an increase in the erosion resistance of the soil.

- An increase in the plasticity index (PI) in general leads to an increase in the erosion resistance in both coarse-grained and fine-grained soils (especially soils with  $D_{50}$  less than 0.3 mm); however, there are a few exceptions to this statement.
- An increase in the plastic limit (PL) leads to an increase in the erosion resistance in fine-grained soils. This influence was found to be more pronounced in the EFA data set than in the JET and HET data sets.
- In many cases, the wet unit weight ( $\gamma$ ) and the undrained shear strength ( $S_u$ ) (for soils with  $D_{50}$  less than 0.3 mm) were directly proportional to the erosion resistance.
- Water content (WC) seemed to have a positive impact on the erosion resistance of finer soils in general. However, WC showed a negative effect on the erosion resistance of coarse-grained soils in the EFA test. It appears that WC alone is poorly correlated with the erosion resistance.

Overall, the geotechnical properties were found to have a mixed and complex relationship with erosion resistance in general. Nevertheless, the aforementioned observations as well as the proposed equations can be used as a first step in estimating the erosion resistance of many soils. If, by using such relationships, the erosion issue is clearly not a problem, it is unlikely that further effort is necessary. However, if the use of such equations leads to uncertainty, it is desirable to run erosion tests on site-specific samples.



# Symbols and Abbreviations

<i>A</i>	soil activity
ASSET	Adjustable Shear Stress Erosion and Transport
BBET	bottom borehole erosion test
BET	borehole erosion test
Ca/Na	calcium/sodium ratio
<i>C<sub>c</sub></i>	coefficient of curvature
CDC	Centers for Disease Control and Prevention
CEC	cation exchange capacity
CFD	computational fluid dynamics
CL	clay of low plasticity
CV	coefficient of variation
C.V.	cross-validation
<i>C<sub>u</sub></i>	coefficient of uniformity
<i>D<sub>50</sub></i>	mean particle size
EC	erosion category
ECDF	empirical cumulative density function
EFA	erosion function apparatus
ER	electrical resistivity
ERT	electrical resistivity tomography
ESTD	ex situ scour testing device
<i>E<sub>v</sub></i>	initial slope of velocity–erosion rate
<i>E<sub>τ</sub></i>	initial slope of shear stress–erosion rate
GEER	Geotechnical Extreme Events Reconnaissance
gpm	gallons per minute
HEC	Hydraulic Engineering Circular
HET	hole erosion test
ISEEP	in situ erosion evaluation probe
ISTD	in situ scour testing device
JET	jet erosion test
LBET	lateral borehole erosion test
LL	liquid limit
LVDT	linear variable differential transformer
MCMC	Markov Chain Monte Carlo
Mg	magnesium
ML	silt
MSE	mean square error
na	not applicable
NA	not available

NSF	National Science Foundation
PC	percent clay
PDF	probability density function
PET	pocket erodometer test
PF	percentage finer than Sieve #200
PI	plasticity index
PL	plastic limit
POO	probability of overpredicting
POU	probability of underpredicting
PP	pocket penetrometer strength
RELLIS	Respect, Excellence, Leadership, Loyalty, Integrity, and Selfless
RETA	rotating erosion testing apparatus
RH	roughness height
SEDFlume	High Sheer Stress flume
SERF	Sediment Erosion Rate Flume
SET	slot erosion test
STAR-CCM+	Star Computational Continuum Mechanics
$S_u$	undrained shear strength
TAMU	Texas A&M University
TTPTA	true triaxial piping test apparatus
USACE	U.S. Army Corps of Engineers
USBR	U.S. Bureau of Reclamation
USCS	Unified Soil Classification System
USGS	U.S. Geological Survey
VST	vane shear strength
$v_c$	critical velocity
WC	water content
$\gamma$	wet unit weight
$\tau_c$	critical shear stress



## References

- Acciardi, R. 1984. Erosion in Relation to Filter Design Criteria in Dams. *Journal of Geotechnical Engineering*, Vol. 110, No. 7, pp. 996–999.
- Amos, C. L., Droppo, I. G., Gomez, E. A., and Murphy, T. P. 2003. The Stability of a Remedial Bed in Hamilton Harbour, Lake Ontario, Canada. *Sedimentology*, Vol. 50, pp. 149–168.
- Al-Madhhachi, A. T., Hanson, G. J., Fox, G. A., Tyagi, A. K., and Bulut, R. 2013. Measuring Soil Erodibility Using a Laboratory Mini Jet. *American Society of Agricultural and Biological Engineers*, Vol. 56, No. 3, pp. 901–910.
- Annandale, G. W. 2006. *Scour Technology: Mechanics and Practice*. McGraw Hill, New York, pp. 430.
- Annandale, G. W. and Parkhill, D. L. 1995. Stream Bank Erosion: Application of the Erodibility Index Method. In *Proceedings of First International Conference on Water Resources Engineering*, San Antonio, Tex.
- Arneson, L. A., Zevenbergen, L. W., Lagasse, P. F., and Clopper, P. E. 2012. *Evaluating Scour at Bridges*, 5th ed. Publication No. FHWA-HIF-12-003. Hydraulic Engineering Circular No. 18. Federal Highway Administration, U.S. Department of Transportation, Washington, D.C.
- Arulanandan, K., and Perry, E. B. 1983. Erosion in Relation to Filter Design Criteria in Earth Dams. *Journal of the Geotechnical Engineering Division*, Vol. 109, No. 5, pp. 682–698.
- Arulanandan, K., Loganathan, P., and Krone, R. B. 1975. Pore and Eroding Fluid Influences on Surface Erosion of Soils. *Journal of the Geotechnical Engineering Division*, ASCE, Vol. 101, pp. 51–66.
- Arulanandan, K., Sargunam, A., Loganathan, P., and Krone, R. B. 1973. Application of Chemical and Electrical Parameters to Prediction of Erodibility. In *Special Report 135: Soil Erosion: Causes and Mechanisms; Prevention and Control*. HRB, National Research Council, Washington, D.C., pp. 42–51.
- ASTM D422-63. 2007. Standard Test Method for Particle-Size Analysis of Soils. ASTM International, West Conshohocken, Pa.
- ASTM D854-14. 2014. Standard Test Methods for Specific Gravity of Soil Solids by Water Pycnometer. ASTM International, West Conshohocken, Pa.
- ASTM D1587/D1587M-15. 2015. Standard Practice for Thin-Walled Tube Sampling of Fine-Grained Soils for Geotechnical Purposes. ASTM International, West Conshohocken, Pa.
- ASTM D2216-10. 2010. Standard Test Methods for Laboratory Determination of Water (Moisture) Content of Soil and Rock by Mass. ASTM International, West Conshohocken, Pa.
- ASTM D2487-17. 2017. Standard Practice for Classification of Soils for Engineering Purposes (Unified Soil Classification System). ASTM International, West Conshohocken, Pa.
- ASTM D4318-17e1. 2017. Standard Test Methods for Liquid Limit, Plastic Limit, and Plasticity Index of Soils. ASTM International, West Conshohocken, Pa.
- ASTM D4647/D4647M-13. 2013. Standard Test Methods for Identification and Classification of Dispersive Clay Soils by the Pinhole Test. ASTM International, West Conshohocken, Pa.
- ASTM D4648. 2016. Standard Test Methods for Laboratory Miniature Vane Shear Test for Saturated Fine-Grained Clayey Soil. ASTM International, West Conshohocken, Pa.
- ASTM D5852. 2007. Standard Test Method for Erodibility Determination of Soil in the Field or in the Laboratory by the Jet Index Method (withdrawn 2016). ASTM International, West Conshohocken, Pa.
- ASTM D7263-09. 2018. Standard Test Methods for Laboratory Determination of Density (Unit Weight) of Soil Specimens. ASTM International, West Conshohocken, Pa.
- ASTM D7928-17. 2017. Standard Test Method for Particle-Size Distribution (Gradation) of Fine-Grained Soils Using Sedimentation (Hydrometer) Analysis. ASTM International, West Conshohocken, Pa.
- Benahmed, N., and Bonelli, S. 2012. Internal Erosion of Cohesive Soils: Laboratory Parametric Study. 6th International Conference on Scour and Erosion, Aug 2012, Paris.
- Blaisdell, F.W., Clayton, L.A., and Hebaus, G. G. 1981. Ultimate Dimension of Local Scour. *Journal of Hydraulics Division*, Vol. 107, No. 3, pp. 327–337.

- Bloomquist, D., Sheppard, D. M., Schofield, S., and Crowley, R. W. 2012. The Rotating Erosion Testing Apparatus (RETA): A Laboratory Device for Measuring Erosion Rates Versus Shear Stresses of Rock and Cohesive Materials. *Geotechnical Testing Journal*, Vol. 35, No. 4. Paper ID GTJ104221.
- Bogdanov, V. I., and Smirnov, R. A. Vlaznost gruntov zony aeracii v usloviyah zastroyki. In *Problemy programirovaniya povysheniya urovny gruntovyh vod na zastroennyh territoriyah I borba s ih podtoplenniem*. Belgorod, 1972. (Богданов В.И., Смирнов Р.А. Влажность грунтов зоны аэрации в условиях застройки. В кн.: Проблемы прогнозирования повышения уровня грунтовых вод на застроенных территориях и борьба с их подтоплением (материалы совещания), Белгород, 1972).
- Bones, E. J. 2014. Predicting Critical Shear Stress and Soil Erodibility Classes Using Soil Properties. MS thesis. School of Civil and Environmental Engineering, Georgia Institute of Technology.
- Briaud, J. L. 2008. Case Histories in Soil and Rock Erosion: Woodrow Wilson Bridge, Brazos River Meander, Normandy Cliffs, and New Orleans Levees. 9th Ralph B. Peck Lecture. *Journal of Geotechnical and Geo-environmental Engineering*, Vol. 134, No. 10.
- Briaud, J. L. 2013. *Geotechnical Engineering: Unsaturated and Saturated Soils*. John Wiley and Sons, New York.
- Briaud, J. L., Bernhardt, M., and Leclair, M. 2012. The Pocket Erodometer Test: Development and Preliminary Results. *Geotechnical Testing Journal*, Vol. 35, No. 2, Paper ID GTJ102889.
- Briaud, J. L., Chedid, M., Chen, H. C., and Shidlovskaya, A. 2017a. Borehole Erosion Test. *Journal of Geotechnical and Geoenvironmental Engineering*, Vol. 143, No. 8. ASCE ISSN 1090-0241.
- Briaud, J. L., Chen, H. C., Kwak, K., Han, S., and Ting, F. 2001a. Multiflood and Multilayer Method for Scour Rate Prediction at Bridge Piers. *Journal of Geotechnical and Geoenvironmental Engineering*, Vol. 127, No. 2, pp. 114–125.
- Briaud, J. L., Govindasamy, A.V., and Shafii, I. 2017b. Erosion Charts for Selected Geomaterials. *Journal of Geotechnical and Geoenvironmental Engineering*, Vol. 143, No. 10, S. 04017072-1–04017072-13.
- Briaud, J. L., Ting, F., Chen, H. C., Cao, Y., Han, S.-W., and Kwak, K. 2001b. Erosion Function Apparatus for Scour Rate Predictions. *Journal of Geotechnical and Geoenvironmental Engineering*, Vol. 127, No. 2, pp. 105–113.
- Briaud, J. L., Ting, F. C. K., Chen, H. C., Gudavalli, R., Perugu, S., and Wei, G. 1999. SRICOS: Prediction of Scour Rate in Cohesive Soils at Bridge Piers. *Journal of Geotechnical and Geoenvironmental Engineering*, Vol. 125, No. 4, pp. 237–246.
- CD-adapco. 2016. STAR-CCM+ 11.0 User Guide. CD-adapco, Inc.
- Chang, D. S., and Zhang, L. M. 2011. A Stress-Controlled Erosion Apparatus for Studying Internal Erosion in Soils. *Geotechnical Testing Journal*, Vol. 34, No. 6. Paper ID GTJ103889.
- Chapuis, R. P., and Gatien, T. 1986. An Improved Rotating Cylinder Technique for Quantitative Measurements of the Scour Resistance of Clays. *Canadian Geotechnical Journal*, Vol. 23, No. 1, pp. 83–87.
- Chedid, M., Shafii, I., and Briaud, J. L. 2018. Erosion Tests on the Teton Dam Soils. Presented at 9th International Conference on Scour and Erosion, Taipei, Taiwan.
- Chen, C., Liu, W., Li, F., Lin, C.-H., Liu, J., Pei, J., and Chen, Q. 2013. A Hybrid Model for Investigating Transient Particle Transport in Enclosed Environments. *Building and Environment*, Vol. 62, pp. 45–54.
- Chen, H. C., Patel, V. C., and Ju, S. 1990. Solutions of Reynolds-Averaged Navier–Stokes Equations for Three-Dimensional Incompressible Flows. *Journal of Computational Physics*, Vol. 88, No. 2, pp. 305–336.
- Chen, Y.-H., and Anderson, B. A. 1987. Methodology for Estimating Embankment Damage Caused by Flood Overtopping. *Transportation Research Record: Journal of the Transportation Research Board*, No. 1151, pp. 1–15.
- Chow, V. T. 1959. *Open-Channel Hydraulics*. McGraw-Hill, New York.
- Clark, L. A., and Wynn, T. M. 2007. Methods for Determining Streambank Critical Shear Stress and Soil Erodibility: Implications for Erosion Rate Predictions. *Transactions of the ASABE*, Vol. 50, No. 1, pp. 95–106.
- Comité Français des Grande Barrages. 1997. Internal Erosion: Typology, Detection, Repair. Bulletin du Comité Français des Grande Barrages. FRCOLD NEWS. No. 6, Special Congress, Commission Internationale des Grands Barrages (CIGB) Florence.
- Cossette, D., Mazurek, K. A., and Rennie, C. D. 2012. Critical Shear Stress from Varied Methods of Analysis of a Submerged Circular Turbulent Impinging Jet Test for Determining Erosion Resistance of Cohesive Soils. In *Proceedings of the 6th International Conference on Scour and Erosion (ICSE6)*, 11–18. Société Hydrotechnique de France (SHF), Paris.
- Croad, R. N. 1981. *Physics of Erosion of Cohesive Soils*. PhD dissertation. Department of Civil Engineering, University of Auckland, New Zealand.
- Daly, E. R., Fox, G. A., and Al-Madhhachi, A. T. 2013. Application of Excess Shear Stress and Mechanistic Detachment Rate Models for the Erodibility of Cohesive Soils. Presented at the 2013 Annual Meeting of the American Society of Agricultural and Biological Engineers, St. Joseph, Mich., Paper No. 131596568.
- Daly, E. R., Fox, G. A., Al-Madhhachi, A. T., and Storm, D. E. 2015. Variability of Fluvial Erodibility Parameters for Streambanks on a Watershed Scale. *Geomorphology*, Vol. 231, pp. 281–291.
- Dunn, I. S. 1959. Tractive Resistance of Cohesive Channels. *Journal of Soil Mechanics and Foundations Division*, Vol. 85, No. 3, pp. 1–24.

## 322 Relationship Between Erodibility and Properties of Soils

- Fleshman, M. S., and Rice, J. D. 2013. Constant Gradient Piping Test Apparatus for Evaluation of Critical Hydraulic Conditions for the Initiation of Piping. *Geotechnical Testing Journal*, Vol. 36, No. 6. DOI 10.1520/GTJ20130066.
- Gabr, M., Caruso, C., Key, A., and Kayser, M. 2013. Assessment of In Situ Scour Profile in Sand Using a Jet Probe. *Geotechnical Testing Journal*, Vol. 36, No. 2, pp. 264–274.
- Ghebreiyessus, Y. T., Gantzer, C. J., Alberts, E. E., and Lentz, R. W. 1994. Soil Erosion by Concentrated Flow: Shear Stress and Bulk Density. *Transactions of the ASAE*. Vol. 37, No. 6, pp. 1791–1797.
- Gibbs, H. J. 1962. A Study of Erosion and Tractive Force Characteristics in Relation to Soil Mechanics Properties: Earth Research Program. Report No. EM-643. U.S. Department of the Interior, Bureau of Reclamation, Division of Engineering Laboratories, Denver, Colo.
- Hanson, G. J. 1990a. Surface Erodibility of Earthen Channels at High Stresses. Part I: Open Channel Testing. *Transactions of the ASAE*, Vol. 33, No. 1, pp. 127–131.
- Hanson, G. J. 1990b. Surface Erodibility of Earthen Channels at High Stresses. Part II: Developing an In Situ Testing Device. *Transactions of the ASAE*, Vol. 33, No. 1, pp. 132–137.
- Hanson, G. J. 1991. Development of a Jet Index to Characterize Erosion Resistance of Soils in Earthen Spillways. *Transactions of the ASAE*, Vol. 34, No. 5, pp. 2015–2020.
- Hanson, G. J. 1992. Erosion Resistance of Compacted Soils. *Transportation Research Record: Journal of the Transportation Research Board*, No. 1369, pp. 26–30.
- Hanson, G. J., and Cook, K. R. 2004. Apparatus, Test Procedures, and Analytical Methods to Measure Soil Erodibility In Situ. *Applied Engineering in Agriculture*, Vol. 20, No. 4, pp. 455–462.
- Hanson, G. J., and Cook, K. R. 1997. Development of Excess Shear Stress Parameters for Circular Jet Testing. Presented at 1997 ASAE Annual International Meeting, Minneapolis, Minn., Paper No. 972227.
- Hanson, G. J., and Hunt, S. L. 2007. Lessons Learned Using Laboratory JET Method to Measure Soil Erodibility of Compacted Soils. *Applied Engineering in Agriculture*, Vol. 23, No. 3, pp. 305–312.
- Hanson, G. J., and Robinson, K. M. 1993. The Influence of Soil Moisture and Compaction on Spillway Erosion. *Transactions of the ASAE*, Vol. 36, No. 5, pp. 1349–1352.
- Hanson, G. J., Robinson, K. M., and Cook, K. R. 2002. Scour Below an Overfall: Part II. Prediction. *Transactions of the ASAE*, Vol. 45, No. 4, pp. 957–964.
- Hanson, G. J., and Simon, A. 2001. Erodibility of Cohesive Streambeds in the Loess Area of the Midwestern USA. *Hydrological Processes*, Vol. 15, No. 1, pp. 23–38.
- Hastings, W. 1970. Monte Carlo Sampling Methods Using Markov Chains and Their Application. *Biometrika*, Vol. 57, pp. 97–109.
- Hobson, P. M. 2008. *Rheologic and Flume Erosion Characteristics of Georgia Sediments from Bridge Foundations*. Master's thesis. Georgia Institute of Technology, Atlanta.
- Hofland, B., Battjes, J. A., and Booij, R. 2005. Measurement of Fluctuating Pressures on Coarse Bed Material. *Journal of Hydraulic Engineering*, Vol. 131, No. 9, pp. 770–781.
- Julian, J. P., and Torres, R. 2006. Hydraulic Erosion of Cohesive Riverbanks. *Geomorphology*, Vol. 76, Nos. 1–2, pp. 193–206.
- Julien, P. Y. 1995. *Erosion and Sedimentation*. Cambridge University Press, Cambridge, United Kingdom.
- Justin, J. D. 1923. The Design of Earth Dams. *Trans. ASCE* 87, pp. 1–61.
- Kandiah, A., and Arulanandan, K. 1974. Hydraulic Erosion of Cohesive Soils. *Transportation Research Record: Journal of the Transportation Research Board*, No. 497, pp. 60–68.
- Karim, M. Z., and Tucker-Kulesza, S. E. 2018. Predicting Soil Erodibility Using Electrical Resistivity Tomography. *Journal of Geotechnical and Geoenvironmental Engineering*, Vol. 144, No. 4.
- Kerr, K. 2001. A Laboratory Apparatus and Methodology for Testing Water Erosion in Rock Materials. M.Eng. thesis. University of Florida, Gainesville.
- Khanal, A., Fox, G. A., and Al-Madhuchi, A. T. 2016. Variability of Erodibility Parameters from Laboratory Mini Jet Erosion Tests. *Journal of Hydrologic Engineering*, Vol. 21, No. 10.
- Lefebvre, G., Rohan, K., and Douville, S. 1985. Erosivity of Natural Intact Structured Clay: Evaluation. *Canadian Geotechnical Journal*, Vol. 22, pp. 508–517.
- Li, Y., Briaud J.-L., Chen H.-C., Nurtjahyo P., and Wang J., 2002. Shear Stress Approach to Pier Scour Predictions. In *Proceedings of the First International Conference on Scour of Foundations*, Texas A&M University, College Station, Tex., pp. 156–161.
- Lyle, W. M., and Smerdon, E. T. 1965. Relation of Compaction and Other Soil Properties to Erosion Resistance of Soils. *Transactions of the ASAE*, Vol. 8, No. 3, pp. 419–422, 284–298.
- Masch, F. D., Jr., Espey, W. H., Jr., and Moore, W. L. 1965. Measurements of the Shear Resistance of Cohesive Sediments. In *Proceedings of the Federal Inter-Agency Sedimentation Conference*, Agricultural Research Service, Publication No. 970, Washington, D.C., pp. 151–155.
- Maslov, N. N. 1968. *Osnovy mechaniki gruntov i inженерной геологии*. Vyshayay skola.

- McNeil, J., Taylor, C., and Lick, W. 1996. Measurements of Erosion of Undisturbed Bottom Sediments with Depth. *Journal of Hydraulic Engineering*, Vol. 122, No. 6, pp. 316–324.
- Medina-Cetina, Z. 2006. *Probabilistic Calibration of a Soil Model*. PhD dissertation. Johns Hopkins University, Baltimore, Md., <https://dspace.library.jhu.edu/handle/1774.2/3069>.
- Metropolis, N., Rosenbluth, A., Rosenbluth, M., Teller, A., and Teller, E. 1953. Equations of State Calculations by Fast Computing Machines. *Journal of Chemical Physics*, Vol. 21, No. 6, pp. 1087–1092.
- Mirzhulava, Z. E. 1967. *Razmyv rulsa I metodika ocenki ego ustoichivosti*. Kolos. Moskva.
- Mitchell, J. K. 1993. *Fundamentals of Soil Behavior*, 2nd ed. John Wiley and Sons Inc., Hoboken, N.J.
- Moody L. F. 1944. Friction Factors for Pipe Flow. *Transactions of the American Society of Civil Engineers*, Vol. 66.
- Moore, W. L., and Masch, F. D., Jr. 1962. Experiments on the Scour Resistance of Cohesive Sediments. *Journal of Geophysical Research*, Vol. 67, and No. 4, pp. 1437–1449.
- Mostafa, T. S., Imran, J., Chaudhry, M. H., and Kahn, I. B. 2008. Erosion Resistance of Cohesive Soils. *Journal of Hydraulic Research*, Vol. 46, No. 6, pp. 777–787.
- Navarro, H. R. 2004. Flume Measurements of Erosion Characteristics of Soils at Bridge Foundations in Georgia. Master's thesis. Georgia Institute of Technology, Atlanta.
- Neill, C. R. 1967. Mean-Velocity Criterion for Scour of Coarse Uniform Bed-Material. *International Association for Hydraulic Research*, Vol. 3, pp. 46–54.
- Osipov V. I., Sokolov V. N., and Rumyanzeva, E. M. 1989. *Microstructure of Clayey Soils* (in Russian). Nedra, Moscow.
- Partheniades, E. 1965. Erosion and Deposition of Cohesive Soils. *Journal of Hydraulic Engineering*, Vol. 91, pp. 105–139.
- Partheniades, E. 2009. *Cohesive Sediments in Open Channels: Properties, Transport and Applications*. Elsevier.
- Richards, K. S., and Reddy, K. R. 2010. True Triaxial Piping Test Apparatus for Evaluation of Piping Potential in Earth Structures. *Geotechnical Testing Journal*, Vol. 33, No. 1. Paper ID GTJ102246.
- Roberts, J. D., Jepsen, R. A., and James, S. C. 2003. Measurement of Sediment Erosion and Transport with the Adjustable Shear Stress Erosion and Transport Flume. *Journal of Hydraulic Engineering*, Vol. 129, No. 11, pp. 862–871.
- Robinson, K. M. 1990. Gully Erosion in Earth Spillways. *Applied Engineering in Agriculture*, Vol. 6, No. 3, pp. 279–284.
- Sargunan, A. 1977. Concept of Critical Shear Stress in Relation to Characterization of Dispersive Clays. In *Dispersive Clays, Related Piping, and Erosion in Geotechnical Projects* (J. L. Sherard and R. S. Decker, eds.), Proceedings of the 79th Annual Meeting of the American Society for Testing and Materials, ASTM Special Technical Publication 623, pp. 390–397.
- Schllichting, H., and Gersten, K. 2000. *Boundary-Layer Theory*. Springer, Berlin.
- Shafii, I., Briaud, J. L., Chen, H. C., and Shidlovskaya, A. 2016. Relationship Between Soil Erodibility and Engineering Properties. In *Scour and Erosion: Proceedings of the 8th International Conference on Scour and Erosion* (J. Harris, R. Whitehouse, and S. Moxon, eds.), CRC Press, London.
- Shafii, I., Zhang, Z., and Briaud, J. L., 2019. Measurement of Hydrodynamic Forces on Gravel Particles in the Erosion Function Apparatus. In *Scour and Erosion IX: Proceedings of the 9th International Conference on Scour and Erosion* (Y. Keh-Chia, ed.), Taylor and Francis Group, London, pp. 519–542.
- Shaikh, A., Ruff, J. F., and Abt, S. R. 1988a. Erosion Rate of Compacted NA-Montmorillonite Soils. *Journal of Geotechnical Engineering*, Vol. 114, No. 3, pp. 296–305.
- Shaikh, A., Ruff, J. F., Charlie, W. A. and Abt, S. R. 1988b. Erosion Rate of Dispersive and Nondispersible Clays. *Journal of Geotechnical Engineering*, Vol. 114, No. 5, pp. 589–600.
- Shan, H., Shen, J., Kilgore, R., and Kerenyi, K. 2015. *Scour in Cohesive Soils*. Publication No. FHWA-HRT-15-033. Federal Highway Administration, U.S. Department of Transportation, Washington, D.C.
- Sheppard, D. M. 2002. Effect of Suspended Fine Sediment on Local Scour. First International Conference on Scour of Foundations, Nov. 17–20, Texas A&M University, College Station, Tex.
- Sheppard, D. M., Bloomquist, D., and Slagle, P. M. 2006. *Rate of Erosion Properties of Rock and Clay*. BD-545, RPWO #3, UF Project 00030890 (4554013-12). Florida Department of Transportation, Tallahassee.
- Sherard, J. L., Dunnigan, L. P., and Decker, R. S. 1976. Identification and Nature of Dispersive Soils. *Journal of the Geotechnical Engineering Division*, Vol. 102, pp. 298–312.
- Simon, A., Curini, A., Darby, S. E., and Langendoen, E. J. 2000. Bank and Near-Bank Processes in an Incised Channel. *Geomorphology*, Vol. 35, pp. 183–217.
- Simon, A., R. E. Thomas, and L. Klimetz. 2010. Comparison and Experiences with Field Techniques to Measure Critical Shear Stress and Erodibility of Cohesive Deposits. In *Proceedings of the 2nd Joint Federal Interagency Conference*. ASCE, Reston, Va.
- Singh, H. V., and Thompson, A. M. 2015. Effect of Antecedent Soil Moisture Content on Soil Critical Shear Stress in Agricultural Watersheds. *Geoderma* Vol. 262, pp. 165–173.

## 324 Relationship Between Erodibility and Properties of Soils

- Smerdon, E. T., and Beasley, R. P. 1961. Critical Tractive Forces in Cohesive Soils. *Journal of Agricultural Engineering*, Vol. 42, No. 1, pp. 26–29.
- Straub, T. D., and Over, T. M. 2010. Pier and Contraction Scour Prediction in Cohesive Soils at Selected Bridges in Illinois. Research Report ICT-10-074. Illinois Center for Transportation, Urbana, Ill.
- Straub, T. D., Over, T. M., and Domanski, M. M. 2013. *Ultimate Pier and Contraction Scour Prediction in Cohesive Soils at Selected Bridges in Illinois*. Research Report No. FHWA-ICT-13-025. Illinois Center for Transportation, Urbana, Ill.
- Terzaghi, K., and Peck, R. B. 1948. *Soil Mechanics in Engineering Practice*. 1st ed. John Wiley and Sons, New York.
- Thoman, R. W., and Niegzoda, S. L. 2008. Determining Erodibility, Critical Shear Stress, and Allowable Discharge Estimates for Cohesive Channels: Case Study in the Powder River Basin of Wyoming. *Journal of Hydraulic Engineering*, Vol. 134, No. 12.
- Tovey, N. K. 1971. Stress Strain Behaviour of Soils. In *Proceedings of the Roscoe Memorial Symposium, Cambridge* (R. H. G. Parry, ed.), Foulis and Co. Ltd., Henley, Oxon, UK, pp. 116–120.
- Trammell, M. 2004. Laboratory Apparatus and Methodology for Determining Water Erosion Rates of Erodible Rock and Cohesive Sediments. MS thesis. University of Florida.
- Von Thun, L. 1996. Understanding Seepage and Piping Failures: The No. 1 Dam Safety Problem in the West. ASDSO Western Regional Conference. Lake Tahoe, Nevada.
- Wahl, T., Hanson, G., and Regazzoni, P. 2009a. Quantifying Erodibility of Embankment Materials for the Modeling of Dam Breach Processes. Presented at ASDSO Dam Safety 2009, Sept. 27–Oct. 1, Hollywood, Fla.
- Wahl, T. L., Regazzoni, P. L., and Erdogan, Z. 2009b. Practical Improvements for the Hole Erosion Test. Presented at 33rd IAHR Congress, August 9–14, Vancouver, British Columbia, Canada.
- Wan, C. F., and Fell, R. 2002. *Investigation of Internal Erosion and Piping of Soils in Embankment Dams by the Slot Erosion Test and the Hole Erosion Test*. UNICIV Report R-412. University of New South Wales, Sydney, Australia.
- Wang, Y. C. 2013. Effects of Physical Properties and Rheological Characteristics on Critical Shear Stress of Fine Sediments. Doctoral dissertation. Georgia Institute of Technology, Atlanta.
- Winterwerp, J. C., and van Kesteren, W. G. M. 2004. *Introduction to the Physics of Cohesive Sediment in the Marine Environment*. Development in Sedimentology, No. 56. Elsevier.
- Wynn, T. M., Mostaghimi, S., and Alphin, E. A. 2004. The Effects of Vegetation on Stream Bank Erosion. Presented at 2004 Meeting of the American Society of Agricultural and Biological Engineers.
- Zhordaniaya, T. G. 1957. Water Content as One of the Major Factors of Soil Erosion (in Russian). In *Proceedings of the Georgian Conference* (GruzNIIGandM), Vol. 1819, pp. 62–69.
- Zinner, M., Meyer, T., Shan, H., Shen, J., Bergendahl, B., and Kerényi, K. 2016. A Field Erodibility Testing Device for Scour Evaluation of Bridges. Proceedings of the 8th International Conference on Scour and Erosion, Sept. 12–15, Oxford, UK.



# Bibliography

- Benedict, S. T., Deshpande, N., Aziz, N. M., and Conrads, P. A. 2006. Trends of Abutment-Scour Prediction Equations Applied to 144 Field Sites in South Carolina. U.S. Geological Survey Open-File Report 2003-295. <https://pubs.er.usgs.gov/publication/ofr2003295>.
- Briaud, J. L. 2015. Scour Depth at Bridges: Method Including Soil Properties. I: Maximum Scour Depth Prediction. *Journal of Geotechnical and Geoenvironmental Engineering*, Vol. 141, No. 2.
- Briaud, J. L., Chen, H. C., Li, Y., Nurtjahyo, P., and Wang, J. 2005. SRCIOS-EFA Method for Contraction Scour in Fine-Grained Soils. *Journal of Geotechnical and Geoenvironmental Engineering*, Vol. 131, No. 10.
- Briaud, J. L., Gardoni, P., and Yao, C. 2014. Statistical, Risk, and Reliability Analyses of Bridge Scour. *Journal of Geotechnical and Geoenvironmental Engineering*, Vol. 140, No. 2.
- Chapuis, R. P. 1986. Quantitative Measurement of the Scour Resistance of Natural Solid Clays. *Canadian Geotechnical Journal*, Vol. 23, No. 2, pp. 132–141.
- Chapuis, R. P. 1986. Use of Rotational Erosion Device on Cohesive Soils. *Transportation Research Record: Journal of the Transportation Research Board*, No. 1089, pp. 23–28.
- Decker, R. S., and Dunnigan, L. P. 1977. Development and use of the Soil Conservation Service Dispersion Test. In *Dispersive Clays, Related Piping, and Erosion in Geotechnical Projects*, ASTM STP 623 (J. L. Sherard and R. S. Decker, eds.), American Society for Testing and Materials, West Conshohocken, Pa., pp. 94–109.
- Grishanin, K.V. 1969. *Dynamics of River Flows* (in Russian). Gidrometeoizdat, Leningrad.
- Hanson, G. J., Robinson, K. M., and Temple, D. M. 1990. *Hydraulic Engineering: In Proceedings of the 1990 National Conference*. American Society of Civil Engineers, New York, pp. 525–530.
- Hanson, G. J., Simon, A., and Cook, K. R. 2002. Non-Vertical Jet Testing of Cohesive Streambank Materials. Joint ASAE Annual International Meeting/CIGR XVth World Congress. Paper No. 022119.
- Lomtadze V. D. 1977. *Engineering Geology. Engineering Geodynamics* (in Russian). Nedra, Moscow.
- Reddi, L. N., Lee, I., and Bonala, M. V. S. 2000. Comparison of Internal and Surface Erosion Using Flow Pump Test on a Sand-Kaolinite Mixture. *Geotechnical Testing Journal*, Vol. 23, pp. 116–122.
- Sanchez, R. L., Strutynsky, A. I., and Silver, M. L. 1983. *Evaluation of the Erosion Potential of Embankment Core Materials Using the Laboratory Triaxial Erosion Test Procedure*. Technical Report GL-83-4. Geotechnical Laboratory, U.S. Army Engineer Waterways Experiment Station, Vicksburg, Miss.
- Sheppard, D. M., Odeh, M., and Glasser, T. 2004. Large Scale Clear-Water Local Pier Scour Experiments. *Journal of Hydraulic Engineering*, Vol. 130, No. 10.
- Sherard, J. L. 1984. Discussions and closure on “Erosion in Relation to Filter Design Criteria in Earth Dams” by K. Arulanandan and E. B. Perry. *Journal of the Geotechnical Engineering*, Vol. 110, No. 7, pp. 996–1005.
- Sherard, J. L. 1985. Hydraulic Fracturing in Embankment Dams. In *Seepage and Leakage from Dams and Impoundments: Proceedings of a Symposium* (R. L. Volpe and W. E. Kelly, eds.), ASCE, New York, pp. 115–141.
- Sherard, J. L., and Dunnigan, L. P. 1989. Critical Filters for Impervious Soils. *Journal of Geotechnical Engineering*, Vol. 115, No. 7, pp. 927–947.
- Sherard, J. L., Decker, R. S., and Ryker, N. L. 1972. Piping in Earth Dams of Dispersive Clay. In *Conference on Performance of Earth and Earth-Supported Structures*, ASCE, New York, Vol. 1, No. 1, pp. 589–626.
- Sherard, J. L., Dunnigan, L. P., Decker, R. S. and Steele, E. F. 1976. Pinhole Test for Identifying Dispersive Soils. *Journal of the Geotechnical Engineering Division*, Vol. 102, pp. 69–85.
- Sherard, J. L., Dunnigan, L. P., and Talbot, J. R. 1984. Filters for Silts and Clays. *Journal of the Geotechnical Engineering Division*, Vol. 110, No. 6, pp. 684–699.
- Sherard, J. L. 1973. Embankment Dam Cracking. In *Embankment Dam Engineering* (R. C. Hirschfeld and S. J. Poulos, eds.), John Wiley and Sons, New York.
- Shidlovskaya, A. V., Briaud, J.-L., Chedid, M., and Keshavarz M. 2016. Erodibility of Soil Above the Groundwater Level: Some Test Results. In *Proceedings of the 3rd European Conference on Unsaturated Soils*, Paris.

**326** Relationship Between Erodibility and Properties of Soils

- Skempton, A. W. 1953. The Colloidal "Activity" of Clays. In *Proceedings of the 3rd International Conference on Soil Mechanics and Foundation Engineering*. ICOSOMEF, Zurich, Switzerland, Vol. 1, pp. 57–61.
- SPSS Inc. 2014. IBM SPSS Statistics 23 Core System User's Guide. Chicago, Ill.
- Terzaghi, K., and Peck, R. B. 1967. *Soil Mechanics in Engineering Practice*. 2nd ed. John Wiley and Sons, New York.
- Trofimov, V. T. 2011. *Engineering Geology of Russia*, Vol. 2. (in Russian). KDU, Moscow.
- United States Society on Dams. 2011. *21st Century Dam Design—Advances and Adaptations*. 31st Annual USSD Conference, San Diego, Calif., pp. 1023–1032.
- Utley, B., and Wynn, T. 2008. Cohesive Soil Erosion: Theory and Practice. World Environmental and Water Resources Congress.
- Wahl, T. L. 2010. A Comparison of the Hole Erosion Test and Jet Erosion Test. Joint Federal Interagency Conference on Sedimentation and Hydrologic Modeling, Las Vegas, Nev.
- Wahl, T. L. 2014. *Measuring Erodibility of Gravelly Fine-Grained Soils*. Hydraulic Laboratory Report HL-2014-05. Bureau of Reclamation, U.S. Department of the Interior, Denver, Colo.
- Wahl, T. L., and Erdogan, Z. 2008. *Erosion Indices of Soils Used in ARS Piping Breach Tests*. Hydraulic Laboratory Report HL-2008-04. Bureau of Reclamation, U.S. Department of the Interior, Denver, Colo.
- Wan, C. F., and Fell, R. 2004a. Investigation of Rate of Erosion of Soils in Embankment Dams. *Journal of Geotechnical and Geoenvironmental Engineering*, Vol. 130, No. 4, pp. 373–380.
- Wan, C. F., and Fell, R. 2004b. Laboratory Tests on the Rate of Piping Erosion of Soils in Embankment Dams. *Geotechnical Testing Journal*, Vol. 27, No. 3, pp. 295–303.
- Zimon, A. D. 1976. *Adhesion of Dust and Powder*. Moscow.
- Zvonkov, V. V. 1962. *Water and Wind Erosion* (in Russian). Isd. Akad. Nauk SSSR, Moscow.



# Appendices

Five appendices to *NCHRP Research Report 915* are gathered in an Appendices Report that is available on the NCHRP Project 24-43 page on the TRB website ([trb.org](http://trb.org)):

- Appendix 1: Erosion Test Results Spreadsheets,
- Appendix 2: Geotechnical Properties Spreadsheets,
- Appendix 3: First and Second Order Statistical Analyses Results,
- Appendix 4: Deterministic Frequentist Regression Analysis, and
- Appendix 5: Probabilistic Calibration Results.



*Abbreviations and acronyms used without definitions in TRB publications:*

A4A	Airlines for America
AAAE	American Association of Airport Executives
AASHO	American Association of State Highway Officials
AASHTO	American Association of State Highway and Transportation Officials
ACI-NA	Airports Council International—North America
ACRP	Airport Cooperative Research Program
ADA	Americans with Disabilities Act
APTA	American Public Transportation Association
ASCE	American Society of Civil Engineers
ASME	American Society of Mechanical Engineers
ASTM	American Society for Testing and Materials
ATA	American Trucking Associations
CTAA	Community Transportation Association of America
CTBSSP	Commercial Truck and Bus Safety Synthesis Program
DHS	Department of Homeland Security
DOE	Department of Energy
EPA	Environmental Protection Agency
FAA	Federal Aviation Administration
FAST	Fixing America's Surface Transportation Act (2015)
FHWA	Federal Highway Administration
FMCSA	Federal Motor Carrier Safety Administration
FRA	Federal Railroad Administration
FTA	Federal Transit Administration
HMCRP	Hazardous Materials Cooperative Research Program
IEEE	Institute of Electrical and Electronics Engineers
ISTEA	Intermodal Surface Transportation Efficiency Act of 1991
ITE	Institute of Transportation Engineers
MAP-21	Moving Ahead for Progress in the 21st Century Act (2012)
NASA	National Aeronautics and Space Administration
NASAO	National Association of State Aviation Officials
NCFRP	National Cooperative Freight Research Program
NCHRP	National Cooperative Highway Research Program
NHTSA	National Highway Traffic Safety Administration
NTSB	National Transportation Safety Board
PHMSA	Pipeline and Hazardous Materials Safety Administration
RITA	Research and Innovative Technology Administration
SAE	Society of Automotive Engineers
SAFETEA-LU	Safe, Accountable, Flexible, Efficient Transportation Equity Act: A Legacy for Users (2005)
TCRP	Transit Cooperative Research Program
TDC	Transit Development Corporation
TEA-21	Transportation Equity Act for the 21st Century (1998)
TRB	Transportation Research Board
TSA	Transportation Security Administration
U.S. DOT	United States Department of Transportation

**TRANSPORTATION RESEARCH BOARD**

500 Fifth Street, NW  
Washington, DC 20001

---

**ADDRESS SERVICE REQUESTED**

---

*The National Academies of*

**SCIENCES • ENGINEERING • MEDICINE**

The nation turns to the National Academies of Sciences, Engineering, and Medicine for independent, objective advice on issues that affect people's lives worldwide.

[www.national-academies.org](http://www.national-academies.org)

ISBN 978-0-309-48075-8



9 780309 480758